Edited by
Jef Poortmans and Vladimir Arkhipov

Thin Film Solar Cells

Fabrication, Characterization and Applications

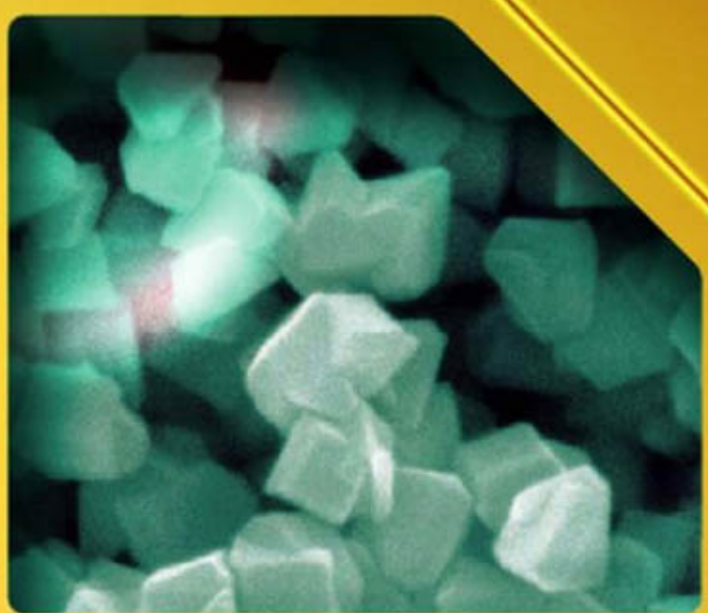

WILEY

Wiley Series in Materials for Electronic & Optoelectronic Applications

VISIT…

Thin Film Solar Cells Fabrication, Characterization and Applications

Edited by

Jef Poortmans

and

Vladimir Arkhipov

IMEC, Leuven, Belgium

John Wiley & Sons, Ltd

Thin Film Solar Cells
Fabrication, Characterization and Applications

Wiley Series in Materials for Electronic and Optoelectronic Applications

Series Editors

Dr Peter Capper, SELEX Sensors and Airborne Systems Infrared Ltd, Southampton, UK
Professor Safa Kasap, University of Saskatchewan, Canada
Professor Arthur Willoughby, University of Southampton, Southampton, UK

Published Titles

Bulk Crystal Growth of Electronic, Optical and Optoelectronic Materials, Edited by P. Capper
Properties of Group-IV, III–V and II–VI Semiconductors, S. Adachi
Optical Properties of Condensed Matter and Applications, Edited by J. Singh
Charge Transport in Disordered Solids with Applications in Electronics, Edited by S. Baranovski

Forthcoming Titles

Liquid Phase Epitaxy of Electronic, Optical and Optoelectronic Materials, Edited by P. Capper and M. Mauk
Dielectric Films for Advanced Microelectronics, Edited by K. Maex, M. R. Baklanov and M. Green

Thin Film Solar Cells Fabrication, Characterization and Applications

Edited by

Jef Poortmans

and

Vladimir Arkhipov

IMEC, Leuven, Belgium

John Wiley & Sons, Ltd

Copyright © 2006 John Wiley & Sons Ltd, The Atrium, Southern Gate, Chichester,
West Sussex PO19 8SQ, England

Telephone (+44) 1243 779777

Email (for orders and customer service enquiries): cs-books@wiley.co.uk
Visit our Home Page on www.wileyeurope.com or www.wiley.com

All Rights Reserved. No part of this publication may be reproduced, stored in a retrieval system or transmitted in any form or by any means, electronic, mechanical, photocopying, recording, scanning or otherwise, except under the terms of the Copyright, Designs and Patents Act 1988 or under the terms of a licence issued by the Copyright Licensing Agency Ltd, 90 Tottenham Court Road, London W1T 4LP, UK, without the permission in writing of the Publisher. Requests to the Publisher should be addressed to the Permissions Department, John Wiley & Sons Ltd, The Atrium, Southern Gate, Chichester, West Sussex PO19 8SQ, England, or emailed to permreq@wiley.co.uk, or faxed to (+44) 1243 770620.

Designations used by companies to distinguish their products are often claimed as trademarks. All brand names and product names used in this book are trade names, service marks, trademarks or registered trademarks of their respective owners. The Publisher is not associated with any product or vendor mentioned in this book.

This publication is designed to provide accurate and authoritative information in regard to the subject matter covered. It is sold on the understanding that the Publisher is not engaged in rendering professional services. If professional advice or other expert assistance is required, the services of a competent professional should be sought.

Other Wiley Editorial Offices

John Wiley & Sons Inc., 111 River Street, Hoboken, NJ 07030, USA

Jossey-Bass, 989 Market Street, San Francisco, CA 94103-1741, USA

Wiley-VCH Verlag GmbH, Boschstr. 12, D-69469 Weinheim, Germany

John Wiley & Sons Australia Ltd, 42 McDougall Street, Milton, Queensland 4064, Australia

John Wiley & Sons (Asia) Pte Ltd, 2 Clementi Loop #02-01, Jin Xing Distripark, Singapore 129809

John Wiley & Sons Canada Ltd, 6045 Freemont Blvd, Mississauga, Ontario, L5R 4J3

Wiley also publishes its books in a variety of electronic formats. Some content that appears in print may not be available in electronic books.

Library of Congress Cataloging-in-Publication Data

Thin film solar cells : fabrication, characterization, and applications /
edited by Jef Poortmans and Vladimir Arkhipov.
p. cm.
Includes bibliographical references and index.
ISBN-13: 978-0-470-09126-5 (cloth : alk. paper)
ISBN-10: 0-470-09126-6 (cloth : alk. paper)
1. Solar cells. 2. Thin film devices. I. Poortmans, Jef. II. Arkhipov, Vladimir.

TK2960.T445 2007
621.31′244—dc22 2006010650

British Library Cataloguing in Publication Data

A catalogue record for this book is available from the British Library

ISBN-10 0-470-09126-6 (HB)
ISBN-13 978-0-470-09126-5 (HB)

Typeset in 10/12pt Times by TechBooks, New Delhi, India.
Printed and bound in Great Britain by Antony Rowe, Chippenham, Wiltshire.
This book is printed on acid-free paper responsibly manufactured from sustainable forestry in which at least two trees are planted for each one used for paper production.

Disclaimer

The publisher and the author make no representations or warranties with respect to the accuracy or completeness of the contents of this work and specifically disclaim all warranties, including without limitation any implied warranties of fitness for a particular purpose. This work is sold with the understanding that the publisher is not engaged in rendering professional services. The advice and strategies contained herein may not be suitable for every situation. In view of ongoing research, equipment modifications, changes in governmental regulations, and the constant flow of information relating to the use of experimental reagents, equipment, and devices, the reader is urged to review and evaluate the information provided in the package insert or instructions for each chemical, piece of equipment, reagent, or device for, among other things, any changes in the instructions or indication of usage and for added warnings and precautions.

The fact that an organization or Website is referred to in this work as a citation and/or a potential source of further information does not mean that the author or the publisher endorses the information the organization or Website may provide or recommendations it may make. Further, readers should be aware that Internet Websites listed in this work may have changed or disappeared between when this work was written and when it is read. No warranty may be created or extended by any promotional statements for this work. Neither the publisher nor the author shall be liable for any damages arising herefrom.

Dedication

The unexpected death of Vladimir Arkhipov on December 10, 2005 was a sad loss for the scientific community and even more so for his young family. Shortly after returning from a conference in Boston, he went to Moscow to visit his mother and while in his hometown he suffered a heart attack. Strangely enough this happened when there was good reason to expect that he could finally settle down in Leuven. However, his destiny was to go back to his Russian roots. His family, friends and colleagues can only mourn the loss of a great personality and a great scientist.

Vladimir Arkhipov was born on January 18, 1952. He studied physics at the Moscow Institute of Physics and Engineering. For his PhD, completed in 1980, he joined the theoretical group of Professor Alexander Rudenko who stimulated his interest in the properties of semiconductors, in particular disordered inorganic materials. Their joint work on dispersive charge transport in amorphous semiconductors featuring an exponential distribution of trap states was well received in the literature. It attracted the interest of the international community and started the reputation of the young scientist. For a young, gifted scientist full of ideas, success is, indeed, an important stimulant for expanding his range of interest. Energetic as he was, he began exploring the fascinating world of charges diffusing, drifting, and recombining in the rough energy landscape of amorphous semiconductors, such as chalcogenides. However, by interacting with a group working on polymers he became aware that his theoretical methodologies could be applied to organic materials as well. A new door was opened to him.

In 1992, Vladimir Arkhipov, a professor at his home institution, received a scholarship from the German Humboldt foundation for a two years' visit to a research group in the Department of Physical Chemistry in Marburg, Germany. This started a very fruitful collaboration. Like chemical bonding, such an interaction does not simply involve addition of the expertise of two individuals but it creates a new state in which exchange interaction plays an important and stabilizing role. His input was his profound knowledge of the theory of hopping phenomena in amorphous solids. He did not only use it to solve problems in the course of our work on optoelectronic properties of organic solids but he set up a comprehensive conceptual framework for hopping transport in organic glasses and polymers featuring a Gaussian distribution of states. Highlights included experimental and theoretical investigations on injection of charge carriers from an electrode into the dielectric layer of a light emitting diode, the intrinsic and extrinsic optical generation of charge carriers in conjugated polymers, charge transport in neat and doped conjugated polymers, and thermally stimulated luminescence caused by the recombination of geminately bound electron hole pairs. One of the last topics he dealt with was photovoltaics. He introduced a new concept for explaining efficient charge carrier generation in organic solar cells.

Altogether Vladimir spent more than five years in Marburg, both the members of my group and I profited greatly from daily discussions. The cooperation continued when he moved to the Catholic University of Leuven and, after 2001, as a senior researcher to IMEC.

Over the years, Vladimir and I became personal friends. I liked his kind, gentle, warm-hearted personality, his keen intellect and his intuition. He was an exceptionally good and open-minded scientist with deep insight into the essence of a physical problem including experiments and, above all, he was able to listen. This is one reason why the research groups at IMEC, at the KU University of Leuven and in Marburg were so eager to interact with him, get his advice and sit together and solve problems. It is sad that he is no longer among us. We will miss him.

Heinz Bässler,
University of Marburg, Germany

Contents

Series Preface **xiii**

Preface **xv**

1 Epitaxial Thin Film Crystalline Silicon Solar Cells on Low Cost Silicon Carriers **1**
Jef Poortmans
1.1 Introduction 1
1.2 Deposition Technologies 4
1.2.1 Thermally Assisted Chemical Vapor Deposition 5
1.2.2 Liquid Phase Epitaxy – Electrodeposition 6
1.2.3 Close Space Vapor Transport Technique 8
1.2.4 Ion Assisted Deposition 9
1.2.5 Low Energy Plasma Enhanced Chemical Vapor Deposition/Electron Cyclotron Resonance Chemical Vapor Deposition 10
1.3 Silicon Based Epitaxial Layer Structures for Increased Absorbance 11
1.3.1 Epitaxial Growth on Textured Substrates 11
1.3.2 Silicon–Germanium Alloys 12
1.3.3 Germanium–Silicon Structures 15
1.3.4 Epitaxial Layers on a Buried Backside Reflector 17
1.4 Epitaxial Solar Cell Results and Analysis 21
1.4.1 Laboratory Type Epitaxial Solar Cells 21
1.4.2 Industrial Epitaxial Solar Cells 22
1.4.3 Special Epitaxial Solar Cell Structures 24
1.5 High Throughput Silicon Deposition 24
1.5.1 Chemical Vapor Deposition Reactor Upscaling 25
1.5.2 Liquid Phase Epitaxy Reactor Upscaling 29
1.6 Conclusions 32
References 32

2 Crystalline Silicon Thin Film Solar Cells on Foreign Substrates by High Temperature Deposition and Recrystallization **39**
Stefan Reber, Thomas Kieliba, Sandra Bau
2.1 Motivation and Introduction to Solar Cell Concept 39
2.2 Substrate and Intermediate Layer 42

Thin Film Solar Cells Edited by J. Poortmans and V. Arkhipov
© 2006 John Wiley & Sons, Ltd

2.2.1 Substrate 42
2.2.2 Intermediate Layer 44
2.3 Zone Melting Recrystallization 48
2.3.1 Introduction 48
2.3.2 Zone Melting Recrystallization Film Growth 51
2.3.3 Features of Silicon Layers Recrystallized by Zone Melting Recrystallization 53
2.3.4 Development of Lamp Heated Zone Melting Recrystallization Processors 59
2.3.5 Zone Melting Recrystallization on Ceramic Substrates 64
2.4 Silicon Deposition 66
2.4.1 Requirements of Silicon Deposition for Photovoltaics 67
2.4.2 Some Basics on Thermal Silicon Atmospheric Pressure Chemical Vapor Deposition from Chlorosilanes 68
2.4.3 R&D Trends in Silicon Atmospheric Pressure Chemical Vapor Deposition for Photovoltaics 71
2.4.4 Silicon Chemical Vapor Deposition on Ceramic Substrates 73
2.5 Solar Cells on Foreign Substrates 75
2.5.1 Options for Solar Cell Fabrication 76
2.5.2 Solar Cells on Model Substrates 78
2.5.3 Solar Cells on Low Cost Substrates 82
2.6 Summary and Outlook 85
Acknowledgments 87
References 87

3 Thin Film Polycrystalline Silicon Solar Cells 97
Guy Beaucarne, Abdellilah Slaoui
3.1 Introduction 97
3.1.1 Definition 97
3.1.2 Why Polycrystalline Thin Film Silicon Solar Cells? 98
3.2 Potential of Polysilicon Solar Cells 98
3.2.1 Light Confinement 98
3.2.2 Diffusion Length 99
3.2.3 Modeling 100
3.3 Substrates for Polysilicon Cells 101
3.4 Film Formation 103
3.4.1 Initial Step for Grain Size Enhancement 103
3.4.2 Techniques for Active Layer Formation 106
3.4.3 Defect Density and Activity 112
3.5 Solar Cell and Module Processing 115
3.5.1 Device Structure 115
3.5.2 Junction Formation 117
3.5.3 Defect Passivation 118
3.5.4 Isolation and Interconnection 118
3.6 Polysilicon Solar Cell Technologies 120
3.6.1 Solid Phase Crystallization Heterojunction with Intrinsic Thin Layer Solar Cells 120
3.6.2 Surface Texture and Enhanced Absorption with Back Reflector Solar Cells 121

3.6.3 Crystalline Silicon on Glass Technology 121
3.6.4 Other Research Efforts Around the World 122
3.7 Conclusion 123
References 123

4 Advances in Microcrystalline Silicon Solar Cell Technologies 133
Evelyne Vallat-Sauvain, Arvind Shah and Julien Bailat
4.1 Introduction 133
4.2 Microcrystalline Silicon: Material Fabrication and Characterization 134
4.2.1 Microcrystalline Silicon Deposition Techniques 134
4.2.2 Undoped Microcrystalline Layers 137
4.2.3 Doped Layers 147
4.3 Microcrystalline Silicon Solar Cells 148
4.3.1 Light Management Issues 149
4.3.2 Single Junction Microcrystalline Silicon Solar Cells 154
4.3.3 Tandem Amorphous/Microcrystalline Silicon Solar Cells: The Micromorph Concept 159
4.4 Conclusions 163
References 165

5 Advanced Amorphous Silicon Solar Cell Technologies 173
Miro Zeman
5.1 Introduction 173
5.2 Overview of Amorphous Silicon Solar Cell Technology Development and Current Issues 174
5.2.1 1970s 174
5.2.2 1980s 174
5.2.3 1990s 174
5.2.4 After 2000 175
5.2.5 Current Technology Issues 175
5.3 Hydrogenated Amorphous Silicon 177
5.3.1 Atomic Structure 177
5.3.2 Density of States 179
5.3.3 Models for the Density of States and Recombination–Generation Statistics 180
5.3.4 Optical Properties 181
5.3.5 Electrical Properties 183
5.3.6 Determination of Density of States 187
5.3.7 Metastability 190
5.3.8 Hydrogenated Amorphous Silicon from Hydrogen Diluted Silane 192
5.3.9 Doping of Hydrogenated Amorphous Silicon 194
5.3.10 Alloying of Hydrogenated Amorphous Silicon 196
5.4 Deposition of Hydrogenated Amorphous Silicon 197
5.4.1 Radio Frequency Plasma Enhanced Chemical Vapor Deposition 198
5.4.2 Direct Plasma Enhanced Chemical Vapor Deposition Techniques 200
5.4.3 Remote Plasma Enhanced Chemical Vapor Deposition Techniques 202
5.4.4 Hotwire Chemical Vapor Deposition 203

5.5 Amorphous Silicon Solar Cells 204
5.5.1 Hydrogenated Amorphous Silicon Solar Cell Structure 204
5.5.2 Hydrogenated Amorphous Silicon Solar Cell Configurations 207
5.5.3 Design Approaches for Highly Efficient Solar Cells 208
5.5.4 Light Trapping and Transparent Conductive Oxides 209
5.5.5 Degradation of Hydrogenated Amorphous Silicon Solar Cells 211
5.5.6 Multijunction Hydrogenated Amorphous Silicon Solar Cells 212
5.6 Performance and Fabrication of Hydrogenated Amorphous Silicon Based Modules 219
5.6.1 Energy Yield 221
5.6.2 Fabrication of Hydrogenated Amorphous Silicon Based Modules 223
5.6.3 Plasma enhanced Chemical Vapor Deposition Systems 223
5.7 Applications 227
5.8 Outlook 229
Acknowledgments 230
References 230

6 Chalcopyrite Based Solar Cells 237
Martha Ch. Lux-Steiner
6.1 Introduction 237
6.2 Potential of Chalcopyrite Photovoltaic Modules 237
6.3 Technology for the Preparation of Chalcopyrite Solar Cells and Modules 239
6.3.1 Absorber 240
6.3.2 Contacts 244
6.4 Characterization and Modeling 247
6.4.1 Cell Concept 248
6.4.2 Carrier Density and Transport 250
6.4.3 Loss Mechanisms 251
6.5 Scaling Up and Production 254
6.5.1 Cost Estimations 257
6.5.2 Module Performance 258
6.5.3 Sustainability 259
6.6 Developing Future Chalcopyrite Technology 260
6.6.1 Lightweight and Flexible Substrates 260
6.6.2 Cadmium Free Cells 261
6.6.3 Indium Free Absorbers 263
6.6.4 Novel Back Contacts 263
6.6.5 Bifacial Cells and Superstrate Cells 263
6.6.6 Nonvacuum Processing 264
6.6.7 Wide Gap and Tandem Cells 265
References 266

7 Cadmium Telluride Thin Film Solar Cells: Characterization, Fabrication and Modeling 277
Marc Burgelman
7.1 Introduction 277

7.2 Materials and Cell Concepts for Cadmium Telluride Based Solar Cells 278
7.2.1 Optical Properties of Cadmium Telluride 279
7.2.2 Electrical Properties of Cadmium Telluride 281
7.2.3 The Buffer Material: Cadmium Sulfide 283
7.2.4 Window Materials for Cadmium Telluride Based Solar Cells 285
7.3 Research Areas and Trends in Cadmium Telluride Solar Cells 286
7.3.1 The Activation Treatment of Cadmium Telluride 286
7.3.2 The Back Contact Structure 288
7.3.3 Environmental Issues 290
7.3.4 Other Research Areas and Trends 291
7.4 Fabrication of Cadmium Telluride Cells and Modules 294
7.4.1 Deposition Methods for Cadmium Telluride Based Solar Cells 294
7.4.2 Design of Series Integrated Cadmium Telluride Modules 296
7.4.3 Production of Cadmium Telluride Solar Modules 297
7.5 Advanced Characterization and Modeling of Cadmium Telluride Solar Cells 298
7.5.1 Characterization and Modeling: Introduction 298
7.5.2 Characterization Methods for Cadmium Telluride Materials and Cells 298
7.5.3 Modeling of Thin Film Cadmium Telluride Solar Cells 303
7.6 Conclusions 314
Acknowledgments 314
References 314

8 Charge Carrier Photogeneration in Doped and Blended Organic Semiconductors 325
Vladimir I. Arkhipov, Heinz Bässler
8.1 Introduction 325
8.2 Exciton Dissociation in Neat and Homogeneously Doped Random Organic Semiconductors 326
8.2.1 Intrinsic Photogeneration in Conjugated Polymers 326
8.2.2 Sensitized Photogeneration of Charge Carriers in Homogenously Doped Conjugated Polymers 328
8.2.3 Photogeneration of Charge Carriers at a Donor–Acceptor Interface 335
8.3 Models of Exciton Dissociation in Homogeneously Doped Conjugated Polymers and in Polymer Based Donor/Acceptor Blends 349
8.3.1 The Onsager–Braun Model 349
8.3.2 Exciton Dissociation in Conjugated Polymers Homogeneously Doped with Electron Scavengers 351
8.3.3 Exciton Dissociation at a Polymer Donor/Acceptor Interface 353
8.4 Conclusions 357
References 358

9 Nanocrystalline Injection Solar Cells 363
Michael Grätzel
9.1 Introduction 363
9.2 Band Diagram and Operational Principle of the Dye Sensitized Solar Cell 364

9.3 The Importance of the Nanostructure 365
9.3.1 Light Harvesting by a Sensitizer Monolayer Adsorbed on a Mesoscopic Semiconductor Film 366
9.3.2 Enhanced Red and Near Infrared Response by Light Containment 368
9.3.3 Light Induced Charge Separation and Conversion of Photons to Electric Current 369
9.3.4 Charge Carrier Collection 371
9.3.5 Quantum Dot Sensitizers 374
9.4 Photovoltaic Performance of the Dye Sensitized Solar Cell 375
9.4.1 Photocurrent Action Spectra 375
9.4.2 Overall Conversion Efficiency Under Global AM1.5 Standard Reporting Conditions 376
9.4.3 Increasing the Open Circuit Photovoltage 377
9.5 Development of New Sensitizers and Redox Systems 378
9.6 Solid State Dye Sensitized Solar Cells 379
9.7 Dye Sensitized Solar Cell Stability 379
9.7.1 Criteria for Long Term Stability of the Dye 379
9.7.2 Kinetic Measurements 380
9.7.3 Recent Experimental Results on Dye Sensitized Solar Cell Stability 381
9.7.4 First Large Scale Field Tests and Commercial Developments 382
9.8 Future Prospects 384
Acknowledgments 384
References 384

10 Charge Transport and Recombination in Donor–Acceptor Bulk Heterojunction Solar Cells 387
A. J. Mozer, N. S. Sariciftci
10.1 Introduction 387
10.2 Development of Bulk Heterojunction Solar Cells 388
10.3 Bulk Heterojunction Solar Cells 391
10.3.1 Operational Principles 391
10.3.2 Nanomorphology–Property Relations 394
10.3.3 Improving the Photon Harvesting 397
10.4 Charge Carrier Mobility and Recombination 399
10.4.1 Measurement Techniques 399
10.4.2 Charge Transport in Conjugated Polymers 401
10.4.3 Charge Transport and Recombination in Bulk Heterojunction Solar Cells 412
10.5 Summary 421
Acknowledgments 421
References 422

11 The Terawatt Challenge for Thin Film Photovoltaics 427
Ken Zweibel
11.1 Prologue 427
11.2 'The Only Big Number Out There – 125 000 TW' (Quote, Nate Lewis, 2004) 428

11.3 Low Cost and the Idea of Thin Films 431
11.4 A Bottom Up Analysis of Thin Film Module Costs 431
11.4.1 Approach 432
11.4.2 Results 435
11.5 Other Aspects of the 'Terawatt Challenge' 455
11.6 Risks and Perspective 458
Acknowledgments 459
Appendix 11.1 459
Appendix 11.2 460
References 460

Index **463**

Series Preface

WILEY SERIES IN MATERIALS FOR ELECTRONIC AND OPTOELECTRONIC APPLICATIONS

This book series is devoted to the rapidly developing class of materials used for electronic and optoelectronic applications. It is designed to provide much needed information on the fundamental scientific principles of these materials, together with how these are employed in technological applications. The books are aimed at postgraduate students, researchers and technologists, engaged in research, development and the study of materials in electronics and photonics, and industrial scientists developing new materials, devices and circuits for the electronic, optoelectronic and communications industries.

The development of new electronic and optoelectronic materials depends not only on materials engineering at a practical level, but also on a clear understanding of the properties of materials, and the fundamental science behind these properties. It is the properties of a material that eventually determine its usefulness in an application. The series therefore also includes such topics as electrical conduction in solids, optical properties, thermal properties, etc., all with applications and examples of materials in electronics and optoelectronics. The characterization of materials is also covered within the series in as much as it is impossible to develop new materials without the proper characterization of their structure and properties. Structure–property relationships have always been fundamentally and intrinsically important to materials science and engineering.

Materials science is well known for being one of the most interdisciplinary sciences. It is the interdisciplinary aspect of materials science that has led to many exciting discoveries, new materials and new applications. It is not unusual to find scientists with chemical engineering backgrounds working on materials projects with applications in electronics. In selecting titles for the series, we have tried to maintain the interdisciplinary aspect of the field, and hence its excitement to researchers in this field.

Peter Capper
Safa Kasap
Arthur Willoughby

Thin Film Solar Cells Edited by J. Poortmans and V. Arkhipov
© 2006 John Wiley & Sons, Ltd

Preface

P.1 STATUS OF PHOTOVOLTAICS AND THE ROLE OF THIN FILM SOLAR CELLS

The large scale production of solar cells during the year 2004 surpassed the symbolic threshold of 1 GW_p [1] and the total cumulative worldwide PV capacity installed is above 3 GW. Photovoltaic applications range from large scale stand alone/grid connected power stations to low power electronics.

The photovoltaic (PV) sector has been growing with a compounded annual growth rate of nearly 30 % over the last five years and in 2004 the growth rate even amounted to a breath-taking 60 % as can be seen in Figure P.1.

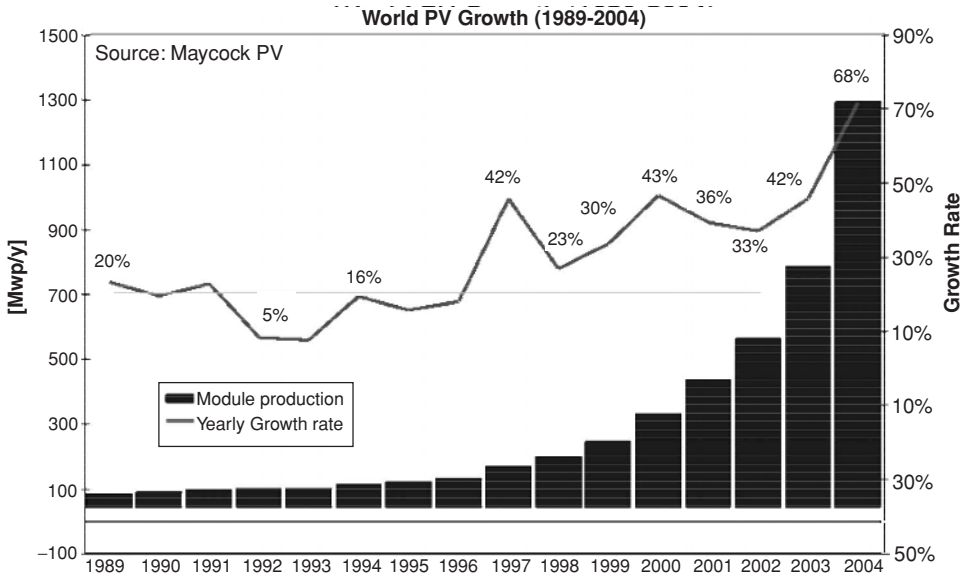

Figure P.1 Evolution of the yearly produced PV modules in terms of MW_p.

The production of solar cells was and is still based mainly on crystalline silicon (Si). More specifically 36 % of the 2004 production is based on single crystal Si but the main part is based on multicrystalline Si cells – substrates and ribbons (58 %). The remainder is based on thin

Thin Film Solar Cells Edited by J. Poortmans and V. Arkhipov
© 2006 John Wiley & Sons, Ltd

film solar cell technologies and consists of 4 % based on thin film amorphous Si solar cells and 2 % on polycrystalline compound solar cells based on CdTe and $CuInSe_2$ (Figure P. 2).

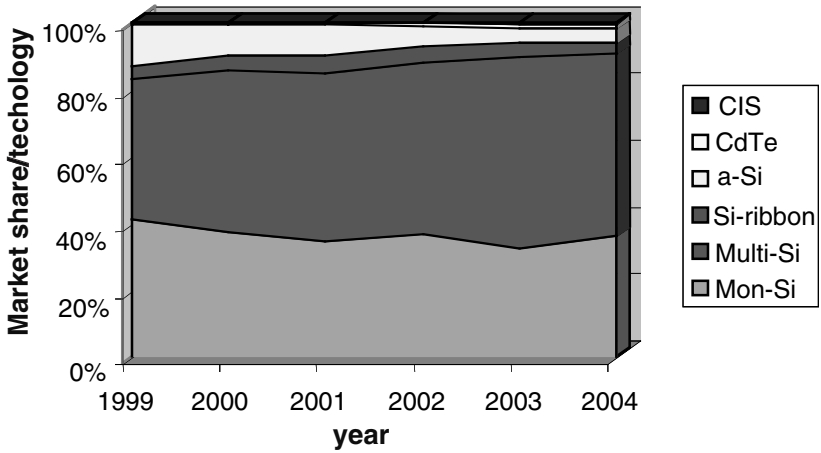

Figure P.2 Market share evolution taken by the different solar cell technologies over the last five years.

Despite tremendous progress in all aspects of production of Si based solar cells and the rapid decrease of production cost for PV modules [2] from 5 $\$/W_p$ at the beginning of the nineties to 2.5$\$/W_p$ in 2004, the cost/kWh is still too high to compete with other sources of electricity generation. In the Northwestern European climate and taking into account the system costs, one arrives at a cost of 0.7$/kWh, which is definitely still too high.

The single most important factor in determining the cost of production is the cost of the 250–300 μm thick Si wafer used for the fabrication of solar cells. It accounts for more than 50 % of the costs at the module level. The problem of the high cost of electronic grade Si was recognized right from the beginning and a lot of effort is being put into developing a source of polysilicon feedstock, which is suited for Si substrate production for solar cells. This solar grade Si will have relaxed specifications in terms of impurities as compared with electronic grade Si. Additionally, thinner wafers, a more efficient usage of Si and an increase of the module efficiency from 13–15 % to 18–20 % will have to contribute to a further reduction by a factor of two to three before 2020 [3]. At the time of publication of this book, there is a tendency for the crystalline Si substrate costs to increase their contribution as there is a situation of scarcity for the polysilicon feedstock material. This situation of scarcity is probably temporary according to the editors' opinion, but it is clear that, presently, there is a real window of opportunity to introduce thin film solar cells on a larger scale onto the market and to set in motion the necessary evolution towards module costs below $1\$/W_p$. This cost reduction will have to be brought about by a combination of upscaling – that is why it is important for thin film solar cells to increase their market share and to use the present opportunity – and intense R&D to tackle the remaining weaknesses of the different thin film solar cell technologies.

Another major consideration when comparing different PV technologies is the energy pay-back period, which refers to the number of years in which the electrical energy generated by the devices will be equal to the energy required for production of these devices. On the module level the thin film technologies perform better by at least a factor of two – less than one year - than multicrystalline Si modules (2–3 years) in southern regions. The comparison of the payback

time can be done at the level of the PV module should also include the other components [4] to find which application field is most suited for the different technologies. In reference [4] it was noted that for grid connected rooftop and array fields, thin film solar cell technology is the better choice. On the other hand, the multicrystalline Si estimates point to its use in free standing applications because of the higher balance of system (BOS) cost associated with these applications. The higher efficiency of multicrystalline Si modules reduces the impact of the higher BOS costs.

P.2 THIN FILM MATERIALS FOR SOLAR CELLS

P.2.1 Thin film: definition

The reader might remark at this point that the term 'thin film solar cell technology' has not yet been defined in the context of this book. The definition given by Chopra *et al.* [5] provides a good starting point and also yields a criterion to discriminate the term 'thin film' from 'thick film'. They define a thin film as a material 'created *ab initio* by the random nucleation and growth processes of individually condensing/reacting atomic/ionic/molecular species on a substrate. The structural, chemical, metallurgical and physical properties of such a material are strongly dependent on a large number of deposition parameters and may also be thickness dependent. Thin films may encompass a considerable thickness range, varying from a few nanometers to tens of micrometers and thus are best defined in terms of the production processes rather than by thickness. One may obtain a thin material (not a thin film) by a number of other methods (normally called thick-film techniques) such as by thinning bulk material, or by depositing clusters of microscopic species in such processes as screen-printing, electrophoresis, slurry spray, plasma gun, ablation, etc.' The given definition still leaves room for a broad field of technologies to deposit the thin film (plasma, sputtering, evaporation, deposition from the liquid phase, etc.) and to tailor its electrical and morphological properties (crystalline, amorphous and intermediary forms). These techniques and their relation with the final morphology and the photovoltaic performance will be discussed in the separate chapters dealing with the different thin film solar cell technologies. For the inorganic non-crystalline Si materials and technologies we will follow the approach of ref. 5.

P.2.2 Thin film absorber materials

Conventionally, photovoltaic materials use inorganic semiconductors. The semiconductors of interest allow the formation of charge-carrier separating junctions. The junction can be either a homojunction (like in Si) or a heterojunction with other materials to collect the excess carriers when exposed to light. In principle, a large number of semiconductor materials are eligible, but only a few of them are of sufficient interest. Ideally, the absorber material of an efficient terrestrial solar cell should be a semiconductor with a bandgap of 1–1.5 eV with a high solar optical absorption ($10^4 - 10^5\,\mathrm{cm}^{-1}$) in the wavelength region of 350–1000 nm, a high quantum yield for the excited carriers, a long diffusion length low recombination velocity. If all these constraints are satisfied and the basic material is widely available, the material allows in principle the manufacturing of a thin-film solar cell device.

From the point of view of processing, manufacturing and reproducibility, *elemental* semiconductors provide a simple and straightforward approach to manufacture thin-film solar cells.

The first material at hand is the material which dominates the PV market nowadays: silicon. Crystalline silicon is a semiconductor material with a bandgap of 1.1 eV. Because of the indirect bandgap character of silicon for photons with energy lower than 3.4 eV, it is clearly not an ideal material for thin-film solar cells. Nevertheless, there is a substantial R&D effort being put into developing thin-film solar cells based on crystalline Si. The thin film of crystalline Si can be grown either by low-temperature deposition techniques which yield microcrystalline Si or by high-temperature techniques. In the latter case the material properties of the grown crystalline Si film are similar to the properties of bulk crystalline Si solar material. Because of its relatively low absorption coefficient, crystalline Si layers have to be at least 30 μm thick to absorb sufficient light unless optical enhancement techniques are used to improve the effective absorption. As a result of its high refractive index (4) crystalline Si allows efficient optical confinement with optical pathlength enhancements up to a factor 50. It will come as no surprise to the reader that optical enhancement is therefore a substantial part of the research in the field of thin-film crystalline Si.

Si can also be deposited in its amorphous form. Amorphous Si as such is a material of little use for photovoltaics because of the extremely high dangling bond density and intragap state density in the material ($>10^{19}\,\mathrm{cm}^{-3}$), resulting in immediate recombination of photo-excited excess carriers and pins the Fermi level, excluding controllable doing. The properties of amorphous Si are drastically improved by alloying it with H, which passivates most of the dangling bonds and reduces the intrap state density to $10^{16}\,\mathrm{cm}^{-3}$ or less. The alloying with H takes place in a natural way during the deposition of the film which is deposited by cracking a Si precursor (most often SiH_4) by means of a plasma and the material formed is denoted as a-Si:H. In comparison with crystalline Si, a-Si:H has a number of properties which make it attractive as an absorber layer for thin-film solar cells. The bandgap of a-Si:H, is to some extent tailorable by the method and conditions of deposition. In addition, the material is relatively easy to dope, which allows the manufacturing of homojunction devices and, last but not least, it has a high optical absorption coefficient over the wavelength range of interest. Under suitable deposition conditions and strong hydrogen dilution, nanocrystalline and microcrystalline materials are obtained. While the crystallite size and volume fraction are very small, these crystallites catalyze the crystallization of the remainder of the amorphous matrix upon annealing. Microcrystalline materials deposited by this method are found to have less defect density and are more stable against light degradation compared with a-Si. Recently developed improved efficiency materials consist of this heterogeneous mixture of the amorphous and an intermediate range order microcrystalline material.

a-Si:H has emerged as an attractive material which, for some time, was challenging the supremacy of crystalline Si cells in the Eighties. Because of stability problems and the lower efficiencies as compared with crystalline Si, the market share of a-Si:H based thin- film solar cells remained limited. Nevertheless, the present shortage of crystalline Si and the developments around multijunction structures and micro/nanocrystalline Si extensions provide a new opportunity for this technology to make it to the marketplace. Recently also carbon came into the picture as a candidate material for thin-film solar cells, with first results being reported for boron-doped diamond-like carbon [6] and fullerene films [7]. These approaches are not very well developed and therefore do not appear within this book.

III–V compound materials like GaAs, InP and their derived alloys and compounds, which most often have a direct bandgap character, are ideal for photovoltaic applications, but are far too expensive for large-scale commercial applications, because of the high cost of the necessary

precursors for the deposition and the deposition systems itself. The deposition systems for these materials are either based on molecular beam epitaxy or metalorganic chemical vapour deposition.

More appealing from the point of view of ease of processability and cost of material and deposition are the "II–VI compound materials" like CdTe or variations on this like $CuInSe_2$. The interest in these materials for thin-film solar cell manufacturing is essentially based on two elements. Because of the chemical structure of these materials the internal (grain boundaries, interfaces) and external surfaces are intrinsically well passivated and characterized by a low recombination velocity for excess carriers. The low recombination activity at the grain boundaries allows high solar cell efficiencies even when the material is polycrystalline with grain sizes in the order of only a few μm. This is to be contrasted with crystalline Si where grain boundaries are normally characterized by a high recombination velocity. Moreover, the polycrystallinity allows a large number of substrates (glass, steel foil, ...) and is compatible with low-cost temperature deposition techniques, as there is no need for epitaxial growth or high temperatures to obtain large grain sizes. A second important property is the possibility to tailor the bandgap e.g. replacing Se by S in $CuInSe_2$ results in a material with a higher bandgap. This property allows one to build in bandgap gradients aiding the collection of excess carriers and, ultimately, could even be used to develop multijunction solar cells. With the increasing number of components in ternaries and even quaternaries, the number of possible material combinations increases.

An interesting alternative to inorganic semiconductor absorbers are organic semiconductors, which combine interesting optoelectronic properties with the excellent mechanical and processing properties of polymeric/plastic materials. In organic semiconductors, absorption of photons leads to the creation of bound electron–hole pairs (excitons) with a binding energy of 0.5 eV rather than free charges. The excitons carry energy, but no net charge, and have to diffuse to dissociation sites where their charges can be separated and transported to the contacts. In most organic semiconductors, only a small portion (30 %) of the incident light is absorbed because the majority of semiconducting polymers have bandgaps higher than 2.0 eV. The typically low charge-carrier and exciton mobility require the active absorber layer thickness to be less than 100 nm. This thickness is sufficient to absorb most of the incident solar photons if light trapping is used, although the low refractive index calls for adapted approaches. More importantly, organic semiconductors can be processed from solutions at or near room temperature on flexible substrates using simple, cheap and low-energy deposition methods such as spinning or printing thereby yielding cheaper devices. Even though the efficiency of these devices is poor at present, they may find immediate applications for disposable solar cell based small power applications. Among the major issues to be addressed before reasonable market penetration of the organic devices takes place are the improvement of the stability of conjugate polymers, and the matching of the bandgap of the organic materials with the solar spectrum for higher conversion efficiency by using blended/composite polymers and suitable dyes.

P.3 DIFFERENT THIN FILM SOLAR CELL TECHNOLOGIES

Based on the available semiconductor absorber materials discussed above one can go systematically over the different related thin film solar cell technologies.

P.3.1 Crystalline silicon thin film solar cells

There are a large variety of crystalline Si thin film approaches. The one that is closest to the classical crystalline Si solar cell structure is the 'epitaxial solar cell approach'. The basic idea behind this thin film approach, is the realization of a thin crystalline Si film of high electronic quality on a low cost Si carrier substrate by means of epitaxial growth as shown in Figure P.3a. The depicted structure strongly resembles the structure of a classical, self supporting bulk crystalline Si solar cell and, as a result, the basic solar cell process to produce the solar cell is very similar to the practices used within the photovoltaics (PV) industry nowadays. Its structural similarity would result in a low acceptance threshold in the solar cell industry, which is presently still dominated by crystalline Si. A special case is the 'lift-off approach' where, by means of a crystalline Si template based on porous Si, a thin cell is realized which is lifted off before or after the cell process.

The epitaxial cell approach relies on the use of a Si substrate. There are also attempts to develop thin film crystalline Si solar cell structures on non-Si substrates. Because of the high temperatures ($>600\,^{\circ}$C) used for the film deposition, glass is not suitable as a substrate. Rather, low cost ceramic substrates and graphite are the substrates of choice. In case the substrate is nonconductive, novel solar cell structures are needed to contact the solar cell as shown in Figure P.3b. The Si layer, deposited on top of these substrates, will be micro or polycrystalline with a grain size determined by the growth temperature and supersaturation conditions during the silicon layer deposition. It turns out to be difficult to realize solar cells with proper energy conversion efficiencies in material with a grain size of 1–10 μm, although substantial progress has been made recently in this field. On ceramic substrates which withstand high temperatures, liquid phase recrystallization is often applied to increase the final grain size, whereas laser recrystallization and rapid thermal annealing is being developed for substrates which can only withstand process temperatures $>650\,^{\circ}$C for a limited time.

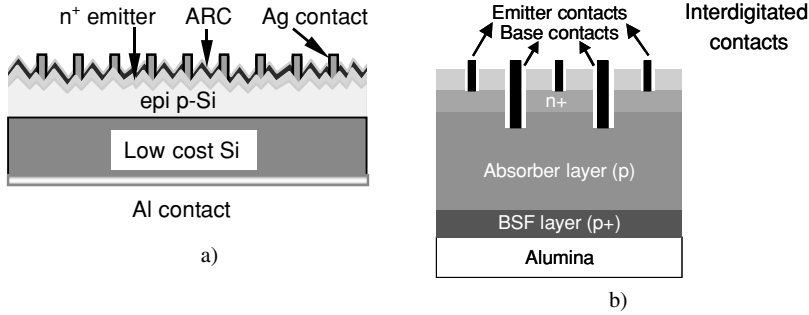

Figure P.3 a) Schematic of a epitaxial cell on a highly doped low cost Si substrate (ARC stands for anti-reflective coating; b) Novel solar cells with a noncoductive substrate.

P.3.2 Amorphous and microcrystalline silicon thin film solar cells

Because a-Si:H can be doped efficiently p- and n-type, the cell structure is based on a homojunction. As a result of the short carrier lifetime and the low carrier mobility collection by pure diffusion of excess carriers is not very effective. Therefore a-Si:H solar cells also

include a drift zone to improve the carrier collection. As a result the structure of the solar cell device is a p-i-n-structure where an intrinsic a-Si:H layer is sandwiched between a thin n^+ and p^+-type layer. Because of the low doping in the intrinsic part, the electrical field will extend all over the intrinsic layer. As mentioned before, the properties of the material and the junction device are severely affected by the light induced creation of metastable defects, known as the Staebler–Wronski effect. Light induced degradation of a-Si:H devices and, as a consequence, a reduction of the electrical field in the intrinsic part of the cell is tackled by reducing the a-Si:H layer thickness so that the photogenerated carriers need to move only a short distance before they reach the electrode. However, thinning down also results in lower light absorption and thus optical confinement techniques employing diffusely reflecting front and back contacts are required to increase the effective layer thickness in order to absorb the photons. Over a period of time, extensive research and development work on deposition techniques and device structure have resulted in development of single junction and multijunction devices with high efficiency and moderately good stability. A typical a-Si:H based multijunction solar cell structure is shown in Figure P.4a.

As the cost of the Ge precursors is high and the electronic quality of the a-SiGe:H layers is lower than for a-Si:H layers, a lot of effort is being done in replacing the a-SiGe:H part of the cell by other solutions like microcrystalline Si. This leads to the 'micromorph' cell concept combining an a-Si:H topcell with a microcrystalline Si bottomcell as shown in Figure P.4b.

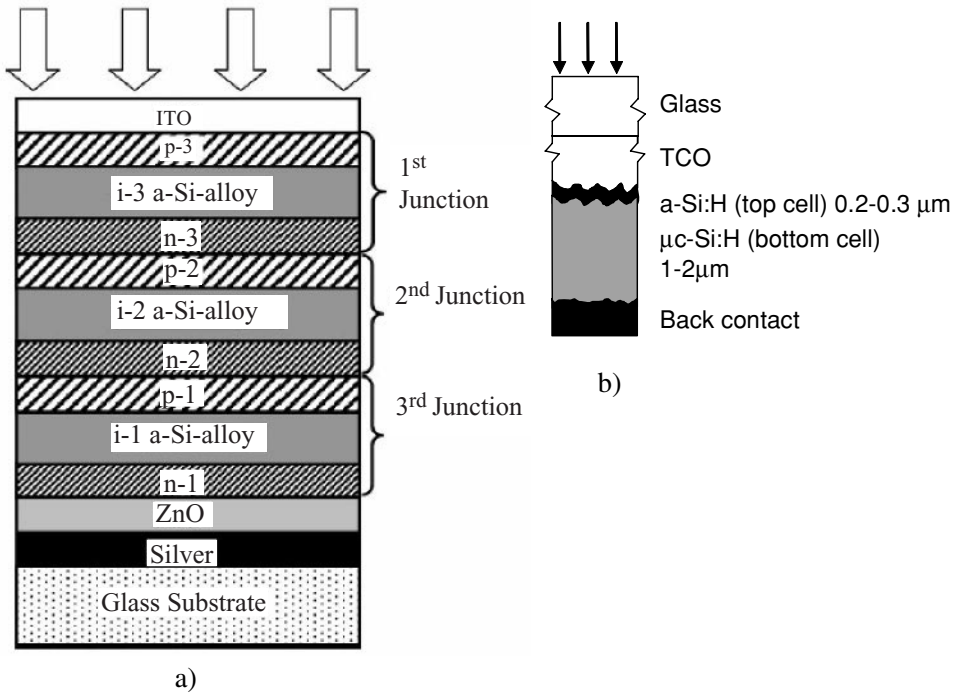

Figure P.4 a) Cross section of typical multijunction solar cell based on a-Si:H. In order to improve the performance the lower a-Si:H subcells are sometimes replaced by a-SiGe:H alloys; b) In the second approach (the micromorph concept) improved stability is obtained by replacing the a-Si:H bottom cell by a microcrystalline Si solar cell (taken from ref. 5).

P.3.3 Copper indium gallium selenide and cadmium telluride solar cell structures

Both superstrate and substrate device structures are currently being pursued for copper indium gallium selenide ($CuIn(Ga)Se_2$, CIGS) device fabrication. The film growth and interdiffusion and hence the device properties are dependent on the device structure. These CIGS solar cells, based on the superstrate structure, are inferior to the substrate structure, because of the interdiffusion of CdS during high temperature CIGS film growth. A best device efficiency of 10.2 % was reported for the superstrate structure. On the other hand, a substrate configuration like the one shown in Figure P.5a with CdS buffer layer resulted in a 19.2 % efficiency device.

Cadmium telluride devices are fabricated preferably in the superstrate configuration because the CdTe surface is exposed for contacting. In addition, the benign feature of CdS diffusion during the processing reduces the lattice mismatch between CdTe and CdS. Cadmium telluride solar cells use borosilicate glass for high temperature deposition (600 °C) and soda lime glass for low temperature deposition (60–500 °C). Cadmium telluride has also been deposited on thin metallic foils such as stainless steel, Mo, Ni and Cu. Molybdenum is best suited for CdTe deposition, owing to better thermal matching.

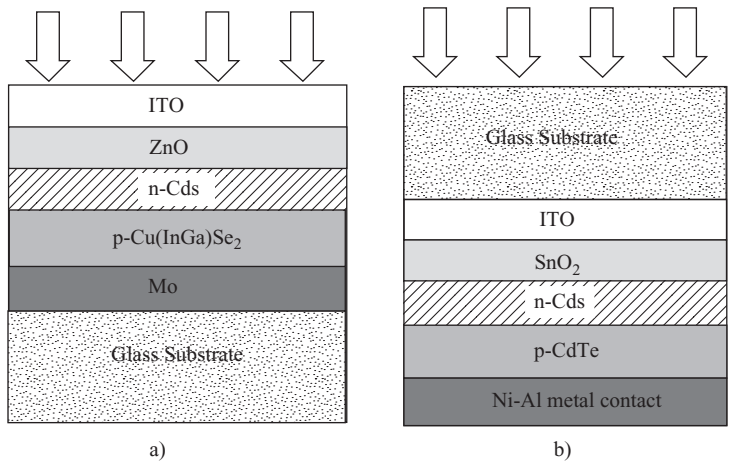

Figure P.5 a) Schematic view of the typical substrate structure of CIGS solar cells; b) Schematic view of the typical superstrate structure of CdTe solar cells (taken from ref. 5).

P.3.4 Basic structure of thin film organic solar cells

The term ‘organic solar cell’ has to be correctly defined. The term covers those photovoltaic devices where the organic layer is an essential part of the photovoltaic process. The basic steps in photovoltaic conversion are light absorbance, charge carrier generation, charge carrier transport and extraction/injection of charge carriers through externally accessible contacts. More specifically, the term ‘organic solar cell’ is applicable whenever at least the two first steps are being realized by means of an organic layer. By this definition, full organic devices as well as hybrid devices are being covered.

Organic solar cells have already been the subject of R&D efforts for a long time because of the potentially very low cost of the active layer material. Originally, most of the attempts to realize organic solar cell devices were based on essentially the same concepts as thin film p-n or p-i-n devices. This resulted in energy conversion efficiencies of about 1 % with the main limitation being the short exciton diffusion length and insufficient exciton dissociation. The breakthrough for solar cells incorporating an organic part came with the advent of concepts that radically deviated from the planar hetero- or homojunction solar cells. The generic idea behind these concepts is the existence of a bulk distributed interface to capture the excited carrier and to increase the exciton dissociation rate. The 'Graetzel cell' is a prominent example of this generic idea belonging to the class of hybrid cells. Within the pores of a porous TiO_2 layer a monolayer of an organic sensitizer is adsorbed on the pore walls as shown in Figure P.6a. After absorption of a photon, the excited electron within the sensitizer molecule is immediately transferred to the conduction band of TiO_2, after which the electron diffuses through the porous network to the contact. The oxidized sensitizer molecule is reduced to the original state by supplying electrons through a liquid electrolyte within the pores. Cells based on this hybrid concept show confirmed energy conversion efficiencies up to 11 % for small area cells, whereas upscaled modules exhibit efficiencies between 5 and 7 %. Standing issues of this type of hybrid solar cells are the replacement of the sensitizer by a material with increased absorption in the red and infrared part of the spectrum, the replacement of the liquid electrolyte by a solid state hole conductor and the improvement of the cell stability.

The full organic counterpart of the hybrid cell is the bulk donor–acceptor heterojunction concept (see Figure P.6b), which is based on blends of two organic compounds, one with donor character, the other with acceptor properties. The excitons dissociate very efficiently at the interfaces between donor and acceptor phases and flow through the percolated donor and acceptor subnetworks to the contacts, which are carrier selective. Efficiencies up to 5 % were reported for this type of cell based on the P3HT/PCBM donor–acceptor couple. This acceptor (PCBM) is often used, because exciton dissociation turns out to be extremely efficient with transfer times in the 100 fs range. Alternatives in which PCBM is replaced by a polymer with acceptor characteristics were also reported (e.g. CN-PPV/MEH-PPV pair). For this type of organic cell, standing issues are the extension of the active layer absorbance towards the red and infrared range, the use of materials with higher mobilities (in this context also tests with liquid crystal materials should be mentioned) and the critical issue of stability. In the framework of improving the red and infrared sensitivity of the donors, the majority of the activities are directed towards thiophenes, which could also improve stability.

For the sake of completeness it should be mentioned that there is also a nonorganic counterpart of these three-dimensional junction devices. These are the ETA (extremely thin absorber) structures, shown in Figure P.6c.

P.4 BASIC MODULE MANUFACTURING SCHEMES

One has to distinguish between two basic module concepts to interconnect the thin film solar cell structures discussed in this book. The first module concept is similar to the modules made with bulk crystalline Si solar cells. The same concept will apply to any thin film structure based on a wafer equivalent, like the epitaxial cell approach or a thin film crystalline Si technology on graphite. This concept is based on an interconnection by means of metallic tabs between the front side of one cell and the back contact of the neighboring cell (see Figure P.7a).

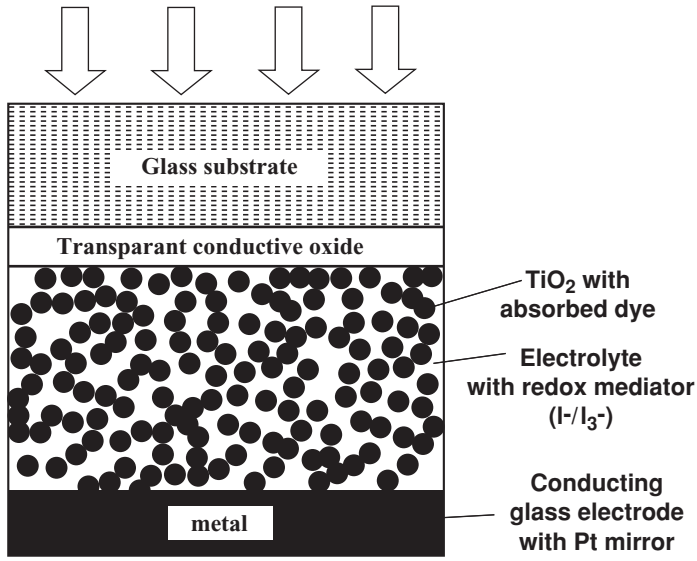

a)

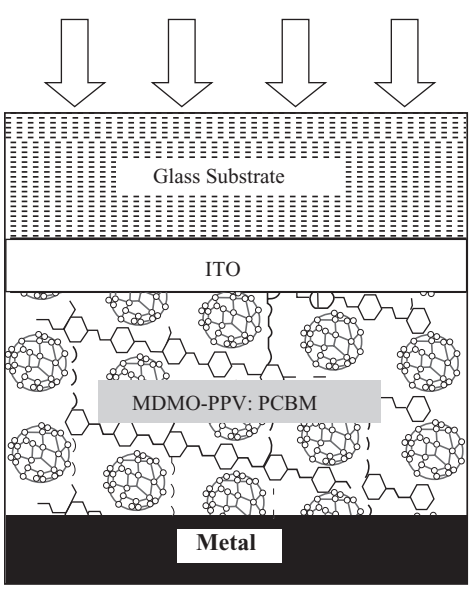

b)

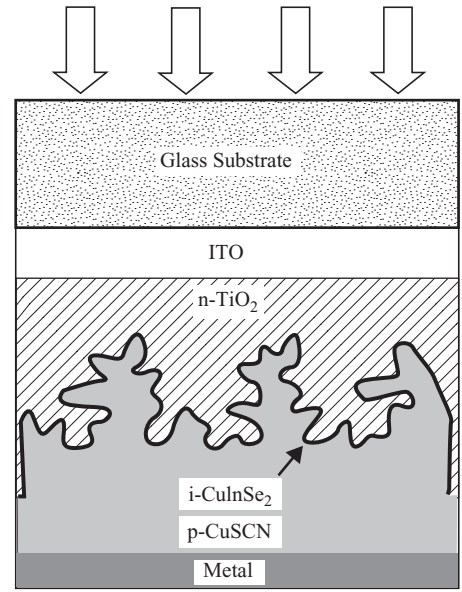

c)

Figure P.6 Structures of a) the Graetzel cell based on nanocrystalline porous TiO_2; b) the bulk donor–acceptor heterojunction concept; c) the structure of ETA cells.

The second manufacturing concept results in a monolithic module, where the cell and the module processing steps are no longer sharply distinguishable. The manufacturing of monolithic photovoltaic modules involves the sequential deposition of different thin films on a large area substrate. A typical polycrystalline superstrate module manufacturing process begins with cleaning of the glass substrate followed by the TCO deposition, window layer and absorber layer formation. Generally three laser or mechanical scribing steps are employed to define, interconnect and isolate the cells. The metallization after the second scribe interconnects the cells defined by the first scribe. The interconnection schemes vary from one module manufacture to another. Modules are then completed by lamination, followed by attaching the current leads. Figure P.7b shows the cross section of a typical monolithic photovoltaic module with a few cells for clarity. The actual process, device structure and materials may vary for different manufacturers. The schematic diagram reveals the advantage of monolithic integration of the cells in the module manufacturing process with minimum area losses in the module. There are several key costing issues such as yield, material cost and capital cost that critically affect the manufacturing of large area photovoltaic modules. The production yield depends on many factors, especially on the uniformity of the deposition process and laser scribing process used to isolate and interconnect the individual cells. Device uniformity over a large area is very critical because a faulty device can severely affect the performance of the entire module. This is, at the same time, the strong and weak point of the monolithic module approach. The monolithic module approach allows, in principle, an important cost saving as the number of steps is reduced as compared with wafer based module manufacturing. However, this potential cost reduction can only be realized with a very high areal yield for the processes to make the modules.

P.5 SHORT OUTLINE OF THIS BOOK

This book provides an overview of the thin film solar cell technologies briefly introduced above. The book aims at introducing the photovoltaic device concepts, to provide the reader with a state-of-the-art overview on the performance of these devices, their characterization and the insights gained in the morphology of the active layers and their optoelectronic characteristics. In this respect it should be appealing to scientists and technologists wanting to acquire updated insights as well as to the more general public wanting to learn more about the thin film solar cell technologies which will conquer an increasing market share of the expanding PV market in the coming decades.

When overviewing the book structure, the reader might remark that the ‘grain size’ of the active layer decreases over the chapters. From grains with a size in the mm range in Chapters 1 and 2, one moves to grain sizes in the μm range in Chapters 3 and 4, whereas in Chapter 5 we are essentially dealing with an amorphous material. In Chapter 1 the ‘epitaxial cell’ approach in which an epitaxial thin film of Si is grown on a low cost Si substrate is dealt with. The resulting structure is equivalent to a multicrystalline Si wafer, which is further processed into a solar cell using the techniques commonly used in the PV industry. In this respect it is a kind of ‘bridge’ between the existing PV industry and the thin film solar cell technologies. In Chapter 2 this is extended to approaches where the crystalline Si layer is deposited on top of a nonSi substrate. A high temperature treatment during which the Si layer is molten turns the crystalline Si layer into a form which is similar to multicrystalline Si. If the substrate is conductive, one ends up with a structure which is still equivalent to a Si wafer. If the substrate is

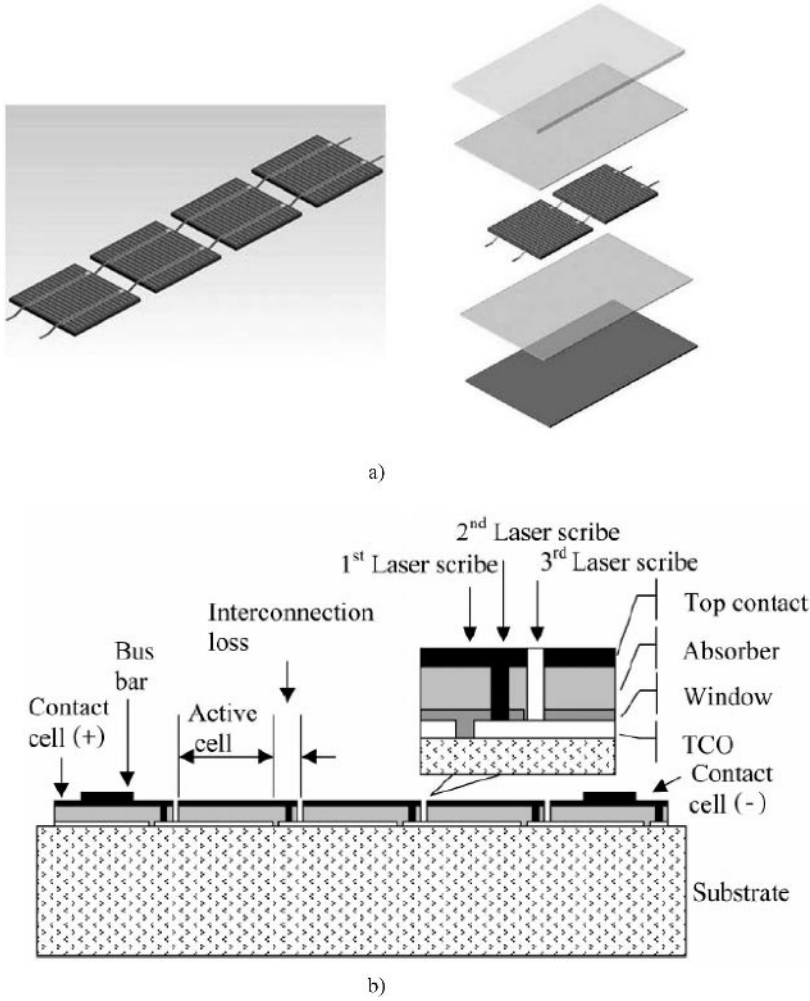

Figure P.7 a) Module concept used for bulk crystalline Si solar cells and valid for any thin film technology based on wafer equivalents. The figure on the left hand side describes the stringing of the solar cells, whereas the right hand side describes the lamination of the cells, courtesy of ECN, the Netherlands; b) typical module cross section for a thin film technology (taken from Reference [5]).

nonconductive, the final structure comes closer to the basic thin film module build-up as shown in Figure P.7b. Because of the high temperature treatment, the nonSi substrates have to satisfy stringent requirements in terms of thermal and mechanical stability whereas impurities have to be contained to impede their diffusion into the active Si layer. This is relaxed in Chapter 3 where the state-of-the-art on polycrystalline Si solar cells on glass and ceramic is reviewed. Because of the absence of any melting step, the grain size of the active layer is in the μm range, but the basic collecting structure is still based on the p-n configuration. This is no longer the case in Chapters 4 and 5, where microcrystalline Si and a-Si:H active layers are being discussed. These active layers are deposited at temperatures $<400\,^{\circ}C$. The electronic quality

of these layers is such that one cannot rely any longer on minority carrier diffusion for carrier collection. Instead carrier collection is aided by a built-in field present throughout the active layer. This built-in field is realized by means of a p-i-n configuration.

Whereas the first five chapters are still based on Si as the active material in a crystalline or amorphous form, the next chapters, 6 and 7, deal with polycrystalline compound semiconductors with a grain size in the μm range. Chapters 6 and 7 deal with polycrystalline compound solar cells. Cadmium telluride solar cells are discussed in Chapter 6 with special emphasis on their characterization and modeling. In Chapter 7 the second type of polycrystalline compound solar cell material, $CuInSe_2$, is reviewed.

In Chapter 8 one is dealing with the fundamental difference between inorganic and organic materials with respect to free carrier generation. This chapter deals with the theoretical insights in exciton generation and dissociation. These insights provide the necessary base for understanding the device concepts in Chapters 9 and 10. In these chapters one is dealing with active layers where the typical domain size is in the nm range as encountered in fully organic bulk donor–acceptor heterojunction solar cell or hybrid approaches like the 'Graetzel cell'. The device concepts of Chapters 9 and 10 are radically different from the concepts in the other chapters in that collection takes place throughout the whole volume of the active layer and that the concept of a 'minority carrier' essentially loses meaning. Chapter 11 is fundamentally different from the other chapters in that it discusses the vision of how the thin film solar cell technologies closest to industrial manufacturing will be introduced in a multi-GW scenario and what the final cost structure will look like.

REFERENCES

[1] D. W. Aitken, L. Billman, S. R. Bull, The climate stabilization challenge: can renewable energy sources meet the target, *Renewable Energy World*, **7(6)**, 56–69 (2004).

[2] See e.g. http://www.ecn.nl/docs/library/report/2004/c04035.pdf.

[3] see e.g. http://www.epia.org/05Publications/EPIAPublications.htm and http://europa.eu.int/comm/research/energy/pdf/vision-report-final.pdf.

[4] E. A. Alsema, P. Frankel, K. Kato, Energy pay-back time of photovoltaic energy systems: present status and prospects, *Proceedings of the 2nd World Conference and Exhibition on Photovoltaic Solar Energy Conversion*, Vienna, 2125–2130 (1998)

[5] K. L. Chopra, P. D. Paulson and V. Dutta, Thin-film solar cells: an overview, *Progress in Photovoltaics: Research and Applications*, **12**, 69–92 (2004).

[6] Z. Q. Ma, B. X. Liu, Boron-doped diamond-like amorphous carbon as photovoltaic films in solar cells, *Solar Energy Materials and Solar Cells*, **69(4)**, 339–344 (2001).

[7] E. A. Katz, D. Faiman, V. Lyubin, Persistent internal photopolarization in C_{60} thin-films: proposal for a novel fullerene–based solar cells, *Conference Digest of the 29th IEEE Photovoltaic Specialists Conference*, New Orleans, May 19–24, 2002, 1298–1301.

1 Epitaxial Thin Film Crystalline Silicon Solar Cells on low Cost Silicon Carriers

Jef Poortmans
IMEC, Leuven, Belgium

1.1 INTRODUCTION

In order to substantially reduce the costs of present crystalline Si solar cells, the material consumption of highly pure Si in a typical solar cell structure should be reduced. Most of the crystalline Si material merely acts as a mechanical carrier for the solar cell device with most of the optical absorption taking place in the upper 30 μm region. When special care is taken to maximize optical confinement active layer thicknesses as low as 0.5 μm would be sufficient [1] for reaching energy conversion efficiencies above 15 %. Moving to thinner Si wafers to reduce Si consumption represents one option, but there are obvious concerns about process yield, showing up when producing cells in Si-wafers with thicknesses below 200 μm. Special substrate types, specifically developed to avoid crack propagation, like the tri-crystalline Si material [2] or thin edge film growth (EFG) ribbons [3], might alleviate this problem.

A more ambitious approach to reduce solar cell costs consists of growing a thin active crystalline Si layer onto a cheap carrier. This carrier can be a ceramic substrate or even a glass substrate when the deposition and solar cell process are performed at low temperature. The Si layer, deposited on top of these substrates, will be micro- or polycrystalline with a grain size determined by the growth temperature and supersaturation conditions during the silicon layer deposition. For microcrystalline Si solar cells on glass, exhibiting grain sizes in the range 1–100 nm, energy conversion efficiencies[1] up to 10 % are reported [4]. On the other hand, it turns out to be difficult to realize solar cells with proper energy conversion efficiencies in material with a grain size of 1–10 μm [5, 6], although substantial progress has been made lately in this field [7]. On ceramic substrates, which withstand high temperatures, liquid phase recrystallization [8, 9], is often applied to increase the final grain size, whereas laser recrystallization and rapid thermal annealing is being developed for substrates which can only withstand process temperatures $>650\,^{\circ}C$ for a limited time [10, 11].

[1] In the remainder of the chapter energy conversion efficiency will be named "efficiency"

Thin Film Solar Cells Edited by J. Poortmans and V. Arkhipov
© 2006 John Wiley & Sons, Ltd

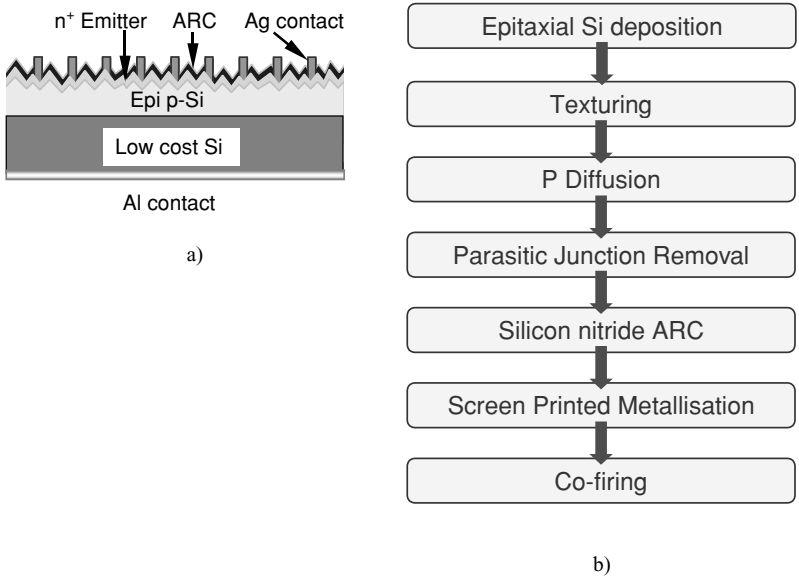

Figure 1.1 a) Schematic cross-section of epitaxial solar cell structure; b) Comparison of generic industrial process flows for epitaxial solar cells versus self-supporting crystalline Si solar cells; only the first process step (the epitaxial deposition) would be added to the normal process flow for industrial crystalline Si solar cells.

The basic idea behind the thin film approach discussed in this chapter, is the realization of a thin crystalline Si film of high electronic quality [12, 13] on a low cost Si carrier substrate by means of epitaxial growth. When discussing thin film solar cell technologies, thin film crystalline Si solar cells, based on an epitaxially grown active layer on an inactive highly doped low cost Si carrier substrate[2] are often left untreated. This is readily understood when looking at Figure 1.1a, showing the generic structure of the type of the solar cell being discussed within this chapter. The depicted structure strongly resembles the structure of a classical, self supporting bulk crystalline Si solar cell and, as a result, the basic solar cell process to produce the solar cell is very similar to the practices used within the photovoltaics (PV) industry nowadays. This is, at the same time, the strongest and weakest point of this technology. Its structural similarity would result in a low acceptance threshold in the solar cell industry, which is presently based at 95 % on crystalline Si. Indeed, the only major change required to introduce this technology within the crystalline Si PV industry would be the introduction of a high throughput epitaxial Si deposition reactor at the beginning of the production line as shown in Figure 1.1b. In this way, additional investments and risks can be minimized, which is a nonnegligible element in major investment decisions.[3] In this context one sometimes uses the term 'wafer equivalents' to emphasize the similarity aspect. Last, but not least, the 'wafer scale' approach has the advantage that process yield can be kept at a high level using the in-line

[2] In the remainder of the chapter the shorter term "epitaxial Si solar cells", will be used, although this is not the only thin-film crystalline technology in which an epitaxial Si layer is being deposited during the formation of the active layer.

[3] The large investment when building thin-film solar cell production lines is often mentioned as a major barrier.

production quality monitoring tools available in crystalline Si production lines. For thin film solar cell technologies which are depositing the active layers on large area substrates of more than 1 m^2, the uniformity and reproducibility requirements are much more severe to obtain a similar yield.

The similarity of the basic epitaxial solar cell structure to classical crystalline Si solar cells also creates the impression that the potential cost savings by using this epitaxial cell technology would be marginal. A closer look reveals that this is not necessarily true. As mentioned in the introductory chapter of this book, when analyzing the cost structure of multicrystalline Si solar cell modules, one sees that more than 50 % of the module cost consists of costs related to the crystalline Si substrate [14, 15]. At the time of redaction of this chapter there is a tendency for the crystalline Si substrate costs to increase as one is facing a situation of scarcity of poly-Si feedstock material. This is temporary in to the author's opinion, because of major investments in additional poly-Si feedstock production specifically tuned to the needs of the Si solar cell industry [16]. Nevertheless, it remains that the cost projections for this specific 'solar grade' poly-Si feedstock material are mostly in the range 15–20 € /kg. Based on such a feedstock cost and a further reduction in the amount of crystalline Si/Watt peak (W_p) in line with the historical trend of 5 %/year [17] the cost of bulk crystalline Si solar cell modules would be in the range of 1.2 $/$W_p$ with industrial efficiencies near 20 % [15]. The epitaxial cell route is based on metallurgical or upgraded metallurgical grade Si substrate material which would cost less than 5 € /kg.[4] In the situation of having a high throughput epitaxial Si deposition process with costs below 10 € /m^2, the final cost of the module would be in the range 0.9–1 $/$W_p$, even with an cell efficiency of only 15 %. Besides this cost potential, the epitaxial cell approach would also render the PV industry independent from any supply issues on the level of poly-Si feedstock material.

The substrates of interest for epitaxial Si solar cells are low cost Si substrates which, because of their doping and impurity levels, do not allow the realization of a solar cell with sufficient efficiency within the substrate. The Si substrate can be a highly doped Si ribbon; see e.g. [18] for chemical vapor deposition (CVD)-grown epitaxial cells on an ribbon growth on substrate (RGS) ribbon or [19, 20] for an liquid phase epitaxy (LPE)-grown layer on the same ribbon type. Also Si substrates from metallurgical grade Si (MG-Si) or upgraded metallurgical grade Si (UMG-Si) ingots are an attractive option [13, 21, 22]. By growth of an epitaxial layer with suitable doping and reduced impurity levels on top of this substrate, a better performing solar cell can be realized on top of this substrate [21]. The secondary ion mass spectrometry (SIMS) profile, shown in Figure 1.2, illustrates that the epitaxial layer on top of the contaminated substrate does indeed contain a substantially lower content of impurities than the substrate.

The objective of this chapter is to outline the different epitaxial cell approaches to the level of deposition technology and epitaxial layer structure. The solar cell process developments will only be discussed insofar as the solar cell results shed more light on the efficiency potential in laboratory conditions or in an industrial environment. Specific attention will be given to those aspects which have to be developed to make the epitaxial cell technology viable for industrial production. The latter aspect does not only concern the concepts and development of high throughput deposition technologies and adaptation of solar cell processes but also covers the

[4] Si as such is not a rare material and the reduction of sand to metallurgical grade is consistent with a cost of 1–2 Euro/kg.

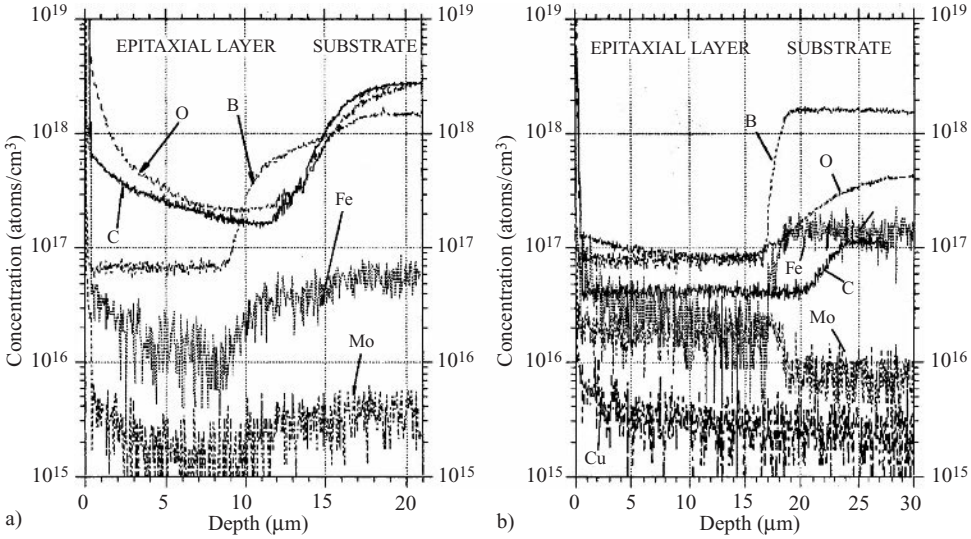

Figure 1.2 SIMS profiles of the impurities O, C, Fe, Mo, Cu in epitaxial layer on a) highly doped multicrystalline Si substrate (SILSO); and b) on a MG-Si substrate. Note the decreasing impurity concentrations in the epitaxial layer for Fe, O and C in both cases.

approaches to keeping the epitaxial layer thickness as low as possible. This can only be realized by enhanced light absorption and/or optical confinement of light within the active volume of the cell. Concerning optical confinement, the reader will immediately remark that this is a difficult issue as the substrate and active material are both crystalline Si, which excludes major reflection of light at the interface between the Si substrate and the active layer. To solve this intrinsic problem innovative schemes based on a buried reflector are required. The different approaches to realizing such a buried reflector will be discussed. Alloying with Ge is one other possibility to enhance the cell's absorbance.

1.2 DEPOSITION TECHNOLOGIES

The different deposition technologies by which epitaxial layers for solar cell applications can be grown are discussed as a function of deposition temperature, starting from the technique using the highest deposition temperature. This classification methodology also reflects the amount of experimental results and the maturity of the respective techniques. This is not a surprising finding since the epitaxial layers needed for epitaxial solar cells are quite thick in comparison with the typical layer thickness needed for other electronic applications (with the exception of epitaxial layers for power devices). The required epitaxial layer thickness which is in the range 5–30 μm requires a high growth rate to avoid excessive deposition times. At lower deposition temperatures the adatom surface mobility decreases resulting in an increasing number of crystallographic defects because the adatoms do not have sufficient time to relax into the lattice sites. As a result, at lower temperatures additional energy besides the thermal energy has to be supplied to increase the surface mobility and to allow high-quality epitaxial growth. This additional energy can supplied by means of accelerated ions or through plasma techniques.

1.2.1 Thermally assisted chemical vapor deposition

The deposition technique, which has been and is still most widely studied in the context of epitaxial solar cells, is based on thermally assisted heterogeneous decomposition of a Si precursor and doping gases at a heated Si -surface. In the text it will be referred to as thermally assisted chemical vapor deposition (TA-CVD). Since the seventies attempts have been made to use this technique in the frame of solar cells [23] and nowadays it is still widely used in Europe [15, 24] and Japan [25] for the realization of thin film crystalline Si solar cells. There are numerous reactor types which have been used for TA-CVD. Batch type as well as single wafer systems have been used. Single wafer systems are often horizontal flow reactors, where gases are introduced at one end of a chamber and exit from the other end. The wafer either lies on a silicon carbide coated graphite susceptor, or is thermally isolated and heated only by radiation. In the latter case, extremely fast heating and cooling rates are achievable and the technique is therefore often referred to as rapid thermal CVD (RT-CVD) [26]. The technique was pioneered in the eighties [27] and the specific study of this technique for thin film crystalline Si solar cells was conducted in the laboratory of the Institut d'Electronique du Solide et des Systèmes (INESS, Strasbourg [26] (see Figure 1.3). It avoids unwanted Si deposition on the cool furnace walls and reduces the time associated with heating and cooling of the substrates with all the energy being used for heating of the substrate and not of the furnace periphery. Batch type multiwafer reactors include pancake and barrel reactors, where rotation of the wafers on flat or cylindrical substrate holders ensures the required uniformity and aerodynamic conditions, and low pressure CVD reactors (LPCVD).

CVD takes advantage of the large process expertise available in the field of microelectronics. The developed epitaxial deposition systems and processes allow highly reproducible and uniform layers, both on the level of thickness and of dopant control. Doping and thickness uniformity are typically in the range of a few % over areas as large as 200–300 mm. In fact, the specifications for microelectronic applications are much more severe than what is being aimed at in photovoltaic applications, where a uniformity requirement of about 10 % for thickness and doping levels is probably sufficient. Nevertheless TA-CVD has a number of inherent disadvantages in the frame of thin film crystalline Si solar cells. First of all, it uses Si precursors which are toxic and/or corrosive and these precursors represent obvious explosion risks. In addition, the temperatures needed to obtain high growth rates in the order of a few μm/min are in the range 1000–1200 °C.

The electronic quality of CVD-grown epitaxial layers has been studied by means of lifetime measurements with typical lifetimes found in the order of a few μs on monocrystalline Si reference substrates and in the order of 1 μs on multicrystalline substrates [28].

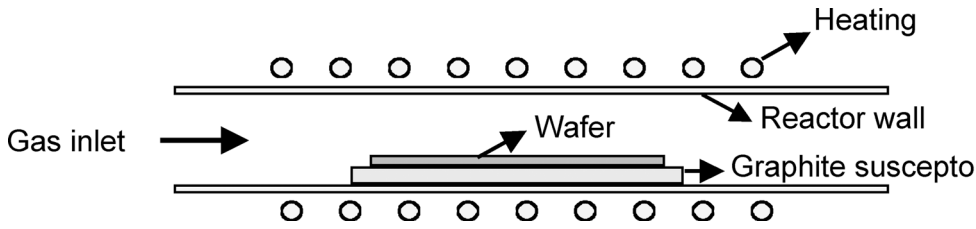

Figure 1.3 Schematic view of typical horizontal TA-CVD system (see reference [26]).

1.2.2 Liquid phase epitaxy – electrodeposition

A technique which is basically different from CVD in that it uses a liquid medium instead of a gaseous environment is solution growth (SG). The technique is also called liquid phase epitaxy (LPE) when this principle is used for the growth of epitaxial layers on a crystalline substrate [29]. In SG the growth of Si proceeds from a molten metal solution, typically Sn, In or sometimes Cu and Al [30, 31]. The molten metal is saturated with Si and afterwards slowly cooled. When cooling down, the melt gets supersaturated and the crystalline Si layer will be deposited from the melt onto a substrate by heterogeneous nucleation. The typical temperatures used range between 700 and 900 °C with growth rates in the order of 1 μm/min.

Besides its conceptual simplicity, the main advantage of the LPE technique lies in the fact that the growth system is close to thermal equilibrium and the Si atoms in the melt exhibit a large diffusion coefficient. Both factors enhance the crystallographic quality of the grown Si film. At the same time the close-to-equilibrium character also represents a serious drawback since nucleation of the Si-layer on a non-Si substrate or along defects at a Si surface becomes very difficult, which often results in non homogeneous and even nonconsistent Si layers on substrates containing crystallographic defects. In case of non-Si substrates like graphite this is often tackled by having a Si seed layer deposited by another technique. When growing epitaxial layers by the LPE technique on RGS [19] or silicon sheets from powder (SSP) ribbons [20] the epitaxial layer thickness in the region of the grain boundaries is often much reduced as compared to the intragrain thickness because the higher energy associated with the defects suppresses the layer growth near these defects, as schematically shown in Figure 1.4. In the regions where the epitaxial layer is much thinner, the n^+-emitter diffusion and p^+-substrate are in direct contact, resulting in leaky junctions and low fill factors. Faster cooling rates provide some improvement but the problem remains for uniform deposition over large areas.

Because of the low supersaturation during LPE growth, the defect density and excess carrier recombination activity in the LPE-grown epitaxial layers are lower as compared to CVD-grown layers. Numerous studies [32, 33] give strong support for this view. Electron beam induced current (EBIC) pictures of partially masked structures give unambiguous evidence of the reduced recombination in the LPE layers as shown in [32]. This reduction is caused by the tendancy to strive for the lowest energy configuration of the dislocation network in the LPE-layer. In addition, impurities will be contained in the molten metal solution because of the distribution coefficient between the liquid and solid phase. Minority-carrier lifetimes of several μs up to 10 μs have been reported in epitaxial layers for solar cells (see e.g. [34]).

A variation of solution growth is the electrodeposition of Si from molten salts (see Figure 1.5), which also allows the growth of epitaxial layers [35].

LPE allows one to easily incorporate an *in situ* doping gradient in the active base layer. The doping gradient will result in a positive electrical field in case of a decreasing dopant incorporation during growth. This positive field aids the collection of minority carriers and results in an increased effective diffusion length (L_{eff}) [36].

$$\frac{1}{L_{\text{eff}}} = \frac{1}{2L}\left(\sqrt{\left(\frac{E}{E_c}\right)^2} + 4 - \frac{E}{E_c}\right) \tag{1.1}$$

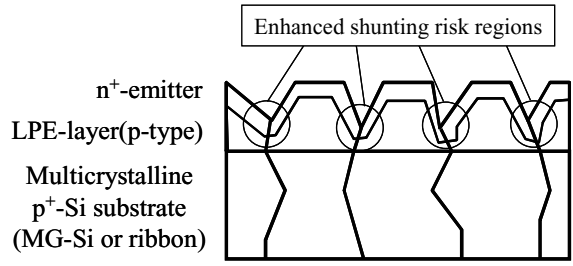

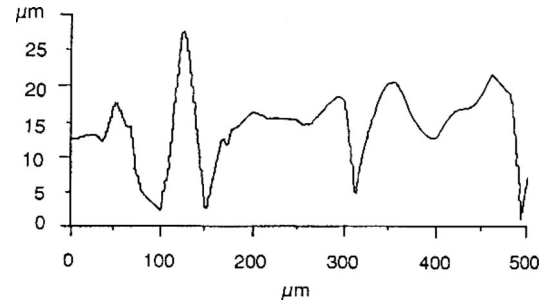

a) b)

Figure 1.4 a) Picture and surface profile showing typical surface morphology of LPE-layer on defected Si substrate (taken from reference [19], courtesy of WIP, Munich, Germany); b) Schematic illustration of LPE growth topology problem in regions near crystallographic defects. It is obvious that during emitter diffusion, these regions are more susceptible to shunting between the n^+-emitter and the highly doped substrate.

with L the minority carrier diffusion length in the absence of an electrical field and

$$E_c = \frac{kT}{q} L \tag{1.2}$$

whereas E is given by:

$$E = \frac{kT}{qW_B} \ln\left(\frac{N_r}{N_f}\right) \tag{1.3}$$

where N_r represents the doping level at the substrate-epilayer interface and N_f is the doping level at the epilayer surface.

Intuitively one would expect a substantial performance increase by this effect. It was proven in [36] that the enhancement in most cases remains very limited and is only relevant in the absence of light trapping and with small minority-carrier diffusion lengths. It was recently pointed out by Majumdar *et al.* [37] that a negative field (i.e. the incorporation of the doping element increasing during the growth of the epitaxial layer) is a better approach. Although this result is to some extent counterintuitive, this can be understood from the consideration that the minority-carrier concentration gradient upon illumination is large anyway and is relatively

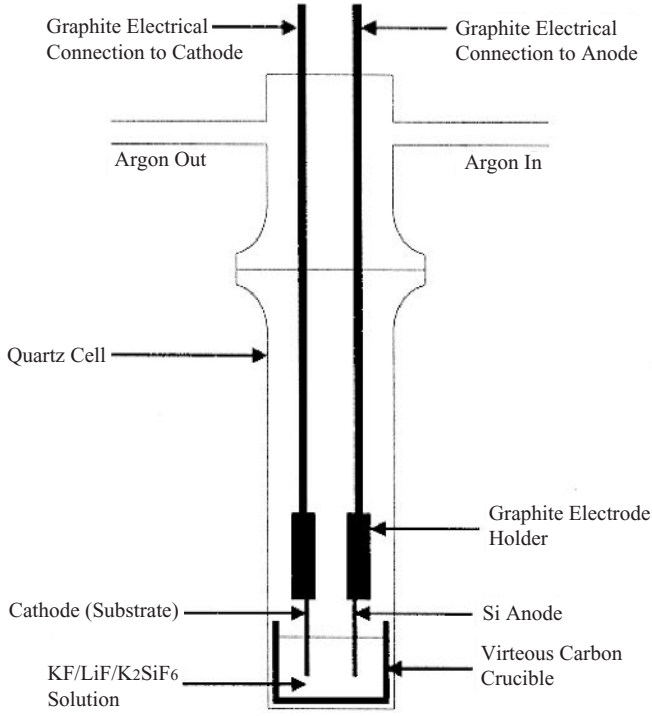

Figure 1.5 Schematic drawing of the electrodeposition technique. Reproduced Figure 1 with permission from J. T Moore, T. H. Wang, M. J. Heben, K. Douglas, T. F. Ciszek, 'Fused-salt electrodeposition of thin-layer silicon', Conference Record of the 26th IEEE Photovoltaic Specialists Energy Conference, Anaheim, 775, 1997. Copyright (1997) IEEE.

unaffected by the doping profile whereas the open circuit voltage is kept high because of the high base doping level near the junction.

1.2.3 Close space vapor transport technique

An alternative technique which yields very high chemical efficiencies[5] is based on so-called close space vapor transport [38]. Although the technique has been known since the sixties [39], it received renewed attention through research performed at the National Renewable Energy Laboratory (NREL), USA. A schematic drawing of this technique is shown in Figure 1.6. In this technique Si is transported from a source to a substrate. The driving force for the Si transfer is the temperature difference between both. A small separation between source and destination allows very high transfer efficiencies, because there is only limited loss of Si to the side walls. By means of this technique, epitaxial layers were deposited on highly doped mono- and multicrystalline Si substrates.

[5] The chemical efficiency describes the ratio between the Si-containing species incorporated in the growing solid Si film and the amount of Si supplied.

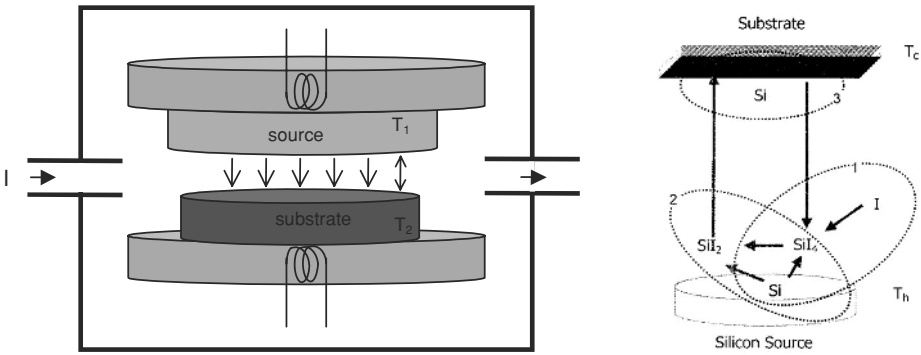

Figure 1.6 a) Schematic drawing of CVST technique for Si-deposition; b) Application of CSVT principle in the APIVT system presented in [38]. Reproduced Figure 1 with permission from T.H. Wang, T.F. Ciszek, M. Page, Y. Yan, R. Bauer, Q. Wang, J. Casey, R. Reedy, R. Matson, R. Ahrenkiel and M.M. Al-Jassim, 'Material properties of polysilicon layers deposited by atomspheric pressure iodine vapor transport', Conference Record of the twenty-eight IEEE Photovoltaic Specialists Conference, Anchorage 15–22 September 2000, p.138–141. Copyright (2000) IEEE.

The electronic quality obtained was remarkably good as evidenced by laboratory solar cells, made in these epitaxial atmospheric pressure iodine vapor transport (APIVT)-grown layers, especially taking into account the elevated deposition rate at a relatively low substrate temperature. The growth rate obtained at substrate temperatures in the range 650–850 °C (with the source temperature kept at 1300 °C) was in the order of 1–3 μm/min and was relatively insensitive to the substrate temperature. A model was constructed to explain this atypical temperature dependence of growth rate. The model incorporates the arrival rate of SiI_2, the departure rate of SiI_4 and surface migration and resulted in an expression for the growth rate R in the form:

$$R \propto (T - T_{\text{source}}) \left(T_{\text{source}}^2 - T^2\right) \exp\left(\frac{-Q}{kT}\right) \tag{1.4}$$

with T being the substrate temperature and Q the activation energy for surface migration. The insensitivity of the growth rate to the substrate temperature is caused by two opposing tendencies. For classical CVD the T dependence of the surface migration increases the deposition rate, but in APIVT this is counteracted by the lower temperature difference between source and substrate (at constant source temperature), resulting in a lower arrival rate.

1.2.4 Ion assisted deposition

Ion assisted deposition (IAD) is based on electron-gun evaporation and subsequent partial ionization of silicon [40]. An applied voltage accelerates silicon ions towards the substrate. Typical acceleration voltages of 20 V are used. This yields the lowest etch-pit densities in monocrystalline epitaxial layers [41]. The principle of the IAD technique is shown in Figure 1.7.

Because of the energy supplied by the accelerated ions, the surface adatom mobility is enhanced. As a result the IAD technique enables epitaxial growth at temperatures as low as 435 °C with high deposition rates up to 0.5 μm/min. The Hall mobility of monocrystalline epitaxial

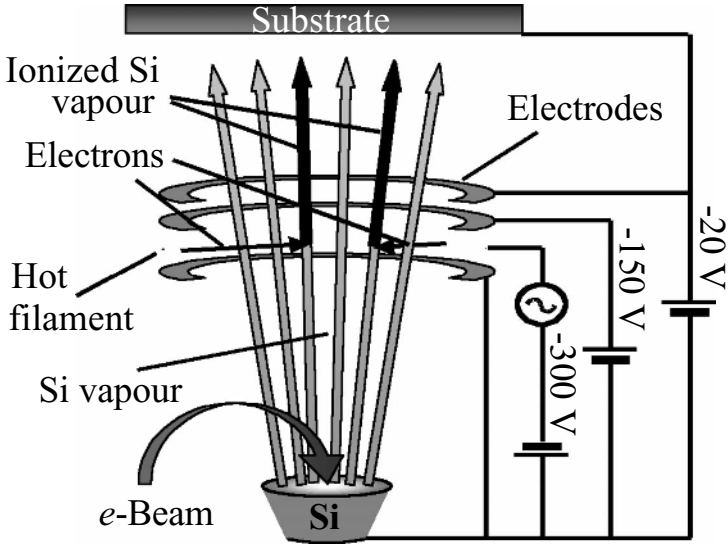

Figure 1.7 Schematic of the ion-assisted deposition technique [after 42].

layers increases with deposition temperature and reaches values comparable to those of bulk Si at $T > 540\,^{\circ}$C. The majority-carrier mobility in IAD boron-doped films almost reaches the theoretical values obtained for crystalline bulk silicon over the doping range 10^{16} to 10^{20} cm^{-3}. The electronic properties of the films are strongly dependent on the substrate orientation. In line with other findings valid for low-temperature epitaxial growth, the diffusion length is up to an order of magnitude lower in (111)-oriented Si films as compared to (100)-oriented Si films, resulting in inhomogeneous current collection in light-beam induced current measurements on epitaxial cells on multicrystalline Si substrates [43]. Photoluminescence and deep level transient spectroscopy revealed broad defect distributions for low deposition temperatures $<550\,^{\circ}$C. The point defect densities are up to four orders of magnitude lower in (100)-oriented Si epitaxial layers than in (111)-oriented Si films. Also temperature-dependent quantum efficiency (TQE) measurements were used to investigate the recombination behaviour in epitaxial silicon thin film solar cells grown by ion-assisted deposition [44]. The diffusion length in this material is dominated by Shockley–Read–Hall recombination via relatively shallow defects with activation energies of 70–110 and 160–210 meV, respectively. At a deposition temperature of 650– $^{\circ}$C with a prebake at 810– $^{\circ}$C [45], ion-assisted deposition produces epitaxial Si films with a minority-carrier diffusion length of 40 μm.

1.2.5 Low energy plasma enhanced chemical vapor deposition/electron cyclotron resonance chemical vapor deposition

Apart from accelerated ions, plasma techniques can also be used to provide additional energy to increase surface mobility and by doing so to allow high-quality epitaxial growth from a low-temperature deposition method.

Low energy plasma enhanced chemical vapor deposition is a technique in which a high current plasma discharge composed of low-energy particles leads to a high deposition rate,

while not damaging the wafer surface [46]. The main application for this technique is the growth of compositionally graded relaxed SiGe buffer layers for high-speed advanced metal-oxide-semiconductor (MOS) devices, but the technique is in principle also of great interest for solar cells.

An ECR source can also be used to provide a dense plasma that greatly enhances surface mobility and allows epitaxy at temperatures below 400 °C [47].

1.3 SILICON BASED EPITAXIAL LAYER STRUCTURES FOR INCREASED ABSORBANCE

Since crystalline Si is an indirect bandgap material, its absorption coefficient at wavelengths >900 nm becomes too small to absorb effectively incoming light at larger wavelengths in an epitaxial layer of only 20 μm. In order to increase the absorbance, one can modify the epitaxial layer by growing specific structures to increase the optical pathlength or through decreasing the bandgap by alloying with Ge.

1.3.1 Epitaxial growth on textured substrates

A first approach consists of chemically texturing the substrate before epitaxial growth. However, this approach also has drawbacks. The textured surface structure tends to flatten during the epitaxial process by facet formation, reducing the effectiveness of the texturing process. Moreover, due to the resulting surface roughness before epitaxy, the defect density in the epitaxial layer will be high and as a result it will be difficult to reach high open circuit voltage (V_{oc}) values.

The texturing can also be done by mechanical means, resulting in structures like the ones shown in Figure 1.8. The approach followed here is straightforward: by grooving the Si substrate

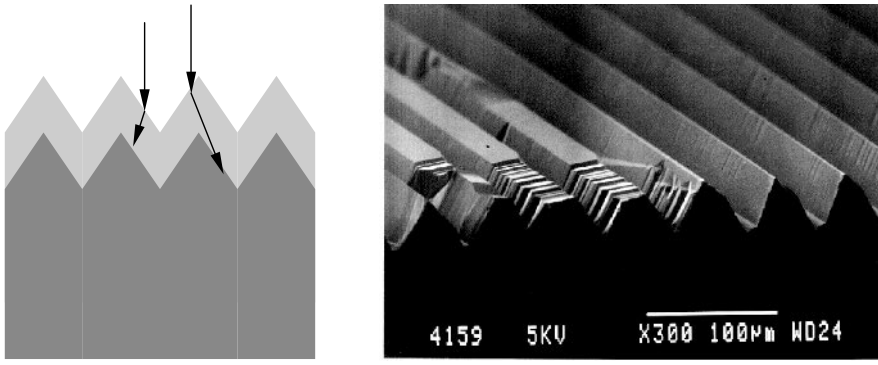

a) b)

Figure 1.8 a) Schematic of the optical enhancement effect when grooving the substrate before the epitaxial growth assuming conformal growth; b) SEM picture illustrating the modification of the mechanically textured Si-surface after growth of an epitaxial layer when growing on a Si-substrate with different grain orientations.

before the epitaxial growth, the optical pathlength within the active layer is enhanced, as shown in Figure 1.8a when conformal growth is assumed. A minimization of the reflectance of the structure before and after grooving was studied [48]. When applying this technique to multicrystalline Si substrates one has to take into account the facetted growth of the epitaxial layer and the different growth rates on different crystallographic orientations. The consequence of this effect is illustrated in Figure 1.8b, showing the cross-section of an epitaxial layer grown on a mechanically textured surface. One can clearly observe the modified texture after epitaxial growth. On grains with orientations near (100) the texture is well preserved, whereas on other grain orientations the original texture has been modified by the development of different facets.

By means of this technique, large-area CVD-grown epitaxial cells (100 cm^2) on UMG-Si were realized. Using an industrial solar cell process with screenprinted contacts, efficiencies between 12 and 13 % were obtained despite the limited thickness of the epitaxial layer which was between 15 and 20 μm [21, 49].

1.3.2 Silicon–Germanium alloys

A straightforward approach to increase the short circuit current is based on increasing the absorption coefficient of a crystalline Si by alloying it with Ge. The lower bandgap of the SiGe alloy allows the increase of the infrared absorption of the cell, although at the expense of a reduced solar cell open circuit voltage. In a bulk crystalline solar cell this loss will outweigh the gain in short circuit current. Solar cells realized in bulk $Si_{1-x}Ge_x$ substrates with $x < 10$ % solar cells were reported [50], confirming the predicted behaviour. However, in thin film cells the reduction in open circuit voltage is, theoretically at least, less severe when surface recombination dominates over bulk recombination. By using a $Si/Si_{1-x}Ge_x$ heterojunction back surface field (BSF, see Figure 1.9a) most of the loss in open circuit voltage can theoretically be recovered. Figure 1.9b shows the typical cross-hatch pattern of a relaxed SiGe layer, epitaxially grown on a (100) Si substrate.

The experimental studies, conducted on relaxed $Si_{1-x}Ge_x$ epitaxial layers on Si for photovoltaic purposes were mostly restricted to alloys with Ge-content below 20 %, although theoretical calculations indicate there might be (limited) benefit from impact ionization at higher Ge-content [51, 52]. Thick relaxed $Si_{1-x}Ge_x$ layers with x ranging from 0 to 20 % were

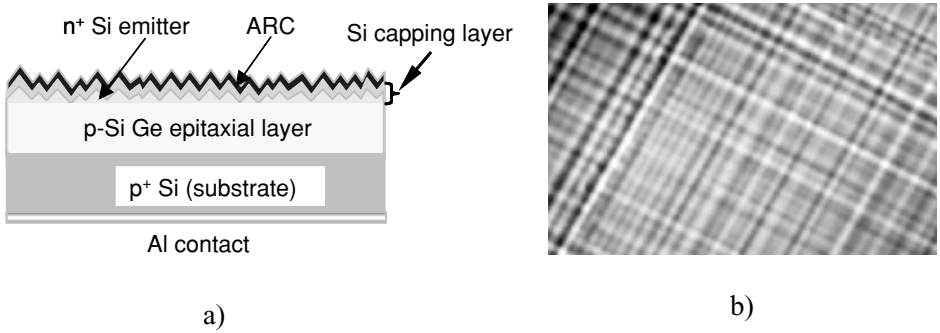

Figure 1.9 a) Basic structure of the SiGe thin film structure on Si; b) Optical micrograph of the typical cross-hatch pattern of a relaxed $Si_{.9}Ge_{.1}$-layer on Si; the magnification is 500x

grown epitaxially by CVD and LPE on highly doped monocrystalline Si substrates for solar cell purposes. Epitaxial SiGe alloys were grown by means of CVD in a lamp-heated system with graphite susceptor at reduced pressure (40 mTorr) and temperatures between 700 and 800 °C [53]. SiH_2Cl_2 and GeH_4 were used as Si and Ge precursors, respectively. Because of the relatively large thickness needed (in comparison with the strained layers needed for micro-elecronic applications), the growth rate should be as high as possible. Increasing the growth rate requires higher deposition temperature, but since the Ge-incorporation efficiency decreases at higher temperatures, a trade-off has to be looked for. This can be seen in Figure 1.10. As a

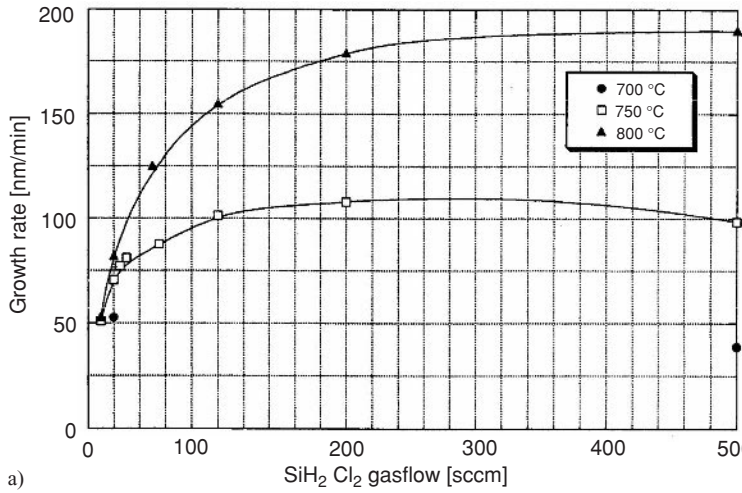

a)

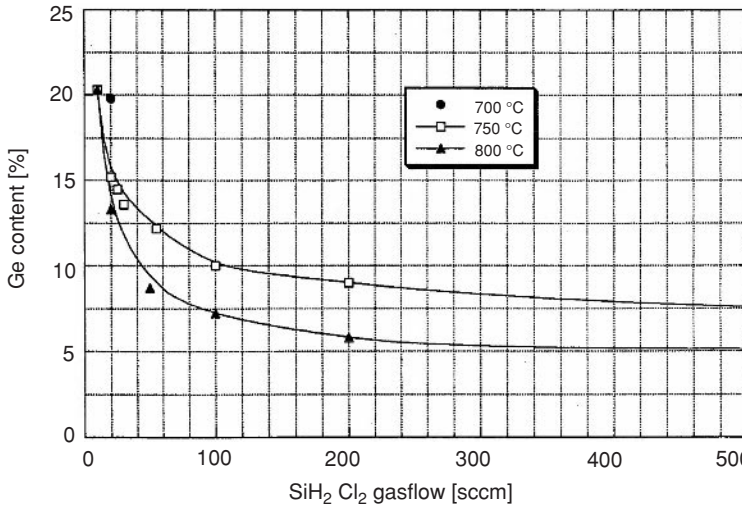

b)

Figure 1.10 a) Growth rate of the epitaxial $Si_{1-x}Ge_x$-layers as a function of the mass flow of SiH_2Cl_2 (the 1 %GeH_4 in H_2 flow was kept constant at 200 sccm); b) Ge-incorporation a.f.o. SiH_2Cl_2 gasflow for different temperatures (the GeH_4/H_2 flow was the same as for a.)

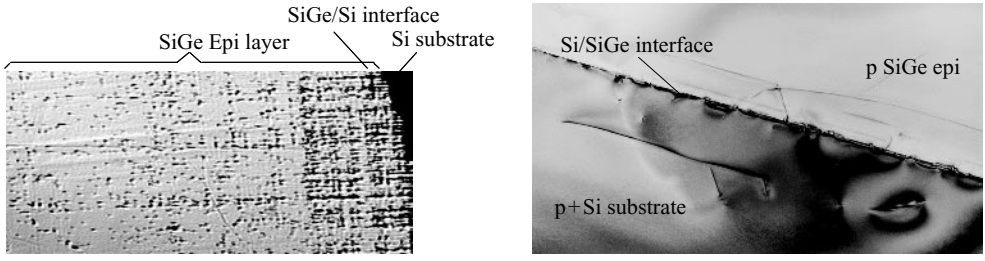

Figure 1.11 a) Defect density a.f.o. depth as revealed by optical analysis of beveled relaxed $Si_{.9}Ge_{.1}$-layers on Si; b) Cross-section TEM picture of dislocations confined within the buffer layer of the same structure as in Figure 1.11a. One can observe the bending of the dislocation lines within the buffer layer.

result, growth rates between 0.15 and 0.2 μm/min were obtained for the layers studied within the solar cells.

Because of the lattice mismatch between the $Si_{1-x}Ge_x$-layer and the Si-substrate it is necessary to incorporate a buffer layer in between the Si substrate and the active layer. When the $Si_{1-x}Ge_x$-thickness (10–15 μm) greatly exceeds the critical thickness [54] for growth on Si (which will always be the case), misfit dislocations relax the lattice strain, resulting from the lattice mismatch.[6] The density of dislocations throughout a bevelled epitaxial $Si_{1-x}Ge_x$-layer on Si can be seen in Figure 1.11a. When grown under suitable conditions and at sufficiently high temperature, the misfit dislocations will partially annihilate within the buffer layer. On bevelled samples which were subjected to a defect etch, the evolution of the defect density as a function of depth was determined. This is shown in Figure 1.11a where a strong reduction of the dislocation density towards the upper surface is clearly seen. The defect density decreases from 10^7 cm^{-2} in the buffer to 10^5 cm^{-2} at the top surface of the layer. The confinement of the misfit dislocations was also verified by cross-section transmission electron microscopy (TEM) (see Figure 1.11b).

By means of EBIC measurements on Schottky diodes on the as-deposited relaxed $Si_{1-x}Ge_x$-layers, the diffusion length was extracted [55]. Despite the defect density being in the order of 10^5 cm^{-2} an effective diffusion length of 80 to more than 100 μm was extracted for CVD layers as well as for LPE layers when a buffer layer was used. The term effective diffusion length is used because the layer thickness is only 20 μm thick. It also proves that, at room temperature at least, the dislocations in a CVD-grown layer are not necessarily more active than in LPE-grown layers.

Solar cells were processed in these relaxed $Si_{1-x}Ge_x$-layers on p^+-Si by a laboratory process comprising solid source diffusion, nitride surface passivation and evaporated contacts, the details of which can be found in [56]. The short circuit current observed for the cells with a relaxed $Si_{1-x}Ge_x$ layer was higher than for a Si thin film crystalline Si solar cell with comparable active layer thickness and similar doping profile, but the enhancement of the short circuit current saturates at Ge-content larger than 10 %. However, open circuit voltage and

[6] The difference in lattice constant between Si and Ge is about 4 %. The lattice constant of the SiGe alloy varies practically in a linear fashion between the lattice constant of Si and Ge (Vegard's law).

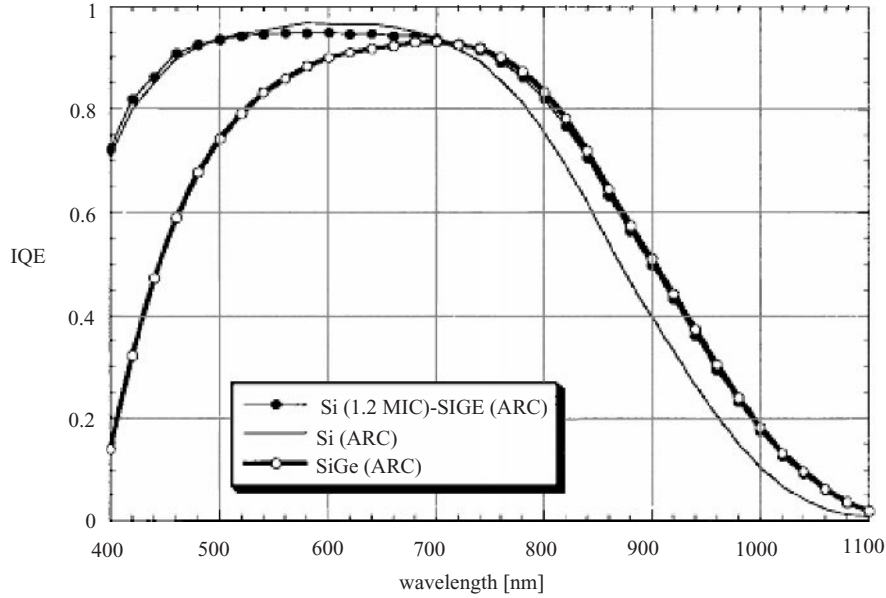

Figure 1.12 IQE-curve of epitaxial solar cell with relaxed SiGe-base ([Ge] = 10 %) and comparison with response of an epitaxial Si solar cell with equal active layer thickness. Reproduced figure 10 with permission from K. Said, J. Poortmans, M. Caymax, J. F Nijs, L. Debarge, E. Christoffel, A. Slaoui, 'Design, fabrication, and analysis of crystalline Si-SiGe heterostructure thin-film solar cells', IEEE Trans. El. Dev. Vol.46, no:10; Oct.1999; p.2103–10. Copyright (1999) IEEE.

fill factor were substantially lower than for the Si reference cell. One of the important items when using $Si_{1-x}Ge_x$-alloys is the surface passivation. Although the use of plasma enhanced chemical vapor deposition (PECVD)-nitride passivates the front surface to some degree, the blue response of the cell is significantly lower than for a Si reference cell. The blue response is improved by the use of a Si capping layer on top of the structure. The positioning of the Si–$Si_{1-x}Ge_x$ transition relative to the junction is very important to avoid excessive recombination near the interface between the Si capping layer in which the emitter is diffused and the $Si_{1-x}Ge_x$ base layer. The Si on top relaxes in its turn resulting in a defect density in the Si layer of the order of 10^7 cm^{-2}. The internal quantum efficiency (IQE) curve in Figure 1.12 shows the effect of enhanced red response in the base resulting from the alloying with Ge and the improved blue response by the use of an optimized Si capping layer. But even under these circumstances the voltage penalty is too high to get an improved efficiency as compared to the thin film crystalline Si reference cell, as can be seen from Table 1.1.

1.3.3 Germanium–Silicon structures

In order to avoid crystallographic defect formation occurring upon relaxation of a SiGe layer with a thickness larger than the critical thickness, other approaches have been proposed and tested recently. One approach consists in growing Ge layers embedded in a Si matrix by forming three-dimensional islands in the Stranski–Krastanov growth mode. The embedded Ge layers

Table 1.1 AM1.5 illuminated I-V-characteristics of a thin film epitaxial $Si_{.9}Ge_{.1}$ solar cell on a p^+-Si substrate in comparison to thin film crystalline Si solar cell on the same substrate. The active layer thickness was 15 μm with a Si capping layer of 1 μm

Active layer material	Short circuit current [mA cm^{-2}]	Open circuit voltage [mV]	Fill factor [%]	Efficiency [%]
$Si_{.9}Ge_{.1}$	28.8	575	77.5	12.8
Si	27.9	634	79.2	14.0

increase the infrared absorption in the base of the cell to achieve higher overall photocurrent and to overcome the loss in open circuit voltage of the heterostructure. Usami *et al.* [57] report on the performance of solar cells with stacked self-assembled Ge dots in the intrinsic region of Si-based p-i-n diode. These dots were epitaxially grown on p-type Si(100) substrate via the Stranski–Krastanov growth mode by gas-source molecular beam epitaxy. The layer stack is shown in Figure 1.13a.

An enhanced external quantum efficiency (EQE) in the infrared region up to 1.45 μm was observed for solar cells with stacked self-assembled Ge dots compared with the structure without Ge dots, as can be seen from Figure 1.13b. Furthermore, the EQE was found to increase with increasing number of stacked layers. Similar work was reported by Presting *et al.* [58]. In an ultra high vacuum molecular beam epitaxy (UHV-MBE) chamber up to 75 layers of Ge, each about eight monolayers thick, separated by Si-spacer layers (9–16 nm) were grown on each other using standard 10 Ω-cm p-type Si-substrates. The density of islands in the layers was increased by the use of antimony as surfactant resulting in densities $>10^{11}cm^{-2}$. The islands were covered by a 200 nm thick Si-layer (n-type) on top which is used as the emitter of

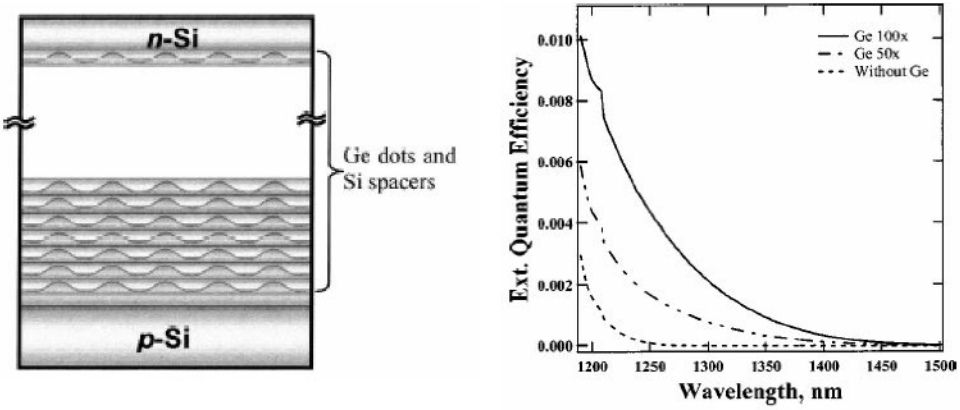

Figure 1.13 a) Cross-section of the Si-Ge layer structure grown in [57]; b) spectral photocurrent extracted from the structure in [57]; Reused with permission from Arnold Alguno, Applied Physics Letters, 83, 1258 (2003). Copyright 2003, American Institute of Physics.

the cell. Photocurrent measurements confirmed the higher response of the fabricated solar cells in the infrared region compared to standard Si-cells. It remains unclear whether the voltage penalty can be overcome by this approach.

For the sake of completeness, it has to be noted that, within the frame of space solar cells, the growth of GaAs layers on a Si-carrier has received a lot of attention. Very often, a Ge template layer is grown between the Si substrate and GaAs active layer to accommodate the lattice mismatch between Si and GaAs [59, 60]. The discussion of these advanced approaches goes beyond the scope of this chapter.

1.3.4 Epitaxial layers on a buried backside reflector

Despite the clear experimental evidence of enhanced photocurrents, no group has been able to prove experimentally that the current increase from including a $Si_{1-x}Ge_x$ alloy or embedded Ge layers in the active layer structure of the solar cell is sufficient to overcome the voltage penalty. As a result the photocurrent increase does not result in an enhanced efficiency as compared to Si solar cells with equal active layer thickness. Therefore substantial effort is being put into developing material systems which allow reflection at the interface between the Si substrate and the Si epitaxial layer and thereby allow optical confinement. Reflection can only occur by having a medium with a different refractive index in between the Si substrate and the epitaxial layer. The main restriction within the context of this chapter is that this medium should allow epitaxial growth. Grossly speaking, one can distinguish two basic solutions, which are shown in Figure 1.14. The first one is based on the use of a porous Si interlayer. By means of the porosity one can control the refractive index while at the same time the porous Si acts a template for epitaxial growth by retaining the crystallographic information of the substrate beneath (at least when the porous Si is formed by anodization in an HF-containing solution). The second solution relies on epitaxial overgrowth over a dielectric or metallic layer with windows allowing a crystallographic connection to the Si substrate.

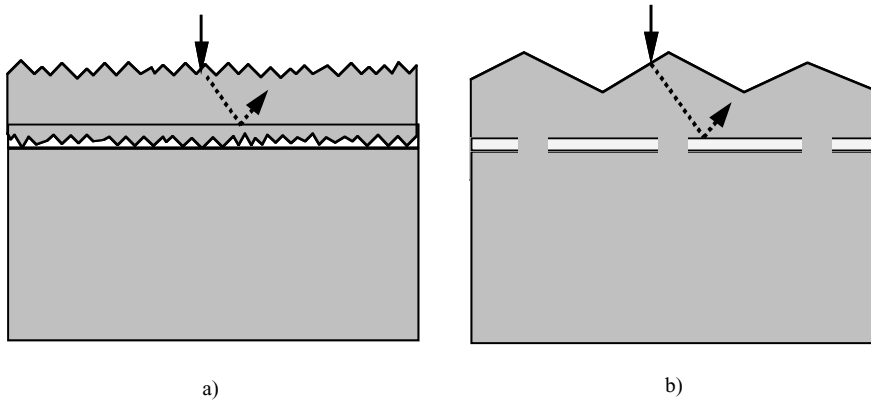

Figure 1.14 a) Schematic of porous Si interlayer approach; b) Schematic illustration of lateral epitaxial overgrowth approach

1.3.4.1 Epitaxial layers on buried porous Si interlayers

Electrochemical etching of porous silicon is an excellent technique to create multiple Bragg reflectors that can be used, for instance, in optical cavities. The refractive index of the different layers of the Bragg reflector are controlled by the porosity, which is determined by the anodization conditions (current density, HF-concentration in the solution). As porous silicon retains the crystallographic information of the original crystal it is etched into, the application of a silicon deposition process can lead to ordered deposition defined by the original crystal structure of the substrate. It therefore seems ideal for the purpose described above [61, 62].

Significant efforts have been made to model and optimize the reflectance of the porous Si interlayer. Zettner *et al.* [61] and Abouelsaood *et al.* developed a model for light propagation in porous silicon (PS) based on the theory of wave propagation in random media [63]. The modeling in the latter is based on silicon being the host material in combination with randomly distributed spherical voids as scattering particles. The specular and the diffuse part of the light scattering were determined and treated separately.

The challenge in the experimental implementation of this concept is to maintain the reflector properties during the silicon deposition process, which often takes place at high temperature, where porous silicon is not stable. Porous silicon tends to reorganize itself towards a low energy configuration with larger, spherical voids. Moreover, a phenomenon of pore filling can occur: some of the deposited silicon enters and gets incorporated in the porous structure, lowering the porosity. Two approaches can be followed. One can attempt to preserve the porous silicon structure as much as possible by carrying out the deposition at low temperature, for instance with LEPECVD [64]. This technique allows one to deposit a Si film with an epitaxial quality on the top of PS without destroying its multilayer structure (as revealed by high-resolution X-ray diffraction and cross-sectional transmission electron microscopy shown in Figure 1.15a). The epilayers of 10 μm are grown at very high deposition rate (around 3 nm/s) at 590 °C. TEM-analysis reveals that during the deposition a high density of defects forms at the interface PS/epi-Si and spreads through the whole epilayer. The defect density is decreased when the deposition temperature is increased to 645 °C. The second approach is to carry out epitaxy at high temperature, and live with the reorganization that will inevitably occur. Remarkable

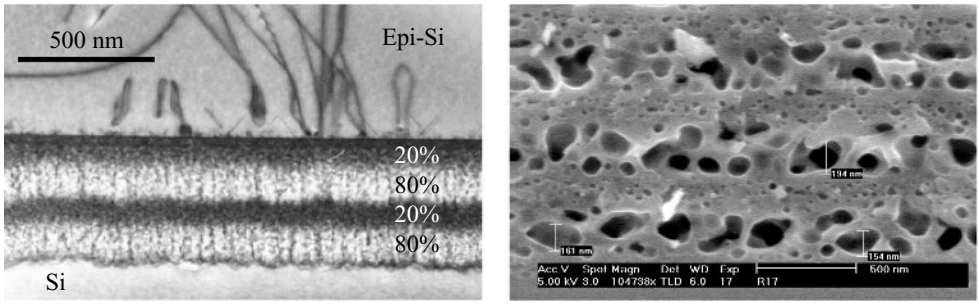

a) b)

Figure 1.15 Buried porous silicon reflectors: a) TEM-picture of epitaxial layer grown on top of a porous Si layer structure at low temperature; b) SEM micrograph of an annealed porous Si reflector consisting of multiple high-porosity/low-porosity bi-layers. The porous layer was subjected to an annealing at T = 1150 °C.

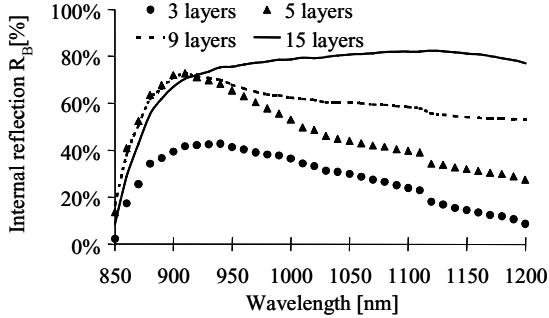

Figure 1.16 Curves of the back reflectance derived from reflectance measurements, achieved with differerent PS reflectors (from reference [[67]).

results with this approach were recently reported [65]. Porous silicon multilayers consisting of several low-porosity/high-porosity stacks were formed by electrochemical etching on highly p-doped single crystalline silicon. The samples were then brought to high temperature and underwent an epitaxial deposition process with thermal CVD. A scanning electron microscopy (SEM) micrograph of the structure in Figure 1.15b clearly shows that the porous silicon, with original pore size in the order of a few nanometers, has completely reorganized into layers with large voids and wide pore walls. The overall structure with alternating high/low porosities is, however, maintained. Strikingly, the structure after reorganization appears to function rather well as a Bragg mirror. This can be seen in Figure 1.16, where the internal back reflectance (R_B) at the porous silicon/epitaxial layer interface, as calculated from the samples' total reflectance, is plotted as a function of the wavelength. The internal reflectance increases with the number of porous silicon layers and reaches a top value around 80 % for a stack of 15 layers in a broad wavelength range. Resistance measurements show that this type of buried reflector does not significantly hinder the vertical flow of majority carriers. It therefore shows great promise for high current epitaxial solar cells.

Liquid phase epitaxy has also been studied for growing Si epitaxial layers on porous Si. In [66] the porous silicon formation by HF anodization on (100) or (111) Si wafers is realized in the first step, followed by annealing in an H_2 atmosphere, and finally LPE silicon growth was made with different temperature profiles in order to obtain a silicon layer on the sacrificial porous silicon (p-Si). Pyramidal growth was found on the surface of the (100) porous silicon but the coalescence was difficult to obtain. However, on a p-Si(111) oriented wafer, homogeneous layers were obtained.

Besides acting as a template for epitaxial growth, the porous Si buried layer can also act as a gettering layer to prevent contaminants from diffusing from the Si carrier substrate into the active epitaxial layer. The principle of using porous-silicon-gettered MG-Si as a low cost epitaxial substrate for polycrystalline silicon thin film growth for solar cells has been proven by Tsuo *et al.* [67].

1.3.4.2 Epitaxial lateral overgrowth

Epitaxial lateral overgrowth (see Figure 1.14b) is a well known technique which is often based on selective epitaxial growth of Si through openings in a dielectricum. The dielectricum

most often studied as a masking layer is thermal oxide. Selectivity in CVD is obtained by controlling the balance between Si etching and growth in a Cl-containing atmosphere. In order to overgrow the dielectricum, the lateral growth rate is preferentially enhanced as compared to the vertical growth rate. As this is a difficult task, the only way to obtain closed Si layers over the dielectricum is to keep the distance between the openings approximately two times the desired layer thickness.

Because of its close-to-equilibrium character, it is most often easier to grow with a selectively high horizontal to vertical growth by means of LPE. The growth is mostly done on (111) Si substrates as this allows the growth of smooth layers [68] (see Figure 1.17a), although the *in situ* texturing during LPE-growth on (100) Si substrates would be a valuable asset. An interesting variation on this theme is the creation of a buried reflector by means of electrodeposition. The proof-of-concept was done on patterned, metal-masked silicon substrates by a liquid-phase electro-epitaxial lateral overgrowth process [69] (see Figure 1.17b). Silicon films were grown from liquid metal solutions (molten bismuth saturated with silicon) by current-induced crystallization on stripe-patterned, W-masked (111) silicon substrates. Tungsten was chosen because it resists the high temperatures during the electrodeposition and is not chemically attacked by the molten metal. Growth temperatures range from 800 to 1150 °C, and a current density of 2–20 A/cm^2 was imposed across the silicon/melt interface to enhance the lateral growth. Continuous (over 1 cm^2 areas) epitaxial layers of silicon were achieved on W-masked substrates patterned with 10 μm wide stripe openings spaced 100 μm apart.

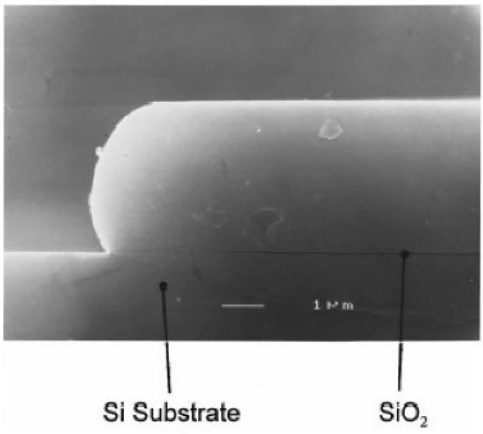

a)

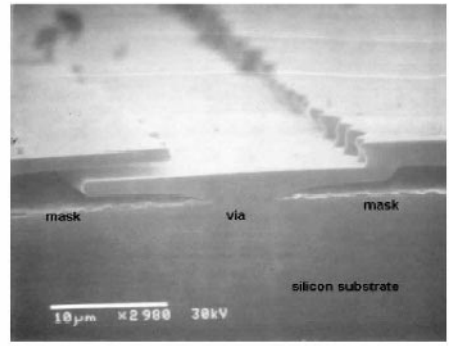

b)

Figure 1.17 a) Epitaxial lateral overgrowth by means of LPE through openings in a dielectricum layer on top of a (111) Si substrate. The experimental aspect layer width/layer height ratio is 43, the picture was taken from ref. [68]; Reused with permission from H. Raidt, Journal of Applied Physics, 80, 4101 (1996). Copyright 1996, American Institute of Physics.; b) Illustration of the electro-epitaxial lateral overgrowth over a tungsten buried reflector (taken from ref. [69]). Silicon is growing from the stripe opening in mask. The right side has been connected with the silicon overlayer seeded at the adjacent via, but the left side is misaligned and interleaved with silicon at adjacent via. Reproduced with permission from *Journal of Crystal Growth,* **225**, M. G. Mauk and J. P. Curran, Electro-epitaxial lateral overgrowth of silicon from liquid-metal solutions', pp. 348–353. Copyright (2001) Elsevier.

1.4 EPITAXIAL SOLAR CELL RESULTS AND ANALYSIS

1.4.1 Laboratory type epitaxial solar cells

Although the substrates of interest for epitaxial solar cells are low cost Si substrates, substantial work has been reported on reference mono- and multicrystalline Si substrates. Epitaxial cells on highly doped monocrystalline Si substrates were reported by several groups in the early nineties to demonstrate the efficiency potential of the epitaxial solar cell approach (see e.g. references [70] for CVD-grown cells and [71, 72] for LPE-grown Si layers). Table 1.2 provides an overview of the best efficiency results obtained in epitaxial layers grown by various techniques and processed according to different *laboratory* solar cell process schemes. The experimental results obtained on monocrystalline highly doped substrates confirm the large efficiency potential of thin film crystalline Si solar cells, especially when combined with a suitable backside reflector (the intermediate oxide layer in case of the silicon-on-insulator by implantation of oxygen (SIMOX substrate or by etching back the Si substrate to improve the optical confinement properties of the structure). Some reports provide an indication that crystallographic defects in the epitaxial layer are created by the lattice mismatch which exists between the highly doped Si substrate and the epitaxial layer. This lattice mismatch is small but in view of the large thickness of the epitaxial layer, strain relaxation occurs through the introduction of misfit dislocations [73].

When epitaxial growth by means of CVD is performed on highly doped multicrystalline substrates (ribbons, MG-Si, p^+-multicrystalline Si), the efficiencies of laboratory type cells are clearly lower as compared to the demonstration epitaxial cells on monocrystalline Si substrates.

Table 1.2 Overview of main results on laboratory type epitaxial cells

Growth technique	Type of substrate	Thickness [μm]	Cell area [cm^2]	Solar cell process	Efficiency [%]
CVD-grown epitaxial layers					
CVD	Mono (SIMOX)	46	4	High-efficiency interdigitated process Evaporated contacts	19.2 [8]
CVD	p^+-Mono	37	4	ISE high-efficiency process	17.6 [78, 79]
CVD	p^+–SILSO	20	4	Homogeneous etched-back emitter Evaporated contacts	13.8 [49]
CVD	p^+-EFG	20	4	Homogeneous etched-back emitter Evaporated contacts	13.2 [49]
LPE-grown epitaxial layers					
LPE	p^+-mono	35	4	Evaporated contacts + back-etch of substrate	18.1 [80]
LPE	p^+-mono	30	4	Evaporated contacts (drift-field in epitaxial layer)	16.4 [76]
LPE	p^+-multi				15.4 [77]

A process step during which H is introduced in the epitaxial layer, either by remote plasma hydrogenation or a firing-through-nitride step has been proven to be crucial to passivate the defects in the epitaxial layers [18, 21, 48, 49]. This has allowed solar cell efficiencies near to 14 % in epitaxial layers of only 20 μm for small-area cells.

Solar cells fabricated on LPE-grown epitaxial layers display open circuit voltages above 660 mV (air mass number (AM) l.5, 25 °C) [74], confirming the high electronic quality of the epitaxial layer. As a result, the best solar cells made in LPE-grown layers have efficiencies in the range 17–18 % [75]. An important step in obtaining these high cell efficiencies is the removal of most of the heavily doped substrate on which the epitaxial layer is grown to boost the backside reflectance. In this way the cell efficiency can be increased by nearly 25 % when the cell is thinned to a thickness of 30 μm. As mentioned earlier, LPE allows the incorporation of a doping profile in a straightforward fashion into the epitaxial layer. In reference [76] a Ga doping gradient was intentionally introduced throughout the film to produce a drift field in the base of the solar cell, thus enhancing the effective minority-carrier diffusion length and increasing the long-wavelength response. An independently confirmed efficiency of 16.4 % was achieved on an LPE drift-field thin film silicon solar cell.

The efficiency potential has been further confirmed by small-area LPE-grown epitaxial cells on multicrystalline Si substrates. Such cells have displayed efficiencies up to 15.4 % [77].

1.4.2 Industrial epitaxial solar cells

Within the context of this chapter, 'industrial solar cell' is equivalent to large-area solar cell ($>20\,cm^2$), made by a production process which is similar to the practices in the PV industry. Although the generic process flow to produce a solar cell in an Si epitaxial layer is very similar to the cell process for a classical Si solar cell, the subject deserves to be treated within a separate chapter for two reasons. First of all, making large-area cells is an indication of the maturity of a certain epitaxial deposition technology (homogeneity in thickness and doping over a larger area). Second by, despite the generic resemblance to the solar cell process, steps like front surface texturing have to be tuned for epitaxial cells. In the latter it does not make sense to use the texturing techniques widely used for bulk crystalline Si solar cells as these techniques would remove most of the epitaxial layer; typically, the texturing step removes 10–20 μm of Si.

The main reported results are summarized in Table 1.3. Efficiencies up to nearly 14 % on Czochralski-silicon (Cz-Si) and 13 % on highly doped multicrystalline Si substrates have been achieved by applying an industrial process scheme based on tube or in-line P diffusion, as well as screen-printed front and back contacts fired through a SiN_x anti-reflection coating [81, 82]. Light-beam induced current measurements show that the diffusion length distribution is quite inhomogeneous over the whole cell area. A maximum effective diffusion length of about 25 μm and mean values around 15 μm were found in typical epitaxial solar cells [83]. Characterization of the solar cells by infrared lock-in thermography revealed local shunts as shown in Figure 1.18. In some circumstances these local shunts were correlated with well defined epitaxial defects [84].

To reduce the front surface reflectance and enhance the optical path length, the front surface of the epitaxial cell should be textured. This is a common step in most industrial processes for bulk crystalline Si solar cells, but the process has to be adapted for epitaxial solar cells. The most crucial element is to minimize the amount of silicon removal to keep the starting thickness of the epitaxal layer as low as possible. One process, already used in industrial solar

Table 1.3 Main efficiency results obtained on epitaxial solar cells produced by industrial process flows

Growth technique	Type of substrate	Thickness [μm]	Cell area [cm^2]	Solar cell process	Efficiency [%]
CVD	p^+-Cz-Si (reclaimed)				13.8[81]
CVD	p^+-SILSO	20	25	Screenprinting (firing through nitride)	12.5 [21]
	Epitaxial layer on grooved p^+-SILSO	20	25	Screenprinting (firing through nitride)	13.2 [21]
	p^+-SILSO	40	20	Laser-grooved buried grid technology	11.9 [21]
CVD	UMG-Si	25	20	Screenprinting (firing through nitride)	12.9[82]
		100	20	Screenprinting (firing through nitride)	12.2[82]
LPE	UMG-Si (melt-back method)	Small area	30	Phosphorus diffusion from pastes	10[86]

cell fabrication to texture multicrystalline silicon solar cells, is based on chemical isotexturing. This wet chemical etching based on HF and HNO_3 starts on the defects of the saw damaged surface, and creates a textured surface with etch pits of 1 to 10 μm in diameter. However, on epitaxially grown layers, this process does not start uniformly because the surface is essentially damage free. Instead of obtaining a homogeneously textured surface, deep holes are formed on the surface at defects in the epitaxial layer. Therefore, a new plasma texturing technique was developed based on SF_6 chemistry and plasma generation with microwave antennas and specifically tuned for epitaxial solar cells. In particular, the amount of Si removal was minimized while keeping the reflectance low. This texturing process removes only 2 μm of the epitaxial

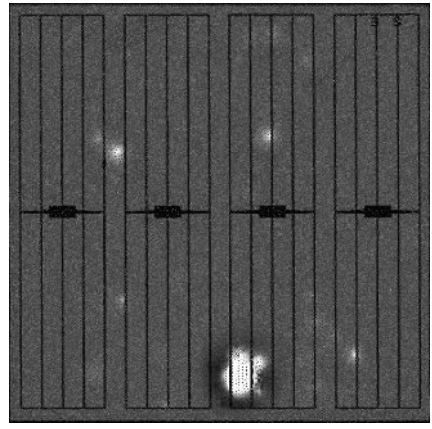

Figure 1.18 Picture showing local shunting paths as revealed by IR-thermography . The fingerstructure is shown in overlay (courtesy of FhG-ISE, Freiburg, Germany).

layer. With this process, efficiencies near 13 % were obtained in CVD-grown epitaxial layers on UMG-Si substrates.

The first modules based on epitaxial solar cells, grown on highly doped monocrystalline or multicrystalline Si substrates, were recently reported [85]. The module based on monocrystalline substrates showed an efficiency of 12.2 % (cell aperture area was 368 cm^2), whereas the one based on multicrystalline Si gave an efficiency of 10.2 % (the aperture area in this case was 576 cm^2). Both results give evidence of the fastly progressing maturity of this solar cell technology.

Industrial type solar cells have also been realized on LPE-grown layers. In comparison with CVD-grown epitaxial layers where the difference between industrial and laboratory type solar cell efficiencies is in the range of 1 % (for layers grown on highly doped multicrystalline Si substrates), the efficiency gap is much larger between laboratory type and industrial LPE solar cells. This is caused by the difficulty in obtaining LPE-layers with uniform topology over the whole area. Solar cells, fabricated by a P paste diffusion, have shown efficiencies up to 10.0 % [86].

1.4.3 Special epitaxial solar cell structures

Front grid contacted thin epitaxial silicon solar cells based on the growth of crystalline silicon films on a substrate or superstrate have been reported for many years, as have wafer based solar cells with alternative contact approaches. Integrating these two concepts into a single device presents an opportunity for simultaneously reducing two major loss mechanisms associated with crystalline silicon solar cells. A proof-of-concept thin epitaxial silicon solar cell with an embedded semiconductor grid as an alternative to a conventional front metallic grid was developed by Aiken *et al.* [87] by means of lateral epitaxial overgrowth (see Figure 1.19). It resulted in a thin epitaxial silicon solar cell with a 7.8 % designated area conversion efficiency, well isolated contacts, negligible series resistive power loss, and less than 1 % shading of the designated area.

1.5 HIGH THROUGHPUT SILICON DEPOSITION

Despite its generic resemblance to a classical bulk crystalline Si solar cell process, the development of a manufacturing technology based on epitaxial solar cells requires two additional issues to be solved. The first is related to the commercial availability of a low cost Si substrate.

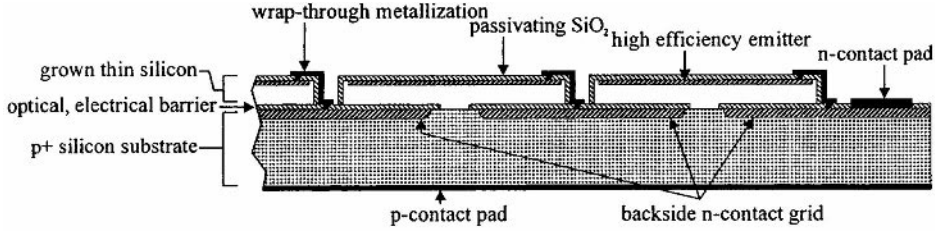

Figure 1.19 Schematic of the novel epitaxial cell structure as developed by Aiken *et al.*

As shown in the previous chapters there is ample evidence that efficiencies near 14–15 % are achievable in the short term with an epitaxial cell process using MG-Si substrates. The availability is mainly a matter of upscaling the infrastructure to produce this feedstock material as well as finding companies willing to crystallize this material to produce large multicrystalline Si ingots and to wafer them.

The second issue concerns the development of high throughput deposition equipment to grow epitaxial layers at a rate of several m^2/h for epitaxial layer thicknesses between 5 and 20 μm. This throughput is definitely higher than typically reached in commercial epitaxial reactors as developed for the microelectronic sector, which are rather aimed at obtaining a very high uniformity of thickness and doping (in the order of 1 %). The same upscaling challenge exists obviously for other thin film technologies based on a-Si:H or μc-Si:H layers, but in the case of epitaxial cells, the technical difficulties to be solved are considerable. In order to achieve high growth rate in the order of a μm/min and high crystallographic quality the temperature range of interest is between 800 °C and 1300 °C, which requires the use of materials withstanding high temperatures. Despite the high temperature prevailing during deposition, contamination of the crystalline Si layer during growth has to be prevented, putting stringent requirements on the purity of the used materials. But both in CVD and LPE one is confronted with potentially corrosive and aggressive gases or liquids. Finally there are conflicting requirements concerning the chemical efficiency[7] of the Si deposition process and the thickness uniformity. A high uniformity normally does not go along with a high efficiency since the latter points to a depletion in the gas phase. Even taking into account that the uniformity requirement for thickness and doping is in the order of 10 %, it remains a considerable issue.

Even when these problems are satisfactorily solved, the reliability and safety of the developed deposition equipment over time as well as its low cost-of-ownership will have to be proven. The allowable cost comprising the depreciation of the investment cost, and the cost of consumables (gases, susceptors, . . .) and maintenance depends obviously on the efficiency reached, but in order to be compatible with 1 € /W_p this should not be higher than 20 € /m^2, assuming a module efficiency of 14 % [15].

Clearly, presently one has not yet reached this point. Rather one sees presently a number of emerging high throughput deposition reactor concepts to tackle the main challenges. These concepts are aimed essentially at upscaling the CVD and LPE methods and will be discussed in the next sections. It should not come as a surprise that the upscaling efforts are mainly focusing on CVD and LPE giving their relative maturity versus other solutions like IAD. It is expected that the build-up of sufficient confidence in these reactor concepts will still require a number of years before one can foresee their integration into existing solar cell production lines.

1.5.1 Chemical vapor deposition reactor upscaling

1.5.1.1 Continuous chemical vapor deposition reactor

The first reactor concept comes closest to the in-line solar cell processing concept which one encounters in most present production facilities for bulk crystalline Si solar cells. It is

[7] Chemical efficiency is defined as the ratio of the Si which ends up in the active layer versus the amount of Si introduced in the gaseous or solid phase.

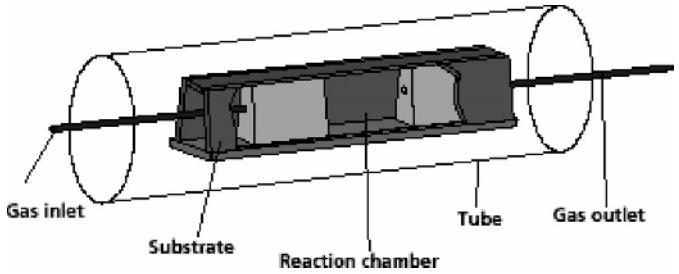

Figure 1.20 Schematic view on the tube-in-tube concept for the continuous CVD system developed at FhG-ISE, Freiburg; courtesy of FhG-ISE, Freiburg.

essentially based on continuous transport of the wafers through the hot reaction zone where the epitaxial deposition takes place. In order to achieve a high conversion efficiency ($Si_{(g)} \rightarrow Si_{(s)}$) with only minor parasitic depositions, this reactor concept relies on a tube-in-tube concept [88, 89]. The rectangular substrates form the side walls of the reaction chamber (the inner tube) and constitute the largest part of its inner surface. The chamber is placed within the outer tube, flooded by H_2 or inert gas. The reactive gases, a mixture of $SiHCl_3$ (TCS) and H_2, are fed into the chamber and deposition occurs. In the continuous CVD (Con-CVD) reactor two rows of substrates slide continuously along the chamber, as shown in Figure 1.20. This also solves the problem of lateral uniformity and gas depletion as all substrates pass through the same reaction profile. To prevent, or at least reduce, the outdiffusion of reactive gases from the chamber into the outer tube, a small overpressure is maintained.

A gas curtain system ensures the separation between the inner atmosphere in the reaction zone and the outer atmosphere. This allows the substrates to be fed into and out of the reactor in a continuous way without gas exchange between reactor and laboratory. It is based on the behaviour of a gas diffusing against the flow of another gas. A small flow in the order of some cm/s reduces the concentration of the diffusing gas after a few centimetres against the flow direction to negligible values. Figure 1.21 shows the principle of the gas curtain systems which are installed at both ends of the reactor tube.

FhG-ISE has built the first test reactors using this concept [88, 89]. The most important features of the ConCVD reactor are shown in Figure 1.22.

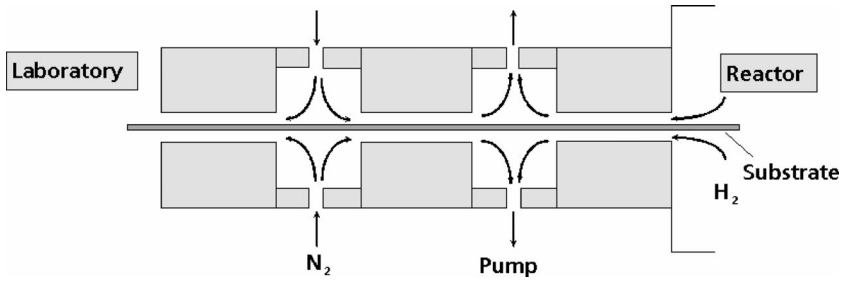

Figure 1.21 Gas curtain system to separate inner reactor atmosphere from outer atmosphere in the continuous CVD apparatus. See also [89].

a)

Open system with gas curtains and two rows of continuously moving substrates

Substrate temperature up to 1300 °C, resistively heated

Reactor tube SiC, 30 cm Ø

Reaction chamber: graphite, 40 cm long

Two rows of graphite carriers for the substrates: substrate width 10 or 20 cm, substrate length up to 40 cm; substrates of 10 cm width are placed in two rows one upon the other on each carrier

Gas lines into the reaction chamber for H_2, $SiHCl_3$ and B_2H_6, for H_2 or inert gas into the tube

Production rate at 5µm/min average deposition rate: 1.4 m_/h for Si layers of 30 µm thickness

b)

Figure 1.22 a) View on the ConCVD apparatus available at FhG-ISE, Freiburg; b) Summary of the main features of the present ConCVD-reactor.

Using this reactor, epitaxial layers were grown at 1150 °C on highly doped multicrystalline Si substrates at a deposition rate of about 1.5 µm/min and a throughput of 1.2 m^2/h. Using a relatively simple solar cell process, an efficiency of 12.5 % was reported [90].

First cost estimations have been made for this type of reactor. A production type ConCVD system featuring a 2m long reaction chamber (instead of the present 0.4 m) at 200 mm width would have a throughput of 150 000 m^2/year which in the end results in an estimated cost for silicon epitaxy of around 10 € /m^2, which is compatible with the cost goal stated before. The major cost share is H_2 consumption, which can be further decreased by application of state-of-the-art H_2 recycling [88].

1.5.1.2 Convection assisted chemical vapor deposition

Convection assisted CVD (COCVD) is a recent development which actively uses thermal convection to control the gas flow inside the reactor and to implement, in a natural manner, recycling of the nonused gaseous precursor. The concept of COCVD is shown in Figure 1.23 [91]. The reactor is tilted by an angle α against the horizontal orientation. Cold gas is fed into the reactor and flows downward along the cold wall that is positioned opposite to the substrate. The gas moves upwards on the substrate side where it is heated, an effect which also drives the convection. Part of the gas leaves the reactor through the outlet while the portion far from the substrate stays in the convection roll for another turn. This corresponds to an internal 'recirculation' mechanism which reduces the amount of TCS that is required to grow a given layer thickness. It is easily understood that the inclination of the substrate and the bottom wall is crucial to the convection.

1.5.1.3 Batch type epitaxial reactors

Despite the tremendous progress achieved with the ConCVD and COCVD reactors there is still a long way to go before the reliability and safety of both concepts will be fully proven. In the microelectronics sector large vertical batch type furnaces, based on SiH_4 as Si-precursor, have been developed for 200 and 300 mm wafers with throughputs in the order of 100 wafers/h, which corresponds to 5 m^2/h. Adapting the poly-Si deposition processes for thicker poly-Si layers (like for power electronics applications) by using slightly higher temperatures (100–200 °C higher) and reducing the uniformity specs to 10 %, the required cost goals might also be attainable with such deposition systems.

The first indications that suitable epitaxial quality is reachable in such systems have been obtained in a batch type LPCVD system [92]. The system consists of a resistively heated quartz tube connected to a pump system at one end and closed with a quartz door at the other (the thermal insulation between door and reaction volume is realized by a vacuum-pumped quartz belljar). Si layers can be grown on 20 wafers simultaneously, using a system which allows removal of the unwanted Si deposition on the reactor walls by using a quartz insert which can be easily removed from the system. The wafers can be arranged in several configurations as shown in Figure 1.24a and b. The horizontal set-up results in a thickness variation below 20 % for five 5 × 5 cm^2 samples, which is acceptable for solar cell applications. High quality epitaxial layers have been obtained, a fact illustrated by solar cells produced in layers grown on p^+-monocrystalline Si substrates [93]. For a process with a low deposition rate (between 20 and 50 nm/min) a defect density of 10^4 defects/cm^2 can be obtained. This value is comparable with

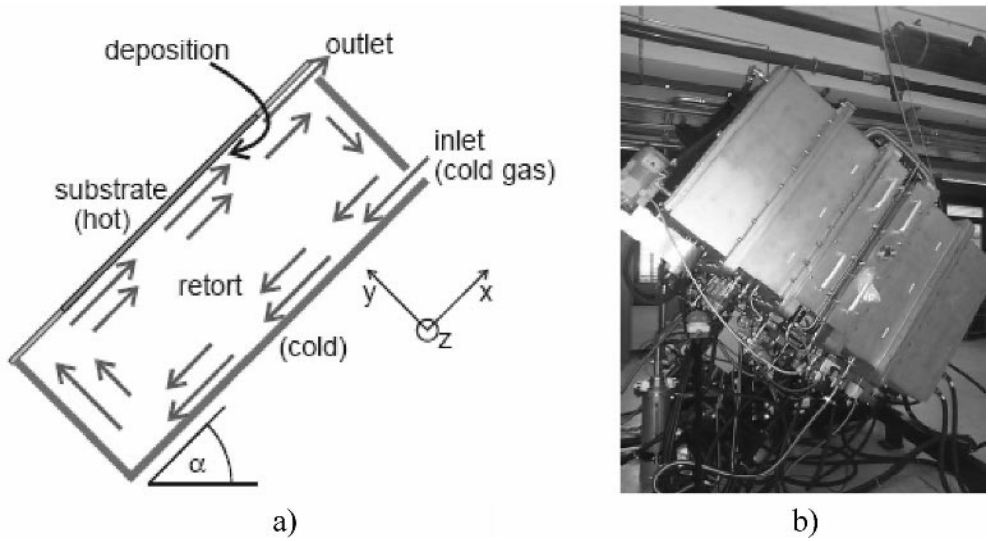

Figure 1.23 a) The concept of convection-assisted chemical vapor deposition. The flow of feed gas is enhanced and stabilized by thermal convection. The convection is governed by the reactor inclination angle α. Reproduced with the permission from Proc. 19th Europ. PVSEC, Paris, (2004), p. 1241. Copyright (2004) Thomas Kunz, ZAE Bayern e.V; b) Photograph of the new CVD system. Reproduced with the permission from Proc. PVSEC-15, Shanghai, (2005), p.190. Copyright (2005) Thomas Kunz, ZAE Bayern e.V.

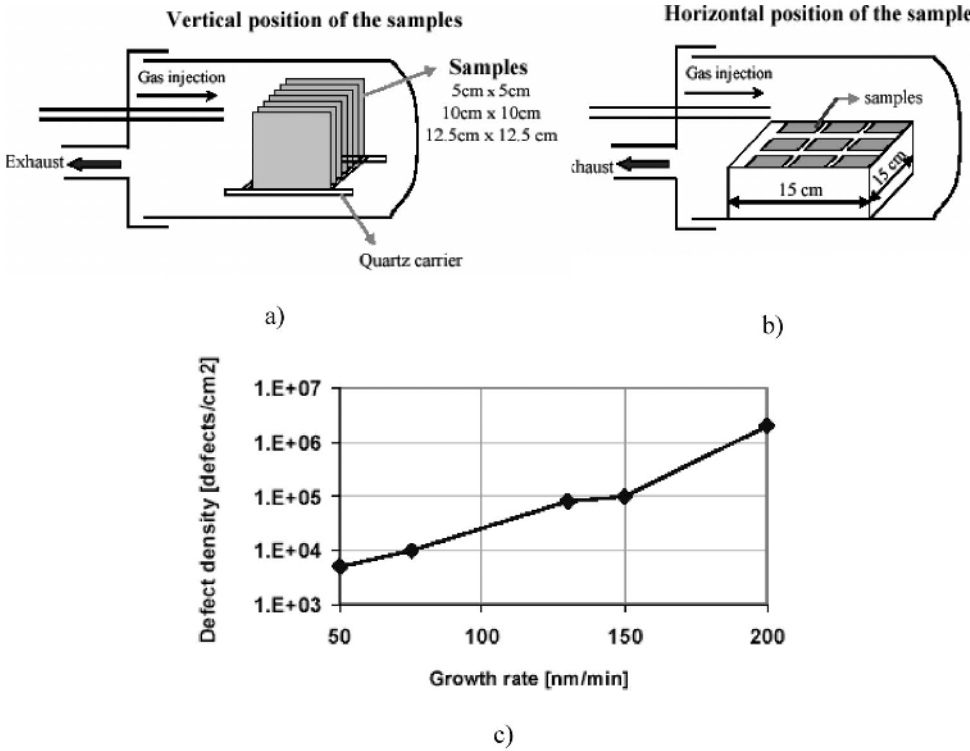

Figure 1.24 a) and b) Basic configuration of the LPCVD system and wafers stacking used in Reference [92] and [93] c) Dependence of the defect density on the deposition rate in the LPCVD-system.

the quality of the epitaxial layers on the same type of highly doped substrates grown in a commercial reactor. By increasing the partial pressure of the SiH_4 flow in the total gas flow, an increase in growth rate can be obtained. The defect density of the grown layers increase strongly as a function of the deposition rate as shown in Figure 1.24c.

An alternative batch type reactor concept is the so-called stacked epitaxial reactor [94] (SER) which is based on densely packed resistively heated graphite susceptors as shown in Figure 1.25a. The concept (shown in Figure 1.25b) is based on pioneering work in the eighties [95]. The shown configuration results in highly efficient and homogeneous heating. Presently, a prototype of this reactor is being built including a H_2 recirculation system. The required H_2 gas flow to the system is high to keep the temperature in the gas bulk sufficiently low as to avoid dust formation. Without H_2 recirculation, the economics of the approach would be endangered. The system is foreseen to operate at atmospheric pressure in a mass transport controlled regime, although in the prototype the possibility is foreseen to also operate at low pressure.

1.5.2 Liquid phase epitaxy reactor upscaling

For LPE reactor upscaling one can also make the same distinction between in-line concepts and batch type concepts. In general, the concepts have not yet reached the same maturity as the CVD concepts.

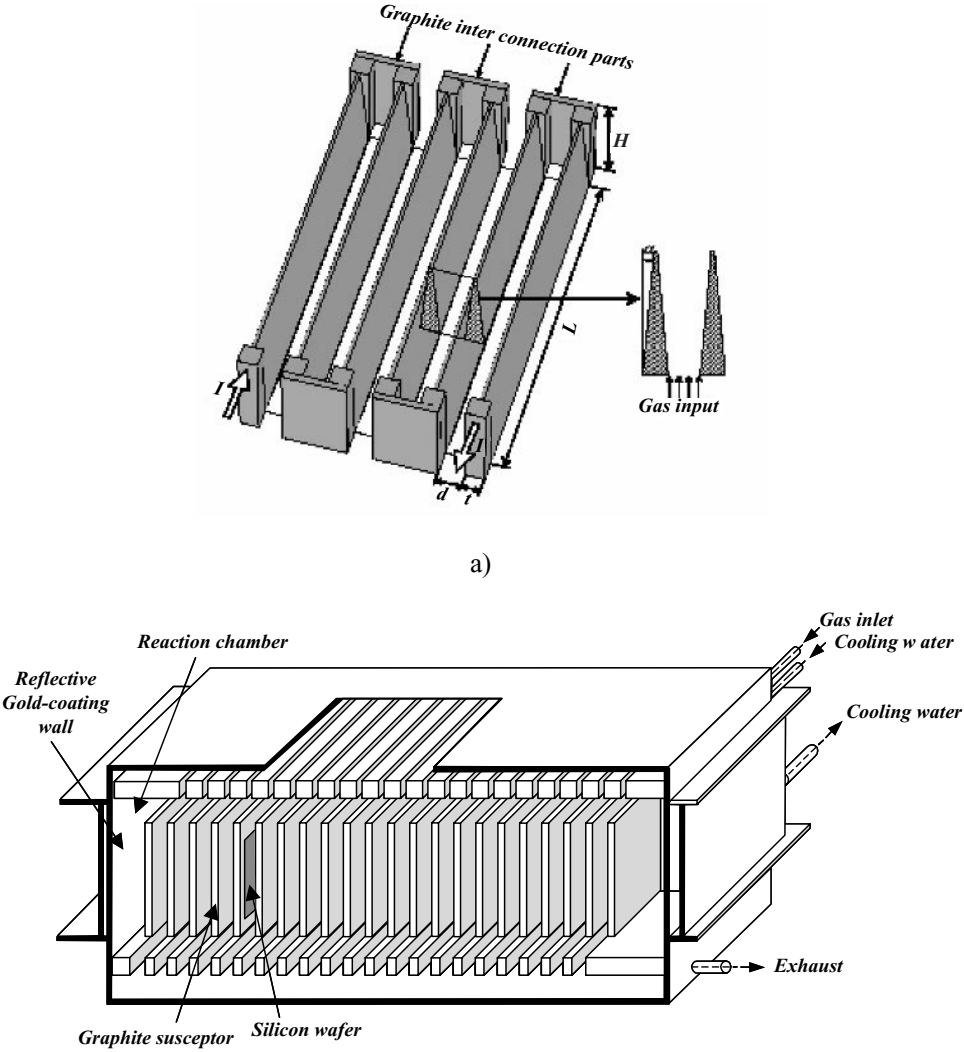

Figure 1.25 a) Graphite susceptor configuration in the SER reactor and detail of the cross-section of an interduct; b) Artists' view of the SER-concept.

1.5.2.1 Temperature difference method

The temperature difference method (TDM) is a promising quasicontinuous technology for the growth of thin film silicon from solution on large-area multicrystalline substrates ($10 \times 10\,\mathrm{cm}^2$) [96, 97]. It was originally developed by Nishizawa [98] and has been used for the deposition of III-V semiconductor layers for luminescent devices. The thermodynamic driving

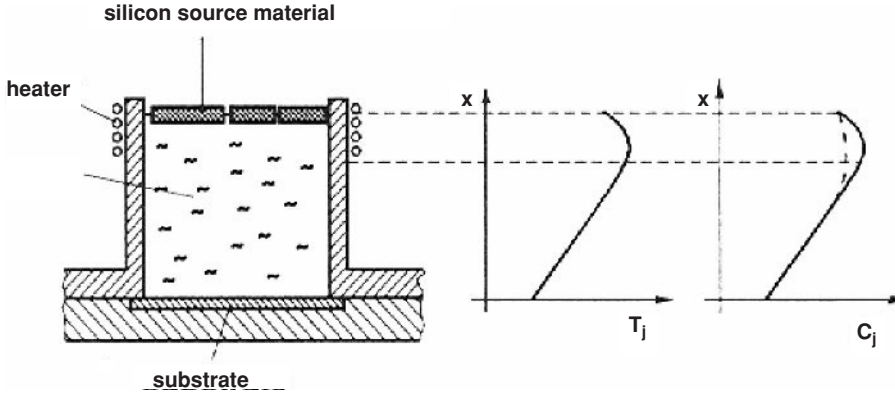

Figure 1.26 Principle of the temperature difference method (taken from reference [97]); the heater at the top ensures the temperature difference between source and substrate; Reproduced Figure 1 with permission from B. Thomas, G. Muller, P.-m. Wilde, and H. Wawra, Properties of silicon thin films grown by the temperature difference method (TDM), *Conference Record of the 26th IEEE Photovoltaic Specialists Energy Conference, Anaheim*, 771–774, 1997. Copyright (1997) IEEE.

force for layer growth by TDM is generated by a temperature gradient perpendicular to the substrate surface as shown in Figure 1.26. This temperature gradient results in a concentration gradient over the melt. This gradient is the driving force for layer growth on the substrate. Because the temperature remains constant during growth, the temperature dependence of the solubility does not influence the layer composition.

Silicon thin films have been grown from In/Ga solutions with growth rates up to 0.3 μm/min. Minority-carrier lifetimes of 5–10 μs were determined in 30 μm thick epitaxial layers both on mono- and multicrystalline Si substrates, which is remarkably high taking into account the absence of any H-passivation treatment

1.5.2.2 Batch type multiwafer liquid phase epitaxy system using melt-back

Standard LPE setups like the 'sliding boat approach' are not compatible with large batch type processes because of the necessity to change the solvent after each epitaxial growth as the amount of dissolved Si has diminished. The University of Konstanz is therefore developing a system, based on dipping the substrates into an 'infinite source' [99, 100], the principle of which is shown in Figure 1.27a. The present system (see Figure 1.27b) is capable of handling 16 substrates at a time, but there is no basic lemitation for further upscaling. An interesting asset of the proposed approach is the melt-back step, carried out before each growth process to supply silicon to the melt from the UMG-Si [100, 101] instead of adding electronic grade silicon to the solution. The upgrading of the Si material, done in this way, is probably more energy efficient than the purification of metallurgical grade Si. Small-area (3 cm^2) solar cells produced in these LPE layers by means of a solar cell process compatible with industrial practice showed efficiencies around 10 %.

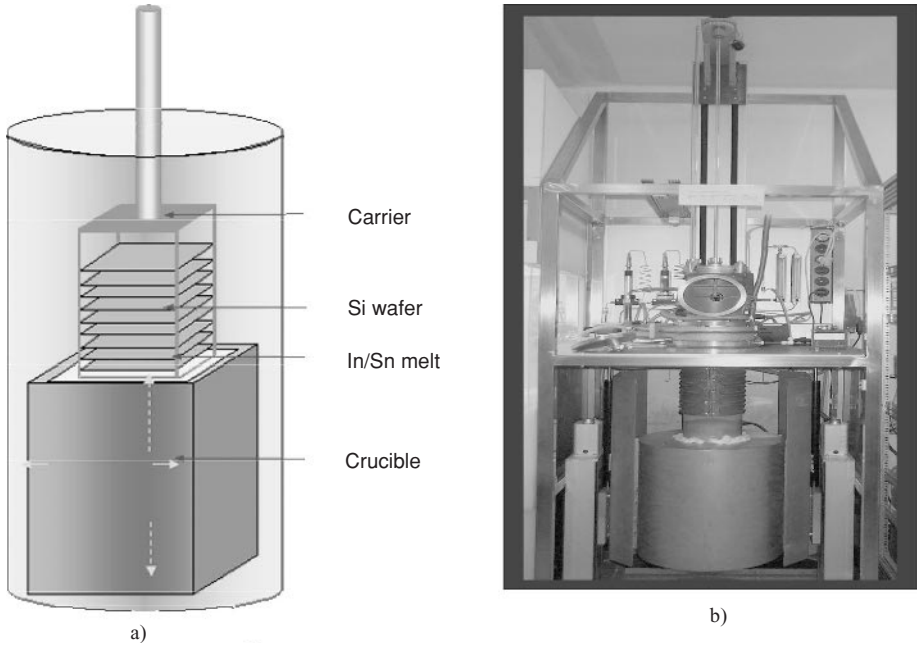

Figure 1.27 a) Schematic view on the batch-type LPE system based on dipping the substrates in an 'infinite source'. b) Present system. Courtesy of University of Konstonz.

1.6 CONCLUSIONS

Epitaxial thin film solar cells represent a technology that is very different from other thin film technologies but is rather close to the dominant bulk silicon solar cells. As such it is an appealing option in scenarios of gradual transition from wafer based solar cells to thin film monolithic modules. The potential cost reduction, while not as dramatic as for some other thin film technologies, is nevertheless substantial. Importantly, the technology would decrease the dependency of the PV industry on poly-Si feedstock. Thin film epitaxial cells show a high level of maturity, with industrial type solar cells reaching efficiencies of about 13 %. To further increase performance, optical confinement is necessary. Recent developments on buried porous silicon reflectors indicate that the path length enhancement necessary to reach efficiencies similar to those of bulk solar cells is achievable. Several deposition techniques have been investigated, but technologies based on thermal CVD are the most mature and give the best results. However, a prerequisite for future commercialization of the technology is the availability of a dedicated high throughput epitaxy system. This is therefore a very important topic in current epitaxial solar cell research and development.

REFERENCES

[1] R. Brendel and D. Scholten, 'Modeling light trapping and electronic transport of waffle-shaped crystalline thin-film Si solar cells', *Applied Physics A (Materials Science and Processing)*. vol.A69, no.2; p.201–213. (1999).

[2] J. Palm, W. Krühler, W. Kusian, A. Lerchenberger, A. L. Endrös, G. Mihalik, B. Fickett and J. Tester, 'Characterization of Tri-crystalline Silicon for photovoltaic applications', *Proceedings of the Twenty-eighth IEEE Photovoltaic Specialists Conference*, Anchorage 15–22 September 2000, p.40–45 (2000).

[3] B. H. Mackintosh, M. P. Ouellette, M. D. Rosenblum, J. P. Kalejs and B. P. Piwczyck, '100 micron thick multicrystalline Si wafers and cells from large diameter EFG cylinders', *Proceedings of the Twenty-eighth IEEE Photovoltaic Specialists Conference*, Anchorage 15–22 September 2000, p.46–49 (2000).

[4] see e.g. A. V. Shah, J. Meier, E. Vallat-Sauvain, N. Wyrsch, U. Kroll, C. Droz, U. Graf, 'Material and solar cell research in microcrystalline silicon', *Solar Energy materials and Solar Cells*. vol.78; p.469–491(2003) and references therein.

[5] R. B. Bergmann, 'Crystalline Si thin-film solar cells: a review', *Applied Physics A (Materials-Science-Processing)*. vol.A69, no.2; p.187–194 (1999).

[6] A. Focsa, A. Slaoui, E. Pihan, F. Snijkers, P. Leempoel, G. Beaucarne and J. Poortmans, 'Poly-Si films prepared by thermal CVD on flowable oxide layers coated ceramic substrates', E-MRS 2005 Spring Meeting, Strasbourg, May 31–June 3 (2005).

[7] see e.g. L. Carnel, D. Van Gestel, I. Gordon, K. van Nieuwenhuysen, G. Beaucarne and J. Poortmans, 'Thin-film polycrystalline Si solar cells with a *V*oc above 500 mV' and I. Gordon, K. Van Nieuwenhuysen, L. Carnel, D. Van Gestel, G. Beaucarne, 'Development of interdigitated solar cell and module processes for polycrystalline-silicon thin films', presented at the E-MRS 2005 Spring Meeting, Strasbourg, May 31–June 3 (2005) and to be published in *Thin Solid Films*.

[8] C. Hebling, S. Reber, K. Schmidt, R. Lüdemann and F. Lutz, 'Oriented recrystallization of silicon layers for silicon thin-film solar cells', *Conference Record of the Twenty-sixth IEEE Photovoltaic Specialists Conference* – 1997 (Cat. No.97CB36026). IEEE, New York, NY, USA; 1997; 1451 p.623–626 (1997).

[9] M. Pauli, T. Reindl, W. Krühler, F. Homberg and J. Müller, 'A new fabrication method for multicrystalline silicon layers on graphite substrates suited for low-cost thin-film solar cells', *Proceedings of the First World Conference on Photovoltaic Energy Conversion*, Hawaii, p.1387–1390 (1994).

[10] G. Andra, J. Bergmann, F. Falk and E. Ose, 'Laser-induced crystallization: a method for preparing silicon thin solar cells', *Proceedings of the Twenty-sixth IEEE Photovoltaic Specialists Energy Conference*, Anaheim, p.639–642, (1997).

[11] M. J. Keevers, A. Turner, U. Schubert, P. A. Basore and M. A. Green, 'Remarkably effective hydrogenation of crystalline Si on glass modules', to be published in *Proceedings of the Twentieth European Photovoltaic Solar Energy Conference*, Barcelona, Spain, June 6–10 (2005).

[12] M. Stemmer, G. Wagner, S. Martinuzzi, D. Ginley, A. Catalano, H. W. Schock, C. Eberspacher, T. M. Peterson and T. Wada, 'Silicon films deposited by LPE on low cost multicrystalline silicon substrates', *Proceedings of Thin Films for Photovoltaic and Related Device Applications Symposium*, p.123–128 (1996).

[13] E. Demesmaeker, M. Caymax, R. Mertens, Le Quang Nam and M. Rodot, 'Solar cells in thin epitaxial layers on metallurgical silicon substrates', *International Journal of Solar Energy*, vol.11, no.1–2; p.37–53 (1992).

[14] See **Preface?** of this book.

[15] J. Poortmans, S. Reber, S. Gall, C. Zahedi and J. Alonso, 'European Cluster on High- and Intermediate thin-film crystalline Si solar cells R & D: overview of running projects and underlying roadmap', *Proceedings of the Nineteenth European Photovoltaic Conference*, Paris, 7–11 June, p.397–402 (2004).

[16] There is one company dedicated to the production of solar grade Si (SGS, USA) whereas several other companies (Hemlock, USA; Wacker, Germany; Tokuyama, Japan) are developing specific production lines for the production of solar grade Si (Fluidized bed reactors for Wacker, vapor to liquid reactor for Tokuyama). Elkem, Norway is developing its own route based on upgrading metallurgical Si see e.g. C. Zahedi, E. Enebakk, K. Friestad, M. G. Dolmen, J. Heide, T. Buseth,

R. Tronstad, C. Dethloff, K. Peter, R. Kopecek, I. Melnyk and P. Fath, 'Solar Grade Silicon from metallurgical route', *Technical Digest of the Fourteenth International Photovoltaic Science and Engineering Conference (PVSEC-14)*, Bangkok, Thailand, January 26–February 1, p. 673–676, (2004).

[17] H. A. Aulich, 'Silicon supply for PV', *Technical Digest of the Fourteenth International Photovoltaic Science and Engineering Conference (PVSEC-14)*, Bangkok, Thailand, January 26–February 1, p. 677, (2004).

[18] T. Vermeulen, O. Evrard, W. Laureys, J. Poortmans, M. Caymax, J. Nijs and R. Mertens, 'Realisation of thin film solar cells in epitaxial layers grown on highly doped RGS-ribbons', *Proceedings of the Thirteenth European Photovoltaic Solar Energy Conference*, Nice, p.1501–1504 (1995).

[19] G. Wagner, G. Steiner, B. Winter, W. Dorsch, A. Voigt, H. P. Strunk, R. Brendel, M. Wolf and J. H. Werner, 'Polycrystalline silicon layers on low cost silicon ribbons for photovoltaic cell application', *Proceedings of the Thirteenth European Photovoltaic Solar Energy Conference*, Nice, p.461–464 (1995).

[20] K. J. Weber, A. Stephens and A. W. Blakers, 'Investigation of the effect of various process parameters during liquid phase epitaxy of silicon on silicon substrates', *Proceedings of the Thirteenth European Photovoltaic Solar Energy Conference*, Nice, p. 1590–1593 (1995).

[21] see e.g. T. Vermeulen, J. Poortmans, M. Caymax, F. Duerinckx, S. Maene, J. Szlufcik, J. Nijs, R. Mertens, N. B. Mason and T. M. Bruton, 'Application of industrial processing techniques to thin-film crystalline solar cells on highly doped defected silicon substrates', '*Proceedings of the Second World Conference on PV Solar Energy Conversion*', p.1209–1214 (1998) and J. Poortmans, J., F. Duerinckx, F, J. Nijs, J., N. Mason, N., T. Bruton, B. Garrard, B., T. Ulset and W. Warta, 'Large-area epitaxial thin-film solar cells on metallurgical-grade Si substrates'. *Proceedings of the Sixteenth European Photovoltaic Solar Energy Conference and Exhibition*; May 2000; Glasgow, Scotland, p. 1549–1552 (2000).

[22] C. Zahedi, F. Ferrazza, A. Eyer, W. Warta, H. Riemann, n. V. Abrasimov, K. Peter and J. Hötzel, 'Thin-film silicon solar cells on low-cost metallurgical silicon substrates by liquid phase epitaxy', *Proceedings of the Sixteenth European Photovoltaic Solar Energy Conference and Exhibition*; May 2000; Glasgow, Scotland, p. 455–458 (2000).

[23] J. Bloem and L. J. Giling, 'Mechanisms of the chemical vapour deposition of silicon', *Current Topics in Materials Science* (Ed. E. Kaldis), North-Holland Publishing Company (1985).

[24] J. Poortmans, A. Diet, A., and A. Räuber, 'A. survey of the European activities and progress in the field of CVD-grown crystalline Si thin-films for solar cells on low-cost insulating substrates'. *Proceedings of the Sixteenth European Photovoltaic Solar Energy Conference and Exhibition*; May 2000; Glasgow, Scotland, p.1077–1082 (2000).

[25] S. Arimoto, H. Morikawa, M. Deguchi, Y. Kawama, Y. Matsuno, T. Ishihara, H. Kumabe and T. Murotami, 'High-efficient operation of large-area 100 cm^2 thin film polycrystalline silicon solar cell based on SOI structure', *Solar Energy Materials and Solar Cells.* vol.34; p.257–262 (1994).

[26] A. Slaoui, R. Monna, D. Angermeier, S. Bourdais and J. C. Muller, 'Polycrystalline silicon films formation on foreign substrates by a rapid thermal CVD technique', *Conference Record of the Twenty-sixth IEEE Photovoltaic Specialists Energy Conference*, Anaheim, p. 627–630 (1997).

[27] J. F. Gibbons, C. M. Gronet, K. E. Williams, 'Limited Reaction Processing: Silicon Epitaxy', *Applied Physics Letters.* Vol.47; p.721–723 (1985).

[28] Z. C. Liang, H. Shen, N. S. Xu and S. Reber Characterisation of direct epitaxial silicon thin film solar cells on a low-cost substrate', *Solar Energy Materials and Solar Cells*, vol. 80, no.2; p. 181–193 (2003).

[29] see e.g. M. Konuma, I. Silier, E. Czech and E. Bauser, 'Semiconductor liquid phase epitaxy for solar cell application', *Solar Energy Materials and Solar Cells*. vol.34, no.1–4; p.251–256, (1994).

[30] T. F. Ciszek, T. H. Wang, X. Wu, R. W. Burrows, J. Alleman, C. R. Schwerdtfeger and T. Bekkedahl, 'Si thin layer growth from metal solutions on single-crystal and cast metallurgical-grade multicrystalline Si substrates', *Conference Record of the Twenty-third IEEE Photovoltaic Specialists Conference,* p.65–72, (1993) (Cat. No.93CH3283–9).

[31] R. Bergmann, S. Robinson, Z. Shi and J. Kurianski, 'Silicon films incorporating a drift-field grown by liquid phase epitaxy for solar cell applications', *Solar Energy Materials and Solar Cells*, vol.31, no.3; p. 447–451 (1993).

[32] M. Albrecht, B. Steiner, Th.Bergmann, A. Voigt, W. Dorsch, H. P. Strunk and G. Wagner, 'The crystalline quality of epitaxial Si layers solution grown on polycrystalline Si substrates', *Materials Research Society Symposium Proceedings.* vol.358; p.889–894 (1995).

[33] B. Steiner and G. Wagner, 'Silicon layers on polycrystalline Si substrates – influence of growth parameters during liquid phase epitaxy', *Journal of Crystal Growth*. vol.146; p. 293–298 (1995).

[34] S. Nishida, K. Nakagawa, M. Iwane, Y. Iwasaki, N. Ukiyo, H. Mizutani and T. Shoji, 'Si-film growth using liquid phase epitaxy method and its application to thin-film crystalline Si solar cell', *Solar Energy Materials and Solar Cells*, p. 525–532 (2001).

[35] J. T. Moore, T. H. Wang, M. J. Heben, K. Douglas and T. F. Ciszek, 'Fused-salt electrodeposition of thin-layer silicon', *Conference Record of the Twenty-sixth IEEE Photovoltaic Specialists Energy Conference*, Anaheim, p. 775 (1997).

[36] K. J. Weber, A. Cuevas and A. W. Blakers, 'The influence of drift fields in thin silicon solar cells', *Solar Energy Materials and Solar Cells*. vol.45; p.151–160 (1997).

[37] D. Majumdar, S. Chattejee, U. Gangopadhyayand H. Saha, 'Role of drift field in thin silicon solar cell developed by liquid phase epitaxial method', *SPIE – International Society For Optical Engineering*, p. 1262–1265, (2000).

[38] T. H. Wang, T. F. Ciszek, M. Page, Y. Yan, R. Bauer, Q. Wang, J. Casey, R. Reedy, R. Matson, R. Ahrenkiel and M. M. Al-Jassim, 'Material properties of polysilicon layers deposited by atmospheric pressure iodine vapor transport', *Conference Record of the Twenty-eighth IEEE Photovoltaic Specialists Conference*, Anchorage 15–22 September 2000, p.138–141 (2000) and T. H. Wang, T. F. Ciszek, M. R. Page, R. E. Bauer, Q. Wang and M. D. Landry, 'APIVT-grown silicon thin layers and PV devices', *Conference Record of the Twenty-nineth IEEE Photovoltaic Specialists Conference*, New Orleans, May, 19–24, 2002, p.94–97 (2002).

[39] J. E. May, *Jourrnal of the Electrochemical Society.* vol.112; p.710 (1965).

[40] L. Oberbeck, R. B. Bergmann, N. Jensen, S. Oeltingand J. H. Werner, 'Low-temperature silicon epitaxy by ion-assisted deposition', *Diffusion Defect Data B, Solid State Phenomena*, vol.67–68; p.459–464 (1999).

[41] L. Oberbeck, T. A. Wagner, R. B. Bergmann, R. W. Collins, H. M. Branz, M. Stutzmann, S. Guha and H. Okamoto, 'Ion-assisted deposition of silicon epitaxial films with high deposition rate using low energy silicon ions', *Amorphous and Heterogeneous Silicon Thin Films – 2000. Symposium* (*Materials Research Society Symposium Proceedings* Vol.609), p. A7.1.1–6, (2001).

[42] Niels-Peter Harder, Ph. D Thesis, University of Leipzig, 2005.

[43] T. A. Wagner, L. Oberbeck, R. B. Bergmannand J. H. Werner, 'Intra-grain defects-limiting factor for low-temperature polycrystalline silicon films?', *Diffusion Defect Data B, Solid State Phenomena.* vol.80–81; p. 95–100 (2000).

[44] T. A. Wagner and U. Rau, 'Density of recombination centers in epitaxial silicon thin-film solar cells by temperature-dependent quantum efficiency measurements', *Applied Physics Letters*. vol.82, no.16; p. 2637–2639 (2003).

[45] L. Oberbeck, J. Schmidt, T. A. Wagner and R. B. Bergmann, 'High-rate deposition of epitaxial layers for efficient low-temperature thin film epitaxial silicon solar cells', *Progress in Photovoltiacs Research And Applications.* vol.9, no.5, p333–340 (2001).

[46] C. Rosenblad, M. Kummer, H.-R. Deller, T. Graf, A. Dommann, T. Hackbarth, G. Hock, E. Muller and H. von Kanel, *Materials Research Society Symposium Proceedings.* vol.696; p. 131 (2002).

[47] S. Brehme, P. Kanschat, K. Lips, I. Sieber and W. Fuhs, *Materials Science & Engineering B* vol.B 69–70; p. 232 (2000).

[48] T. Vermeulen, 'Epitaxial solar cells on low-cost, highly doped defected Si substrates' Ph.D thesis, Katholieke Universiteit Leuven.

[49] T. Vermeulen, F. Duerinckx, K. De Clercq, J. Szlufcik, J. Poortmans, P. Laermans, M. Caymax, J. Nijs and R. Mertens, 'Cost-effective thin film solar cell processing on multicrystalline

silicon', *Conference Record of the Twenty-sixth IEEE Photovoltaic Specialists Conference* – 1997 (Cat. No.97CB36026), p. 267–269 (1997).

[50] K. Said, J. Poortmans, M. Libezny, M. Caymax, J. Nijs and R. Mertens, 'Low-temperature passivation for SiGe-alloy solar cells', *Proceedings of the Fourteenth European Photovoltaic Solar Energy Conference*, Barcelona, p.986, (1997).

[51] J. H. Werner, S. Kolodinski and H. J. Queisser, 'Novel optimization principles and efficiency limits for semiconductor solar cells', *Physical Review Letters*. vol.72, no.24; p.3851–3854 (1994).

[52] M. Wolf, R. Brendel, J. H. Werner and H. J. Queisser, 'Solar cell efficiency and carrier multiplication in $Si_{1-x}Ge_x$ alloys', *Journal of Applied Physics*. vol.83; p.4213–4221 (1998).

[53] K. Said, J. Poortmans, M. Caymax, R. Loo, A. Daami, G. Bremond, O. Kruger and M. Kittler, 'High quality, relaxed SiGe epitaxial layers for solar cell application'. *Thin Solid Films*. vol. 337, no.1–2; p. 85–89 (1999).

[54] U. Jain, S. C. Jain, J. Nijs, J. R. Willis, R. Bullough, R. P. Mertens and R. Van Overstraeten, 'Calculation of critical-layer-thickness and strain relaxation in Ge_xSi_{1-x} strained layers with interacting 60 and 90 degrees dislocations', *Solid State Electronics*. vol.36, no.3; ; p.331–337 (1993).

[55] O. Kruger, W. Seifert, M. Kittler, A. Gutjahr, M. Konuma, K. Said and J. Poortmans, 'Electrical properties of SiGe epitaxial layers for photovoltaic application as studied by scanning electron microscopical methods', *Diffusion and Defect Data Part B (Solid-State-Phenomena)*. vol.63–64; p.509–518 (1998).

[56] K. Said, J. Poortmans, M. Caymax, J. F. Nijs, L. Debarge, E. Christoffel and A. Slaoui, 'Design, fabrication, and analysis of crystalline Si-SiGe heterostructure thin-film solar cells', *IEEE Transactions on Electron Devices* vol.46, no.10; p.2103–2110 (1999).

[57] A. Alguno, N. Usami, T. Ujihara, K. Fujiwara, G. Sazaki, K. Nakajima and Y. Shiraki, 'Enhanced quantum efficiency of solar cells with self-assembled Ge dots stacked in multilayer structure', *Applied Physics Letters* vol.83, no. 6, 1258–1260 (2003).

[58] H. Presting, J. Konle and H. Kibbel, 'Self-assembled Ge-dots for Si solar cells', *International Journal of Modern Physics B*, vol.16, no.28–29; p. 4347–4351, (2003).

[59] C. L. Andre, J. A. Carlin, J. J. Boeckl, D. M. Wilt, M. A. Smith, A. J. Pitera, M. L. Lee, E. A. Fitzgerald and S. A. Ringel, 'Investigations of high-performance GaAs solar cells grown on Ge-Si_{1-x}/Ge_x-Si substrates', *IEEE Transactions on Electron Devices.* vol.52, no.6; p. 1055–1060 (2005).

[60] G. Flamand, S. Degroote, K. Dessein and J. Poortmans, 'Cheap virtual germanium substrates by CSVT deposition on porous Si', *Conference Record of the Thirty-first IEEE Photovoltaic Specialists Conference*, Orlando, January 2005 (2005).

[61] J. Zettner, M. Thoenissen, T. Hierl, R. Brendel and M. Schulz, 'Novel porous silicon backside light reflector for thin silicon solar cells', *Progress in Photovoltaics: Research and Applications.* vol.6, no.6; 423–432 (1998).

[62] L. Stalmans, J. Poortmans, M. Caymax, H. Bender, S. Jin, J. Nijs and R. Mertens, 'Realization of light confinement in thin crystalline Si films grown on porous silicon', *Proceedings of the Second World Conference on Photovoltaic Solar Energy Conversion,* Vienna, 1998, p. 124 (1998).

[63] A. A. Abouelsaood, M. Y. Ghannam, L. Stalmans, J. Poortmans and J. F. Nijs, 'Experimental testing of a random medium optical model of porous silicon for photovoltaic applications', *Progress in Photovoltaics: Research and Aplpications*, p. 15–26 (2001).

[64] R. Bilyalov, C.S. Solanki, J. Poortmans, O. Richard, H. Bender, M. Kummer and H. von Kanel, *Solar Energy Materials and Solar Cells*. vol.72; p. 221 (2002).

[65] F. Duerinckx, K. Van Nieuwenhuysen, H. J. Kim, I. Kuzma-Filipek, G. Beaucarne and J. Poortmans, to be published in *Proceedings of the Twentieth European Photovoltaic Solar Energy Conference*, Barcelona, June 6–10, (2005).

[66] S. Berger, S. Quoizola, A. Fave, A. Ouldabbes, A. Kaminski, S. Perichon, N. –E. Chabane-Sari, D. Barbier and A. Laugier, 'Liquid phase epitaxial growth of silicon on porous silicon

for photovoltaic applications', *Crystal Research and Technology*. vol.36, no.8–10; p.1005–1010 (2000).

[67] Y. S. Tsuo, P. Menna, J. R. Pitts, K. R. Jantzen, S. E. Asher, M. M. Al-Jassim and T. F. Ciszek, 'Porous silicon gettering', *Conference Record of the Twenty-fifth IEEE Photovoltaic Specialists Conference* – 1996 (Cat. No.96CH35897), 461–464 (1996).

[68] H. Raidt, R. Kohler, F. Banhart, B. Jenichen, A. Gutjahr, M. Konuma, I. Silier and E. Bauser, 'Adhesion in growth of defect-free silicon over silicon oxide', *Journal of Applied Physics.* vol.80, no.7; p.4101–4107, (1996).

[69] M. G. Mauk and J. P. Curran, 'Electro-epitaxial lateral overgrowth of silicon from liquid-metal solutions', *Journal of Crystal Growth*. vol.225, no.2–4; p. 348–353, (2001).

[70] O. Evrard, T. Vermeulen, J. Poortmans, M. Caymax, P. Laermans, J. Nijs and R. Mertens, 'The study of the influence of the layer resistivity of thin epitaxial Si cells', *Proceedings of the First IEEE World Conference on Photovoltaic Energy Conversion. Conference Record of the Twenty Fourth IEEE Photovoltaic Specialists Conference-1994* (Cat.No.94CH3365-4), 1567–1570 (1994).

[71] J. H. Werner, S. Kolodinski, U. Rau, J. K. Arch and E. Bauser, 'Silicon solar cell of 16.8 μm thickness and 14.7 % efficiency', *Applied Physics Letters*. vol.62, no.23; p.2998–3000 (1993).

[72] A. W. Blakers, J. H. Werner, E. Bauser and H. J. Queisser, 'Silicon epitaxial solar cell with 663-mV open-circuit voltage', *Applied Physics Letters*. vol.60, no.22; p.2752-2754 (1992).

[73] O. Evrard, E. Demesmaeker, T. Vermeulen, M. Zagrebnov, M. Caymax, W. Laureys, J. Poortmans, J. Nijs and R. Mertens, 'Analysis of the limiting recombination mechanisms on high-efficiency thin-film cells grown with CVD epitaxy', *Proceedings of the Thirteenth European Photovoltaic Solar Energy Conference*, Nice, p.440 (1995).

[74] A. W. Blakers, J. H. Werner, E. Bauser and H. J. Queisser, 'Silicon epitaxial solar cell with 663-mV open-circuit voltage', *Applied Physics Letters*, 2752–2754 (1992).

[75] A.W. Blakers, K. J. Weber, M. F. Stuckings, S. Armand, G. Matlakowski, A. J. Carr, M. J. Stocks, A. Cuevas and T. Brammer, '17 % efficient thin-film silicon solar cell by liquid-phase epitaxy', *Progress in Photovoltaics: Research and Applications*. vol.3, no.3; p. 193–195 (1995).

[76] Guang Fu Zheng, Wei Zhang, Zhengrong Shi, D. Thorp and M. A. Green, 'High-efficiency drift-field thin-film silicon solar cells by liquid-phase epitaxy and substrate thinning', *Conference Record of the Twenty-fifth IEEE Photovoltaic Specialists Conference – 1996* (Cat. No.96CH35897), 693–696 (1996).

[77] G. Ballhorn, K. J. Weber, S Armand, M. J. Stocks and Blakers,, 'High-efficiency multicrystalline silicon solar cells by liquid phase-epitaxy', *Solar Energy Materials and Solar Cells*. vol.52, no.1–2; p.61–68 (1998).

[78] F. R. Faller, V. Henninger, A. Hurrle and N. Schillinger, 'Optimization of the CVD process for low-cost crystalline-silicon thin-film solar cells', *Proceedings of the Second World Conference on PV Solar Energy Conversion*, p.1278–1283 (1998).

[79] F. R. Faller and A. Hurrle, 'High-temperature CVD for crystalline-silicon thin-film solar cells', *IEEE Transactions on Electron Dev*ices. vol.46, no.10; 2048–2054 (1999).

[80] A. W. Blakers, K. J. Weber, M. F. Stuckings, S. Armand, G. Matlakowski, M. J. Stocks and A. Cuevas, '18 % efficient thin silicon solar cell by liquid phase epitaxy', *Proceedings of the Thirteenth European Photovoltaic Solar Energy Conference*, Nice, p.33 (1995).

[81] J. Rentsch, S. Bau and D. M. Huljic,' Screen-printed epitaxial silicon thin-film solar cells with 13.8 % efficiency', *Progress in Photovoltaics: Research and Applications*. vol.11, no.8; p.527–534 (2003).

[82] K. Van Nieuwenhuysen, F. Duerinckx, R. Bilyalov, H. Dekkers, G. Beaucarneand J. Poortmans, *Proceedings of the Nineteenth European Photovoltaic Solar Energy Conference*, Paris, June 7–11, 2004, p. 1178. (2004).

[83] Z. C. Liang, H. Shen, N. S. Xu and S. Reber,' Characterisation of direct epitaxial silicon thin film solar cells on a low-cost substrate', *Solar Energy Materials and Solar Cells*, vol.80, no.2; p. 181–193 (2003).

[84] S. Bau, D. M. Huljic, J. Isenberg and J. Rentsch, 'Shunt-analysis of epitaxial silicon thin-film solar cells by lock-in thermography', *Conference Record of the Twenty-ninth IEEE Photovoltaic Specialists Conference 2002 (Cat. No.02CH37361)*, New Orleans, May 21–24, 1335–1338 (2002).

[85] S. Reber, H. Schmidhuber, H. Lautenschlager, J. Rentsch and F. Lutz, 'Solar minimodule made with epitaxial crystalline silicon thin-film wafer equivalents', *Proceedings of the Nineteenth European Photovoltaic Conference*, Paris, 7–11 June, 1311 (2004).

[86] K. Peter, R. Kopecek, P. Fath, E. Bucher and C. Zahedi, 'Thin film silicon solar cells on upgraded metallurgical silicon substrates prepared by liquid phase epitaxy', *Solar Energy MaterIals and Solar Cells*, vol.74, no.1–4; p.219–223 (2002).

[87] D. J. Aiken and A. M. Barnett, 'Alternative contact designs for thin epitaxial silicon solar cells', *ProgRess in Photovoltaics: Research and Applications*. vol.7, no.4; p.275–285, (1999).

[88] S. Reber, N. Schillinger, S. Bau, B. Waldenmayer, 'Progress in high-temperature silicon epitaxy using the RTCVD 160 processor', *Proceedings of the Nineteenth European Photovoltaic Conference*, Paris, 7–11 June, p. 471 (2004).

[89] A. Hurrle, S. Reber, N. Schillinger, J. Haase and J. G. Reichart, 'High-throughput continuous CVD reactor for silicon deposition', *Proceedings of the Nineteenth European Photovoltaic Conference,* Paris, 7–11 June, p. 459 (2004).

[90] S. Reber, A. Eyer, F. Haas, N. Schillinger, S. Janz and E. Schmich, 'Progress in crystalline Si thin-film solar cell at Fraunhofer ISE', *Proceedings of the Twentieth European Photovoltaic Conference,* Barcelona, 6–10 June, p. 459 (2004).

[91] T. Kunz, I. Burkert, R. Auer, R. Brendel, W. Buss, H. v. Campe, and M. Schulz, 'Convection-assisted Chemical Vapor Deposition (COCVD) of silicon on a 40 $\times$ 40 cm^2 substrate for photovoltaics', *Proceedings of the Nineteenth European Photovoltaic Conference*, Paris, 7–11 June, p. 903 (2004).

[92] J. Poortmans, J. G. Beaucarne and S. Sivoththaman, 'Study of Si deposition in a batch-type LPCVD-system for industrial thin-film crystalline Si solar cells', *Conference Record of the Twenty-eighth IEEE Photovoltaic Specialists Conference* – 2000 (Cat. No.00CH37036), p. 347–350 (2000).

[93] K. Van Nieuwenhuysen, D. Van Gestel, I. Kuzma, F. Duerinckx, G. Beaucarne and J. Poortmans, 'Characterization of thin silicon films grown in a batch-type LP-CVD system', *Twentieth European Photovoltaic Solar Energy Conference and Exhibition*, Barcelona, June, 2005.

[94] H. J. Rodriguez, J. C. Zamorano, I. Tobias, C. Del Canizo and A. Luque, 'High-throughput epitaxial reactor prototype for thin-film solar cells on low grade Si substrates', *Proceedings of the Nineteenth European Photovoltaic Conference,* Paris, 7–11 June, p. 903 (2005).

[95] A. Luque, V. Ortuno, J. Alonso and E. Gomez, 'New concepts on epitaxial reactors for solar cells' *Proceedings of the Ninth European Photovoltaic Conference,* Freiburg, p. 459 (1989).

[96] B. Thomas, G. Müller, P. Heidborn and H. Wawra, 'Growth of polycrystalline silicon thin films using the temperature difference method', *Proceedings of the Fourteenth European Photovoltaic Conference*, Barcelona, June 30–July 4, p. 1483 (1997).

[97] B. Thomas, G. Muller, P.-M. Wilde and H. Wawra, 'Properties of silicon thin films grown by the temperature difference method (TDM)', *Conference Record of the Twenty-sixth IEEE Photovoltaic Specialists Conference* – 1997 (Cat. No.97CB36026, p. 771–774 (1997).

[98] J. Nishizawa, Y. Okuno and H. Tadano, 'Nearly perfect crystal growth of III–V compounds by the temperature difference method under controlled vapour pressure', *Journal of Crystal Growth.* Vol.31; p. 215–222 (1975).

[99] K. Peter, G. Willeke and E. Bucher, 'Rapid growth of high quality crystalline silicon by a novel temperature gradient liquid phase epitaxy', *Proceedings of the Thirteenth European Photovoltaic Conference,* Nice, p. 379–381 (1995).

[100] K. Peter, R. Kopecek, P. Fath, E. Bucher and C. Zahedi, 'Thin-film silicon solar cells on upgraded metallurgical silicon substrates prepared by liquid phase epitaxy', *Solar Energy Materials and Solar Cells*. vol.74; p. 219 (2002).

[101] M. Mueller, R. Kopecek, P. Fath, C. Zahedi and K. Peter, *Proceedings of Third World Conference on Photovoltaic Energy Conversion*, p. 1221 (2003).

2 Crystalline Silicon Thin Film Solar Cells on Foreign Substrates by High Temperature Deposition and Recrystallization

Stefan Reber
Fraunhofer Institute for Solar Energy Systems ISE, Freiburg, Germany

Thomas Kieliba
Former member of Fraunhofer ISE, now with ErSol Solar Energy AG, Erfurt, Germany

Sandra Bau
Former member of Fraunhofer ISE, now with AMD, Dresden, Germany

2.1 MOTIVATION AND INTRODUCTION TO SOLAR CELL CONCEPT

The idea of using foreign substrates, i.e. nonsilicon materials or coated silicon for the subsequent deposition and processing of a thin film silicon solar cell has been in the minds of scientists for several decades. This concept has some major principal advantages: consumption of expensive solar grade silicon can be dramatically decreased, and wafer formation by sawing can be omitted completely. The consequence is an inherent potential for large cost savings compared to a 'conventional' module manufactured from silicon wafer solar cells.

To realize the idea, approx. 30 years ago research started on amorphous silicon films (a-Si), usually using glass sheets as substrates. Glass substrates have many advantages, such as low cost, abundance and transparency, to name just a few. However with ongoing research, the solar cell efficiency of a-Si solar cells reached a kind of saturation, with a limit on typical module conversion efficiency at around 6–8 %. This efficiency is too low to let the inherent cost reduction potential of thin film silicon solar cells become visible, due to high area-related costs. Efficiency was then increased by the introduction of a new cell concept involving two or three pn-junctions stacked monolithically upon each other to separate light-generated charge carriers more effectively [1]. Hydrogenated microcrystalline silicon (μc-Si:H) was, in addition, found as a new material to exhibit beneficial properties for this purpose. It consists of

Thin Film Solar Cells Edited by J. Poortmans and V. Arkhipov
© 2006 John Wiley & Sons, Ltd

silicon crystallites of submicrometer grain size, with its numerous dangling silicon bonds being passivated by hydrogen. The optical and electrical properties of μc-Si:H are similar to large-grained crystalline silicon (c-Si). Two-junction ("tandem") solar cells were fabricated using a-Si cells as the top cells (faced to the illuminating light) and μc-Si:H as the bottom cells. Thus efficiency could be increased to higher than 13 % before light-soaking, for large laboratory modules [2], with stable efficiencies in the range of 10 % [3]. However this improvement also did not lead to a deep market penetration until now. Still and without a decreasing trend conventional silicon wafers dominate the photovoltaics (PV) market at a share higher than 93 % [4]. One of the important reasons leading to this situation surely is the possibility for reliable manufacturing of silicon wafers, as well as their potential for stable and predictable high efficiency due to the underlying material, crystalline silicon. The obvious thing to do in order to exploit the cost potential for thin silicon solar cells on foreign substrates would consequently be the combination of 'crystalline silicon' and 'thin film'. Crystalline silicon thin film (CSiTF) solar cells would combine the principal advantages discussed above and the high solar cell efficiency potential of crystalline silicon. Intense research on CSiTF solar cells started about 10 to 15 years ago. Soon research showed that – as for 'thick' wafer solar cells – the diffusion length of minority carriers of the active silicon layer has to exceed the silicon layer thickness about a factor two to three, if solar cell efficiency is not to be limited by the layer quality (see e.g. Ref. [5]). Bergmann and Werner have calculated a quantitative correlation between solar cell conversion efficiency potential and grain size of the multicrystalline silicon layer, taking into account the detrimental influence of grain boundaries [6, 7]. According to these calculations, in order to achieve e.g. conversion efficiencies exceeding 15 %, the size of the silicon grains has to be at least in the order of 100 μm.

Direct deposition of silicon on a foreign substrate, however, yields crystal grains smaller than approx. 5 μm, independent of deposition method and temperature used. Therefore, the key issue in all research activities on CSiTF solar cells on foreign substrates is to increase the grain size of the as-deposited silicon layer, also called 'recrystallization'. All approaches to realize recrystallized CSiTF solar cells use some kind of heat treatment to achieve this aim. Depending on the substrate type used, process temperatures can be limited. In the so-called 'low-temperature approach' the use of glass substrates prohibits temperatures exceeding approx. 550 °C. Maximum grain size achieved is therefore in the 10 μm range and respective solar cell efficiencies are limited to approx. 8 % up to now [8]. More information on this topic is found in Chapter 3.

In the 'high temperature approach', the substrate does, by definition, not limit process temperature. It is allowed to even exceed the melting point of silicon at 1420 °C, which gives room for the most effective method to create grains exceeding 100 μm from a microcrystalline layer: liquid phase recrystallization.

This chapter deals with issues regarding preparation of CSiTF solar cells on foreign substrates following the high temperature approach. Key issues for the discussed technology are: (i) availability of a suitable substrate material, (ii) development of an in-line silicon deposition method and (iii) progress in high-speed recrystallization. In this section we will give an overview of the requirements for materials, layers and processes, of the current research work and of the challenges and problems which have emerged. The most important topics are treated in separate sections in detail. We will often use examples to spot-light typical effects and results encountered during experimental work, in order to achieve a more vivid description of the research results.

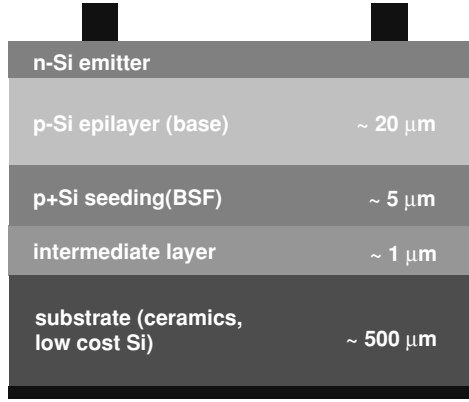

Figure 2.1 Generic structure of a CSiTF solar cell on foreign substrate.

In the following pages, the layers and key processes to prepare a CSiTF solar cell on a foreign substrate using high temperatures shall be introduced. A typical ('generic') device structure is shown in Figure 2.1.

The CSiTF solar cell can be based on any suitable high temperature stable substrate, e.g. ceramics or low-cost silicon ribbons. The substrate is coated by an intermediate layer (IL), which is mainly needed to suppress diffusion of impurities from the substrate into the silicon layer. Requirements for the substrate and intermediate layer, as well as current achievements, are discussed in detail in Section 2.2.

A process consisting of three major steps is usually applied to form the silicon layer. In the first step, a highly boron doped ($\sim 10^{19}$at/cm^3) silicon layer is deposited onto the intermediate layer. Section 2.4 discusses basics and results achieved for the most commonly used silicon deposition technique for this purpose, thermal atmospheric-pressure chemical vapor deposition (APCVD).

Since the as-deposited silicon layer is microcrystalline, it is recrystallized in the second step. Large-area melting [9] and zone-melting recrystallization (ZMR) are possible methods. The latter is more commonly used, therefore we will focus only on the ZMR method in this chapter. Details of the ZMR principle, ZMR silicon film features and ZMR processor development are given in Section 2.3.

The recrystallized silicon layer (also called 'seeding layer') serves as 'seed' for a subsequent epitaxial deposition of a ($\sim 10^{17}$ at/cm^3) normal boron doped silicon layer, which forms the active solar cell absorber. Challenges and achievements concerning this processing step, as well as current work on CVD processor development are also described in Section 2.4.

The three-step process to create the silicon layers enables the formation of a p^+/p high-low junction at the interface between the seeding and epitaxial absorber layers, where it acts as a back surface field (BSF) and thus reduces the effective surface recombination at the rear of the epitaxial layer.

There are, in principle, two ways to process a solar cell using the layer stack as described up until now. If the substrate and/or intermediate layer are nonconductive, both metal contacts for base and emitter have to be applied to the front side. This allows manufacturing of an integrated module on one large-area substrate by interconnection of (e.g. laser) isolated solar cell stripes. If both the substrate and the intermediate layer are conductive, a conventional metallization

structure can be realized for contacting base and emitter, as sketched in Figure 2.1. Base contacting is done on the rear side of the substrate, and emitter contacts are formed on the front side of the stack. If this processing is possible, the layer stack (i.e. substrate, IL and silicon layers) may be called 'recrystallized wafer equivalent' [10], since in principle it can be processed to a solar cell and module like a standard wafer. It has the potential to replace a conventional wafer in a typical silicon wafer solar cell production, therefore the term 'wafer equivalent' applies. Section 5 deals in detail with solar cell results and challenges in processing recrystallized wafer equivalents.

2.2 SUBSTRATE AND INTERMEDIATE LAYER

Nearly all thin film concepts are based on the deposition of the electrically active absorber film onto substrates. In most cases, intermediate layers between the substrate and film are used in order to avoid the diffusion of impurities which are detrimental to solar cell performance. Requirements of both the substrate and IL are especially high for the high temperature concept for CSiTF solar cells to be realized. They will be discussed, together with an overview of the respective state of the art in R&D in the following two sections.

2.2.1 Substrate

2.2.1.1 Material requirements

The high temperature concept described in this work enables high silicon deposition rates, grain enlargement by recrystallization and low defect epitaxial growth. However, the necessary temperature stability restricts the choice of potential substrate materials. The following requirements have to be satisfied:

- *Mechanical and chemical stability*. A basic requirement of the substrate is its mechanical stability during all high temperature processes. Screen-printing and lamination demand a bending strength of ~150 MPa [11]. As to chemical stability, the substrate material has to be inert to any interaction with liquid silicon during ZMR. Diffusion of harmful impurities from the substrate into the active silicon film is also not tolerable. In both cases the introduction of an intermediate barrier layer may lower requirements on the substrate. As a last point, the substrate has to withstand different chemicals used for solar cell processing. Replacing standard wet processes by dry processing can make this issue less critical [12].
- *Flatness and thickness uniformity*. For ZMR to be successful a certain degree of substrate flatness is necessary to keep the focal line in a fixed plane. The maximum acceptable bow is in the range 0.5 mm to 1.0 mm for a $150 \times 150\,mm^2$ wafer. Substrates with a bow exceeding this value would not only be problematic for ZMR but also could not be processed into solar cells with today's standard solar cell manufacturing equipment. Thickness uniformity is important for various processes and again especially for ZMR, where uniformity is a prerequisite in order to achieve a homogeneous temperature and therefore stable recrystallization.

- *Small surface roughness*. Small surface roughness and small surface pores are necessary to ensure the formation of a closed film during Silicon (Si) deposition and recrystallization. As a rule of thumb, the maximum roughness should be less than one third of the seed film thickness [13].
- *Matched thermal expansion coefficient (TEC)*. During Si deposition the substrate is heated up to around 1200 °C, and during recrystallization to even more than 1400 °C locally. The substrate's thermal expansion has to match that of Si (for experimental data see e.g. Ref. [14]) in order to avoid the formation of cracks in the cooling phase after high temperature processing.
- Another thermal property to be mentioned is the material's 'thermoshock resistance', which must be compatible with the heat up and cool down ramps applied during the high temperature processes.
- *Low costs*. The cost of the substrate plus the active Si thin film must be substantially lower than that of standard multicrystalline wafers, otherwise the CSiTF solar cell cannot be cost effective. Cost calculations conclude that the upper cost limit is in the range of 50 to 70 €/m^2, assuming a conversion efficiency around 12 % [15]. For high volume production, substrate costs of 20 €/m^2 to 50 €/m^2 have been projected [15, 16][1]. If ceramics are chosen as a substrate material, the ability to produce it by tape casting[2] is a prerequisite since other forming techniques like hot pressing are rather cost intensive.

2.2.1.2 Low cost and 'Model' substrates

For the research on CSiTF solar cells two different types of substrates were used. On one hand Silicon ribbon and ceramic materials with low cost potential were tested. On the other hand standard mono- and multicrystalline Si wafers were employed as 'model' substrates for Si thin film optimization.

Examined materials belonging to the first group were silicon nitride (Si_3N_4) [19, 20], zirconium silicate ($ZrSiO_4$) [21], silicon infiltrated silicon carbide (SiSiC) [22] and reaction bonded silicon carbide (RBSiC) [23] ceramics, aluminum oxide based ceramics like Al_2O_3 [24], Mullite [25, 26], SiAlON [27, 28], graphite [12, 29], and silicon sheets from powder (SSP) ribbons [28, 30]. Not all of these materials match the criteria listed in the previous section. Al_2O_3, for example, has a large difference in TEC to silicon, therefore it was only used in direct deposition of silicon, not for ZMR purposes. For a better understanding of the following sections, it is necessary to describe some of the more promising materials in more detail. All of them were used in the work reported in the respective references cited above.

Silicon nitride ceramics were produced by two different methods: sintering of silicon nitride powder (sintered silicon nitride, SSN) and reaction bonding through nitridation (reaction bonded silicon nitride, RBSN). A benefit of SSN material is its higher material density compared to that of RBSN (see e.g. Ref. [18], p. 215 ff). However, for possible application as thin film solar cell substrate, RBSN material is preferred for cost reasons. Both silicon nitride

[1] Pursuing a similar concept AstroPower Inc. (now taken over by GE Energy) calculated with 9 $/$m^2$ for substrate costs [17].

[2] For details on this technique see, e.g. [18], p. 41ff.

materials are characterized by a TEC slightly smaller than that of silicon and a very good thermal shock resistance. Both the SSN and warm pressed RBSN materials were produced by Ceramic for Industries (CFI), Germany[3]. Tape cast SSN ceramics were produced by the Energy Research Centre of the Netherlands (ECN) [20].

Zirconium silicate ($ZrSiO_4$) occurs as the natural mineral zircon and is mined as sand. This raw material is especially well suited to meet the cost goals. The resulting substrates are nonconductive, and their white color makes optical confinement issues easier. The $ZrSiO_4$ substrates reported were uniaxially pressed, however it is possible to tape cast the material.

One of the most important nonoxide ceramics is SiSiC. The pores of the SiC ceramic matrix are filled with liquid silicon and yield a very dense material without open pores. A high temperature stability and good thermal and electrical conductivity characterize SiSiC. Basic information on these ceramic types can be found, e.g., in [18], p. 210 ff. Usually SiSiC ceramics are manufactured by isostatic hot pressing, thus yielding a substrate cost which would probably be too high. A more economic approach is the tape casting and reaction bonding of SiC based ceramics [23]. Here, a slurry containing silicon, carbon, silicon carbide particles and binder is tape cast to up to 40 cm wide tapes, shaped, debindered and sintered at temperatures exceeding 1500 °C.[4] During the sintering step, silicon and carbon react to create SiC, thus binding the already present SiC particles together. The resulting RBSiC tape has the potential to be cost effective for PV purposes. In contrast to SiSiC, it contains open pores which make wet chemical processing difficult.

The SSP ribbon growth process was developed by Fraunhofer Institute for Solar Energy Systems (Fraunhofer ISE) and Siemens AG [31, 32]. Originally it featured a surface melting as well as a zone melting step. Later the process was modified to yield substrates for thin film solar cells, employing surface melting only [30]. Substrates made of SSP ribbons had a thickness around 600 μm and were used without any mechanical or chemical leveling of the surface.

All the ceramic and silicon ribbon substrates mentioned above have been developed in research projects on CSiTF solar cells. Substrate compositions and fabrication methods are still under investigation, and they can therefore not yet be fabricated with the same reproducibility as that of routinely manufactured products. In addition, more often than not the available quantity of such substrates is not sufficient for silicon thin film optimization. At the moment, no substrate is available on the market which is really suitable for high temperature CSiTF solar cells. However their development is continuing with good progress.

Oxidized or SiC coated standard Czochralski silicon (Cz-Si) and multicrystalline silicon (mc-Si) are commonly used as 'model' substrates for ZMR, silicon deposition and solar cell optimization. Both monocrystalline Cz-Si semiconductor industry monitor wafers, and wire-sawn and damaged etched mc-Si wafer are employed for this purpose.

2.2.2 Intermediate layer

Low costs and chemical purity of the substrate material cannot usually be achieved simultaneously. Metals which are especially harmful are those which are present in free form, while those bound in the form of oxides are less detrimental [33]. However, the required purity cannot

[3] Now H.C. Starck Ceramics, Germany.

[4] This process to produce RBSiC was developed for PV by H.C. Starck Ceramics, Germany.

normally be achieved without an intermediate barrier layer. A good intermediate layer has to meet the following requirements:

- The most important requirement is mechanical and chemical stability at process temperatures as high as 1450 °C, including in the zone melting process. If not met, it leads to either nonideal silicon seeding layer deposition, to inhomogeneous ZMR up to complete destruction of the seeding layer structure, or to the contamination of the silicon layer by substrate impurities.
- The intermediate layer has to act as an effective diffusion barrier for electrically active impurities from the substrate. It also may not serve as a source of impurities by itself. Considering the high temperatures of the ZMR process, these requirements are extremely demanding and narrow the range of possible materials extremely.
- Good wetability of both the substrate and the silicon layer makes ZMR processing more reliable. However, most publications report the use of SiO_2 as an intermediate layer, which has a comparatively bad wetting behavior with respect to liquid silicon.

Besides the barrier properties an intermediate layer can serve two other purposes: firstly, it may be a functional part of an advanced contacting scheme like an integrated series interconnection; secondly, the intermediate layer can act as a back reflector and be part of a light trapping structure.

On the mc-Si and Cz-Si wafers which are used as model substrates, an intermediate layer (IL) is not necessary to create a barrier, however it serves other purposes. Here the intermediate layer assures the same Si seed film growth as on coated ceramics. Further it provides electrical separation of the active Si thin film from the substrate if needed.

In principle, all carbides, nitrides and oxides could be investigated for IL purposes. Also other compounds (e.g. silicates) or even elemental layers (e.g. from pyrocarbon) could be suitable. Of course transition metals and other harmful elements should be avoided both as anions in those compounds and for applications as bare metal IL, since they would probably be dissolved by liquid silicon and thus contaminate it.

At the moment, however, only silicon dioxide (SiO_2), silicon nitride (SiN_x) and silicon carbide layers have been tested as intermediate layers. Silicon dioxide was either deposited by PECVD or by the spin-on coating of a commercial spin-on dopant (SOG). Thermal oxidation has also been applied to form SiO_2 layers. For the preparation of SiN_x layers PECVD was the only deposition method used. Stacks of SiO_2 and SiN_x (e.g. the combination $SiO_2/SiN_x/SiO_2$, 'ONO') have also been examined [22, 26, 34].

Both SiO_2 and SiN_x layers are nonconductive. Their conductive counterpart are SiC layers, which were prepared either at low temperature by PECVD, or by atmospheric pressure CVD at high temperature [35, 36]. Thickness of the intermediate layers ranged from 0.5 μm to 4 μm for the low temperature deposited layers, and up to several 10 μm for the high temperature SiC layers.

2.2.2.1 Light trapping

Since crystalline Si is an indirect semiconductor, light trapping must play a major role if thin film solar cells with high conversion efficiency are to be realized. Without light path enhancement it is not possible to profit from the advantages of thin cells compared to thick

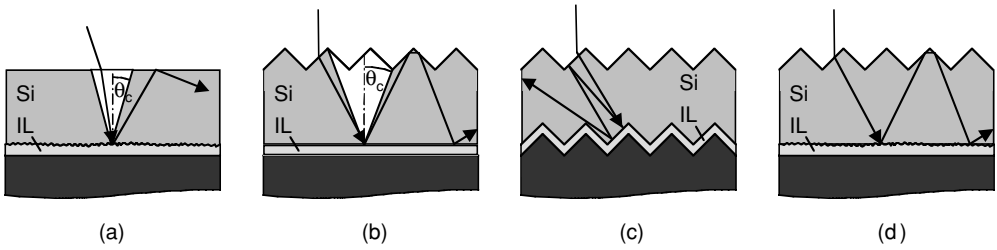

Figure 2.2 Different options for light trapping. The change in refraction at the interface of Si and the intermediate layer (IL) results in total reflection for rays with angles greater than θ_c. (a) Diffuse back reflector. (b) Structured front and planar back side. (c) Front and back side both structured. (Note: in reality this is a three dimensional pyramidal structure). (d) Structured surface and diffuse back side.

cells, i.e. the potential for a high open circuit voltage V_{oc} with reduced requirements regarding material quality. Indeed, companies with low temperature concepts close to commercialization like Kaneka [37] and CSG Solar[5] [8, 38] put a lot of emphasis on light trapping technology.

Using an analytical approach, Goetzberger demonstrated that the combination of a planar surface with an ideal diffuse reflector (Figure 2.2a) provides a very effective light trapping structure [39]. The key to this concept is the Lambertian reflector – defined as a reflector with uniform radiance (brightness) in all directions, regardless of the angle of incidence. Using such a reflector, only a small fraction of scattered rays can escape at the front surface while all rays with an angle θ greater than the critical angle θ_c experience total reflection.

In the wavelength region between 800 nm and 1200 nm, the critical angle θ_c is approx. 16 ° for silicon and air, and approx. 24 ° for silicon and SiO_2.[6]

Yablonovitch and Cody have calculated a maximum light path enhancement of $4n_{21}^2$ for such a randomizing structure, where n_{21} is the ratio of the refractive index of silicon to that of the adjacent material [41, 42]. For silicon and air the enhancement factor has a value of around 50. Numerical simulations show that even with more elaborate structures it is difficult to exceed the performance of the ideal diffuse reflector structure described above [5, 43]. However, in practice, this ideal Lambertian behavior cannot be achieved [44] and more realistic simulations of diffuse reflection use the Phong model [5, 45]. In addition, the IL at the rear surface of the silicon layer is in all cases reported to be not ideally reflecting, but represents a dielectric mirror. This dielectric mirror of course also has a loss cone, with a θ_c depending on its refractive index n. For IL made from material of high refractive index (e.g. SiC: $n \approx 2.5$), the loss cone can become a significant drawback.

The numerical investigations cited above show that the most efficient structure is one with pyramids on both sides (Figure 2.2c) or one with a pyramidal structured surface in combination with a diffuse back reflector (Figure 2.2d). Slightly less efficient is a combination of a pyramidal structured front side and a planar back reflector (Figure 2.2b).

The structure used in various publications often corresponds to Figure 2.2b for the case of model substrates. Damage etched mc-Si wafers and ceramic substrates provide some surface roughness and the structure corresponds to an intermediate state between Figure 2.2b and d.

[5] Former Pacific Solar Ltd.

[6] Calculated from the data given in Ref. [40].

Since ZMR yields crystal grains which are preferentially (100) oriented, texturing of the silicon surface is easily possible by applying a standard wet chemical anisotropic alkaline texture (e.g. by a KOH isopropanol solution). This way a randomized pyramid surface is achieved as sketched in Figure 2.2b.

2.2.2.2 Diffusion of impurities

In principle nearly every chemical element is unwelcome in the silicon layer of CSiTF solar cells. Transition metals like iron, nickel or titanium as well as other elements like aluminium can be found in metallurgical silicon and silicon based ceramics [46]. Their concentrations can reach up to 10^{20} at/cm^3, and a large part can be mobile in the substrate at high temperatures. Even if only a small fraction is transported to the active silicon layer, it can have a dramatic negative influence on the solar cell's performance. Elements from the group of transition metals are especially harmful, as they seriously degrade the solar cell's efficiency [47, 48]. In the case of CSiTF solar cells, the diffusion velocity of the respective elements in silicon during the high temperature treatments also has to be considered. Compared to other elements, the transition metals diffuse very fast in silicon at high temperatures. Among these, iron, chromium and vanadium are the elements with extraordinarily high diffusion coefficients [49]. If they can penetrate the IL, they are expected to be distributed nearly homogeneously throughout the thin silicon layer at high temperatures in a short amount of time. Titanium also has a high diffusion coefficient, but tends to segregate at the silicon surface and is therefore not as mobile as iron, chromium and vanadium [50].

Considering these three criteria, the transition metals iron, chromium and vanadium are the most critical ones for CSiTF solar cells. Consequently, intermediate layers have to be especially effective as a diffusion barrier against these metals. Systematic studies yielding quantitative parameters of diffusion barrier properties of SiO_2, SiN_x and SiC layers with respect to iron, chromium and vanadium are very rare, especially in the temperature range of interest for CSiTF solar cells. In Ref. [51] diffusion barrier data from non-PV work is reviewed, and detailed information on experiments yielding temperature dependent diffusion coefficients for iron chromium and vanadium in PECVD SiO_2 and SiN_x layers is given. Simulations created in this work predict that SiO_2 and SiN_x can effectively prevent the diffusion of impurities in a generic process for the preparation of CSiTF solar cells as described in Section 2.1. Referring to PECVD layers it has been shown that SiN_x is a more effective barrier than SiO_2 [52].

A more practical method to evaluate the effectiveness of diffusion barriers is the compositional analysis of silicon layers on foreign substrates after all processing steps have been completed. In Ref. [20], the use of glow discharge mass spectrometry (GDMS) is described in the case of a SiSiC substrate coated with a 2 μm thick PECVD SiO_2 intermediate layer. Figure 2.3 shows the respective impurity concentration profile of the layer stack after ZMR and epitaxy.

The measurement reveals a large contamination of the ceramic substrate by boron and various transition metals like iron, titanium, vanadium, chromium, manganese and nickel. Within the barrier and BSF layer (labeled 'p^+-Si' in the figure) the concentration of all impurity elements decreases substantially, and in the base layer only iron and nickel are detected in concentrations exceeding 0.01 ppma. Compared to the substrate concentration, this corresponds to a reduction of three and two orders of magnitude, respectively. The author also reports that the application of an ONO intermediate layer stack similarly leads to a decrease in transition metal

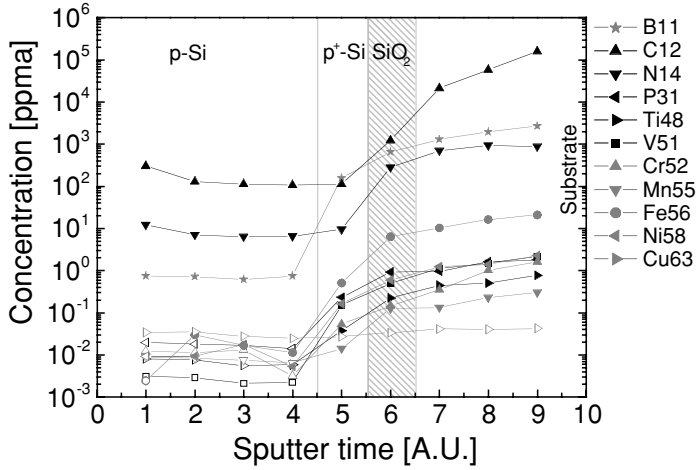

Figure 2.3 GDMS impurity profile of a silicon film prepared on a SiO_2 encapsulated SiSiC ceramic substrate. Hollow symbols denote measurement signals below the detection limit.

contamination in the p^+-region, but the impurity concentration drops below the detection limit within the epitaxial layer.

Compositional analysis of CSiTF structures can be a very efficient way of evaluating the effectiveness of diffusion barriers. The analysis showed that SiO_2 and SiN_x layers can be effective diffusion barrier layers even when applying them to very impure ceramics and to extreme process temperatures up to 1450 °C. This proof is still missing for SiC intermediate layers.

2.3 ZONE MELTING RECRYSTALLIZATION

For the thin film concept presented in this chapter, ZMR is a key technology. This process largely determines the crystallographic and electronic quality of the silicon thin film. This section starts with a short historical introduction to ZMR and then describes characteristics of ZMR film growth. Subsequently, typical features of ZMR thin films are discussed. A central aspect concerns the effect of scan speed on film quality, since this parameter mainly determines process costs. Further, concrete realizations of ZMR systems are presented. *In situ* process control is an important feature for automated high speed processing. The section concludes with the discussion of ZMR results on ceramic substrates.

2.3.1 Introduction

Typically, the crystallite or 'grain' size of Si films deposited on foreign substrates by high temperature CVD is in the micron range. So far, using conventional solar cell processes with p-n structure, the maximum conversion efficiency obtained on such thin films has been below 6 % [26, 53, 54]. Through solid or liquid phase recrystallization, grain size can be increased by several orders of magnitude, allowing much higher solar cell conversion efficiencies to be reached.

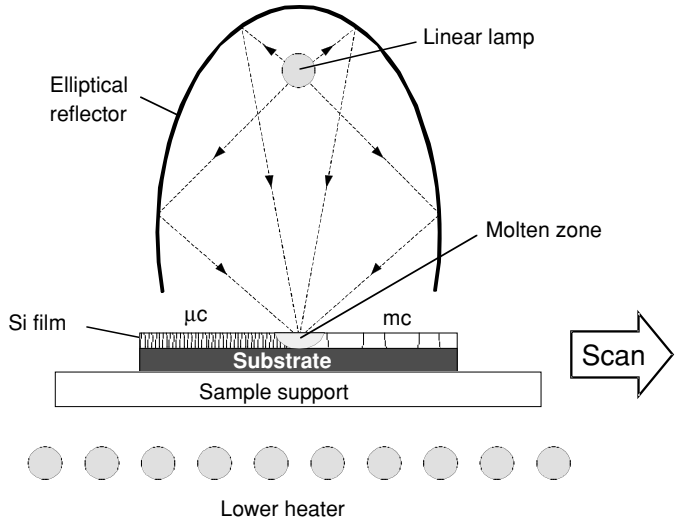

Figure 2.4 Principle of ZMR using linear halogen lamp heaters.

A recrystallization technique for PV has to fulfil the following requirements:

- Costs for this process step have to be lower than $\sim 20\,€/m^2$.
- The throughput of a respective processor needs to be at least $5\,m^2/h$.
- A processor for recrystallization needs to be uncomplicated and reliable; the process should be controlled automatically.
- Grain sizes larger than 100 µm should be achieved.

Zone melting recrystallization is one of the few techniques able to meet these requirements. The principle of this technique is shown in Figure 2.4, where halogen lamps are used as heat sources. Common to all ZMR methods is the creation of a narrow molten zone that is scanned across the thin film. Behind the focal line, the melt cools below the melting point and heterogeneous nucleation starts. Stable crystallites develop and act as seeds for further growth. Due to the anisotropic crystal growth speed (see, e.g. [55]) grains with a particular crystal direction soon prevail. This kind of geometric selection is well known from the Bridgman technique [56], one of the preferred methods for multicrystalline ingot growth in photovoltaics [57]. Grains grown by ZMR reach up to several millimeters in width and several centimeters in length.

A pioneer of ZMR was Leitz who, in 1950, patented a technique for growing single-crystal films of luminescent materials [58]. In the 1960s ZMR was investigated for the growth of low melting point semiconductors like germanium or InSb [59]. At this time initial experiments with silicon failed, but interest in ZMR was renewed in the 1980s when research into technologies able to produce silicon on insulator (SOI) films became of interest. Such films were desirable for high-speed integrated complementary metal oxide semiconductor (CMOS) circuits realized with small structures, little capacitance and avoidance of parasitic transistors, as well as for high power devices built up on insulators. A comprehensive review on activities and results

Table 2.1 Characteristics of different ZMR film growth methods

Heat source	Electron beam	Laser	Graphite stripe	Incoherent lamp
Temp. gradient	high	high	low	low
Grain size	μm–mm	μm–mm	mm–cm	mm–cm
Defect density	high	high	medium	medium
Substrate requirements	medium	medium	high	high
Film contamination	oxygen	oxygen	carbon, oxygen	oxygen
Investment costs	very high	high	low	low

during this period is given by Givargizov [60]. An overview with focus on modeling is provided by Miaoulis *et al.* [61].

For use in SOI technology ZMR wafers could not carry through in the face of other technologies like separation by implantation of oxygen (SIMOX) or wafer bonding. However, several research groups have examined the ZMR technique for an application in photovoltaics. As listed in Table 2.1, four different methods to generate the molten zone are being investigated:

- *Electron beam ZMR* An electron beam is generated in a vacuum environment and very rapidly melts a thin silicon layer [62]. Scan speed is very high (up to several cm/s), therefore the thermal load of the substrate can be kept low. Defect density in grains is comparatively high, but due to the low substrate temperature this method is especially useful for glass substrates.
- *Laser ZMR* A laser beam is scanned two-dimensionally across the silicon layer generating a zone of molten silicon [63]. Throughput is limited since the laser spots have to overlap and the resulting scan speed is comparatively low. Similar to electron beam melting, the thermal load of the substrate is also low due to extremely fast heating up and cooling down ramps, leading to highly defective crystals. Laser melting is preferentially used with glass as a substrate.
- *Graphite stripe melting* A graphite stripe located very close to the silicon surface is heated by an electrical current in a vacuum or inert gas environment [64]. The thermal load of the substrate is high, but temperature gradients are small and cooling ramps are smooth. As a result of this, crystal quality can be very high.
- *Incoherent lamp heating* Usually linear halogen lamps focused by an optical system, as shown in Figure 2.4, are used as energy sources to generate the molten zone. Layer properties are similar to those of strip heater ZMR, however, a higher reliability and a better process control can be achieved. In addition, contamination of the silicon layer by carbon is completely avoided.

The following sections focus on ZMR using linear halogen lamps.

Regarding this technique, it is especially worth mentioning the work of a group at Mitsubishi Electric Corp. [65]. Following the high temperature route using strip and lamp heater ZMR, this group reported remarkable conversion efficiencies of 16.45 % and16 % for $1 \times 1\,\mathrm{cm}^2$ [66] and $10 \times 10\,\mathrm{cm}^2$ thin film solar cells [67], respectively.

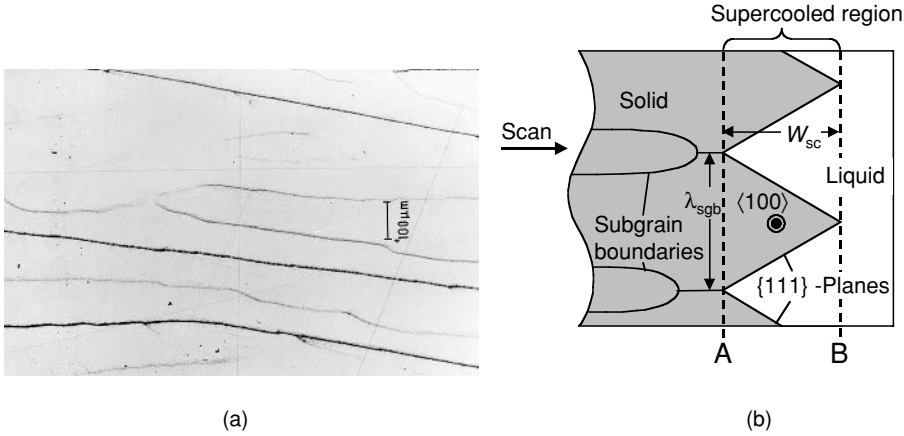

Figure 2.5 (a) Structure of Subboundaries in an epitaxially thickened ZMR Si film revealed by etching and optical microscopy [76]. (b) Scheme of crystallization front morphology and subboundary formation. For faceted growth there is a direct relationship between subboundary spacing λ_{sgb} and the depth of the supercooled region $W_{sc.}$

In the last decade progress in ZMR technology has mainly been made in three fields: (i) equipment development, (ii) process control and (iii) numerical modeling, the latter being enabled by the advances in computer technology. References and details regarding these developments are given in Sections 2.3.4.1, 2.3.4.2 and 2.3.2.

2.3.2 Zone melting recrystallization film growth

When ZMR grown thin films are preferentially etched (e.g. with a Secco[7] solution) they typically exhibit a defect structure as shown in Figure 2.5a. The defects visible as dark lines are caused by low angle grain boundaries. They run nearly parallel to the scan direction and most of the time they are regularly spaced. Other typical features are the development of new boundaries and the coalescence in a Y-shaped connection. Since these boundaries are found within a single grain they are called subgrain boundaries, or short subboundaries. Their origin has been the subject of various experimental and theoretical studies [69–75]. A historical overview with detailed discussion on the different models is given in the above mentioned book by Givargizov (see Ref. [60] p. 168ff).

Important progress in the understanding of subboundary formation was made with the analysis of crystallization front morphology. First hints on the structure were obtained by quenching experiments [70, 73]. The structure resulting from very rapid cooling was interpreted as an instant image of the crystallization front. Not a planar, but a faceted morphology was found, as sketched in Figure 2.5b. Further knowledge was gained from *in situ* observations using charge coupled device (CCD) cameras. These techniques were first developed for laser [77, 78] and electron beam ZMR [79]. Later they were also implemented for strip [74] and lamp heater sources [80]. Unlike the quenching results, *in situ* observations additionally yielded

[7] Mixture of HF (48 %) and $K_2Cr_2O_7$ (0.15 molar solution) in the ratio 2:1 [68].

information on temporal development and the stability of the crystallization front. *In situ* observations are also the base for advanced process control, as discussed in Section 2.3.4.2.

Today, it is generally agreed that subboundary formation and the particular crystallization front morphology are caused by an instability of the solid–liquid interface due to supercooling.

Leamy *et al.* [81] and Lemons *et al.* [82] attributed subboundary formation to constitutional supercooling, i.e. supercooling due to the segregation of impurities ahead of the crystallization front. This mechanism is well known to be responsible for microcellular morphologies in other growth techniques like the Czochralski method [83, 84].

However, nonplanar morphologies have also been observed for stationary heating where constitutional supercooling is not present. By careful microscopic *in situ* observations Im and coworkers verified the development of nonplanar solidification front morphologies for stationary strip heater ZMR [74]. Im *et al.* attributed the observed morphologies to a 'radiative' supercooling. In this model, supercooling is explained by the difference in reflectivity between the solid and liquid phase. The reflectivity of liquid Si [$R_l(0.6\ \mu m) = 0.7$] is much higher than that of solid Si [$R_s(0.6\ \mu m) = 0.3$].[8] Therefore, in the liquid state it absorbs less radiation than in the solid state. The effect is a supercooling of the liquid Si and a superheating of the solid Si near the solid–liquid interface.

Although constitutional and radiative supercooling are caused by different processes, both lead to the same effect and result in a fundamental relationship between the temperature gradient at the solid–liquid interface and the depth of the supercooled region. This connection is explained with reference to Figure 2.5b. Assuming an initially planar solid–liquid interface, this interface is located at line A. The supercooled region extends up to line B with a depth $W_{sc.}$ This configuration is highly unstable. Small perturbations can cause the development of protrusions that extend up to the front given by line B.

This way the solid–liquid interface may self-adjust into a form that is more stable. For the cellular structure shown in Figure 2.5b, within the supercooled region, close to the solidification front (line A) most of the Si, on average, is solid while at the opposite site (line B) most of the Si is liquid. The experimentally observed maximum distance between tips and inner corners of the growth cells is a measure of the depth of the supercooled region W_{sc}.

In both cases, constitutional or radiative supercooling, the depth of the supercooled region depends on the temperature gradient at the solid–liquid interface. The smaller the gradient, the deeper the supercooled region. With the increase in temperature a transition of interface morphology has been observed, from dendritic, to cellular,[9] to planar [74, 87]. For the faceted cellular interface as shown in Figure 2.4b there is a direct relationship between subboundary spacing λ_{sgb} and the depth of the supercooled region W_{sc}. This configuration yields the lowest defect density, which is confirmed by experimental results [61, 87, 88]. Films grown with a dendritic or planar interface are much more defective.

The choice of heat source significantly effects the temperature gradient and therefore the film quality (Table 2.3.1). Strip or lamp heater sources produce much lower temperature gradients

[8] Reflection values for liquid silicon calculated from refractive index and extinction coefficient at $\lambda = 0.6\ \mu m$ given in Ref. [85]. For solid silicon and wavelengths $\geq 0.6\ \mu m$ the extinction coefficient is negligible [40]. A more detailed analysis additionally has to take into account the corresponding emissivity values. They differ from the former ones since temperatures of silicon film and lamp filament are not the same [86].

[9] The nomenclature for this growth morphology is not consistent. Some authors distinguish between *cellular* and *faceted* growth (e.g. see Ref. [80]). Here we follow the naming in Ref. [60], where *cellular* is the main category divided into the subcategories of *rounded* and *faceted* cellular growth.

than laser or electron beam heat sources. This explains why lamp or strip heater ZMR produce better crystallographic quality than laser or electron beam ZMR [89].

Another aspect discussed in Table 2.3 is common impurities. During ZMR processing the silicon film is typically in contact with at least one SiO_2 layer: (i) eventually an SiO_2 intermediate layer and (ii) a SiO_2 or SiO_2/SiN capping layer to prevent agglomeration of molten Si (balling-up effect). Therefore oxygen concentrations up to the solubility limit are found in recrystallized layers [71, 90]. For strip heater ZMR an additional source of contamination is the graphite stripe, which is thought to be responsible for high carbon concentrations [69].

As discussed before, the most stable ZMR growth and the lowest defect density is observed for cellular interface morphologies. In the case of faceted cells, the interface is composed of $\{111\}$ planes, which for silicon are the slowest growing faces. Both scan direction and surface normal are then in a $\langle 100 \rangle$ direction. The phenomenon of preferred orientation of the crystallites in a polycrystalline solid is referred to as texture.

Experimental investigations showed that the percentage of $\{100\}$ oriented grains depends on the silicon film thickness and the scan speed [91]. It was determined that critical thicknesses below which the $\langle 100 \rangle$ orientation dominates range from 2 μm to 5 μm [77, 92]. Biegelsen *et al.* have given an explanation for the preferential orientation based on the anisotropic interfacial free energy between crystalline silicon and SiO_2 [93]. The $\langle 100 \rangle$ texture is especially useful for the implementation of a light trapping structure since it allows an easy to apply surface texturization by anisotropic etching.

2.3.3 Features of silicon layers recrystallized by zone melting recrystallization

2.3.3.1 Grain size enhancement

The most prominent effect of ZMR is the enlargement of silicon grains, by the mechanism explained in Section 2.3.2. Figure 2.6 shows Secco etched cross-sections illustrating the effect: (a) is a typical view of an as-deposited silicon layer, grain size is in the micron range. The

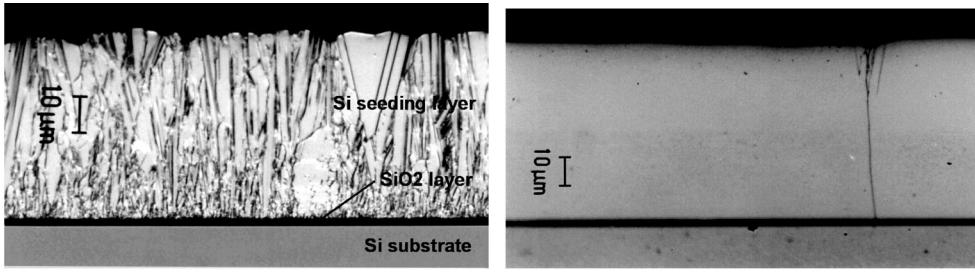

Figure 2.6 Cross-sectional Nomarski photographs of a silicon layer on top of a SiO_2 coated Cz-Si substrate before (a) and after (b) ZMR. Images taken from C. Hebling, Die kristalline Silicium-Dünnschichtsolarzelle auf isolierenden Substraten, Ph.D thesis, Universität Konstanz (1998).

first 5 μm deposited consist of even smaller grains of submicron size; (b) shows the result after ZMR, where the cross-section was taken perpendicular to the scanning direction. In the selected area one grain boundary is visible. The microcrystalline structure has been replaced by a coarse grained structure with grain widths usually significantly larger than 100 μm.

ZMR works extraordinarily well for 1–5 μm thick silicon layers on polished and SiO_2 coated Cz-Si substrates. For optimized ZMR conditions (i.e. extremely homogeneous power distribution in the melt zone, very homogeneous thickness of substrate and all functional layers, and a very stable capping layer – sometimes even the use of a combined SiO_2/SiN_x layer is reported) the resulting layer can be nearly monocrystalline. The more imperfections present (e.g. variation in layer thickness or in temperature/radiation distribution), the higher the deviations from this ideal result. For minor imperfections, the resulting grain width decreases to a value of approximately 1 cm. Still, grains have substrate length, with crystal orientations slightly deviating from the ideal <100> direction. The grain area enhancement is from $\sim 1\ \mu m^2$ to $\sim 10\ cm^2$, i.e. a factor of 10^9. If the sample and ZMR processor setup exhibit more severe imperfections, the grain size decreases further. For applications in PV, the very stringent cost requirements lead to non-ideal (e.g. ceramics) substrates, less homogeneous layers and less sophisticated ZMR processors. In consequence, processing with these conditions typically yields a state as shown in Figure 2.7. Grain width usually ranges between 0.5 mm and 5 mm, and grain length is in the order of several 10 mm, which is still a increase in grain area by a factor of 10^7 to 10^8. The grains do not run perfectly parallel anymore, but they are tilted against the scanning direction. This leads to the formation of new grains at the intersection of two tilted grains, so grains generally become shorter than the substrate length. At the edges of the sample in Figure 2.7 the silicon layer is non-recrystallized and the surface appears homogeneously grayish, clearly illustrating the grain enlargement effect of ZMR.

Figure 2.7 Top view of a ZMR recrystallized layer on a $50 \times 50\ mm^2$ SiO_2 coated mc-silicon substrate. Scan direction was from bottom to top, the molten zone was in the horizontal direction. Images taken from C. Hebling, Die kristalline Silicium-Dünnschichtsolarzelle auf isolierenden Substraten, Ph.D thesis, Universität Konstanz (1998).

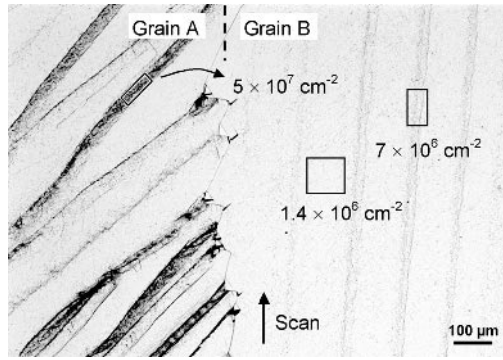

Figure 2.8 Polished and Secco-etched surface of a ZMR seed film thickened by epitaxy (optical micrograph). Subgrain boundaries in the seed film yield stripes with high dislocation density.

2.3.3.2 Microstructure and origin of defects

In Section 2.3.2 it was discussed how defects – namely subgrain boundaries – are created during the ZMR process. After the recrystallization process, however, the highly doped silicon films are usually thickened by epitaxial growth with normally doped Si. At this stage the films are used for solar cell processing. Therefore, the relationship between defects in the ZMR seed film and the epitaxially grown film is of importance. The surface of such a film after polishing and treatment with Secco etch [68] is shown in Figure 2.8. Areas with dislocation density (macroscopically detectable as etch pit density, EPD) much higher than the background are visible as characteristic dark stripes. Two typical grains are labeled: grain B, where the direction of subgrain boundaries was nearly parallel to the scanning direction; and grain A, with subgrain direction tilted significantly to the scanning direction. In the two grains the value of the EPD varies strongly. The 'background' value e.g. in grain B is around $1 \times 10^6\ \mathrm{cm}^{-2}$, whereas the EPD in the areas with higher dislocation density in this grain is seven times higher. The background EPD value in grain A is very similar to that of grain B. The areas with higher dislocation density, however, are both more frequent, i.e. they take a larger area fraction, and their EPD values are about ten times higher than those areas with higher dislocation density of grain B. This example shows a typical feature of the microstructure of ZMR films for PV: the defect density, i.e. the quality of neighboring grains can differ dramatically.

The origin of the high dislocation stripes are subgrain boundaries in the ZMR seed film, as can be deduced from Figure 2.9. This figure shows a beveled section of an epitaxially thickened ZMR silicon film. It proves that the defects visible in Figure 2.8 originate at the subgrain boundaries.

Figure 2.10a–c show details of the beveled section of Figure 2.9. The images show a clear correlation between dislocation density in the seed film and the epitaxial film. Three different types of structures can be distinguished. In Figure 2.10a the dislocation density in the area between the two subgrains is higher than that in the surrounding area, but no explicit boundary is visible. Compared to Figure 2.10a, dislocation density in Figure 2.10b is much higher. Etch pits overlap and form clusters. The dislocation density in the epitaxial film is also much higher than in the former case. Figure 2.10c differs from the other two images by a straight subgrain boundary line. Here the dislocation density in the epitaxial film is at its highest.

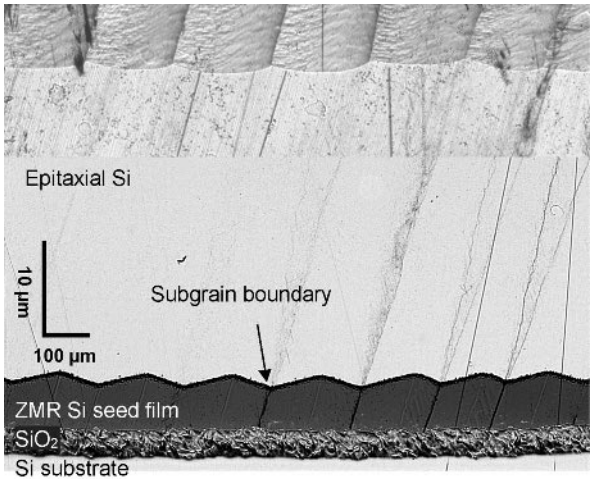

Figure 2.9 Beveled section of a ZMR Si film thickened by epitaxy. The vertical scale drawn is a projection of the Z-scale on the beveled surface which is declined 2 °52' relative to the sample's surface.

Figure 2.10a–c further show that dislocation density is generally higher in the epitaxial film compared to the seed film.

The following can be deduced from these observations about ZMR of layers for PV: if the seed layer concept is used for CSiTF, i.e. an epitaxy is done to thicken the seed layer, the key to high quality layers is an optimum ZMR process, with uniform layers on uniform substrates. Therefore, very strong R&D efforts are needed to attain these requirements, whilst remaining within the cost constrains.

2.3.3.3 High speed recrystallized silicon layers

Remaining within the maximum allowable processing costs directly translates into increasing the ZMR scan speed. In principle ZMR is not a consumable intensive process, so investment costs per processed area dominate the overall processing costs. Detailed calculations show that in order to achieve a ZMR cost below 10 €/m^2, the process scan speed must be higher than

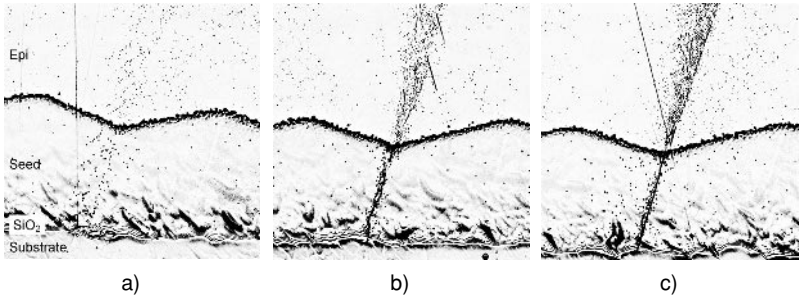

Figure 2.10 Details of the beveled section shown in Figure 2.9 exhibiting a different number and structure of dislocations at the boundary between neighboring subgrains in the seed film. To enhance the contrast the dark background in the seed film region was removed by image processing.

100 mm/min and the throughput per processor must be higher than 10 000 m^2/a [95]. Most publications report the use of a scan speed in the range 10–20 mm/min. Investigations into the influence of a higher scan speed on crystal structures and defect density were done in the early 90s by the group at Mitsubishi Corp. [64, 91, 96]. Their focus was on comparatively thin seeding layers of up to 1 μm thickness. Scan speeds up to 360 mm/min were investigated. The main results of their work can be summarized as follows:

- For thick layers (1 μm and above), an increase in the scan speed is quite detrimental, since defect density already increases dramatically even at moderate speed.
- The thinner the seeding layer, the less pronounced is the increase in defect density. With thin layers (∼0.3 μm) defect densities below 10^6 cm^{-2} could be achieved even at very high scanning velocities.

These results, which apply to ideal substrates, clearly suggest using very thin layers, if high crystal qualities are to be achieved. Unfortunately, this conclusion cannot be adapted to CSiTF layers for PV where low cost substrates have to be used. Very thin seeding layers are not compatible with ZMR silicon layers on low cost substrates due to the prevelant high surface roughness. Typical values for average surface roughness are in the range of 2–5 μm, exceeding the optimum layer thickness used in the Mitsubishi experiments roughly by a factor of ten. At Fraunhofer ISE an experiment similar to that of the Mitsubishi group was performed, using 2 μm and 8 μm thick films, and scan speeds in the range of 10–100 mm/min [97]. Although the relationship between scan speed and EPD was in accordance with the Mitsubishi results, the behavior concerning thickness was contradictory: 8 μm thick layers resulted in better quality than 2 μm layers. New experiments by the Fraunhofer ISE group did not focus on layer thickness (8 μm and 12 μm thick layers were used) but on scan speed (20–400 mm/min), and the difference in EPD before and after epitaxy [98].

Shape of the melting zone

Melting zone morphology shows significant differences in three criteria when using low or high scan speeds, respectively. Illustrated in Figure 2.11 is an example of each of those two scanning conditions. The first criterion is the width of the melting zone: the higher the speed the wider the melting zone has to be to achieve complete melting and faceted growth. A typical melt zone width at scan speed $v_s = 200$ mm/min is more than three times higher than the width at $v_s = 20$ mm/min (1.1 mm). Secondly, the average size of faceted growth cells increases with higher scan speed. According to Section 2.3.2 the size of the growth cells is directly related to the subgrain boundary spacing and the generated defect density can therefore be expected to be lower. A possible explanation for the larger size of growth cells is a lower temperature gradient at the solidification front, also proposed in the models of constitutional and radative supercooling described in Section 2.3.2. In fact, since at high scan speeds the solidification front is no longer directly heated by the focus lamp, it seems plausible that the temperature gradient between liquid and solid silicon is more gentle than at lower speeds. The third observation is a higher geometric instability of the facets in time. They move laterally, vanish and emerge much more frequently at higher speeds than at lower speeds. Translated to subgrain boundaries this means that at high speeds they do not run parallel any more, but they combine and split up frequently. Consequently, the gain in size of subgrains due to larger growth cells, and with that a possibly lower defect density, is probably compensated or maybe even over-compensated.

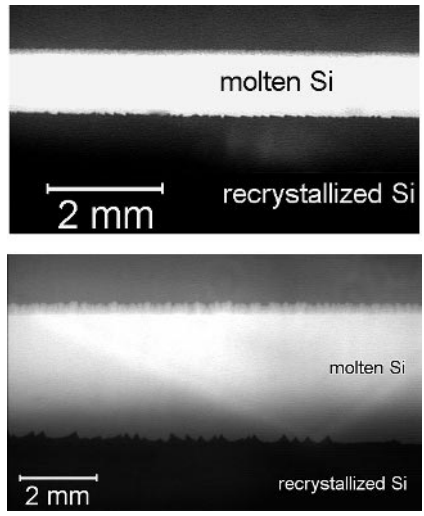

Figure 2.11 Snapshot of a typical melting zone at 20 mm/min (top) and 200 mm/min (bottom) recrystallization speeds. Note the different scale of the two images. Reprinted from *Journal of Crystal Growth*, **287**, S. Reber, A. Eyer, and F. Haas, High-throughput zone-melting recrystallization, 391–398. Copyright (2005), with permission from Elsevier.

Grain shape

Figure 2.12 shows photographs of seeding layers (12 µm thick) recrystallized at low (20 mm/min, left) and high speed (300 mm/min, right). Obviously, the structure of the low speed sample is much more regular. This reflects the stability of the crystallization front described above.

Grain width of the low speed sample is in a typical range of 1–3 mm, with single grains achieving widths up to 13 mm. The typical grain length is several centimeters. The number of small grains with a size of less than 1 mm is very rare. The situation is different for the high speed sample. Grain size is limited to only a few millimeters in width. Within large grains small grains visible as little dark spots or line shaped areas in Figure 2.12 (right) are included, the difference in color indicates a different crystal orientation. A closer look shows that the size of these grains is still in the order of several hundred micrometers, therefore their size does not necessarily limit the solar cell's performance.

Defect density

Intragrain defects are the crystal features influencing CSiTF solar cell performance most severely, as shown above. Counting of EPD is very useful for characterizing the defect density of silicon layers. However the method has its limitations. Since the typical diameter of etch pits used for this investigation is in the range of 0.3 µm, etch pits start overlapping at an EPD of around 3×10^7 cm^{-2}. EPD values higher than this value therefore have to be regarded as a lower limit of the true EPD value (which of course remains unknown).

Figure 2.13 summarizes the results of an experiment which examined the EPD of layers recrystallized at different speeds [98], either with (graph b) or without[10] (graph a) additional

[10] In the following also called "bare ZMR layer".

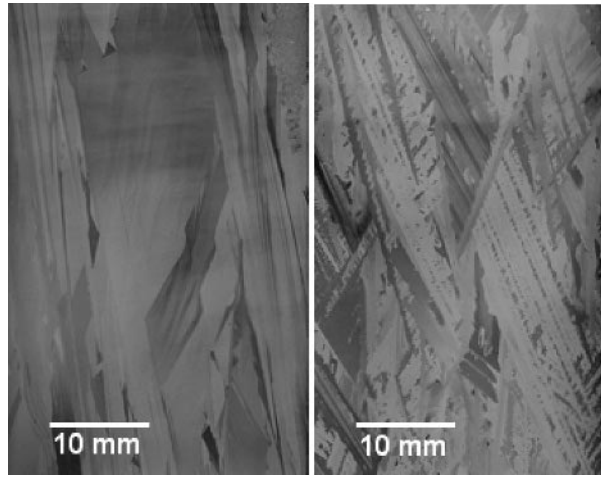

Figure 2.12 Photograph of silicon layers after recrystallization at a scan speed of 20 mm/min (left) and 300 mm/min (right). Reprinted from *Journal of Crystal Growth*, **287**, S. Reber, A. Eyer, and F. Haas, High-throughput zone-melting recrystallization, 391–398. Copyright (2005), with permission from Elsevier.

epitaxial layer. The limitations of the EPD method affect only graph b, the curve for the epitaxially thickened ZMR layers: the curve shapes for EPD values exceeding $10^7\,\mathrm{cm}^{-2}$ as well as the calculated mean values only denote a lower limit of the EPD.

Mean values of EPD for bare ZMR layers do not vary significantly with scan speed for the range of 50–350 mm/min. Their values of $3–5 \times 10^6\,\mathrm{cm}^{-2}$ are still moderate and can be acceptable for CSiTF solar cells. The lower limit of the mean EPD for epitaxial layers, as calculated from the curves shown in Figure 2.13 (bottom), is around $3 \times 10^7\,\mathrm{cm}^{-2}$, nearly one order of magnitude larger than that for bare ZMR layers. This result is in good accordance with the data given by the Mitsubishi group [99]. In addition it reflects the qualitative observations of an increasing defect density with thicker epitaxial layers, as described in Section 2.3.3.2.

In terms of EPD the bare ZMR layers are therefore clearly superior to those with an additional epitaxial layer. This finding extends the conclusion drawn at the end of Section 2.3.3.2: concerning defect density, an alternative way to achieve high quality ZMR layers at high speed, is to skip the seeding layer concept and just use the ZMR layer as the active solar cell base. Of course this recommendation raises further questions, like the performance of bare ZMR layers in thin film solar cells, or the realization of low surface recombination velocity at the rear side, which is of utmost importance for the high conversion efficiency of thin film solar cells.

2.3.4 Development of lamp heated zone melting recrystallization processors

As described above, lamp heated ZMR processors are the ones which deliver the best layer quality concerning grain structure, defect density and process related contamination. Consequently, the best solar cell results have also been achieved using lamp heated ZMR processors,

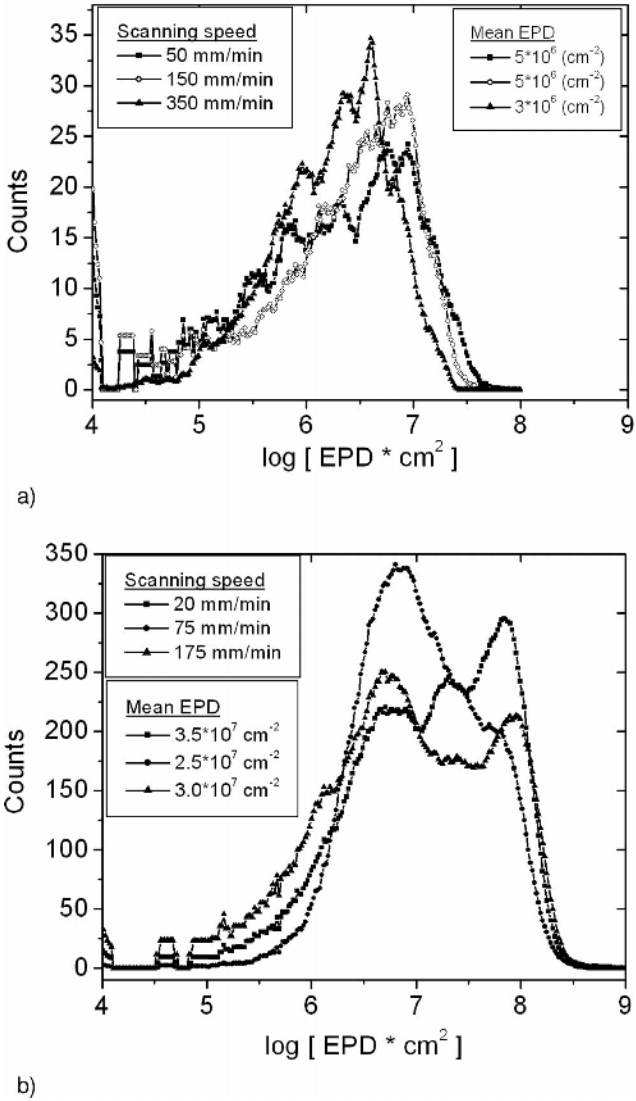

Figure 2.13 Distribution of etch pit density measured at the surface of ZMR silicon layers a) without and b) with an additional epitaxial silicon layer. Sample size was $8 \times 8\,\text{mm}^2$. Reprinted from *Journal of Crystal Growth*, **287**, S. Reber, A. Eyer, and F. Haas, High-throughput zone-melting recrystallization, 391–398. Copyright (2005), with permission from Elsevier.

and they are now routinely used in several R&D groups. The main issue concerning ZMR processor development is increasing the throughput by scaling up the width, reducing the sample loading/unloading time, increasing the ZMR speed and improving the automated process control. Probably the most advanced ZMR processor with respect to this main issue is currently operative at the Fraunhofer Institute for Solar Energy Systems [98, 100]. Therefore, the following description focuses on this high throughput processor.

2.3.4.1 System setup

Lamp heated processors for ZMR of thin silicon films were already reported in the early 80s for SOI applications in microelectronics [101]. Their application for PV was published more than one decade later, by the Mitsubishi group in 1996 [102] and by the Fraunhofer ISE in 1998 [94]. An advanced version was reported by the Fraunhofer ISE in 2001 [103]. The setups of the first and the latter ZMR processors already featured the core part of the setup used today (see Figure 2.4): a linear halogen lamp is located in the first focal line of a reflecting cylindrical ellipse ('focus mirror'); the second focal line lies in the plane of the silicon film of the sample. The sample is moved perpendicular to the focal line for ZMR. It is homogeneously preheated by the base heater located below the sample, consisting of an array of linear halogen lamps. The molten zone generated by the focus heater can be observed by CCD cameras; the images are analyzed to extract its width. The Mitsubishi group uses a hardware analyzer for this purpose, Fraunhofer ISE applies vision software (see Section 2.3.4.2). The respective sample size which can be homogeneously recrystallized is 6" (round) for the Mitsubishi processor and 100 mm for the Fraunhofer ISE processor.

A scaled up processor for up to 400 mm wide substrates was reported in Ref. [100]. This processor, called 'ZMR400', had a larger furnace body with accordingly larger lamps, a load lock at the loading side and a sealed feedthrough for sample transportation, but has left the principle used in the smaller sized processors otherwise unchanged. Homogeneous recrystallization was feasible for samples larger than 300 mm in width, however throughput of the ZMR400 was limited.

Therefore the ZMR400 was extended to a fully in-line, continuous ZMR processor named 'ZMR400con' (see Ref. [98]). Figure 2.14 sketches the principle of this processor: the load lock is replaced by gas curtain sections on the front and rear side of the furnace body, the sample is transported from loading station to unloading station by a walking beam mechanism. A crossed lamp array was realized which allows control of the power density, both in the transport direction and perpendicular to it, in order to improve the lateral homogeneity of the molten zone. This setup of the base heater had already proved to be effective in the ZMR processor of the Mitsubishi group.

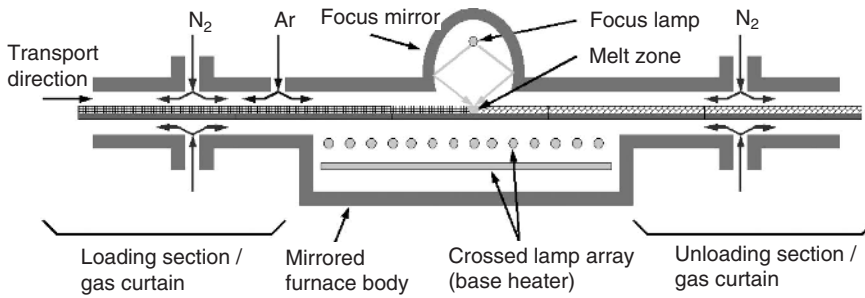

Figure 2.14 Sketch of a section of the ZMR400con. Reprinted from *Journal of Crystal Growth*, **287**, S. Reber, A. Eyer, and F. Haas, High-throughput zone-melting recrystallization, 391–398. Copyright (2005), with permission from Elsevier.

The modified sample loading and transport system increased the throughput of the ZMR400con to a maximum value of approx. 10 m^2/h.

The authors reported homogeneous recrystallization of four 100 × 100 mm^2 large silicon coated substrates, placed next to each other to form a 400 mm wide substrate array. Good results also have been achieved when using 200 × 200 mm^2 large silicon or ceramic substrates with a silicon layer (see also Section 2.3.5) [95].

2.3.4.2 Process control

The connection between temperature gradient, growth morphology and defect density has already been discussed in detail. According to this discussion, the precise control of the temperature gradient at the crystallization front is of immense importance for the growth of high quality ZMR thin films.

Unfortunately, the value of the temperature gradient is not easily determined by direct measurements. However, the good visibility of molten Si, due to the change in reflectivity, can be utilized for an indirect measurement. The width of the molten zone is connected to the thermal gradient at the crystallization front as demonstrated by Robinson and Miaoulis using numerical modeling [86]. The smaller the molten zone, the lower the thermal gradient. This result is consistent with experimental observations of the crystallization front morphology [87, 104]. Therefore image analysis can be used to detect the width of the molten zone and to implement a ZMR process control.

Wong and Miaoulis were the first to report such a control for the recrystallization of gallium films [105]. Their system implemented two control parameters: (i) crystallization front position and (ii) crystallization front pattern. A successful control of the crystallization front position was demonstrated. However, the system suffered from unstable lighting conditions and a relatively long sampling time.

Kawama and coworkers at Mitsubishi Electric Corp. implemented a process control for ZMR of silicon films, employing a CCD camera with a subsequent commercial width analyzer [102]. Their experiments confirmed that the width of the molten zone is a useful parameter to control crystallization front morphology. The authors claimed to keep the width of the molten zone constant within ±10 % relative (usually approx. 0.1 mm) [64].

An advanced ZMR process control realized in the processor described in Section 2.3.4.1 was developed originally by one of the authors [76]. Image acquisition is done by several miniature CCD cameras. A software application realizes the process control, including analyzing the width of the molten zone and implementing closed-loop feedback using this parameter to control the focused lamp (Figure 2.15):

For standard substrates, this automatic control is able to keep the width of the molten zone within a range of ±5 % from the desired value. Successful ZMR process control for scan speeds up to 400 mm/min has been demonstrated [98], the ZMR results having already described in the previous section. At such speed manual control would cancel out.

As an example, Figure 2.16 shows data recorded during an automatically controlled ZMR process of a 50 mm long sample. The actual width of the molten zone only deviates slightly from the desired value of 1.0 mm. Noticeably, the power of the focus lamp is significantly lower in the center than at the start, a behavior also reported by the Mitsubishi group [102]. This finding can be explained by an effect well known from rapid thermal processing: wafers

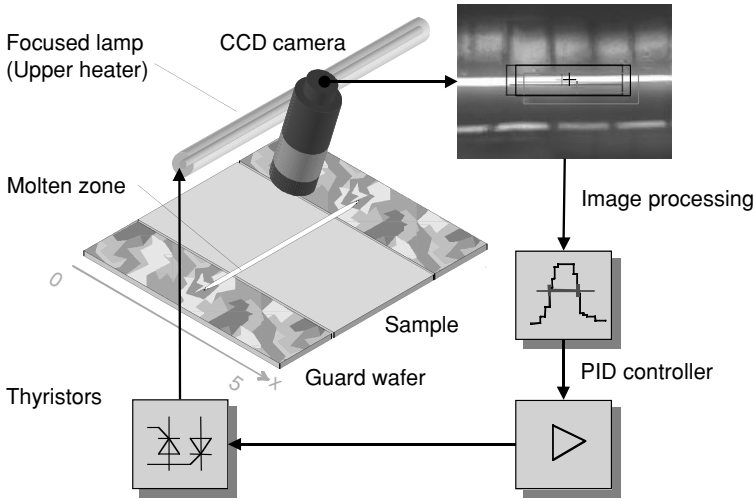

Figure 2.15 Closed-loop control implemented in the ZMR 100 system.

homogeneously irradiated from top or bottom are colder at the edges than at the center due to radiation losses at the unheated sides. This effect is often diminished by the use of so called 'guard rings' that artificially extend the wafer area [106]. Analogously, in the ZMR reactor 'guard stripe' wafers are placed parallel to the sample (Figure 2.15). Without guard wafers the width of the molten zone would decrease at the wafer edges, yielding a cigar like form.

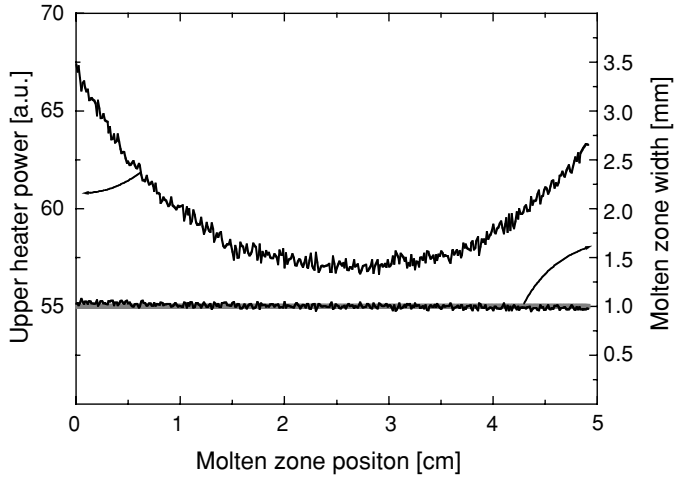

Figure 2.16 Upper heater power (focused lamp) and width of the molten zone as a function of the zone position for an automatically controlled ZMR process. The thick gray line indicates the desired value, the lower thin line the actual width. The PID controller adjusts the lamp power (upper thin line) to minimize the difference between desired and actual width.

2.3.5 Zone melting recrystallization on ceramic substrates

The discussions in the previous sections show that the quality of a ZMR silicon layer depends on many parameters, even if model substrates are used. The situation gets much more difficult if not 'ideal' but ceramic substrates are used. Usually a ceramic differs from a silicon substrate in the following most prominent 'material intrinsic' properties important for ZMR behavior:

- *Surface roughness* A silicon substrate can be made quite smooth on a microscopic scale by simple isotropic etching, e.g. by a CP133[11] chemical polish etch. However, the surface of a ceramic substrate usually cannot be altered by chemical etching, and remains in the state achieved after sintering. Depending on the substrate material and manufacturing processes, the average roughness can be in the range of 0.1–10 μm, usually being higher than 2 μm for cost effective ceramics. The minimum thickness of the seeding layer should exceed this value roughly by a factor of three.
- *Open porosity and pore diameter* Some ceramic types, especially tape cast ceramics, feature an 'open porosity' of 30 % and higher. The term "open porosity" means that pores agglomerate to form open paths throughout the whole ceramic. If the intermediate layer is not dense, liquid silicon can vanish through those open pores into the bulk of the substrate during ZMR, i.e. the silicon from the seeding layer is soaked up by the substrate. More important than the open porosity itself is the average diameter of the pores. Due to the high surface tension of liquid silicon, the tendency to vanish in the bulk of the substrate decreases with smaller pores. In any case, a well suited intermediate layer closing all open pores of the substrate surface makes ZMR much more reliable.
- *TEC* The TEC for a ceramic usually differs from that of silicon. Depending on the type of ceramic, the difference can be up to a factor of two e.g. for Al_2O_3 ceramics. Even better matched material relevant for PV substrates like SiC based ceramics or Si_3N_4 can deviate significantly in TEC. To avoid cracks or blisters, length difference between the silicon layer and substrate due to different TEC's has to be lower than 0.1 % of the total length in the whole temperature range.
- *Thermal conductivity* Due to compositional variation (pores e.g. are the most severe ones), thermal conductivity of the ceramics can vary locally. This leads to temperature variations in the recrystallization front during ZMR and consequently to nonideal ZMR behavior.

In addition to these material intrinsic effects, geometrical issues can also limit the ZMR success: substrate warpage can occur before or during ZMR, the seeding layer then gets locally out of the focus of the focal lamp, changing the power distribution and lateral homogeneity. In addition, thickness variations of the substrate can lead to the same effects as the locally varying thermal conductivity mentioned above.

In the following few pages some exemplary results on suited and nonsuited ceramic substrates are given.

Figure 2.17 shows a silicon layer on top of a PECVD-SiC coated RBSiC ceramic successfully recrystallized using the ZMR400con [95]. The grains are up to several millimeters wide, and partially nearly as long as the substrate itself. In this case, TEC matched well, and warping

[11] CP 133: Chemical Polish consisting of HF (50 %), HNO_3, CH3COOH in the ratio 1:3:3.

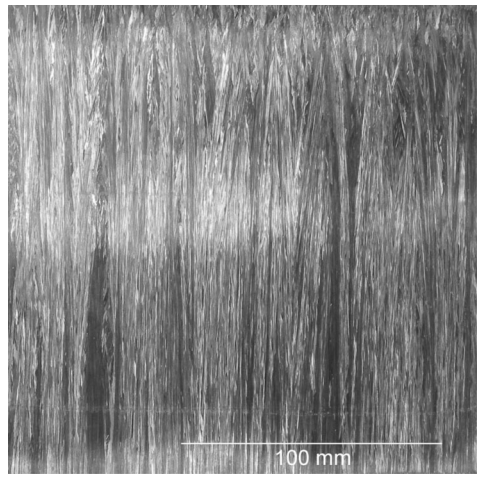

Figure 2.17 ZMR silicon layer on top of a SiC coated tape cast RBSiC substrate. Scanning direction was from top to bottom. Reproduced with permission from S. Reber et al., Progress in crystalline silicon thin-film solar cell work at Fraunhofer ISE. In *Proc. 20th European Photovoltaic Solar Energy Conference and Exhibition*, edited by H. O. W. Palz and P. Helm. pp 694–697. Copyright (2005) WIP-Renewable Energies, Minuch, Germany.

was below a critical value and hence did not influence ZMR too severely. Only approx. 1 cm of the edges width were affected and they were cut away after ZMR.

At first sight, ∼1 mm thick hot pressed RBSiN substrates as shown in Figure 2.18 seem to exhibit perfect properties for ZMR: the resulting grains are very large with nearly ideal structures (left part of the picture). A closer look at the epitaxially thickened silicon layer reveals that a network of cracks has affected its integrity. The obvious reason for this negative effect is the small difference in TEC between ceramics and the silicon layer. Although the

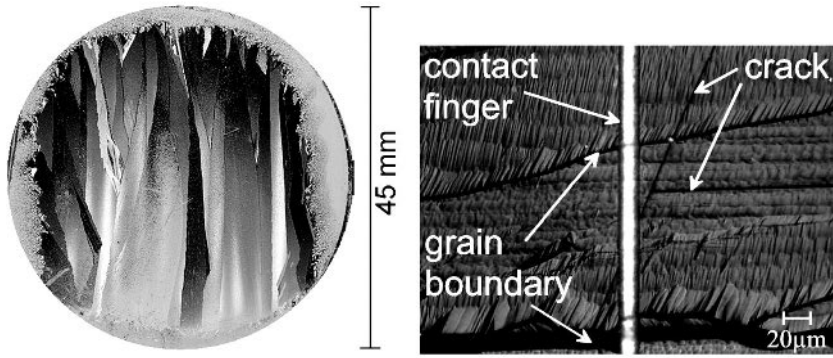

Figure 2.18 Silicon layer on hot pressed RBSiN ceramic substrate after ZMR and epitaxy (Ref. [19]). Left: photograph of the whole sample. Right: close-up after solar cell processing. From S. Reber *et al.*, Crystalline silicon thin-film solar cells on silicon nitride ceramics, in *Proc. 16th European Photovoltaic Solar Energy Conference*, B.M.H. Scheer, W. Palz, H.A. Ossenbrink, and P. Helm (Eds.), James & James Publishers Ltd., 2000.

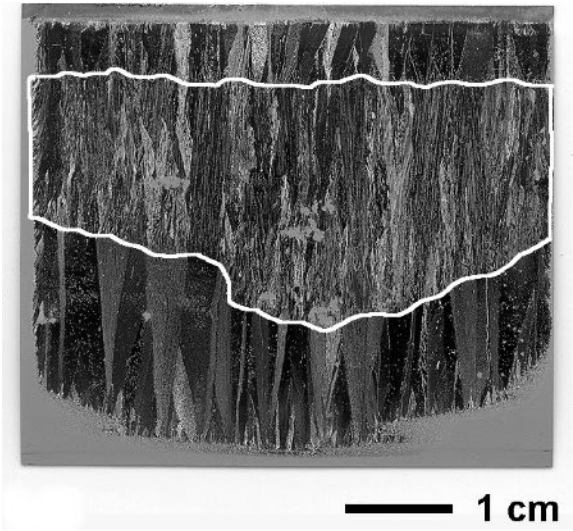

Figure 2.19 Silicon layer on top of a ONO coated tape-cast Si_3N_4 ceramic substrate after ZMR and epitaxy. The white line was drawn to highlight the badly recrystallized area of the sample.

cracks are quite small, their detrimental influence on the solar cell performance is dramatic, as shown later in Section 2.5.3.

An inhomogeneous width of the molten zone characterized the recrystallization process on ONO capped, 250 μm thin tape cast Si_3N_4 ceramics, with the results being shown in Figure 2.19. In some areas, encircled by the white line in Figure 2.19, the power intensity was high enough to melt even parasitic silicon depositions on the rear surface of the sample. Due to the resulting low temperature gradient, the crystal structure of the recrystallized silicon film was characterized by small grains in these regions. A faceted growth front was observed on part of the samples, indicating oriented crystal growth. In this case, large grains several millimeters in width and centimeters in length were developed. Inhomogeneous thermal properties, which are the reason for the inhomogeneous ZMR results, could have influenced this case in two ways: firstly, incomplete mixing of the starting powders or nonuniform sintering conditions may have caused inhomogeneous Si_3N_4 tapes; secondly, severe warpage was the reason that the sample's back side was only in local contact with the carrier quartz plate during ZMR, thus generating 'hot spots' where the parasitic rear deposits were molten.

To summarize, for successful ZMR on ceramics the substrate/intermediate layer system has to be chosen very well. If so, ZMR can yield silicon layers with grain size and defect density of a sufficient quality to realize solar cells with a conversion efficiency significantly exceeding 10 %.

2.4 SILICON DEPOSITION

The basic step in any CSiTF solar cell concept is the deposition of the silicon layer. For the concept presented in this chapter, thermal CVD from chlorosilanes turned out to be the

optimum method. After discussing the reasons why this method is the best choice in the first section, some basics on the chemistry of thermal CVD from chlorosilanes will be given. The chapter continues with an overview of real life reactor and process developments. Finally, the application of the processes to ceramic substrates and zone melted silicon layers is given, with a focus on the effect of non-suited substrates on deposition quality.

2.4.1 Requirements of silicon deposition for photovoltaics

Nearly all R&D efforts in PV are related to the reduction of cost per W_p (watt peak). Cost effectiveness is also the most important requirement on a future silicon deposition processor and process. Simple calculations give an upper limit of about 30 €/m^2 for the deposition of a silicon layer suitable for c-Si thin film solar cells. The term 'suitable' here relates to the quality of the layer, which has to be sufficiently high depending on the application, as described in Section 2.4.3. Some general basic requirements of a silicon deposition tool and process can be specified:

- High throughput (5–10 m^2/h).
- High growth rates ($\geq$5 µm/min).
- High chemical yield of silicon precursor.
- Possibility to process rectangular or square wafers.
- Deposition possible on rough and porous ceramic substrates.
- Sufficient layer quality (diffusion length in epitaxial layers exceeding 2–3 times layer thickness).
- Controllable doping profiles.
- Simple setup with limited complexity.

Of all deposition methods (for an overview see e.g. [20]), thermal atmospheric pressure chemical vapor deposition (APCVD) from chlorosilanes at high temperatures is probably the most promising method capable of meeting all of these demands. Thermal CVD is based on the decomposition of silicon containing source gases at the heated sample surface and the subsequent incorporation of silicon atoms into the growing film. It can be carried out under different operational regimes depending on the process temperature and pressure. At high deposition temperatures up to 1300 °C, APCVD operates in the mass transport limited regime. Under these operating conditions, deposition rates up to 10 µm/min can be achieved. Trichlorosilane ($SiHCl_3$, TCS) highly diluted in hydrogen is typically used as a silicon source gas. *In -situ* layer doping is achieved by adding suitable dopant gases, e.g. diborane (B_2H_6) and phosphine (PH_3) diluted in hydrogen for p-type and n-type doping respectively. The APCVD process is better suited to epitaxial depositions because the high process temperature enables an optimal arrangement of deposited atoms in the silicon crystal matrix, and hence crystals with extremely low defect densities can be grown. Typically, silicon epitaxy by APCVD is carried out in a temperature range of 950–1250 °C. Compared to other deposition techniques,

which use high vacuums and complex systems, little technological effort is needed for CVD at atmospheric pressure and continuous systems are feasible.

In the microelectronic industry, CVD is a key technology which is commonly used for silicon epitaxial deposition. In this area, excellent crystallographic quality, thickness and doping uniformity in the 2 % range, and high purity are absolutely necessary [107]. Batch type systems (barrel reactors) or single wafer reactors are traditionally used. Operation at high gas flow rates enables one to achieve the required thickness and doping homogeneity, at the expense, however, of low chemical yield, low throughput and a therefore high cost per m^2. Regarding the total cost for the final microelectronic device, silicon deposition makes up only a small fraction even if cost intensive deposition techniques are used. From this point of view, the development of high throughput, low cost silicon deposition reactors is of no interest to the microelectronics industry. In contrast to that, the silicon deposition process constitutes a large fraction of the final cost for a silicon thin film solar cell, making the development of a cost effective silicon deposition reactor the most important subject of research. The most commonly used technique in CSiTF solar cell research is currently APCVD of silicon from chlorosilanes. In the following sections, the focus is only on work where APCVD deposition was applied for layer formation.

2.4.2 Some basics on thermal silicon atmospheric pressure chemical vapor deposition from chlorosilanes

The description of the silicon growth process in CVD is a complex issue where gas transport phenomena have to be coupled to chemical reactions on the substrate surface and in the gas phase. A general model describing the entire deposition process therefore involves the solution of many coupled partial differential equations. Because of the large complexity of the problem many authors restrict their analysis to a simplified model at specific operating regimes e.g. by neglecting gas flow dynamics. The development of improved models and simulation tools is still a current topic of research, the interested reader is referred to the literature, e.g. Refs. [108–110].

There are two key parameters for silicon deposition for PV which influence the throughput and cost of the deposition process: growth rate and chemical yield. Some important basic information shall be given for these two parameters.

2.4.2.1 Silicon growth rate in a $SiHCl_3$-H_2 system

Growth rate (also called deposition rate) in a TCS/H_2 precursor system is influenced by deposition temperature, gas phase composition and total pressure, as can be shown easily in experiments. For the definition of an optimum working point as well as an optimum reactor geometry, modeling of the deposition reaction is unavoidable. In Ref. [111] a theoretical growth model is presented and experimentally verified for a silicon deposition process based on the decomposition of TCS in a horizontal atmospheric pressure reactor at high temperatures. The chemical reaction leading to silicon deposition is assumed to be a two step reaction: firstly, $SiHCl_3$ molecules impinging on the substrate surface are chemisorbed to yield $SiCl_2$ and volatile HCl; in a further step, the $SiCl_2$ molecule reacts with H_2 to form HCl and solid silicon, the latter being incorporated into the crystal.

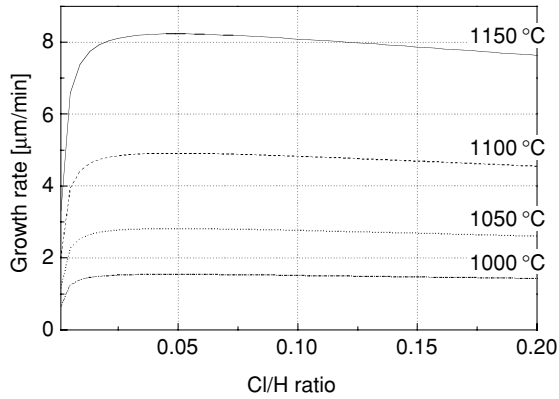

Figure 2.20 Growth rate depending on the temperature and the Cl/H ratio calculated according to the model of Habuka [112].

In a simplified form, the overall chemical reaction can be described by:

$$SiHCl_3 + H_2 \rightarrow Si + 3HCl$$

A simple calculation yields an expression for the growth rate, which is dependent on the $SiHCl_3$ and H_2 concentrations, as well as on reaction rates for chemisorption and decomposition. The main parameter describing the reaction is the Cl/H ratio, which is given by the composition of those process gases and which does not alter throughout the reaction.

Figure 2.20 illustrates the effect of the temperature and the Cl/H ratio on the growth rate deduced by this calculation.

Depending on the Cl/H ratio, the growth rate curve can be characterized by three regimes. At Cl/H ratios below 0.5 % the growth rate increases strongly with rising Cl/H ratio. Small changes in gas composition result in large changes in growth rate. With a further increase of the Cl/H ratio a saturation level is reached, where the growth rate changes only slightly with increasing Cl/H ratio and eventually the growth rate even decreases with increasing Cl/H ratio. In this regime the growth rate is comparatively insensitive to the Cl/H ratio.

The validity of the presented model was proven by Habuka in a wide temperature range of 800–1120 °C and gas compositions with molecular weights between 2.7×10^{-3} and 11×10^{-3} kg/mol, covering the operating regimes typically used for industrial APCVD processes.

In Ref. [107] a similar model is presented to describe the growth rate in a horizontal single wafer reactor with TCS as a precursor gas. The predicted growth rates were also successfully verified by experiments.

The combined results for CVD in the PV industry and the modeling of growth rates leads to the conclusion that when using TCS as silicon precursor gas, the Cl/H ratio should be higher than approximately 2 % to achieve a deposition process with high growth rates and good tolerance towards parameter fluctuations. It also shows that a temperature of at least 1150 °C is necessary to achieve mean deposition rates exceeding 5 µm/min.

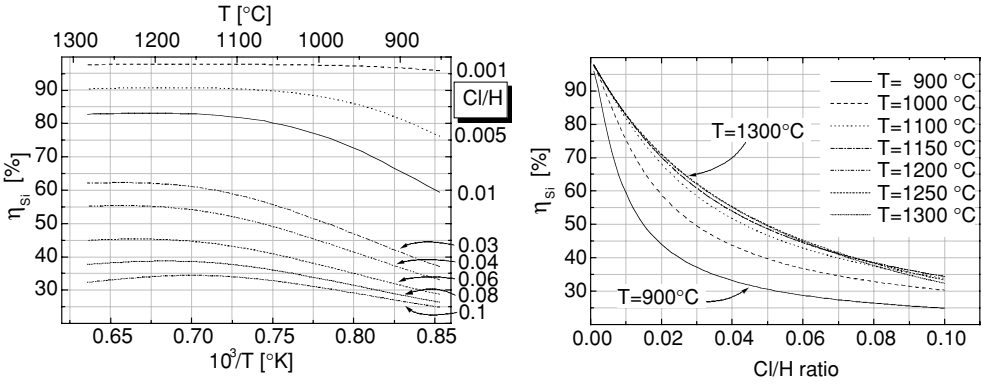

Figure 2.21 Dependence of chemical yield on temperature and Cl/H ratio in thermal equilibrium [113].

2.4.2.2 Chemical yield

The chemical yield (or silicon conversion efficiency) is defined as the efficiency to convert silicon contained in the initial gas phase into solid silicon. Comparing the initial Si/Cl mole ratio in the gas to the final Si/Cl ratio at deposition temperature under thermal equilibrium gives information about the amount of TCS which is theoretically consumed in reactions leading to silicon deposition. Using TCS as a precursor gas the initial Si/Cl ratio is 0.33. If the final Si/Cl ratio exceeds this value, etching of silicon dominates the process instead of deposition. For Si/Cl ratios lower than 0.33, silicon deposition occurs. The final Si/Cl ratio depends on the process temperature and the initial gas composition i.e. Cl/H ratio. The chemical yield is defined by:

$$\mu_{Si} = 1 - \frac{(Si/Cl)}{(Si/Cl)_i}$$

Assuming thermal equilibrium, the chemical yield can be calculated from the partial pressures of silicon and chlorine containing species as a function of temperature and the Cl/H ratio. In Ref. [113] the effect of the temperature and the Cl/H ratio on the chemical yield has been evaluated by means of thermal equilibrium calculations. The results are depicted in Figure 2.21.

The Cl/H ratio and the temperature determine the maximum chemical yield which can be reached at the chemical equilibrium. The lower the Cl/H ratio, the larger the chemical yield at a given temperature. With increasing temperature the chemical yield rises due to the enhanced reactivity. The largest yields can be achieved at high process temperatures and low Cl/H ratios. Given that the lower limit for the Cl/H ratio is 2 % due to growth rate, maximum chemical yield for a CVD process would be around 70 %.[12] The choice of the actual set of parameters for the production of silicon layers also depends, however, on economic data like the cost of silicon precursors and hydrogen.

[12] This is of course only true if a chemical equilibrium is reached at some stage in the deposition process.

2.4.3 R&D trends in silicon atmospheric pressure chemical vapor deposition for photovoltaics

2.4.3.1 Reactor development

As already pointed out in Section 2.4.2, the epitaxy reactors used in microelectronics are not suitable for PV for cost reasons. Research in PV therefore focuses either on large area batch reactors, or on high throughput continuous reactors. Reactor development for PV has been started by several groups in order to fulfil the requirements stated in Section 2.4.1. All studies are based on the well known TCS/H_2 APCVD reaction.

Kunz *et al.* [114] reported the development of an optically heated silicon epitaxy reactor for $40 \times 40\,cm^2$ wafer deposition area per batch. The substrates are mounted face down in the inner side of a tilted stainless steel cuboid, parallel to one large face. A reaction chamber is formed by quartz windows on both sides of the substrate carrier, some distance apart from the substrates. Heating is enabled by halogen lamps. The process gas enters near the lower quartz window parallel to the substrate surface and flows downwards following this quartz window. As the gas stream heats up, it revolves at the lower end of the reaction chamber and flows back towards the gas outlet, which is located above the gas inlet at the same face of the cuboid. Due to convection, the gas stream now moves directly beneath the substrate surface. During this travel to the outlet, silicon deposition occurs on the substrate surface. Due to the tilting of the stainless steel cube, gas depletion effects can, in principle, be avoided. The whole principle is called 'convection roll'. Up to now, no further experimental results have been published.

Rodriguez *et al.* [115] are working on a batch APCVD reactor for deposition of 60 $10 \times 10\,cm^2$ substrates per run. The substrates are mounted on the tilted vertical walls of 50 cm long graphite cuboids serving as susceptors. Six of these susceptors are mounted in the form of an array parallel to each other. Heating is realized by direct electrical heating of the susceptors. The process gas enters the reactor below the susceptor array, flows upwards perpendicular to the array area through slits between the single susceptors, passing the substrates and leaving the reactor through its ceiling. Depletion and temperature effects should be equalized by the setup, especially the tilting of the susceptor walls. To decrease process costs, reuse of process gas by a feedback loop is planned. For this reactor development, no experimental data has yet been published.

The third and final published development of a high throughput reactor was done at the Fraunhofer ISE. Hurrle *et al.* [116] reported the development of a high throughput silicon CVD reactor in cooperation with the company Centrotherm, which features continuous movement for higher throughput by using gas curtains for separation of reactor atmosphere from laboratory environment, resistance heating for high temperature uniformity and optimum electrical power utilization as well as operation in a depletion regime to increase chemical yield. The reactor (called ConCVD due to its capability for continuous in-line deposition) is an open system where sample carriers are continuously fed into the reactor. Nitrogen gas curtains located at both ends of the machine separate the interior atmosphere of the reactor from the laboratory environment. Figure 2.22 shows a schematic of the reactor tube and reaction chamber. The reaction chamber, where the deposition takes place, consists of a frame with the front and back plate being connected by rods. Together with the moving samples, a closed volume is generated into which the process gases are injected. After deposition the samples enter the cooling zone,

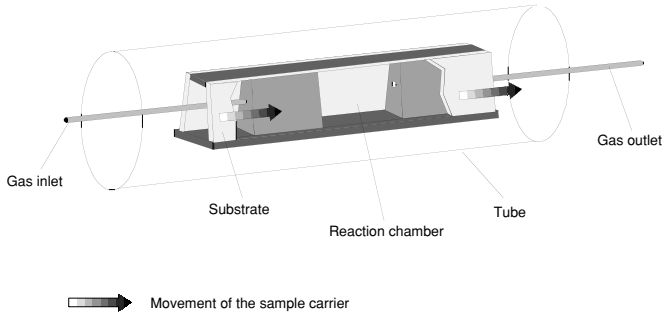

Figure 2.22 Schematic of the reactor tube and deposition chamber of the ConCVD.

where they are cooled down before they leave the reactor. Samples with a maximum width of 200 mm can be processed and by adjusting the transport speed, layers of nearly arbitrary thickness can be grown.

The sample movement allows the deposition process to be run under depletion conditions, i.e. with a high chemical yield, and a high homogeneity in layer thickness is still being achieved. The manual design components of the reactor are: an average deposition rate of 5 μm/min, a reaction chamber length of 400 mm and a substrate width of 200 mm, yielding a calculated throughput of 2.1 m^2/h for a 20 μm silicon layer.

Among the three concepts described, experimental data for silicon layers were reported only for the ConCVD [116]. The best chemical yield achieved was 30 % (nearly 90 % of the theoretical limit for the Cl/H ratio used), homogeneity in transport direction was close to 100 %, and deviation in layer thickness across the substrate width perpendicular to the transport direction was lower than 20 %. An average deposition rate of 3.3 μm/min was reported for these conditions. Solar cells on highly doped mc-Si substrates with 20 μm thick silicon layers deposited epitaxially in the ConCVD achieved solar cell conversion efficiencies up to 12.5 % [95].

2.4.3.2 Process development

The seeding layer concept for CSiTF on foreign substrates creates the need for two different types of silicon layer depositions. The first deposition takes place onto the substrate/intermediate layer and results in polycrystalline silicon films with a typical grain size in the micron range. The subsequent ZMR process requires layers of 1–5 μm thickness, with homogeneity of 90–95 % and very good structural integrity, i.e. no whiskers or holes can be present. Usually a high doping concentration of larger than 10^{19} at/cm^3 is needed to realize a back surface field layer in the CSiTF solar cell. If SiO_2 deposited by PECVD is used as an intermediate layer material, silicon growth has to be performed at temperatures below 1000 °C in order to prevent a decomposition of the silicon dioxide by hydrogen, therefore damaging the dielectric layer. Silicon deposition at low temperatures is determined by reaction kinetics, and consequently growth rates using TCS are comparatively low (around 1 μm/min). Depletion of process gas can therefore already be avoided with low precursor gas flows, and higher thickness homogeneity can be achieved, especially in reactors with a stationary sample setup.

After ZMR, the now coarse grained silicon seeding layer has to be thickened epitaxially at a lower doping level, in order to produce the electrically active solar cell absorber layer. The resulting high-low junction at the rear surface of this epitaxial layer reduces the effective rear surface recombination for light generated electron hole pairs. Since the epitaxial layer determines the performance of the solar cell, it's electrical and crystallographic quality is of major importance.

The crystal quality of epitaxial layers depends on the substrate material, preepitaxial cleaning and the process conditions [117]. Epitaxial layers are known to have larger defect densities compared to standard wafers but the oxygen concentration is typically lower compared to Cz-Si [118]. Epitaxial defects can be categorized according to their origin in substrate related defects (i.e. for the setup of Figure 2.1: defects in the seeding layer) and defects related to process conditions. Grain boundaries or other crystal imperfections intersecting the substrate surface are continued in the epitaxial layer and therefore belong to the first category. Stacking faults and spikes are the most common epitaxial defect type belonging to the second category. Stacking faults are reported to have the most detrimental effect on the electrical quality of epitaxial wafers of all defect types [119]. They are generally attributed to the presence of impurities (organic or metallic) on the substrate surface [120]. Contamination of the sample surface can be caused by incomplete cleaning prior to epitaxy and unclean process conditions (wafer handling, laboratory cleanliness, purity of the process gases etc).

Process development for epilayers has to focus on both the economic issues of deposition (chemical yield, throughput etc.), and the electrical excellence of the layers. Usually a trade-off between those two demands is necessary. Wet chemical precleaning of the samples is a good example of this trade-off: comparatively time consuming standard RCA (three step) cleaned surfaces yield the lowest defect density layers on monocrystalline substrates. However, one step cleaning like KOH or CP etching yield only slightly worse crystallographic results, and results which are nearly as good after solar cell processing [121]. A similar result was described for the influence of epilayer growth rates on a solar cell's performance in Ref. [20]. Two processes with growth rates of 5 μm/min and 9 μm/min, were compared. Although the 9 μm/min process yielded a higher defect density, the respective solar cell conversion efficiency was only 5 % worse, relatively. An economic evaluation would probably be in favor of this nearly two-fold higher throughput process. These two examples show that in many cases, reasonable trade-offs are feasible. In addition, for foreign substrate based solar cells, the quality of the epilayer is strongly related to the quality of the seeding layer, therefore the main R&D effort has to be focused on the recrystallization process.

2.4.4 Silicon chemical vapor deposition on ceramic substrates

The deposition of polycrystalline silicon by APCVD using chlorosilanes on SiO_2 or other layers is a routine process in microelectronics. The adapted reactors and principles described in Section 2.4.3 can also be applied in PV processes to deposit polycrystalline silicon layers on SiO_2 coated silicon substrates, which are later used as seeding layers. Figure 2.6 (left) shows a cross-section of such a layer after preferential defect etching. Nucleation took place on the SiO_2 layer every 0.5 μm or even more frequently and the columnar grains get larger the thicker the layer becomes. The seeding layer thickness was only chosen to be extraordinarily high for demonstration purposes. It is important to mention that the SiO_2 layer is closed and smooth and that the APCVD grown seeding layer does not exhibit any holes or other irregularities.

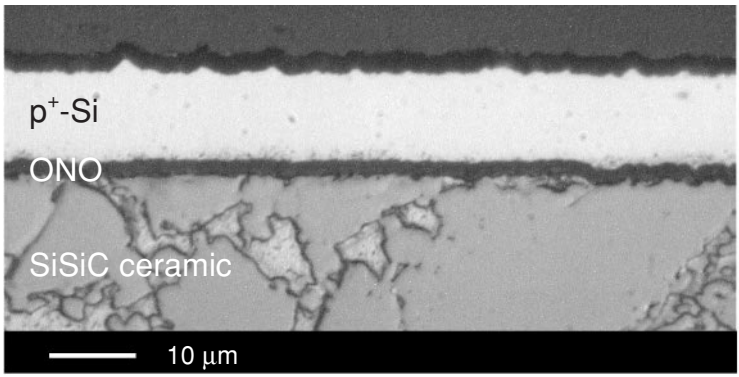

Figure 2.23 Cross-section of a polycrystalline silicon seeding layer on SiSiC ceramic substrate coated with a stack of SiO_2, SiN_x, SiO_2 (ONO).

This result can also be transferred to suitable ceramic substrates. Figure 2.23 shows a smooth SiSiC ceramic substrate surface covered by undamaged and equally smooth intermediate and silicon seeding layers. Important parameters to guarantee a successful seeding layer deposition are:

- Intermediate layer surface may not be contaminated by (metallic) impurities. These can cause whisker growth by generating a local eutectic of metal silicide [122].
- The intermediate layer has to have a homogeneous surface without holes. Otherwise selective growth rates can lead to local inhomogeneity of layer thickness, or whisker growth due to substrate impurities can occur.

Figure 2.24 shows an example where silicon was deposited onto an unsuitable substrate. The rough, porous SiAlON substrate surface chemically reacted with the ONO intermediate

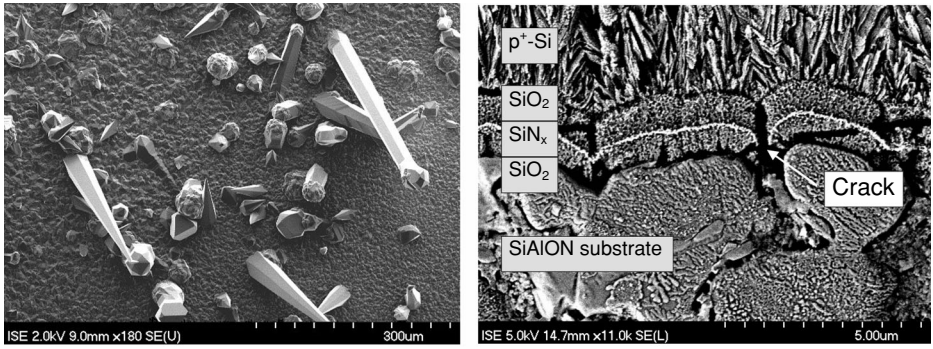

Figure 2.24 SEM pictures of surface (left) and cross-section (right) of a CVD silicon layer on unsuitable SiAlON ceramic substrate. From S. Bau *et al.*, Chemical vapour deposition of silicon on ceramic substrates for crystalline silicon thion-film solar cells, in *Proc. 17th European Photovoltaic Solar Energy Conference*, 2001.

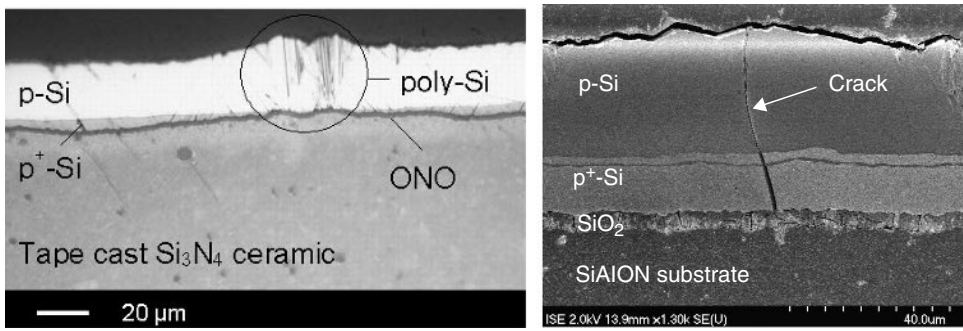

Figure 2.25 Cross-sections of silicon epitaxy exhibiting major failures. Left: Nomarski micrograph of a polycrystalline silicon region. Right: Crack due to unmatched TEC.

layer thus destroying its structural integrity and forming cracks (left). As a result, whiskers have developed during silicon deposition (right).

The situation is similar for epitaxy on recrystallized silicon layers. Any major deviation from the ideal state, i.e. a closed, low defective, clean silicon surface, leads to nonideal epitaxy. Cleaning of silicon layers on ceramics prior to epitaxy is a difficult task, as ceramics often consist of metallurgical raw material. Cross contamination of the seeding layer surface can therefore occur during wet chemical sample cleaning, leading to whisker growth or enhanced defect density during epitaxy. If the substrates are porous, wet chemical cleaning is sometimes even harder due to safety reasons. Cross contamination can also occur during the high temperature epitaxy process itself, when impurities out-diffused from the substrate are transported via gas phase to the growing silicon layer.

These effects can still be minor effects, i.e. the epitaxy can be still of decent quality. Major failure of the grown layer happens when the seeding layer is no longer closed, or if the thermal expansion coefficients of the substrate and the silicon do not fit well together. Figure 2.25 shows two respective examples. In the left picture a region of polycrystalline silicon neighbored by regular epitaxial layers is highlighted. Here, the IL is not covered by the recrystallized seeding layer any more, leading to the growth of a fine grained silicon layer during epitaxy. In the sample shown in the picture on the right, a crack already present in the recrystallized seeding layer was carried through into the epitaxial layer. Such cracks break up lateral conductivity in the epitaxial layer, and can initiate short cuts between the emitter metallization and the base during solar cell processing.

To summarize, silicon deposition on ceramics can, in principle, be done using the standard CVD technique, well known for its application in the microelectronics industry. The quality of the silicon layer is, however, directly related to the quality of the substrate: imperfect substrates lead to poor quality of the deposited silicon layer. Impurities and holes or cracks in the intermediate layer and seeding layer catalyze cracks, whiskers and other growth defects up to polycrystalline growth during epitaxy.

2.5 SOLAR CELLS ON FOREIGN SUBSTRATES

Solar cell processing of silicon layers prepared at temperatures up to 1400 °C should, in principle, be straightforward: all known technologies used to process silicon wafer solar cells

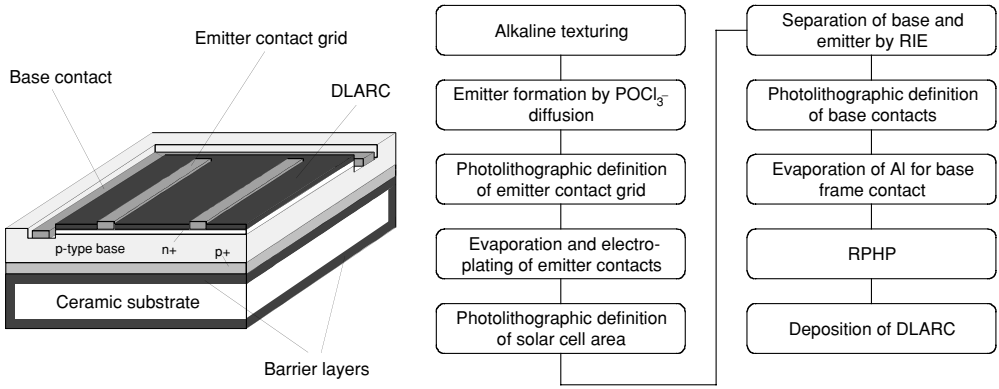

Figure 2.26 Solar cell scheme and processing sequence for one side contacted solar cells on insulating substrates (after Ref. [20]). 'RPHP': Remote plasma hydrogen passivation.

should be applicable. The use of foreign substrates, however, makes some processing options unsuitable. In the first part of this section, the principle requirements for a suitable cell process, as well as the resulting cell and processing options are discussed. The subsequent segment summarizes work done on model substrates to investigate the influence of hydrogen passivation and ZMR scan speed on the open circuit voltage of the cell. In addition, some work to check the feasibility of the concept for large area solar cells is presented. The section closes with a description of some selected CSiTF solar cells on ceramic substrates, which illustrate very nicely the influence of the substrate/layer system on the solar cell's performance.

2.5.1 Options for solar cell fabrication

The big advantage of c-Si thin films prepared at a high temperature is their compatibility to conventional solar cell processing, since the active layer consists of multicrystalline silicon just like a conventional mc-Si wafer. A processing scheme including the typical steps for processing CSiTF on nonconductive ceramics is shown in Figure 2.26. For the special case shown in this figure, both emitter and base contacts are applied at the front of the solar cell, which is necessary if intermediate layers and/or ceramics are nonconductive. As for standard silicon wafer solar cells, an emitter is formed by diffusion, an antireflection coating[13] is deposited to reduce reflective losses, and metal contacts enable the extraction of current from the cell. However the following features of the cell are more important for thin films than for wafer based devices:

- *A textured surface* In combination with a difference in refractive index at the rear side of the silicon layer, a surface texture realizes the light trapping described in Section 2.2.2.1. Using conventional wet chemical alkaline anisotropic etching, very well shaped random pyramids can be formed on the silicon surface, a feature which is also used in high efficiency cell processing. The resulting internal reflection exceeds 90 % easily [76]. However, texturing

[13] Labeled "DLAR" for "double layer anti reflection coating" in the figure.

by KOH/isopropanol removes up to 10 μm of the silicon layer. The amount of silicon lost during texturing can consist of up to more than one third of the total deposited silicon, which increases the overall cost of the CSiTF system. An alternative is plasma texturing, which is described below in more detail.

- *Front surface passivation* Recombination at front and rear surfaces affects CSiTF solar cell performance more severely than in the case of "thick" wafer solar cells. This is due to the higher ratio of bulk volume (approx. depth of one diffusion length), which is influenced more negatively by high recombination activity at the surface when compared to a thick silicon wafer. Effective rear surface recombination is lowered in the seed layer concept by the BSF high-low junction. In principle, passivation of the front surface can be done either by thermal oxidation, or by the deposition of SiN_x. However for CSiTF on ceramics, no systematic work concerning front surface passivation has been reported thus far.
- *Bulk passivation* As will be shown in Section 2.5.2.1, passivation of bulk defects by hydrogenation is very beneficial for the solar cell performance of ZMR silicon layers. There are two principal ways to create the atomic hydrogen required for PV passivation: either through the formation of a hydrogen plasma in a furnace in which the samples are loaded, or by offering atomic hydrogen from the SiN_x:H antireflection coating directly. In the literature, only the first method has been reported for CSiTF on ceramics substrates.

Although, in principle, nearly every conventional technology for solar processing can be applied to CSiTF solar cells, the use of ceramic substrates can impose severe problems. Porosity is surely the most important issue to be listed here: if the ceramics have open pores, wet chemical processing can be difficult, sometimes even dangerous. Chemicals used during etching or plating fill the pores, and due to the large inner surface area proper cleaning of the wafer by water rinsing is sometimes virtually impossible. The dispersal of hazardous chemicals and the detrimental influence on subsequent process steps can be the result. For this reason, solar cell processes adapted to this special situation have to be developed. Two strategies are available: firstly, one can hermetically seal any open pores, e.g. by deposition of a thick intermediate layer, or by coating with resins which are resistant against all chemicals used in the process. In fact, this strategy was reported e.g. in Ref. [12], where a graphite substrate was coated with an SiC intermediate layer to close all open pores of the graphite substrate. The drawback of the hermetic sealing, however, is its cost, as additional layers or layer thickness, and/or resins can be quite expensive when applied over a large area. Therefore the second strategy involves dry process technologies. Most prominently the use of plasma etching has to be mentioned here. Plasma etching is a well known technique, whose application for silicon wafer solar cells is currently of great interest (see e.g. Ref. [123]). There are groups trying to adapt the plasma etching processes to c-Si films on ceramics. Using a fluorine based plasma, all problematic wet chemical etching steps can be replaced: removal of the capping layer after ZMR, surface preparation before epitaxy, sample cleaning prior to emitter diffusion, texturing featuring a small amount of silicon removal, phosphosilicate glass removal and silicon etching (for example trench formation), see e.g. Refs. [124–126]. Applying a completely 'dry' process to manufacture CSiTF solar cells on low cost ceramics is however not yet routine.

Even more sophisticated solar cell processes are necessary if substrate and/or intermediate layers are electrically insulating. Trenches have to be cut or etched into the silicon layer to realize one-side contacting (i.e. both metal contacts are located on the illuminated front side of the solar cell), or an integrated interconnection of cell stripes. While the first technique is applied

by several groups routinely, only a few authors have reported on an integrated interconnection (e.g. Refs. [127–130]). Challenges in realizing an error free interconnection arise from the comparatively rough surface of an epitaxially thickened ZMR layer due to the different grain orientations with subsequently different growth rates. Rentsch *et al.* reported on the difficulties faced when trying to realize a metallization by screen printing for integrated interconnection on epitaxially thickened ZMR layers due to shunting caused by such surface steps [127]. Other concepts involve either photolithography [129], trench dicing and metal dispensing [128], shadow mask evaporation [130] or wire bonding [131]. Brendel *et al.* presented a concept to create a metal free interconnection through the use of a special shadow-mask epitaxy of the base and the emitter [132]. None of these concepts, however, are well suited for cost effective, large scale production, except probably the one reported by Sims *et al.* using trench dicing and metal dispensing [128]. Remarkably, these authors reported the best conversion efficiency of an integrated interconnection of solar cells on a ceramic substrate: a four segment integrated module of 5.6 cm^2 achieved a conversion efficiency of 5.6 % and a V_{oc} of 2.2 V.

The maximum solar cell efficiency on ZMR silicon layers on model substrates was published by Gazuz *et al.* [130]. This group prepared an 86 cm^2 large module consisting of nine cell stripes, with a maximum solar cell efficiency of 6.3 % at a mean V_{oc} per cell of 544 mV.

In conclusion, wet chemicals are the cause of many problems in the solar cell processing of CSiTF on ceramics, due to the common porous structure of the substrate. For high throughput solar cell production, only dry processing techniques like plasma etching seem to be able to offer a satisfying solution to this issue.

2.5.2 Solar cells on model substrates

2.5.2.1 Zone melting recrystallization scan speed and hydrogen passivation

Most results published for ZMR silicon thin film solar cells were achieved on model substrates as defined in Section 2.2.1.2. They give important information about principle performance issues of ZMR layers. The best cell efficiency using ZMR layers on oxidized silicon wafers was reported by the Mitsubishi group (see Section 2.3.1): 16.45 % for a $1 \times 1\,cm^2$ [66], and 16 % for a $10 \times 10\,cm^2$ large thin film solar cell [67]. The solar cell process applied for both cells was very sophisticated, but the result demonstrates the potential for ZMR silicon to be used on foreign substrates.

In order to understand how to achieve such results on more cost effective substrates, various parameters involved in the preparation process of ZMR layers were studied systematically. Where a low cost silicon substrate is used (e.g. an SSP ribbon), promising results can be transferred fairly easily, whereas in the case of ceramics this is often still a difficult task.

In the following pages, two of the parameters influencing the solar cell performance of ZMR silicon layers shall be treated in more detail: ZMR scan speed and hydrogen passivation.

As already described in Section 2.3.3.3, scan speed is the most important cost parameter for the ZMR process. The experiments on defect density reported in this section have already raised the question of how much defect density can influence a solar cell's performance. The Mitsubishi group observed a strong decrease in solar cell performance (mainly V_{oc}) with increasing scan speed and defect density [64, 91, 96]. In Ref. [97], the Fraunhofer ISE group confirmed these results concerning scan speed. However, the Fraunhofer ISE group also showed that a remote plasma hydrogen passivation (RPHP) treatment can increase V_{oc} of samples

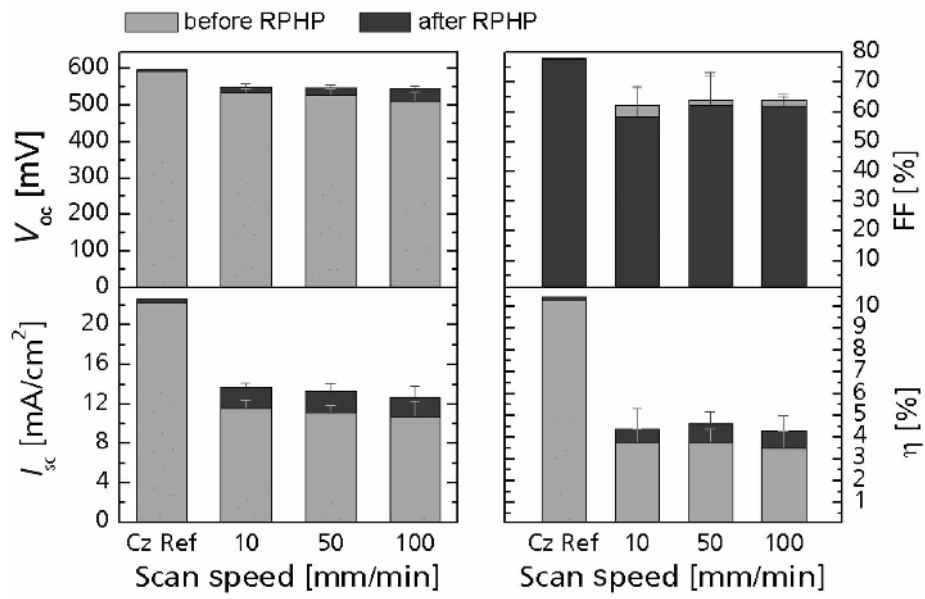

Figure 2.27 Solar cell parameters of ZMR recrystallized cells with epitaxial layers before and after hydrogen passivation. After T. Kieliba *et al*., Optimization of c-Si films formed by zone-melting recrystallization for thin-film solar cells, in *Proc. 3rd World Conference on Photovoltaic Solar Energy Conversion*, L.L.K.K. Kurokawa, B. McNelis, M. Yamaguchi, C. Wronski, and W.C. Sinke (Eds.), WCPEC-3 Organizing Committee, 2003 (© 2003 IEEE).

recrystallized at a higher speed more than that of samples recrystallized at a lower speed, as presented in Figure 2.27 (after Ref. [97]). Consequently, large differences in V_{oc} and efficiency are more or less cancelled out by hydrogenation.

As a follow-up to this experiment, a comparison was done on two sets of solar cells, prepared from the layers described in Section 2.3.3.3 [133]. The first set used the normally doped ZMR silicon layer without any further treatment, the second set was made from highly doped ZMR samples thickened with a normally doped epitaxial layer before cell processing. The effectiveness of remote plasma hydrogen passivation was evaluated by measuring the solar cell parameters before and after this step. Figure 2.28 graphically presents the V_{oc} values of the first set before and after hydrogen passivation. V_{oc} is increased by about ~30 mV independent of ZMR speed, so the shape of the curve remains the same and just shifts to higher values. For higher scan speed samples, hydrogen passivation seems to lower the V_{oc} scattering of layers recrystallized at the same speed. The hydrogen passivation result is in good accordance with the result of EPD measurements described in the above mentioned section, showing that at all ZMR speeds basically the same amount of defects is present, which can be passivated. The trend in V_{oc} also correlates well with the defect density: V_{oc} does not change very much with ZMR speed, only a slight decrease of ~15 mV in mean value is found when increasing the speed by about 20 times from 20 mm/min to 350 mm/min. This result is very promising, since it leads to the conclusion that highly efficient solar cells can be processed even from layers prepared at very high ZMR speed.

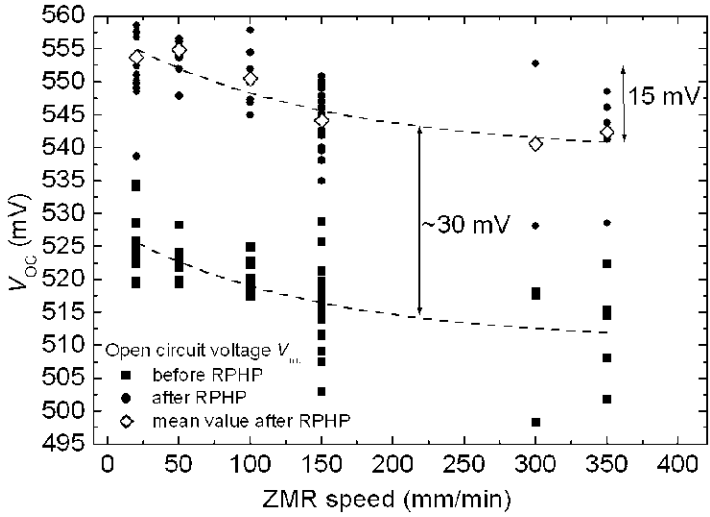

Figure 2.28 Open circuit voltage V_{oc} of solar cells without an additional epitaxial silicon layer. The lines are least squares fits and are only a guide.

A comparison of V_{oc} for cells with and without epitaxial layers is presented in Figure 2.29. It shows two significant differences of the V_{oc} curves:

Firstly, the overall level of V_{oc} shown in this figure is significantly lower for epitaxial cells at all scan speeds. The overproportional improvement of the V_{oc} by hydrogen passivation for scan speeds up to 100 mm/min found in [97] could not be reproduced. This result correlates to the difference in absolute values of EPD of at least one order of magnitude described in Section 2.3.3.3.

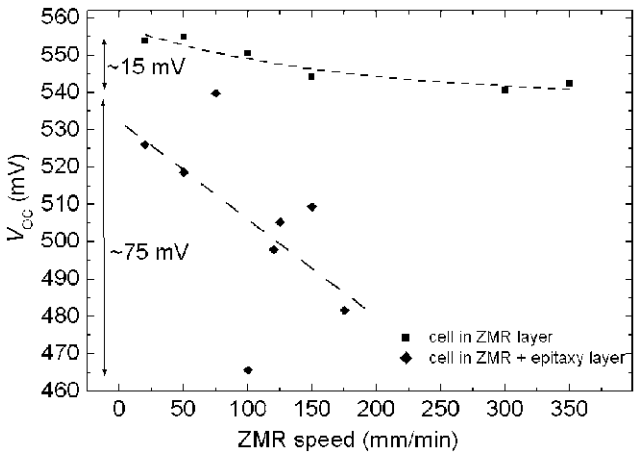

Figure 2.29 Comparison of mean values of the open circuit voltage V_{oc} of solar cells after hydrogen passivation with and without additional epitaxial silicon layer.

Secondly, the shape of the curves of V_{oc} vs. scan speed are significantly different: while the V_{oc} of solar cells from bare ZMR layers saturates at a high level, the V_{oc} for epitaxial cells decreases dramatically with scan speed.

The findings reported in this section support the conclusion drawn in Section 2.3.3.3.: to achieve the best recrystallized CSiTF solar cells, the seeding layer concept which involves an epitaxy to realize the base layer is probably not the best choice, especially if a high ZMR scan speed is involved. Hydrogen passivation helps to boost the cell efficiency by about 5–10 % relative, but it is not capable of cancelling out the detrimental effect of larger defect density when epitaxial layers are used.

2.5.2.2 Largearea recrystallized wafer equivalents

Large area ($>50\,cm^2$) solar cells on ZMR silicon layers were first processed by the Mitsubishi group mentioned already several times in this text. They used a cell process in which the whole silicon layer is detached from the substrate by removing the SiO_2 intermediate layer wet chemically. This process is called 'VEST' (via-hole etching for the separation of thin films), and is usually applied to approx. 80 μm thick silicon layers [99]. The best result achieved was 16.0 %, as already mentioned in the previous section. An attempt to produce recrystallized wafer equivalents (i.e. the layer is still attached to the substrate) of large areas was recently published by Reber *et al.* [95]. A process called 'laser-fired rear access' (LFA) enables the epitaxially deposited base layer to contact the substrate wafer through laser via-holes fired into the intermediate layer. A 'standard' solar cell process with emitter metallization at the front surface and base metallization at the rear surface was used to prepare LFA solar cells. The best cell parameters reported were $V_{oc} = 556\,mV$, short circuit current density $J_{sc} = 25.0\,mA/cm^2$, fill factor $FF = 60.7\,\%$ and energy conversion efficiency $\eta = 8.4\,\%$ for an area of $86\,cm^2$. The solar cell efficiency was mainly limited by high series resistance due to an improper design of the via-hole pattern. These results clearly prove the feasibility of the wafer equivalent concept (see also the left image of Figure 2.30). A further proof of this concept was achieved by series

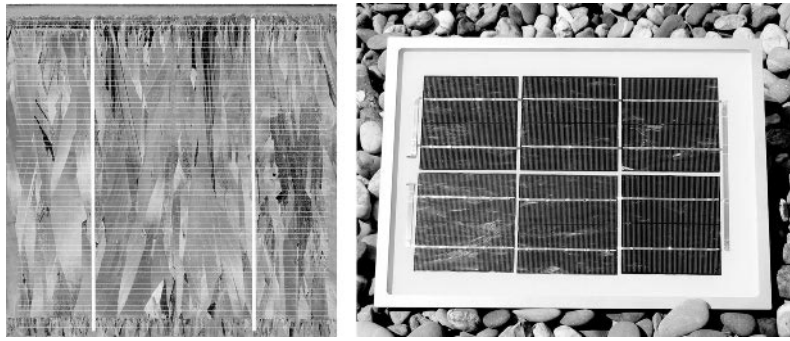

Figure 2.30 Left: Photograph of a 92 cm^2 LFA recrystallized wafer equivalent solar cell processed on a $100 \times 100\,mm^2$ silicon wafer substrate. Right: Mini module of six series connected LFA cells. Reproduced with permission from S. Reber et al., Progress in crystalline silicon thin-film solar cell work at Fraunhofer ISE. In *Proc. 20th European Photovoltaic Solar Energy Conference and Exhibition*, edited by H. O. W. Palz and P. Helm. pp 694–697. Copyright (2005) WIP-Renewable Energies, Minuch, Germany.

Table 2.2 Overview of best solar cell results on ceramic substrate where ZMR was involved

Substrate	Intermediate layer	Thickness of active Si layer, approx.	Conversion efficiency	Reference
SSP-Si	PECVD-SiO_2	30 µm	11.3 %	[134]
SiSiC ceramics	PECVD-SiO_2/SiN_x	25 µm	10.7 %	[20]
Si_3N_4 ceramics	PECVD-SiO_2/SiN_x	30 µm	9.4 %	[19]
$ZrSiO_4$ ceramics	PECVD-SiO_2/SiN_x	30 µm	8.3 %	[21]
Mullite (tape cast) ceramics	none	51 µm	8.2 %	[25]
Graphite	SiC		11.0 %	[12]
unknown	none	30–35 µm	9.2 %	[128]

interconnection via the soldering of tabs ('stringing') and lamination the of six LFA cells into a minimodule by using conventional technologies. The module shown in Figure 2.30 (right) exhibited an V_{oc} of 3.2 V, which is nearly equal to the sum of the single cell voltages.

2.5.3 Solar cells on low cost substrates

So far not many groups have reported solar cell results on ceramics or low cost silicon. Table 2.2 gives an overview of the best efficiencies published for solar cells where lamp or strip heater ZMR was involved. The highest confirmed value of 11.3 % has been achieved on an electronically pure, but SiO_2 capped, SSP ribbon substrate. Where metallurgical raw material was used, the SiSiC based solar cell with 10.7 % efficiency is leading the list. However all results reported were based on small batches of solar cells, in most cases only ~20 cells were produced. Therefore this table cannot give information on the suitability of the respective substrates.

Three of the cell types listed in the table shall be evaluated in more detail below: the cell on mullite ceramics because it is interesting from the viewpoint of light trapping, a cell on Si_3N_4 ceramics to show the detrimental effect of cracks due to unmatched TEC, and the cell on SiSiC ceramics as the best one.

2.5.3.1 Effect of light trapping: solar cells on mullite ceramics

In Ref. [25], Bourdais *et al.* reported on 1 cm^2 large solar cells on tape cast mullite substrates fabricated with the same cell process as described in Figure 2.26. The mullite used is of bright white in color, and scatters light diffusely at the small crystallites in its bulk. Three selected samples of the solar cell batch demonstrate how the effectiveness of light trapping properties can be influenced by layer engineering. The different layer setups are summarized in Table 2.3, Figure 2.31 shows the corresponding external quantum efficiency(EQE) curves. Cell B, made from a 20 µm silicon layer on a bare mullite substrate, has the highest current density of 26.1 mA/cm^2. The EQE value of 50 % at 1000 nm wavelength of this cell is relatively high. The light trapping by a textured front surface and a diffuse reflection from the substrate probably realizes the best possible light trapping scheme sketched in Figure 2.2d very well. However due to the lack of an intermediate layer, the bulk of this cell was contaminated by impurities, as is reflected by the low V_{oc} value of 351 mV. The EQE of cells A and C is similar at long

Table 2.3 Layer and solar cell parameters of the cells on mullite substrate

Cell	Intermediate layer	Thickness of active Si layer (μm)	J_{sc} (mA/cm^2)	V_{oc} (mV)
A	None	50	23.8	525
B	None	20	26.1	351
C	ONO	20	20.3	534

wavelengths, but completely different to cell B: only a small hump can be seen in the EQE starting from 900 nm wavelength, so the EQE values of 21 % at 1000 nm are much lower than for cell B. The thickness of cell A is too high to make the diffuse scattering at the rear surface effective, so the short circuit current density (J_{sc}) value of 23.8 mA/cm^2 is significantly lower than that of cell B. The setup of cell C is, in principle, similar to the light trapping structure of Figure 2.2b, which should theoretically also be quite effective: for a similar structure on a model substrate, Kieliba *et al.* reported a conversion efficiency of 13.5 % and a J_{sc} of 30.9 mA/cm^2 [97]. However, cell C exhibits the lowest current of all three cells. Obviously light trapping did not work as expected – one possible reason could be that the silicon grains were not (100) oriented, resulting in a worse random pyramid coverage. In the case of a diffusely scattering substrate this does not affect light trapping too badly (it would be described by the case of Figure 2.2a), however, with a smooth ONO intermediate layer, a lot of light would be lost due to the missing texture and with that the missing internal reflection.

This example demonstrates that intelligent light trapping schemes are also very important on ceramic substrates, if high currents are to be achieved. However, methods to improve light trapping can, on the other side, lead to a decrease in the electronic quality of the layer, which is much more severe than a lack of collected electrons. In conclusion, any attempt to increase

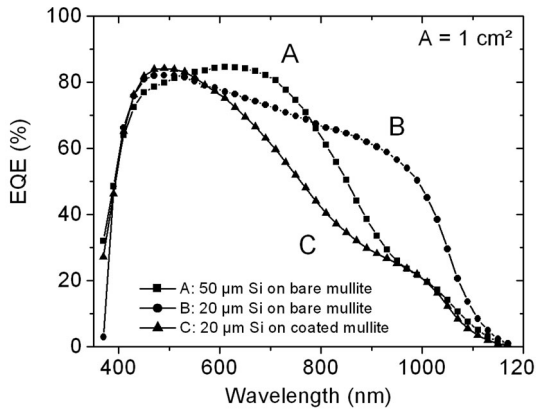

Figure 2.31 External quantum efficiency of CSiTF solar cells on mullite substrate. Case A: ∼50 μm Si on bare mullite. Case B: ∼20 μm Si on bare mullite, Case C: ∼20 μm Si on coated mullite. From S. Boursais *et al.*, Recrystallized silicon thin film solar cells on mullite ceramic substrates, in *Proc. 16th European Photovoltaic Solar Energy Conference*, B.M.H. Scheer, W. Palz, H.A. Ossenbrink, and P. Helm, James & James Scientific Publishers Ltd, 2000.

the efficiency of a CSiTF solar cell on ceramics has to be cross-examined for its detrimental influence on other properties of the layer(s) and solar cells.

2.5.3.2 Effect of the thermal expansion coefficient: solar cells on Si_3N_4 substrate

The second example in this section deals with the detrimental effects of nonmatched TEC on a solar cell's performance [20]. Bau reported one very illustrative cell processed from a cracked silicon layer on top of an ONO coated hot pressed sintered Si_3N_4 ceramic substrate. The solar cell process was identical to the one used for the cell presented in the previous section. The corresponding effective diffusion length map (Figure 2.32) reveals two interesting features: firstly and most obviously, rectangular regions of very low lifetime are located at the corners of an otherwise undisturbed ZMR silicon layer. These regions are attributed to deep cracks, where the base current cannot flow to the frame-like base contact surrounding the active cell area any more. Quantum efficiency is zero in these regions. Secondly, detectable by a thorough examination, one can identify lines of increased effective short circuit current (visible also in Figure 2.32, e.g. starting from the bottom edge of the picture at $x = 6\,mm$ to the left edge at an angle of approx. -45°). These lines are also cracks, but they do not separate the base regions they cross electrically. At the side walls of these cracks, a vertical emitter forms during normal emitter diffusion, which can effectively collect carriers generated within a distance of approximately one diffusion length from the crack. In such areas quantum efficiency is enhanced compared to the rest of the layer. Unfortunately, the loss of collecting area due to the cracks is more severe than the gain due to vertical emitter channels, so the overall cell performance turns out to be worse.

Geometrical integrity of the silicon layer is consequently of basic and utmost importance to develop high quality CSiTF solar cells. Efforts must start with the proper choice of ceramics.

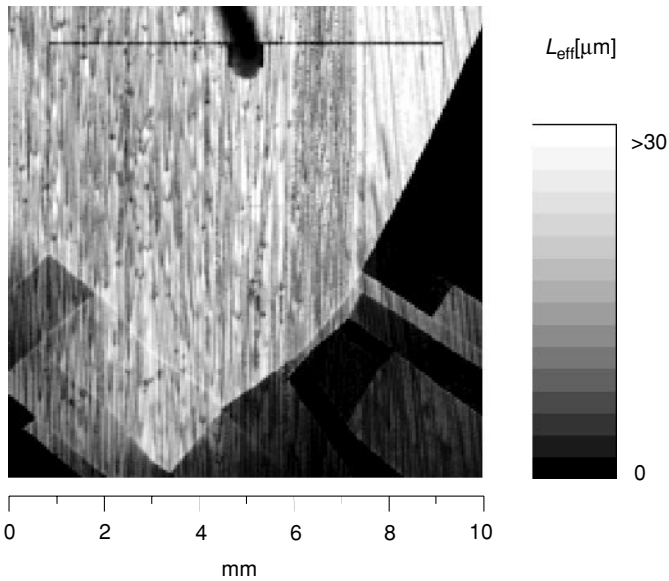

Figure 2.32 Map of effective diffusion length of a CSiTF solar cell on hot pressed Si_3N_4 substrate.

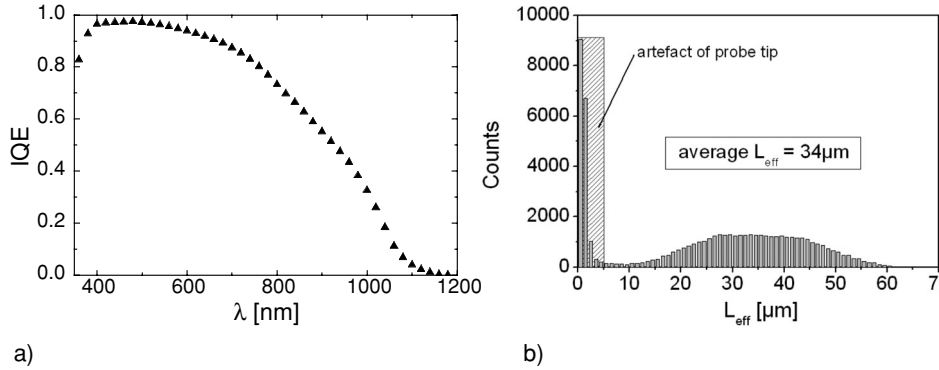

Figure 2.33 a) Internal quantum efficiency and b) histogram of a map of L_{eff} for the best silicon thin film solar cell on a SiSiC ceramic substrate. From S. Boursais et al., Recrystallized silicon thin film solar cells on mullite ceramic substrates. In *Proc. 16th European Photovoltaic Solar Energy Conference*, B.M.H. Scheer, W. Palz, H.A. Ossenbrink, and P. Helm, James & James Scientific Publishers Ltd, 2000.

2.5.3.3 Suitable substrate: solar cells on SiSiC ceramic

The final solar cell presented, on SiSiC ceramic, is a good example of the potential of CSiTF solar cells if suitable substrates are used. The SiSiC ceramic is a material with practically no pores and its surface is ideally closed and flat. Subsequently, standard processing involving wet chemical etching could also be applied to fabricate solar cells of 1 cm^2 area. The cell process was similar to the one sketched in Figure 2.26, however, an additional thermal oxide was grown to passivate the front surface. Solar cell parameters of the best cell reported in Ref. [20] are: $V_{\text{oc}} = 554\,\text{mV}$, $J_{\text{sc}} = 28.9\,\text{mA/cm}^2$, FF = 66.8 % and $\eta = 10.7\,\%$. The internal quantum efficiency (IQE) curve of this cell (see Figure 2.33a) gives more information about bulk and process quality: the comparatively high value at 400 nm indicates the effectiveness of the thermal oxide layer as a front surface passivation technique. The fact that the IQE already starts decreasing at 600 nm hints at a non optimum layer quality e.g. due to impurity contamination. A little hump at around 900 nm indicates some degree of optical confinement, reflected also in a comparatively good J_{sc} value.

The histogram of a map of the effective minority carrier diffusion length (L_{eff}) (see Figure 2.33b) shows a broad L_{eff} distribution, ranging from ~5 µm to 60 µm. Only a small part of the measured L_{eff} values exceeds the base layer thickness of 25 µm by about two times, but the average L_{eff} of 34 µm is still higher than the base layer thickness. This again confirms the effectiveness of surface passivation as well as the comparatively good crystal quality of the epitaxial layer.

A strategy to further increase efficiency of such a cell would have to involve: lowering layer thickness (to achieve a ratio of average diffusion length/thickness of about two), further improving front surface passivation (thermal oxide, or SiN_x) and BSF (higher doping of BSF layer), and using microrough rear surfaces to improve optical confinement.

2.6 SUMMARY AND OUTLOOK

A detailed overview on research activities in the field of recrystallized silicon thin film solar cells on foreign substrates has been presented. Only a few groups worldwide have taken

on the challenge of working on CSiTF solar cells on low cost foreign substrates. The high temperature path, which was the topic of this chapter, has an enormous potential to achieve both high solar cell efficiencies and low cell and module costs. The generic manufacturing process for such a cell starts from a suitable high temperature ($>1400\,^{\circ}C$) stable substrate onto which an intermediate layer (SiO_2, SiN_x or SiC) is deposited. A silicon layer is formed on top of this stack, and after confining this layer by a top SiO_2 capping layer, it is processed by ZMR. This step is a key process characterizing the investigated technology. It increases the area of single grains of the deposited silicon layer dramatically, up to nine orders of magnitude. After the removal of the capping layer, the ZMR silicon layer ('seeding layer') can be epitaxially thickened to form the solar cell absorber layer. The main advantage of the finished stack is its temperature stability and the crystallinity of the silicon layer, which is very similar to a conventional multicrystalline silicon wafer.

Most of the work on ZMR silicon layers has been done using model substrates, i.e. silicon wafers which have beene coated with SiO_2. These substrates are especially useful for parameter studies, since they can easily be reproduced. Progress has been achieved mainly in understanding the response of the sample system to high-speed recrystallization and hydrogenation. Crystalline silicon thin film solar cells with a ZMR layer yield a V_{oc} higher only than cells with an epitaxially deposited active layer. The curve of V_{oc} versus ZMR scan speed for the first cell type is a very important result: V_{oc} tends to saturate for scan speeds higher than approx. 150 mm/min, up to at least 400 mm/min. Future high throughput production of ZMR layers with a layer quality which is still high seems therefore quite realistic.

In addition to the work on model substrates, in the last few years a wide variety of ceramics have been tested as foreign substrates. The experiments have shown that efficiencies higher than 10 % can be achieved (on 'realistic' ceramics the top value is 10.7 %), if suitable substrates and intermediate layers are chosen. However substrates which do not fully meet the requirements demanded can completely prevent any success in layer formation. A significantly better understanding of the processes involved has been gained through experiments which used such 'unsuited' substrates.

This has led to a narrowing of the parameter field defining a suitable ceramic material, enabling substrate manufacturers to focus their R&D work. There is still however no ceramic type which can be regarded as fully developed and which is available in large quantities as a substrate on the market.

Silicon deposition on ceramics has become nearly a standard process over the years. The best approach turned out to be thermal chemical vapor deposition using chlorosilanes as precursor gases. Atmospheric pressure was essentially applied to the deposition processes due to the relative simplicity of the respective processors. Microcrystalline silicon layers with a sufficient quality (so that very good ZMR results can be achieved) can be deposited on suitable ceramics and of course also on model substrates. The deposition of epitaxial layers is also feasible on well recrystallized silicon layers. The defect density of the resulting layers can now be low enough to enable the processing of solar cells exceeding 16 % conversion efficiency on model substrates. Epitaxial quality can be high on ZMR seeding layers on ceramic substrates as well. However as already mentioned above, the suitability of the sandwich 'ceramic substrate, intermediate layer and seeding layer' is a prerequisite for successful silicon deposition. Research has shown that there is no parameter present in this process step to ensure growth of high quality microcrystalline or epitaxial silicon layers on top of low quality substrates or seeding layers.

Significant progress has also been achieved in the field of processor development for ZMR and silicon deposition. These two processes require tools specially developed for PV. This is one reason why progress in sample processing issues seemed to be comparatively slow: the necessary processors just had not been built yet. However, with the development of a ZMR processor for 400 mm wide samples at Fraunhofer ISE this issue can hopefully be overcome. In the area of fast and low cost silicon deposition for CSiTF solar cells on foreign substrates significant progress has also been made by several groups. All of them have focused on thermal APCVD using trichlorosilane. Prototype silicon deposition processors have been built, and first results confirm the principal expectation that these processors can deposit high quality epitaxial layers at high throughput. The latter two developments will make preparation of samples faster and easier, and thus enable better research work on ZMR silicon layers.

The similarity of the ZMR silicon layer to a conventional multicrystalline silicon wafer enables, in principle, the usage of nearly all process technology applied for wafer solar cells. However if porous ceramics are used as substrates, process technology has to be adapted, since the porosity can make processing by dangerous wet chemicals quite complex. Dry process technologies could be an answer to this problem in the future. The current developments in wafer solar cell processing, where large scale plasma processors for deposition and etching have been developed and commercialized, are also beneficial for CSiTF on ceramics: it is expected that process parameters will not deviate too much from standard processes.

Regarding the progress in the past as well as the efficiency potential, the chances that a high temperature recrystallized c-Si thin film solar cell on a foreign substrate will at some stage achieve maturity at a production scale are very high. To reach this nevertheless ambitious aim, research has to focus on suitable dry solar cell processing, reliable layer preparation on improved substrates, and on scaling the cell size from the current 1 cm^2 to at least 100 cm^2 in a medium timescale.

ACKNOWLEDGMENTS

The authors thank all members of the Fraunhofer ISE and other research institutes for their support of the work on the ‘foreign substrates’ topic. We gratefully acknowledge the financial support by the European Commission, the German Federal Ministry for Conservation of the Environment and for Nuclear Safety, the Ministry of Science, Research and the Arts of the State of Baden-Württemberg, Germany, as well as many industrial companies.

REFERENCES

[1] J. Meier, E. Vallat-Sauvain, S. Dubail, U. Kroll, J. Dubail, S. Golay, L. Feitknecht, P. Torres, S. Faÿ, D. Fischer, A. Shah, Microcrystalline/micromorph silicon thin film solar cells prepared by VHF-GD technique, *Solar Energy Materials and Solar Cells* **66** 73 (2001).

[2] K. Yamamoto, A. Nakajima, M. Yoshimi, T. Sawada, S. Fukuda, T. Suezaki, M. Ichikawa, Y. Koi, M. Goto, T. Meguro, T. Matsuda, M. Kondo, T. Sasaki, Y. Tawada, Large Area Thin Film Silicon Hybrid Solar Cell and Module With Inter-Layer, in *Proceedings of the 14th International Photovoltaic Science and Engineering Conference* (Program Committee PVSEC-14) 447–449 (2004).

[3] B. Rech, T. Repmann, J. Hüpkes, M. Berginski, H. Stiebig, W. Beyer, V. Sittinger, F. Ruske, Recent progress in amorphous and microcrystalline silicon based solar cell technology, in *Proceedings of*

the 20th European Photovoltaic Solar Energy Conference and Exhibition, H. Ossenbrink W. Palz, P. Helm (Eds.) (WIP-Renewable Energies, Munich, Germany) 1481–1486 (2005).

[4] M. Schmela, Super sonic solar market–market survey on global cell and module production in 2004, *Photon International* **March 2005** 66–82.

[5] B. F. Wagner, J. O. Schumacher, Light confinement and influence of electrical parameters on thin silicon solar cells, in *Proceedings of the 13th European Photovoltaic Solar Energy Conference*, W. Freiesleben, W. Palz, H.A. Ossenbrink, and P. Helm (Eds.) (H.S. Stephens & Associates, Bedford, UK) 465–468 (1995).

[6] R. B. Bergmann, Crystalline Si Films on Foreign Substrates for Electronic Applications, *Recent Research Deveopments, Crystal Growth Research* **1** 241–256 (1999).

[7] J. H. Werner, Perspectives of Crystalline Silicon Thin Film Solar Cells, in *Technical Digest 13th Sunshine Workshop on Thin Film Solar Cells*, M. Konagai (Ed.) (NE-DO, Tokyo, Japan) 41–48 (2000).

[8] P. A. Basore, Simplified processing and improved efficiency of crystalline silicon on glass modules, in *Proceedings of the 19th European Photovoltaic Solar Energy Conference*, J.-L. Bal, W. Hoffmann, H. Ossenbrink, W. Palz, P. Helm (Eds.) (WIP-Munich and ETA-Florence) 455–458 (2004).

[9] C. Hebling, S. Reber, K. Schmidt, R. Lüdemann, F. Lutz, Oriented recrystallization of silicon layers for silicon thin-film solar cells, *in Proceedings of the 26th IEEE Photovoltaic Specialists Conference* (IEEE; New York, NY, USA) 623–626 (1997).

[10] S. Reber, A. Hurrle, A. Eyer, G. Willeke, Crystalline silicon thin-film solar cells – recent results at Fraunhofer ISE, *Solar Energy* **77** 865–875 (2004).

[11] S. Reber, W. Wettling, High temperature processing of crystalline silicon thin film solar cells, *Applied Physics* **A 69** 215–220 (1999).

[12] R. Lüdemann, S. Schäfer, C. Schüle, C. Hebling, Dry processing of mc-silicon thin-film solar cells on foreign substrates leading to 11 % efficiency, in *Proceedings of the 26th IEEE Photovoltaic Specialists Conference* (IEEE; New York, NY, USA) 159 (1997).

[13] R. Brendel, *Thin-Film Crystalline Silicon Solar Cells: Physics and Technology*, Wiley-VCH, Weinheim, 2003.

[14] T. Soma, H.-M. Kagaya, u. b. M. R. Bronzel, Thermal expansion coefficients of c-Si, in *Properties of Crystalline Silicon*, Robert Hull (Ed.) EMIS Datareview Series No. 20 INSPEC, The Institution of Electrical Engineers, London, UK, 1999 p. 153–154.

[15] J. Poortmans, G. Beaucarne, R. M. Mertens, Thin film crystalline Si solar cells: facts and challenges, in *Proceedings of the 14th International Photovoltaic Science and Engineering Conference* (Program Committee PVSEC-14) 13–16 (2004).

[16] A. Räuber, *'Commercial Process Outline For Crystalline Silicon Thin Film Solar Cells (COMPOSIT), Publishable Report'*, European Commission (2000).

[17] K. Zweibel, Thin film PV manufacturing: materials costs and their optimization, *Solar Energy Materials and Solar Cells* **63** 375–386 (2000).

[18] H. Salmang, H. Scholze, *Keramik*, Vol. 2, Springer, Berlin, 1982.

[19] S. Reber, G. Stollwerck, D. Osswald, T. Kieliba, C. Häßler, Crystalline silicon thin-film solar cells on silicon nitride ceramics, in *Proceedings of the 16th European Photovoltaic Solar Energy Conference*, B. McNelis, H. Scheer, W. Palz, H.A. Ossenbrink, P. Helm (Eds.) (James & James Scientific Publishers Ltd) 1136 (2000).

[20] S. Bau, *High-temperature CVD silicon films for crystalline silicon thin-film solar cells*, Ph.D. Thesis, University of Konstanz (2003).

[21] T. Kieliba, S. Bau, R. Schober, D. Oßwald, S. Reber, A. Eyer, G. Willeke, Crystalline silicon thin-film solar cells on $ZrSiO_4$ ceramic substrates, *Solar Energy Materials and Solar Cells* **74** 261–266 (2002).

[22] S. Reber, F. R. Faller, C. Hebling, R. Lüdemann, Crystalline Silicon Thin-Film Solar Cells on SiC based Ceramics, in *Proceedings of the 2nd World Conference on Photovoltaic Solar Energy*

Conversion, J. Schmid, H.A. Ossenbrink, P. Helm, H. Ehmann, and E.D. Dunlop (Eds.) (Joint Research Centre, European Commission, Ispra, Italy) 1782 (1998).

[23] S. Janz, S. Reber, H. Habenicht, C-Si Thin-film solar cells on ceramic substrates with SiC intermediate layers, in *Proceedings of the 15th International Photovoltaic Science and Engineering Conference*(Organization Committe PVSEC-15) 873–874 (2005).

[24] B. von Ehrenwall, A. Braun, H.G. Wagemann Growth mechanism of silicon deposited by atmospheric pressure chemical vapor deposition on different ceramic substrates, *Journal of The Electrochemical Society* **147** 340–344 (2000).

[25] S. Bourdais, S. Reber, H. Lautenschlager, A. Hurrle, A. Slaoui, Recrystallized silicon thin film solar cells on mullite ceramic substrates, in *Proceedings of the 16th European Photovoltaic Solar Energy Conference*, B. McNelis, H. Scheer, W. Palz, H.A. Ossenbrink, P. Helm (Eds.) (James&James Scientific Publishers Ltd) 1492 (2000).

[26] A. Slaoui, S. Bourdais, G. Beaucarne, J. Poortmans, S. Reber, Polycrystalline silicon solar cells on mullite substrates, *Solar Energy Materials and Solar Cells* **71** 245–252 (2002).

[27] A. v. Keitz, J.A.M. van Roosmalen, C.J.J. Tool, S. E. A. Schiermeier, A. J. M. M. v. Zutphen, F. Fung, G. M. Christie, Improvement of low cost ceramic substrates for use in thin film silicon solar cells, in *Proceedings of the 2nd World Conference on Photovoltaic Solar Energy Conversion*, J. Schmid, H.A. Ossenbrink, P. Helm, H. Ehmann, and E.D. Dunlop (Eds.) (Joint Research Centre, European Commission, Ispra, Italy) 1829 (1998).

[28] S. Reber, W. Zimmermann, T. Kieliba, Zone melting recrystallization of silicon films for crystalline silicon solar cells, *Solar Energy Materials and Solar Cells* **65** 409–416 (1999).

[29] R. Monna, D. Angermeier, A. Slaoui, J. C. Muller, G. Beaucarne, J. Poortmans, C. Hebling, Poly-Si thin films on graphite substrate by rapid thermal chemical vapor deposition for photovoltaic application, in *Proceedings of the 14th European Photovoltaic Solar Energy Conference*, 1456–1459 (1997).

[30] W. Zimmermann, S. Bau, F. Haas, K. Schmidt, A. Eyer, Silicon sheets from powder as low cost substrates for crystalline silicon thin film solar cells, in *Proceedings of the 2nd World Conference and Exhibition on Photovoltaic Solar Energy Conversion*, J. Schmid, H.A. Ossenbrink, P. Helm, H. Ehmann, and E.D. Dunlop (Eds.) (Joint Research Centre, European Commission, Ispra, Italy) 1790–1793 (1998).

[31] A. Eyer, R. Schindler, I. Reis, N. Schillinger, J. G. Grabmaier, Crystal structure and electrical properties of Silicon Grown from Powder (SSP-Method), in *Proceedings of the 19th IEEE Photovoltaics Specialists Conference*, IEEE) 951–954 (1987).

[32] A. Eyer, A. Räuber, N. Schillinger, J. G. Grabmaier, Silicon ribbons for solar cells grown from powder by the SSP method, in *Proceedings of the 20th IEEE Photovoltaic Specialists Conference*, 1565–1568 (1988).

[33] G. Beaucarne, S. Bourdais, A. Slaoui, J. Poortmans, Impurity diffusion from uncoated foreign substrates during high temperature CVD for thin film Si solar cells, *Solar Energy Materials & Solar Cells* **61** 301–309 (2000).

[34] S. Reber, J. Aschaber, A. Hurrle, High-temperature diffusion of iron in PECVD-SiO_2 barrier layers for crystalline silicon thin-film solar cells, in *Proceedigns of the 2nd World Conference on Photovoltaic Solar Energy Conversion*, J. Schmid, H. A. Ossenbrink, P. Helm, H. Ehmann, and E. D. Dunlop (Eds.) (Joint Research Centre, European Commission, Ispra, Italy) 1798 (1998).

[35] S. Bau, S. Janz, T. Kieliba, C. Schetter, S. Reber, F. Lutz, Application of PECVD-SIC as intermediate layer in crystalline silicon thin-film solar cells, in *Proceedings of the 3rd World Conference on Photovoltaic Energy Conversion*, L.L. Kazmerski, K. Kurokawa, B. McNelis, M. Yamaguchi, C. Wronski, W.C. Sinke (Eds.) (WCPEC-3 Organizing Committee) 1178–1181 (2003).

[36] T. Kunz, I. Burkert, R. Auer, R. Brendel, W. Buss, H. von Campe, M. Schulz, Silicon carbide barrier layer on ceramic substrates for crystalline silicon thin-film modules with an integrated series connection, in *Proceedings of the 3rd World Conference on Photovoltaic Energy Conversion*,

K. Kurokawa, L. L. Kazmerski, B. McNelis, M. Yamaguchi, C. Wronski, and W. C. Sinke (Eds.) (WCPEC-3 Organizing Committee) 1255–1258 (2003).

[37] K. Yamamoto, A. Nakajima, M. Yoshimi, T. Sawada, S. Fukuda, K. Hayashi, T. Suezaki, M. Ichikawa, Y. Koi, M. Goto, H. Takata, Y. Tawada, High Efficiency Thin Film Silicon Solar Cell and Module, in *Proceedings of the 29th IEEE Photovoltaic Specialists Conference*, 1110–1112 (2002).

[38] P. A. Basore, Large-area deposition for crystalline silicon on glass modules, in *Proceedings of the 3rd World Conference on Photovoltaic Energy Conversion* (WCPEC-3 Organizing Committee) 935–938 (2003).

[39] A. Goetzberger, Optical confinement in thin film Si-solar cells by diffuse back reflectors, in *Proceedings of the 15th IEEE Photovoltaic Specialists Conference* (IEEE) 867–870 (1981).

[40] D. E. Aspnes, Optical functions of intrinsic c-Si for photon energies up to 7.5 eV, in *Properties of Crystalline Silicon*, Robert Hull (Ed.) EMIS Datareview Series No. 20 (INSPEC, The Institution of Electrical Engineers, London, UK) 1999 p. 683–690.

[41] E. Yablonovitch, Intensity enhancement in textured optical sheets for solar cells, in *Proceedings of the 16th IEEE Photovoltaic Specialists Conference* (IEEE) 501–506 (1982).

[42] E. Yablonovitch, G. Cody, Intensity enhancement in textured optical sheets for solar cells, *IEEE Transactions on Electron Devices* **ED-29** 300–305 (1982).

[43] P. Campbell, M. A. Green, Light trapping properties of pyramidally textured surfaces, *Journal of Applied Physics* **62** 243–9 (1987).

[44] P. Campbell, M. Keevers, Light trapping and reflection control for silicon thin-films deposited on glass substrates textured by embossing, in *Proceedings of the 28th IEEE Photovoltaics Specialists Conferernce* (IEEE) 355–358 (2000).

[45] H. Iwata, T. Ohzone, Numerical solar cell simulation including multiple diffused reflection at the rear surface, *Solar Energy Materials and Solar Cells* **61** 353–63 (2000).

[46] M. A. Green, *Solar cells: operating principles, technology and system applications* (Prentice-Hall, Englewood Cliffs, NJ) 1982.

[47] J. R. Davis, A. Rohatgi, P. Rai-Choudhury, P. Blais, R. H. Hopkins, Characterization of the effects of metallic impurities on silicon solar cell performance, in *Proceedings of the 13th IEEE Photovoltaic Specialists Conference* (IEEE) (1978).

[48] G. Zoth, W. Bergholz, A fast, preparation-free method to detect iron in silicon, *Journal of Applied Physics* **67** 6764–6771 (1990).

[49] INSPEC, *Properties of Silicon* (INSPEC, Institution of Electrical Engineers, London, New York) 1988.

[50] L.-H. Chang, W. G. Cowden, J. Cristiansen, D. Werho, N. D. Theodore, Is Ti Contamination in Si Wafer processing an Issue?, *Journal of the Electrochemical Society* **143** (1996).

[51] S. Reber, *Electrical Confinement for the Crystalline Silicon Thin-Film Solar Cell on Foreign Substrate*, (ibidem Verlag, Stuttgart, Germany) 2000.

[52] J. Isenberg, S. Reber, J. Aschaber, W. Warta, Silicon dioxide and silicon nitride as diffusion barrier for transition metals in solar cell applications, in *Proceedings of the 16th European Photovoltaic Solar Energy Conference*, B. McNelis, H. Scheer, W. Palz, H.A. Ossenbrink, P. Helm (Eds.) (James & James Scientific Publishers Ltd) 1463 (2000).

[53] G. Beaucarne, S. Bourdais, A. Slaoui, J. Poortmans, Thin-film polysilicon solar cells on foreign substrates using direct thermal CVD: material and solar cell design, *Thin Solid Films* **403–404** 229–237 (2002).

[54] S. Bourdais, G. Beaucarne, J. Poortmans, A. Slaoui, Electronic transport properties of polycrystalline silicon films deposited on ceramic substrates, *Physica B* **273–274** 544–548 (1999).

[55] P. Hartman, *Crystal Growth: an Introduction* (North-Holland Pub. Co., American Elsevier, Amsterdam, New York) 1973.

[56] W. Kleber, *Einführung in die Kristallographie* (Verlag Technik, Berlin) 1990.

[57] A. Schönecker, L. J. Geerligs, A. Müller, Casting technologies for solar silicon wafers: block casting and ribbon-growth-on substrate, in *Proceedings of the 10th International Autumn Meeting on Gettering and Defect Engineering in Semiconductor Technology (GADEST)* H. Richter and M. Kittler (Eds.) Solid State Phenomena, **95–96** 149–158 (2003).
[58] E. Leitz, British Patent No. 691355 (1950).
[59] E. I. Givargizov, N. N. Sheftal, V. I. Klykov, Diataxy (graphoepitaxy) and other approaches to oriented crystallization on amorphous substrates, *Current Topics in Materials Science* **10** 1–53 (1982).
[60] E. I. Givargizov, *Oriented Crystallization on Amorphous Substrates* (Plenum Press, New York) 1991.
[61] I. N. Miaoulis, P. Y. Wong, S. M. Yoon, R. D. Robinson, C. K. Hess, Thermal analysis of zone-melting recrystallization of silicon-on-insulator structures with an infrared heat source: an overview, *Journal of the Electrochemical Society* **139** 2687–2696 (1992).
[62] M. Pauli, T. Reindl, W. Krühler, F. Homberg, J. Müller, A new fabrication method for multicrystalline silicon layers on graphite substrates suited for low-cost thin film solar cells, *Solar Energy Materials and Solar Cells* **41/42** 119–126 (1996).
[63] G. Andrä, J. Bergmann, F. Falk, E. Ose, Laser induced liquid phase crystallization of amorphous silicon films on glass for thin film solar cells, in *Proceedings of the 14th European Photovoltaic Solar Energy Conference*, P. Helm, H.A. Ossenbrink, H. Ehmann (Eds.) (H.S. Stephens, Bedford, UK) 1400 (1997).
[64] H. Naomoto, S. Hamamoto, A. Takami, S. Arimoto, T. Ishihara, Characterization of thin-film silicon formed by high-speed zone-melting recrystallization process, *Solar Energy Materials and Solar Cells* **48** 261–267 (1997).
[65] T. Ishihara, Zone-melting recrystallization of Si films for solar cells, in *Growth, Charecterization and Electronic Applications of Amorphous and Crystalline Si Thin Films*; Ralf B. Bergmann (Ed.) (Research Signpost, Kerala) 2002 p. 79–100.
[66] A. Takami, S. Arimoto, H. Morikawa, S. Hamamoto, T. Ishihara, H. Kumabe, T. Murotani, High efficiency (16.45 %) thin film silicon solar cells prepared by zone-melting recrystallization, in *Proceedings of the 12th European Photovoltaic Solar Energy Conference* (1994).
[67] H. Morikawa, Y. Nishimoto, H. Naomoto, Y. Kawama, A. Takami, S. Arimoto, T. Ishihara, K. Namba, 16 % Efficiency of large area (10 cm × 10 cm) thin film polycrystalline silicon solar cell, *Solar Energy Materials and Solar Cells* **53** 23–28 (1997).
[68] F. Secco D'Aragona, Dislocation etch for (100)-planes in silicon, *Journal of the Electrochemical Society* **119** 948–951 (1972).
[69] R. F. Pinizzotto, H. W. Lam, B. L. Vaandrager, Subgrain boundaries in laterally seeded silicon-on-oxide formed by graphite strip heater recrystallization, *Applied Physics Letters* **40** 388–90 (1982).
[70] M. W. Geis, H. I. Smith, B. Y. Tsaur, J. C. C. Fan, D. J. Silversmith, R. W. Mountain, Zone-melting recrystallization of Si films with a moveable-strip-heater oven, *Journal of the Electrochemical Society* **129** 2812–18 (1982).
[71] J. C. C. Fan, B. Y. Tsaur, C. K. Chen, J. R. Dick, L. L. Kazmerski, Oxygen in zone-melting recrystallized silicon-on-insulator films: its distribution and possible role in sub-boundary formation, *Applied Physics Letters* **44** 1086–1088 (1984).
[72] J. M. Gibson, L. N. Pfeiffer, K. W. West, D. C. Joy, Thermal stress during zone-melting-recrystallization of silicon on insulator films: the origin of subboundaries and in-plane orientation of SOI, in *Proceedings of the Semiconductor-on-Insulator and Thin Film Transistor Technology Symposium* (Materials Research Society Symposium Proceedings) 289–298 (1986).
[73] B. Tillack, R. Banisch, H. H. Richter, Origin of defects and their influence on electrical properties of thick SOI films, in *Proceedings of the 2nd International Autumn Meeting: Gettering and Defect Engineering in the Semiconductor Technology (GADEST '87)* 308–312 (1987).

[74] J. S. Im, H. Tomita, C. V. Thompson, Cellular and dendritic morphologies on stationary and moving liquid-solid interfaces in zone-melting recrystallization, *Applied Physics Letters* **51** 685–687 (1987).
[75] L. Pfeiffer, A. E. Gelman, K. A. Jackson, K. W. West, J. L. Balstone, Subboundary-free zone-melt recrystallization of thin-film silicon, *Applied Physics Letters* **51** 1256–1258 (1987).
[76] T. Kieliba, *Optimierung zonengeschmolzener Siliciumschichten für kristalline Dünnschichtsolarzellen*, Diploma thesis, Albert-Ludwigs-University Freiburg (1999).
[77] A. B. Limanov, E. I. Givargizov, Control of the structure in zone-melted silicon films on amorphous substrates, *Materials Letters* **2** 93–96 (1983).
[78] A. Ogura, N. Aizaki, H. Terao, High-speed video observation of laser recrystallization for semiconductor-on-insulator fabrication, *Journal of Applied Physics* **65** 752–754 (1989).
[79] T. Inoue, T. Hamasaki, Direct observation of growth front movement in electron beam recrystallization of silicon layer on insulator, *Applied Physics Letters* **50** 971–973 (1987).
[80] D. Dutartre, *In situ* observation of lamp zone melting of Si films on patterned SiO_2, *Applied Physics Letters* **48** 350–352 (1986).
[81] H. J. Leamy, C. C. Chang, H. Baumgart, R. A. Lemons, J. Cheng, Cellular growth in microzone melted silicon, *Materials Letters* **1** 1944–1947 (1982).
[82] R. A. Lemons, M. A. Bösch, D. Herbst, Crystallization of silicon films on glass: a comparison of methods, in *Conference Proceedings of Laser-Solid Interactions and Transient Thermal Processing of Materials*, J. Narayan, W.L. Brown, and R.A. Lemons (Eds.) (Elsevier, New York) 581–592 (1982).
[83] S. R. Coriell, G. B. McFadden, Morphological Stability, in *Handbook of Crystal Growth*; D.T.J. Hurle (Ed.) 1b(North-Holland Elsevier Science Publishers, Amsterdam) 785–857 (1993).
[84] D. T. J. Hurle, B. Cockayne, Czochralski growth, in *Handbook of Crystal Growth*; D.T.J. Hurle (Ed.) 2a (North-Holland Elsevier Science Publishers, Amsterdam) 99–212 (1994).
[85] D. E. Aspnes, Optical functions of liquid Si, in *Properties of Crystalline Silicon*, Robert Hull (Ed.) EMIS Datareview Series No. 20 (INSPEC, The Institution of Electrical Engineers, London, UK). 696 (1999).
[86] R. D. Robinson, I. N. Miaoulis, Thermal analysis of incandescent lamp zone-melting recrystallization of thin silicon films, *Journal of Applied Physics* **73** 439–447 (1993).
[87] L. Si-Woo, J. Seung-Ki, Effects of process parameters on the defect formation in SOI-ZMR, in *Proceedings of Diagnostic Techniques for Semiconductor Materials and Devices*, D. K. Schroder, J. L. Benton, and P. Rai-Choudhury (Eds.)(Electrochem. Society, Pennington, NJ, USA) 283–294 (1994).
[88] C. K. Chen, J. S. Im, Zone-melting recrystallization with enhanced radiative heating for preparation of subboundary-free silicon-on-insulator thin films, *Applied Physics Letters* **55** 1238–1240 (1989).
[89] H. Richter, B. Tillack, H. Andrä, W. Weinelt, Einfluß des Temperaturgradienten bei der Rekristallisation dicker Poly-Si-Schichten auf SiO_2, *Experimentelle Technik der Physik* **37** 11–21 (1987).
[90] P. W. Mertens, J. Leclair, H. E. Maes, W. Vandervorst, Oxygen distribution in silicon-on-insulator layers obtained by zone melting recrystallization, *Journal of Applied Physics* **67 (12)** 7337–7347 (1990).
[91] A. Takami, S. Arimoto, H. Naomoto, S. Hamamoto, T. Ishihara, H. Kumabe, T. Murotani, Thickness dependence of defect density in thin film polycrystalline silicon formed on insulator by zone-melting recrystallization, in *Proceedings of the 1st World Conference on Photovoltaic Energy Conversion* (IEEE, New York) 1394–1397 (1994).
[92] H. A. Atwater, H. I. Smith, C. V. Thompson, M. W. Geis, Zone-melting recrystallization of thick silicon on insulator films, *Materials Letters* **2** 269–273 (1984).
[93] D. K. Biegelsen, L. E. Fennell, J. C. Zesch, Origin of oriented crystal growth of radiantly melted silicon on SiO_2, *Applied Physics Letters* **45** 546–548 (1984).
[94] C. Hebling, *Die kristalline Silicium-Dünnschichtsolarzelle auf isolierenden Substraten*, Ph.D thesis, Universität Konstanz (1998).

[95] S. Reber, A. Eyer, F. Haas, N. Schillinger, S. Janz, E. Schmich, Progress in crystalline silicon thin-film solar cell work at Fraunhofer ISE, in *Proceedings of the 20th European Photovoltaic Solar Energy Conference and Exhibition*, H. Ossenbrink, W. Palz, P. Helm (Eds.) (WIP-Renewable Energies, Munich, Germany) 694–697 (2005).

[96] T. Ishihara, S. Arimoto, H. Morikawa, H. Kumabe, T. Murotani, S. Mitsui, High efficiency thin film silicon solar cells prepared by zone-melting recrystallization, *Applied Physics Letters* **63** 3604–3606 (1993).

[97] T. Kieliba, J. Pohl, A. Eyer, C. Schmiga, Optimization of c-Si films formed by zone-melting recrystallization for thin-film solar cells, in *Proceedings of the 3rd World Conference on Photovoltaic Solar Energy Conversion*, L.L. Kazmerski, K. Kurokawa, B. McNelis, M. Yamaguchi, C. Wronski, W.C. Sinke (Eds.) (WCPEC-3 Organizing Committee) 1170–1173 (2003).

[98] S. Reber, A. Eyer, F. Haas, High-throughput zone-melting recrystallization for Crystalline Silicon Thin-Film solar cells, *Journal of Crystal Growth* **287** 391–396 (2006).

[99] S. Hamamoto, H. Morikawa, H. Naomoto, Y. Kawama, A. Takami, S. Arimoto, T. Ishihara, K. Namba, Development of the VEST cell process for low-cost fabrication, in *Proceedings of the 14th European Photovoltaic Solar Energy Conference*, P. Helm, H. A. Ossenbrink, H. Ehmann (Eds.) (H.S. Stephens, Bedford, UK) 2328–2332 (1997).

[100] A. Eyer, F. Haas, T. Kieliba, A zone melting recrystallisation (ZMR) processor for 400mm wide samples, in *Proceedings of the 19th European Photovoltaic Solar Energy Conference, 7–11 June 2004*, J.-L. Bal, W. Hoffmann, H. Ossenbrink, W. Palz, P. Helm (Eds.) (WIP – Munich, ETA-Florence) 931–934 (2004).

[101] T. J. Stultz, J. F. Gibbons, Arc lamp zone melting and recrystallization of Si films on oxidized silicon substrates, *Applied Physics Letters* **41** 824–826 (1982).

[102] Y. Kawama, A. Takami, H. Naomoto, S. Hamamoto, T. Ishihara, *In situ* control in zone-melting recrystallization process for formation of high-quality thin film polycrystalline Si, in *Proceedings of the 25th IEEE Photovoltaic Specialists Conference* (IEEE; New York, NY, USA) 481–484 (1996).

[103] S. Reber, W. Zimmermann, T. Kieliba, Zone melting recrystallization of silicon films for crystalline-silicon thin-film solar cells, *Solar Energy Materials and Solar Cells* **65** 409 (2001).

[104] T. Kieliba, S. Reber, Enhanced zone melting recrystallization for crystalline silicon thin-film solar cells, in *Proceedings of the 16th European Photovoltaic Solar Energy Conference*, H. Scheer, B. McNelis, W. Palz, H. A. Ossenbrink, E Dunlop, and P. Helm (Eds.) (James & James Ltd, London UK) 1455–1458 (2000).

[105] P. Y. Wong, I. N. Miaoulis, Real-time image analysis and control of the solid/liquid interface during zone-melting recrystallization of thin films, in *Proceedings of Microelectronic Processes, Sensors, and Controls*, 358–368 (1993).

[106] F. Roozeboom, Introduction: history and perspectives of rapid thermal processing, in *Advances in Rapid Thermal and Integrated Processing*; Fred Roozeboom (Ed.) NATO ASI Series: Series E (Applied Sciences) 318 (Kluwer Academic Publishers, Dordrecht, Boston, London) 1–34 (1996).

[107] S. Kommu, G. M. Wilson, B. Khomami, A theoretical/experimental study of silicon epitaxy in horizontal single-wafer chemical vapor deposition reactors, *Journal of The Electrochemical Society* **147** 1538–1550 (2000).

[108] L. Kadinski (Ed.) *PAR-CVD: Entwicklung leistungsfähiger paralleler Berechnungsverfahren zur Untersuchung und Optimierung von CVD-Prozessen*; (Shaker Verlag Aachen) (1999).

[109] C. R. Kleijn, Computational modeling of transport phenomena and detailed chemistry in chemical vapor deposition – a benchmark solution, *Thin Solid Films* **365** 294–306 (2000).

[110] G. Valente, C. Cavallotti, M. Masi, S. Carrà, Reduced order model for the CVD of epitaxial silicon from silane and chlorosilanes, *Journal of Crystal Growth* **230** 247–257 (2001).

[111] H. Habuka, T. Nagoya, M. Mayusumi, M. Katayama, M. Shimada, K. Okuyama, Model on transport phenomena and epitaxial growth of silicon thin film in $SiHCl_3$–H_2 system under atmospheric pressure, *Journal of Crystal Growth* **169** 61–72 (1996).

[112] H. Habuka, T. Otsuka, W. F. Qu, M. Shimada, K. Okuyama, Model of boron incorporation into silicon epitaxial film in a B_2H_6-$SiHCl_3$-H_2 system, *Journal of Crystal Growth* **222** 183–193 (2001).

[113] F. R. Faller, *Epitaxial Silicon Thin-Film Solar Cells*, Ph.D. Thesis, Albert-Ludwigs-University, Freiburg (1998).

[114] T. Kunz, H. von Campe, *Verfahren und Vorrichtung zum Behandeln und/oder Beschichten einer Fläche eines Gegenstandes*, European Patent No. EP 1 247 587 A2 (2002).

[115] H. J. Rodriguez, J. C. Zamorano, I. Tobias, C. del Canizo, A. Luque, High-throughput epitaxial reactor prototype for thin-film Si solar cells on low-grade Si substrates, in *Proceedings of the 19th European Photovoltaic Solar Energy Conference, 7–11 June 2004*, J.-L. Bal W. Hoffmann, H. Ossenbrink, W. Palz, P. Helm (Eds.) (WIP – Munich, ETA-Florence)(2004).

[116] A. Hurrle, S. Reber, N. Schillinger, J. Haase, J. G. Reichart, High throughput continuous CVD reactor for silicon deposition, in *Proceedings of the 19th European Conference on Photovoltaic Energy Conversion*, J.-L. Bal, W. Hoffmann, H. Ossenbrink, W. Palz, P. Helm (Eds.) (WIP - Munich, ETA-Florence) 459 (2004).

[117] S. M. Sze, *VLSI Technology* (McGraw-Hill, New York) (1983).

[118] S. A. Campbell, Critical review of the epitaxial growth of semiconductors by rapid thermal chemical vapor deposition, *Materials Science and Engineering* **R20** 1–36 (1997).

[119] F. Passek, R. Schmolke, U. Lambert, G. Puppe, P. Wagner, Discrimination of defects on epitaxial silicon wafers, in *Proceedings of the Symposium on Crystalline Defects and Communication: Their Impact and Control in Device Manufacturing II*, Electrochemical Society, 438–447 (1997).

[120] M. J. Stowell, Defects in epitaxial deposits, in *Epitaxial Growth, Part B*; Matthews (Ed.) (Academic Press, New York) 437–492 (1975).

[121] N. König, *Durchlauf Silicium-Epitaxie für kristalline Silicium-Dünnschichtsolarzellen*, Diploma Thesis, Albert-Ludwigs-University, Freiburg (2005).

[122] E. I. Givargizov, Growth of whiskers by the vapor-liquid-solid mechanism, in *Current Topics in Materials Science Vol.1*; E. Kaldis (Ed.) (North-Holland Publishing Company) (1978)

[123] F. W. Dekkers, G. Agostinelli, D. Dehertoghe, G. Beaucarne, Improved performances of mc-Si solar cells by isotropic plasma texturing, in *Proceedings of the 19th European Photovoltaic Solar Energy Conference, 7–11 June 2004*, J.-L. Bal, W. Hoffmann, H. Ossenbrink, W. Palz, P. Helm (Eds.) (WIP – Munich, ETA-Florence) 412–415 (2004).

[124] R. Lüdemann, *Plasmatechnologie für die Photovoltaik* (Hartung-Gorre, Konstanz) (1999).

[125] S. Schäfer, *Plasmaätzen für die Photovoltaik* (UFO Atelier für Gestaltung und Verlag, Allensbach) (2000).

[126] K. V. Nieuwenhuysen, F. Duerinckx, R. Bilyalov, H. Dekkers, G. Beaucarne, J. Poortmans, Epitaxial Si thin films by high-temperature CVD, in *Proceedings of the 19th European Photovoltaic Solar Energy Conference, 7–11 June 2004*, J.-L. Bal, W. Hoffmann, H. Ossenbrink, W. Palz, P. Helm (Eds.) (WIP – Munich, ETA-Florence) 1178–1181 (2004).

[127] J. Rentsch, D. M. Hulijc, T. Kieliba, R. Bilyalov, S. Reber, Screen printed c-Si thin film solar cells on insulating substrates, in *Proceedings of the 3rd World Conference on Photovoltaic Energy Conversion*, L.L. Kazmerski, K. Kurokawa, B. McNelis, M. Yamaguchi, C. Wronski, W.C. Sinke (Eds.) (WCPEC-3 Organizing Committee) 1486–1489 (2003).

[128] P. E. Sims, A. E. Ingram, D. E.J., J. P. Yaskoff, D. H. Ford, J. A. Rand, A. M. Barnett, Silicon-on-ceramic monolithically interconnected solar cell modules, in *Proceedings of the 3rd World Conference on Photovoltaic Energy Conversion*, K. Kurokawa, L. L. Kazmerski, B. McNelis, M. Yamaguchi, C. Wronski, and W. C. Sinke (Eds.) (WCPEC-3 Organizing Committee) 1217–1220 (2003).

[129] M. E. Nell, B. Müller, U. Kerst, S. Kühn, R. Leihkauf, M. Rochel, H. G. Wagemann, Series-interconnection of silicon solar cells on a SOI-wafer, in *Proceedings of the 16th European Photovoltaic Solar Energy Conference* (James & James Ltd, London UK) 1755–1758 (2000).

[130] V. Gazuz, R. Auer, M. Schulz, R. Brendel, Series connection in thin-film crystalline Si solar modules on Insulating Substrates, in *Proceedings of the Proceedings of the 14th International Photovoltaic Science and Engineering Conference* (Program Committee PVSEC-14) 323–324 (2004).

[131] C. Hebling, S. W. Glunz, J. O. Schumacher, J. Knobloch, High efficiency (19.2 %) silicon thin-film solar cells with tnterdigitated emitter and base front-contacts, in *Proceedings of the 14th European Solar Photovoltaic Solar Energy Conversion*, P. Helm, H. A. Ossenbrink, H. Ehmann (Eds.), (H. S. Stephens & Associates), 2318–2323 (1997).

[132] R. Brendel, K. H. Feldrapp, S. Oelting, Shadow-epitaxy for flexible crystalline thin-film silicon solar cell design, *Solar Energy Materials & Solar Cells* **64** 251–260 (2000).

[133] S. Reber, A. Eyer, F. Haas, unpublished work.

[134] T. Kieliba, S. Bau, D. Oßwald, A. Eyer, Coarse-grained Si films for crystalline Si thin-film solar cells prepared by zone-melting recrystallization, in *Proceedings of the 17th European Photovoltaic Solar Energy Conference*, W. Palz, B. McNelis, H.A. Ossenbrink, P. Helm (Eds.) (WIP-Renewable Energies) 1604–1605 (2001).

3 Thin Film Polycrystalline Silicon Solar Cells

Guy Beaucarne
Microsystems, Components and Packaging Division, Silicon Solar Cells Group, IMEC, Kapeldreef 75 B-3001 Leuven, Belgium

Abdelilah Slaoui
PV Group, InESS (Institut d'Électronique du Solide et des Systémes) CNRS, 23 rue du Loess, F-67037 Strasbourg, France

3.1 INTRODUCTION

As the world energy needs continue to rise and concerns about the environmental impact of traditional energy technologies become more pressing, photovoltaics increasingly appears as a key technology for mankind. At present the wafer based crystalline Si technology dominates the market, with a share of more than 90 %. Several thin film technologies have been proposed, the main ones being amorphous silicon (a-Si), cadmium telluride (CdTe) and copper indium gallium selenide (CIGS) but so far none of these have been able to challenge the supremacy of bulk crystalline silicon, which combines an impressive number of advantages such as high performance, stability, abundance and nontoxicity. This chapter deals with an alternative thin film technology that aims to combine these advantages by sticking to crystalline Si as active material, with the low cost that thin film technology in principle enables. This is the thin film polycrystalline silicon solar cells technology.

3.1.1 Definition

There is unfortunately no consensus on the terminology used to classify Si materials, and this has resulted in a somewhat confusing situation today. Polysilicon is nowadays defined as having a grain size between 1 μm and 1 mm [1]. We extend this range a little, by taking 0.1 μm as the lower bound, because many relevant examples have grain sizes not quite reaching 1 μm. In any case, this type of material has much smaller grains than standard material used for solar cells, namely multicrystalline silicon, which confusingly is still often referred to as 'polycrystalline'. The grain size is however much larger than for the material commonly called 'microcrystalline silicon', but also 'nanocrystalline silicon', a material typically obtained by plasma enhanced chemical vapor deposition (PECVD) at very low temperature (∼200 °C). This material has a typical grain size of a few tens of nanometers, still contains a substantial

Thin Film Solar Cells Edited by J. Poortmans and V. Arkhipov
© 2006 John Wiley & Sons, Ltd

fraction of amorphous silicon, and in fact has the best quality in the transition region between amorphous and microcrystalline [2]. In contrast, polysilicon has a crystalline fraction close to 100 %, the disordered regions being confined to the very thin and relatively sparse grain boundaries. By 'thin film', we refer to layers that have been deposited rather than cast, pulled from a melt or obtained through a layer transfer process. In general the thickness of the silicon film is lower than 30 μm, typically between 3 and 10 μm.

3.1.2 Why polycrystalline thin film silicon solar cells?

As mentioned earlier, thin film polycrystalline Si (pc-Si) solar cells want to capitalize on the known advantages of traditional bulk Si solar cells. The material is one of the most abundant elements on Earth and the technology is therefore compatible with very large volume scenarios. Toxicity (real or perceived) has proved to be a major hurdle for some thin film technologies (e.g. CdTe solar cells), but is just not an issue for Si. The stability and reliability of crystalline Si modules has probably been so far the most decisive advantage, contrasting with many thin film products plagued with reliability problems in the infancy stage of the technology. The potential for high efficiency remains, in principle, even for very thin layers, as will be discussed in the next section.

The next question is then, why choose thin film *poly* crystalline silicon, rather than microcrystalline, multicrystalline silicon (as can for instance be obtained by recrystallization through the melt, see e.g. Chapter 2 in this book) or monocrystalline silicon (obtained for instance through a layer transfer technique, see e.g. Reference [4])? The jury is still out on the question of which Si thin film material is best for the purpose, and research is taking place in parallel, none of the approaches having been validated as 'the' solution. Among the various options polycrystalline silicon is less known and may appear a bad choice at first sight. Film formation takes place at temperatures substantially higher than for microcrystalline silicon, and generally, the more heat resistant the substrate, the more expensive they are. Yet, the crystalline quality of these layers is far below that of thin film multi or monocrystalline layers. More importantly, some experts have raised doubts in the literature as to whether efficient solar cells could ever be made in this grain size range, refering to an absence of good results. In some high profile presentations, this grain size range was named 'the Valley of Suffering' [3], situated between the 'mountains' of thin film multi and mono, and of microcrystalline. According to the authors, this is a mistaken interpretation of the data. There are in fact several examples giving a lot of hope for thin film polysilicon, and there is a good chance that it will be the first thin film technology able to challenge the supremacy of bulk Si.

3.2 POTENTIAL OF POLYSILICON SOLAR CELLS

3.2.1 Light confinement

Although Si is an indirect bandgap semiconductor and therefore a relatively poor light absorber, efficient solar cells with reasonable currents can, in principle, be achieved even in thin layers of only a few microns thickness. This is because light confinement can be applied to obtain a high absorbance of the impinging light [4 (Chapter 2)], [5].

Light confinement can be realized by texturing the front side of the active Si layer to obliquely couple the light into the layer, combined with a back reflector. In theory, close to optimal optical confinement can be obtained by a Lambertian scheme, with one of the

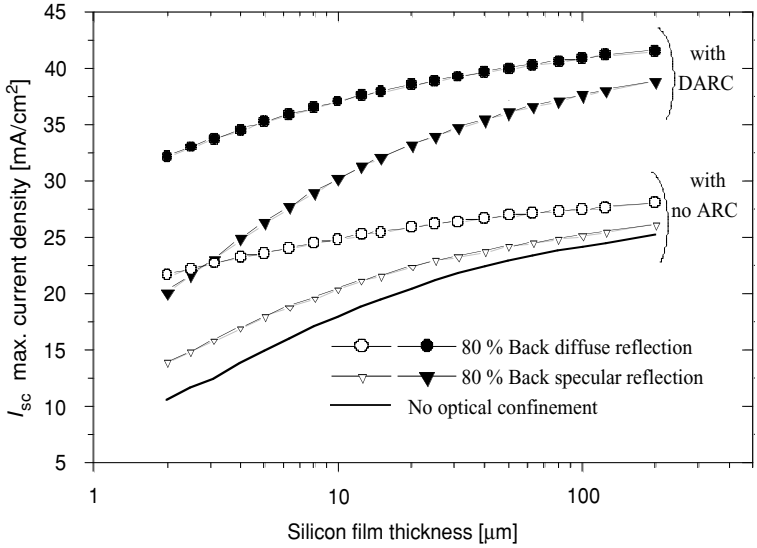

Figure 3.1 Maximum current density I_{max} as a function of silicon film thickness of cells with different configurations: flat surface (solid line); with no ARC but 80 % back diffuse (open triangle) or diffuse (full triangle) reflectance; with double ARC MgF_2/ZnS and 80 % back diffuse (open circle) or diffuse (full circle).

two film surfaces displaying a perfectly diffusing behaviour. In practice however, best results are obtained if both surfaces have a diffused reflection. Optical confinement is particularly important for wavelengths larger than 800 nm, which are weakly absorbed in silicon.

The efficiency of light absorption can be monitored through the theoretical maximal short circuit current density of an illuminated silicon cell under normalized solar spectrum. The maximum current that can be calculated assuming an infinite silicon thickness and total photocarriers collection is about 47 mA/cm^2. Similarly, it is possible to calculate the maximum current density that can be extracted from a thin silicon film versus its thickness. The results are plotted in Figure 3.1. Even for 2 μm thick films, currents above 30 mA/cm^2 are achievable if a good reflector and light diffusion is used. Note that a back reflectance of 80 % is lower than can be achieved with Si on low refractive index materials such glass or ceramic (typical values above 90 %), so the potential current is in fact even larger.

These calculations assume that 100 % of the photogenerated carriers are collected. In practice of course the number of collected carrier will be lower and will primarily depend on minority carrier properties.

3.2.2 Diffusion length

Minority carrier transport is conveniently described by a 'diffusion length'. In polysilicon, the diffusion length is not a fundamental material property, but is the result of different diffusion and recombination processes in the various areas of the device. A lumped effective diffusion length (L_{eff}) has to be defined. Among the various existing models [6, 7], [4 (Chapter 3)], the one based on Shockley's filament theory is probably the most useful as it is both fairly accurate and simple. It considers the material as an array of identical grains with square cross-section.

The L_{eff} is given by:

$$\frac{1}{L_{\text{eff}}^{\ 2}} = \frac{1}{L_n^{\ 2}} + 2b_0^2$$

with L_n the intragrain diffusion length and b_0 the first solution of

$$\left(4\frac{D_n}{S_{gb}a}\right) b\frac{a}{2} = \cot\left(b\frac{a}{2}\right)$$

with a the grain size, S_{gb} the recombination velocity at the grain boundary and D_n the intragrain electron diffusion coefficient. For small grain size, and moderate recombination velocity ($S_{\text{gb}}\ a/D \ll 4$), and relatively high intragrain lifetime the equation simplifies to:

$$L_{\text{eff}} = \sqrt{\frac{D_n a}{2S_{gb}}}$$

For an efficient solar cell, the effective diffusion length must be well above the thickness of the active layer, while at the same time the rear surface recombination velocity should be moderate. Since the active layer is only a few microns thick, the requirements on the effective diffusion length are quite relaxed compared to bulk Si solar cells, 10 μm being sufficient to reach high efficiencies.

3.2.3 Modeling

Different theoretical papers have been dedicated to the topic of modeling thin film polysilicon solar cells, reporting, in particular, the effects of grain size, grain boundary recombination velocity and dislocation density [8–12]. Recently, some papers addressed simulations of the pc-Si based solar cells taking into account the doping spikes due to preferential diffusion of dopants along grain boundaries during the emitter formation (see Section 3.5.2). In columnar structures, the dopant spikes extend deep, over a part or the whole depth of the active layer, along the grain boundaries. Such a structure is called a TREBLE (ThRee-dimensional Emitter Based on Locally Enhanced diffusion) cell [13]. A scheme of the TREBLE cell is shown in Figure 3.2a. The vertical junctions created by this preferential diffusion can enhance collection in materials with low minority carrier diffusion length and therefore increase the cell efficiency. This is clearly shown in Figure 3.2b which reports the calculated efficiency as a function of the dopant diffusion depth along the grain boundary X_{gb} for a 10 μm thick Si based cell with an average grain size of 3 μm. The analysis was done using ISE-DESSIS, a commercial two-dimensional semiconductor device simulator. A conversion efficiency of ∼12 % can be expected with $S_{\text{gb}} = 10^4$ cm/s and $\text{X}_{\text{gb}} = 2.5$ μm. With well passivated grain boundaries ($S_{\text{gb}} = 10^3$ cm/s), the effect of preferential doping is less significant and efficiencies above 13 % can be reached regardless of X_{gb}.

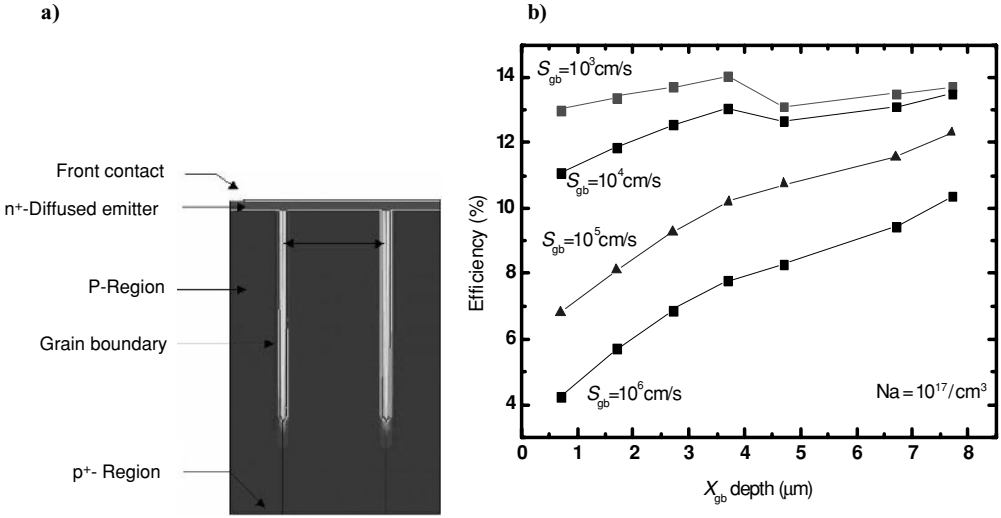

Figure 3.2 (a) Scheme of a TREBLE cell; (b) computed efficiency versus diffusion depth along grain boundary (X_{gb}) and for different surface recombination velocity at grain boundary (S_{gb}). The Si base cell is 8 μm thick, doped at $N_a = 10^{17}$ cm^{-3}, a grain size of 3 μm and a lifetime of 0.5 μsec; the Si-BSF is 2 μm thick and doped at 10^{19} cm^{-3}.

3.3 SUBSTRATES FOR POLYSILICON CELLS

In contrast to bulk crystalline Si solar cells, thin film Si solar cells rely on a foreign material for the mechanical strength. If this material is an insulator and can be produced in the form of large sheets, a monolithic interconnection scheme can be implemented, which potentially can lead to lower processing and module manufacturing costs.

The choice of substrate depends on several criteria. As thin film solar cells aim at cost reduction, the primary criterion is low cost. A second important criterion is the temperature the substrate can withstand, which has to be higher than the maximum temperature in the cell production process. Another crucial parameter is the thermal expansion coefficient (TEC) of the substrate, which should preferably be close to that of crystalline Si ($\sim 4\times10^{-6}\,\mathrm{K}^{-1}$). Mismatch can lead to excessive stress, breakage and/or cracks, as a result of differential extension or contraction while ramping the temperature up or down. This requirement can be more or less stringent according to the maximum process temperature. Transparency is also required if a superstrate configuration is chosen (where light enters the device through the supporting substrate).

In Table 3.1, we list the properties of a few substrate materials considered for polysilicon solar cells. Soda lime glass is an attractive option as this is mass-produced with a large volume float process that delivers very low cost per unit area. Soda lime glass is already used as a standard material in photovoltaic module production, for the front cover and, in glass–glass modules also as back sheet. Front cover glass most often has a low metallic impurities content (‘extra white’ glass) and is hardened. Standard soda-lime glass has a softening point of around 580 °C and therefore cannot withstand temperatures above this value for an extended period

Table 3.1 Properties of substrate materials for thin film polysilicon solar cells

Material	Soda-lime glass	Borosilicate glass	High temperature glass	Stainless steel	Mullite ceramic
Price of substrate (€ /m^2)	3–7	20–40	Unknown for large volumes	4–10	30–40 (estimate for large volumes)
Softening point (°C)	∼580	∼820	∼1000	>1000	>1460
Coefficient of thermal expansion (10^{-6} K^{-1})	80	3	3.8	12	3.5
Transparent	yes	yes	yes	no	no

of time. The TEC of soda-lime glass is much larger than that of Si, which can lead to problems for large polysilicon devices.

Metal substrates can, in principle, be very cost effective. An obvious choice is a steel foil or substrate, as used in some amorphous Si technologies. The TEC, which for metals is usually much larger than that of Si, can here also create problems of cracks and breakage. The fact that the substrate is conductive can be seen as an advantage (easier cell manufacturing with contacts on either side), however it prevents a monolithic module concept and the associated potential cost reduction in module manufacturing. A potential way around this problem is to coat the substrate with an insulating layer. This was suggested in reference [14] for amorphous and microcrystalline Si solar cells, but has not yet been applied for polysilicon cells.

Borosilicate glass is in many cases a more suitable substrate as it has a TEC closer to that of Si, while it can withstand temperatures up to 800 °C. For short times, this type of glass can even withstand temperatures above 900 °C, as, for instance, in the defect anneal step used at CSG Solar [15]. For processes that require even higher temperatures, up to 1000 °C, some special glasses could be used, so called 'high temperature glasses' [16, 17]. Their TEC is tuned to match that of Si and it is predicted that they could be produced at a low cost in large volumes. If temperatures substantially above 1000 °C are required, only ceramic substrates can be considered. Several different ceramics have been investigated. Alumina (microcrystalline aluminium oxide) is a material widely used in the electronic packaging industry. Some of alumina's properties are excellent for thin film Si solar cells. It has good mechanical characteristics and shows a large diffuse reflection. However, its TEC is about twice that of Si. Mullite is a ceramic material formed as a solid state solution of Al_2O_3 and SiO_2 within a certain concentration ratio. It has similar optical properties to alumina, but its TEC is much better matched to that of Si [18]. Cost calculations indicate that it could be produced at a cost compatible with low cost solar cells. Other nitride based ceramics have been investigated, among which SiAlON ceramic [19], which is made from Si_3N_4, AlN and Al_2O_3 powders. The TEC of this material is close to that of Si and its mechanical properties are excellent, while its optical properties are less optimal.

Before closing the discussion on the substrate requirements the authors would like to stress a fact that is obvious from Table 3.1, but that contradicts incorrect statements made in many papers. Glass is not limited to very low temperatures, but can in fact be of application for

technologies going to high temperatures. According to the maximum temperature in the process, borosilicate glass, aluminosilicate glass or a glass-ceramic can be selected. Too often, 600 °C is wrongly presented as a fundamental and absolute limit to the use of glass.

As the active layer of polysilicon cells is very thin compared to bulk Si cells, while they share the same limited absorption, properties it is imperative to implement light confinement in these layers (see Section 3.2.1). For this, internal reflectance should be maximized while light should be coupled into the cell at an oblique angle. Light scattering by rough surfaces is often an excellent means to achieve the latter goal. In Kaneka's STAR concept, both the front surface and the rear reflector are textured [20], while at CSG Solar, flat glass panels are textured by coating them with tiny beads [15]. Other possibilities for texturing glass are sand blasting [21], plasma texturing [22] or chemical reaction with Al [23].

3.4 FILM FORMATION

Crystalline silicon can been grown by a variety of techniques, each suited to the needs of particular semiconductor device technologies. Technical and economic requirements for photovoltaic application impose an optimum thickness of about 10 μm or less. Such thin poly-silicon films on foreign substrates can be grown by different methods that can be distinguished by the principle of the deposition process: chemical vapor deposition (CVD), plasma enhanced CVD (PECVD), ion assisted deposition (IAD), liquid phase epitaxy (LPE) and finally the solid phase crystallization (SPC) of amorphous silicon. In this section we review the different steps for the formation of the Si films as well as the properties of the resulting silicon layers in terms of grain size and prefential orientation.

3.4.1 Initial step for grain size enhancement

In order to make use of the high efficiency potential of polysilicon thin film solar cells, researchers strive to obtain as ideal layers as possible, therefore with grains as large as possible. If Si is deposited directly onto a foreign substrate, the resulting material is usually of rather poor crystallographic quality, with very small grains. That is why an initial step is often carried out aiming to reach large grains (>10 μm). Two different approaches are followed.

3.4.1.1 Nucleation control

Any formation of a polycrystalline film on a foreign substrate starts with a nucleation phase, the followed by a phase in which the nuclei grow further until they form a complete layer. In general, the larger the number of nuclei ('nucleus density') formed during, the nucleation phase, the smaller the grain size in the final layer will be. On the other hand, if nucleus density is too low, the nuclei are too far from each other and it will take an impractically long time to reach a complete layer, or total coalescence might not be reached at all. In order to obtain an optimal layer, one can therefore attempt to control nucleation in the early phase of the crystallization or deposition process, aiming at the nucleus density predicted to give the largest grain size in a continuous layer.

Nucleation control takes on different forms according to the film formation technique used, and will therefore be dealt with in dedicated sections.

3.4.1.2 Seed layer approach

In contrast with the nucleation control approach, the seed layer approach totally decouples initial nucleation from the actual growth of the active layer. First, a thin continuous layer with large grains is formed, the seed layer. This seed layer shows good crystallographic quality, but is either too thin or too highly doped, or both, to be used as an active layer in a solar cell. In the second phase, an epitaxial deposition process is applied, that is a deposition process that reproduces the underlying crystal structure, to create the absorber layer. Note that two completely different film formation techniques can be used for the seed layer and the active layer.

The seed layer approach decouples the issues of achieving good crystallographic quality on one hand, and of depositing a layer with the required doping profile and with an adequate growth rate on the other hand. Two prominent techniques to make a seed layer for thin film polysilicon solar cells are laser crystallization and aluminium induced crystallization (AIC).

Laser crystallization makes use of laser light pulses to melt the silicon locally, inducing crystallization. As only a small volume of silicon is liquid for only a very short time, the substrate itself remains at low temperature. Laser crystallization is therefore compatible with cheap low temperature substrates. High electronic quality can be achieved, with excellent homogeneity over large areas, even on ordinary glass substrates. Laser crystallized silicon is used by the electronics industry to obtain thin film transistors (TFTs) for flat panel displays. There are several different techniques used to laser crystallize materials over large areas. The standard technique for TFT's at present is excimer laser annealing (ELA), in which a thin amorphous Si layer is crystallized by repeated pulses of a wide excimer laser beam. This technique results in a material with a relatively small grain size (0.1–0.5 μm). Newer techniques are being investigated, which generate polysilicon layers with better structural quality and larger grains. The most promising is the sequential lateral solidification (SLS) process [24, 25]. The idea is to generate grains that serve as seeds for further lateral crystallization. Local melting and crystallization is spatially and temporally displaced from the previous crystallization event. The grain width has been found to depend on the a-Si thickness, the laser power and the pulse frequency. The lower the film thickness, the laser power or the pulse frequency, the higher the quenching rate is [26]. A high quenching rate means fast crystallization and small grains. The SLS process has been successfully used for the formation of polysilicon materials with typical grain size in the range 2–4 μm [27] and up to 7 mm under some specific conditions [28].

In principle, if the a-Si is moderately doped, active layers for solar cells can be formed directly by laser crystallization. This was done, for instance, by a team at the Electrotechnical Laboratories in Tsukuba, reporting efficiencies of up to 6.5 % on very small area devices on ceramic [29, 30]. However, it seems difficult to achieve large devices in this way, due to the lack of dopant profile control. As the whole Si volume goes through the liquid phase, the resulting doping level is uniform over the whole thickness. It is therefore impossible to create a highly doped back region, which is needed for lateral transport of the majority charge carrier. Therefore, laser crystallization is mainly applied on highly doped layers to create seed layers for subsequent epitaxial deposition [31].

The main advantage of laser processing is the possibility to use cheap glass or flexible substrates. Critical issues for a possible industrial application are throughput (scanning over the whole device area with a narrow beam is usually slow) and maintenance costs. However, with constant progress in laser technology, these issues might be successfully addressed.

Another way to reach large grain sizes while keeping the substrate temperature low is to apply some kind of metal induced crystallization. Some metals, such as Al, Ni or Pd [32–34] are known to affect crystallization of amorphous silicon, lowering the crystallization temperature and/or leading to larger grains. In the case of Ni, silicide precipitates are formed at the initial stage of thermal annealing and act as the sites for crystallization. The amorphous silicon layer is fully crystallized before the onset of random nucleation, with each nickel particle seeding one grain, achieving grain sizes $>100\,\mu m$. These grains, however, contain many low angle subgrain boundaries and are heavily metal contaminated. To avoid contamination, aluminum is preferred, as it acts as an acceptor dopant in Si and diffuses relatively slowly in Si. The AIC technique leads to a thin crystalline layer with a high Al concentration. Such a p^+ layer is not a problem in a photovoltaic device. It is in fact a feature that is present in most Si solar cell designs. Aluminium induced crystallization (also called ALILE or Al induced layer exchange) is based on the overall layer exchange of adjacent Si and Al films and transformation of amorphous to polycrystalline Si during thermal annealing [35, 36]. The Si and Al layers, each a few hundreds of nm thick, are generally deposited by evaporation, magnetron sputtering or PECVD. Importantly, a thin (a few nm) Al_2O_3 membrane should be formed between the two layers. This is usually done by oxidation of the Al prior to Si deposition. Figure 3.3 depicts the AIC process on silicon oxide substrate through cross-sectional focused ion beam (FIB) micrographs. Figure 3 a) shows the Al and a-Si layer before annealing. The Al and Si exchange is performed during annealing at temperatures in the range 450–550 °C and for durations of 30 min to 20 h. During the thermal treatment, the dissolved Si atoms crystallize within the aluminium. The Si grain first grows in three dimensions until it reaches the substrate and the membrane at the a-Si/Al interface. Then the grain grows sideways until the end of the crystallization process. If right parameters are chosen, a continuous polycrystalline silicon layer is formed. Some secondary crystallites (sometimes called 'islands') are formed in the top layer. Figure 3.3c) illustrates the resulting polysilicon layer as well as the residual Al+Si structure obtained after annealing at 500 °C for 2 h. It can be noticed that the layer exchange has successfully taken place.

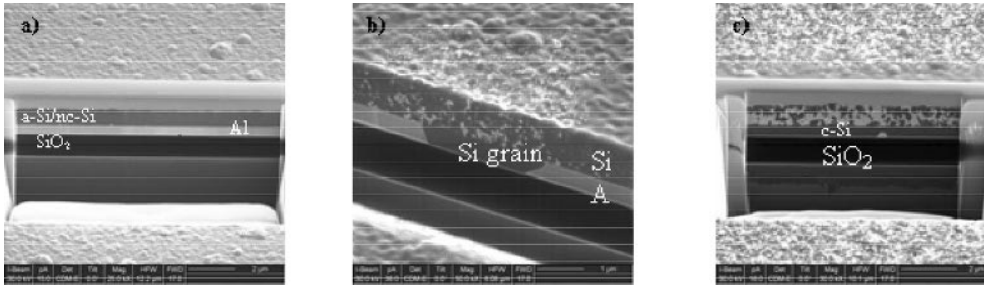

Figure 3.3 Section view micrographs by FIB illustrating the crystallization process on oxidized silicon substrate: (a) as-deposited Al/a-Si films; (b) silicon grain growth in the aluminium layer after 10 minutes annealing at 500 °C; (c) complete layer exchange after 2 hours annealing at 500 °C.

The Al is removed by selective etching (e.g. by phosphoric acid treatment) after the AIC process is complete. Grain sizes range between a few microns and larger than 50 μm, depending on the substrate and the process. The grain aspect ratio is extremely small, as grain thickness is only in 100–500 nm thick, depending on the thickness of the deposited Al layer. The exact mechanism of AIC is still unclear, although general principles have been established based on nucleation theory and diffusion limited kinetics [37]. Many parameters appear to play a role in the process, including annealing temperature and time, but also Al grain size [38, 39], the deposition technique used [40, 41], the roughness of the substrate, etc. In general, if the parameters are chosen for fast crystallization, there will be more nuclei and eventually smaller grains. The grain structure is therefore a compromise between acceptable process time and best crystallographic structure. Most of the work on AIC has been carried out on glass substrates, which have close to perfect flatness. The process can also be applied to other types of substrates such as ceramics [42, 43], but a problem arises of excessive nucleation due to substrate roughness. This can be solved by depositing a flattening layer on the substrate prior to AIC, such as a flowable oxide [44, 45]. AIC seed layers show a preferred <100> orientation [36, 46, 47], which is very beneficial for the subsequent epitaxy. The degree of preferential orientation is to some extent tunable through the process parameters. The secondary islands on the seed layer are undesirable because they lead to imperfect epitaxy and more grain boundaries. They can be removed by chemical mechanical polishing (CMP) [48] or by a high temperature (T >130 °C) ultrasonic phosphoric acid treatment that causes a lift-off of the remaining aluminium oxide layer [49, 50]. Alternatively, one can ensure that the secondary crystallites are completely embedded in the to Al layer at the end of the process, so that they are easily removed during Al etching [51].

3.4.2 Techniques for active layer formation

3.4.2.1 Chemical vapor deposition

In CVD a solid material is deposited through a chemical reaction from gaseous reactants. It is widely used in microelectronics to grow thin epitaxial layers because it allows excellent dopant concentration and layer thickness control. The starting product or 'precursor' for Si deposition is most often silane (SiH_4) or a chlorinated compound such as dichlorosilane (SiH_2Cl_2) or trichlorosilane ($SiHCl_3$). Si deposition is the result of a chain of processes including gas phase reaction (decomposition of the precursor gas into smaller molecules), gas phase diffusion and surface reactions. When the process is based on thermal decomposition of the precursor, the term 'thermal CVD' or simply 'CVD' is used. Depending on the precursor, deposition takes place between 800 and 1200 °C. Chemical vapor deposition is one of the main techniques investigated for thin film polysilicon solar cells. A detailed review on that topic is given in a recent review paper [52].

Chemical vapor deposition is applied either as the second step in the seed layer approach, i.e. epitaxy on an existing seed layer, or as the only deposition technique to create the whole Si structure, in which case one may attempt nucleation control in the initial stage of the deposition.

As part of the seed layer approach, the use of CVD is relatively straightforward. In contrast to other epitaxial techniques, good epitaxy is obtained irrespective of the crystal orientation and H-coverage prior to epitaxy. Low defect density can, in principle, be achieved if the epitaxial template is smooth and continuous. This has been demonstrated many times for epitaxial solar

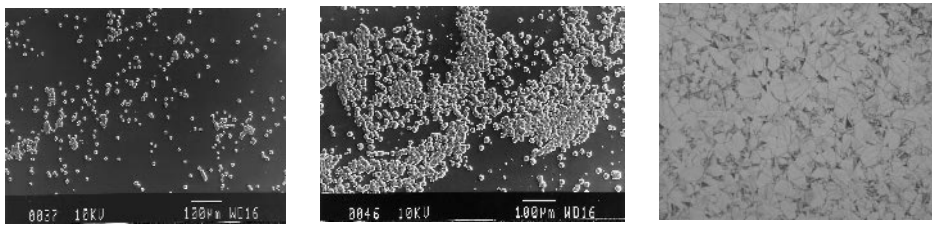

Figure 3.4 SEM pictures of Si nuclei grown after 5 s, 15 s and 120 s on amorphous thermal SiO_2 in an APCVD reactor at 1150 °C.

cells [53] and high temperature thin film multicrystalline silicon solar cells [54]. For thin film *poly* silicon solar cells with the seed layer approach, results are less numerous and more recent, but also indicate that good epitaxy is possible on the various crystal orientations provided the seed layer is of good quality [44].

Until recently, however, most of the work on thermal CVD for thin film polysilicon solar cells involved direct deposition on foreign substrates. Uniform layers on large areas were obtained on oxidized silicon wafer [55–57], but also on other foreign substrates: graphite [58], high temperature glass [59], alumina [60–65], SiAlON and Si-SiAlON [66] and mullite [67, 64]. When Si is directly deposited on the foreign substrate, the grain size is going to be determined by the nucleation phenomenon in the early stage of deposition (see Figure 3.4). During the nucleation phase, nuclei are formed and start capturing free Si atoms on the substrate surface. While these existing grains grow, new ones may be formed in the spaces between them. After coalescence, however, grains grow further epitaxially, continuing the underlying crystalline structure throughout the layer. As the crystallites have different crystal orientations, they form grain boundaries when they reach each other.

Clearly the number of nuclei just before coalescence determines the grain size in such a coalesced layer. The lower the nucleus density, the larger the grains will be. The relationship between n_x (the nucleus density) and L_g (the grain size in the final layer) can be roughly approximated by $n_x \approx L_g^{-2}$. For an average grain size of 10 µm, for instance, the nucleus density to be obtained should be in the order of $10^6\ cm^{-2}$. A second factor that affects grain size is competitive growth. During further growth after the initial stage of deposition, some grains grow at the expense of others, leading to V-shaped grains and a grain size at the surface significantly larger than at the interface between the substrate and the layer. This is linked to the orientation dependence of the deposition rate. Finally, grain boundary mobility is another potentially important factor. If grain boundaries are highly mobile during the deposition process, the final grain size can be much larger than what is expected from the nucleus density obtained in the early phase of deposition. Grain boundary mobility depends primarily on the temperature. Under normal conditions of conventional CVD, grain boundary mobility is so low [68] that this effect should have only a minor impact on the timescale of the deposition process. However, some influences can strongly increase grain boundary mobility, like a very high doping level [69] and the presence of point defect injecting mechanisms such as oxidation [70] and Al alloying [71]. The studies of nucleation and growth carried out on oxidized Si wafers (used as an 'ideal' model of foreign substrates) show that the grain size is indeed determined by the nucleus density [57, 72, 73]. The average grain size in the complete layer can be fairly accurately predicted based on the nucleus density after less than a minute's deposition. For a grain size of

10 μm, one should target a nucleus density of about $10^6\,cm^{-2}$. On foreign substrates as well, many experiments indicate that the nucleation process also determines the final layer structure. As the surface offers a lot of preferential nucleation sites, the nucleus density is usually very large, leading to layers with a grain size of 1 μm or below. Attempts to control the nucleus density include adding HCl to the gas flow [55], using intermittent injection of the precursor gas instead of a constant flow [57, 65] and introducing an intermediate dielectric layer on the substrate to affect the nucleation behaviour [74].

Many reports of direct CVD on foreign substrates mention a strong <110> preferential orientation [75–78]. However, it has to be said that the observed preferential orientation (110) is not specific to a high temperature CVD process, as it appears to be common to many deposition techniques at high growth rates [79–82]. The dominance of this orientation is found for fine grained layers, and is linked to some properties of <110> grains, which make them highly successful in competitive growth, namely the high growth rate of the {110} planes and a low probability of developing slow growing {111} facets [83, 84]. The films with strong <110> preferential orientation usually feature many grains with extensive twinning. The preferential orientation in CVD layers is therefore not a sign of good material quality. Layers with large grains, where competitive growth plays a much smaller role, do not show a strong <110> preferential orientation and tend towards totally random grain orientations [85].

An alternative technique to CVD is iodine vapor transport deposition. Iodine vapor reacts with a Si source to form the transport agent SiI_4, which then decomposes on the substrate to form a polycrystalline Si layer [86, 87]. The process is claimed to be fast and to yield layers with large grain sizes (∼20 μm) at a temperature of about 900 °C.

A very original approach to increase the grain size is to carry out the deposition of the Si-layer on a layer with low viscosity. As a result of the enhanced mobility of the Si adatoms over the surface of this low viscosity layer and the ability of the Si nuclei to rotate on this surface, large Si grains can be formed with grain boundaries which take a low energy configuration. This should favor the development of large flat grains. The name CVDOLL (CVD on liquid layer) was introduced by Graef, Gilling and Bloem, who obtained layers with grain sizes up to 100 μm using Sn layers [88], but the principle had been proposed earlier under the name of rheotaxy by Rasmanis [89] in the sixties. Using a glass layer that became liquid at the temperature of Si CVD, he was able to create layers with very large grains on alumina substrates and to make bipolar devices with good characteristics. The potential of this approach is under investigation and might be very large, although achieving a layer with controlled viscosity at high temperature, and which, additionally, is benign in terms of contamination is far from straightforward.

3.4.2.2 Plasma enhanced chemical vapor deposition

Plasma enhanced CVD is a technique that also involves a gaseous precursor, but the energy required to break chemical bonds is provided by a plasma. Therefore the temperature required to achieve a given growth rate can be lower than with thermal CVD. The high energy electrons in the plasma collide with the gas molecules and dissociate them, initiating the chemical reaction. In addition, the bombardment of the substrate surface by positive ions from the plasma can change the surface chemistry. Depending on the reactor configuration, one distinguishes between direct and remote PECVD, if the sample is directly exposed to the plasma or placed in the afterglow of the plasma, respectively. Different types of excitation can be used, with

frequencies ranging from a few kHz to several GHz. The most common PECVD reactors are based on parallel plates using RF frequencies. Two promising techniques that prevent ion bombardment and give high deposition rates are hot-wire CVD (HWCVD) [90] and electron cyclotron resonance CVD (ECR-CVD) [91]. In Hot-Wire CVD source gases like SiH_4 and H_2 are pyrolytically decomposed on a filament catalyzer which is heated to 1300–2000 °C and located several centimeters from the surface of the substrate. Electron cyclotron resonance CVD makes use of the cyclotron resonance, which occurs when the frequency of an alternating electric field matches the frequency of electrons orbiting the line of force of a magnetic field. This allows very high plasma densities to be reached.

Plasma enhanced CVD is most commonly used at low temperature (100–300 °C) to deposit amorphous or microcrystalline Si. To deposit fully crystalline layers as needed for thin film polycrystalline Si solar cells, higher temperatures are needed. Here again, we make a distinction between the use of the technique in a seed layer approach and direct deposition.

As an epitaxial technique to thicken the seed layer, the focus is on achieving epitaxy with sufficient quality and thickness. Low temperature epitaxy in general is challenging, even more so on imperfect seed layers. In general, it appears very difficult to reach epitaxial quality on grains that depart too much from the <100> orientation, and epitaxy tends to break down after a few hundreds of nm. Nevertheless, epitaxial layers on AIC seed layers with epitaxy on more than 70 % of the area with a thickness of 2 μm have been achieved with ECR-CVD at a temperature of 585 °C [48].

There has been much less research on direct deposition of polysilicon with PECVD than with CVD, even though it can potentially combine a simple process, very high growth rates and low temperature substrates. Fuyuki *et al*. studied the influence of the deposition conditions on preferential orientation and growth rates on oxidized Si wafers [82]. Reehal *et al*. achieved promising results with complete solar cell structures obtained with Si PECVD on graphite substrates at 800 °C [92]. It is also assumed that Kaneka used some kind of high temperature PECVD for the excellent results of the STAR cells (see further).

3.4.2.3 Ion assisted deposition

Ion-assisted deposition is based on electron gun evaporation and subsequent partial ionization of silicon [93, 94]. An applied voltage accelerates silicon ions towards the substrate. Typical acceleration voltages of 20 V are used. Because of the energy supplied by the accelerated ions, the surface adatom mobility is enhanced. As a result the IAD technique enables epitaxial growth at temperatures as low as 435 °C with high deposition rates up to 0.5 μm/min. On monocrystalline Si, epitaxial layers with very decent quality, considering the low temperature, have been achieved. Epitaxial films on <100> wafers with a minority carrier diffusion length of 40 μm and dislocation densities below 10^3 cm^{-2} have been obtained at a deposition rate of 0.8 μm/min and a deposition temperature of 650 °C [95]. However, as for most low temperature epitaxial deposition techniques, epitaxial quality is found to be highly dependent on the substrate orientation [96], the dislocation density on <111> oriented wafers being at least two orders of magnitude higher.

In the context of thin film polysilicon cells, IAD has been applied to thicken AIC seed layers formed on borosilicate glass at a substrate temperature of around 600 °C [97]. Special precautions have to be taken to avoid surface contamination and to provide the hydrogen termination at the surface, which is crucial for low temperature epitaxy. A low deposition rate

in the initial phase is also needed to achieve epitaxy on grains with less favourable orientation. Devices were made with these samples, showing V_{oc} up to 420 mV after rapid thermal annealing (RTA) and hydrogenation.

3.4.2.4 Liquid phase epitaxy

Liquid phase epitaxy (also called solution growth) consists of exposing the substrate to a metal solvent bath saturated with Si and then lowering the temperature. As a result of supersaturation, Si is driven out of the solution and is deposited onto the substrate. Various metal solvents (indium, gallium, aluminium, ...) are used and the process takes place in the temperature range of 700–950 °C. The thermodynamic driving force in solution growth is relatively small, so that no undesired deposition occurs on the walls of the deposition apparatus.

On Si wafers, LPE is known to lead to epitaxial layers with low defect densities and high minority carrier lifetime [98]. On foreign substrates, however, it appears difficult to grow device quality layers. Because of the low driving force, it is a serious challenge to obtain enough nucleation on non-Si substrates. Insufficient nucleation leads to isolated Si crystallites with large empty spaces in between. The absence of a continuous layer prevents device fabrication. In that context, one might expect that the seed layer approach is more successful for LPE, as a continuous layer is then formed *before* solution growth is started. Different attempts have been made at combining the deposition of a seed layer with subsequent LPE deposition [99–101], but none so far has led to device worthy layers. In many cases, Si does not cover the substrate completely. Even when coverage is complete, the Si deposit usually does not look like a compact layer but rather like many large separate grains close to each other but without connecting tissue. Kühnle *et al.* gave an explanation for this observation based on the low supersaturation of LPE and its impact on the critical grain size [102]. Low supersaturation implies a large critical grain size. All small grains in the seed layer are smaller than the critical size and therefore get dissolved during the solution growth process. This is beneficial for the average grain size, but leads to discontinuous layers.

3.4.2.5 Solid phase crystallization

The most extensively studied method to obtain poly-Si, and until now the most successful at solar cell level, is SPC of amorphous silicon [15, 103, 104]. The amorphous silicon can be deposited either by PECVD, sputtering or simple evaporation.

Typically the amorphous silicon films are between 1 and 3 μm thick, and can either be undoped, moderately doped or highly doped, or consist of multiple layers with different doping levels. After deposition, the films are annealed at temperatures between 550 and 700 °C, for a long period of time, typically several tens of hours. The higher the temperature, the faster full crystallization will be reached, but the smaller the grains will be. If the temperature is too low, full crystallization is not reached within a reasonable time. A workable compromise is 600 °C. In Figure 3.5, a TEM cross-section of an SPC film obtained from annealing evaporated amorphous silicon is shown. Solar cell grade SPC films have a typical grain size of 1–2 μm [105, 106]. For all SPC annealing temperatures, there is generally a log-normal distribution of grain sizes [107–109] which inevitably results in a large proportion of small grains. The average grain size is a factor of 3–5 times smaller than the maximum grain size. Moreover, the intragrain

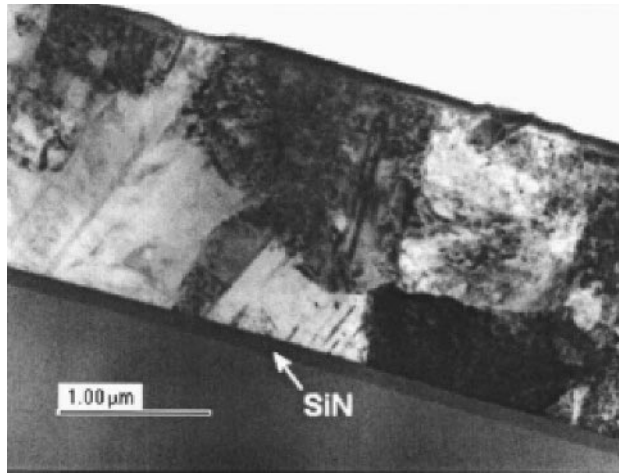

Figure 3.5 Cross-sectional transmission electron image of a SPC polysilicon film made on planar SiN-coated glass. Reprinted with permission from Figure 1, M. Terry, A. Straub, D. Inns, D. Song, A. Aberle, Large open circuit voltage improvement by rapid thermal annealing of evaporated solid-phase-crystallized thin film silicon solar cells on glass, Applied Physics Letters, 86, 172108. Copyright (2005), American Institue of Physics.

quality is far from being perfect, featuring many defects such as twins and dislocations. As grown, the electronic quality is rather poor. If devices are made in such layers, V_{oc} values below 200 mV are obtained [104-105]. However, the electronic quality of this type of polysilicon is greatly improved by post processing (defect annealing and hydrogen passivation, see later), leading to V_{oc} values around 500 mV and above. Note that diffusion of typical dopants (P, B and Al) is very slow at 600 °C. Provided the thermal budget after crystallization remains low, the doping profile created during the amorphous silicon deposition is retained in the crystallized state.

In contrast with other types of polysilicon, SPC material tends to show a <111> preferential orientation [110, 105]. This has been attributed to the anisotropic rate of crystallization, which favours grain growth of grains with a <111> direction perpendicular to the substrate [110].

Several approaches can be used to try to improve the material quality of SPC silicon further. A first approach consists of controlling nucleation by depositing the first layer of amorphous silicon under such conditions that it will nucleate first and influence the crystallization of the whole stack. High doping levels are known to lower the threshold to crystallization, particularly in n type Si. Another parameter is the presence of small crystallites in the amorphous silicon. Sanyo reached their best SPC polysilicon quality using a highly doped n-type initial layer with nanocrystallites with <110> preferential orientation [103]. A true seed layer approach can also be used, where a large grained seed layer is first created, an amorphous silicon is deposited on this seed layer and then solid phase crystallized. This is in fact the solid phase epitaxy (SPE) method applied to thin film polysilicon. Such an approach has been tried on several seed layer types, notably on AIC seed layers [111], however, with less success so far than standard SPC.

SPC has several advantages compared to other film formation techniques. It is rather simple and cost effective, requires a low process temperature, produces a relatively high quality

active layer, is easy to scale up and allows the possibility of *in situ* junction formation. The disadvantages are the very long cycle time and the difficulty to reach the structurally excellent material quality that will probably be needed for thin film polysilicon solar cells with efficiencies beyond 12 %.

3.4.3 Defect density and activity

In this section, we first briefly introduce some concepts that are useful in the study of polysilicon thin films and then describe the ongoing discussion on the electrical activity of grain boundaries in this type of material.

A first crucial concept is the 'grain size'. Grains in real polycrystalline layers are not uniform in size, but come in a variety of sizes, which is best expressed in a distribution. For the sake of simplicity, one usually refers to the 'average grain size' in a layer. Although this looks like a straightforward concept, it is not unambiguous. As discussed in [112], the *average grain size* determined by averaging the diameter of each grain is not the same as the *area weighted average grain size*. They can easily differ by a factor of two. In practice, a convenient approach to determine a characteristic grain size from optical or electron microscope pictures is to use the 'grain boundary crossing technique' [68, Chapter 2]. For TEM pictures, the grain size is taken as the average of the distance between two grain boundaries for each visible grain, taken over as many grains as possible. With SEM top views, the grain size at the top of the layer is measured in a similar way: a straight line is drawn across the picture, and the grain size is considered to be equal to the length of the line divided by the number of grain boundaries crossed by the line. This procedure is repeated several times to average extreme values. It has been found that the average grain size derived in this way is slightly higher than the area weighted average grain size derived by an extensive counting method.

As extended defects in a semiconductor, grain boundaries give rise to energy states within the bandgap. The most appropriate description of these defect states is to define distributions of acceptor and donor states in the bandgap, distinguishing between deep and tail states, and this for each grain boundary. For a practical analysis, it is, however, useful to lump these states into one characteristic value, the grain boundary defect density, considered an average of all the different grain boundaries present in the material. A typical grain boundary defect density is $10^{12}\,\mathrm{cm}^{-2}$ for unhydrogenated material, and below $10^{11}\,\mathrm{cm}^{-2}$ when effectively passivated. These defects trap majority carriers and give rise to depletion regions on either side of the grain boundaries. In most thin film polysilicon layers, however, the grains are so large that the material is only partly depleted, most of the grain being undepleted. The defect density at grain boundaries can conveniently be derived from resistivity versus temperature measurements. Indeed, the activation energy corresponds to the potential barrier at grain boundaries, which can be linked through the Seto theory [113] to the grain boundary defect density:

$$\varphi_{\mathrm{b}} = \frac{q N_{\mathrm{t}}^2}{8 \varepsilon_{\mathrm{s}} N}$$

with ϕ_{b} the height of potential barrier at a grain boundary, q the electronic charge, N_{t} the defect density at grain boundaries, ε_{s} the permittivity of Si and N the doping level. For low doping, high grain boundary defect density and the smaller grains in the grain size distribution, complete depletion might occur.

In contrast to microcrystalline silicon where doping drastically increases defect density [114], the electronic quality of thin polysilicon films decreases relatively slowly as the doping level increases up to 10^{17} cm^{-3} [44, 115]. In many reports, grain boundary defect densities and recombination velocities are reported to be very large. Values of S_{gb} derived from the device parameters are often larger than 10^5 cm/s [11]. In particular, as-deposited material has extremely active grain boundaries, in contrast with as-deposited microcrystalline material that shows values of S_{gb} below 1000 cm/s. It has been suggested that the <110> prefential orientation which is typical for microcrystalline Si results in low recombination activity at grain boundaries, because two adjacent grains with a vertical <110> axis in principle can only form low energy grain boundaries ([110]-tilt type) [12, 116]. However experiments certainly do not show that it is *sufficient* for good performance, as many layers with strong <110> preferential orientation result in very low values of V_{oc}. Moreover, some of the best thin film polysilicon solar cells are based on SPC. However, SPC layers generally do not show a <110> preferential orientation. (Note that the claim in [116] and [12] that Sanyo's SPC layers had a <110> texture is not substantiated in Sanyo's papers [103, 117] and is in fact unlikely to be true. There has been a confusion between the nucleation layer and the active layer.) Since it is neither sufficient nor necessary, an explanation based on the favourable properties of the <110> orientation is not satisfactory.

It has been suggested that even if grain boundaries have moderate recombination velocities, the presence of very small grains (as in the tail of the grain size distribution) have a disproportionately negative effect on the open circuit voltage. Indeed, very small grains can potentially become completely depleted, in which case the Fermi level is pinned at midgap [118]. Since these regions extend deep into the base, and since the Shockley–Read–Hall mechanism is most efficient as electron and hole concentrations are of the same order, one could indeed expect that they would have a very detrimental impact on performance. Although this effect might indeed play a role, alone it cannot explain the difference between microcrystalline and polysilicon in terms of grain boundary recombination. In fact, microcrystalline devices, with a much larger depleted volume, should, according to this suggested mechanism, suffer more from enhanced recombination, which is not the case.

A difference between grain boundaries in micro- and polycrystalline silicon might be the level of impurity segregation at grain boundaries. Segregation to grain boundaries can alter the electronic properties of polycrystalline semiconductor materials quite dramatically, and it has been suggested that the electrical activity of grain boundaries is wholly a result of impurity segregation [119]. The higher temperatures used to form polysilicon film might favour segregation. Oxygen is known to diffuse to grain boundaries during annealing treatments at over 600 °C [120, 121]. The increasing concentration of oxygen at the grain boundaries as the annealing time or temperature is increased has been linked with a larger grain boundary potential barrier.

While these explanations may indeed explain the very high electrical activity of some polysilicon materials, an analysis of the results obtained in the past and more recently suggests that this problem is not fundamental, and that grain boundaries in polysilicon can be passivated to a very large extent. In Figure 3.6, the best V_{oc} values reported for thin film polysilicon cells are plotted as a function of the grain size. As reference, a value recently published for state-of-the-art microcrystalline Si is given as well. The references are as follows: 'microcrystalline': [122]; Kaneka: [20]; Sanyo: [103]; CSG: [89]; IMEC98: [123]; UNSW: [124]; IMEC05: [125]; ETL: [30]; IMEC02: [115]; IPHT: [126]. There is no indication that V_{oc} drastically decreases with decreasing grain size. In fact, the best V_{oc} as obtained by Sanyo was on layers with

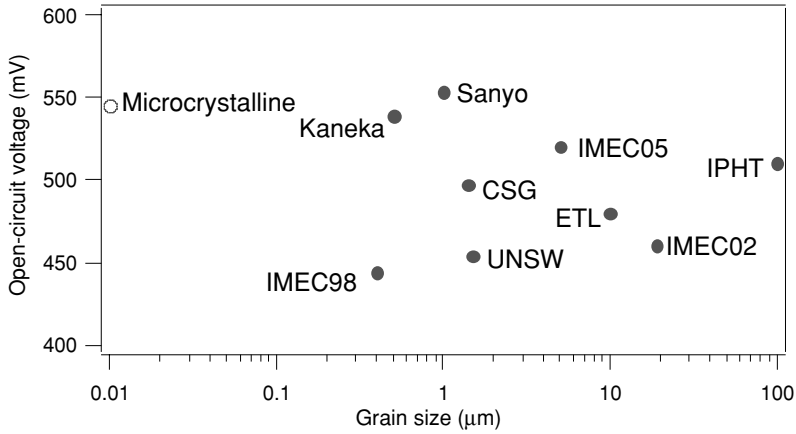

Figure 3.6 Compilation of the best open circuit values obtained with thin film polysilicon solar cells, plotted as a function of the grain size.

1 μm grain size! In Figure 3.7, the calculated diffusion lengths of the same devices are given (using Taretto's method to derive the effective diffusion length from device parameters [12]. Theoretical lines with the expected diffusion length for a given grain boundary recombination velocity are also given, and allow one to situate the degree of grain boundary activity.

Three of the data points in Figure 3.7 have estimated grain boundary recombination velocities below 10 000 cm/s, some being close to 1000 cm/s. Note that, in contrast to reference [12], we do not find two distinct groups. There are data points over the whole range of recombination velocities, from 1000 to 10^7 cm/s. The main difference between bad and good polysilicon is the degree of defect passivation. In microcrystalline silicon, grain boundaries are passivated *in*

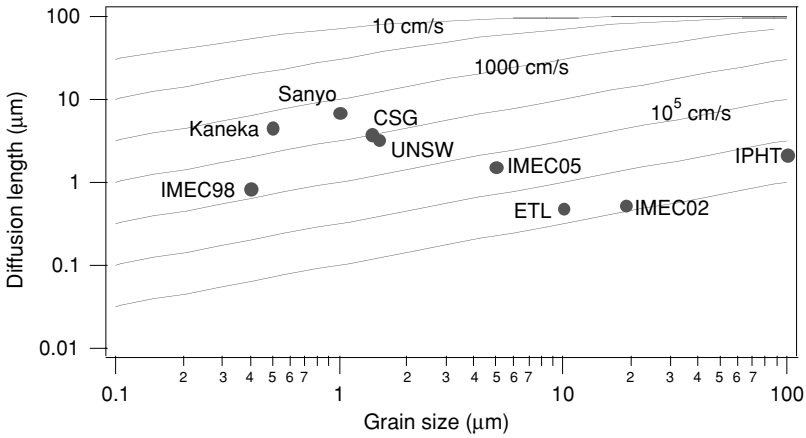

Figure 3.7 Diffusion lengths in thin film polysilicon solar cells reported in the literature, as calculated from IV parameters using the Taretto formula [12]. The continuous lines give the theoretical diffusion length as a function of the grain size, for given grain boundary recombination velocities.

situ by hydrogen. In polysilicon, defect passivation has to be done subsequently. Although it is a challenge, the examples of excellent polysilicon show that almost as efficient grain boundary passivation can be achieved.

3.5 SOLAR CELL AND MODULE PROCESSING

3.5.1 Device structure

Thin film polysilicon devices have, in fact, a similar structure to that of standard bulk crystalline Si solar cells, in spite of the much thinner active layer. The collecting structure is a p-n junction, with a highly doped side (the emitter) and a moderately or lowly doped side (the base). In several polysilicon technologies, the base doping is chosen to be very low, in the order of 10^{15} cm^{-3}. Often the base is not intentionally doped, although significant doping is found to be present, either through O related donor formation, or dopant diffusion. Yet, the space charge region does not extend over the whole thickness of the base. In contrast to amorphous Si where drift is the main mechanism, collection in these devices mainly relies on diffusion. All devices have a highly doped region at the rear, which is necessary for easy contacting. This layer also induces a field effect that tends to repel minority carriers from the rear surface ('back surface field'), which is important if the diffusion length approaches or exceeds the base thickness.

As for other thin film solar cell technologies, two basic configurations can be envisaged, namely the superstrate or the substrate configuration (see Figure 3.8). In the superstrate configuration, light enters the cell through the support onto which the active layer has been deposited, whereas it enters through the other side in the substrate configuration. Although we have depicted the superstrate configuration for a device with a p type base, an n type base is of course also possible in this configuration. Conversely, a p type base is used in many examples of polysilicon cells in the substrate configuration. The superstrate configuration has a few inherent advantages. If large enough, the superstrate can act as the module front cover, apart from providing mechanical strength. This entails a major cost reduction in module manufacturing, as no additional front cover glass panel is then required. Since none of the contacts are covering the layer, shadow losses are very low if not negligible. Finally, the metallization pattern can be designed for low series resistance with no adverse consequence for the short circuit current due to shading losses.

With most thin film solar cells, extracting current from the sublayer that is in contact with the substrate presents a challenge. The only exception is if the substrate is conductive (e.g. uncoated stainless steel), in which case the substrate itself can be in ohmic contact with the layer and serve as the back electrode. However, most thin film polysilicon solar cells use an insulating substrate. One can, in principle, cover the substrate with a conductive layer prior to the deposition of the active layer, as is done in most thin film solar cell technologies (e.g. transparent conductive oxide (TCO) layer for amorphous p-i-n modules, and molybdenum layer for CIGS modules). The fact that the preparation of polysilicon layers usually requires high temperatures severely limits the possibilities for such an intermediate conductive layer. A possible candidate is a TiB_2 layer, which has been shown to have the required thermal stability and conductivity [127]. However, a more appealing possibility is to make use of the natural conductivity of polysilicon. In contrast with amorphous and microcrystalline Si, polysilicon can have a low resistivity, depending on the grain structure and the doping level. A thin layer

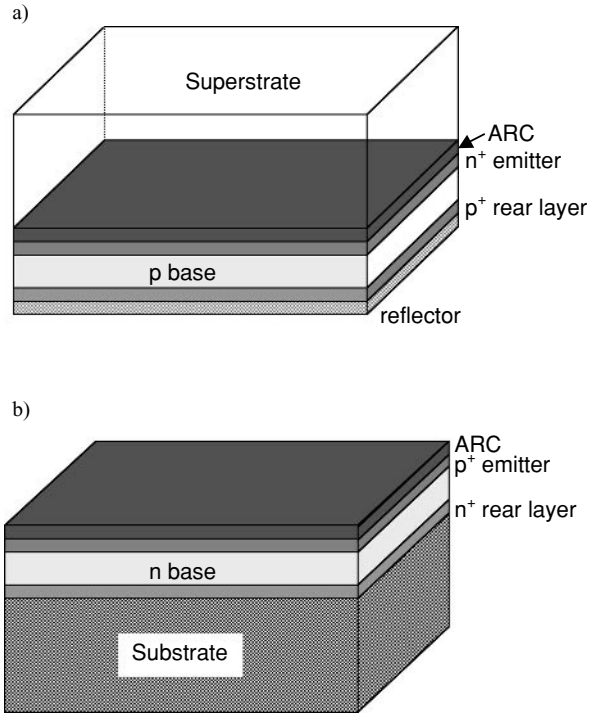

Figure 3.8 Possible configuration for thin film polysilicon solar cells: a) superstrate configuration (as used, for instance, by CSG Solar), b) substrate configuration (as used, for instance, by Sanyo).

of highly doped polysilicon can provide a conductance that is sufficient to prevent a significant voltage drop over hundreds of micrometers. This enables local contacting schemes, where access is made to the rear sublayer through the other sublayers (e.g. by etching) and local contacting. One local contact then collects current from a relatively large area around it (see example in Figure 3.9). The optimal contact density is determined by a trade-off between series resistance losses, dead area losses and technological limitations for local contact formation.

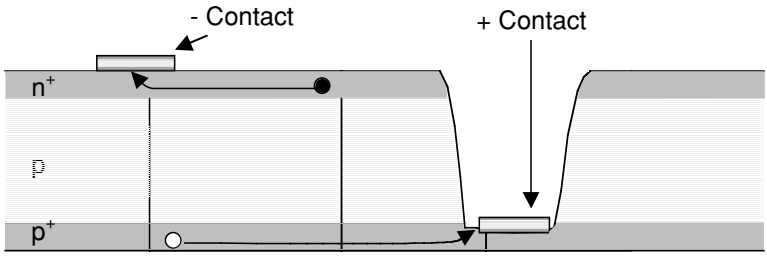

Figure 3.9 Example of contacting scheme enabled by the high conductivity of doped polysilicon layers. In this example, both holes in the rear p+ layer and electrons in the front n+ emitter travel laterally over large distances in the silicon layer itself before reaching the contacts.

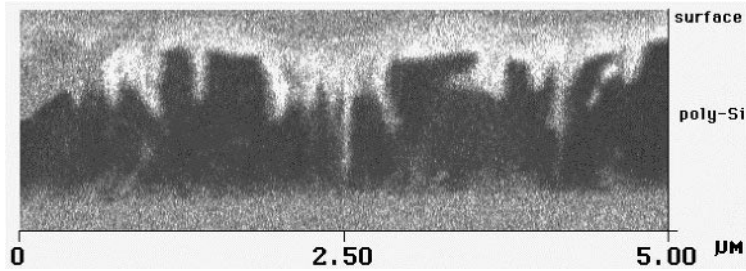

Figure 3.10 Scanning capacitance microscopy image of a p–n^+ polysilicon diode, featuring peaks of preferential doping. Reprinted from Solid State Phenomena, 67–68, G. Beaucarne, J. Poortmans, M. Caymax, J. Nijs, R. Mertens, "Properties of p-n diodes made in polysilicon layers with intermediate grain size", 577–582 Proceedings of the the 5th International Conference on Polycrystalline Semiconductors POLYSE'98. 13–18 Sept. 1998; Schwabisch Gmund, Germany. Copyright (1998) with permission from Transtech Publications.

3.5.2 Junction formation

A straightforward way of creating a junction in a polysilicon thin film is to apply the standard technique for bulk Si solar cells, namely to diffuse P at high temperature (700–900 °C) into a p-type material. The diffusion profile is, however, not as easy to predict as on standard mono or multicrystalline material. In general, faster diffusion is observed because of enhanced diffusion along extended crystallographic defects such as grain boundaries and dislocations. Preferential doping along grain boundaries leads to the creation of dopant 'spikes', n-doped zones penetrating vertically into the base. Evidence of this can be gathered with advanced microscopy techniques. An example is given in Figure 3.10 [128]. It is believed that the impact of these peaks on carrier collection can be considerable, particularly in polysilicon with electrically very active grain boundaries [129]. It has been suggested to make active use of this phenomenon to improve performance (see Section 3.2.3 and references [13, 115, 130]). However, the increase of the junction area can potentially lead to a worsened space charge region recombination current and adversely affect the V_{oc} of the cells. The extent of enhanced diffusion within grains and grain boundaries depends on various parameters of the polysilicon film such as preferential orientation and the growth rate at which the film was deposited [131].

An alternative to high temperature diffusion of dopants for emitter formation is to grow the emitter *in situ*, in the same deposition step as the base layer. This has been successfully done for high temperature PECVD deposition [92] and solid phase crystallization [15, 105]. A grown junction may entail a significant simplification of the process, as it makes an additional junction formation step unnecessary. However its implementation may present a difficult technological challenge because of reduced control over doping profiles, particularly if the deposition process takes place at high temperature.

A last possible junction formation technique that can be used for thin film polysilicon solar cells is to create a heterojunction by depositing thin amorphous Si layers. Sanyo was a pioneer with this approach, with the development of the heterojunction with intrinsic thin layer (HIT) and reporting a poly-Si HIT solar cell as early as 1990 [132]. Here a thin intrinsic layer (∼5 nm) is first deposited on the polysilicon, followed by a doped p^+ layer. Because the amorphous

silicon layer does not provide lateral conductance this type of emitter has to be combined with a TCO. Although Sanyo only reported results on n-type base devices, heterojunction emitters can also be applied on p type base devices, the thin amorphous emitter being then n^+ doped. Recently, V_{oc} values up to 520 mV have been reported on p type CVD deposited polysilicon on ceramic [125].

3.5.3 Defect passivation

In comparison with standard solar grade crystalline Si material, thin polysilicon layers contain a lot of defects (in the order of $10^{16}\,cm^{-3}$), both at grain boundaries and inside the grains. It is of crucial importance to passivate these defects to reach high device performance. Some of the defects can be annealed away with a short high temperature treatment. This has proved to be very beneficial for SPC polysilicon on glass, for which a rapid rhermal anneal brings about an increase in V_{oc} of more than 30 mV [105, 133]. However, so-called 'smearing' of the doping profiles takes place during high temperature annealing, making transitions less sharp and increasing the doping level of the most lowly doped region. If the thermal budget is excessive, two regions of high and opposite doping might get in contact and lead to shunting.

Defect passivation is usually achieved by introducing atomic hydrogen into the material. The effect is of considerable complexity and still the topic of much research. The simple picture is that hydrogen atoms bind with dangling bonds at extended or point defects, thereby removing energy states in the bandgap. There have been many studies about hydrogenation of multicrystalline silicon [134–136]. For this material, hydrogen passivation from a short anneal of a silicon rich PECVD nitride has appeared to be very effective and most convenient as it fits very well in a straightforward process sequence (silicon nitride is deposited anyway as an anti-reflection coating) [137, 138], and is now applied in most industrial solar cell processes. While one can expect V_{oc} improvements of up to a few tens of mV with multicrystalline Si, the effect is much more far-reaching for thin-film polycrystalline cells. It is not uncommon to observe increases of 200 mV or more in V_{oc} as a result of hydrogenation [97, 106, 133, 139].

The plasma hydrogenation process is typically done at a temperature of 400 °C, although studies indicate that more effective passivation can be obtained at higher temperatures (see Figure 3.11) [97]. At CSG Solar, it is carried out at a temperature as high as 610 °C, but the plasma is kept on during the cooling down phase [106].

A typical hydrogenation time is 30 min. Longer hydrogenation may lead to the creation of new defects in the grains that counteract the beneficial passivation effect [140]. Recently, it has been demonstrated that hydrogenation through rapid thermal annealing of silicon nitride (as used in standard solar cell processing) can also effectively be applied to thin film polysilicon layers [141].

3.5.4 Isolation and interconnection

Production processes of thin film polysilicon solar cells start with the formation of a film with the required structure and properties on a large area substrate. Afterwards, this large film needs

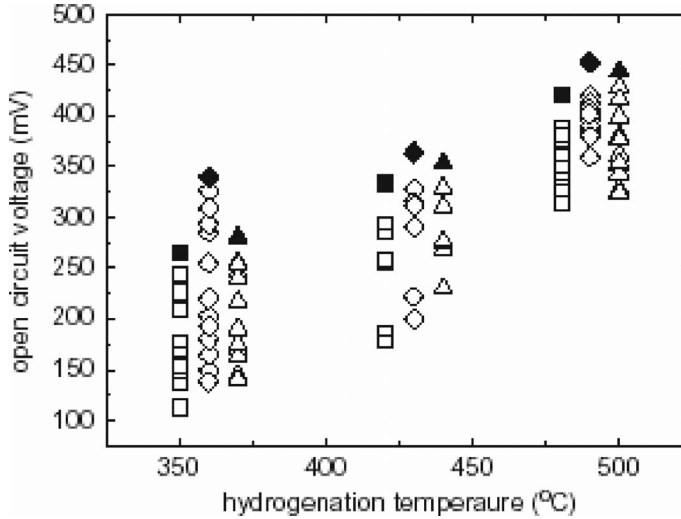

Figure 3.11 Effect of hydrogenation temperature on V_{oc} of polysilicon pn junction obtained by AIC crystallization followed by IAD. The squares are the V_{oc} values, whereas the diamonds and the triangles indicate the first and second diode influences, respectively. Reprinted from A. Straub, D. Inns, M. L. Terry, Y. Huang, P. I. Widenborg, A. G. Aberle, Optimisation of low-temperature silicon epitaxy on seeded glass substrates by ion-assisted deposition, Journal of Crystal Growth, 280, 385–400. Copyright (2004),with permission from Elsevier.

to be isolated into islands or segments, which become separate cells. For research, a mesa structure formed by shallow etching is useful [52]. To enable series connection of the cells, however, the isolation has to be carried out down to the substrate. This can be done by dry or wet etching, or by laser grooving. If the latter technique is used, special care has to be taken to ensure that no p^+ n^+ junction is created as a result of the local remelting, as this would lead to shunting.

Once the separate cells have been isolated, they have to be connected with each other in series. This is most conveniently done simultaneously with the cell metallization. The positive polarity contacts of one cell are connected with the negative polarity contacts of the next cell, and both may in fact consist of the one single strip of metal, bridging the isolation groove. This is, for instance, illustrated in Figure 3.12, a picture of the metallization and interconnection scheme of a CSG Solar module [15]. Note that a collecting busbar is not needed in monolithic polysilicon modules. The current flows from one cell to the next in the cell 'string' in a distributed way over the whole length of the cell segments. Large collecting contacts are only needed at the two ends of the module (left of the first and right of the last cell). This greatly simplifies module manufacturing and is a major advantage compared to traditional module production, where carrying very large currents from one cell to the other without excessive series resistance losses is a major issue.

As a result of the edge isolation process, it is likely that both cell polarities surface in the vicinity of the isolation groove. To avoid short circuiting the cell with the interconnection metal, some kind of bridge over the groove is needed. This is achieved by applying an insulating

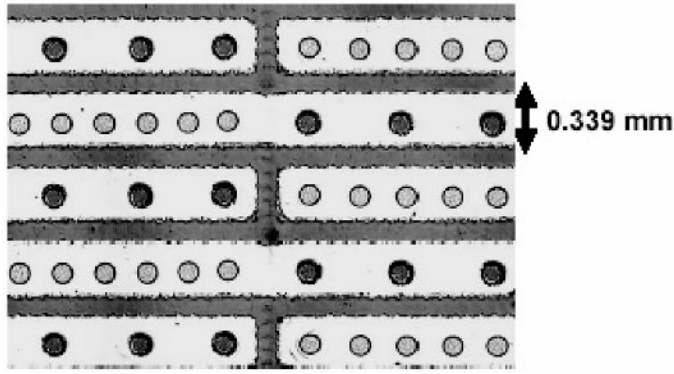

Figure 3.12 Metallization and interconnection scheme of a CSG Solar module. The positive contacts (lighter dots) are connected with the negative contacts (darker dots) of the next cell. The isolation groove runs vertically in the middle of the picture and is filled by an insulating resin. Figure 2 in: P.A. Basore, Simplified processing and improved effciency of crystalline silicon on glass modules, Proceedings 19th European Solar Energy Conference, 455–458. Copyright (2004) WIP.

material covering the edges of the isolation groove (or, optionally, the whole isolation groove area). In the CSG Solar modules, this is done with a resin which completely fills the groove [15].

3.6 POLYSILICON SOLAR CELL TECHNOLOGIES

In this section we will review some of the major thin film polysilicon technologies and research efforts on this type of solar cells. In contrast with the development of bulk crystalline Si solar cells, the development has not been a continuous, gradual but steady flow of improvements, through the contributions of many institutes and companies. On the contrary, it has been fragmented and characterized by many stops and starts.

The first studies for thin film polysilicon solar cells were carried out in the USA in the seventies. The approaches were mostly based on high temperature deposition from the gas phase. While the achieved efficiencies at the time were only in the range of 1 to 3 %, a wealth of knowledge was gained, which could have been the start of a successful development. However, the programmes were discontinued at the end of the seventies. A more detailed description of these early research efforts is given in reference [52]. Research on this type of materials for solar cells resumed only in the nineties, starting in Japan.

3.6.1 Solid phase crystallization-heterojunction with intrinsic thin layer solar cells (SPC-HIT)

Sanyo did extensive research on SPC polysilicon for solar cells and started reporting about it in 1990 [132]. The amorphous Si was deposited on quartz or metal substrates by PECVD. The layers were not intentionally doped but got a marked n-type doping after crystallization [117]. For the emitter, they used their HIT structure (thin intrinsic a-Si/thin p^+ a-Si). The best solar cell results were presented in 1995, with an efficiency on a 1 cm^2 device of 9.2 % [103]. The results

at the time were remarkable, better than what had been achieved up to then with microcrystalline Si. It is therefore puzzling that this research path was apparently discontinued in 1996. Sanyo did continue the development of its HIT emitter, but in combination with high lifetime bulk wafers, and has since then demonstrated outstanding results with laboratory cells (up to 21.5 % [142]) and successfully upscaled the concept into a high efficiency commercial product.

3.6.2 Surface texture and enhanced absorption with back reflector solar cells (STAR)

Kaneka is well known for its hybrid amorphous Si–microcrystalline Si modules, which they were first to bring on the market. These modules have an amorphous Si top cell deposited on TCO covered glass, onto which a microcrystalline silicon layer is deposited by PECVD. Note that, as the amorphous top cell is sensitive to temperature, the second active film also has to be deposited at low temperature, and therefore is bound to feature very small grains and substantial amorphous material. However, a lot of the work carried out by Kaneka in the nineties seems to have been on polysilicon. For a large part of the nineties, Kaneka reported that it produced *poly* silicon with substantial grain size (not clearly mentioned, but should be at least 0.1 μm), with a substantial effective active doping of $10^{16}\,\mathrm{cm}^{-3}$ [143, 144]. The details of the deposition were not given, only mentioning that the PECVD deposition took place at a temperature below 550 °C. All these parameters are very different from microcrystalline silicon, which has grains of a few tens of nm, has to be intrinsic and is deposited around 200 °C. This therefore suggests that the cells presented in those publications (called STAR cells for Surface Texture and enhanced Absorption with back Reflector) were made of real polysilicon (grain size 0.1 μm or higher and complete crystallinity) by a high temperature (just below 550 °C) PECVD process. Outstanding results were achieved with the STAR concept, with efficiencies up to 10.1 % [145]. This is probably the best thin film polysilicon solar cell ever made. Emphasis was put on achieving effective light confinement by the use of a front texture and a good and rough reflector at the rear. The confusing part is that the results for the STAR cells were often presented alongside hybrid cell results (e.g. in [143]), in which the bottom cell has to be microcrystalline. It seems that, at some point, Kaneka completely switched to a microcrystalline technology and gave up the polysilicon route they had been investigating. Even in recent papers, Kaneka maintains ambiguity, referring to the material used in its hybrid modules as polysilicon, but equating it to microcrystalline silicon [146].

3.6.3 Crystalline silicon on glass technology (CSG)

The thin film polycrystalline silicon technology that is closest to industrial implementation is arguably the crystalline silicon on glass (CSG) technology developed by the company previously called Pacific Solar (now CSG Solar). Although Pacific Solar was founded in 1995, they only published their first technical paper in 2002, mentioning a best module efficiency of 7.3 % [147]. Other publications have since followed, releasing an increasing amount of details [15, 106, 148–150]. The best efficiency so far is 8.8 % for a 96 cm^2 mini-module, while the V_{oc} of individual cells is close to 500 mV. In 2004, the company stopped its activities

under the name Pacific Solar, but continued with the same technology and new investors as a new company CSG Solar. This led to the construction of a production line in East Germany. Production start is foreseen in 2006.

The devices feature a p-n^+ junction, the standard structure for a crystalline silicon cell. The technology is based on SPC of PECVD deposited amorphous Si. All layers are deposited directly on a borosilicate glass substrate previously textured with a sol-gel coating containing small silica beads. The polysilicon layer is just 1.5 μm thick, which is extremely thin for crystalline silicon. Nevertheless, decent currents are achieved (up to 28 mA/cm^2), thanks to the application of a very effective light confinement scheme. Post deposition treatment of the polysilicon films, such as defect anneal and hydrogenation, are crucial for the high performance of the produced modules. The defect anneal is done in a short RTA treatment at 900 °C, well above both the strain point and the softening point of the substrate material. CSG Solar's plasma hydrogenation process is quite remarkable. It is extremely effective on their SPC material, leading to very large increases in V_{oc} (+ 260 mV) and efficiency (a factor of 4.6!). A prototype has been built to apply this process with a high throughput, and a full size industrial system is going to be installed at the CSG Solar factory.

It should be noted that efficiencies achieved so far already come close to those of record single junction microcrystalline cells. Moreover, upscaling appears relatively easy and durability is excellent [149].

3.6.4 Other research efforts around the world

Several photovoltaic research groups are investigating thin film polysilicon technologies. Most of the efforts are directed towards producing a material with much higher crystallographic quality than state-of-the-art SPC material, with a high growth rate. It is believed that enhancing the crystallographic quality (larger grains) gives rise to a higher efficiency potential, which will eventually lead to efficiencies in the range of 14–15 %. Here, we highlight the work of a few groups that have already produced functioning devices. This should be considered as a snapshot taken at the time of writing. Because of the fast progress, it is expected that the mentioned V_{oc} and efficiencies values will greatly increase in the next few years.

The thin film group at the University of New South-Wales investigates different routes, all based on intermediate temperature substrates and nonUHV evaporation techniques, based on the assumption that these choices will eventually lead to solar cells with the lowest cost [151]. The EVA concept is similar to the CSG Solar approach but uses evaporated amorphous silicon layers instead of PECVD a-Si. The other two routes use AIC seed layers on glass in combination with epitaxy. The ALICIA cell uses IAD to create the epitaxial absorber layer, whereas the ALICE concept applies a solid phase epitaxy process on amorphous Si layers deposited on the AIC layer. Values of V_{oc} above 400 mV have been reached with the three techniques, the best value at the time of writing being 454 mV with EVA. Efficiencies are still very low (1–2 % range), because the solar cell process is not yet optimized.

The Hahn-Meitner Institute (HMI) has a similar approach but has focused on AIC on glass and low temperature epitaxial deposition with ECR-CVD [152]. Devices have been made using a heterojunction emitter. Values of V_{oc} of up to 378 mV and a best efficiency so far of 1 % have been reported [153].

The Institute for Physical High Technology (IPHT) in Jena, Germany is developing a technique called layered laser crystallisation (LLC) [126]. A seed layer is first created by laser crystallization of a p^+ layer. On this seed layer, an epitaxial layer is formed in a PECVD system equipped with a pulsed KrF excimer laser. The regular laser pulses lead to the *in situ* crystallization of the deposited amorphous silicon, creating high quality epitaxial layers. Values of V_{oc} up to 510 mV and efficiencies up to 3.6 % have been reached on small area devices.

While the groups mentioned so far are only investigating devices on 'intermediate temperature substrates' (that is substrates that can withstand temperatures above 600 °C only for a very limited time), others are investigating high temperature substrates such as ceramic substrates. The Interuniversity Microelectronics Centre (IMEC) started research in thin film polysilicon cells in the mid-nineties, using thermal CVD. The focus was first on attempting to control nucleation in the early stages of deposition for optimal grain size. A best efficiency of 5.5 % was reached on a model oxidized silicon substrate [115]. The approach has now shifted towards the combination of AIC seed layer on ceramic substrates and epitaxial thickening of that layer with thermal CVD [154]. The best efficiency so far is 5.9 % using a heterojunction emitter and interdigitated contacts [155] (presently InESS).

The PHASE Laboratory in Strasbourg, France is applying various approaches to grain size control for polysilicon on various ceramics (alumina, mullite, SiN . . .), including AIC and CVDOGL (CVD on glassy layers), while silicon deposition is carried out in a rapid thermal CVD (RT-CVD) system at atmospheric pressure. The best efficiency so far is 3.3 %.

NAIST in Japan is focusing on direct polysilicon deposition on foreign substrates by thermal CVD, controlling the grain size by the intermittent supply method [57, 65]. Grain sizes of around 10 μm are reproducibly achieved and V_{oc} values up to 410 mV have been reached [156], with efficiencies so far in the range 2–3 %.

NREL in the USA is investigating the use of the iodine vapour transport method for thin film solar cells on foreign substrates. With a heterojunction emitter, solar cells with V_{oc} values of 460 mV and efficiencies up to 3.5 % have been reached [87].

3.7 CONCLUSION

Thin film polysilicon solar cells are a rather new thin film photovoltaic technology, combining a large cost reduction potential with a large efficiency potential. State-of-the-art polysilicon solar cells are made with SPC, with efficiencies presently reaching around 9 % at minimodule level. To reach higher performance, a lot of research is going on aiming to achieve better crystallography. In order to be successful, thin film polysilicon devices need to improve further and reach 12 % module efficiency with a single juntion, with a process that is industrially applicable. Considering the fast pace of progress, particularly in the last few years, it is possible that thin film polysilicon will emerge as the major technology to succeed bulk Si.

REFERENCES

[1] P. A. Basore, Defining terms for crystalline silicon solar cells, *Prog. Phot. Res. Appl.*, **2**, 177–179 (1994).

[2] A. V. Shah, J. Meier, E. Vallat-Sauvain, N. Wyrsch, U. Kroll, C. Droz, U. Graf, Material and solar cell research in microcrystalline silicon, *Sol. En. Mat. Sol. Cel.*, **78**, 469–491 (2003).

[3] R. B. Bergmann, J. H. Werner, The future of crystalline silicon films on foreign substrates, *Thin Solid Films*, **403–404**, 162–169 (2002).
[4] R. Brendel, *Thin-film crystalline silicon solar cells*, Wiley-VCH (2003).
[5] T. Tiedje, E. Yablonovitch, G. D. Cody, B. G. Brooks, Limiting efficiency of silicon solar cells, IEEE Trans. Electr. Dev., **ED-31**, 711–716 (1984).
[6] C. Donolato, Effective diffusion length of multicrystalline solar cells, *Semicond. Sci. Technol.*, 13, 781–787 (1998).
[7] J. Dugas, J. Oualid, Modeling of base doping concentration influence in polycrystalline silicon solar cells, *Solar Cells*, **20**, 145–154 (1987).
[8] T. I. M. Imaizumi, M. Yamaguchi, K. Kaneko, Effect of grain size and dislocation density on the performance of thin film polycrystalline silicon solar cells, *J. Appl. Phys.*, **81**, 7635–7640 (1997).
[9] K. Kurobe, Y. Ishikawa, Y. Yamamoto, T. Fuyuki, H. Matsunami, Effects of grain boundaries in polycrystalline silicon thin-film solar cells based on the two-dimensional model, *Solar Energy Materials and Solar Cells*, 65, 201–209 (2001).
[10] A. B. Arab, Analytical solutions for the photocurrent and dark diffusion current of preferentially doped polysilicon solar cells, *Solar Energy Materials and Solar Cells*, **37**, 239–258 (1995).
[11] P. P. Altermatt, G. Heiser, Development of a three-dimensional model of grain boundaries in highly doped polycrystalline silicon and applications to solar cells, *J. Appl. Phys.*, **91**, 4271–4274 (2002).
[12] K. Taretto, U. Rau, J. H. Werner, Method to extract diffusion length from solar cell parameters – application to polycrystalline silicon, *J. Appl Phys.*, **93**, 5447–5455 (2003).
[13] S. Bourdais, A. Slaoui, G. Beaucarne, J. Poortmans, E. Christoffel, A. Zerga, The ThRee-dimensional Emitter Based on Locally Enhanced diffusion (TREBLE) structure: modeling and formation, *Solid State Phenomena*, **82—84**, 713–18 (2002).
[14] P. van der Vleuten, Thin film silicon solar cells on insulated metal substrates, *Proceedings 19th European Photovoltaic Solar Energy Conversion Conference*, 1352–1354 (2004).
[15] P. A. Basore, Simplified processing and improved efficiency of crystalline silicon on glass modules, *Proceedings 19th European Photovoltaic Solar Energy Conference*, 455–458 (2004).
[16] *British patent application No. GB9603028.3* filing date 14.02.96, publication No. GB2310314 dated 20.08.1997.
[17] N. I. Nemchuk, J. G. Couillard, D. G. Ast, F. P. Fehlner, L. R. Pinckney, Novel glass-ceramic substrates for thin film polycrystalline silicon solar cells, *Proceedings 9th Workshop on crystalline silicon solar cell materials and processes*, 90–93 (1999).
[18] S. Bourdais, F. Mazel, G. Fantozzi, A. Slaoui: Silicon deposition on mullite ceramic substrates for thin-film solar cells, *Prog. Photovolt: Res. Appl.*, **7**, 437–447 (1999).
[19] A. von Keitz, J. A. M. van Roosmalen, C. J. J. Tool, S. E. A. Schiermeier, A. J. M. M. van Zutphen, F. Fung, G.M. Christie: Improvement of low cost ceramic substrates for use in thin film silicon solar cells, *Proceedings 2nd WCPVSEC*, 1829–1832 (1998).
[20] K. Yamamoto, Very thin film crystalline silicon solar cells on glass substrate fabricated at low temperature, *IEEE Trans. Electr. Dev.*, **46**, 2041–2047 (1999).
[21] K. Roth, J. C. Goldschmidt, T. Puzzer, N. Chuangsuwanich, B. Vogl, A. G. Aberle, Structural properties of polycrystalline silicon seed layers made on glass by solid-phase crystallisation, *Proceedings 3rd World Conference on Photovoltaic Energy Conversion*, 1202–1205 (2003).
[22] N.-P. Harder, U. Blieske, D. Le Bellac, E. Royer, B. Rech, G. Schöpe, J. Müller, Light-trapping in a-Si:H and μc-Si solar cells via nano-textured glass superstrates made by plasma etching, *Proceedings 19th EPVSEC*, 1355–1358 (2004).
[23] N. Chuangsuwanich, P. I. Widenborg, P. Campbell, A. G. Aberle, Light trapping properties of thin silicon films on AIT-textured glass, *Proceedings 14th International Photovoltaic Science and Engineering Conference*, 325–326 (2004).
[24] J. S. Im, H. J. Kim, On the super lateral growth phenomenon observed in excimer laser-induced crystallization of thin Si films, *Appl. Phys. Lett.*, **64**, 2303–2305 (1994).

[25] Y. Helen, R. Dassow, M. Nerding, K. Mourges, F. Raoult, J. R. Köhler, T. Mohammed-Brahim, R. Rogel, O. Bonnaud, J. H. Werner, and H. P. Strunk, *Thin Solid Films*, **383**, 143 (2001).
[26] M. Nerding, S. Christiansen, J. Krinke, R. Dassow, J. R. Köhler, J. H. Werner, H. P. Strunk, *Thin Solid Films*, **383**, 112 (2001).
[27] M. Nerding, R. Dassow, S. Christiansen, J. R. Köhler, J. Krinke, J. H. Werner, H.-P. Strunk, Microstructure of laser-crystallized silicon thin films on glass substrate, *J. Appl. Phys.*, **91**, 4125 (2002).
[28] A. Bonfiglietti, A. Valletta, P. Gaucci, L. Mariucci, G. Fortunato, S. D. Brotherton, Electrical characterization of directionally solidified polycrystalline silicon, *J. Appl. Phys*, **98**, 033702 (2005).
[29] K. Ishii, H. Nishikawa, T. Takahashi, Y. Hayashi, Sub- 5 μm thin film crystalline silicon solar cell on alumina ceramic substrate, *Jpn. J. Appl. Phys.*, **32**, L770-L773 (1993).
[30] R. Shimokawa, K. Ishii, H. Nishikawa, T. Takahashi, Y. Hayashi, I. Saito, F. Nagamine, S. Igari, Sub-5 μm thin film c-Si cell and optical confinement by diffuse reflective-substrate, *Sol. En. Mat. Sol. Cells*, **34**, 277–283 (1994).
[31] G. Andra, J. Bergmann, F. Falk, Laser crystallized multicrystalline silicon thin films on glass, *Thin Solid Films*, **487 (1–2)**, 77 (2005).
[32] M. S. Haque, H. A. Nasseem, W. D. Brown, Interaction of aluminium with hydrogenated amorphous silicon at low temperatures, *J. Appl. Phys.*, **75**, 3928–3935 (1994).
[33] G. Liu, S. Fonash, Polycrystalline silicon thin film transistors on Corning 7059 glass substrates using short time, low-temperature processing, *Appl. Phys. Lett.*, **62**, 2554–2556 (1992).
[34] S. Y. Yoon, K. H. Kim, J. Y. Oh, Y. J. Choi, W. S. Shon, C. O. Kim, J. Jang, A high-performance polycrystalline silicon thin-film transistor using metal-induced crystallization with Ni solution, *Jpn. J. Appl. Phys.*, **37**, 7193–7197 (1998).
[35] O. Nast, T. Puzzer, L. M. Koschier, A.B. Sproul and S.R. Wenham, Aluminum-induced crystallization of amorphous silicon on glass substrates above and below the eutectic temperature, *Appl. Phys. Lett.*, **73**, 3214–3216 (1998).
[36] O. Nast, S. Wenham, Elucidation of the layer exchange mechanism in the formation of polycrystalline silicon by aluminium-induced crystallization, *J. Appl. Phys.*, **88**, 124–132 (2000).
[37] J. Schneider, J. Klein, A. Sarikov, M. Muske, S. Gall, W. Fuhs, Suppression of nucleation during the aluminum-induced layer exchange process, *Proceedings MRS spring meeting 2005*, A2.2.1–A2.2.6 (2005).
[38] O. Nast, S. Brehme, S. Pritchard, A. Aberle and S.R. Wenham, in *Technical Digest of the Intern. PVSEC-11*,.727 (1999).
[39] O. Nast, A. J. Hartmann, Influence of interface and Al structure on layer exchange during aluminium-induced crystallisation of amorphous silicon, *J. Appl. Phys.*, **88**, 716–724 (2000).
[40] C. Ornaghi, G. Beaucarne, J. Poortmans, J. Nijs, R. Mertens, Aluminium induced crystallization of amorphous silicon: Influence of materials characteristics on the reaction, *Thin Solid Films*, **451–452**, 476–480 (2004).
[41] P. I. Widenborg, S. Von Chan, D. Inns, A. G. Aberle, Fabrication of poly-Si seed layer by Aluminium-induced crystallisation of a-Si deposited by PECVD or sputtering, *Technical Digest 15th Photovoltaic Science and Engineering Conference* 814–815 (2005).
[42] A. Slaoui, E. Pihan, M. Rusu, Formation of polycrystalline silicon on foreign substrates by combination of CVD and Aluminium-induced crystallisation techniques, *Proceedings 17th European Photovoltaic Solar Energy Conference*, 1462–1465 (2001).
[43] C. Ornaghi, M. Stöger-Pollach, G. Beaucarne, J. Poortmans, P. Schattschneider, Thin film polycrystalline silicon solar cell on ceramics with a seeding layer formed via aluminium-induced crystallisation of amorphous silicon, *IEE Proc.-Circuits Devices Syst.*, **150**, 287–293 (2003).
[44] G. Beaucarne, D. V. Gestel, I. Gordon, L. Carnel, K. Van Nieuwenhuysen, C. Ornaghi, J. Poortmans, M. Stöger-Pollach, P. Schattschneider, Aluminium-induced crystallization of silicon on high temperature substrates for thin-film crystalline silicon solar cells, *Proceedings 19th European Photovoltaic Solar Energy Conference*, 467–470 (2004).

[45] D. Van Gestel, I. Gordon, L. Carnel, K. Van Nieuwenhuysen, G. Beaucarne, J. Poortmans, Influence of substrate roughness on the quality of thin-film polycrystalline-silicon solar cells made by aluminium-induced crystallization, *Proceedings 15th Photovoltaic Science and Engineering Conference*, 853–854 (2005).
[46] S. Gall, J. Schneider, M. Muske, I. Sieber, O. Nast, W. Fuhs, Poly-Si seeding layers by aluminium-induced crystallization, *Proceedings PV in Europe*, 87–90 (2002).
[47] E. Pihan, A. Focsa, A. Slaoui, C. Maurice, Crystallographic analysis of polysilicon films formed on foreign substrates by aluminium induced crystallization and epitaxy, to be published in *Thin Solid Films* (2006).
[48] B. Rau, J. Schneider, M. Muske, I. Sieber, S. Gall, M. Stoger-Pollach, P. Schattschneider and W. Fuhs, *Proceedings 19th European Photovoltaic Solar Energy Conference*, 1131–1134 (2004).
[49] A. Aberle, P. Widenborg, A. Straub, D. Neuhaus, O. Hartley, World Intellectual Property Organization, WO 2004/033769 A1.
[50] D. Van Gestel, I. Gordon, L. Carnel, K. Van Nieuwenhuysen, J. D'Haen, J. Irigoyen, G. Beaucarne, J. Poortmans, Influence of seed layer morphology on the epitaxial growth of polycrystalline silicon solar cells, *Thin Solid Films*, 511–512, 35–40, (2006).
[51] E. Pihan, A. Slaoui, P. Roca i Cabarrocas, A. Focsa, Polycrystalline silicon films by aluminium-induced crystallisation: growth process vs. silicon deposition method, *Thin Solid Films*, **451–452**, 328–333 (2004).
[52] G. Beaucarne, S. Bourdais, A. Slaoui, J. Poortmans, Thin-film film polycrystalline Si solar cells on foreign substrates: Film formation at intermediate temperatures (700–1300 °C), *Appl. Phys. A*, **79**, 469–480 (2004).
[53] G. Beaucarne, F. Duerinckx, I. Kuzma, K. Van Nieuwenhuysen, H. J. Kim, J. Poortmans, Epitaxial thin-film Si solar cells, *Thin Solid Films*, 511–512, 533–542 (2006).
[54] S. Reber, W. Wettling, High-temperature processing of crystalline silicon thin-film solar cells, *Appl. Phys. A*, **69**, 215–220 (1999).
[55] G. Beaucarne, J. Poortmans, M. Caymax, J. Nijs, R. Mertens, Tailored Si-layers on silicon oxide obtained by thermal CVD, *Proceedings Material Research Symposium 'Thin-Film Structures for Photovoltaics'*, **485**, 89–94 (1998).
[56] Y. Ishikawa, Y. Yamamoto, T. Hatayama, Y. Uraoka, T. Fuyuki: Crystallographic analysis of high quality poly-Si thin films deposited by atmospheric pressure chemical vapor deposition *Technical digest 12th PVSEC*, 437–438 (2001).
[57] Y. Ishikawa, Y. Uraoka, T. Fuyuki: Nucleation control towards the poly-Si thin films with large grain size utilizing intermittent supply of dichlorosilane, *Proceedings 3rd World Conference on Photovoltaic Energy Conversion*, 1503–1506 (2003).
[58] R. Monna, D. Angermeier, A. Slaoui, J. C. Muller, G. Beaucarne, J. Poortmans, C. Hebling, Poly-Si films on graphite substrates by rapid thermal chemical vapor deposition for photovoltaic application, *Proceedings of the 14th EPVSEC*, 1456–1459 (1997).
[59] R. B. Bergmann, R. Brendel, M. Wolf, P. Lšlgen, J. Krinke, H. P. Strunk, J. Werner, Growth of polycrystalline silicon films on glass by high-temperature chemical vapour deposition, *Semicond. Sci. Technol.*, **12**, 224–227 (1997).
[60] G. Beaucarne, J. Poortmans, M. Caymax, J. Nijs, R. Mertens, D. Angermeier, S. Bourdais, R. Monna, A. Slaoui, CVD-growth of crystalline Si on amorphous or microcrystalline substrates, *Proceedings of the 14th European Photovoltaic Solar Energy Conference*, 1007–1010 (1997).
[61] A. Slaoui, R. Monna, D. Angermeir, S. Bourdais, J.C. Muller, Polycrystalline silicon films formation on foreign substrates by a rapid thermal-CVD technique, *Proceedings 26th IEEE-PVSEC*, 627–630 (1997).
[62] C. Schmidt, B.v. Ehrenwall, A. Braun, A. Püschel, S. Ruckmich, B. Tierock, M. Nell, H.-G. Wagemann, Silicon deposition on structured ceramic substrates for thin film solar cells, *Proceedings 14th EPVSEC*, 2694–2697 (1997).
[63] M. E. Nell, A. Braun, B. von Ehrenwell, C. Schmidt, L. Elstner: Solar cells from thin silicon layers on Al2O3, *Technical digest 11th Int. PVSEC-11*, 749–750 (1999).

[64] A. J. M. M. van Zutphen, A. von Keitz, M. Zeman, J. W. Metselaar: Film-silicon deposition followed by phosphorus diffusion for photovoltaic application *Proceedings 2nd WCPVSEC*, 1762–1765 (1998).

[65] A. Ogane, T. Yamazaki, T. Yamazaki, Y. Uraoka, T. Fuyuki, Large grain poly-Si thin films deposited on ceramic substrate by intermittent source gas supply, *Proceedings 20th European Photovoltaic Solar Energy Conference*, 1028–1031 (2005).

[66] A. J. M. M. van Zutphen, M. Zeman, J. W. Metselaar, A. von Keitz, C. J. J. Tool, G. Beaucarne, J. Poortmans: Film silicon on ceramic substrates for solar cells *Proceedings 16th EPVSEC*, 1412–1415 (2000).

[67] S. Bourdais, F. Mazel G. Fantozzi, A. Slaoui, Silicon deposition on mullite ceramic substrates for thin-film solar cells, *Prog. Photovolt: Res. Appl.*, **7**, 437–447 (1999).

[68] T. I. Kamins: *Polycrystalline silicon for integrated circuit applications*, Norwell, MA: Kluwer (1988).

[69] D. A. Smith, T. Y. Tan, Effect of doping and oxidation on grain growth in polysilicon, *Mat. Res. Soc. Symp. Proc.*, **5**, 65–70 (1982).

[70] R. E. Proano, D. G. Ast, Effects of the presence/absence of HCl during gate oxidation on the electrical and structural properties of polycrystalline silicon thin-film transistors, *J. Appl. Phys.*, **66**, 2189–2199 (1989).

[71] B. L. Sopori, J. Alleman, W. Chen, T. Y. Tan, N. M. Ravindra, Grain enhancement of thin silicon layers using optical processing, *Mat. Res. Soc. Symp. Proc.*, **470**, 419–424 (1997).

[72] G. Beaucarne, *Crystalline Si solar cells in thin layers deposited on foreign substrates using high-temperature chemical vapour deposition* Ph.D. Thesis, K. U. Leuven (2000).

[73] S. Bourdais: *Etude du dépôt et des propriétés physiques du silicium polycristallin obtenu par le procédé RTCVD sur substrats de mullite. Application aux cellules photovoltaïques en couches minces* Ph.D. thesis, Université Louis Pasteur de Strasbourg (2000).

[74] A. Focsa, A. Slaoui, E. Pihan, M. Rusu, F. Snijkers, P. Leempoel, G. Beaucarne, J. Poortmans, E. Alvarez, Silicon thin films on spin-on intermediate layer coated mullite ceramics for photovoltaic application, *Proceedings 19th EPVSEC*, 1281–1284 (2004).

[75] G. Beaucarne, J. Poortmans, M. Caymax, J. Nijs, R. Mertens, R. Monna, D. Angermeier, A. Slaoui, CVD-growth of crystalline Si on amorphous or microcrystalline substrates, *Proceedings 14th European Photovoltaic Solar Energy Conference*, 1007–1010 (1997).

[76] Y. Ishikawa, K. Nishioka, Y. Yamamoto, T. Hatayama, Y. Uraoko, T. Fuyuki, Effect of hydrogen lasma assivation for columnar poly-Si thin film deposited, *Proceedings 17th European Photovoltaic Solar Energy Conference*, 1682–1685 (2001).

[77] A. Slaoui, R. Monna, D. Angermeier, S. Bourdais, J.C. Muller, Polycrystalline silicon films formation on foreign substrates by a rapid thermal-CVD technique, *Proceedings of the 26th IEEE Photovoltaic Specialists Conference*, 627–630 (1997).

[78] Shen Hui, Ai Bin, Study on growth behavior of polycrystalline silicon thin films on the foreign substrates, *Technical Digest 15th Photovoltaic Science and Engineering Conference*, 810–811 (2005).

[79] T. Suzuki, A. Mimura, T. Ogawa, The formation of polycrystalline-silicon deposited on oxide-covered single crystal silicon substrates, *J. Electrochem. Soc.*, **124**, 17(1977).

[80] T. I. Kamins, J. Manoliu, R. N. Tucker, Diffusion of impurities in polycrystalline silicon, *J. Appl. Phys.*, **43**, 83–91 (1972).

[81] J. C. Liao, J. L. Crowley, T. I. Kamins, *Mat. Res. Soc. Symp. Proc.* **146**, 97 (1989).

[82] T. Fuyuki, H. Yoshida, H. Matsunami, Preferentially-oriented polycrystalline Si growth for thin-film solar cells using SiH_2Cl_2 decomposed in plasma, *Proceedings First World Conference on Photovoltaic Energy Conversion*, 1383–1386 (1994).

[83] D. Meakin, J. Stoemenos, P. Migliorato, N. A. Economou: Structural studies of low-temperature low-pressure chemical deposited polycrystalline silicon, *J. Appl. Phys.*, 61, 5031–5037 (1987).

[84] R. Bisaro, J. Magarino N. Proust, K. Zellama, Structure and crystal growth of atmospheric and low-pressure chemical-vapor-deposited silicon films, *J. Appl. Phys.*, **59**, 1167–1178 (1986).
[85] A. Ogane, Y. Takahashi, Y. Uraoka, T. Fuyuki, Crystallographic properties of large grain poly-Si thin films deposited by intermittent source gas supply, *Technical Digest of the 15th Photovoltaic Science and Engineering Conference*, 806–807 (2005).
[86] T. H. Wang, T. F. Ciszek, M. Page, Y. Yan, R. Bauer, Q. Wang, J. Casey, R. Reedy, R. Matson, R. Ahrenkiel, M. M. Al-Jassim: Material properties of polysilicon layers deposited by atmospheric pressure iodine vapor transport, *Proceedings 28th IEEE Photovoltaic Specialists Conference*, 138–141 (2000).
[87] T. H. Wang, M. R. Wang, R. E. Bauer, M. D. Landry, Q. Wang, T. F. Ciszek, Material improvements and device processing on APIVT-grown poly-Si thin layers, *Proceedings NCPV and Solar Program Review Meeting*, 1–3 (2003).
[88] M. W. M. Graef, L. J. Gilling, J. Bloem, Enhanced crystallinity of silicon films deposited by CVD on liquid layers (CVDOLL process): silicon on tin layers in the presence of hydrogen chloride, *J. Appl. Phys.*, **48**, 3937–3940 (1977).
[89] E. Rasmanis: Thin film p-n junction silicon devices, *Semiconductor Products*, **June 1963**, 30–33 (1963).
[90] J. K. Rath, H. Meiling, R. E. I. Schropp, Purely intrinsic poly-silicon films for n-i-p solar cells, *Jap. J. Appl. Phys.*, **36**, 5436 (1997).
[91] P. Muller, I. Beckers, E. Conrad, L. Elstner, W. Fuhs, Application of low-temperature electron cyclotron resonance CVD to silicon thin-film solar cell preparation, *Proceedings 25th Photovoltaic Specialists Conference*, 673–676 (1996).
[92] H. S. Reehal, M. J. Thwaites, T. M. Bruton: Thin film polycrystalline silicon solar cells prepared by plasma CVD *Phys. Stat. Sol. A*, **154**, 623–633 (1996).
[93] S. Oelting, D. Martini, D. Bonnet, Crystalline thin film silicon solar cells by ion-assisted deposition, *Proceedings 12th European Photovoltaic Solar Energy Conference*, 1815–1818 (1994).
[94] L. Oberbeck, R. B. Bergmann, N. Jensen, S. Oelting, J. H. Werner, *Diffus. Defect Data B, Solid State Phenom.*, **67–68**, 459 (1999).
[95] L. Oberbeck, J. Schmidt, T. Wagner, R. B. Bergmann, High-rate deposition of epitaxial layers for efficient low-temperature thin film epitaxial silicon solar cells, *Prog. Photovolt: Res. Appl.*, **9**, 333–340 (2001).
[96] T. A. Wagner, L. Oberbeck, R. B. Bergmann, Low temperature epitaxial silicon films deposited by ion-assisted deposition, *Mat. Sci. Eng. B*, **89**, 319 (2002).
[97] A. Straub, D. Inns, M. L. Terry, Y. Huang, P. I. Widenborg, A. G. Aberle, Optimisation of low-temperature silicon epitaxy on seeded glass substrates by ion-assisted deposition, *J. Cryst. Growth*, **280**, 385–400 (2005).
[98] M. Albrecht, B. Steiner, Th.Bergmann, A. Voigt, W. Dorsch, H. P. Strunk and G. Wagner, The crystalline quality of epitaxial Si layers solution grown on polycrystalline Si substrates, *Mat. Res. Soc. Symp. Proc.*, **358**, 889–894 (1995).
[99] A. Gutjahr, I. Silier, G. Cristiani, M. Konuma, F. Banhart, V. Schöllkopf, H. Frey, Silicon solar cell structure grown by liquid phase epitaxy on glassy carbon, *Proceedings of the 14th EPVSEC*, 1460–1462 (1997).
[100] S. Bourdais, R. Monna, D. Angermeier, A. Slaoui, N. Rauf, A. Laugier, F. Mazel, Y. Jorand, G. Fantozzi, Combination of RT-CVD and LPE for thin silicon-film formation on alumina substrates, *Proceedings 2nd WCPVSEC, (Vienna)*, 1774–1777 (1998).
[101] S. E. A. Schiermeier, C. J. J. Tool, J. A. M. van Roosmalen, L. J. Laas, A. von Keitz, W. C. Sinke, LPE-growth of crystalline silicon layers on ceramic substrates, *Proceedings 2nd WCPVSEC*, 1673–1676 (1998).
[102] J. Kühnle, R. B. Bergmann, J. Krinke, J. H. Werner, Comparison of vapor phase and liquid phase epitaxy for deposition of crystalline Si on glass, *Mat. Res. Soc. Symp. Proc.*, **426**, 111–116 (1996).

[103] T. Baba, M. Shima, T. Matsuyama, S. Tsuge, K. Wakisaka, S. Tsuda, 9.2% efficiency thin-film polycrystalline silicon solar cell by a novel solid phase crystallization method, *Proceedings 13th European Photovoltaic Solar Energy Conference*, 1708–1711 (1995).

[104] D. Song, A. Straub, P. Widenborg, B. Vogl, P. Campbell, and Y. Huang, A. G. Aberle, *Proceedings 19th European Photovoltaic Solar Energy Conference*, 1193 (2004).

[105] M. L. Terry, A. Straub, D. Inns, D. Song, A. G. Aberle, Large open-circuit voltage improvement by rapid thermal annealing of evaporated solid-phase-crystallized thin-film silicon solar cells on glass, *Appl. Phys. Lett.*, **86**, 172108 (2005).

[106] M. J. Keevers, A. Turner, U. Schubert, P. A. Basore, M. A. Green, Remarkably effective hydrogenation of crystalline silicon on glass modules, *Proceedings 20th European Photovoltaic Solar Energy Conference*, 1305–1308 (2005).

[107] P. Kwizera and R. Reif, Solid phase epitaxial recrystallization of thin polysilicon films amorphized by silicon ion implantation, *Appl. Phys. Lett.*, **41**, 379–381 (1982).

[108] R. B. Bergmann, F. G. Shi, H. J. Queisser and J. Krinke, *Appl. Surf. Sci.* **123–124**, 376 (1998).

[109] H. Kumoni, F. G. Shi, Phys. Rev. Lett. 82, 2717 (1999).

[110] L. Haji, P. Joubert, J. Stoemenos, N. A. Economou, Mode of growth and microstructure of polycrystalline silicon obtained by solid-phase crystallization of an amorphous silicon film, *J. Appl. Phys.*, **75**, 3944–3952 (1994).

[111] P. I. Widenborg, A. Straub, A. G. Aberle, Epitaxial thickening of AIC poly-Si seed layers on glass by solid phase epitaxy, J. Cryst. Growth, **276**, 19–28 (2005).

[112] R. B. Bergmann, R. Brendel M. Wolf, P. Lolgen, J. H. Werner, J. Krinke, H.P. Strunk, Crystalline silicon films by chemical vapor deposition on glass for thin film solar cells, *Proceedings 25th IEEE Photovoltaic Specialists Conference*, 365–370 (1996).

[113] J. Y. Seto, The electrical properties of polycrystalline silicon films, *J. Appl. Phys.*, **46 (12)**, 5247–5254 (1975).

[114] V. L. Dalal, P. Sharma, Defect density and diffusion length of holes in nanocrystalline silicon devices, *Appl. Phys. Lett.*, **86**, 103510 (2005).

[115] G. Beaucarne, S. Bourdais, A. Slaoui, J. Poortmans, Thin-film polysilicon solar cells on foreign substrates using direct thermal CVD: material and solar cell design, *Thin Solid Films*, **403–404**, 229–237 (2002).

[116] J.H. Werner, K. Taretto and U. Rau, Grain boundary recombination in thin-film silicon solar cells', *Sol. State Phenom.*, **80–81**, 209–304 (2001).

[117] T. Matsuyama, N. Terada, T. Baba, T. Sawada, S. Tsuge, K. Wakisaka, S. Tsuda, High-quality polycrystalline silicon thin film prepared by a solid phase crystallization method, *J. Non-Cryst. Sol.*, 198–200, 940–944 (1996).

[118] G. Beaucarne, J. Poortmans, M. Caymax, J. Nijs, R. Mertens, On the behavior of p-n junction solar cells made in fine-grained silicon layers, *IEEE Trans. Electr. Dev.*, **47**, 1118–1120 (2000).

[119] C. R. M. Grovenor, Grain boundaries in semiconductors, *J. Phys. C*, **18**, 4079–4120 (1985).

[120] L. L. Kazmerski, Chemistry of hydrogen and arsenic interactions at silicon grain boundaries, *J. Vac Sci. & Technol.*, **A 4**, 1638 (1986).

[121] G. Harbeke, *Polycrystalline Semiconductors*, Berlin: Springer-Verlag, (1985).

[122] Y. Mai, S. Klein, R. Carius, J. Wolff, A. Lambertz, F. Finger, X. Geng, Microcrystalline silicon solar cells deposited at high rates, *J. Appl. Phys.*, **97**, 114913 (2005).

[123] G. Beaucarne, J. Poortmans, M. Caymax, J. Nijs, S. Bourdais, D. Angermeier, R. Monna, A. Slaoui, Recrystallization-free thin-film crystalline silicon solar cells on foreign substrates, *Proceedings 2nd World Conference on Photovoltaic Energy Conversion*, 1814–1817 (1998).

[124] A. G. Aberle, P. I. Widenborg, D. Song, A. Straub, M.L. Terry, T. Walsh, A. Sproul, P. Campbell, D. Inns, B. Beilby, M. Griffin, J. Weber, Y. Huang, O. Kunz, R. Gebs, F. Martin-Brune, V. Barroux, S.R. Wenham, Recent advances in polycrystalline silicon thin-film solar cells on glass at USNW, *Proceedings 31st IEEE Photovoltaic Specialist Conference*, 877–882 (2005).

[125] L. Carnel, I. Gordon, D. Van Gestel, K. Van Nieuwenhuysen, G. Agostinelli, G. Beaucarne, J. Poortmans, Thin-film polycrystalline silicon solar cells on ceramic substrates with a V_{oc} above 500 mV, *Thin Solid Films*, 511–512, 21–25 (2005).

[126] G. Andrä, J. Bergmann, F. Falk, E. Ose, Multicrystalline silicon thin film solar cells on glass, *Proceedings 19th European Photovoltaics Solar Energy Conference*, 872–875 (2004).

[127] C. Feldman, N. A. Blum, F. G. Satkiewicz, Vacuum deposited polycrystalline silicon solar cells for terrestrial use, *Proceedings 14th IEEE Photovoltaic Specialists Conference*, 391–396 (1980).

[128] G. Beaucarne, J. Poortmans, M. Caymax, J. Nijs, R. Mertens, Properties of p-n diodes made in polysilicon layers with intermediate grain size, *Sol. State Phenom.*, **67–68**, 577–582 (1999).

[129] G. Beaucarne, S. Bourdais, A. Slaoui, J. Poortmans, Carrier collection in fine-grained p-n junction polysilicon solar cells, *Proceedings 28th IEEE PVSC*, 128–133 (2000).

[130] T. H. DiStefano, J. J. Cuomo, Reduction of grain boundary recombination in polycrystalline silicon solar cells, *Appl. Phys. Lett.*, **30**, 351–353 (1977).

[131] G. Beaucarne, M. Caymax, I. Peytier and J. Poortmans, Polysilicon thin-film solar cells: influence of the deposition rate on enhanced diffusion and on cell performance, *Sol. State Phenom.*, 80–81, 269–274 (2001).

[132] T. Matsuyama, K. Wakisaka, M. Kameda, M. Tanaka, T. Matsuoka, S. Tsuda, S. Nakano, Y. Kishi, Y. Kuwano, Preparation of high-quality n-type poly-Si films by the solid phase crystallization (SPC) method, *Jpn. J. Appl. Phys.*, **11**, 2327–2331 (1990).

[133] M. L. Terry, A. Straub, D. Inns, D. Song, A. G. Aberle, V_{oc} improvement of evaporated SPC thin-film Si solar cells on glass by rapid thermal annealing, *Proceedings 31st Photovoltaic Specialists Conference*, 971–974 (2005).

[134] M. Spiegel, G. Hahn, W. Jooss, S.Keller, P. Fath, G.Willeke and E. Bucher, Investigation of hydrogen diffusion, effusion and passivation in solar cells using different multicrystalline silicon base materials, *Proceedings 2nd WCPVSEC, Vienna*, 1685–1688 (1998).

[135] R. Plieninger, H. N. Wanka, J. Kuhnle, J. H. Werner, Efficient defect passivation by hot-wire hydrogenation, *Appl. Phys. Lett.*, **71**, 2169–2171 (1997).

[136] H. E. A. Elgamel, J. Nijs, R. Mertens, M. G. Mauk, A. M. Barnett, Hydrogen in polycrystalline silicon solar cell material: its role and characteristics, *Sol. En. Mat. Sol. Cel.*, **53**, 277–284 (1998).

[137] F. Duerinckx, J. Szlufcik, Defect passivation of industrial multicrystalline solar cells based on PECVD silicon nitride, *Sol. En. Mat. Sol. Cel.*, **72**, 231–246 (2002).

[138] J. H. W. J. Soppe, W. M. M. Kessels, M. C. M. van den Sanden, W. M. Arnoldbik, H. Schlemm, C. Devilee, H. Rieffe, S. E. A. Schiermeier, J. H. Bultman, A. W. Weeber, On combining surface and bulk passivation of SiNx:H layers for mc-Si solar cells, *Proceedings 29th IEEE PVSC*, 158–161 (2002).

[139] L. Carnel, I. Gordon, K. Van Nieuwenhuysen, D. Van Gestel, G. Beaucarne, J. Poortmans, Defect passivation in chemical vapour deposited fine-grained polycrystalline silicon by plasma hydrogenation, *Thin Solid Films*, **487**, 147–151 (2005).

[140] S. Honda, T. Mates, M. Ledinsky, J. Oswald, A. Fejfar, J. Kocka, T. Yamazaki, Y. Uraoka, T. Fuyuki, Effect of hydrogen passivation on polycrystalline silicon thin films, *Thin Solid Films*, **487**, 152–156 (2005).

[141] L. Carnel, I. Gordon, H.F.W. Dekkers, D. Van Gestel, K. Van Nieuwenhuysen, G. Beaucarne, J. Poortmans, Direct plasma hydrogenation and SiN:H hydrogenation of thin-film polycrystalline-silicon solar cells, *Technical Digest 15th Photovoltaic Science and Engineering Conference*, 907–908 (2005).

[142] M. Taguchi, H. Sakata, Y. Yoshimine, E. Maruyama, A. Terakawa, M. Tanaka, An approach for the higher efficiency in the HIT cells, *Proceedings 31st IEEE Photovoltaic Specialists Conference*, 866–817 (2005).

[143] K. Yamamoto, T. Suzuki, M. Yoshimi, A. Nakajima, Optical confinement effect for below 5 μm thin film poly-Si solar cell on glass substrate, *Jpn. J. Appl. Phys.*, **36**, L569–L572 (1997).

[144] K. Yamamoto, M. Yoshimi, Y. Tawada, Y. Okamoto, A. Nakajima, S. Igari, Thin-film poly-Si solar cells on glass substrate fabricated at low temperature, *Appl. Phys. A*, **69**, 179–185 (1999).

[145] K. Yamamoto, M. Yoshimi, T. Suzuki, Y. Tawada, Y. Okamoto, A. Nakajima, Below 5 μm thin film poly-Si solar cell on glass substrate fabricated at low temperature, *Proceedings 2nd WCPVSEC, Vienna*, 1284–1289 (1998).

[146] K. Yamamoto, A. Nakajima, M. Yoshimi, T. Sawada, S. Fukuda, T. Suezaki, M. Ichikawa, Y. Koi, M. Goto, H. Takata, T. Sasaki, Y. Tawada, Novel hybrid thin-film silicon solar cell and module, *Proceedings 3rd World Conference on Photovoltaic Energy Conversion*, 2789–2792 (2003).

[147] P. A. Basore, Pilot production of thin-film crystalline silicon on glass modules, *Proceedings 29th IEEE Photovoltaic Specialists Conference*, 49–52 (2002).

[148] P. A. Basore, Pilot production of thin-film crystalline silicon on glass modules, *Proceedings From PV Technology to Energy Solutions*, 236–239 (2002).

[149] P. A. Basore, Large-area deposition for crystalline silicon on glass modules, *Proceedings 3rd World Conference on Pphotovoltaic Energy Conversion*, 935–938 (2003).

[150] M. A. Green, P. A. Basore, N. Chang, D. Clugston, R. Egan, R. Evans, J. Ho, D. Hogg, S. Jarnason, M. Keevers, P. Lasswell, J. O'Sullivan, U. Schubert, A. Turner, S.R. Wenham, T. Young, Crystalline silicon on glass (CSG) thin-film solar cell modules, *J. Solar Energy*, **77**, 857–863 (2004).

[151] A. G. Aberle, Crystalline silicon thin-film solar cells: where are we? Where to go from here?, *Proceedings 20th European Photovoltaic Solar Energy Conference*, 1108–1111 (2005).

[152] S. Gall, J. Schneider, J. Klein, K. Hübener, M. Muske, B. Rau, E. Conrad, I. Seiber, K. Petter, K. Lips, M. Stöger-Pollach, P. Schattschneider, W. Fuhs, Large-grained polycrystalline silicon on glass for thin-film solar cells, *Thin Solid Films*, 511–512, 7–14 (2006).

[153] B. Rau, J. Schneider, E. Conrad, S. Gall, W. Fuhs, Polycrystalline Si thin-film solar cells with absorber layers grown at temperatures below 600 °C by ECRCVD, *Technical Digest 15th Photovoltaic Science and Engineering Conference*, 778–779 (2005).

[154] I. Gordon, D. Van Gestel, K. Van Nieuwenhuysen, L. Carnel, G. Beaucarne, J. Poortmans, Thin-film polycrystalline silicon solar cells on ceramic substrates by Aluminium-Induced Crystallization, *Thin Solid Films*, **487**, 113–117 (2005).

[155] I. Gordon, L. Carnel, D. Van Gestel, K. Van Nieuwenhuysen, J. Irigoyen, G. Beaucarne, J. Poortmans, Development of efficient thin-film polycrystalline silicon solar cells based on aluminium-induced crystallization, *Technical Digest 15th International Photovoltaic Science and Engineering Conference*, 937–938 (2005).

[156] T. Yamazaki, Y. Matsumura, Y. Urakoka, T. Fuyuki, Analysis of electronic properties at grain boundary of poly-Si thin film solar cells deposited with nucleation control using intermittent supply method, *Proceedings 19th European Photovoltaic Solar Energy Conference*, 742–745 (2004).

4 Advances in Microcrystalline Silicon Solar Cell Technologies

Evelyne Vallat-Sauvain, Arvind Shah and Julien Bailat
Institute of Microtechnology, University of Neuchâtel, Switzerland

4.1 INTRODUCTION

Thin film silicon constitutes, from many points of view, an ideal option for future low-cost mass production of photovoltaic (PV) solar modules:

- Material requirements are reasonable: no rare or toxic raw materials are used in large quantitites.
- Energy payback times are much lower than for the present wafer based PV technology.
- An upscaling to large area modules (with areas over 1 m^2) has already been demonstrated for industrial plants with production capacities of more than 10 MW_p/year.
- Monolithic integrated series connection of cells to form entire modules is possible.
- Typical processes involved are low-temperature processes and, thus, a large variety of substrate materials, including low cost flexible plastic substrates are possible.

In the first two decades of development (approx. 1970–1990) thin film silicon solar cells were restricted to hydrogenated amorphous silicon (a-Si:H) and its alloys with germanium (a-Si,Ge:H) and carbon (a-Si,C:H). This topic is discussed in Chapter 5 of this volume. Amorphous silicon photovoltaic technology is now an industrially mature technology, but has so far not been able to capture a significant share of the PV market. Hydrogenated amorphous silicon solar cells had indeed initially been largely confined to applications for powering small systems, and only rarely used in actual electrical power applications. One of the main reasons for this is the relatively low efficiency (5 to 7 %) obtained for commercial amorphous silicon modules. This limitation is due in part to the Staebler–Wronski effect or light-induced degradation effect. Inspite of this limitation, a-Si:H PV modules are now gradually entering into the energy field and especially into the building integrated PV (BIPV) area, where they offer interesting structural and aestethic advantages.

In the early 90s, hydrogenated microcrystalline silicon (μc-Si:H) was pioneered by our group at the Institute of Microtechnology of the University of Neuchâtel (IMT) as a new thin film material for photovoltaic applications. Microcrystalline silicon layers and solar cells can

Thin Film Solar Cells Edited by J. Poortmans and V. Arkhipov
© 2006 John Wiley & Sons, Ltd

be produced in virtually the same manner and with the same equipment as amorphous silicon, but have quite different material properties:

- A complex material microstructure, that varies drastically with deposition conditions.
- An increased sensitivity to layer contamination.
- A lower bandgap (1.1 eV instead of 1.7 to 1.8 eV for a-Si:H). Due to this, there is a capacity for usefully absorbing and converting incoming light in the near infrared region of the solar spectrum.
- An indirect bandgap, i.e. a lower absorption coefficient in the visible range of the solar spectrum compared with a-Si:H. Due to this, there is a necessity for using thicker absorbing layers than in the case of a-Si:H and more efficient light trapping within the solar cell.
- A much milder form of light induced degradation.

Microcrystalline silicon solar cells are still very much a research topic. Many aspects of the material properties and the device physics are just being investigated. The present chapter will give a comprehensive report on some of the more important of these issues.

Looking at solar cell efficiencies, one notes that presently the best laboratory single junction microcrystalline silicon solar cells have efficiencies in the 9 to 10 % range; individual record cells even reach values slightly over 10 %. As microcrystalline silicon is yet in the early stages of development, one can hope that these values will be susbtantially increased during the next few years, especially through more efficient light management schemes.

However, the best way of using microcrystallline silicon for photovoltaics appears at present to be in the "micromorph" tandem, i.e. in the combination of a microcrystalline silicon bottom cell with an amorphous silicon top cell. Here, stabilized efficiencies in the range of 11 to 12 % are obtained for small area laboratory cells. The world record initial efficiency for such tandem small area cells has now reached 14.7 %. Kaneka Corp. has brought out commercial PV modules based on the tandem approach with stabilized efficiencies of over 8 %.

In this chapter, limitations and prospects for the micromorph tandem will therefore also be discussed.

4.2 MICROCRYSTALLINE SILICON: MATERIAL FABRICATION AND CHARACTERIZATION

4.2.1 Microcrystalline silicon deposition techniques

4.2.1.1 Introduction

One usually employs the term 'microcrystalline silicon' (μc-Si:H) or, alternatively 'nanocrystalline silicon' to designate layers that are deposited at low temperatures (below 400 °C) by plasma enhanced chemical vapor deposition (PECVD) or similar techniques, either from pure silane (SiH_4) or, more commonly, from a mixture of silane and hydrogen. The term 'polycrystalline silicon' has been commonly used to designate layers that are deposited e.g. by chemical vapor deposition at higher temperatures (usually 600 °C and above). There are two advantages

of selecting a low temperature process such as the plasma processes used for microcrystalline silicon: (a) a large variety of substrates becomes possible and contamination problems are reduced, (b) hydrogen is incorporated into the layers, thereby passivating the electronic defects and grain boundaries.

The possibility for low temperature synthesis of microcrystalline silicon was discovered in 1968 by Veprek and Marecek [1] by a chemical transport technique. This technique is comparable to the currently employed PECVD process with respect to two aspects: in both cases, the deposition precursors are silane related radicals and in both cases atomic hydrogen plays a crucial role in layer growth. The fabrication of μc-Si:H using PECVD of silane was introduced in 1979–1980 [2,3]. Its application to solar cells was first limited to p type window layers in p-i-n type amorphous silicon solar cells [4]. There, the high conductivity and low absorption coefficient in the visible range of these microcrystalline silicon layers are particularly useful [5]. Fully microcrystalline thin film silicon solar cells incroporating a μc-Si:H i-layer as photoactive layer were at first not considered feasible due to the poor quality and the n type character of undoped layers. In 1994, the Neuchâtel group showed, however, that it is possible to obtain fully microcrystalline single junction solar cells with conversion efficiencies over 7 % [6] using the very high frequency (VHF) plasma technique [7]. Currently, the growth rate of microcrystalline silicon is the limiting step in the industrialization of microcrystalline silicon modules, and a large effort is devoted to the development of high rate (>5 Å/s) deposition of μc-Si:H layers for their incorporation into solar cells. We will discuss in more detail below the advantage of using VHF plasmas for the deposition of μc-Si:H layers, but shall mention here the use of higher plasma pressures (the so-called 'high pressure depletion' regime) [8,9], as well as that of microwave plasmas [10,11]. Hot wire deposition [12,13] as an alternative to plasma deposition will also be cited. These techniques are currently under investigation, but although, in the laboratory, deposition rates up to 10 Å/s can be obtained for state-of-the-art solar cells with some of these methods, regular large scale production at such high rates has not yet been reported, except by Kaneka Corp.

4.2.1.2 Very high frequency glow discharge deposition technique

In 1987, IMT introduced the so-called very high frequency glow discharge (VHF-GD) deposition technique, allowing for considerable improvement in the deposition rates of amorphous (and later) μc-Si:H silicon. Typically, standard PECVD deposition of μc-Si:H is performed in a diode type reactor. For the VHF-GD deposition technique, the conventional plasma power source generator working at an excitation frequency of 13.56 MHz is replaced by a power source with an excitation frequency between 30 MHz and 300 MHz. Since the electrons in a plasma have a much larger thermal velocity than the positive ions, the bulk plasma is required to have a positive potential in order to maintain charge neutrality. The plasma sheath near the substrate leads to the acceleration of positive ions and also to electron confinement within the plasma. As a direct consequence of the use of a higher plasma excitation frequency, the plasma sheath thickness is reduced; this leads to a reduced plasma impedance at higher frequencies, an enhanced dissociation of silane and a reduced energy of the ions impinging on the growing surface. It seems that due to the softer (but more intense) ion bombardment on the growing surface, the VHF process favors the formation of microcrystalline silicon, as compared to conventional plasma deposition at 13.56 MHz. Furthermore, it has now been shown that VHF plasma has the potential for constituting a high-rate deposition process. Several groups have

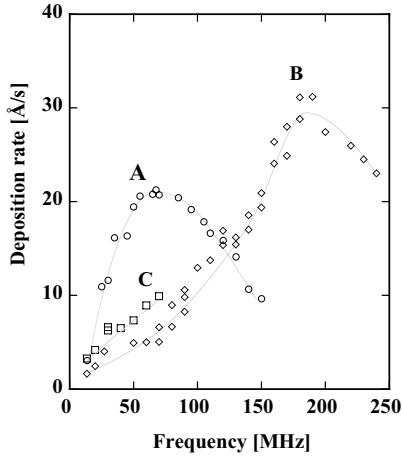

Figure 4.1 Deposition rate of hydrogenated amorphous silicon versus plasma excitation frequency as obtained in different reactors by independant research groups. Curve A: data taken from [7], curve B: data taken from [16], curve C: data taken from [104].

demonstrated that an increase in plasma excitation frequency from the standard 13.56 MHz to values in the VHF range permits an increase in deposition rate by a factor of four to ten for amorphous silicon. A similar trend is also observed for microcrystalline silicon. The curve of deposition rate versus excitation frequency (Figure 4.1) shows in general a maximum for a given deposition reactor. The decrease occuring at higher frequencies can be attributed to engineering aspects like reactor design and leads to parasitic shunt capacitance within the reactor. On the other hand, the generally observed increase of deposition rate with increasing excitation frequency can be attributed to fundamental physical changes in the capacitively coupled glow discharge plasma, linked with the observed modifications in the plasma impedance and with the reduced sheath thickness. Heintze *et al*. [14] measured an enhanced ion flux on the growing surface at higher frequencies and suggested that the higher ion flux and lower energy of the ion bombardment lead to a 'softer' but intensified bombardment. As an important consequence of these physical modifications, a significantly better coupling of the RF power into the bulk plasma rather than into the sheath can be obtained at higher excitation frequencies. Due to this, higher electron densities and better SiH_4 dissociation in the bulk plasma [15,16], as well as increased radical and ion flux onto the growing surface, can be achieved. The end result of all this is a net increase in the deposition rate and the promotion of microcrystalline growth.

4.2.1.3 Alternative deposition techniques

In the high pressure depletion regime (HPD), higher gas pressures within the plasma reactor are used during deposition (typically 7 to 10 Torr instead of about 0.3 Torr in the 'conventional' deposition regime). Due to the prevailing higher pressure , the ions that bombard the surface lose a large part of their energy in collisions within the plasma. Thus, the power fed to the plasma can be susbtantially increased and, in this way, the deposition rate is enhanced without adversely affecting material quality. However, in order to obtain μc-Si:H rather than a-Si:H growth, it is,

at the same time, necessary to have plasma conditions where silane is depleted and where there is relatively more hydrogen present in the plasma. High hydrogen consumption, formation of powder and layer inhomogeneity are problems that are to be faced when optimizing HPD deposition. Excellent μc-Si:H solar cells have been obtained by the Juelich group with HPD at a deposition rate of 5 Å/s with 13.56 MHz excitation frequency [17] and by a combination of HPD and VHF (95 MHz excitation frequency) with a growth rate of 11 Å/s [18], resulting in a 9.8 % conversion efficiency for single junction μc-Si:H solar cells. Some Japanese groups report the fabrication of μc-Si:H cells with slightly reduced efficiencies at rates in the range of 20 to 40 Å/s [19,20]. One of the main ongoing tasks here is to design a production type large area reactor based on a combination of HPD and VHF principles [21].

In microwave plasma, here again the ion bombardment is reduced compared with the standard 13.56 MHz plasma deposition process, and high deposition rates are achieved for μc-Si:H deposition, although so far no significant results on full single junction μc-Si:H have been reported [22].

Hot wire (HW) deposition is an alternative to plasma deposition: the silane gas is thermally dissociated by using a metal filament (e.g tungsten wire) heated up to 1600–2000 °C. As there is no plasma, the ion bombardment, which is, in general, detrimental for layer quality, is completely avoided. So far, high rate μc-Si:H layers have been deposited by HW deposition and relatively good single junction μc-Si:H at low rates have been obtained [13,23], but no satisfactory solar cells have been obtained at high rates. The total lack of ion bombardment in HW, may, however, actually be a disadvantage. It would seem that some amount of low energy ion bombardment is beneficial for μc-Si:H growth. Indeed, a combination of HW with VHF has so far yielded the most encouraging results [24]. Further technical problems to be solved for succesful HW deposition are large area homogeneity, periodic replacement of the filament and overheating of the growing layer by thermal radiation from the filament. It would seem that these problems are all in the process of being tackled by specialized equipment manufacturers.

4.2.2 Microcrystalline silicon layers

Since its discovery in 1968, it has been known that a necessary condition for growth of microcrystalline silicon is a high density of atomic hydrogen at the growing surface [25,26]. The density of atomic hydrogen can be enhanced by adding hydrogen to the plasma or by increasing plasma power as observed from plasma optical emission spectra [27], as well as by increasing plasma excitation frequency. Thus, studies of μc-Si:H layers are often performed on series of layers deposited with varying values of silane concentration ($SC = [SiH_4]/[SiH_4 + H_2]$). Adhesion of micrometer thick layers on glass subtrates is another issue, due to the large internal mechanical stress present in μc-Si:H layers [28].

In the following paragraph, we will describe the main physical characteristics of undoped and doped μc-Si:H layers in view of their incorporation into solar cell devices.

4.2.2.1 Undoped microcrystalline layers

The study of intrinsic microcrystalline silicon layers deposited on various substrates is used in practice in order to monitor the fundamental chemicophysical properties of the material, in view of its incorporation as photogeneration layer within solar cell devices. As mentioned

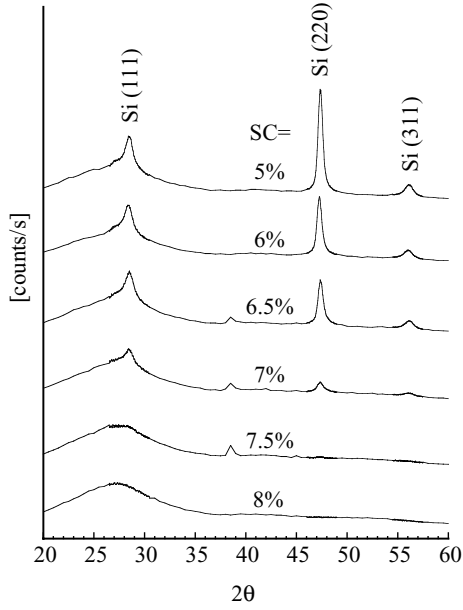

Figure 4.2 X-ray diffraction spectra obtained for a series of μc-Si:H layers deposited on glass substrates at various silane concentrations (SC). The curves are shifted for clarity. The three main diffraction peaks corresponding to the (111), (220) and (311) silicon crystallographic planes are indicated. In some spectra, a small peak around 38.5° is observed. It is due to the presence of aluminium used for electrical contacts on these layers. In this example, the amorphous to microcrystalline transition occurs for SC between 7 % and 7.5 %.

above, μc-Si:H layers can be fabricated by PECVD from a mixture of silane and hydrogen. The variation of the silane concentration in the plasma results in a 'transition' from hydrogenated amorphous silicon (a-Si:H) to hydrogenated microcrystalline silicon (μc-Si:H), as seen in X-ray Diffraction (XRD) (see Figure 4.2) and Raman spectra [29]. In this example, the μc-Si:H layer deposited with a silane concentration value of 7.5 % presents a XRD spectrum characteristic of amorphous silicon, whereas the layer deposited with a silane concentration value of 7 % exhibits diffraction peaks that are related to crystalline silicon. Here, the occurrence of crystallinity appears suddenly with a small variation of SC, giving rise to a phenomenon that looks like a transition. Although the term transition might, strictly speaking, be incorrect [30], we shall use it in this chapter.

Here, we will discuss in more detail the microstructural evolution of layers deposited for various values of SC and focus on the microsctructure of layers deposited close to the amorphous/microcrystalline transition. Nucleation and growth of layers deposited on different substrates will be discussed and a simple growth model will be presented. Optical and electronic transport properties of device grade material will then be given.

4.2.2.2 Microstructural properties

Microcrystalline silicon is a complex material (see Figure 4.3). Its microstructure consists of the microcrystalline phase itself, made of silicon nanocrystals packed, with some amorphous

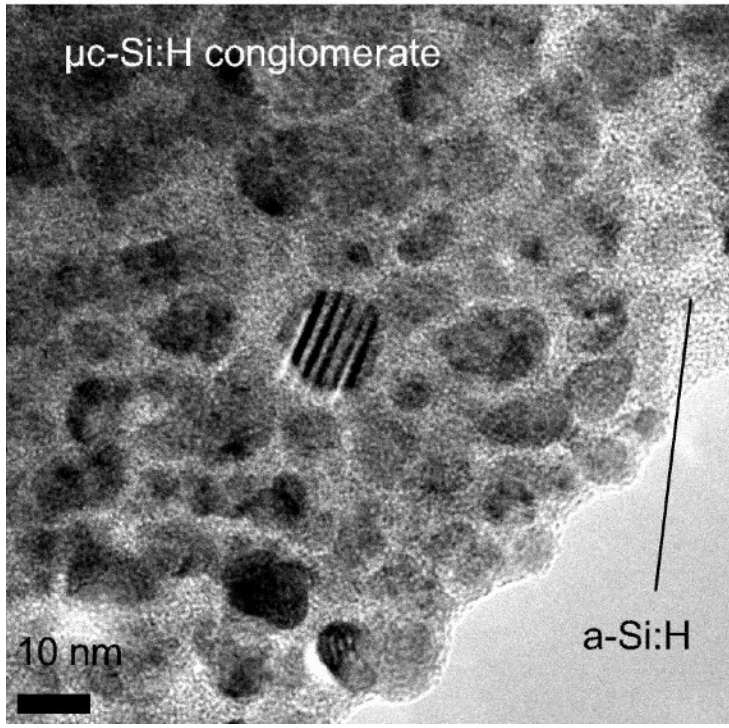

Figure 4.3 High resolution transmission electron microscopy micrograph of a plane view taken within a microcrystalline conglomerate. Spherical nanocrystals embedded in amorphous tissue constitute the microcrystalline phase itself.

silicon, into conglomerates. Figure 4.3 shows a plane view of a μc-Si:H conglomerate consisting of silicon nanocrystals possessing a diameter between 10 and 20 nm, embedded into amorphous silicon. The conglomerates are separated by a varying amount of amorphous silicon, grain boundaries and/or cracks. The silicon crystallites in the material are of nanometer scale and this is why μc-Si:H is also sometimes designated as 'nanocrystalline silicon' [31]. The term 'microcrystalline', on the other hand, comes from the micrometer scale conglomerate dimensions, which, as we shall see later, limit coplanar electronic transport in this material [32].

In general, the microstructure of μc-Si:H depends on the fabrication conditions and ultimately on the underlying substrate on which nucleation and growth take place. A sketch of the evolution of microstructure μc-Si:H as a function of SC is given in Figure 4.4. At low values of silane concentration, μc-Si:H consists of elongated nanocrystals separated by cracks that extend through the whole layer. Such layers with a high density of grain boundaries and a columnar structure are prone to post oxidation [33], a phenomenon that is responsible for a variation in the dark conductivity activation energy (i.e. for a variation of the position of the Fermi level), and thus, leads to a change in many of the electronic transport properties, on a timescale of a few hours to a few days. As the value of SC is increased, the material becomes denser and at the same time less crystalline; it is also less affected by post oxidation. Close to the amorphous/microcrystalline transition, μc-Si:H consists of conical conglomerates

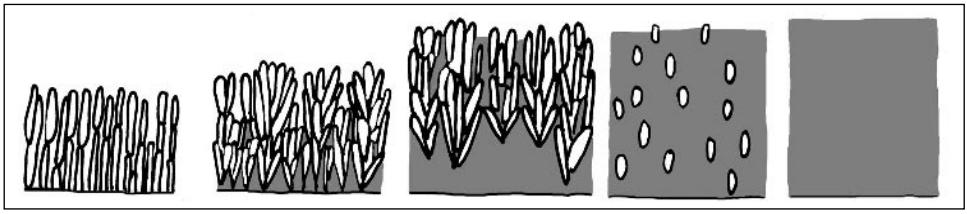

Figure 4.4 Schematic evolution of the microstructure of microcrystalline silicon layers as a function of crystallinity. Nanocrystallites of silicon are white in this sketch, whereas amorphous silicon is gray. The increasing thickness is a schematic representation of the increasing growth rate of microcrystalline silicon with decreasing crystallinity.

of microcrystalline silicon separated by amorphous silicon, as shown in Figures 4.4 and 4.7. A vertical section through the microstructure of such layers can be described as follows: first, just above the substrate, is a continuous, fully amorphous layer below the nuclei (so-called incubation layer), this is followed by a mixed phase layer (consisting of amorphous and microcrystalline phases), starting at the nucleation points and extending laterally up to the colaescence threshold. From there on, the conical conglomerates grow as microcrystalline columns. Typically, the cone aperture angle is between 15 and 20° [34,35]. The diameter of the silicon nanocrystals is typically of a few nanometers (see Figure 4.3) and relatively insensitive to the deposition conditions. Preferential crystallographic growth of the nanocrystallites in the (220) direction increases when one increases the value of SC that one uses (see Figure 4.2). In a XRD spectra of randomly. oriented Si powder, a peak intensities ratio of 1:0.55:0.3 among the (111), (220) and (311) peaks is observed. This is obviously not the case in this series, where the (220) peak intensity is, relatively, much higher than the (111) peak intensity, indicative of a preferred (220) orientation for the nanocrystallites. Such a (220) preferential orientation is frequently observed in device grade material [36], although preferential orientation along (400) directions have been reported as well [37]. The growing surface as observed with atomic force microscopy (AFM) performed on a thickness dependent series [38] or on micrometer thick layers [39] typically reveals large conglomerates with a diameter of the order of a fraction of micrometer, composed of much smaller nanocrystals (see Figure 4.5). These general features of μc-Si:H microstructure and their variation with i-layer deposition conditions are in essence also observed in i-layers incorporated within p-i-n type and n-i-p type solar cells, as long as the i-layer thickness has a similar value [34]. Layer crystallinity is one of the main material parameters for incorporation into solar cell devices. As described above, growth of microcrystaline silicon leads to depth dependent crystallinity, with, in general, a less crystalline material growing on top of the substrate. Experimental methods allowing the evaluation of i-layer crystallinity are, thus, of practical importance for the characterization of μc-Si:H. Transmission electron microscopy (TEM) is a very powerful technique that allows for direct observation of the presence of amorphous and microcrystalline phases. Numerical evaluation of the TEM micrographs allows one to determine the crystalline volume fraction [40]. The drawbacks of this technique are the lengthy sample preparation and the resulting destruction of the sample layer. X-ray diffraction can be used for the evaluation of the i-layer average crystallinity, although experimental evaluation of the volume crystalline fraction based on this technique is subject to relatively large experimental errors. Raman spectroscopy is the fastest and easiest experimental technique for crystallinity measurement in μc-Si:H. In Raman spectroscopy, amorphous silicon leads to the occurence of a broad peak at about

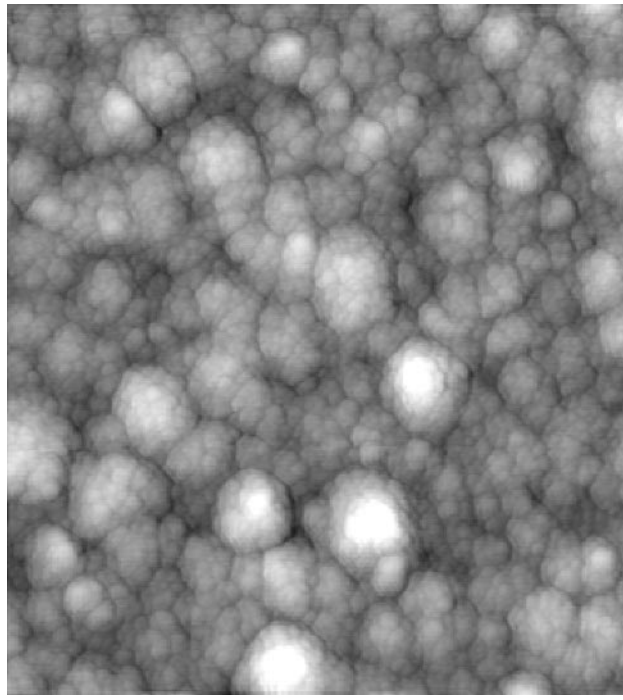

Figure 4.5 Atomic force microscopy micrograph of the surface topography of a 2 μm thick μc-Si:H layer deposited on a glass substrate with deposition conditions close to the amorphous/microcrystalline transition. Scanned area is 3 μm×3 μm and rms roughness of this sample is 16 nm.

480 cm^{-1}. The integrated intensity of this peak I_a is proportional to the amorphous volume fraction in the excited volume. The signature of microcrystalline silicon is an asymetrical peak at 520 cm^{-1}, which is the position of the transverse optic mode in monocrystalline silicon. The asymetry of this peak occurs as a tail towards lower wavenumbers (around 510 cm^{-1}); this tail has been attributed to the 'defective' part of the crystalline phase (crystallites smaller than 10 nm [41] or to a silicon wurtzite phase [42] that results from twinning [43]). The integrated intensity I_c of the two microcrystalline silicon related peaks (520 cm^{-1} and 510 cm^{-1}) can therefore be considered proportional to the crystalline volume fraction. Thus, the ratio $I_c/(I_c + I_a)$ resulting from the deconvolution and integration of the Raman lines allows us to define a 'Raman crystallinity' factor which is quite useful for qualitative characterization of the crystallinity of μc-Si:H layers, both individually and also within solar cells. For a more precise, quantitative evaluation of the crystalline volume fraction, the Raman crystallinity has to be corrected by a calibration factor in order to obtain the actual value for the crystalline volume fraction [44].

4.2.2.3 Nucleation and growth

One of the critical microstructural parameters that has to be controlled carefully so as to obtain high values of the open circuit voltage value with μc-Si:H solar cells is the crystallinity of the

intrinsic layer. As described above, the crystallinity of μc-Si:H layers is depth dependent as the layers consist of conglomerates that nucleate either on the substrate or, for layers deposited close to the transition, above a continuous amorphous incubation layer. The nucleation density of the microcrystalline phase is, thus, an important parameter for controlled growth of μc-Si:H. Measurements of the nuclei density of μc-Si:H deposited close to the transition on various flat and rough substrates showed that the density of nuclei depends mainly on the chemical nature of the substrate (see Figure 4.6). Another important consideration for nucleation of μc-Si:H is the role of local epitaxy. It has been shown that local epitaxy is involved in the growth of i-layers onto doped microcrystalline layers [45], a situation systematically encountered in p-i-n type and n-i-p type devices where the doped layer plays the role of a nucleation layer. A first highly microcrystalline doped layer will, thus, be beneficial in obtaining a high density of nuclei for the subsequent i-layer growth.

Growth of the microcrystalline phase has the particularity of extending perpendicular to the local substrate plane from the first tens of nanometers onwards. This aspect is not relevant for the study of layers grown on flat substrates, but plays an important role for layers grown

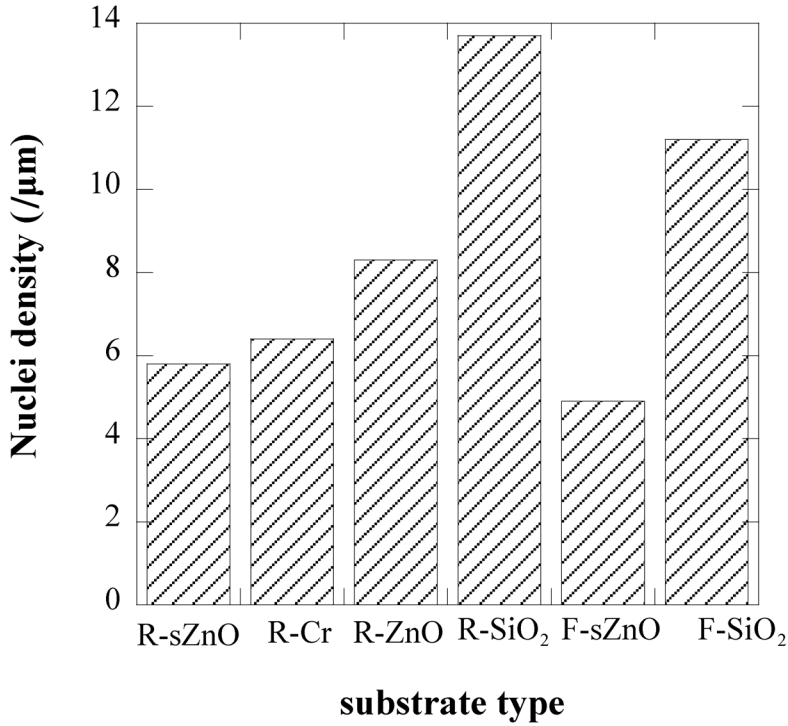

Figure 4.6 Nuclei density of μc-Si:H layers deposited on six different substrates with a value of the silane concentration (SC) close to the SC value needed to reach the amorphous/microcrystalline 'transition'. R stands for 'rough', whereas F stands for 'flat'. The rms value of the surface roughness is 60 nm for the rough substrates; this is a typical value observed in transparent conductioe oxides used for light trapping within μc-Si:H solar cells. For both flat and rough substrates, silicon dioxide SiO_2 (deposited by PE-CVD) is the most favourable layer for nucleation, whereas sputtered ZnO is the least favourable layer for nucleation of μc-Si:H.

on rough substrates such as the rough transparent conductive oxide (TCO) layer generally used as contact layers in order to obtain efficient light trapping in solar cells. In this case, the typical rms roughness of the substrate is of the order of a few tens of nanometers. Here, the geometrical consequences of this peculiar aspect of growth lead to the accumulation of amorphous material at the bottom of the substrate grooves [40], with grain boundaries that extend from the bottom of the grooves up to the top of the device. In this way, substrate topography can play an important role on the average crystallinity of the layer and on the grain boundary density [46]. One of the most remarkable aspects of microcrystalline silicon growth is that crystallites grow at temperatures much lower than the silicon melting temperature. The formation of the crystalline phase at such low temperatures is occuring far from equilibirum and consequently involves dynamical aspects. Current physicochemical models of μc-Si:H growth describe the possible gas phase reactions between silane and hydrogen (such as $H + SiH_4 \rightarrow SiH_3 + H_2$) whose balance determines the atomic hydrogen density. A correlation between a high density of atomic hydrogen and the appearence of crystalline growth has been observed experimentally for a wide range of deposition conditions [25]. The microscopic role of atomic hydrogen is extensively discussed in terms of: (a) etching, where atomic hydrogen selectively etches away amorphous silicon (but does not create the crystalline structure) [47], (b) the surface diffusion model [48], in which exothermic recombination of atomic hydrogen occurs on the surface, which could locally provide sufficient energy for crystallization [49], and (c) the chemical annealing model [50] in which subsurface structural relaxation mediated by permeating atomic hydrogen gives rise to crystallization. Even if these models allow one to predict the necessary physicochemical conditions to be fullfilled for crystallization, they do not allow one to account for the fact that crystal growth can occur here with the peculiar conical microstructure mentioned above.

Models allowing one to simulate the growth of crystalline domains generally treat growth from the point of view of statistical mechanics, but until now no statistical growth model could reproduce the peculiar conical shape of the crystalline domains. Nor could these models explain the observations that growth occurs perpendicular to the local substrate plane and that layer roughness evolution with accumulated layer thickness increases steadily after the occurrence of crystallization.

In order to reproduce the above mentioned characteristic features of μc-Si:H microstructure resulting from the low temperature, out-of-equilibrium growth process, a simple discrete dynamical crystalline growth model inspired from a Potts model was introduced by our group and will now be described. In this numerical model, aimed to simulate the microstructure and roughness evolution of a growing μc-Si:H layer [51,52], each cubic particle falls down a randomly chosen column of the lattice towards the growing surface. Note that here, a particle describes the statisical behavior of several radicals or atomic species contributing to film growth. When the particle reaches the surface, it relaxes to the column of lowest height around the surrounding sites (first neighbors only). The state of this newly arriving growth unit is then chosen according to the following selection rules: the new state will be the state most represented in the neighborhood, provided that the number of similar neighbors is higher than a threshold value, the so-called 'crystalline threshold value'; otherwise, the state of the particle is randomly chosen among all possible states. The state attributed, thus, to each growth unit corresponds to its crystallographic orientation. A crystalline domain is in this way filled with particles in the same state (same 'gray level'), whereas an amorphous domain is filled with particles in different states. In this model, the number of parameters is then reduced to three: the total number of possible states (i.e. of crystallographic orientations), the crystalline threshold value and the etching

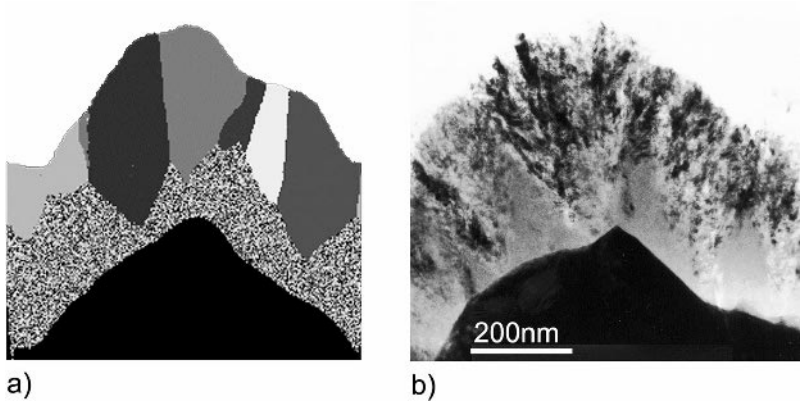

Figure 4.7 a) Cross-sectional view of a simulated microstructure of μc-Si:H and b) typical cross-sectional transmission electron micrograph of a μc-Si:H layer deposited by VHF-PECVD. The main features of the microstructure of μc-Si:H that can be observed on the simulation as well as on the TEM micrograph are: amorphous incubation layer, heterophase layer and conically shaped microcrystalline domains.

probability. The result of the simulation is a discrete representation of the microstructure of the layer that compares directly with TEM micrographs (Figure 4.7). Furthermore, this model permits one to simulate the time evolution of the growing microstructure. This model is the first one that simulates the main features of growth (microstructure and surface roughness evolution) of μc-Si:H from simple selection rules. It shows that growth can be explained in terms of local self assembly of particles ruled by the influence of first neighbors. In this very simple form, the simulation model does not give rise to the appearance of cracks and substructure (nanocrystals) within the conglomerates, but a corresponding extension of the model is now under way.

4.2.2.4 Optical properties

In order to play the role of the main 'photovoltaically active' layer (i.e. 'absorber' and 'photogeneration' layer) in a solar cell, the i-layer has to possess a high optical absorption coefficient in the useful spectral range of solar radiation. For the AM1.5 spectrum, the range containing some 85 % of the total incident energy extends from 1 to 4 eV. Figure 4.8 shows the optical asborption coefficient α as a function of photon energy for three different silicon based materials: monocrystalline silicon (c-Si), hydrogenated amorphous silicon (a-Si:H) and hydrogenated microcrystalline silicon (μc-Si:H). In this figure, the data for μc-Si:H have been corrected in order to suppress the effect of light scattering on the actual measurements, according to [53]. Without this correction, the apparent optical absorption of μc-Si:H is higher than that of monocrystalline silicon. From the corrected curve given in Figure 4.8, one can see that the optical bandgap of μc-Si:H ($\approx$1.1 eV) is pratically identical to the bandgap of monocrystalline silicon. In the weak absorption region (photon energy range below 1.1 eV), apparent, as-measured absorption coefficients are five to ten times higher than the values plotted in Figure 4.8, because of light trapping caused by layer nanoroughness. Such absorption spectra that vary over seven decades can be readily measured in layers deposited on

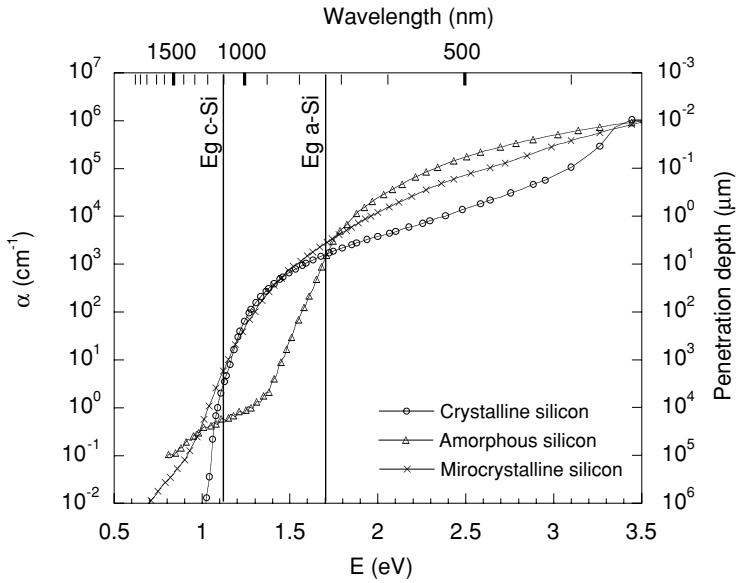

Figure 4.8 Optical absorption spectrum of microcrystalline silicon compared with those of amorphous silicon and monocrystalline silicon. Data taken from [105] Thin Film Silicon and Solar Technology, *Progress in Photovoltaics: Research and Applications,* Vol. 12, A. Shah *et al*., p 113–142. Copyright (2004) John Wiley & Sons Ltd. Reproduced with permission.

glass by combining two measurement methods: in the high absorption range by using transmission/reflection measurements and in the low absorption range by more sensitive techniques such as photothermal deflection spectroscopy (PDS), constant photocurrent spectroscopy (CPM) [54,55] and more recently with the Fourier transform photocurrent spectroscopy (FTPS) technique [56,57]. The latter will be described and discussed in more detail in Section 4.3.

The absorption spectra can be divided into three parts: the high absorption part, where band-to-band electronic excitations are involved. This region of band-to-band absorption is followed by an exponentially decreasing tail towards lower energies. Such an absorption tail is also observed as a function of temperature in c-Si but there it is merely attributed to the effect of thermal disorder [58]. On the other hand, more pronounced exponential absorption tails are observed in disordered semiconductors such as a-Si:H and are there due to the static structural disorder (strained bonds); they are then called Urbach tails. Urbach tails attributed to structural disorder are also observed in μc-Si:H. Urbach tails result from electronic transitions involving bandtail states in the electronic density of states. The measured slope of the Urbach tail is obtained by fitting the data below 1.1 eV in μc-Si:H with a decreasing exponential function whose exponent is called the Urbach parameter. Typically, the values of the Urbach parameter are between 35 meV and 40 meV in device grade μc-Si:H. They are thus lower than the values measured in device grade a-Si:H. As charges stored in the bandtail states can lead to a decrease in the electrical field within the intrinsic layer, a lower Urbach tail value is beneficial for the application of the material in a solar cell and may be one of the reasons why it is possible to implement relatively thick (>2 μm) μc-Si:H solar cells.

In the low photon energy range (photon energy around 0.8 eV), the value of the absorption coefficient is related to the density of defects in the center of the gap, i.e. to defects that are

acting as recombination centers. This absorption value is, thus, characteristic of the material quality used for device applications; indeed recombination within the i-layer is one of the major factors limiting thin film solar cell performance. Typically, device grade μc-Si:H is characterized by a "true" absorption coefficient at $h\nu = 0.8$ eV as low as 0.1–0.3 cm^{-1} (after correction for light scattering) or an as-measured value of 1–3. cm^{-1}. This value is lower than the defectrelated absorption coefficient measured in devicegrade a-Si:H at $h\nu = 1.2$ eV after light induced degradation. One can therefore assume the defect density also to be lower for μc-Si:H intrinsic layers. This is a further reason why thicker μc-Si:H p-i-n diodes are feasible.

The critical step in obtaining absolute FTPS absorption spectra is calibration. Whereas calibration procedures are well known for amorphous silicon, the calibration procedure for microcrystalline silicon is more critical. Because of the natural, as-grown surface roughness, the apparent (i.e. as-measured) absorption coefficient is overestimated due to light scattering. The parameter of the spectrum which is independent of the calibration procedure is the Urbach slope, whereas the defect related absorption coefficient critically depends on the calibration procedure. A convienient way to calibrate the spectrum is to adjust the absorption coefficent of the measured curve for μc-Si:H to the known value of the absorption coefficient value of c-Si at 1.35 eV. Nevertheless, even if one carries out such a calibration, one should be cautious when comparing absolute values of defect related absorption coefficients measured on devices with varying light scattering properties (e.g layers of different thicknesses, or layers deposited on TCO's with varying roughnesses and absorption coefficients).

4.2.2.5 Electronic transport properties

Electronic transport properties are convienently characterized by the mobility × lifetime product (μτ-product) for electrons and holes. This is because the μτ-products appear as physical characteristics of the material properties both in drift and diffusion lengths which, in turn, are involved in the physical description of charge collection within the solar cell devices. In μc-Si:H, the majority carrier μτ-product can be evaluated from the photoconductivity measurement and the minority carrier μτ-product can be evaluated from the steady state photocarrier grating experiment [33,59]; thereby, one has to take care to perform the experiments soon after deposition in order to avoid post-oxidation effects. Both techniques are performed in coplanar geometry, i.e. in a configuration where electronic transport takes place parallel to the substrate, whereas transport within a p-i-n type or n-i-p type solar cell is in a direction orthogonal to the substrate plane. As discussed above, μc-Si:H microstructure is columnar, and anisotropic electronic transport properties have indeed been observed in highly microcrystalline layers with marked columnar growth and cracks; this was shown by determining the μτ-products in the growth direction with the surface photovoltage measurement technique and comparing these μτ-products with those obtained from the coplanar measurements described above [60]. For device grade μc-Si:H that is obtained near the microcrystalline/amorphous transition, we may assume that this anisotropy is small. In the following, the values given for the μτ-products are therefore all measured parallel to the substrate and are taken as an estimation of the physical characteristics of the material as they intervene in the drift controlled collection mechanism prevalent in thin film silicon solar cells. The corresponding values are summarized in Table 4.1.

From this table, one can note that μτ-products for μc-Si:H are of the same order of magnitude as μτ-products for annealed amorphous silicon, which, in turn, is one decade higher than

Table 4.1 $\mu^o\tau^o$ products, computed from σ_{photo} and L_{amb} measurements, of amorphous and microcrystalline silicon layers (thickness 1 to 2 μm) deposited on glass substrates

	Measured $\mu^o\tau^o$ –value [32, 61–63]	Corresponding L_{drift} if $E = 1\,V/\mu m$
a-Si:H (initial state)	2×10^{-7}	20
a-Si:H (degraded state)	2×10^{-8}	2
μc-Si:H	1×10^{-7}	10
Units	cm^2/Vs	μm

μτ-products for degraded amorphous silicon. These μτ-products are much lower than those measured in solar grade 'multisilicon' wafers. Therefore, a p-n diode configuration which is diffusion limited cannot be used for efficient charge collection in a-Si:H or μc-Si:H. Thus, drift assisted devices such as p-i-n or n-i-p cells have generally been used for μc-Si:H solar cells just as has been the case for a-Si:H. Thereby, the internal electric field present in the i-layer assists the charge carrier collection. The values of corresponding drift length for an electric field of 1V/μm are also given in Table 4.1. From these values, one can extrapolate that μc-Si:H solar cells should show satisfactory collection up to a few micrometers i-layer thickness, which is indeed observed [64]. This can be related to the observation [65] that in a μc-Si:H p-i-n solar cell, the electric field can be considered uniform up to i-layer thicknesses of several μm, which can presumably be due to a relatively low defect density (see also Section 4.2.2.3).

A detailed study of the effect of microstructure on the coplanar transport properties [32] has shown that the μτ-product is not affected by the size of the nanocrystals but decreases as the conglomerate size decreases (see Figure 4.9). In these samples, one can note that the value of the ambipolar diffusion length value is approximatively half the value of the conglomerate diameter. This can be expected if the ambipolar diffusion length is limited by recombination at the conglomerate boundaries. According to [66], when microcrystalline silicon no longer consists of conical conglomerates but consists mostly of nanocrystals embedded in an amorphous silicon matrix, such as within the amorphous/microcrystalline transition, then the dark conductivity activation energy (E_{act})is larger than 0.5 eV and electronic transport properties become limited by the size of the nanocrystals and are no longer dependent on the microcrystalline conglomerate size.

4.2.3 Doped layers

Historically, μc-Si:H was first incorporated in devices as high quality doped layers in amorphous silicon solar cells. Indeed, doping in μc-Si:H is more easily achieved than in a-Si:H; by doping one can push the Fermi level nearer to the conduction/valence band in μc-Si:H more easily than in a-Si:H. The dark conductivity activation energy can be taken as a rough estimate for the separation between the Fermi level and the conduction/valence band. In doped a-Si:H, E_{act} hardly ever reaches values below 200 meV, whereas in doped μc-Si:H, E_{act} can readily be below 50 meV, thus leading to doped layers with much higher values of conductivity. For these layers, as well, crystallinity is a critical parameter: here we need high crystallinity in order to reach a high conductivity. In particular, this point is critical for p-doped layers as boron doping and low deposition temperature are sensitive

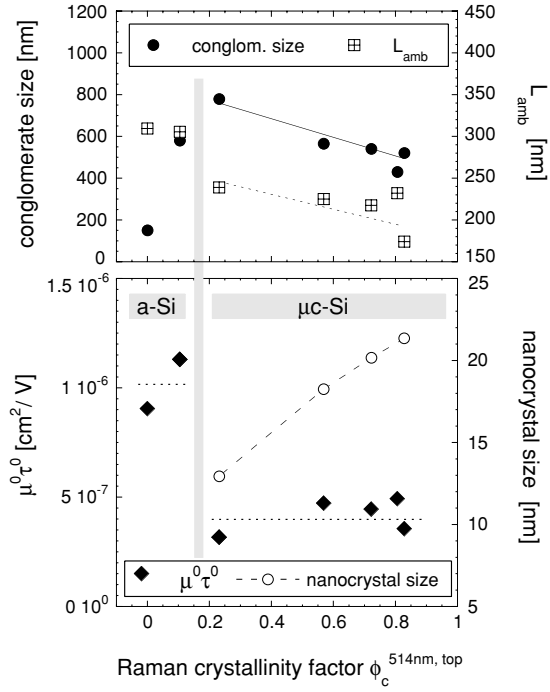

Figure 4.9 Microstructural and transpert properties as a function of Raman crystallinity factor, for a SC series of silicon layers deposited on glass. Top: Conglomerate size (Δ) evaluated from AFM surface topography and ambipolar diffusion length (L_{amb}), with corresponding linear fits (for the μc-Si:H samples); Bottom: mobility × lifetime product ($\mu^0\tau^0$) and nanocrystal size (δ) evaluated from the (220) XRD peaks, as a function of the Raman crystallinity for a SC series of silicon layers deposited on glass. The lines are here merely guides to the eyes. Reproduced with permission from [32] Corinne Droz, Proceedings on the 3rd World Conference in Photovoltaic Energy Conversion Osaka 2003.

parameters that can adversely affect the growth of highly microcrystalline layers. In particular, deposition temperature has been shown to have a rather narrow optimum around 180 °C for maximum crystallinity of diborane doped μc-Si:H layers [31]. The thickness of the p-layer is another critical parameter for high crystallinity. It is indeed difficult to obtain highly crystalline thin p-layers. In general, maximal conductivity is reached for p-layer thickness above 20 nm [31]. Like for i-layers, growth of doped layers is affected by the substrate roughness and chemical nature: on rough LP-CVD ZnO p-layer crystalline growth starts at the top of the substrate's features [67]. Crystallinity of n-doped layers codeposited on various transparent conductive oxides has been observed to depend on the substrate type [34]. This implies that, in practice, doped layers deposition conditions have to be reoptimized whenever the underlying substrate is modified.

4.3 MICROCRYSTALLINE SILICON SOLAR CELLS

Hydrogenated microcrystalline silicon (μc-Si:H) was confirmed as a promising thin film absorber material roughly ten years ago [6]. It became, thus, a complement to hydrogenated

amorphous silicon (a-Si:H) for thin film silicon photovoltaic applications. The main differences between μc-Si:H and a-Si:H as viewed for solar cell applications are:

- The bandgap of μc-Si:H is about that of monocrystalline silicon (≈1.1 eV at room temperature) whereas that of a-Si:H is significantly higher, i.e. around 1.75 eV.
- Because of the crystalline nature of μc-Si:H, its indirect bandgap leads, in the visible range of wavelengths, to lower values of absorption than for a-Si:H; therefore, thicker i-layers (of the order of 1 μm or more) are required in μc-Si:H solar cells; this compares with typical values of 0.3 μm for a-Si:H.
- The light induced degradation effect (or Staebler–Wronski effect [68]) which causes a reduction of the initial efficiency of a-Si:H cells is not present in μc-Si:H (or, rather, is only present in a much milder form than in a-Si:H) (see also Section 4.3.2).

So far, the best μc-Si:H single junction solar cells attain, in the laboratory (as small area test cells), AM1.5 conversion efficiencies of slightly over 10 % [18,69]. Values of the same solar can be achieved today with the best single junction a-Si:H cells after degradation (stabilized efficiency) [70]. The production of commercial single junction μc-Si:H modules is therefore, at the present moment, not an interesting application. Indeed, because of the higher i-layer thickness, the deposition of μc-Si:H solar cells takes much longer than that of a-Si:H solar cells and is therefore more expensive. This may, however, change if single junction μc-Si:H solar cells make further progress in obtaining higher conversion efficiency values. At present, the best way to use μc-Si:H solar cells is in a tandem structure, as a bottom cell together with an a-Si:H top cell; this is the so-called 'micromorph' tandem solar cell (see Section 4.3.3). It can be easily shown [71,72] that the bandgap combination 1.1 eV and 1.75 eV is very near to the ideal 'theoretical' bandgap combination needed to obtain maximum efficiency under AM1.5 illumination, assuming that all photons with an energy above the bandgap are usefully absorbed in the solar cell and that fill factor (FF) and open circuit voltage (V_{oc}) are not too far from ideal theoretical values. The condition of absorbing all photons with energy above the bandgap is far from being fullfilled in micrometer thick μc-Si:H i-layers and therefore light trapping/light managment becomes a key issue. This issue will be dealt with in the next paragraph (Section 4.3.1). Thereafter, in Section 4.3.2, single junction μc-Si:H solar cells will be described, giving their structure, their typical electric characteristics and indications on how one may hope to improve the solar cell performances. Finally, in Section 4.3.3., the authors will give a detailed description (including optoelectrical characteristics) of the micromorph tandem solar cell.

4.3.1 Light management issues

For all thin film silicon solar cells it is essential to keep the cell thickness as low as possible and to increase the effective optical path within the solar cell by proper light management/light trapping schemes. This is already an important issue in a-Si:H solar cells, but is even more important for μc-Si:H solar cells. This is because (as already mentioned), the absorption coefficient is lower (due to the indirect bandgap nature of the optical gap in μc-Si:H) in μc-Si:H as compared with a-Si:H. Furthermore, the deposition rate of μc-Si:H is limited and therefore i-layer thickness and i-layer deposition time are critical cost factors for the mass production of PV modules with μc-Si:H cells. The light management schemes, however, depend very much on the type of substrate chosen. We shall therefore first have a look at the possible substrate choices.

4.3.1.1 Substrates

The choice of the substrate material is essential for the production of low cost photovoltaic modules. To date, the majority of PV thin film module manufacturers use glass substrates coated with transparent conductive oxide (TCO). Commercial TCO producers provide TCO on inexpensive soda-lime glass for minimum cost. However, higher conversion efficiencies are obtained with more expensive, low iron content glass, which, due to its lower absorption in the red and near infrared, allows one to exploit in a better way the extended long wavelength response of μc-Si:H solar cells. With such fully transparent substrate and contact layers, the device structure for thin film silicon solar cells is a p-i-n stack, into which light enters through the p-player (see Figure 4.10). This configuration is called the 'superstrate' configuration. In this configuration, light trapping within the silicon based device is achieved by using rough TCO layers, i.e. by having a rough TCO-p μc-Si:H interface. This effect will be discussed in more detail in Section 4.3.1.2, where we will deal more specifically with TCO properties. On the other hand, in the superstrate configuration, the glass substrate plays the role of cover in the encapsulation scheme. Although breakable and relatively heavy, a glass substrate offers excellent protection against the damaging influence of weather, guaranteeing, thus, the long term outdoor stability of the module.

Another well established substrate option is the use of stainless steel. This option lends itself to roll-to-roll processing. So far, however, it does not allow for an integrated series connection of individual cells to form a whole monolithic module, which otherwise is an attractive feature of thin film PV technology. The use of a nonconductive flexible substrate such as plastic for the development of low weight, unbreakable modules is a current research topic [72–74]. The performances of laboratory μc-Si:H single junction cells on plastic substrates are starting to reach values comparable with those initally obtained for μc-Si:H cells deposited on TCO coated glass. The device structure used on all opaque (or UV degradable) substrates is a n-i-p stack, where light enters the device from the p side. In this case, the p-layer is the last semiconductor layer deposited during the deposition sequence of the device. It is followed by a top TCO layer (indium tin oxide (ITO) or ZnO) and by the encapsulation (protecting layer). In general, the

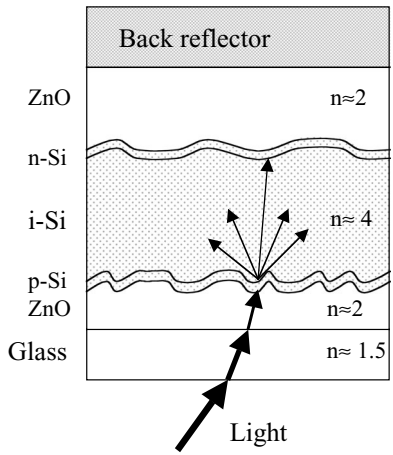

Figure 4.10 Schematic device structure for a single junction μc-Si:H p-i-n solar cell.

n-i-p, or 'substrate' configuration allows one to exploit the whole versatility in the choice of substrate types as allowed by the low temperatures of the PECVD deposition process. On the other hand, in this configuration, one of the main cost factors is the top protective foil that has to be transparent and UV resistant and provide long term stability. Obtaining a low cost solution here is still very much a research and development topic.

In the 'substrate' (i.e. n-i-p type) configuration schemes for efficient light trapping into the silicon based layers can be obtained by tailoring the back reflector's roughness. This is often achieved either by texturing the substrate itself [75] or by using a textured layer directly above the substrate. In n-i-p-type μc-Si:H solar cells, one can use e.g. random metallic reflectors (such as hot silver [76]) or periodic optical gratings with specifically tuned broadband reflectivity [75]. The conformally grown TCO layer deposited on top of the metallic reflector or on top of the optical grating takes on the back reflector's topography and thus light scattering is obtained at the μc-Si:H/TCO interface. One of the main advantages of the substrate (or n-i-p) configuration is that texturing for light trapping is done at the bottom of the solar cell, i.e. before the deposition sequence of the silicon based layers, and offers, therefore, more flexibility in the choice of structuration methods and substrate materials.

4.3.1.2 Transparent Conductive oxides

Transparent conductive oxide layers are used in both superstrate and substrate configurations, and are, in general, located both on the front side (where light enters into the solar cell), where they consitute transparent contacts, as well as on the back side (just before the back reflector), where they are employed in order to improve the optical properties (refractive index matching) and as diffusion barrier.

The various requirements for TCO layers in microcrystalline silicon solar cells are summarized in Table 4.2.

The most stringent requirements on TCO layers come to bear on front TCO layers in the superstrate configuration, so we will center the discussion in the present section on this specific case.

All front TCO layers have to fullfill the following two requirements:

(1) High transparency for the whole useful spectral range, so as to minimize optical losses (absorption and/or reflection) (typically the average absorbance between 400 nm–1100 nm should be below 6–7 %)

(2) High conductivity, so as to constitute a low value of series resistance for the solar cell (typically, the sheet resistance should not be larger than about 10 Ω sq).

Furthermore, for the front TCO layers in the superstrate configuration, the following two additional requirements have to be fulfilled:

- Excellent light scattering capability through surface roughness.
- Chemical stability with respect to subsequent deposition of silicon layers by PECVD. Basically, there are three materials commonly suggested as TCO layers for solar cell applications: Indium tin oxide (ITO), tin oxide (SnO_2) and zinc oxide (ZnO).

Table 4.2 Summary of the physical properties required for front and back TCO layers incorporated as contact/reflector layers in the p-i-n type (superstrate configuration) or n-i-p type (substrate configuration) of μc-Si:H based solar cells

	Front TCO	Back TCO
p-i-n type (superstrate)	Low sheet resistance ($<10\ \Omega_{sq}$)	Low sheet resistance if the reflector is nonconductive.
	High optical transmission in the range 350–1100 nm.	Sheet resistance not limiting if conductive back reflector conducting.
	High surface roughness, while fulfilling above requirements (typically rms 50–200 nm).	High optical transmission (>80 %) in the range 650–1100 nm for single junction μc-Si:H solar cell, range 650–1100 nm for tandem micromorph solar cell.
n-i-p-type (substrate)	Low sheet resistance ($<10\ \Omega_{sq}$)	Low sheet resistance ($<10\ \Omega_{sq}$) if non.conductive reflector. Not a limiting factor if conductive reflector.
	High optical transmission (>80 %) in the range 350–1100 nm	High optical transmission (>80 %) in the range 650–1100 nm for single junction μc-Si:H solar cells, in the range 650–1100 nm for micromorph tandems.
	Surface nanoroughness: not a limiting factor (roughness partly given by the μc-Si:H layers)	Surface roughness not limiting: use back reflector texture or substrate texture.

Indium tin oxide is a TCO that very effectively fulfills both conditions (1) and (2) and it is indeed used as front contact for substrate (n-i-p type) μc-Si:H solar cells [10]. However, ITO does not remain stable within a silane plasma, and is therefore certainly excluded as front TCO for glass superstrate (p-i-n type) μc-Si:H solar cells; indeed the deposition of the silicon based layers on top of an ITO layer invariably leads to serious problems with indium diffusion and lifetime reduction in the silicon layers.

Tin oxide is another commonly used TCO. Glass coated with fluorine doped SnO_2 is indeed available on a commercial basis. It is regularly used as front TCO for a-Si:H solar cells and modules. Here, the surface roughness of the SnO_2:F layer is instrumental in obtaining good light scattering/light trapping performances. However, SnO_2:F cannot be directly used as front TCO for superstrate type μc-Si:H solar cells, because subsequent microcrystalline silicon layer deposition requires a hydrogen rich plasma that chemically partly reduces the oxide layer and affects its transparency. Some laboratories have, however, used SnO_2:F layers covered with a thin layer of ZnO [77] or of TiO_2 [78] as front TCO for μc-Si:H solar cells.

Our own laboratory has concentrated on the use of zinc oxide (ZnO) as TCO layer for a-Si:H and μc-Si:H solar cells. In fact, ZnO is an abundant and nontoxic material that can be easily deposited at low temperatures, is a good diffusion barrier and is not reduced by exposure to

a subsequent hydrogen rich plasma. Zinc oxide can be convienently deposited by sputtering or by low pressure chemical vapor deposition (LP-CVD). Sputtered aluminium doped ZnO is basically flat and, thus does not possess, as deposited, the light scattering properties needed in the solar cell front TCO. However, surface nanotexturing can be obtained, in a second step, by chemical wet etching, allowing one, thereby, to obtain the necessary light scattering properties. For a complete and recent review of sputtered, post etched ZnO:Al, the reader is referred to [79].

On the other hand, ZnO deposited by LP-CVD has several distinct advantages [80,81]. Low pressure CVD is basically a very simple process and upscaling up to 1 m^2 is easily achievable, with deposition rates over 2 nm/s. Zinc oxide grown by this technique has a high as-grown texturing, resulting from a highly marked (110) crystallographic preferential columnar growth. The resulting surface topography of a ZnO layer deposited by LP-CVD is shown in Figure 4.11, with a cross-sectional view displaying the columnar microstructure of a typical 1 μm thick layer. A typical optical transmission spectrum of such a ZnO layer is given in Figure 4.12. In the short wavelength region, transmission is limited by the optical bandgap of ZnO (3.2 eV). In the near infrared, transmission decreases due to free carrier absorption. For the application of ZnO as a front contact, an optimum compromise between ZnO sheet resistance and optical transmission has to be found. Sheet resistance is given by the specific resistivity of the layer divided by the layer thickness. By increasing the layer thickness, one decreases the sheet resistance, but also increases optical absorption. In order to minimize the sheet resistance, the layer resistivity has to be minimized. This should be achieved by increasing carrier mobility in the TCO rather than by raising carrier density, as the latter also enhances the optical absorption in the near infrared range. Thus, high mobility TCO's are currently an important field of research and development. They are specially important for μc-Si:H solar cells, where the useful spectral range extends into the near infrared. To achieve high mobility TCO, one must not only try to improve the ZnO layers, but also try out novel combinations of TCO layer materials [82].

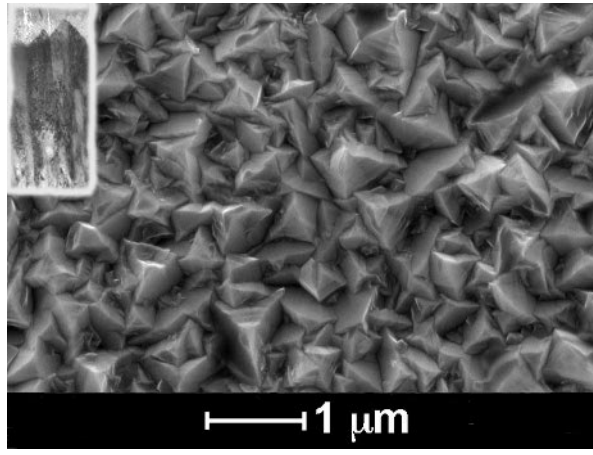

Figure 4.11 Scanning electron micrograph of the surface topography of LP-CVD ZnO. A dark field transmission electron micrograph of the layer is shown in inset; both micrographs are at the same scale. The inset shows that each pyramid emerging at the surface consists of a single crystallite of ZnO.

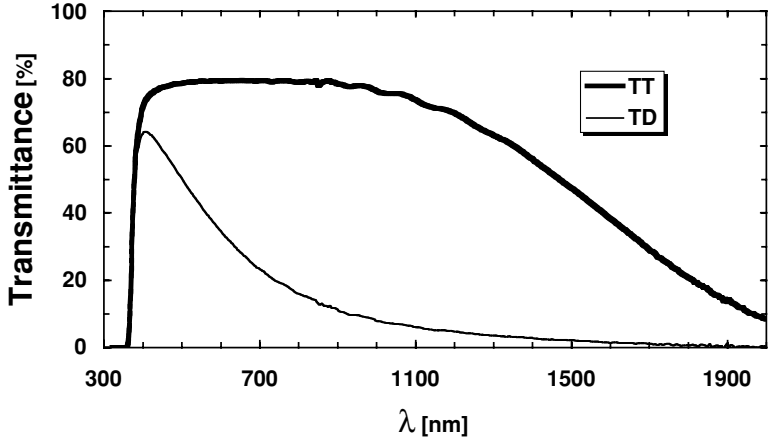

Figure 4.12 Typical total transmittance (TT) and diffuse transmittance (TD) curves of LP-CVD ZnO layers as used for photovoltaic applications.

Light managment in the superstrate (p-i-n type) configuration depends in two ways on the TCO p-layer interface roughness. Optically, a rough interface between a low refractive index material ($n_{ZnO} \approx 2$) and a high refractive index material ($n_{Si} \approx 3.7$) results in reduced reflection due to gradual refractive index matching (the effective refraction index being then given by the volume fraction across the interface). This effect applies to the entire wavelength range of the spectral response of the cell. In order to increase this effect, rather high rms values of surface roughness are needed. The second effect of a rough TCO-p interface is light trapping into the silicon layer; by diffusively transmitting some of the incoming light into the silicon layer at an angle smaller than the total reflection angle, light is trapped into the silicon based layer and its optical path is, thus, increased. This effect is important for weakly absorbed light (800 nm to 1100 nm) that has to be as well reflected at the back contact of the device. In this case, back and forth scattering at the interfaces can result typically in a four to five fold increase in the optical path within the silicon layer. For even more efficient light managment in μc-Si:H devices, a precise knowledge of the optimal TCO rms roughness and geometry (optimal feature shape at the TCO surface and optimal feature dimensions) is as yet still lacking. However, numerical simulations allow one at least to predict the effect of incorporating a given TCO on the spectral response curve and on the short circuit current density J_{sc} of μc-Si:H solar cells [83]. In general, one can say that higher surface roughness gives higher J_{sc} values. On the other hand, there are indications [46] that TCO layers with too high roughness values and with steep slopes may lead to reduced V_{oc} and FF values for μc-Si:H solar cells. Thus, a lot of further research is needed in the field of TCO optimization for single junction μc-Si:H solar cells.

4.3.2 Single junction microcrystalline silicon solar cells

Single junction microcrystalline solar cells have been fabricated, first by our laboratory and, subsequently, by many other laboratories in the p-i-n type and n-i-p type configurations with

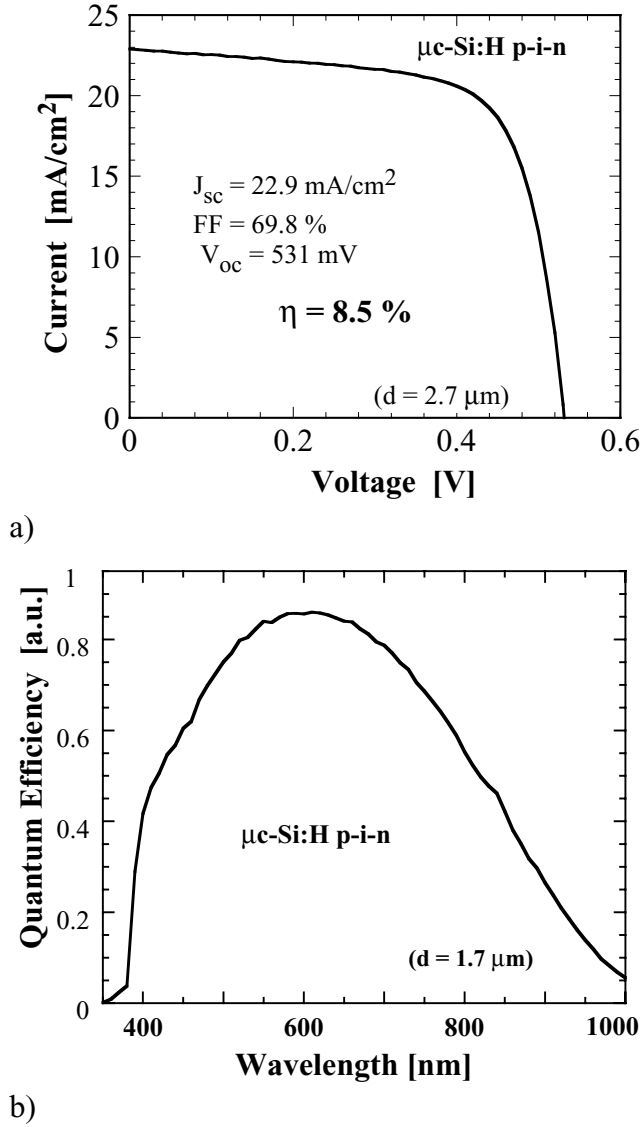

Figure 4.13 a) Typical $I(V)$ curve and b) external quantum efficiency of μc-Si:H single.junction solar cells deposited on LP-CVD ZnO layers. Note that the i-layer thickness is not the same on both graphs. Data reproduced from [105] Thin Film Silicon and Solar Technology, *Progress in Photovoltaics: Research and Applications,* Vol. 12, A. Shah *et al*., p 113–142. Copyright (2004) John Wiley & Sons Ltd. Reproduced with permission.

conversion efficiencies in the range of 8 to 10 % [18,69,84]. Typical p-i-n type cell structure is shown in Figure 4.10. Figure 4.13 (a) represents the $I(V)$ curve and Figure 4.13 (b) the external quantum efficiency curve of a typical p-i-n type single junction μc-Si:H solar cell with an AM1.5 efficiency of 8.5 % [84]. Here, LP-CVD ZnO was used as TCO. It has been

shown that the cells with the best efficiencies are fabricated with i-layers deposited near the a-Si:H/μc-Si:H transition, i.e. with i-layers that contain a substantial amount of amorphous tissue, but are still in the microcrystalline regime [23,85]. In this deposition regime, the open circuit voltage (V_{oc}) increases substantially with increasing silane concentration [8,84]. This effect is attributed to the variation in i-layer crystallinity: a linear relationship between V_{oc} and the average Raman crystallinity of p-i-n type and n-i-p type devices has indeed been observed [44]. Best μc-Si:H cells have V_{oc} values around 530 mV to 550 mV; although record values approaching 600 mV [23] for cells that still show microcrystalline type behaviour in their quantum efficiency curves have indeed been reported. The fundamental process determining V_{oc} is recombination within the i-layer. The measurement of the i-layer quality (recombination center density) within fully operating devices is a challenging task; the recently developed FTPS technique allows for the measurement of the defect-related absorption of the i-layer as incorporated into entire p-i-n type and and n-i-p type devices. In this experiment, the solar cell is used as an external photodetector (see Figure 4.14) and its absorption spectra is obtained by calibration with the internal detector of the FT-IR spectrometer [56,57]. Thus, the absorption coefficient within the i-layer can be measured for photon energies well below the bandgap. In μc-Si:H, the absorption coefficient at photon energies of 0.8 eV is taken as an estimate for the recombination center (dangling bond) density [57]. The principal reason for obtaining high values of V_{oc} near the μc-Si:H/a:Si:H transition appears to be the passivating effect of the amorphous material on grain boundaries and internal surfaces; this is documented, as shown in Figure 4.15, by a corresponding decrease in i-layer defect-related absorption coefficient (i.e recombination center density) evaluated at 0.8 eV by the FTPS method [86]. In principle, it should be possible to obtain, with μc-Si:H, similar V_{oc} values as with crystalline silicon wafer based cells, i.e. around 700 mV; however, in practice this is certainly unrealistic, because of the higher defect density and higher recombination losses always present in microcrystalline

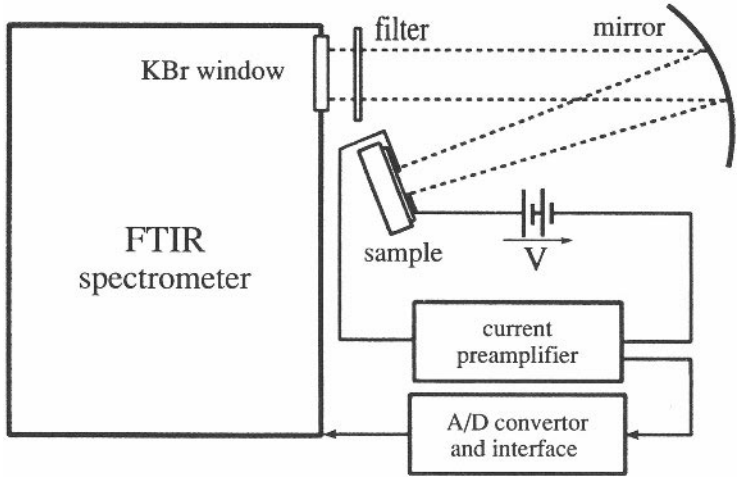

Figure 4.14 Schematic set-up of the Fourier transform photocurrent spectroscopy (FTPS). Reused with permission from M. Vanecek and A. Poruba, Applied Physics Letters, 80, 719 (2002). Copyright 2002, American Institute of Physics.

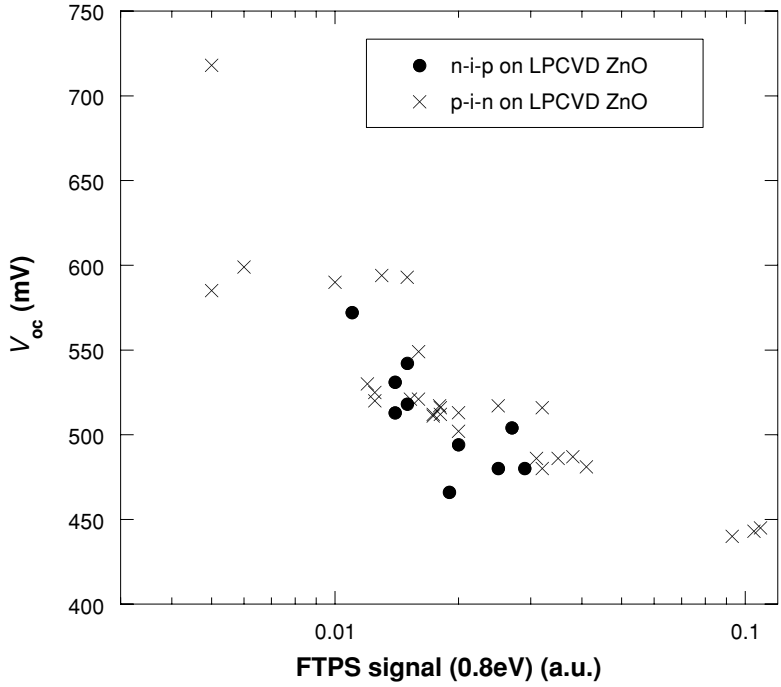

Figure 4.15 Open circuit voltage V_{oc} of a large number of p-i-n and n-i-p μc-Si:H single junction solar cells as a function of the defect-related absorption coefficient at 0.8 eV as measured by FTPS.

material due to the grain boundaries (even if they are well passivated), and also because in the p-i-n type (or n-i-p type) structure, the internal electric field that allows for drift assisted collection is severely reduced as open circuit conditions are approached, causing even further recombination losses that limit the values of V_{oc}.

The fill factors (FF) of state-of-the-art μc-Si:H solar cells are generally around 70 %. Values approaching 77 % have been achieved for individual record cells [69], and values above 70 % are also reported for solar cells with very thin i-layers [23]. On the other hand, shunts and other technological problems easily reduce the FF to values below 60 %, this being invariably a signal for a major problem within the whole cell fabrication process.

The largest spread of values reported, as well as the largest uncertainty, in all electrical solar cell parameters is related to the short circuit current density J_{sc}. Generally, in solar cells where the i-layer thickness is kept constant and is fabricated with varying silane dilution, J_{sc} remains nearly constant in the μc-Si:H regime and decreases abruptly at the transition into the amorphous regime [23,87]. Values of J_{sc} up to 30mA/cm^2 [88,89] have been mentioned, whereas most published values lie around 20–25 mA/cm^2[23,69,90]. In order to obtain reliable J_{sc} values, the μc-Si:H solar cell has to be properly structured, so as to avoid lateral collection; furthermore, a well calibrated AM1.5 spectrum is mandatory for measuring the $J(V)$ characteristics and assessing J_{sc}. Besides these technical aspects that may account for the uncertainty in some of the published values, J_{sc} also critically depends on i-layer thickness [23] and on light management schemes (see Section 4.3.1) and these vary considerably from laboratory to

laboratory. On the other hand, J_{sc} probably also holds the greatest scope for contributing to a further increase in μc-Si:H cell efficiency, provided the whole light management scheme can be systematically optimized.

In the early stages of development, the i-layers in single junction μc-Si:H solar cells were highly crystalline, as they were deposited under conditions rather far from the a-Si:H/μc-Si:H transition; under these conditions, they were shown to be stable with respect to light induced degradation [6,91]. More recent studies on series of solar cells with i-layers of varying crystallinity show, however, that cells deposited close to the transition do indeed suffer from a mild form of light induced degradation if they are exposed to the whole AM1.5 light spectra [92,93]. On the other hand, μc-Si:H solar cells are fully stable when exposed to red light only [94]. These studies report that solar cells with lower crystallinity have a stronger light induced degradation effect; this fact may suggest that the observed light induced degradation is due to the degradation of the amorphous tissue within μc-Si:H layers [92,94]. Typically, 2 μm thick solar cells deposited near the transition show a relative decrease in efficiency of about 5 to 10 % after 1000 h of light soaking with 100 mW/cm^2 AM1.5 like light at 50 °C [93]. This decrease is mainly due to a decrease in FF and partly also to a reduction of J_{sc}. The degradation of solar cell performances is accompanied by a corresponding increase, by a factor of about two, in defect-related absorption, as measured by the FTPS method. Even if cells with higher i-layer crystallinity remain practically stable, their defect related absorption is higher than those of degraded cells deposited closer to the a-Si:H/μc-Si:H transition (see Figure 4.16). The observation of light-induced degradation in μc-Si:H raises important questions for further research: what is the exact mechanism of light-induced degradation? Does the extent of degradation depend on factors other than i-layer crystallinity? It should, however, be immediately mentioned that light-induced degradation of the μc-Si:H bottom cell in an amorphous/microcrystalline

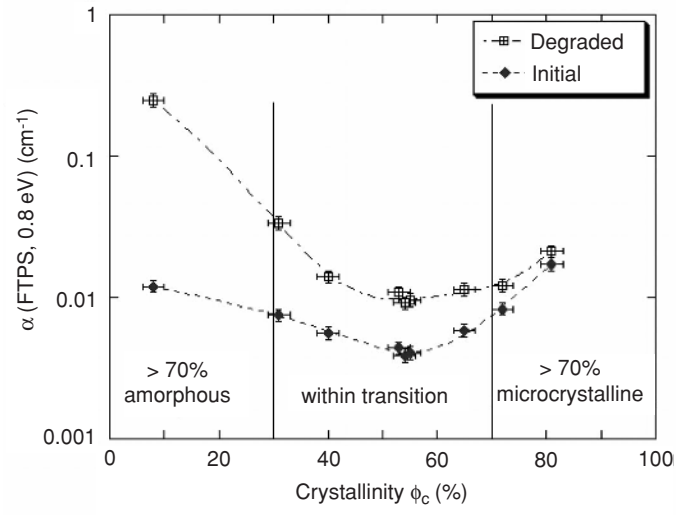

Figure 4.16 Defect related absorption in initial and degraded state (AM1.5-like spectrum, 100 mW/cm^2, 1000h at 50 °C) for a series of p-i-n type single-junction μc-Si:H solar cells with varying Raman crystallinity ϕ_c of the i-layer. Reproduced from [93] F. Meillaud *et al*. Proceedings of the 31st IEEE photovoltaic specialist conference. P. 1412–1415, Copyright (2005) IEEE.

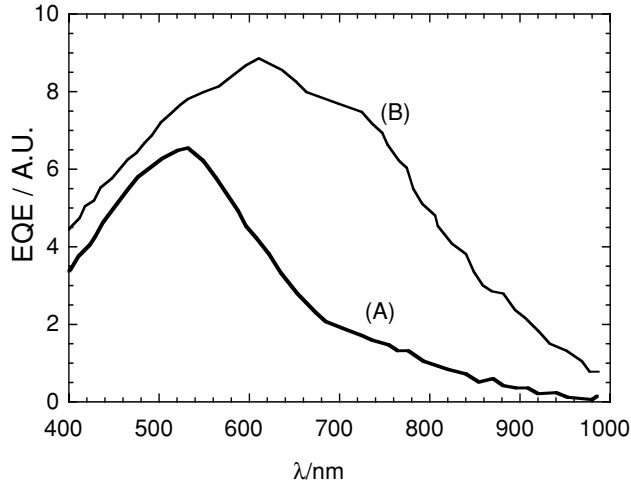

Figure 4.17 External quantum efficiency curve for single-junction μc-Si:H solar cells effect of oxygen contamination in the i-layer. Curve A: without source gas purifier. Curve B: with source gas purifier. Reused with permission from P. Torres, J. Meir, R. Fluckiger, U. Kroll, J. A. Anna Selvan, H. Keppner, A. Shah, S. D. Littelwood, I. E. Kelly, and P. Giannoules, Applied Physics Letters, **69**, 1373 (1996). Copyright 1996, American Institute of Physics.

(or 'micromorph') tandem cell so far plays only a minor role (if it is at all observable), because high energy photons are definitively absorbed in the amorphous top cell.

In order to obtain high enough external quantum efficiency in μc-Si:H solar cells in the long wavelength range, a necessary condition is a low level of contaminants which can act as dopants within the i-layer. Any dopant like contaminant will reduce the internal electric field, which is responsible for the collection of carriers within the whole i-layer thickness, resulting in a loss of quantum efficiency, possibly over the whole wavelength range [95]. Oxygen is easily incorporated into plasma-deposited layers through contamination of the feedstock gases and from the reactor walls [96]. Oxygen can act as a donor in silicon, and will therefore cause a reduction in the electric field in the entire i-layer. This will affect the external quantum efficiency curve, especially in the long wavelength part of the spectrum (see Figure 4.17). Boron, which is used for the deposition of the first deposited p-layer in p-i-n type solar cells, may contaminate the initial part of the i-layer, especially if deposition temperature its is higher than 200 °C [97] or if the deposition of the subsequent layer is carried out directly in a single chamber system without further precautions. Boron contamination will affect the quantum efficiency curve in the short wavelength region, and will also limit values of V_{oc} and FF.

4.3.3 Tandem amorphous/microcrystalline silicon solar cells: the micromorph concept

In order to achieve a substantial increase in efficiency for thin film silicon solar cells deposited at low temperatures, the use of stacked double and triple junction structures, in which multiple

cells with different optical bandgaps are stacked together, is basically one of the most interesting approaches. Conceptually, the advantages of this approach are the following: (a) it is possible to combine materials with different bandgaps so that the incoming light is used more efficiently, (b) it is possible to obtain a higher open circuit voltage and, at the same time, work with lower current densities, so that the problems for electrical series resistance are relatively reduced, and (c) it is possible to reduce light induced degradation by the use of a 'thin' amorphous top cell.

Tandem and multijunction solar cells with photogeneration layers based on amorphous silicon as well as on amorphous silicon/germanium (a-Si,Ge:H) alloys have been studied since the 80s and are now commercially produced by various companies. See Chapter 5 of this volume for more details. Two main problems are encountered with this approach: (a) a basic difficulty in making device grade a-Si:Ge:H intrinisc layers with a good stability and a bandgap lower than 1.5 eV [98,99] and (b) the relatively high cost of germane (GeH_2) source gas. The introduction of hydrogenated microcrystalline silicon as an efficient photogeneration layer having a bandgap as low as 1.1 eV thus opened up the possibility for a microcrystalline/amorphous silicon tandem solar cell, also called the 'micromorph' tandem [100], and known in Japan as the 'hybrid' cell [69]. This novel tandem concept provides a new avenue of R&D, where one can hope to reach higher conversion efficiencies and lower production costs.

Indeed, from very elementary theoretical considerations one could consider the bandgap combination of 1.1 eV with 1.75 eV to be very near the ideal combination for tandem solar cells [71]. If we assume that all photons with an energy higher than the bandgap can be usefully absorbed both in the top and bottom cells, and if we assume reasonable values for *FF* and V_{oc} based on bandgaps and on a p-i-n type structure (see [72] for details), we arrive at the semi-theroetical efficiency limits shown in the diagram in Figure 4.18. From Figure 4.18 one

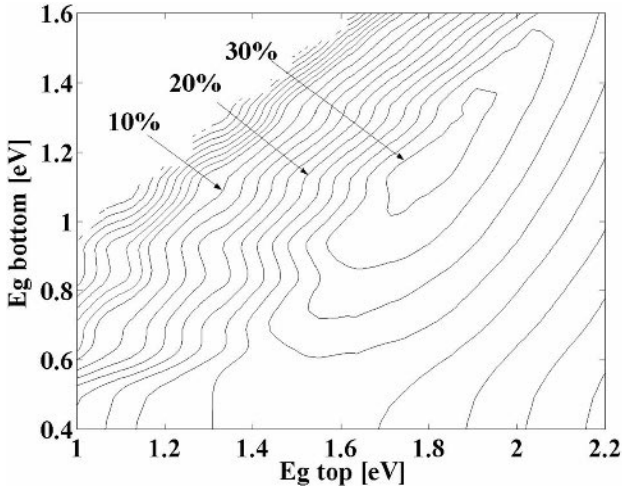

Figure 4.18 Semi-empirical limit of the efficiency as a function of the energy gap E_g of the bottom and top cells of a tandem solar cell, based on an assumed minimum value for the reverse saturation current of a p-i-n type diode. All AM1.5 light with photon energies above the bandgap energy is assumed to be usefully absorbed and to contribute to the short circuit current density J_{sc}. Reprinted from [72] *Journal of Non-Crystalline Solids*, Vol. 338–340, Shah *et al*., Basic efficiency limits. . . , p. 693–645. Copyright (2004) with permission from Elsevier.

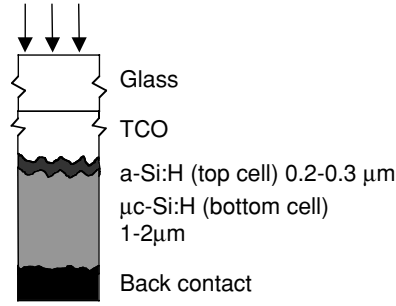

Figure 4.19 Schematic device structure of the micromorph tandem cell in the 'superstrate' configuration, i.e. in the configuration glass/TCO/p-i-n a-Si:H/p-i-n μc-Si:H.

can indeed deduce that the ideal bandgap combination is close to 1.1 eV for the bottom cell and 1.75 eV for the top cell. In practice, the photogeneration layer thickness (i-layer thickness) of the first and second cell should be designed in such a way that the photogenerated currents are the same in both cells, so as to obtain current matching, in accordance with the current continuity law. As μc-Si:H is a material with an indirect bandgap (see Figure 4.8) the optical absorption coefficient for energies just above the bandgap is relatively low. This means that in a micromorph tandem, the microcrystalline bottom cell will have to be thicker than the amorphous top cell in order to obtain current matching conditions. Figure 4.19 shows a sketch of the typical structure of a micromorph tandem solar cell. With this configuration, one is, in practice, still very far away from usefully absorbing all photons with an energy higher than the bandgap energy. This is because one is forced to use relatively thin absorbing layers: around 0.25 μm for the a-Si:H top cell because of the Staebler–Wronski effect or light induced degradation, and around 1 to 2 μm for the microcrystalline bottom cell, because of deposition time and its relatively large contribution to fabrication costs. Due to these constraints, stabilized efficiencies currently obtained for small area micromorph test cells (1cm^2 size) are in the range of 11–12 %. Figures 4.20 and 4.21 show typical $I(V)$ [101] and quantum efficiency curves obtained with such a tandem structure in our laboratory.

Industrially, the first 'micromorph' or 'hybrid' modules have been brought out by Kaneka Corp. of Japan. They have stabilized efficiencies over 8 % and are commercially available in Japan. For test purposes, large area modules of 0.41 m^2 size with initial average efficiencies in the range of 11 % and with a confirmed highest initial module efficiency of 12.5 % have been fabricated by this company.

In Figure 4.20, we can see the effect of light induced degradation on a micromorph tandem with a high initial efficiency (over 12 %) combined with a high open-cricuit voltage of 1.4 V. After light soaking, a stabilized efficiency of 10.8 % could be obtained. In this configuration, the degradation of the tandem is due only to the Staebler–Wronski effect in the amorphous top cell, whereas the microcrystalline bottom cell within the tandem shows no degradation at all (even if its i-layer has been deposited near the microcrystalline/amorphous transition). To date and to the authors' knowledge, light induced degradation of the microcrystalline bottom cell of a micromorph tandem has so far never been observed. The reason is probably that the bottom cell is not exposed to the whole AM1.5 spectrum, but mainly to the red and infrared parts of the spectrum, i.e. to those parts which are transmitted through the amorphous top cell.

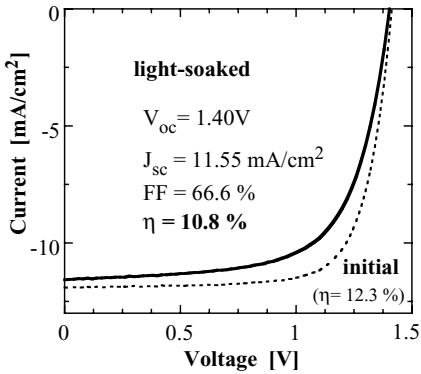

Figure 4.20 $I(V)$ curve of a 'micromorph' p-i-n type a-Si:H/μc-Si:H tandem cell, as fabricated by IMT Neuchâtel, both in the initial and light soaked state (after 336 h under AM1.5 like spectra, 100 mW/cm^2 and 50 °C). Data reproduced from [105] Thin Film Silicon and Solar Technology, *Progress in Photovoltaics: Research and Applications,* Vol. 12, A. Shah *et al*., p 113–142. Copyright (2004) John Wiley & Sons Ltd. Reproduced with permission.

Even so there is, at present, a significant difference for the micromorph tandem between the values reported for initial efficiencies (over 14 %) and those reported for stabilized efficiencies (11–12 %). In order to reduce degradation in a micromorph tandem, two options can be chosen:

(1) One can use a bottom limited tandem, i.e. a tandem in which the short circuit current density is lower in the microcrystalline bottom cell than in the amorphous top cell. In such a case, the properties of the tandem cell are governed by the limiting cell: the tandem is more stable, but also has a relatively high temperature coefficient, i.e. a significant loss of efficiency at high operating temperatures.

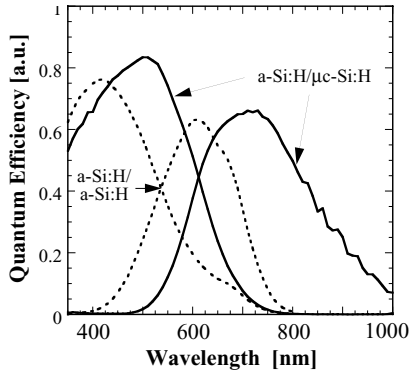

Figure 4.21 External quantum efficiency curve of a 'micromorph' tandem p-i-n type solar cell, compared with that of a a-Si:H/a-Si:H tandem p-i-n type solar cell. Note the extended long wavelength spectral response of the 'micromorph' cell. Data reproduced from [105] Thin Film Silicon and Solar Technology, *Progress in Photovoltaics: Research and Applications,* Vol. 12, A. Shah *et al*., p 113–142. Copyright (2004) John Wiley & Sons Ltd. Reproduced with permission.

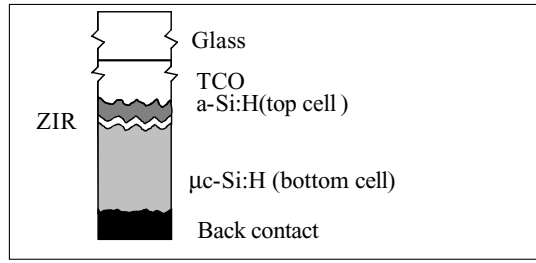

Figure 4.22 Schematic device structure of the 'micromorph' tandem cell in the 'superstrate' configuration with a ZnO intermediate reflector (ZIR) i.e. with the configuration glass/TCO/p-i-n a-Si:H/ZnO/p-i-n μc-Si:H.

(2) One can use a very thin amorphous silicon top cell (i.e. a cell with an i-layer thickness below 0.2 μm). Such very thin amorphous top cells hardly degrade, they also have low temperature coefficients, i.e. little loss of efficiency at high operating temperatures [27]. However, in the simple tandem configuration sketched in Figure 4.19, such a very thin amorphous silicon top cell will only provide a very low short circuit current density and limit the tandem too severely. This is because in the simplest configuration no effective light trapping is achieved within the amorphous top cell. For this reason, our Institute introduced an intermediate optical reflector (constituted of a ZnO layer) between the top and the bottom cell [102]. This structure and results obtained will be described in more details below.

Figure 4.22 shows a schematic sketch of a tandem cell with an intermediate reflector. This type of tandem is technologically more complicated to produce, both in the laboratory and especially industrially, but it represents one of the most promising avenues for further increasing the stabilized efficiencies in micromorph tandem cells. In this approach, the total micromorph current can be increased by increasing the top a-Si:H current (thanks to light reflection at the a-Si:H/ZnO interface) without increasing its thickness; thereby maintaining a acceptable device stability in the top a-Si:H cell. With this structure, IMT fabricated a fully stable laboratory cell with 10.8 % efficiency [101]. With the same structure, Kaneka fabricated a laboratory tandem cell with 14.7 % initial efficiency [69]. The optical behavior and the photogenerated current of such tandem micromorph cells incorporating an intermediate ZnO reflector has been simulated numerically with a Monte Carlo approach, based on measured absorption data for the amorphous and microcrystalline silicon layers. Assuming TCO and doped layers with reduced absorption as well as an ideal back reflector, a stabilized efficiency of 15 % is predicted [103]. A more recent simulation based on actual absorption data for ZnO and doped layers arrives at a stabilized short circuit current density of 14 mA/cm^2 which may translate into 13 to 14 % stabilized efficiency [76].

4.4 CONCLUSIONS

Microcrystalline silicon is a material that has only recently been introduced for use as photogeneration layers (intrinsic i-layer) in thin film silicon solar cells of p-i-n and n-i-p types.

The development of devices with higher conversion efficiencies incorporating μc-Si:H is, thus, still a research topic. Microcrystalline silicon is generally deposited with the same PE-CVD equipment as a-Si:H, by using a mixture of silane and hydrogen, and by increasing the ratio of hydrogen to silane in the feed gas, so as to obtain microcrystalline growth. This technology has the advantage of using non-toxic materials and of being based on low temperature processes; it also easily allows for large area deposition. It has, therefore the clear potential for future cost reduction of photovoltaic modules.

Microcrystalline silicon is a complex material consisting of conglomerates of silicon nanocrystallites embedded into amorphous silicon. It can be more easily doped than a-Si:H; but, on the other hand, it is also more sensitive to contaminants than a-Si:H. The nucleation and growth of μc-Si:H are determinant for device quality; a certain amount of amorphous material is needed for the passivation of the nanocrystallites and for the reduction of defect related absorption. This is obtained by reducing the hydrogen dilution so as to approach the microcrystalline/amorphous transition. Solar cells (p-i-n and n-i-p type diodes) produced with intrinsic i-layers with increasing amorphous volume fraction have, indeed, increasing values of V_{oc}.

The optical properties of μc-Si:H are quite different from those of a-Si:H; indeed μc-Si:H possesses an indirect optical bandgap at 1.1 eV and has, thus, relatively low optical absorption for higher photon energies ($h\nu > 1.1$. eV) whereas a-Si:H has a bandgap of about 1.75 eV and higher optical absorption for photon energies above the bandgap ($h\nu > 1.75$ eV), as is characteristic for amorphous semiconductors. On the other hand, μc-Si:H absorption spectra exhibit, for photon energies below the bandgap, features that are characteristic of a certain amount of disorder prevailing in the material, such as an Urbach tail and defect related absorption at about 0.8 eV. These features are absent in the absorption spectra of monocrystalline silicon (wafers). The optical features can be measured by specialized methods like Fourier transform photocurrent spectroscopy (FTPS) and are used in order to assess material quality for photovoltaic applications.

Coplanar electronic transport properties of μc-Si:H are strikingly similar to those characteristic of a-Si:H and this resemblance can be understood by assuming that electronic transport is limited by the amorphous/disordered material present in μc-Si:H layers. Because of the limited electronic transport properties and the resulting limitation in diffusion length, a p-i-n type or n-i-p type device structure is used for μc-Si:H solar cells. In this type of device, carrier collection is enhanced by drift, i.e. by the internal electric field prevailing in the i-layer. Currently, the conversion efficiency of the best single junction μc-Si:H solar cell is around 10 %. Single junction μc-Si:H solar cells show a very mild form of light induced degration, depending on the amorphous volume fraction and the spectrum of illumination used for degradation. One expects a further increase in the efficiency of μc-Si:H single junction solar cells mostly by implementation of improved light trapping schemes and by a corresponding increase in short circuit current density. Improved light trapping will be based on the development of new and better suited transparent conductive oxides, structured substrates (periodic gratings or rough random substrates). This field is indeed currently an important research topic.

The development of thin film silicon devices relies at present mainly on the development of tandem 'micromorph' solar cells consisting of a stack with a top a-Si:H cell and a bottom μc-Si:H cell. This combination of materials can be shown theroretically to possess bandgaps that are very near to the best combination of bandgaps for optimum conversion of the AM1.5 spectrum. The highest initial efficiency achieved with such a thin film silicon tandem solar cell is currently 14.7 %. For reaching maximum efficiency, an intermediate reflector is used

between the bottom and the top cell. Such tandem devices generally suffer less from light induced degradation in the amorphous top cell. In general, the microcrystalline bottom cell inside the tandem is stable (as it is only exposed to the long wavelength part of the solar spectrum). In order to gain both in conversion efficiency and in device stability, one should reduce the thickness of the amorphous top cell and further optimize light trapping. This may hopefully lead to solar cells with stabilized efficiencies of 13–14 %. The industrial production of tandem modules has currently been started by a single Japanese module manufacturer. Several other firms (mainly Japanese) are doing research in this subject and a few of them have even developed prototype modules.

Thin film silicon offers interesting applications in building-integrated photovoltaics, thanks to its esthetical appearance and the versatility it provides in the choice of a substrate material. On the other hand, the 'micromorph' tandem concept allows for an increase in module efficiency towards a stabilized value above 10 %. Because of these factors, one may reckon that the industrial development of thin film silicon tandem modules based on a combination of amorphous and microcrystaline silicon will be intensified during the next few years, leading to a clear reduction in module costs, probably down to values below $2\$/W_p$.

REFERENCES

[1] S. Veprek and V. Marecek, The preparation of thin layers of Ge and Si by chemical hydrogen plasma transport, *Solid State Electronics*, **11**, 683–684 (1968).

[2] R. Tsu, M. Izu, S. R. Ovshinsky and F. H. Pollack, Electroreflectance and Raman scattering investigation of glow-discharge amorphous Si:F:H, *Solid State Communications*, **36**, 817–822 (1980).

[3] T. Hamasaki, H. Kurata, M. Hirose and Y. Osaka, Low temperature crystallization of doped a-Si:H alloys, *Applied Physics Letters*, **37**, 1084–1086 (1980).

[4] Y. Hattori, T. Kruangam, T. Toyama, H. Okamoto and Y. Hamakawa, High efficiency amorphous heterojunction solar cell employing ECR-CVD produced p-type microcrystalline SiC film, *Technical Digest of the International PVSEC-3*, 171 Tokyo, Japan (1987).

[5] Y. Uchida, T. Ichimura, M. Ueno and H. Haruki, Microcrystalline Si: H film and its application to solar cells, *Japanese Journal of Applied Physics*, **21**, L586–L588 (1982).

[6] J. Meier, R. Fluckiger, H. Keppner and A. Shah, Complete microcrystalline p-i-n solar cell – crystalline or amorphous cell behavior, *Applied Physics Letters*, **65**, 860–862 (1994).

[7] H. Curtins, N. Wyrsch and A. Shah, High-rate deposition of amorphous hydrogenated silicon: effect of plasma excitation frequency, *Electronic Letters*, **23**, 228–230 (1987).

[8] T. Roschek, T. Repmann, J. Müller, B. Rech and H. Wagner, Comprehensive study of microcrystalline silicon solar cells deposited at high rate using 13.56 MHz plasma-enhanced chemical vapor deposition, *Journal of Vacuum Science and Technology A*, **20**, 492–498 (2002).

[9] C. Niikura, M. Kondo and A. Matsuda, High rate growth of microcrystalline silicon films assisted by high density plasma, *Proceedings of the 3rd World Conference on PVSEC, Osaka*, 1710–1713 (2003).

[10] B. Yan, G. Yue, J. Yang, K. Lord, A. Banerjee and S. Guha, Microcrystalline silicon solar cells made using RF, MVHF and microwave at various deposition rates, *Proceedings of the 3rd World Conference on PVSEC, Osaka*, 2773–2778 (2003).

[11] H. Shirai, Y. Sakuma, K. Yoshino and H. Uemaya, Fast deposition of microcrystalline silicon films using the high density microwave plasma utilizing a spoke wise antenna, *Proceedings of the Materials Research Society Symposium*, **609**, A.4.4.1–6 (2001).

[12] M. Mastumoto, M. Shima, S. Okamoto, K. Murata, M. Tanaka, S. Kiyama, H. Kakiuchi, K. Yasutake, K. Yoshii, K. Endo and Y. Mori, Extremely high rate deposition of silicon thin-film prepared by atmospheric plasma CVD method with a rotary electrode, *Proceedings of the 3rd World Conference on PVSEC, Osaka*, 1552–1555 (2003).

[13] Y. Ide, Y. Saito, A. Yamada and M. Konagai, Microcrystalline silicon thin film solar cells prepared by the hot wire method, *Proceedings of the 3rd World Conference on PVSEC, Osaka*, 1772–1775 (2003).

[14] M. Heintze, R. Zedlitz and G. H. Bauer, Analysis of high-rate a-Si:H deposition in a VHF plasma, *Journal of Physics D: Applied Physics*, **26**, 1781–1786 (1993).

[15] J. Perrin and J. P. M. Schmitt, Emission cross-sections from fragments produced by electron impact on silane, *Chemical Physics*, **67**, 167–176 (1982).

[16] A. A. Howling, J.-L. Dorier, C. Hollenstein, U. Kroll and F. Finger, Frequency effects in silane plasma for plasma enhanced chemical vapor deposition, *Journal of Vacuum Science &Technology A*, **10**, 1080–1085 (1992).

[17] T. Repmann, W. Appenzeller, B. Sehrbrock, H. Stiebig and B. Rech, Advanced PECVD processes for thin film silicon solar cells on glass, *Proceedings of the European Photovoltaic Specialist Conference, Paris, France, June 2004*, 1334–1351 (2004).

[18] Y. Mai, S. Klein, J. Wolff, A. Lambertz, X. Geng and F. Finger, Microcrystalline silicon solar cells deposited at high rates by combination of VHF-PECVD and high working pressure, *Proceedings of the 19th EU Photovoltaic Solar Energy Conference, Paris, France, June 2004*, 1399–1402 (2004).

[19] S. Goya, I. Nakano, T. Watanabe, N. Yamashita and Y. Yonekura, The effect of narrow gap length on the high-rate deposition of microcrystalline silicon, *Proceedings of the 19th EU Photovoltaic Solar Energy Conference, Paris, France, June 2004*, 1625–1628 (2004).

[20] M. Kondo, Critical processing steps for microcrystalline silicon bottom cells, *Proceedings of the 31st IEEE Photovoltaic Specialist Conference, Lake Buena Vista, FL, USA, January 2005*, 1377–1382(2005).

[21] H. Takatsuda, M. Noda, Y. Yonekura, Y. Takeuchi and Y. Yamauchi, Development of high efficiency large area silicon thin film modules using VHF-PECVD, *Solar Energy*, **77**, 951–960 (2004).

[22] H. Shirai, G. Ohkawara and M. Nakajima, High-density microwave plasma-enhanced chemical vapor deposition of crystalline silicon films for solar cell devices, *Solid State Phenomena (Diffusion and Defect Data Part B)*, **93**, 109–114 (2003).

[23] S. Klein, F. Finger, R. Carius, B. Rech, L. Houben, M. Luysberg and M. Stutzmann, High efficiency thin film solar cells with intrinsic microcrystalline silicon prepared by hot wire CVD, *Material Research Society Symposium Proceedings*, **715**, A26.22.21–26 (2002).

[24] H. Hakuma, K. Niira, H. Senta, T. Nishimura, M. Komoda, H. Okui, K. Aramaki, Y. Okada, K. Tomita, H. Higuchi and H. Arimune, Microcrystalline-Si solar cells by newly developed novel PECVD method at high deposition rate, *Proceedings of the 3rd World Conference on Photovoltaic Energy Conversion, Osaka, 2003*, 1796–1799 (2003).

[25] A. Matsuda, Formation kinetics and control of microcrystallite in μc-Si:H from glow discharge plasma, *Journal of Non-Crystalline Solids*, 59&60, 767–774 (1983).

[26] A. Matsuda, Growth mechanism of microcrystalline silicon obtained from reactive plasmas, *Thin Solid Films*, **337**(1–6) 1–2 (1999).

[27] H. Keppner, J. Meier, P. Torres, D. Fischer and A. Shah, Microcrystalline silicon and micromorph tandem solar cells, *Applied Physics A*, **69**, 169–177 (1999).

[28] U. Kroll, J. Meier, A. Shah, S. Mikhailov and J. Weber, Hydrogen in amorphous and microcrystalline silicon films prepared by hydrogen dilution, *Journal of Applied Physics*, **80**, 4971–4975 (1996).

[29] L. Houben, M. Luysberg, P. Hapke, R. Carius, F. Finger and H. Wagner, Structural properties of microcrystalline silicon in the transition from highly crystalline to amorphous, *Philosophical Magazine A*, **77**, 1447–1460 (1998).

[30] P. M. Voyles, J. E. Gerbi, M. M. J. Treacy, J. M. Gibson and J. R. Abelson, Absence of an abrupt change from polycrystalline to amorphous in silicon with deposition temperature, *Physical Review Letters*, **86**, 5514–5517 (2001).

[31] M. Kondo and A. Matsuda, **title**in *Thin Film Solar Cells*, ed. Y. Hamakawa (Springer Verlag, Berlin Heidelberg, 2004), p. 139–149.

[32] C. Droz, E. Vallat-Sauvain, J. Bailat, L. Feitknecht, J. Meier, X. Niquille and A. Shah, Electrical and microstructural characterisation of microcrystalline silicon layers and solar cells, *Proceedings of the 3rd World Conference on Photovoltaic Energy Conversion, Osaka, 2003*, 1544–1547 (2003).

[33] M. Goerlitzer, P. Torres, N. Beck, N. Wyrsch, H. Keppner, J. Pohl and A. Shah, Structural properties and electronic transport in intrinsic microcrystalline silicon deposited by the VHF-GD technique, *Journal of Non-Crystalline Solids*, **227–230**, 996–1000 (1998).

[34] J. Bailat, E. Vallat-Sauvain, L. Feitknecht, C. Droz and A. Shah, Microstructure and open circuit voltage of n-i-p microcrystalline silicon solar cells, *Journal of Applied Physics*, **93**, 5727–5732 (2003).

[35] R. W. Collins, A. S. Ferlauto, G. M. Ferreira, C. Chen, Joohyun Koh, R. J. Koval, Yeeheng Lee, J. M. Pearce and C. R. Wronski, Evolution of microstructure and phase in amorphous, protocrystalline, and microcrystalline silicon studied by real time spectroscopic ellipsometry, *Solar Energy Materials and Solar Cells*, **78**, 143–180 (2003).

[36] E. Vallat-Sauvain, U. Kroll, J. Meier, A. Shah and J. Pohl, Evolution of the microstructure in microcrystalline silicon prepared by very high frequency glow-discharge using hydrogen dilution, *Journal of Applied Physics*, **87**, 3137–3142 (2000).

[37] T. Kamiya, K. Nakahata, K. Ro, C. Fortmann and I. Shimizu, Comparison of microstructure and crystal structure of polycrystalline silicon exhibiting varied textures fabricated by microwave and very high frequency plasma enhanced chemical vapor deposition and their transport properties, *Japanese Journal of Applied Physics*, **38**, 5750–5756 (1999).

[38] A. Fejfar, B. Rezek, P. Knapek, J. Stuchlik and J. Kocka, Local electronic transport in microcrystalline silicon observed by combined atomic force microscopy, *Journal of Non-Crystalline Solids*, **266–269**, 309–314 (2000).

[39] E. Vallat-Sauvain, U. Kroll, J. Meier, N. Wyrsch and A. Shah, Microstructure and surface roughness of microcrystalline silicon prepared by very high frequency-glow discharge using hydrogen dilution, *Journal of Non-Crystalline Solids*, **266–269**, 125–130 (2000).

[40] E. Vallat-Sauvain, J. Bailat, J. Meier, X. Niquille, U. Kroll and A. Shah, Influence of the substrate morphology and chemical nature on the nucleation and growth of microcrystalline silicon, *Thin Solid Films*, to be published, (2005).

[41] M. N. Islam and S. Kumar, Influence of crystallite size distribution on the micro Raman analysis of porous Si, *Applied Physics Letters*, **78**, 715–717 (2001).

[42] R. J. Kobliska and S. A. Solin, Raman spectrum of wurtzite silicon, *Physical Review B*, **8**, 3799–3802 (1973).

[43] M. Luysberg, P. Hapke, R. Carius and F. Finger, Structure and growth of hydrogenated microcrystalline silicon: investigation by transmission electron microscopy and Raman spectroscopy of films grown at different plasma excitation frequencies, *Philosophical Magazine A*, **75**, 31–47 (1997).

[44] C. Droz, E. Vallat-Sauvain, J. Bailat, L. Feitknecht, J. Meier and A. Shah, Relationship between Raman crystallinity and open-circuit voltage in microcrystalline silicon solar cells, *Solar Energy Materials and Solar Cells*, **81**, 61–71 (2004).

[45] M. Luysberg, C. Scholten, L. Houben, R. Carius, F. Finger and O. Vetterl, Structural properties of microcrystalline silicon solar cells, *Material Research Society Symposium Proceedings*, **664**, A15.12.11–16 (2001).

[46] Y. Nasuno, M. Kondo and A. Matsuda, Microcrystalline silicon thin-film solar cells prepared at low temperature using PECVD, *Solar Energy Materials and Solar Cells*, **74**, 497–503 (2002).

[47] C. C. Tsai, G. B. Anderson and R. Thompson, Growth of amorphous, microcrystalline and epitaxial silicon in low temperature plasma deposition, *Material Research Society Symposium Proceedings*, **192**, 475 (1990).

[48] A. Matsuda, Formation kinetics and control of microcrystallite in μc-Si:H from glow discharge plasma, *Journal of Non-Crystalline Solids*, **59/60**, 767–774 (1983).

[49] S. Veprek, Z. Iqbal and F. A. Sarott, A thermodynamic criterion of the crystalline-to-amorphous transition in silicon, *Philosophical Magazine B*, **45**, 137–145 (1982).

[50] T. Akasaka and I. Shimizu, *In situ* real time studies of the formation of polycrystalline silicon film on glass grown by a layer-by-layer technique, *Applied Physics Letters*, **66**, 3441–3443 (1995).

[51] J. Bailat, E. Vallat-Sauvain, A. Vallat and A. Shah, Simulation of the growth dynamics of amorphous and microcrystalline silicon, *Journal of Non-Crystalline Solids*, **338–340**, 32–36 (2004).

[52] J. Bailat, E. Vallat-Sauvain, A. Vallat and A. Shah, Phase diagrams and microstructure of microcrystalline and amorphous silicon studied by dynamical simulation of the growth of microcrystalline silicon, *Material Research Society Symposium Proceedings*, **808**, 221–226 (2004).

[53] A. Poruba, A. Fejfar, Z. Remes, J. Springer, M. Vanecek, J. Kocka, J. Meier, P. Torres and A. Shah, Optical absorption and light scattering in microcrystalline silicon thin films and solar cells, *Journal of Applied Physics*, **88**, 148–160 1 (2001).

[54] M. Vanecek, J. Kocka, A. Poruba and A. Fejfar, Direct measurement of the deep defect density in thin amorphous silicon films with the 'absolute' constant photocurrent method, *Journal of Applied Physics*, **78**, 6203–6210 (1995).

[55] M. Vanecek, J. Kocka, J. Stuchlik and A. Triska, Direct measurement of the gap states and band tail absorption by constant photocurrent method in amorphous silicon, *Solid State Communications*, **39**, 1199–1202 (1981).

[56] M. Vanecek and A. Poruba, Fourier-transform photocurrent spectroscopy of microcrystalline silicon for solar cells, *Applied Physics Letters*, **80**, 719–721 (2002).

[57] A. Poruba, M. Vanecek, J. Meier, and A. Shah, Fourier transform infrared photocurrent spectroscopy in microcrystalline silicon, *Journal of Non-Crystalline Solids*, **299–302**, 536–540 (2002).

[58] J. D. Cody, Urbach edge of crystalline and amorphous silicon: a personal review, *Journal of Non-Crystalline Solids*, **141**, 3–15 (1992).

[59] M. Goerlitzer, N. Beck, P. Torres, J. Meier, N. Wyrsch and A. Shah, Ambipolar diffusion length and photoconductivity measurements on 'midgap' hydrogenated microcrystalline silicon, *Journal of Applied Physics*, **80**, 5111–5115 (1996).

[60] J. Kocka, A. Fejfar, H. Stuchlikova, J. Stuchlik, P. Fojtik, T. Mates, B. Rezek, K. Luterova, V. Svrcek and I. Pelant, Basic features of transport in microcrystalline silicon, *Solar Energy Materials and Solar Cells*, **78**, 493–512 (2003).

[61] N. Beck, N. Wyrsch, C. Hof, and A. Shah, Mobility-lifetime product – a tool for correlating a-Si:H film properties and solar cell performances, *Journal of Applied Physics*, **79**, 9361–9368 (1996).

[62] V. Daudrix, C. Droz, N. Wyrsch, Y. Ziegler, X. Niquille and A. Shah, Development of more stable amorphous silicon thin film solar cells deposited at 'moderately high' temperature, *Proceedings of the 16th European Photovoltaic Solar Energy Conference, Glasgow*, 385–388 (2000).

[63] C. Droz, M. Goerlitzer, N. Wyrsch and A. Shah, Electronic transport in hydrogenated microcrystalline silicon: similarities with amorphous silicon, *Journal of Non-Crystalline Solids*, **266–269**, 319–324 (2000).

[64] J. Meier, P. Torres, R. Platz, S. Dubail, U. Kroll, J. A. Anna Selvan, N. Pellaton-Vaucher, C. Hof, D. Fischer, H. Keppner, and A. Shah, On the way towards high efficiency thin film silicon solar cells by the 'micromorph' concept, *Proceedings of the Materials Research Society Symposium*, **420**, 3–14 (1996).

[65] N. Wyrsch, N. Beck, J. Meier, P. Torres and A. Shah, Electric field profile in μc-Si:H p-i-n devices, *Proceedings of the Materials Research Society Symposium*, **507**, 181–186 (1998).

[66] J. Kocka, H. Stuchlikova, J. Stuchlik, B. Rezek, T. Mates, V. Svrcek, P. Fojtik, I. Pelant and A. Fejfar, Model of transport in microcrystalline silicon, *Journal of Non-Crystalline Solids*, **299–302**, 355–359 (2002).

[67] E. Vallat-Sauvain, S. Dubail, U. Kroll, J. Meier and A. Shah, Improved Interface Between Front TCO and Microcrystalline Silicon p-i-n Cells, *Proceedings of the Materials Research Society Symposium*, **664**, A15.13.11– 16. (2001).

[68] D. L. Staebler and C. R. Wronski, Reversible conductivity changes in discharge-produced amorphous silicon, *Applied Physics Letters*, **31**, 292–294 (1977).

[69] K. Yamamoto, A. Nakajima, M. Yoshimi, T. Sawada, S. Fukuda, T. Suezaki, M. Ichikawa, Y. Koi, M. Goto, T. Meguro, T. Matsuda, M. Kondo, T. Sasaki and Y. Tawada, A high efficiency thin-film silicon solar cell and module, *Solar Energy Materials and Solar Cells*, **77**, 939–949 (2004).

[70] J. Meier, High efficiency amorphous and micromorph silicon solar cells, *Proceedings of the 3rd World Conference on Photovoltaic Energy Conversion, Osaka, 2003*, 2801–2805 (2003).

[71] H. Takakura, Optimum design of thin-film-based tandem-type solar cells, *Japanese Journal of Applied Physics*, **31**, 2394–2399 (1992).

[72] A. Shah, M. Vanecek, J. Meier, F. Meillaud, J. Guillet, D. Fischer, C. Droz, X. Niquille, S. Faÿ, E. Vallat-Sauvain, V. Terrazzoni-Daudrix and J. Bailat, Basic efficiency limits, recent experimental results and novel light trapping schemes in a-Si:H, μc-Si:H and micromorph tandem solar cells, *Journal of Non-Crystalline Solids*, **338–340**, 639–645 (2004).

[73] H. Mase, M. Kondo and A. Matsuda, Microcrystalline silicon solar cells fabricated on polymer substrate, *Solar Energy Materials and Solar Cells*, **74**, 547–552–(2002).

[74] A. Takano, T. Wada and M. Shimosawa, Working pressure effects on deposition of large area microcrystalline silicon films on flexible plastic substrate at 130 °C, *Japanese Journal of Applied Physics*, **41**, L978–980 (2002).

[75] V. Terrazzoni-Daudrix, J. Guillet, X. Niquille, L. Feitknecht, F. Freitas, P. Winkler, A. Shah, R. Morf, P. Parriaux and D. Fischer, Enhanced light trapping in thin film silicon solar cells deposited on PET and glass, *Proceedings of the 3rd World Conference on Photovoltaic Energy Conversion, Osaka, May 2003*, 1596–1600 (2003).

[76] A. Shah, J. Bailat, E. Vallat-Sauvain, M. Vanecek, J. Meier, S. Faÿ, I. Pola, V. Terrazzoni-Daudrix and C. Ballif, Microcrystalline and micromorph solar cells and modules: status and potential, to be published in the *Proceedings of the 31st IEEE Specialists conference, Orlando USA*, (2005).

[77] T. Ikeda, K. Sato, Y. Hayashi, Y. Wakayama, K. Adachi and H. Nishimura, Surface microstructures of ZnO coated SnO_2: F films, *Solar Energy Materials and Solar Cells*, **34**, 379 (1994).

[78] H. Natsuhara, N. Ohashi, S. Ogawa, N. Y. Oshida, T. Itoh, S. Nonomura, M. Fukawa and K. Sato, Hydrogen-radical durability of TiO_2 thin films for protecting transparentconducting oxide for Si thin film solar cells, *Thin Solid Films*, **430**, 253–257 (2003).

[79] J. Müller, B. Rech, J. Springer and M. Vanecek, TCO and light trapping in silicon thin film solar cells, *Solar Energy*, **77**, 917–930 (2004).

[80] R. G. Gordon, Deposition of transparent conducting oxides for solar cells, NREL/SNL Photovoltaics Program Review, *14th Conference – A Joint Meeting, 18–22 Nov, 1996, Lakewood, CO, USA*, 39–48, (1997) (AIP Press New-York).

[81] S. Faÿ, U. Kroll, C. Bucher, E. Vallat-Sauvain and A. Shah, Low pressure chemical vapour deposition of ZnO layers for thin-film solar cells: temperature induced morphological changes, *Solar Energy Materials and solar cells*, **86**, 385–397 (2004).

[82] J. A. Anna Selvan, Y.-M. Li, S. Guo, and A.-E. Delahoy, Development of μc-Si:H solar cells on novel transparent conducting light trapping oxide (TCLO) superstrate with IMO, ITiO or surface textured i-ZnO/IMO & i-ZnO/ITiO bilayer, *Proceedings of the 19th EU Photovoltaic Solar Energy Conference, Paris, France, June 2004*, 1346–1351 (2004).

[83] J. Springer, A. Poruba and M. Vanecek, Improved three-dimensional optical model for thin-film silicon solar cells, *Journal of Applied Physics*, **96**, 5329–5337 (2004).

[84] J. Meier, H. Keppner, J. Dubail, U. Kroll, P. Torres, P. Pernet, Y. Ziegler, J. A. Anna Selvan, J. Cuperus, D. Fischer and A. Shah, Microcrystalline single junction and micromorph tandem thin film silicon solar cells, *Material Research Society Symposium Proceedings*, **507**, 139–144 (1998).

[85] O. Vetterl, F. Finger, R. Carius, P. Hapke, L. Houben, O. Kluth, A. Lambertz, A. Mück, B. Rech and H. Wagner, Intrinsic microcrystalline silicon: a new material for photovoltaics, *Solar Energy Materials and Solar Cells*, **62**, 97–103 (2000).

[86] J. Bailat, E. Vallat-Sauvain, M. Dubey, F. Meillaud, X. Niquille, J. Guillet, A. Shah, A. Poruba, L. Mullerova, J. Springer and M. Vanecek, Quality of i layer investigated within the complete solar cells by absorption spectroscopy, *Proceedings of the 19th EU Photovoltaic Solar Energy Conference, Paris, France, June 2004*, 1541–1544 (2004).

[87] O. Vetterl, F. Finger, R. Carius, P. Hapke, L. Houben, O. Kluth, A. Lambertz, A. Muck, B. Rech and H. Wagner, Intrinsic microcrystalline silicon: a new material for photovoltaics, *Solar Energy Materials and Solar Cells*, **62**, 97–108 (2000).

[88] K. Saito, M. Sano, A. Sakai, R. Hayashi and K. Ogawa, High efficiency microcrystalline silicon solar cells deposited at high deposition rates, *Technical Digest of the 12th International PVSEC, Jeju, Korea, 2001*, 429 (2001).

[89] K. Saito, M. Sano, K. Matzuda, T. Kondo, M. Higasikawa and T. Karyia, High efficiency microcrystalline silicon solar cells by the low temperature plasma CVD method, *Proceedings of the International PVSEC-11, Sapporo, Japan*, 229–230 (1999).

[90] Y. Mai, S. Klein, X. Geng and F. Finger, Structure adjustment during high-deposition-rate growth of microcrystalline silicon solar cells, *Applied Physics Letters*, **85**, 2839–2841 (2004).

[91] K. Yamamoto, Very thin film crystalline silicon solar cells on glass substrate fabricated at low temperature, *IEEE Transactions on Electron Devices*, **46**, 2041–2047 (1999).

[92] S. Klein, F. Finger, R. Carius and H. Stiebig, Light-induced degradation of microcrystalline silicon thin-film solar cells prepared by hot-wire CVD, *Proceedings of the 19th EU Photovoltaic Solar Energy Conference, Paris, France, June 2004*, 1579–1582 (2004).

[93] F. Meillaud, E. Vallat-Sauvain, X. Niquille, M. Dubey, J. Bailat, A. Shah and C. Ballif, Light-induced degradation of thin-film microcrystalline silicon solar cells, *Proceedings of the 31st IEEE Photovoltaic Specialist Conference, Lake Buena Vista, FL, USA, January 2005*, to be published (2005).

[94] B. Yan, G. Yue, J. Owens, J. Yang and S. Guha, Light-induced metastability in hydrogenated nanocrystalline silicon solar cells, *Applied Physics Letters*, **85**, 1925–1927 (2004).

[95] Y.-M. Li, J. A. Anna Selvan, L. Li, R. A. Levy and A.-E. Delahoy, A study of single chamber RF-PECVD μc-Si:H solar cells, *Proceedings of the 3rd World Conference on Photovoltaic Energy Conversion, Osaka, 2003*, 1788–1791 (2003).

[96] P. Torres, J. Meier, R. Flückiger, U. Kroll, J. A. Anna Selvan, H. Keppner, A. Shah, S. D. Littlewood, I. E. Kelly and P. Giannoulès, Device grade microcrystalline silicon owing to reduced oxygen contamination, *Applied Physics Letters*, **69**, 1373–1375 (1996).

[97] M. Kondo, Critical processing steps for microcrystalline silicon bottom cells, *Proceedings of the 31st IEEE Photovoltaic Specialist Conference, Lake Buena Vista, FL, USA, January 2005*, 1377–1382(2005).

[98] J. Fölsch, F. Finger, T. Kulessa, F. Siebke, W. Beyer and H. Wagner, Improved ambipolar diffusion length in a-$Si_{1-x}Ge_x$:H alloys for multijunction solar cells, *Proceedings of the Materials Research Society Symposium*, **377**, 517–522 (1995).

[99] S. Guha and J. Yang, Amorphous silicon alloy materials, cells and modules, *Proceedings of the 29th IEEE PVSEC, New Orleans*, 1070–1075 (2002).

[100] J. Meier, S. Dubail, R. Fluckiger, D. Fischer, H. Keppner and A. Shah, Intrinsic microcrystalline silicon (μc-Si:H)– a promising new thin film solar cell material, *1st World Conference on Photovoltaic energy conversion*, **1**, 409–412 (1994).

[101] J. Meier, J. Spitznagel, S. Faÿ, C. Bucher, U. Graf, U. Kroll, S. Dubail and A. Shah, Enhanced light trapping for micromorph tandem solar cells by LP-CVD ZnO, *Proceedings of the 29th IEEE Photovoltaic Specialists Conference, New Orleans*, 1118–1121 (2002).

[102] D. Fischer, S. Dubail, J. A. Anna Selvan, N. Pellaton-Vaucher, R. Platz, C. Hof, U. Kroll, J. Meier, P. Torres, H. Keppner, N. Wyrsch, M. Goetz, A. Shah and K.-D. Ufert, The micromorph solar cell: extending a-Si:H technology towards thin film crystalline silicon, *Proceedings of the 25th IEEE Photovoltaic Energy Conference*, 1053–1056 (1996).

[103] M. Vanecek, Light trapping and optical losses in microcrystalline silicon and micromorph silicon solar cells, *Proceedings of the 3rd World Conference on Photovoltaic Energy Conversion, Osaka, 2003*, 1527–1532 (2003).

[104] R. Zedlitz, M. Heintze and G. H. Bauer, Analysis of VHF glow discharge of a-Si:H over a wide frequency range, *Proceedings of the Materials Research Society Symposium*, **258**, 147–151 (1992).

[105] A. Shah, H. Schade, M. Vanecek, J. Meier, E. Vallat-Sauvain, N. Wyrsch, U. Kroll, C. Droz and J. Bailat, Thin film silicon and solar cell technology, *Progress in Photovoltaics: Research and Applications*, **12**, 1–30 (2004).

5 Advanced Amorphous Silicon Solar Cell Technologies

Miro Zeman
Delft University of Technology

5.1 INTRODUCTION

The first amorphous silicon layers were reported in 1965 as films of 'silicon from silane' deposited in a radio frequency glow discharge [1]. Ten years later, Walter Spear and Peter LeComber from Dundee University reported that amorphous silicon had semiconducting properties. They demonstrated that the conductivity of amorphous silicon can be manipulated by several orders of magnitude by adding some phosphine or diborane gas to the glow discharge gas mixture [2]. This was a far reaching discovery since until that time, it had generally been thought that amorphous silicon could not be made n type or p type by substitutional doping. It was not recognized immediately that hydrogen plays an important role in the newly made amorphous silicon doped films. In fact, amorphous silicon suitable for electronic applications, requiring doping, is an alloy of silicon and hydrogen. Electronic grade amorphous silicon is therefore called hydrogenated amorphous silicon (a-Si:H).

The successful doping of amorphous silicon created tremendous interest in this material for two reasons. First, the material had several interesting properties that opened up many opportunities for semiconductor device applications. For example, due to the high absorption coefficient of a-Si:H in the visible range of the solar spectrum, a 1 micrometer (μm) thick a-Si:H layer is sufficient to absorb 90 % of the usable solar energy. Second, the glow discharge deposition technique, also referred to as plasma enhanced chemical vapour deposition (PECVD), enabled the production of a-Si:H films over a large area (larger than 1 m^2) and at a low temperature (100 to 400 °C). The low processing temperature allows the use of a wide range of low cost substrates such as glass sheet, metal or polymer foil. The a-Si:H is simply doped and alloyed by adding the appropriate gases to a source gas, usually silane. These features have made a-Si:H a promising candidate for low cost thin film solar cells. At present, besides solar cells, this material is used for thin film transistors in flat panel displays and photoconductive layers in electrophotography.

Since the first a-Si:H solar cell Carlson and Wronski made in 1976, which had an energy conversion efficiency of 2.4 % [3], a-Si:H solar cell technology has improved considerably, and today, it is capable of producing solar cells with initial efficiencies exceeding 15 % [4]. Today, amorphous silicon solar cell technology is a mature thin film solar cell technology that in 2003 already delivered modules with a total output power of 25.8 MW_p [5].

Thin Film Solar Cells Edited by J. Poortmans and V. Arkhipov
© 2006 John Wiley & Sons, Ltd

5.2 OVERVIEW OF AMORPHOUS SILICON SOLAR CELL TECHNOLOGY DEVELOPMENT AND CURRENT ISSUES

5.2.1 1970s

Carlson and Wronski announced that they had made the first experimental a-Si:H solar cell at the RCA Laboratory in 1976 [3]. This single junction p-i-n a-Si:H solar cell deposited on a glass substrate coated with transparent conductive oxide (TCO) and aluminium back contact exhibited a 2.4 % conversion efficiency. In order to increase the output voltage of a-Si:H solar cells, the concept of a stacked (also called multi-junction) solar cell structure was introduced [6]. A key step to industrial production was the development of a monolithically integrated type of a-Si:H solar cell [7]. Using the monolithic series integration of a-Si:H solar subcells, a desired output voltage from a single substrate can easily be achieved. In 1980, the integrated type a-Si:H solar cells were commercialized by Sanyo and Fuji Electric and applied in consumer electronics such as calculators and watches.

5.2.2 1980s

Much research in the field of a-Si:H solar cells was devoted to developing and optimising a-Si:H based alloys in the 1980s. A p type hydrogenated amorphous silicon carbide (*a*-SiC:H) was incorporated in solar cells as a low absorbing layer, usually denoted as a window layer [8]. Hydrogenated amorphous silicon germanium (a-SiGe:H) became an attractive low bandgap material for stacked solar cells [9]. Surface textured substrates were introduced to enhance optical absorption [10]. The laboratory cells reached an initial efficiency in the range of 11 to 12 %. The next generation of a-Si:H modules came on the market in the second half of the 1980s and was aimed at off grid power generation. These modules were single junction p-i-n a-Si:H solar cells, produced mainly in a single chamber batch process. The typical area of the modules ranged from 0.1 to 0.3 m^2 and they were aimed to deliver a power of around 14 W (stabilized efficiency up to 5 %). However, this promising technology suffered from some setbacks that gave it a bad reputation: pronounced initial degradation due to illumination, insufficient protection and framing of these modules against moisture, which resulted in the corrosion of contacting electrodes.

5.2.3 1990s

In the 1990s, the main research and manufacturing efforts were directed towards achieving 10 % stabilized module efficiency and a high throughput process. Several companies optimized and implemented an a-SiGe:H alloy in tandem (BP Solar [11], Sanyo [12], Fuji Electric [13]) and triple junction (United Solar [14]) solar cell structures. The main characteristics of a-Si:H modules developed in the 1990s were a multijunction solar cell structure, improved encapsulation and framing. Lightweight frames from organic materials that provided better protection against corrosion substituted the aluminium frames. The module area reached 1 m^2 and the total area stabilized module efficiency was increased to 6–7 %. The improved environmental protection of the modules enabled the producers to guarantee more than 20 years of power

output. At the end of the 20th century, the annual total production capacity for amorphous silicon single and multijunction modules reached around 30 MW_p. The focus on the application of the modules shifted from off grid to building integrated applications.

Hydrogenated microcrystalline silicon deposited by the low temperature PECVD technique emerged in this period as a new candidate for the low bandgap material in multijunction *a*-Si:H based solar cells. The University of Neuchâtel introduced a micromorph tandem solar cell in 1994, which comprized an *a*-Si:H top cell and a μc-Si:H bottom cell [15]. The promising potential of the micromorph cell concept was soon demonstrated by the fabrication of micromorph tandem and triple solar cells with stabilized efficiencies in the range of 11 to 12 % [16, 17], and Kaneka Corporation started the development of micromorph module production technology [17]. The introduction and implementation of μc-Si:H in thin film silicon solar cells shifted attention to increasing the deposition rate. Several new deposition techniques [18] started to be investigated and developed for fabricating absorber layers at high deposition rates (10 to 20 Å/s), such as very high frequency and microwave PECVD, hot wire CVD, and expanding thermal plasma CVD.

5.2.4 After 2000

Research has concentrated on understanding and improving light trapping techniques, where surface textures as well as new TCO materials play a crucial role. This activity has resulted in the commercialization of novel deposition techniques for ZnO as an alternative TCO material for SnO_2 [19, 20]. Several deposition machine manufacturers have started developing commercial production machines for the fabrication of thin film silicon solar cells [21, 22]. Today the most advanced a-Si:H production lines are characterized by fully automated facilities and large area deposition over more than 1 m^2, with an annual production capacity in the range of 10 MW_p to 30 MW_p (Mitsubishi Heavy Ind. 10 MW_p, Kaneka Corporation 20 MW_p, United Solar 30 MW_p).

5.2.5 Current technology issues

In order to increase the competitiveness of a-Si:H modules on the market, several cost-to-performance aspects of the a-Si:H solar cell technology are of importance, which can be divided into the following performance and production related issues:

1. Increase of the conversion efficiency of a-Si:H solar cells. Based on fundamental considerations, major performance improvement is expected in the near future from an increase in the current of thin film silicon solar cells [23]. This increase has to result from improved light management schemes such as light trapping and reduction of light absorption losses. For solar cells deposited on glass plates, also called *superstrate type* cells, the development of a TCO front electrode material with an optimal surface morphology that results in improved light scattering properties is essential. Essential for solar cells deposited on (flexible) opaque carriers, often denoted as *substrate type* solar cells, is improvement of the texturing and reflectivity of the back contact. Ongoing attention has to be paid to further improvement of the optoelectronic quality of a-Si:H and a-SiGe:H absorbers, the doped layers and the interfaces between the doped layers and intrinsic absorbers.

2. Elimination of the light induced degradation known as the Staebler–Wronski effect [24]. This effect is responsible for a decrease in the initial performance of an a-Si:H solar module of typically 15–30 %. Full understanding of the Staebler–Wronski effect in a-Si:H based materials is necessary for fabricating a-Si:H with improved stability against light exposure. The light induced degradation of the modules can be suppressed by using thin absorber layers. However, the use of the thin absorbers strongly depends on the implementation of efficient light trapping techniques in the solar cells, which have to provide for sufficient absorption in these layers.

3. The deposition rate of absorber layers is required to be 10 to 20 Å/s in order to limit the investment in the a-Si:H deposition machine, which is strongly reflected in the cost of the modules. The central question regarding the deposition rate is how to avoid the increased light induced degradation of films deposited at elevated deposition rates [25]. In addition to the radio frquency (rf) PECVD technique, several deposition techniques are being intensively investigated capable of fabricating absorber layers with sufficient quality at high deposition rates, such as very high frequency PECVD, hot wire CVD, and expanding thermal plasma CVD.

4. The choice of mass production technology. Although the deposition of a-Si:H based layers is the most important part of solar cell fabrication, complete production includes several fabrication steps which substantially contribute to the total cost of the solar module. These include the deposition of the TCO front electrode, the deposition of the multilayer back electrode, laser scribing for the subcell series connection, and encapsulation and framing. The solar cell structure and module design determine the choice of sequence of fabrication steps and the deposition and processing techniques to be applied. At present, there are three major approaches to depositing a-Si:H based layers: the one chamber batch process, the multichamber process, and the roll-to-roll process. The advantages and disadvantages of particular a-Si:H production systems are discussed in reference [18]. The general trend is to increase the substrate size, which reduces the cost per unit area, by lowering the relative contribution of the edges. The experience gained in the display industry regarding the deposition of a-Si:H on large area substrates is being transferred to solar cell production. The general requirements for the production machines include sufficient reliability of the deposition process, high production uptime, high yield and the right choice of procedure for cleaning the process chambers.

5. Lowering of material costs. The material costs contribute considerably to the overall cost of a-Si:H modules. A substantial part is formed by the cost of the substrate carrier, the glass plate or high temperature resistant polymer foil. Therefore, cheaper thin metal foils that also allow the use of the continuous roll-to-roll technology are a preferable choice. In case of flexible modules, usually a relatively thick fluoropolymer type encapsulant is applied in order to guarantee a module lifetime of 20 years. The encapsulant dominates the cost of the module and the development of a cheap encapsulant is therefore one of the most important cost issues. The choice of substrate carrier determines the acceptable process temperatures and the sequence of processing steps. The choice of gasses for the deposition of a-Si:H based layers, their purity and the gas utilization also have financial consequences. For example, the use of germane for multijunction solar cells with a-SiGe:H absorbers can substantially increase the material costs.

5.3 HYDROGENATED AMORPHOUS SILICON

In order to understand the design and operation of a-Si:H based solar cells, which are different from those for crystalline silicon solar cells, we will summarize the structural and material properties of a-Si:H and compare them to those of single crystal silicon. Some widely used techniques to characterize a-Si:H are also described in this section.

5.3.1 Atomic structure

Figure 5.1 illustrates the difference in atomic structure between single crystal silicon and a-Si:H. Figure 5.1a shows the structure of single crystal silicon schematically. Each silicon atom is covalently bonded to four neighboring atoms. All bonds have the same length, and the angles between the bonds are equal. The number of bonds of an atom with its immediate neighbors in the atomic structure is called the coordination number or coordination. Thus, in single crystal silicon, the coordination number for all silicon atoms is four; we can also say that silicon atoms are fourfold coordinated. A unit cell can be defined, from which the crystal lattice can be reproduced by duplicating the unit cell and stacking the duplicates next to each other. Such a regular atomic arrangement is described as a structure with a long range order.

Figure 1b illustrates that a-Si:H does not exhibit a structural order over a long range. Nevertheless, there is a similarity in atomic configuration on a local atomic scale, where most silicon atoms have covalent bonds with four neighbors. Though a-Si:H lacks the long range order, it has the same short range order as single crystal silicon. This conclusion about the bonding structure in a-Si:H has been obtained from X-ray diffraction measurements [26]. The small deviations in bonding angles and bonding lengths between the neighboring atoms in a-Si:H lead to a complete loss of the locally ordered structure on a scale exceeding a few atomic distances. The resulting atomic structure of a-Si:H is called a continuous random network.

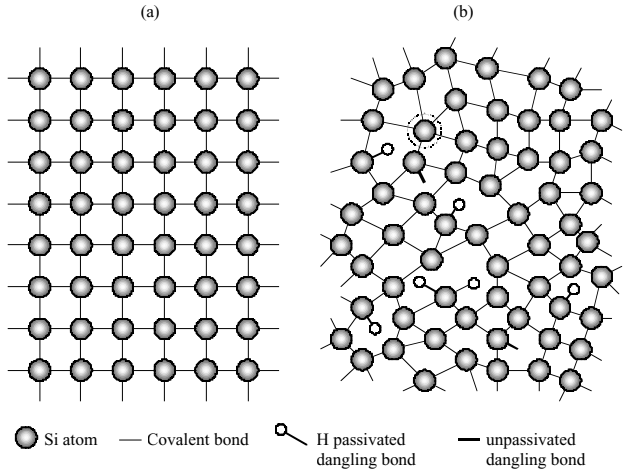

Figure 5.1 Schematic representation of the atomic structure of (a) single crystal silicon, (b) hydrogenated amorphous silicon.

Due to the short range order, the common semiconductor concept of the energy state bands, represented by the conduction and valence bands, can still be used in a-Si:H.

The larger deviations in bonding angles and bonding lengths between the neighboring atoms in a-Si:H result in so-called weak or strained bonds. When enough energy is available, for example in the form of heat, weak bonds can easily be broken. This process leads to the formation of defects in the atomic network. We note that in the continuous random network, the definition of a defect is modified with respect to the crystal structure. In a crystal, any atom that is out of place in a lattice forms a defect. In the continuous random network, an atom cannot be out of place. Because the only specific structural feature of an atom in the continuous random network is the coordination to its neighbors, a defect in a-Si:H is a coordination defect [26]. This happens when an atom has too many bonds or too few. In a-Si:H, defects are mainly silicon atoms that are covalently bonded to only three silicon atoms (threefold coordinated) and have one unpaired electron, a so-called dangling bond. Since this configuration is the dominant defect in a-Si:H, the defects in a-Si:H are often related to dangling bonds. Some dangling bond defects are depicted in Figure 5.1b. Another defect configuration is a silicon atom bonded to five silicon atoms (fivefold coordinated). This configuration is referred to as a floating bond. A silicon atom representing this floating bond defect is indicated in Figure 5.1b by a dotted circle.

In *pure* a-Si (amorphous silicon that contains no other atoms than silicon), there is a large concentration of about 10^{21} defects per cm^3 in the amorphous atomic structure. Material with such a large defect density cannot be used for a functional device. When amorphous silicon is deposited in such a way that hydrogen can be incorporated in the atomic network (as by glow discharge deposition from silane), then hydrogen atoms bond with most of the silicon dangling bonds. Strong silicon–hydrogen bonds are formed, which are illustrated in Figure 5.1b. Hydrogen passivation of dangling bond defects reduces the defect density from about 10^{21} cm^{-3} in pure a-Si to 10^{15}–10^{16} cm^{-3} in a-Si:H, i.e. less than one dangling bond per one million silicon atoms. It is this material, an alloy of silicon and hydrogen, in which substitutional doping has been demonstrated and which is suitable for electronic applications.

5.3.1.1 Electron spin resonance

An experimental technique that can provide information on the microscopic structure of defects in semiconductors, including the amorphous ones, is electron spin resonance (ESR) [27]. Electron spin resonance measurements on a-Si:H have identified a single type of defect that is associated with a neutral dangling bond [26, 28]. The ESR is regarded as an experimental standard for determining defects in a-Si:H, and the ESR results are considered unambiguous. However, the sensitivity of this method is limited for thin films with a low spin density and the method only gives information about paramagnetic defects, i.e. defects with an unpaired electron. For this reason, ESR can underestimate the defect density, because the charged dangling bonds do not possess an unpaired spin signal. Therefore, the results from ESR strongly depend on the Fermi level position, which determines the electron occupation of defects.

5.3.1.2 Hydrogen characterization in hydrogenated amorphous silicon

Since hydrogen plays an important role in defect passivation, the incorporation and stability of hydrogen in a-Si:H has been the topic of intensive research. Infrared absorption spectroscopy

is widely used to provide information about Si–H_x bonding configurations in a-Si:H [26]. Three characteristic infrared absorption bands are observed in a-Si:H: a peak at 640 cm^{-1}, a doublet at 840–890 cm^{-1}, and absorption peaks in the range of 2000–2200 cm^{-1}. The peak at 640 cm^{-1} reflects the rocking mode of hydrogen covalently bonded in all possible bonding configurations, i.e. silicon mono ($x = 1$), di ($x = 2$), and trihydride ($x = 3$) and polymeric $(Si–H_2)_n$ bonding configurations, and therefore this peak is used to determine the hydrogen content in a-Si:H [18]. The doublet at 840–890 cm^{-1} is assigned to the dihydride wagging mode. A peak around 2000 cm^{-1} is assigned to the stretching mode of the isolated Si–H bonds (also referred to as the low stretching mode (LSM) in the literature) and a peak in the range of 2060–2160 cm^{-1} includes contributions from the stretching mode (referred to as the high stretching mode (HSM)) of Si–H bonds at internal surfaces, e.g. voids, dihydride and trihydride bonds. A 'microstructure parameter,' denoted as R^*, is determined from the LSM and HSM absorption peaks. The R^* is widely used to characterize the microstructure in the a-Si:H network as it roughly indicates two different 'phases', namely a dense network and a fraction of the network containing voids. The microstructure parameter is defined as:

$$R^* = \frac{I_{\mathrm{HSM}}}{I_{\mathrm{LSM}} + I_{\mathrm{HSM}}} \tag{5.1}$$

where I_{HSM} and I_{LSM} are the integrated absorption strength of the LSM and HSM, respectively. In general, device quality a-Si:H contains less than 10 atomic % of hydrogen and is characterized by $R^* < 0.1$.

Hydrogen diffusion and evolution measurements help to characterize hydrogen motion, trapping and evolution in a-Si:H [29]. Nuclear magnetic resonance (NMR) gives information about the local atomic environment in which the hydrogen atoms reside [30]. Recently, it has been reported, based on NMR experiments, that molecular hydrogen forms up to 40 % of the total hydrogen content in a-Si:H [31].

5.3.2 Density of states

An essential component for determining the distributions and concentrations of charge carriers in a semiconductor material is information about the energy distribution of states, often called the density of states. For an ideal intrinsic silicon crystal, the valence band and the conduction band are separated by a well defined bandgap, E_g, and there are no allowed energy states in the bandgap. Due to the long range disorder in the atomic structure of a-Si:H, the energy states of the valence band and the conduction band spread into the bandgap and form regions of states that are called band tails. In addition, the defects introduce allowed energy states that are located in the central region between the valence band and conduction band states. This means that there is a continuous distribution of density of states in a-Si:H and that there is no well defined bandgap between the valence band and the conduction band.

The energy states in which the charge carriers can be considered as free carriers are described by wave functions that extend over the whole atomic structure. These states are nonlocalized and are called extended states. The disorder in a-Si:H causes the wave functions of the tail and defect states to become localized within the atomic network. These states are called localized states. Consequently, mobility that characterizes transport of carriers through the localized states is strongly reduced. This feature of a sharp drop in the mobility of carriers

in the localized states in comparison to the extended states is used to define the bandgap in a-Si:H. This bandgap is denoted by the term mobility gap, E_{mob}, because the presence of a considerable density of states in the mobility gap is in conflict with the classical concept of a bandgap without any allowed energy states. The energy levels that separate the extended states from the localized states in a-Si:H are called the valence band, E_{V}, and the conduction band, E_{C}, mobility edges. The mobility gap of a-Si:H is larger than the bandgap of single crystal silicon and has a typical value between 1.7 eV and 1.8 eV.

5.3.3 Models for the density of states and recombination–generation statistics

In general, the energy distribution of states in a-Si:H is characterized by three different regions: (i) extended states above the mobility edge of the conduction band, (ii) extended states below the mobility edge of the valence bandand (iii) localized states between the mobility edges. The continuous distribution of the localized states is a superposition of the conduction and valence band tail states and the defect states.

In Figure 5.2, we present a standard model of the density of states distribution. In this model, the valence and conduction band states are represented by a parabolic dependence on energy that merges with exponentially decaying valence and conduction band tail states. The defect states are represented by two equal Gaussian distributions, which are shifted from each other by the correlation energy, U. The correlation energy is assumed to be constant and positive. As mentioned earlier, dangling bonds are considered the dominant defect in a-Si:H. A dangling bond can be in three charge states: positive (D^+), neutral (D^0) and negative (D^-). An imperfection with three possible charges, such as a dangling bond, is represented in the band diagram by two energy levels $E^{+/0}$ and $E^{0/-}$, which, depending on the position of the Fermi level, characterize the charge occupation of the imperfection. These two energy levels are

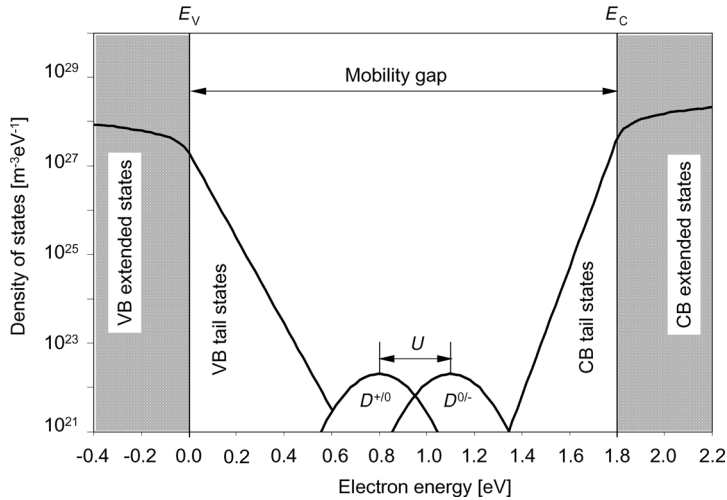

Figure 5.2 The standard model for density of states in a-Si:H.

called the transition energy levels. The two Gaussian distributions, $D^{+/0}$ and $D^{0/-}$, represent the energy distributions of states corresponding to $+/0$ and $0/-$ charge transitions of dangling bonds, respectively. Since the dangling bonds are represented by both the donor like $(+/0)$ and acceptor like $(0/-)$ states, dangling bonds are called amphoteric defects.

The Gaussian distribution that is used to describe the defect states in a-Si:H reflects the concept that the structural disorder results in a distribution of states rather than in states located at a particular energy level. However, the Gaussian representation of defect states does not contain any information about the origin of the defect states. The defect pool theory based on the weak bond–dangling bond conversion model [32] has attracted a lot of attention because it can successfully describe the defect state distribution in a-Si:H [33–35]. The theory assumes that the energy of the defect state can take a range of values due to the inherent disorder of the amorphous network and that the defects can be formed in different charge states. The resulting total defect density of states is the sum of three energy distributions, D_h, D_z, and D_e, which correspond to positive, neutral and negative defects. The defect pool model predicts that the total number of dangling bonds in the intrinsic a-Si:H increases when the Fermi level shifts from the midgap towards the mobility edges of the bands. The position of the Fermi level also determines the energy dependence of the defect state distribution.

The energy states in the bandgap act as trapping and recombination centers and therefore strongly affect many electronic properties of a-Si:H and the performance of a-Si:H devices. In contrast to crystalline semiconductors, in which the recombination process is typically dominated by a single energy level in the bandgap, in a-Si:H, contributions from all bandgap states to the recombination–generation (R–G) rate are included. In order to model the recombination process through the single level states, such as localized tail states, Shockley—Read–Hall R–G statistics [36] is used and Sah and Shockley multilevel R–G statistics [37] are applied for the amphoteric defect states. A detailed analysis and comparison of the modeling approaches of the R–G rate in a-Si:H is given in reference [18].

A large number of experimental techniques have been applied to obtain information about the density of states in a-Si:H [26]. In particular the distribution of localized tail and defect states is of interest. There is no direct method to obtain the energy distribution of states in a-Si:H. The energy distribution of states is determined indirectly from measurements of optical and electrical properties of a-Si:H films or from properties of a space–charge region that is formed at a-Si:H interfaces. In order to provide an understanding of procedures to determine the density of states, we first discuss the optical and electrical properties of a-Si:H.

5.3.4 Optical properties

The optical properties of a-Si:H are usually characterized by the absorption coefficient, the refractive index, and the value of the optical bandgap.

Figure 5.3a shows the typical absorption coefficient of a-Si:H as a function of photon energy. In Figure 5.3b, the absorption coefficient of a-Si:H is plotted with the absorption coefficient of a-SiGe:H, p type a-SiC:H, and crystalline silicon. In the visible part of the solar spectrum, a-Si:H absorbs almost 100 times more than crystalline silicon. This means that a 1 μm thick a-Si:H layer is sufficient to absorb 90 % of the usable solar energy. In practice, the thickness of a-Si:H solar cells is around than 0.3 μm, that is about 1000 times thinner than a typical single crystal silicon cell.

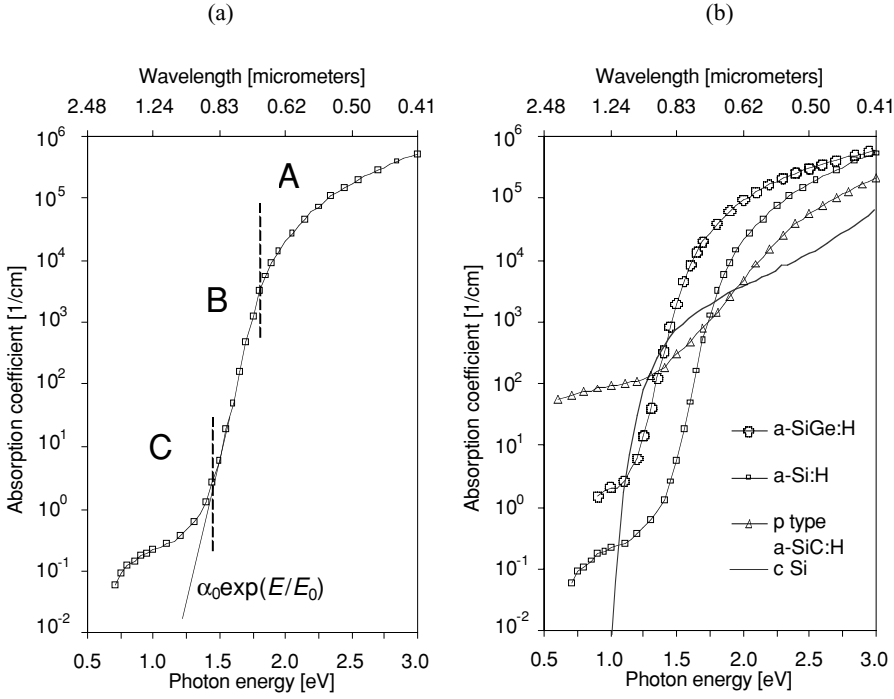

Figure 5.3 (a) Absorption coefficient of a-Si:H as a function of photon energy, (b) absorption coefficient as function of photon energy for a-Si:H, p type a-SiC:H and a-SiGe:H fabricated at Delft University of Technology. The absorption coefficient of c-Si is shown for reference.

Due to the lack of translational symmetry of a unit cell in the structural network of a-Si:H, the law of crystal momentum conservation is relaxed in a-Si:H, and it behaves like a direct semiconductor. The optical absorption coefficient, $\alpha(E)$, is therefore determined by optical transitions involving all pairs of occupied and unoccupied electronic states that are separated by the same photon energy E. For this reason, optical absorption measurements are widely used to determine the density of states distribution in a-Si:H. The absorption coefficient curve is of fundamental importance for evaluating the quality of both amorphous and microcrystalline silicon films.

As indicated in Figure 5.3a, the absorption spectrum of a-Si:H exhibits three regions. In region A, absorption occurs predominantly by transitions between the extended states of the valence and conduction bands. The absorption coefficient in this region is higher than 10^3–$10^4\,\mathrm{cm}^{-1}$ and is commonly determined by reflection-transmission spectroscopy measurement. Region B extends from $\alpha \sim 1$ to $10^3\,\mathrm{cm}^{-1}$ and is characterized by an exponential dependence of the absorption coefficient on the photon energy. This region is called the Urbach edge. When assuming that the optical matrix element is energy independent in this region, as experimentally observed [38], the Urbach edge reflects the transitions between the valence and conduction band tail states. The absorption coefficient in region B can be fitted to

$$\alpha = \alpha_0 \exp(E/E_0), \tag{5.2}$$

where α_0 is a constant and E_0 is the Urbach energy that characterizes the exponential slope of the energy dependence. Because the conduction band tail state distribution is narrower than the valence band tail state distribution, the Urbach energy reflects the slope of the exponential region of the valence band tail. A typical value for device quality a-Si:H film is $E_0 \leq 50 \times 10^{-3}$ eV. Region C, where the absorption coefficient is less than 1 cm^{-1}, is associated with the transitions involving the defect states. Regions B and C are denoted as subbandgap absorption since the absorption coefficient reflects transitions involving states within the bandgap.

From the absorption coefficient of a-Si:H based materials, the so-called optical bandgap is determined. The optical bandgap is a useful material parameter for comparing the light absorption properties of a-Si:H based materials. Generally, the higher optical bandgap of a material, the less light it will absorb. The optical bandgap, E_{opt}, is determined by extrapolating a linear part of the following function $[\alpha(E) \times n(E) \times E]^{1/(1+p+q)}$ versus the photon energy E to $\alpha(E) = 0$, for $\alpha \geq 10^3\ cm^{-1}$:

$$(\alpha(E) \times n(E) \times E)^{1/(1+p+q)} = B(E - E_{opt}) \tag{5.3}$$

where $\alpha(E)$ is the absorption coefficient, $n(E)$ is the refractive index, p and q are constants that describe the shape of the density of extended states distribution for the conduction band and valence band, respectively, and B is a prefactor. When the density of state distribution near the band edges has a square root energy dependence ($p = q = 1/2$), as is commonly the case in crystalline semiconductors, Equation (5.3) describes the so-called Tauc plot [26], and the corresponding optical bandgap is called the Tauc optical gap. When the distribution near the band edges is assumed to be linear ($p = q = 1$), E_{opt} is called the cubic optical gap. The Tauc gap of device quality intrinsic a-Si:H is in the range of 1.70 to 1.80 eV; usually 0.1 to 0.2 eV smaller than this is the cubic gap of the same material. The optical bandgap increases with increasing hydrogen concentration in the film [39].

The refractive index of a-Si:H shows a maximum of almost 5.0 around 425 nm and then decreases as a function of wavelength in the region of interest (350 nm to 900 nm). The refractive index slightly decreases above 900 nm. For device quality a-Si:H, the refractive index at 900 nm is above 3.6.

5.3.5 Electrical properties

The electrical properties of a-Si:H are usually characterized in terms of dark conductivity, photoconductivity and mobility lifetime product. Measuring these properties is a standard approach to obtain information about the quality of a-Si:H material for application in solar cells.

5.3.5.1 Dark conductivity

The dark conductivity σ_d of device quality intrinsic a-Si:H is less than $1 \times 10^{-10}\ \Omega^{-1}\ cm^{-1}$. To determine it and its activation energy, a very low current is measured, in the order of picoamperes. Such measurements are usually carried out on samples with two 1 to 2 cm long coplanar metal electrodes deposited less than 1 mm apart from each other on a single a-Si:H layer on highly resistive glass, such as Corning 1737. Care has to be taken that moisture or

diffusing impurities do not affect the measurement of current. Therefore, the measurement is usually taken in vacuum or in an inert atmosphere and before the measurement, the sample is annealed at 150 °C for half an hour to evaporate all moisture present on the surface of the film. A voltage of typically 100 V is applied to a sample with an a-Si:H layer of about 1 μm thick in order to obtain a current of tens of picoamperes through the sample that can be reliably measured.

The dark conductivity is determined as:

$$\sigma_{\mathrm{d}} = \frac{I}{U}\frac{w}{ld} \tag{5.4}$$

where U is the applied voltage, I is the measured current, l is the length of the electrodes (~1 to 2 cm), w is the distance between the electrodes (0.5 to 1 mm), and d is the thickness of the film.

5.3.5.2 Activation energy of the dark conductivity

The measurement of the temperature dependence of the dark conductivity is used to evaluate the activation energy of the dark conductivity, E_{A}, which gives a good approximation of the position of the Fermi level in a-Si:H films. The temperature dependence of the dark conductivity $\sigma_{\mathrm{d}}(T)$ is described as

$$\sigma_{\mathrm{d}}(T) = \sigma_0 \exp\left(-E_{\mathrm{A}}/kT\right) \tag{5.5}$$

where σ_0 is a conductivity prefactor, T the absolute temperature and k Boltzmann's constant. From the slope of the Arrhenius plot, which in this case is the relationship between $\log(\sigma_{\mathrm{d}}(T))$ and $1/T$, the activation energy is determined. In combination with the optical bandgap, the activation energy is a good measure to evaluate the presence of impurities in the film. The impurities often act as dopants, and even a small concentration of impurities, $1 \times 10^{17}\,\mathrm{cm}^{-3}$ of O or N, causes a shift of the Fermi level. For undoped a-Si:H, the activation energy should be higher than 0.80 eV.

The low dark conductivity of undoped a-Si:H is a result of the low mobility of charge carriers and the high mobility gap of a-Si:H. This is also reflected by the high activation energy of the dark conductivity. The mobility of the charge carriers in the extended states of a-Si:H is about two orders of magnitude lower than in single crystal silicon. Typically, intrinsic a-Si:H is characterized by electron mobility values of 10 to 20 $\mathrm{cm}^2\ \mathrm{V}^{-1}\ \mathrm{s}^{-1}$, and the hole mobility is 1 to 5 $\mathrm{cm}^2\ \mathrm{V}^{-1}\ \mathrm{s}^{-1}$.

5.3.5.3 Photoconductivity

The photoconductivity can be determined by illuminating the same samples as used for the dark conductivity measurement with appropriate light. Often the AM1.5 light spectrum with an incident power of 100 $\mathrm{mW\,cm}^{-2}$ is used. With these conditions, the photoconductivity of device quality undoped a-Si:H, calculated from the photocurrent similarly to Equation (5.4), should be higher than $1 \times 10^{-5}\,\Omega^{-1}\,\mathrm{cm}^{-1}$. The ratio of the photoconductivity and dark conductivity is called the photoresponse. This parameter gives an indication of the suitability of a material

for use as a photoactive layer in a solar cell. A good photoresponse value for a-Si:H is higher than 10^5.

Photoconduction is a complex process of generation, transport and recombination of excess photogenerated carriers. The optical generation rate of carriers G depends on the absorption coefficient, α, and the quantum efficiency for carrier generation η_g. The latter represents the number of electron–hole pairs generated by one absorbed photon. When we assume that the current in a-Si:H is dominated by electrons, transport and recombination are characterized by the extended state mobility μ of electrons and their lifetime, τ. Its photoconductivity can be written as:

$$\sigma_{\text{ph}} = q\,\mu\Delta n = q\,\mu\tau G \tag{5.6}$$

where q is the unit charge and Δn the concentration of photogenerated electrons. The average optical generation rate over the whole thickness, d, of the film is related to the absorbance, A, which can be calculated from the Lambert–Beer absorption formula:

$$A = \Phi^0(1 - R)(1 - \exp(-\alpha\, d)), \tag{5.7}$$

where Φ^0 is the incident photon flux density and R the reflectance of the air–a-Si:H interface. Neglecting the spectral dependence of the reflectance, the average generation rate can be approximated by:

$$G = \eta_{\text{g}}\frac{A}{d} = \eta_{\text{g}}\frac{\Phi^0(1 - R)(1 - \exp(-\alpha\, d))}{d} \tag{5.8}$$

By combining Equations (5.6), (5.7) and (5.8), the photoconductivity can be expressed as:

$$\sigma_{\text{ph}} = q\,\mu\tau\eta_{\text{g}}\frac{\Phi^0(1 - R)(1 - \exp(-\alpha\, d))}{d} \tag{5.9}$$

The quantum efficiency mobility lifetime product $\eta_{\text{g}}\ \mu\tau$ is a useful and often used figure of merit that combines the photoabsorption, transport and recombination in an a-Si:H film. This quantity is determined by measuring photocurrent when illuminating the sample with a monochromatic light of a relatively long wavelength. At such a wavelength, the absorption coefficient is small, which results in almost uniform carrier generation in the a-Si:H film. Usually, 600 nm light is chosen as the probe beam. Using Equation (5.9) combined with the geometry factors of the sample as in Equation (5.4), the $\eta_{\text{g}}\ \mu\tau$ product is obtained as:

$$(\mu\tau\eta_{\text{g}})_{600} = \frac{I_{\text{ph}}w}{qUl\Phi^0(1 - R)(1 - \exp(-\alpha\, d))} \tag{5.10}$$

When we assume that $\eta_{\text{g}} = 1$ in amorphous silicon, it means that one absorbed photon generates one electron–hole pair and the mobility lifetime product at 600 nm for device quality a-Si:H is $\mu\tau \geq 1 \times 10^{-7}\,\text{cm}^2\,\text{V}^{-1}$.

5.3.5.4 Ambipolar diffusion length

The $\mu\tau$ product determined from the photoconductivity measurement characterizes the charge carriers that dominate the transport, i.e. the electrons in amorphous silicon. However, solar

cell performance is often determined by the transport properties of minority carriers, which are holes in a-Si:H. Commonly the steady state photocarrier grating (SSPG) technique is used to determine the ambipolar diffusion length in amorphous silicon [40, 41], from which the mobility lifetime product of the holes is calculated.

When an excess of photogenerated carriers is not distributed uniformly throughout a semiconductor, diffusion of the excess carriers takes place. The excess carriers will diffuse in the semiconductor until they recombine. In the absence of an electric field, the photogenerated electrons and holes diffuse in the same direction. This process is called ambipolar transport. The average distance that the excess carriers can diffuse due to ambipolar transport before being annihilated is defined as the ambipolar diffusion length. The ambipolar diffusion length is therefore a good figure of merit for applying a semiconductor material as a photoactive layer in a solar cell. In case of intrinsic amorphous silicon, ambipolar transport is determined by the mobility of the less mobile charge carriers, holes.

The same samples as for the conductivity measurements can be used for the SSPG technique. The principle of the SSPG technique is based on the creation of a steady state interference pattern in the concentration of photogenerated carriers in the a-Si:H film. This concentration pattern is made by illuminating the sample with two interfering beams generated from one laser. The concentration fringes are parallel to the electrodes of the sample. The photocarriers diffuse from highly populated regions to regions of lower concentration, which leads to a reduction of the amplitude of the modulated carrier population. This reduction depends on the period of the grating pattern and results in a change in the photoconductivity of the sample, which is measured perpendicular to the grating fringes.

In the SSPG experiment, the laser beam is split into two beams, where the intensity of one beam I_1 is larger than that of the second beam I_2. First, the sample is illuminated with both beams which interfere. The weak excitation beam is chopped and the resulting photocurrent is measured using a lock-in amplifier. The obtained signal is proportional to $\sigma_g - \sigma(I_1)$, where σ_g represents the photoconductivity in the presence of the light interference pattern and $\sigma(I_1)$ is the photoconductivity due to the illumination with only beam I_1. Then the sample is illuminated again, but this time the beam with the intensity I_1 is incoherent with the second beam. The obtained signal is proportional to $\sigma_g\,(I_1 + I_2) - \sigma(I_1)$. The ratio between these signals defines the parameter β:

$$\beta = \frac{\sigma_g - \sigma(I_1)}{\sigma(I_1 + I_2) - \sigma(I_1)} \tag{5.11}$$

The parameter β depends on the ambipolar diffusion length L_{amb} and the grating period Λ in the following way (as derived in reference [40]):

$$\beta = 1 - \frac{2\gamma\gamma_0^2}{[1 + (2\pi L_{amb}/\Lambda)^2]^2} \tag{5.12}$$

In Equation (5.12), γ is a power exponent in the relation of the photoconductivity with the generation rate ($\sigma_{ph} \propto G^{\gamma}$), and γ_0 is a factor that characterizes an interference contrast that can change due to, for example, partial coherence between the beams or light scattering ($0 < \gamma_0 \leq 1$). The ambipolar diffusion length is a fitting parameter in the dependence of β on the grating period Λ and is obtained either from the slope of a plot Λ^{-2} versus $(1 - \beta)^{-1//2}$, or from the intersection of the line with the Λ^{-2} axis. The exponent γ is determined from a

plot of the photoconductivity as a function of the light intensity, which is varied using neutral density filters.

5.3.6 Determination of density of states

In the following, we present widely used methods to evaluate the density of states in thin amorphous and microcrystalline silicon layers.

5.3.6.1 Optoelectrical methods

A large group of methods is based on correlating the optical absorption in a-Si:H films or devices with the density of states distribution. The subbandgap absorption especially is of major interest since it reflects transitions involving the localized states within the bandgap. However, the subbandgap absorption is weak and therefore indirect methods, which are based on measurement of some secondary effect, are used to determine the absorption coefficient. In photothermal deflection spectroscopy [42], the deflection of a probe laser beam reflects a change in the refractive index of a medium which is in contact with the a-Si:H film. The change of the refractive index depends on the amount of heat generated by the absorption of monochromatic light in the a-Si:H film and dissipated from the film into the medium. Other techniques, such as constant photocurrent method [43], dual beam photoconductivity [44], and the recently introduced Fourier transform photocurrent spectroscopy [45] are based on measurement of the spectral dependence of the photoconductivity.

5.3.6.2 Photothermal deflection spectroscopy

Photothermal deflection spectroscopy (PDS) is based on the conversion of a fraction of the absorbed photon energy in a film into thermal energy (heat), which dissipates and causes a change in the index of refraction of a medium adjacent to the surface of the film. By probing the medium's refractive index change with a laser beam, one can relate the probe beam deflection to the optical absorption of the film. A sample with a-Si:H film is immersed in an optically transparent and thermally conductive liquid. A chopped, monochromatic beam, which is called a pump beam, illuminates the sample. The deflection signal is measured by a position sensitive detector, which is connected to a lock-in amplifier.

The attractive feature of this technique is its high sensitivity: absorbance values of $\alpha d \approx 10^{-5}$ can be measured on thin films. For a-Si:H films with a typical thickness of 1 μm, an absorption coefficient as low as 10^{-1} cm^{-1} can be determined. The PDS technique is sensitive to surface states, and for this reason, PDS results can overestimate the bulk density of states.

5.3.6.3 Constant photocurrent method

The constant photocurrent method (CPM) is based on measurement of the photoconductivity as described in the previous section. In CPM measurement, the steady state photocurrent is measured as a function of photon energy in the subbandgap region. In this region, the absorption

is weak, which means that $\alpha d \ll 1$. The exponential function can be expanded to a power series and $\exp(-\alpha d) \approx 1 - \alpha d$. Using this approximation in Equation (5.9), the photoconductivity can be expressed as:

$$\sigma_{\mathrm{ph}} = q\mu\tau\eta_{\mathrm{g}}\Phi^0(1-R)\alpha \tag{5.13}$$

Equation (5.4) describes the relation between the photocurrent I_{ph} and the photoconductivity σ_{ph}. Combining Equations (5.4) and (5.13), the photocurrent can be expressed as :

$$I_{\mathrm{ph}} \propto \Phi^0\alpha\eta_{\mathrm{g}}\mu\tau \tag{5.14}$$

The basic idea of CPM measurement is to ensure that the term $\eta_{\mathrm{g}}\mu\tau$ is kept constant during measurement. This is achieved by keeping the photocurrent constant while changing the photon flux density. The constant photocurrent means that the positions of the quasi-Fermi levels for holes and electrons in the bandgap, which determine the number of recombination centres, do not change during the experiment. During the whole measurement, the carrier lifetime is, in this way, kept constant. When we assume that the mobility of the carriers and the generation quantum efficiency are not spectrally dependent, then the absorption coefficient is dependent only on the incident photon flux:

$$\alpha_{\mathrm{CPM}}(E) \approx \frac{C_{\mathrm{CPM}}}{\Phi^0(E)} \tag{5.15}$$

where C_{CPM} is an energy independent constant and $\Phi^0(E)$ the number of photons necessary to keep the photocurrent constant. The relative absorption coefficient α_{CPM} is calibrated to the absolute absorption coefficient, which is determined from reflection–transmission measurement. This original CPM method was later adapted in order to measure the optical (photocurrent) absorption spectrum directly in absolute units without additional calibration and undisturbed by interference fringes [46].

5.3.6.4 Dual beam photoconductivity

The basic idea of dual beam photoconductivity (DBP) measurement is that in addition to a chopped probe beam of monochromatic light, a second light source is used to illuminate the sample. This additional 'bias' light keeps the splitting of the quasi-Fermi levels constant during the measurement. The ac fraction of the photocurrent is measured using a lock-in amplifier and depends on both the monochromatic photon flux and the absorption coefficient of the a-Si:H film [44]. The absorption coefficient can be extracted from the measured photocurrent and photon flux density by:

$$\alpha_{\mathrm{DBP}}(E) \approx C_{\mathrm{DBP}}\frac{I_{\mathrm{ph}}(E)}{\Phi^0(E)} \tag{5.16}$$

where C_{DBP} is an energy independent constant and $\Phi^0(E)$ the photon flux density. As in the case of the CPM, the relative absorption coefficient α_{DBP} has to be normalized to the absolute absorption coefficient. The advantage of the DBP measurement in comparison to the CPM is a shorter measurement time since it is not necessary to adjust the photon flux density of monochromatic light in order to keep the photocurrent constant.

5.3.6.5 Fourier transform photocurrent spectroscopy

Recently, the Fourier transform photocurrent spectroscopy method [45] has been introduced for determining the sub-bandgap absorption. A Fourier transform infrared (FTIR) spectrometer is used as the interferometer and an a-Si:H sample as the external detector. The spectrometer can be equipped with a globar and white light source in order to measure in 0.4 to 1.8 eV spectrum range. The sample, which can be a thin film deposited on a substrate or a complete solar cell, is connected to an electrical circuit with a low noise voltage source and a current preamplifier. The photocurrent of the sample is amplified, and an A/D converter digitizes the output of the preamplifier. Using a computer, the signal is finally translated from the time domain to the frequency domain by Fourier transformation. The FTIR signal from the sample is normalized to the FTIR signal from a spectrally independent detector. The advantage of this method is its sensitivity to low photon energies; the measurement of the subbandgap absorption is extended from ~0.8 eV, typical for the CPM and DBP measurement, to 0.4 eV. The measurement time is strongly reduced and is only a few minutes.

5.3.6.6 Determination of defect concentration from absorption coefficient

Using the subbandgap region of the absorption coefficient (see Figure 5.3a), the defect concentration in a-Si:H is determined using a simple procedure. First, the absorption due to the defect states is determined as:

$$\alpha_{\text{def}} = \alpha - \alpha_0 \exp\left(E/E_0\right) \tag{5.17}$$

where α_0 and E_0 are obtained from the fit to the exponential absorption in region B. Assuming that the optical matrix element is constant in this region, α_{def} is related to the defect density concentration, N_{d}, by [42]:

$$N_{\text{d}} = K_{\text{d}} \int \alpha_{\text{def}} \cdot \text{d}E \tag{5.18}$$

where K_{d} is a correlation factor that depends on the measurement method used to determine the absorption coefficient in region B and C. For two widely used approaches, photothermal deflection spectroscopy and the photoconductivity methods, the correlation factor has been determined to be $K_{\text{d}} = 7.9 \times 10^{15}\,\text{cm}^{-2}\,\text{eV}^{-1}$ [42] and $K_{\text{d}} = 1.6 \times 10^{16}\,\text{cm}^{-2}\,\text{eV}^{-1}$ [47], respectively. Another approach often encountered in the literature is to correlate the value of the absorption coefficient at 1.2 eV to the density of states in the following way [48]:

$$N_{\text{d}} = 2.4 - 5.0 \times 10^{16}\,\alpha_{\text{CPM}}(1.2\,\text{eV}) \quad \text{or} \quad N_{\text{d}} = 1.2 - 2.5 \times 10^{16}\,\alpha_{\text{PDS}}(1.2\,\text{eV}) \tag{5.19}$$

Information about the energy dependence of the density of states in the mobility gap can be extracted from the absorption coefficient using the deconvolution approach [43]. In this approach, the energy distribution of the density of states is extracted by matching the simulated absorption coefficient to the experimental one.

5.3.6.7 Space charge methods

Several methods use the properties of a space charge region that is formed at a-Si:H interfaces. The field effect technique [49], deep level transient spectroscopy (DLTS) [50] and space charge limited current [51, 52] are the main representatives of these techniques.

5.3.6.8 Deep level transient spectroscopy

Deep level transient spectroscopy (DLTS) is an extremely sensitive technique and different from ESR measurements in that it also detects energy levels from nonparamagnetic defects. It is routinely used to determine energy levels and defect concentrations in semiconductors, and it is perhaps the most common technique for measuring deep levels in crystalline semiconductors. It has been demonstrated [50, 53] that in a-Si:H, DLTS is also a valuable method for evaluating the electronic density of states. Originally, a capacitance version of DLTS was used to characterize lightly doped a-Si:H films. Undoped a-Si:H films can be characterized using a charge version of DLTS (Q-DLTS) [54].

The Q-DLTS sample is usually a metal/oxide/semiconductor (MOS) structure consisting of a 1 μm thick a-Si:H layer deposited on a highly doped n^+ type crystalline silicon substrate, which acts as a back contact. For successful Q-DLTS experiments on undoped a-Si:H, a very thin insulating layer has to be created in the surface region of a-Si:H. This insulating layer strongly reduces the leakage current of the sample, which is then negligible with respect to charge transients, and enables shifting of the Fermi level in the a-Si:H film with an applied bias voltage. An Al (semitransparent) layer usually forms the top electrode. By applying bias voltage pulses to the MOS sample, the Fermi level is shifted towards the conduction band mobility edge and the states in the gap of a-Si:H are filled with charge carriers. After each *filling* pulse, the transient current in the external circuit is measured as a function of temperature. The charge emitted from the occupied trap states is determined by integrating the measured current. The charge released at a specific temperature is proportional to the concentration of states at a specific energy in the mobility gap of the a-Si:H material. This technique is suitable for investigating the evolution of the gap states distribution due to light or particle induced degradation, providing new insights in the complex behaviour of a-Si:H under light or particle exposure [55].

Table 5.1 summarizes the criteria for device quality intrinsic amorphous silicon.

5.3.7 Metastability

Inherent to a-Si:H are changes in its electronic properties under light exposure. This is known today as the Staebler–Wronski effect [24]. Since the observation of the Staebler–Wronski effect, a large effort has been put into obtaining an understanding of the processes that cause the light induced structural and optoelectronic changes in a-Si:H [56–59]. An essential feature of the light induced effects on a-Si:H films and solar cells is that most of the effects are 'metastable,' which means they are reversible and can be removed by annealing at temperatures above 150 °C.

Light soaking is thought to lead to the creation of additional dangling bond defects, which is regarded as the principal cause of the Staebler–Wronski effect. The increase of the density of

Table 5.1 Requirements for device quality a-Si:H and a-SiGe:H films for solar cells

Property	a-Si:H	a-SiGe:H
Dark conductivity [Ω^{-1} cm^{-1}]	$<5 \times 10^{-10}$	$<5 \times 10^{-9}$
AM1.5 conductivity [Ω^{-1} cm^{-1}]	$>1 \times 10^{-5}$	$>5 \times 10^{-6}$
Urbach energy [meV]	<47	<55
Activation energy [eV]	≈ 0.8	≈ 0.7
Bandgap, Tauc [eV]	<1.8	~1.45
Bandgap, cubic [eV]	<1.6	1.32
Absorption coefficient (600 nm) [cm^{-1}]	$\geq 3.5 \times 10^4$	$\geq 1 \times 10^5$
Absorption coefficient (400 nm) [cm^{-1}]	$\geq 5 \times 10^5$	$\geq 6 \times 10^5$
Density of defect states		
(CPM, DBP) methods [cm^{-3}]	$\leq 1 \times 10^{16}$	$\leq 1 \times 10^{17}$
ESR method [cm^{-3}]	$\leq 8 \times 10^{15}$	
Mobility-lifetime product (600 nm) [cm^2/V]	$\geq 1 \times 10^{-7}$	
H content [at. %]	9–11	10–15
Microstructure parameter	<0.1	<0.2
Ge content [at. %]		40

defects in a-Si:H due to light soaking is demonstrated in Figure 5.4, which shows the change in the absorption coefficient determined by the DBP technique. The sample was illuminated using a He–Ne red laser ($\lambda = 633$ nm) with an intensity of ~40 mW cm^{-2}. Shown by Figure 5.4, the subbandgap absorption increases with illumination time in the photon energy range between 0.8 and 1.4 eV, which reflects an increase in the defect density. An important aspect of light induced defect generation in a-Si:H is that it saturates. The saturation value of the defect density near room temperature has been found to be $\sim 2 \times 10^{17}$ cm^{-3} and is almost independent of illumination intensity and sample temperature up to 70 °C [60].

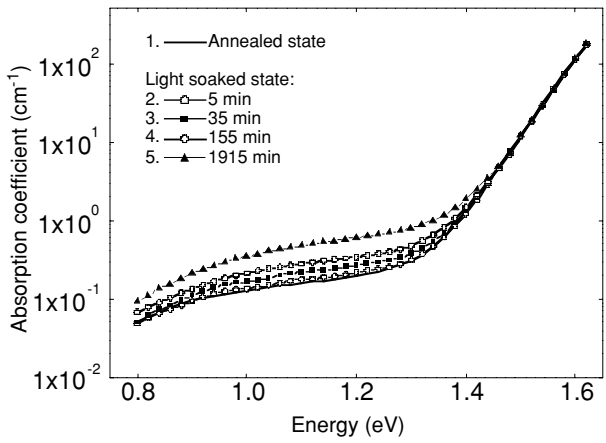

Figure 5.4 The change in subbandgap absorption coefficient of a-Si:H due to light soaking.

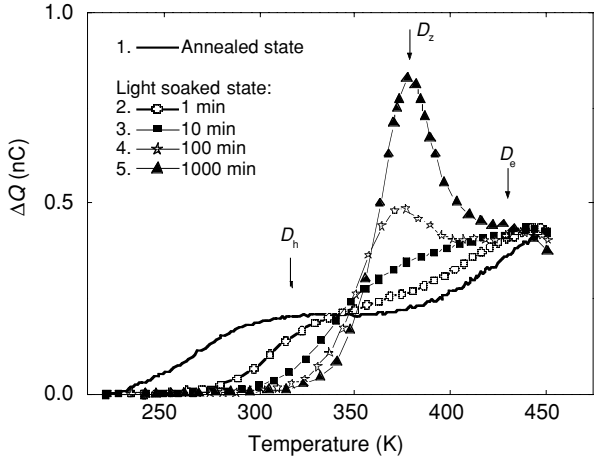

Figure 5.5 The Q-DLTS signal of a-Si:H after light soaking for different exposure times.

Figure 5.5 presents the evolution of the Q-DLTS signal measured after light soaking, which gives information about the energy distribution of the defect states. Light soaking was effected with a He–Ne red laser ($\lambda = 633$ nm) with an intensity of $\sim$250 mW cm^{-2}. The time evolution of the Q-DLTS spectrum shows complex behaviour. At a low temperature the signal disappears, while at 370 K a peak grows significantly with increasing illumination time. The Q-DLTS response around 450 K does not seem to be influenced by moderate light soaking. These three components in the Q-DLTS signal are related to the positively charged, D_h, neutral, D_z, and negatively charged, D_e, defect state distributions, respectively, as predicted by the defect pool model [34]. The arrows in Figure 5.5 indicate the peak positions of D_h, D_z, and D_e gap state distributions in the Q-DLTS spectra. The Q-DLTS measurements indicate that a substantial amount of positively charged defects is removed, the concentration of negatively charged defects remains unchanged and additional neutral defects representing dangling bonds [61] are created. Using the Q-DLTS technique, new insights in the origin and behaviour of different types of defects in a-Si:H have been obtained recently [55]. In this work, it is proposed that in addition to dangling bonds, other types of defects exist in a-Si:H that play an important role in the Staebler–Wronski effect. Positively charged states above midgap are related to a complex formed by a Si dangling bond and a hydrogen molecule. The origins of negatively charged states below midgap are attributed to the floating bonds. Nevertheless, the Staebler–Wronski effect remains a complex phenomenon in a-Si:H and many unresolved issues still remain. The exact role of hydrogen, weak Si–Si bonds and Si–H bonds and complexes in the creation of the metastable defects is still under investigation. Computer simulations of an a-Si:H network support these investigations [62, 63]. Still, there is no commonly accepted model for the metastable defect creation in a-Si:H that is able to explain all experimental observations [58].

5.3.8 Hydrogenated amorphous silicon from hydrogen diluted silane

So far, the effort to fabricate more stable a-Si:H using the PECVD technique has demonstrated the beneficial effect of hydrogen dilution of the source gas on the quality of a-Si:H.

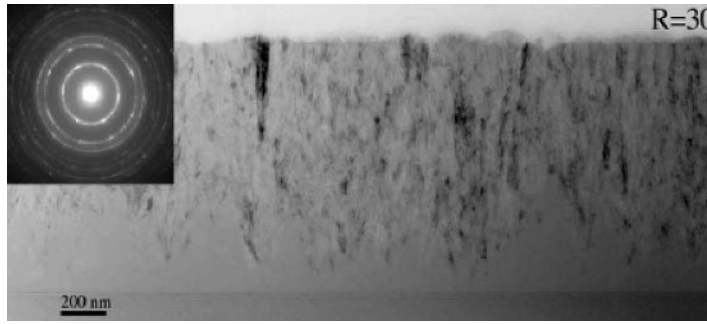

Figure 5.6 TEM photograph of 1 μm thick silicon layer grown in the protocrystalline regime.

Solar cells with a-Si:H absorbers prepared with hydrogen dilution of silane showed a better performance after light exposure than their conventional undiluted counterparts [64, 65]. Hydrogen diluted a-Si:H has received a lot of attention since then and owing to several specific properties, this material is now described in the literature as protocrystalline silicon [66]. The hydrogen–silane dilution ratio ($R = H_2/SiH_4$) roughly defines the deposition conditions at which the so-called protocrystalline Si:H growth regime occurs. In the protocrystalline Si:H growth regime, unique evolutionary growth behaviour is observed, when the film evolves from an amorphous phase into first a mixed amorphous–microcrystalline and subsequently into a single microcrystalline phase. This behaviour is clearly demonstrated in Figure 5.6, which shows a transmission electron microscopy photograph of a layer of about 1 μm thick deposited on a glass substrate at $R = 30$. It is important to note that protocrystalline Si:H material is defined as being fully amorphous, and once the transition from the amorphous to the mixed phase occurs, the film is no longer considered to be protocrystalline. Based on *in situ* real time spectroscopic ellipsometry studies, amorphous-to-microcrystalline silicon phase diagrams have been determined, which predict the thickness at which the transition from amorphous to microcrystalline material for a given R occurs [67]. For lower dilutions ($R < 10$), films are invariably amorphous; this means that there is no evolutionary growth that is characteristic for the protocrystalline growth regime ($R > 10$). For $R < 10$, a critical thickness is observed beyond which the growing amorphous silicon surface becomes rough. The improved stability and quality of protocrystalline Si:H layers compared to conventional a-Si:H deposited from pure silane or using a low hydrogen dilution is attributed to an improved structural order. An enhanced medium range order is determined by measuring the full width at half the maximum ($\Delta 2\theta$) of the first X-ray diffraction (XRD) peak for a-Si:H, which is centred at a scattering angle of $2\theta \sim 28.5^\circ$. A typical value for a-Si:H is $\Delta 2\theta \sim 6^\circ$, which decreases for protocrystalline Si:H to $\Delta 2\theta \sim 5^\circ$ [68]. For the protocrystalline growth regime, an important practical feature is that the phase of the growing film strongly depends on the substrate [66]. Under protocrystalline growth conditions, local epitaxial growth is favoured on crystalline silicon substrates. For this reason, it is difficult, in solar cells, to grow intrinsic protocrystalline Si:H layers directly on doped microcrystalline silicon layers without incorporating a conventional a-Si:H interlayer. On amorphous silicon, the nucleation of crystallites is suppressed. The phase diagrams are important tools for optimization of amorphous and microcrystalline silicon solar cells, as they help to keep the growth of the film within the desired phase.

Among the materials deposited from highly diluted silane in hydrogen, polymorphous silicon (pm-Si:H) is an interesting alternative to a-Si:H [69]. This material is characterized by the presence of dispersed nanocrystallites, which are formed in plasma, embedded in an amorphous network that is more relaxed than that found in standard a-Si:H. Contrary to protocrystalline silicon films, pm-Si:H films can be made thick, because their structure does not depend on thickness or the nature of the substrate. The concentration of small crystallites is approximately 2 %. Spectroscopic ellipsometry measurements demonstrated that pm-Si:H films are more dense than standard a-Si:H, in spite of their high hydrogen content, in the range of 15–20 %. This peculiar structure of pm-Si:H results in a low defect density ($\sim 5 \times 10^{14}\,\mathrm{cm}^{-3}$) and a higher resistance to light soaking than a-Si:H. In particular improved hole transport appears to be a key point for the application of this material in solar cells.

5.3.9 Doping of hydrogenated amorphous silicon

The purpose of doping is to manipulate the type of electrical conductivity and its magnitude by adding a controlled amount of special impurity atoms. The principal doping elements used in a-Si:H are the same as in crystalline silicon: boron for p type and phosphorus for n type material. In 1975 Spear and LeComber from Dundee University first reported that amorphous silicon could be doped by addition of boron and phosphorus [2]. They achieved a change in conductivity of a-Si:H by mixing the silicon source gas, silane (SiH_4), with phosphine (PH_3) or diborane (B_2H_6) during deposition using the glow discharge method. Figure 5.7 shows the

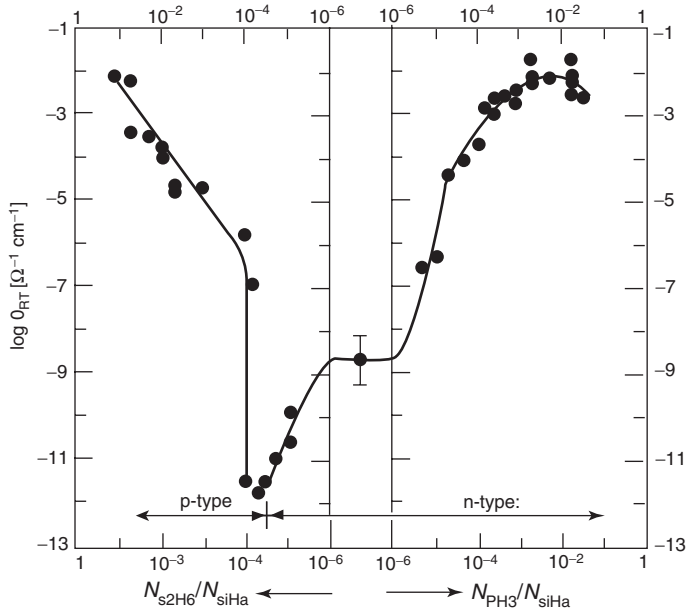

Figure 5.7 Room temperature conductivity, σ_{RT}, of n and p type a-Si:H, plotted as a function of fraction of doping gases in the gas mixture with silane [70]. Reproduced from Figure 3, *Philosophical Magazine* 33, W. E. Spear, *et al.*, "Electronic properties of substitutionally doped amorphous Si and Ge", p. 935–949. Copyright (1976) with permission from Taylor & Francis Ltd, http://www.tandf.co.uk/journals.

room temperature conductivity, σ_{RT}, of their a-Si:H as a function of the fraction of doping gases in a mixture with silane [70]. The conductivity of a-Si:H could be varied by more than a factor of 10^8. The activation energy decreased from 0.7–0.8 eV in the intrinsic material to about 0.15 eV in the phosphorus doped material and 0.3 eV in the boron doped material.

The demonstration of effective doping of a-Si:H was an important breakthrough, because for a long time it was believed that effective doping of amorphous silicon could not be achieved. The continuous random network was assumed to be able easily to incorporate impurity atoms, such as phosphorus and boron, with a coordination corresponding to the bonding configuration of the impurity atoms with the lowest energy. This property of the continuous random network is in contrast to the crystalline structure, in which, due to the long range order, the impurity atoms are forced to adopt the coordination of the host atoms. In a continuous random network, the optimum number of covalent bonds (coordination), Z, for an atom with N valence electrons is:

$$Z = 8 - N \quad \text{for } N \geq 4 \qquad (5.19)$$
$$Z = N \quad \text{for } N < 4$$

This prediction of the atom coordination in the continuous random network is known as the '$8 - N$ rule' and was introduced by Mott in 1969 [71].

For example, following the $8 - N$ rule, a phosphorus atom with five valence electrons would incorporate itself in the continuous random network by forming three covalent bonds with neighboring atoms. This situation is illustrated in Figure 5.8a. In order to describe the configuration of the atoms in the structural network, the notation T_z^q is used, where T is the atom, z is the coordination number, and q is the charge state of the atom; P_3^0 denotes a phosphorus atom that is covalently bonded to three neighboring atoms and is neutral. In a-Si:H, most of the phosphorus atoms are incorporated according to the $8 - N$ rule. They adopt the optimal threefold coordination that represents the nondoping state and is thus electrically inactive. The doping efficiency in a-Si:H, which is defined as the fraction of dopant atoms with fourfold coordination, is rather low. In comparison to single crystal silicon, where the doping efficiency at room temperature is almost unity, it is in the range of 10^{-2}–10^{-3} in a-Si:H. This means that relatively high concentrations of phosphorous atoms must be introduced in order to obtain material with high conductivity. A phosphorous atom can also be incorporated in

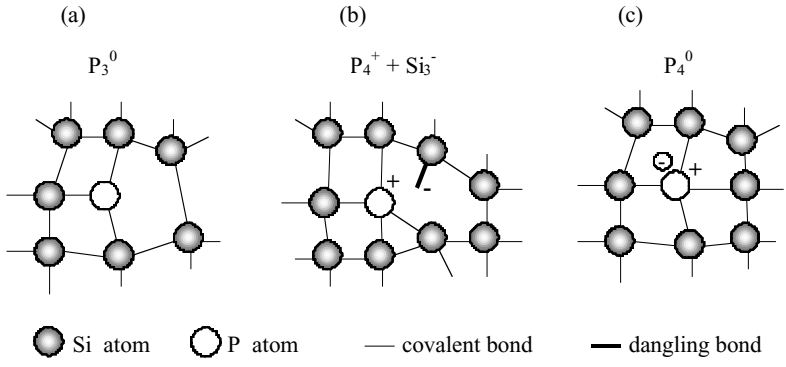

Figure 5.8 Possible configurations of a phosphorous atom in an a-Si:H network: (a) the nondoping state P_3^0, (b) the defect compensated donor state $P_4^+ + Si_3^-$, (c) the neutral donor P_4^0.

the network as the neutral donor P_4^0 like in single crystal silicon (see Figure 5.8c), but this configuration is characterized by a much higher energy than the optimal P_3^0 configuration and is therefore unstable in the continuous random network. Most of the phosphorous atoms which contribute to doping are not P_4^0 neutral donors but charged phosphorus atoms P_4^+. The formation of the P_4^+ charged state is accompanied by formation of negatively charged dangling bond Si_3^-, as illustrated in Figure 5.8b. The P_4^+ and Si_3^- configuration is energetically more favourable than the P_4^0 donor and is called the defect compensated donor.

The formation of defect compensated donors in the case of phosphorus atoms and defect compensated acceptors in the case of boron atoms is the major doping mechanism in a-Si:H. This mechanism was explained by Street and is known as the autocompensation model [72]. The most important result of this model is that doping of a-Si:H inevitably leads to the creation of dangling bonds. Doped a-Si:H has a defect density two or three orders of magnitude larger than intrinsic a-Si:H. The diffusion length of charge carriers in doped a-Si:H is very small compared to single crystal silicon. For this reason, a-Si:H solar cells cannot function successfully as a p-n junction, a relatively defect free intrinsic layer has to be inserted between the p type and n type layers.

An additional important difference between a-Si:H and single crystal silicon is that when the concentration of boron and phosphorous atoms in a-Si:H increases, the Fermi level does not move closer to the valence and conduction band mobility edges than 0.30 eV and to 0.15 eV, respectively. The presence of tail and defect states in the bandgap does not allow a full shift of the Fermi level towards the band edges. A shift towards the band edges is accompanied by the building up of a large space charge in the exponentially increasing tail states that compensates the charge created by ionized doping atoms. This shift also decreases the probability that the doping state configurations of incorporated dopant atoms are formed. The limited shift of the Fermi level in doped layers restricts the built-in potential in the junction of an a-Si:H solar cell, resulting in a lower value of the open circuit voltage, V_{oc}, than expected from the value of the bandgap energy.

5.3.10 Alloying of hydrogenated amorphous silicon

The purpose of alloying a-Si:H for photovoltaic application is to shift the optical absorption spectrum to higher or lower photon energies and in this way to adjust the optical sensitivity of *a*-Si:H to different parts of the solar spectrum. The absorption of a-Si:H can be slightly changed by varying the hydrogen content in a film [39]. This is done by changing the deposition conditions, such as the substrate temperature or dilution of silane with hydrogen. A substantial shift of the absorption coefficient can be achieved by alloying a-Si:H with carbon, oxygen, nitrogen or germanium. Alloying, like doping, can easily be accomplished by adding the appropriate gases to the silane source gas in the CVD process. Mixing silane with methane or germane results in hydrogenated amorphous silicon carbide (a-SiC:H) or hydrogenated amorphous silicon germanium (a-SiGe:H), respectively. In the case of a-SiC:H, the absorption edge is shifted to higher photon energies. The absorption edge of a-SiGe:H alloys, however, is shifted to the lower photon energies in comparison to a-Si:H. The absorption coefficients of p type a-SiC:H and a-SiGe:H are shown in Figure 5.3b. Easy alloying of a-Si:H allows the design of solar cell structures in which these alloys are used as absorber layers.

At present, only a-SiGe:H alloys have proved to be good candidates for the absorber layers in multijunction a-Si:H solar cells. Early studies on this material demonstrated that by changing the ratio between silane and germane in the gas mixture, a-$Si_{1-x}Ge_x$:H layers can be fabricated

with an optical bandgap ranging from 1.7 eV ($x = 0$) to 1.0 eV ($x = 1$). However, they also revealed that the photoelectronic properties of a-SiGe:H alloys of relevance for photovoltaic applications deteriorate as the germanium content in the film increases compared to device quality a-Si:H [73]. The traditional deposition parameters that led to device quality a-Si:H could not produce high quality a-$Si_{1-x}Ge_x$:H material for $x > 0.3$. The deposition process was studied intensively in order to obtain improved a-SiGe:H material. This was achieved mainly by diluting the silane and germane mixture with hydrogen [74]. The application of a strong hydrogen dilution of the silane–germane mixture allowed lowering of the deposition temperature of a-SiGe:H from 250 °C to 180 °C while maintaining high quality material [75]. The implementation of the a-SiGe:H absorbers deposited at low temperatures resulted in improved solar cell performance, which was explained by the reduction of the thermal damage to the underlying layers.

The crucial parameter that determines the photovoltaic quality of amorphous silicon based materials is the density and distribution of the gap states. Measurements of the subbandgap absorption of a-SiGe:H alloys have demonstrated that the Urbach energy remains unchanged as the bandgap is lowered down to 1.25 eV with values similar to those of device quality a-Si:H (about 50 meV) [76]. These also show that the density of defect states in a-SiGe:H alloys generally tends to increase with increasing Ge content in the material. At present, a-SiGe:H layers are used in the bottom cell of the tandem cells and in the middle and bottom component cells of the triple junction solar cells to more effectively capture the long wavelength photons. The hydrogen dilution of the source gas mixture is carefully optimized in order to grow a-SiGe:H in the protocrystalline regime (near the transition edge material) [77]. The magnitude of V_{oc} is used as an indicator of the amorphous to microcrystalline transition. The criteria for device quality a-SiGe:H alloy with a Tauc optical gap around 1.45 eV used in the tandem cells are listed in Table 5.1.

Boron doped a-SiC:H has become a standard p type layer in a-Si:H solar cells [8]. Since boron incorporation reduces the bandgap of a-SiC:H, an optimal p type layer is a trade-off between conductivity and absorption. In addition, a-SiC:H with a low defect density is applied in highly efficient solar cells as a thin buffer layer at the p/i interface. The buffer layer prevents diffusion of boron from the p type into the intrinsic layer and back diffusion of the photogenerated electrons from the intrinsic into the p type layer.

5.4 DEPOSITION OF HYDROGENATED AMORPHOUS SILICON

The first amorphous silicon layers were deposited in a radio frequency driven glow discharge using silane [1]. Since then, many other deposition methods have been investigated in order to improve the quality of a-Si:H and increase the deposition rate. The methods used for depositing thin films of a-Si:H can be divided in two groups. The first group includes methods that form a-Si:H from a gas phase by decomposition of silicon bearing gas and are known as chemical vapor deposition (CVD) methods. The second group represents the physical deposition methods in which silicon atoms for a-Si:H growth are obtained by sputtering a silicon target. The sputtering technique for a-Si:H is not commonly used and therefore not addressed in detail in this chapter. The radio frequency glow discharge method, today known as rf PECVD, is still the method most commonly used, both in the laboratory and on an industrial scale. The bottleneck of the rf PECVD technique is its relatively low deposition rate ($R_d \approx 1 - 2\,\text{Å}\,s^{-1}$). When scaling a-Si:H solar cell technology to a mass production scale, the deposition rate of a-Si:H becomes an important issue and a deposition rate of 10–20 Å s^{-1} is required.

5.4.1 Radio frequency plasma enhanced chemical vapor deposition

The deposition method most widely used to produce device quality a-Si:H is rf (the excitation frequency of plasma is 13.56 MHz) PECVD. The role of the plasma is to provide a source of energy to dissociate silicon bearing gas, which is usually silane . This is done by collisions with electrons, which originate as secondary electrons in the plasma and build up their energy by acceleration in an electric field. The growth of an a-Si:H film is accomplished by attaching reactive particles of dissociated silane molecules, called radicals, to the surface of the growing film. As the thickness of the a-Si:H film for device applications is around half a micrometer, a-Si:H must be deposited on an appropriate substrate carrier. Some of the energy transferred to silane molecules in the collisions with electrons is radiated as visible light, for which reason the deposition method is also referred to as glow discharge. An important advantage of plasma enhanced CVD deposition is that the deposition temperature of device quality a-Si:H is usually between 200 °C and 250 °C. The low temperature process allows the use of a variety of low cost materials as a substrate, such as glass, stainless steel and flexible plastic foils.

The PECVD deposition system is relatively simple and consists of five main parts (see Figure 5.9):

- A stainless steel high vacuum reaction chamber with capacitatively coupled parallel electrodes, rf power feedthrough, substrate holder and substrate heating assembly.
- A gas handling system containing mass flow controllers and several gas valves to handle gas flows required for the deposition of the intrinsic and doped layers and pressure in the chamber.
- A pumping system that usually consists of a turbomolecular pump and a mechanical rotary pump, which can handle reactive gasses.

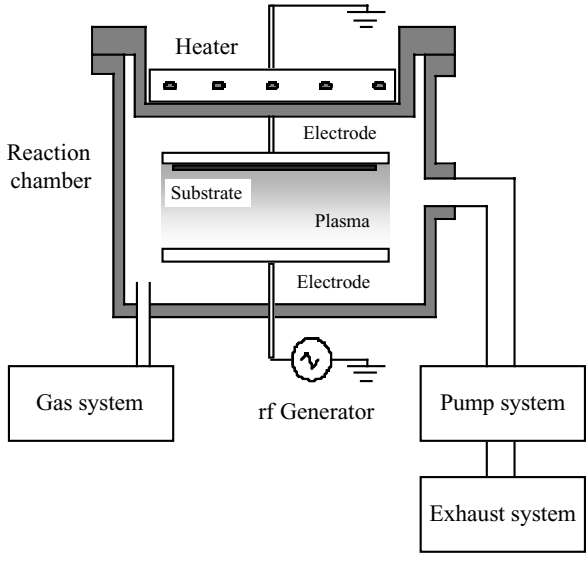

Figure 5.9 Schematic diagram of an rf PECVD deposition system.

- An exhaust system with a scrubber or a burn box to process the outlet gasses.
- An electronic and control part that consists of a dc or rf power generator with a matching box and vacuum, pressure and temperature gauging.

The deposition of *a*-Si:H layer from a silane plasma can be described as a four step process [18]:

(1) The primary reactions in the gas phase, in which SiH_4 molecules are decomposed by electron impact excitation, generate various neutral radicals and molecules, positive and negative ions, and electrons.

(2) The secondary reactions in plasma between molecules and ions and radicals result in the formation of reactive species and eventually in large silicon–hydrogen clusters, which are described in the literature as dust or powder particles. Neutral species diffuse to the substrate, positive ions bombard the growing film, and negative ions are trapped within the plasma.

(3) Interaction of radicals with the surface of the growing film, such as radical diffusion, chemical bonding, hydrogen sticking to the surface or abstraction from the surface.

(4) The subsurface release of hydrogen and relaxation of the silicon network.

The SiH_3 radical is generally considered to be the dominant radical in a-Si:H growth [78, 79]. Since most of the growing substrate is terminated by hydrogen [80], the SiH_3 radical does not readily bond to the growing film but diffuses over the surface until it encounters a dangling bond. By bonding to the dangling bond, the SiH_3 radical contributes to the growth. Bonding of the SiH_3 to the growing surface requires available dangling bonds, which are created when hydrogen is removed from the surface. Hydrogen can be removed by thermal excitation or by abstraction by a SiH_3 radical, in which a dangling bond and a SiH_4 molecule are formed [78]. Though other radicals contribute much less to the growth, they do play an important role in determining the properties of the film. The SiH_2 and higher silane radicals have higher sticking coefficients than SiH_3 and can be incorporated directly into the hydrogen terminated surface [26]. However, the contribution of these radicals to the growth results in poor quality films, and therefore the presence of these radicals in the plasma should be avoided. Ions have been estimated to be able to contribute 10 % to the growth of a-Si:H [81].

Concluding, the deposition process is a complex phenomenon of gas and surface reactions that are controlled by deposition parameters such as the gas composition, flows and pressure, the power density and frequency, the substrate temperature, the electrode geometry, etc. The textbook by Luft and Tsuo discusses in detail the deposition conditions of hydrogenated amorphous silicon alloys [82]. Additional information is to be found in reference [79]. Typical deposition parameters to obtain uniform films of device quality a-Si:H in a laboratory rf PECVD deposition system are: silane flow 20–50 sccm[1], process pressure 0.5–0.7 mbar, substrate temperature 200–250 °C, rf power density 20–50 mW cm^{-2}, electrode distance 1–3 cm. A typical deposition rate is 1–2 Å s^{-1}. One can easily calculate that using these conventional

[1] sccm: standard cubic centimetre per minute. It is a measure for gas flow. One standard cubic centimetre refers to the amount of gas under standard conditions (1 bar, 0 °C) in one cm^3.

conditions, depositing a 300 nm thick a-Si:H absorber layer in a solar cell takes from 25 to 50 minutes. For high volume mass production this is too long, and a deposition rate of 10–20 Å/s is required. Considerable research is therefore being devoted to increasing the deposition rate of a-Si:H without deteriorating the material quality.

The central parameter governing the deposition rate is the power absorbed by the plasma. Higher power results in a higher electron density and electron temperature in the plasma [79], which facilitates the dissociation of SiH_4 molecules. The resulting higher concentrations of SiH_3 and other radicals contribute to a higher deposition rate. However, increasing power leads to deposition conditions which favor the generation of higher silane radicals and eventually powder formation. These deposition conditions result in films with an inferior quality characterized by an increased concentration of H and SiH_2 bonds in the film [83]. In order to facilitate the formation of a compact Si network under high deposition rate conditions, the suppression of formation of SiH_2 bonds is desired [84]. This can be achieved by lowering the electron temperature in the plasma and/or by increasing the deposition temperature. A lower electron temperature in the plasma can be achieved by using a higher plasma excitation frequency. A high deposition temperature of up to 350 °C is required at high deposition rates to promote the diffusion of higher silanes onto and the elimination of hydrogen from the growing surface. However, such a high deposition temperature for absorber layers causes thermal damage to the underlying layers in solar cells [75].

Suppression of higher silane radicals and short lifetime radicals in the gas phase at a high deposition rate has become a general approach for depositing a-Si:H with sufficient material quality. In order to achieve higher deposition rates, two approaches have been taken. In the first, the operating conditions of the PECVD technique were further investigated, which resulted in a high pressure high power rf PECVD [85], a PECVD with very high plasma excitation frequency (vhf) [86], and microwave PECVD [87]. The second approach has concentrated on the investigation and development of novel deposition techniques, such as the hot wire CVD (HWCVD) technique, known also as catalytic CVD [88] and the expanding thermal plasma CVD (ETPCVD) technique [89].

5.4.2 Direct plasma enhanced chemical vapor deposition techniques

5.4.2.1 High pressure high power radio frequency plasma enhanced chemical vapor deposition

Device quality a-Si:H films have been fabricated at a deposition rate of 12 Å s^{-1} using the deposition regime of high deposition pressure (5–10 mbar) and high rf-power density (270–530 mW cm^{-2}) from source gas mixtures of silane and hydrogen [85]. It has been observed that by varying the silane to hydrogen flow ratio or by changing the deposition pressure at a fixed flow ratio, a transition from amorphous to microcrystalline silicon growth can be obtained. Single junction a-Si:H solar cells having a-Si:H absorbers deposited at 190 °C and R_d = 12 Å s^{-1} achieved a stabilized efficiency of 6.5 % [85]. An increase in the bandgap for high rate a-Si:H cells by about 50 meV was observed as compared to the standard a-Si:H intrinsic layers prepared at the same deposition temperature of 190 °C with a low hydrogen dilution at a low rate (1.5 Å s^{-1}). The wide bandgap and corresponding high V_{oc} (typically 0.88–0.9 V)

make these high rate a-Si:H cells interesting candidates for top cells in a-Si:H/a-Si:H or a-Si:H/a-SiGe:H stacked solar cells.

Similar widening of the bandgap is observed for pm-Si:H characterized by a high hydrogen content [69]. This material is deposited in a regime that is close to powder formation. The powder formation is achieved by using plasma conditions that favor secondary reactions including: the increase of pressure, power, interelectrode distance and the decrease of the substrate temperature. The key factor to deposit pm-Si:H is to keep the plasma close to the transition regime conditions. Under this regime, small crystalline particles of 3–5 nm can be formed in the plasma, which are embedded in the growing amorphous film. To keep the plasma in the transition regime, high dilutions of SiH_4 in H ($R > 30$) are used. The larger optical gap of pm-Si:H with respect to a-Si:H and the improved stability of pm-Si:H solar cells make them an ideal material for the top cell with high V_{oc} in tandem and triple junction devices.

5.4.2.2 Very high frequency plasma enhanced chemical vapor deposition

Researchers at the University of Neuchâtel investigated the influence of increasing the plasma excitation frequency in PECVD from 13.56 MHz up to 150 MHz [86], a process today known as the very high frequency (vhf) range (30 to 300 MHz). They demonstrated that by increasing the excitation frequency from 13.56 MHz to 70 MHz at constant plasma power, the deposition rate increases monotonously from 3 to 10 Å s^{-1}, maintaining good quality a-Si:H films [90]. The shift to higher excitation frequencies modifies the electron energy distribution function in plasma, which leads to a faster dissociation rate of source gases and thus higher deposition rates. The higher operating frequencies allow the application of higher power densities in plasma, while remaining in a powder free operational regime [91].

Using the vhf PECVD technique, the researchers at the University of Neuchâtel recently fabricated a p-i-n a-Si:H cell with a stabilized efficiency of 9.5 % [92], which is the highest stabilized efficiency achieved for the p-i-n a-Si:H cell structure. The deposition rate for the a-Si:H intrinsic layer was around 5 Å s^{-1}. This p-i-n cell has an absorber layer thickness of only ~0.25 μm and reveals a very high, stabilized short circuit current density, J_{sc}, of over 17.5 mA cm^{-2} (initial > 18 mA cm^{-2}). The cell was deposited on a glass substrate coated with LP CVD ZnO. The light trapping has also been improved by applying an antireflective (AR) coating.

Recently, the Unaxis KAI PECVD commercial deposition system has been adapted to allow the deposition of a-Si:H and μc-Si:H silicon at an excitation frequency of 40 MHz [21]. In the KAI-M reactor, in which a sheet of glass of 1.4 m^2 size is processed, single junction a-Si:H solar cells were deposited with initial efficiencies of 10 %.

Mitsubishi Heavy Industries have developed a large area vhf PECVD apparatus for depositing on 1.1 × 1.4 m^2 substrate implementing a ladder shaped electrode and using a phase modulation method [93]. The base frequency in the process is 60 MHz and the other frequency is selected based on the degree of uniformity of the deposition. The average deposition rate is 11 Å s^{-1} and the thickness uniformity is kept within ±18 %. Amorphous silicon p-i-n modules with stable aperture efficiency of 8 % have been developed, and the commercial production of a-Si:H modules using this type deposition system started in October 2002.

The principle challenges to apply vhf PECVD on an industrial scale are: (i) the uniformity of the deposited layers on a large substrate when the effect of standing electrical waves at high frequencies (>60 MHz) limits its application and (ii) effective coupling of the power to the plasma.

5.4.3 Remote plasma enhanced chemical vapor deposition techniques

5.4.3.1 Expanding thermal plasma chemical vapor deposition

An important feature of the ETPCVD [89] technique is that it is a remote plasma technique. The ETPCVD deposition set-up is schematically shown in Figure 5.10. The plasma generation and film deposition are spatially separated. The set-up consists of a high pressure plasma source and a low pressure deposition chamber. The plasma is generated by a dc discharge in a cascaded arc in a mixture of nondepositing gasses such as argon and/or hydrogen. The power used to maintain the plasma is typically in the 2 to 8 kW range. The pressure in the plasma source is 200 to 700 mbar, from which the plasma expands supersonically into the deposition chamber, where the pressure is typically 0.1 to 0.3 mbar. Pure SiH_4 is injected into the plasma jet from an injection ring several centimetres behind the expansion nozzle. The silane is dissociated by the reactive species emanating from the plasma source. Hydrogen flow plays an important role in the growth of good quality a-Si:H, since it determines the availability of the atomic hydrogen that is responsible for generating SiH_3 radicals. The deposition rate of a-Si:H layers depends on a number of factors, such as gas flows and arc current, and can reach 800 Å s^{-1} [89]. In order to deposit device quality a-Si:H at high deposition rates (>70 Å s^{-1}), elevated substrate

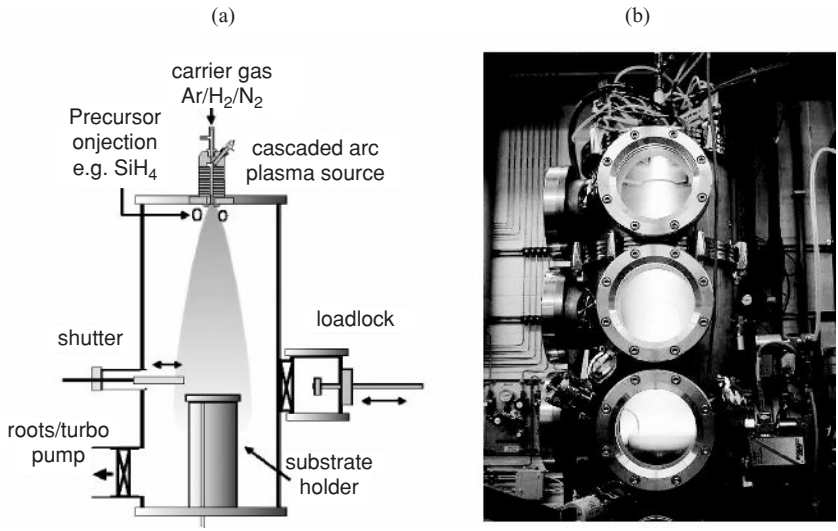

Figure 5.10 (a) A schematic representation of the ETPCVD deposition system, (b) a photograph of the ETPCVD chamber of the CASCADE deposition system at Delft University of Technology during operation. (Courtesy of Richard van de Sanden, Eindhoven University of Technology.)

temperatures around 400 °C have to be used [94]. The need for higher temperatures originates from the competition between the deposition rate and the surface diffusion processes during growth [95]. Applying an external rf bias to the substrate during ETPCVD deposition of a-Si:H has proved to provide extra energy to the surface due to a moderate ion bombardment of the growing surface. The energy delivered to the surface by ion bombardment makes it possible to reduce the deposition temperature by ∼100 °C while preserving good material properties [94]. The ETPCVD method offers excellent possibilities to study the growth of a-Si:H and has already contributed to a better understanding of the importance of the surface processes and the role of different gas species during growth [96].

In order to employ the ETPCVD deposition method for fabricating a-Si:H solar cells, a three chamber system, called CASCADE, has been built [97]. The deposition set-up consists of three vacuum chambers: a load lock, an rf PECVD chamber for the deposition of the doped layers, and an ETPCVD chamber for the growth of the intrinsic layers (see Figure 5.10b). Using rf bias voltage during the ETP CVD growth, compact a-Si:H films are fabricated at high deposition rates, $R_d \geq 10\,\text{Å}\,s^{-1}$, at a substrate temperature lower than 300 °C. A single junction a-Si:H solar cell, using an ETPCVD a-Si:H absorber deposited at 250 °C and $R_d = 11\,\text{Å}\,s^{-1}$, has recently achieved an initial efficiency of 8.0 % [98].

5.4.4 Hotwire chemical vapor deposition

Hot wire CVD is based on the dissociation of gas molecules by a catalytic cracking reaction on a hot filament. A laboratory HW-CVD deposition chamber in its simplest form can be made similar to a PECVD one (see Figure 5.9), where the filaments replace the rf electrode. The filaments are usually made of tungsten or tantalum and placed in the vicinity of the substrate holder. The decomposition of SiH_4 into single silicon and hydrogen radicals is efficient for filament temperatures above 1600 °C. Since the generation of deposition species is different in HW-CVD compared to conventional PECVD, where the species are generated by collisions between energetic electrons and gas molecules, one can expect the resulting a-Si:H films to have different properties to PECVD films. The NREL group demonstrated that by using the HW-CVD technique, a-Si:H films with a hydrogen concentration well below the optimal value of 10 atomic % can be fabricated at substrate temperatures higher than those for the rf PECVD. Electronic properties of these films such as the Urbach energy and defect concentration were similar to a PECVD device quality material [99]. The low hydrogen content, down to 1 atomic %, suggests that these films should be stable against light induced degradation. This work has initiated considerable interest in the HWCVD deposition method and today, many groups all over the world study HWCVD a-Si:H and μc-Si:H materials for various applications such as solar cells [100] and thin film transistors [101].

Like the ETPCVD technique, in the beginning HWCVD produced a-Si:H films with device quality at higher temperatures than used for PECVD [102]. The films deposited at $30\,\text{Å}\,s^{-1}$ and asubstrate temperature of 380 °C exhibited a low defect density of around $10^{16}\,cm^{-3}$ and a low H content: less than 5 atomic %. Recently, a-Si:H films were fabricated at a relatively low substrate temperature (250 °C) that demonstrate properties of protocrystalline silicon [103]. While in conventional PECVD using a high hydrogen dilution of silane, protocrystalline Si can be fabricated at a low deposition rate ($\sim 3\,\text{Å}\,s^{-1}$), researchers at Utrecht University deposited HWCVD protocrystalline Si films from pure silane at high deposition rates ($\sim 10\,\text{Å}\,s^{-1}$). Solar cells in the n-i-p configuration incorporating these HWCVD protocrystalline layers at a

substrate temperature of 250 °C have demonstrated excellent stability against light soaking: after 1500 hours of light soaking, the change in fill factor was within 10 %. The stability of these layers against degradation is correlated with a special void nature and enhanced medium range order [103]. The record single junction n-i-p a-Si:H solar cells with an HWCVD absorber layer deposited at 16.5 Å s^{-1} had an initial efficiency of 9.8 % [104]. Recently, p-i -n single junction a-Si:H solar cells on glass/SnO_2:F substrates with HWCVD absorber layers deposited at 32 and 16 Å s^{-1} reached the initial efficiencies of 7.5 and 8.5 %, respectively [105].

The remarkable features of the HWCVD process make it very attractive for industrial productions: its high deposition rate, high gas utilization, low pressure process avoiding dust formation and therefore the need for frequent chamber cleaning, its large area deposition achieved by the use of multiple filaments and/or filament grids [106] and its decoupling of the gas dissociation from the deposition on the substrate [107]. Scaling up of the HWCVD technique for production has to overcome issues regarding uniform deposition over the large area, filament lifetime and ageing, and the contamination of layers from the filaments. Recent developments show that these issues can be solved successfully and the Japanese company Anelva [106] has introduced the HWCVD deposition system for large area deposition.

5.5 AMORPHOUS SILICON SOLAR CELLS

5.5.1 Hydrogenated amorphous silicon solar cell structure

In a-Si:H, the diffusion length of the charge carriers is much shorter than in crystalline silicon. In device quality intrinsic a-Si:H the ambipolar diffusion length ranges from 0.1 to 0.3 μm. In doped a-Si:H layers, in which the defect density due to doping is two or three orders of magnitude higher than in intrinsic a-Si:H, the diffusion length of the minority carriers is even lower. A solar cell structure based on the transport of the minority carriers in the quasi-neudal regions of the p-n junction as in the case of crystalline silicon does not work for a-Si:H. Due to the very short diffusion length the photogenerated carriers would virtually all recombine in the doped a-Si:H layers before reaching the depletion region of the p-n junction. Therefore, an a-Si:H solar cell is designed differently compared to the standard p-n junction of a crystalline silicon cell.

A schematic structure of a single junction a-Si:H solar cell is shown in Figure 5.11. The active device consists of three principal layers: a p type a-SiC:H layer, an intrinsic a-Si:H layer, and an n type a-Si:H layer, which form a p-i-n junction. This structure is called the single junction a-Si:H solar cell. The doped layers are usually very thin: a p type a-SiC:H layer is ∼10 nm thick, and an n type a-Si:H is ∼20 nm thick. The doped layers have two functions in an a-Si:H solar cell. First, they set up an internal electric field across the intrinsic a-Si:H layer. The electric field should be high enough to ensure that the photogenerated carriers in the intrinsic a-Si:H layer are collected. The strength of the electric field depends on the doping level in the doped layers and the thickness of the intrinsic layer. Second, the doped layers establish low loss ohmic electrical contacts between the a-Si:H part of the solar cell and the external electrodes. Therefore, a sufficiently high electrical conductivity is required for both p and n type layers in order to form a high built-in voltage across the p-i-n junction and low resistance contacts with the electrodes. The intrinsic layer with an optical bandgap of about 1.75 eV serves as an ‘absorber’ layer. The electron–hole pairs that are generated in the absorber

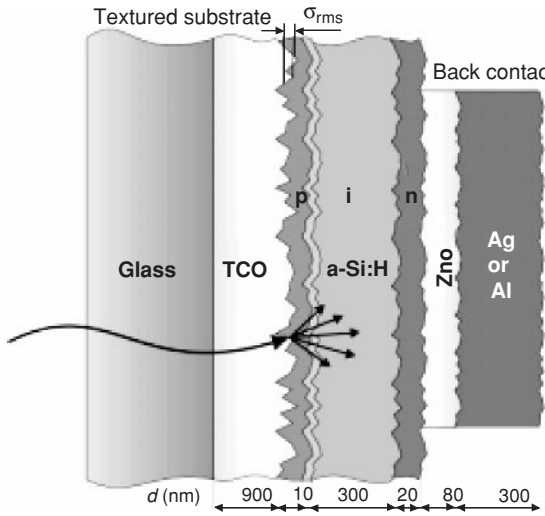

Figure 5.11 A single junction p-i-n a-Si solar cell structure.

layer experience the internal electric field, which facilitates separation of electrons and holes. The material quality of the intrinsic layer and the strength and profile of the internal electric field determine the collection of the photogenerated charge carriers and thus the solar cell performance. The electric field profile in the absorber layer strongly depends on the defect density and its distribution in the bulk of the intrinsic layer and at the interfaces with the doped layers. The photogenerated carriers move towards the doped layers (electrons towards the n type layer and holes towards the p type layer) and are collected by the electrodes. The dominant transport mechanism of the photogenerated carriers is drift in the internal electric field, and therefore, an a-Si:H solar cell is often denoted in the literature as a drift device.

Determining the optimal thickness of the intrinsic a-Si:H layer in the solar cell is the crucial part of the solar cell structure design. The thickness of the intrinsic layer is a delicate trade-off between the absorption, which is higher in a thicker layer, and the collection, which improves when the layer gets thinner. Since the collection depends on the drift of the photogenerated carriers in the internal electric field, it is the magnitude of the electric field across the intrinsic layer and the mobility and lifetime of the carriers that determine the collection. The positions of the Fermi levels in the doped layers determine to a large extent the built-in potential across the device. The built-in potential together with the thickness of the intrinsic layer determine the magnitude of the electric field. However, the electric field is not uniform across the intrinsic layer but strongly depends on the distribution of the space charge in this layer. The space charge in this intrinsic a-Si:H layer, resulting from trapped carriers in the gap states, cannot be neglected as is often possible in crystalline silicon solar cells. Due to the large density of the localized states in the bandgap, the charge trapped in these states substantially contributes to the overall charge in the device and determines the electric field profile. The presence of large defect densities at the interfaces with the doped layers can lead to a strong electric field in these interface regions, while in the bulk of the intrinsic layer, the electric field is relatively low. This is illustrated in Figure 5.12, which shows the influence of two different distributions of defect states in a 320 nm thick intrinsic layer on the internal parameters and dark and illuminated

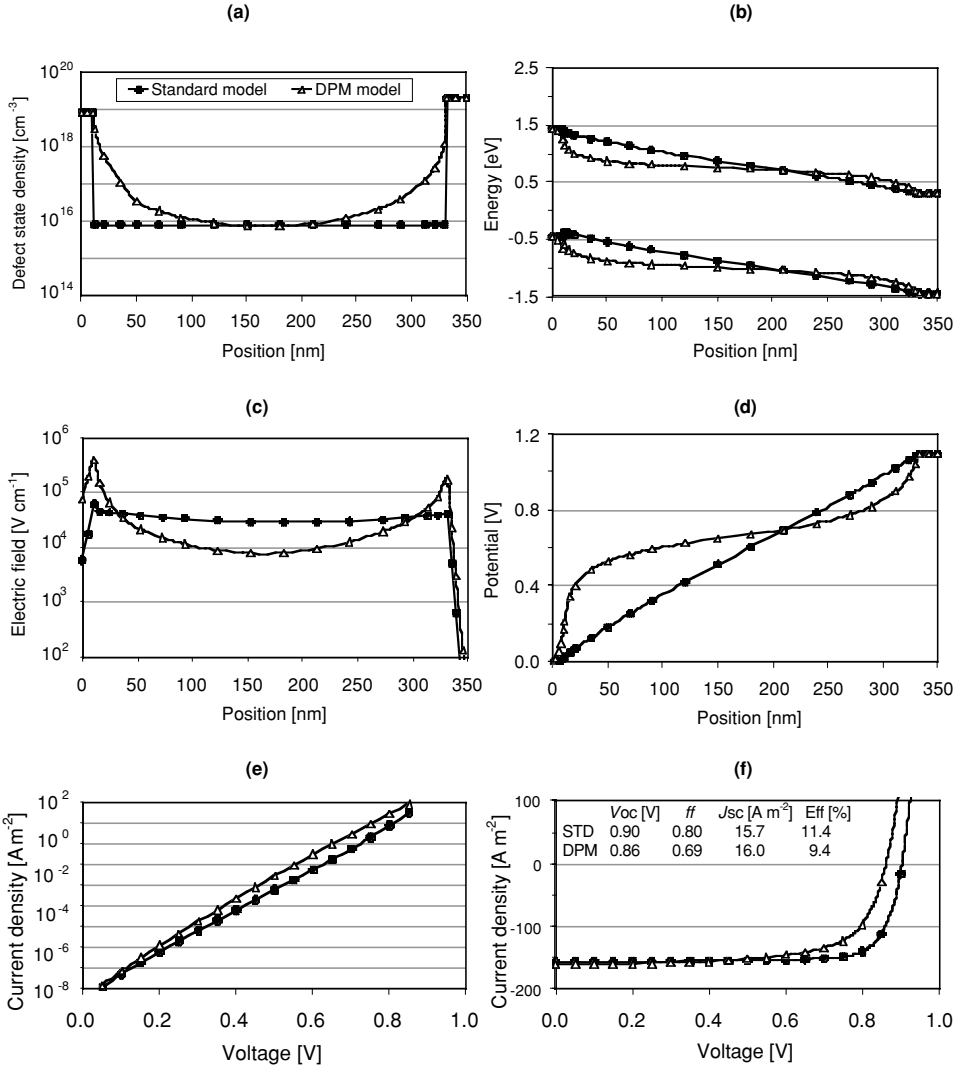

Figure 5.12 Computer simulations of the internal parameters of a p-i-n a-Si:H solar cell with 320 nm thick intrinsic layer. The solar cell structure is shown in Figure 5.11. (a) Defect concentration profile, (b) energy band diagram, (c) electric field profile, (d) potential profile, (e) dark J-V characteristic, (f) illuminated J-V characteristic. The simulations were carried out with the ASA program developed at Delft University of Technology [108].

J-V characteristics of a solar cell. The internal parameters, such as band diagram, electric field profile and potential profile, and the J-V characteristics of the solar cell were calculated with the ASA program [108]. In the first case, denoted as 'standard model,' the standard model of the density of states with the uniform defect density across the intrinsic layer was used in the simulations. In the second case, we used the defect density profile and the energy distribution of defect states calculated according to the defect pool model (DPM). In simulations, only the

description of the defect states was different; all other input parameters were kept the same. The density of states models in a-Si:H are presented in Section 5.3.3.

When the cell is illuminated, high concentrations of photogenerated carriers also influence the space charge in the cell. When the densities of photogenerated carriers become too large, the holes, due to their low mobility, build up a large space charge, which results in a collapse of the electric field at the back side of the cell, as illustrated in the review article by Deng and Schiff [109]. By using computer simulations, they demonstrated that as the thickness of the intrinsic layer increases, the generated power saturates. Power saturation depends on the level of absorbed illumination. For strongly absorbed illumination (photons of about 2.3 eV), the power saturates for thicknesses greater than 100 nm, which is a typical distance at which the photons are already absorbed. For weakly absorbed light (photons of 1.8 eV), the power saturates for thicknesses above 300 nm. This thickness represents the collection length of the carriers, which is determined by the collapse of the electric field. The collection length is determined as the product of the electric field and carrier mobility and lifetime. These simulations also show that the asymmetry in the drift of electrons and holes explains why a-Si:H based solar cells are more efficient when illuminated through the p type layer. The creation of the additional defects in the intrinsic layer due to the Steabler–Wronski effect deteriorates the collection of carriers by decreasing their lifetime and also distorts the electric field. For single junction a-Si:H solar cells, the optimal thickness of the intrinsic layer is in the range of 250 nm to 320 nm [92, 110].

5.5.2 Hydrogenated amorphous silicon solar cell configurations

There are two basic configurations of a-Si:H silicon solar cells, namely the p-i-n superstrate configuration and the n-i-p substrate configuration, which reflect the sequence of silicon layer deposition. In the p-i-n configuration, the p type layer is deposited first, then the intrinsic layer and the n type layer is deposited last. In the n-i-p configuration, the sequence of the deposition is vice versa.

In the case of the superstrate configuration, the p-i-n deposition sequence requires a transparent substrate carrier. Usually a glass plate coated with a TCO film is used. The TCO film serves as the top electrode. It has to fulfil several stringent requirements, such as high optical transmission in the spectrum of interest (350 nm to 800 nm in case of a-Si:H absorbers, 350 nm to 1000 nm for a-SiGe:H absorbers), low sheet resistance, temperature durability and good chemical stability. In addition, the TCO layer has to be surface textured in order to enhance light absorption inside the solar cell due to the scattering at internal rough interfaces. The use of glass substrates allows a deposition temperature of the TCO films up to 600 °C, which makes it possible to employ the atmospheric pressure CVD technique. This technique delivers widely used high quality fluorine doped tin oxide (SnO_2:F) films. The p-i-n amorphous silicon based layers are deposited on the TCO. The back contact is a metal layer, usually deposited onto a TCO interlayer. The TCO interlayer is used to improve the reflection from the back contact by matching the refractive indices between the n type silicon and metal layer and by preventing the intermixing of silicon and metal. An encapsulant and/or another glass plate usually form the back side of the superstrate type cell.

In case of the substrate configuration, the substrate carrier forms the back side of the cell. This allows the use of opaque substrates, such as stainless steel. Alternatively a polymer foil may be used as a substrate. Since the polymer need not be transparent, a temperature resistant type of polymer can be applied, such as polyimid. The foils can be thin enough to be flexible,

which opens up the possibility to employ roll-to-roll processing. A highly reflecting back contact with textured surface that consists of a metal layer of silver or aluminium and a TCO layer is deposited on the substrate carrier. The surface texture is required in order to scatter the reflected light back to the cell at angles facilitating total internal reflection. In the case of stainless steel, the optimal surface texture is obtained by depositing a bilayer of silver and zinc oxide at a temperature between 200 and 350 °C [14]. After depositing the sequence of n-i-p a-Si:H based layers, a TCO top layer with a metal grid is formed as the top contact. The front side of the substrate cell is created by a transparent encapsulant layer with or without an additional glass plate. The use of conductive carriers such as stainless steel complicates the monolithic series interconnection of cells on the substrate.

In practice, glass plates are used as carriers for superstrate type solar cells and flexible metal or polymer foils for substrate type cells. Therefore, the manufacturing technologies for amorphous silicon solar cells can be divided into two routes: the technologies for glass plates and for flexible substrates.

5.5.3 Design approaches for highly efficient solar cells

Since only the absorption in the a-Si:H intrinsic layer contributes to the current generation, the optimal optical design of the cell structure maximizes absorption in the intrinsic layer and minimizes it in all the other layers. This design is often denoted in the literature as optical confinement. The approaches applied to achieve optical confinement in the intrinsic layer are commonly described by the term light trapping. In addition to light trapping, there are other design rules that facilitate the collection of photogenerated carriers.

The following are some important practical design approaches for making highly efficient a-Si:H solar cells, which are schematically depicted in Figure 5.11:

- In practice, light enters the a-Si:H solar cell through the p type layer. The lower mobility of holes in comparison to electrons in a-Si:H is the reason for this design. Since most of the photogenerated carriers are generated in the front part of the solar cell, on average, holes have to travel over a shorter distance to the collecting electrode than electrons. In this way, the collection efficiency of the holes is enhanced.
- Because light enters the solar cell through the p type layer, there is substantial absorption in this layer. The photogenerated carriers in the p type layer do not contribute to the photocurrent because in this layer the electrons, here the minority carriers, quickly recombine. It is therefore desirable to minimize the absorption in the p type layer, which is done by minimizing the thickness and alloying the p type a-Si:H layer with carbon. This p type a-SiC:H layer has an optical bandgap of about 2 eV and is referred to as the window layer.
- The solar cell performance is sensitive to the p-i interface region. The p-i interface is a heterojunction with band offsets between the energy bands of a wide bandgap p type and an intrinsic layer. The band offset in the valence band forms a barrier for the photogenerated hole to the doped layer. One has to keep in mind that the generation rate of the carriers in this region is the highest in the intrinsic layer. A lot of attention is paid to the p-i interface region in order to accommodate the band offset, to optimize the electric field profile in this region, and to prevent back diffusion of the photogenerated electrons into the p type layer [111]. Usually, wide bandgap, thin, high quality layers of intrinsic or lightly doped a-Si:H or

a-SiC:H are introduced at the p-i interface. These layers can also serve as diffusion barriers, preventing boron from diffusing from the p type into the intrinsic layer. These layers are called the buffer layers.

- The substrate that is used for deposition of a-Si:H layers is practically always surface textured. The surface texture of the top TCO layer in the superstrate configuration and the TCO/metal back contact in the substrate configuration introduces rough interfaces into a solar cell. When light reaches a rough interface, part of it will be scattered in various directions instead of propagating in the specular direction. In this way the average light path in the absorber layer is increased and light absorption enhanced.
- Typically, the back contact consists of a ZnO layer and a metal layer, usually Ag. This combination results in a highly reflective back contact that helps to enhance the absorption of light in the absorber layer in the long wavelength region (wavelengths above 600 nm) due to effective reflection from the back side of the cell.

5.5.4 Light trapping and transparent conductive oxides

At present, the most important research area in the field of a-Si:H based solar cells is considered to be further development and implementation of efficient light trapping. Light trapping techniques help to capture light in the desired parts of a solar cell, which are the absorber layers, and prevent it from escaping. Efficient light trapping in a-Si:H silicon solar cells is based on scattering of light at rough interfaces and the employment of highly reflective back contacts and refractive index matching layers in order to manipulate reflection in the cell. Scattering of light at rough interfaces results in a longer average optical path through the absorber layer. Repeated reflection at the back and front contacts causes multiple passes of light through the absorber layer. These processes ensure efficient light confinement that substantially enhances light absorption in the absorber layer and increases the photocurrent of the solar cell. The interested reader will find a comprehensive treatment of the principles for the optical design of a-Si:H based solar cells in the monograph by Schropp and Zeman [18]. Transparent conductive oxide layers play a central role in light trapping approaches and, at present, determine the efficiency of the state-of-the-art solar cells. The development of TCO materials with required optical and electrical properties and optimal surface texture is today the most important issue in the field of thin film silicon solar cells.

In the superstrate configuration, it is the TCO layer that introduces rough interfaces into the solar cell. Since it also serves as the top electrode this layer has to fulfil several material requirements. Table 5.2 presents these requirements and the properties of several TCO films used in a-Si:H solar cells. Traditionally, a surface textured SnO_2:F deposited by APCVD above 500 °C is used as the TCO top contact layer. Today the so-called U type SnO_2 film deposited by Asahi Company in Japan serves as a reference substrate in the field of thin film silicon solar cells [112]. However, this optimized TCO substrate material is not being mass produced. Recently, ZnO has attracted a lot of attention as a potential substitute of SnO_2 because it allows deposition at low temperatures (less than 300 °C) and is stable against hydrogen plasma and high temperature processes. A ZnO layer also acts as a barrier against diffusion of impurities from the substrate. Furthermore, while having comparable optical and electrical properties, ZnO is cheaper than most other TCO materials. Zinc oxide films can be prepared by several deposition techniques, such as LPCVD [19], ETP CVD [113], and

Table 5.2 Properties of several TCO front electrode films

Property	Requirement	ITO	SnO_2:F APCVD	ZnO:B LPCVD	ZnO:Al sputtering
Transmission (350–1000 nm)	>90 %	95 %	90 %	90 %	90–95 %
Bandgap [eV]	>3.5	3.7	4.3	3.4	≈3.45[a]
Sheet resistance [Ω/]	<10	3–5	6–15	6–15	4–15
Contact resistance to amorphous p^+ layer	low ohmic	low ohmic	low ohmic	forms barrier	forms barrier
Roughness	textured	negligible	excellent	excellent	excellent (after treatment)
Plasma durability	resistant	low	good	excellent	excellent

[a] depends on electrical properties (mobility, carrier density, Burstein—Moss shift).

sputtering [20]. The surface texture of ZnO can be obtained naturally during the growth [19, 113] or be created by post deposition chemical etching [20]. The stability of ZnO against hydrogen plasma, especially, allows deposition of amorphous and microcrystalline silicon layers from hydrogen rich plasmas.

The TCO-p interface region has a substantial influence on the solar cell performance [114]. The reduction of the SnO_2 during the deposition of the p type a-SiC:H layer can limit the J_{sc} of the cell. The reduction is pronounced for high deposition temperatures and high hydrogen dilutions. For this reason, a thin layer of ZnO is usually deposited on the SnO_2 film to prevent its reduction in hydrogen rich plasma. The ZnO coating of SnO_2 increases the J_{sc}, but lowers the V_{oc} and fill factor of the cell. This is the result of a pronounced depletion of the thin p type layer at the junction with the degenerated n type ZnO, which creates a contact barrier with the ZnO and lowers the built-in voltage in the cell. The ZnO-p contact problem can be solved by using a highly conductive microcrystalline Si interlayer.

In the substrate technology it is a textured back reflector that introduces rough interfaces into the solar cell. However, increasing the surface texture of the back reflector has not resulted in the expected current enhancement [115]. The current enhancement is limited by higher absorption at the back contact due to the increased texture, which is explained by the surface plasmon absorption [116]. In the case of a stainless steel substrate, the optimal surface texture is obtained by depositing a bilayer of silver and ZnO at a temperature between 200 and 350 °C [14].

The front TCO film has to be designed for low absorption and reflection. This goal is achieved when the thickness of the TCO film fulfils the condition for minimum reflection, which is described as:

$$d_{TCO} \times n_{TCO} = \lambda/4 \tag{5.20}$$

The refractive index of TCO films is typically close to two, which means that the optimal thickness of a TCO film for minimum reflection is around 80 nm. However, this TCO thickness does not yet provide a sufficiently low resistance and therefore, additional current collecting

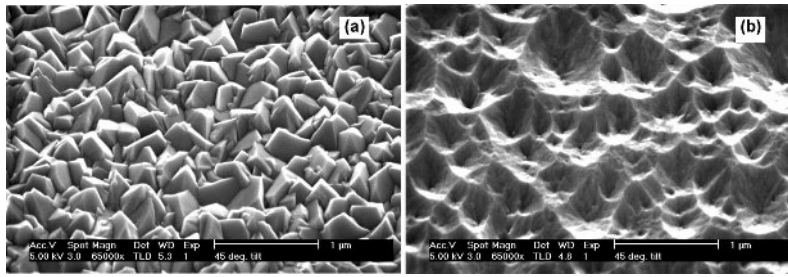

Figure 5.13 Scanning electron microscopy pictures of surface textured TCO substrates: (a) SnO_2:F Asahi U and (b) 10 s etched ZnO:Al TCO surface.

schemes are applied, such as a metal grid on the top of the TCO layer or special current collecting designs such as series connection through apertures formed on film (SCAF) [13].

The surface texture of TCO films depends on the deposition conditions and/or post deposition treatment and can vary a lot, as demonstrated in Figure 5.13. Since enhancement of the photogenerated current in a-Si:H solar cells due to the use of surface textured substrates was demonstrated [10], extensive work has been carried out to investigate the influence of the surface morphology of the TCO films on the photocurrent of cells. The process of light scattering on rough TCO films has been intensively investigated in order to discover relations between the topological properties of a rough interface and its scattering parameters [117–119]. Knowledge about the scattering properties of rough interfaces is of major importance for computer modeling. Optical modeling has become a powerful tool to analyze and optimize the complex optical situation in solar cells where multiple scattering processes take place at internal rough interfaces [118, 120]. Results of simulations have clarified the contributions of the front and back contact surface texture and the choice of materials for the back contact to enhance the current of the solar cells. At the same time, computer modeling helps to analyze optical losses in nonphotoactive layers of the cell. In general, the enhancement of the spectral response in the wavelength range between 450 to 600 nm comes from light scattered at the front interfaces, while above 600 nm, scattering at the back contact plays a dominant role. Therefore, both the front and back contact interfaces have to be rough in order to achieve enhanced absorption in the whole wavelength spectrum. Even when no antireflection coating is used, the total reflection is reduced due to the antireflective properties of the rough interfaces, which result from the profiled refractive index at the rough interface [120].

5.5.5 Degradation of hydrogenated amorphous silicon solar cells

The performance of single junction a-Si:H solar cells decreases during the initial stage of operation due to light induced degradation. After the initial degradation, the performance of solar cells stabilizes. The stabilized performance of high quality solar cells is 70 to 85 % of their initial one. The degradation can be recovered by annealing. Therefore attention has to be paid to whether the reported efficiency of a-Si:H solar cells is the initial efficiency (as-deposited) or the stabilized efficiency (after a degradation test). Most countries have their own conditions

for carrying out degradation tests, or often called light soaking tests. In Japan, 'temporarily defined stabilized efficiency' is the value after 310 h exposure under the following conditions: light intensity 1.25 sun equivalents, temperature 48 °C, and open circuit conditions. In the USA, the stabilized efficiency is defined as efficiency after 600 h of continuous exposure to 1 sun equivalent at 50 °C under open circuit conditions. In PV language, 1 sun equivalent means a solar irradiance of 1000 W m^{-2}.

The solar cell degradation due to illumination is the manifestation of the Staebler–Wronski effect. The drop in performance is ascribed to the creation of additional metastable defects in the absorber layer, which act as extra trapping and recombination centers. As a result of trapping, the space charge distribution in the intrinsic a-Si:H layer is changed in such a way that the internal electric field across this layer is distorted. This leads to a lower drift and thus to a lower carrier collection. Therefore, the a-Si:H solar cell structure and the properties of the individual a-Si:H based layers must be optimized for the light soaked state.

The performance degradation of a-Si:H based solar cells due to illumination can partly be avoided by using thinner absorber layers. Then the internal electric field across the layer is higher and therefore less sensitive to any distortion. However, the employment of thinner absorber layers results in a lower absorption and consequently low short circuit current densities of the cells. One way to overcome the trade-off between carrier generation and carrier collection in thin solar cells is to develop efficient light trapping schemes. Another is the use of a stacked or multijunction structure. By stacking one or more solar cells on top of each other, a total absorption is obtained that is the same or even higher than in a single junction solar cell with comparable total thickness. Because the component cells in the stacked structure are thinner, they are less sensitive to the increased density of light induced defects.

Single junction a-Si:H solar cells, which today exhibit the highest stabilized efficiencies, have a-Si:H absorber layers in the range of 250 nm to 320 nm. The optimal thickness mainly depends on the efficiency of light trapping. Figure 5.14 shows the illuminated J-V characteristic and quantum efficiency of the superstrate type single junction a-Si:H cell with the world's highest stabilized efficiency of 9.47 %, which was fabricated in the Institute of Microtechnology (IMT) at the University of Neuchâtel [92].

5.5.6 Multijunction hydrogenated amorphous silicon solar cells

The concept of the stacked solar cell was introduced to increase the output voltage of a-Si:H solar cells [6]. Only later it was recognized that stacked cells also offer a practical solution for improving the stabilized performance of a-Si:H based solar cells [121]. Different terms such as tandem or dual junction or double junction solar cells are used in the literature to describe a cell in which two junctions are stacked on top of each other. A stack of three junctions is named a triple junction solar cell. The multijunction solar cell structure is far more complex than the single junction solar cell. An example of it is shown in Figure 5.15. For its successful operation there are two crucial requirements: (i) the current generated at the maximum power point has to be equal in each component cell (current matching) and (ii) an internal series connection between the component cells has to feature low electrical and optical losses. The internal series connection is accomplished at the n-p junction, where the recombination of oppositely charged carriers arriving from the adjacent component cells takes place. Tunneling of the carriers through the doped layers facilitates the recombination and therefore the junction is called a tunnel recombination junction.

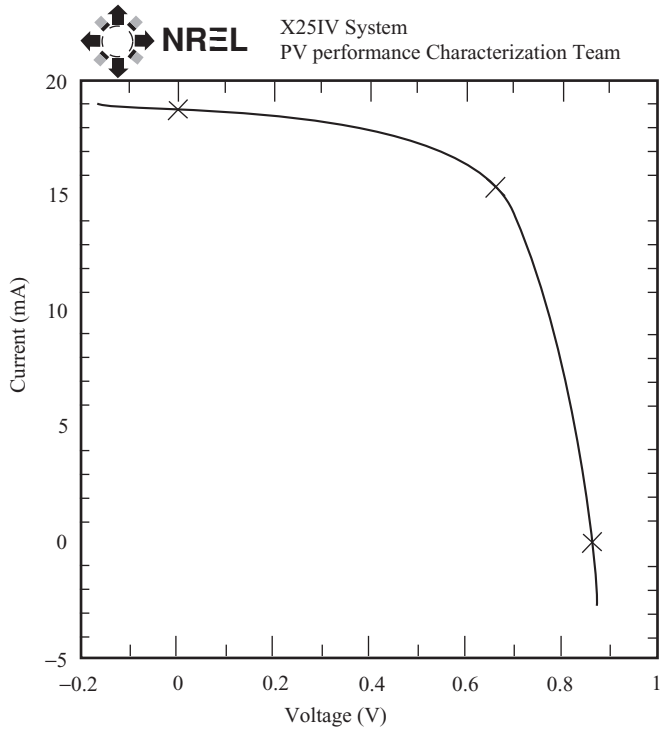

(a)

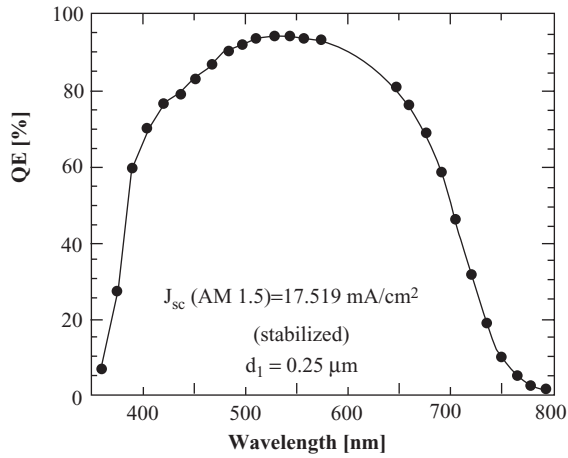

(b)

Figure 5.14 (a) The illuminated I-V characteristic and (b) quantum efficiency of a stabilized single junction a-Si:H solar cell fabricated at the University of Neuchâtel. Reproduced with permission from J. Meier *et al*., High-efficiency amorphous and micromorf silicon solar cells, Proceedings of WCPEC 3, Osaka 2003, S20-89-06. Copyright (2003) with permission from WCPEC-3 Organizing Committee and Masafami Yamaguchi *et al*.

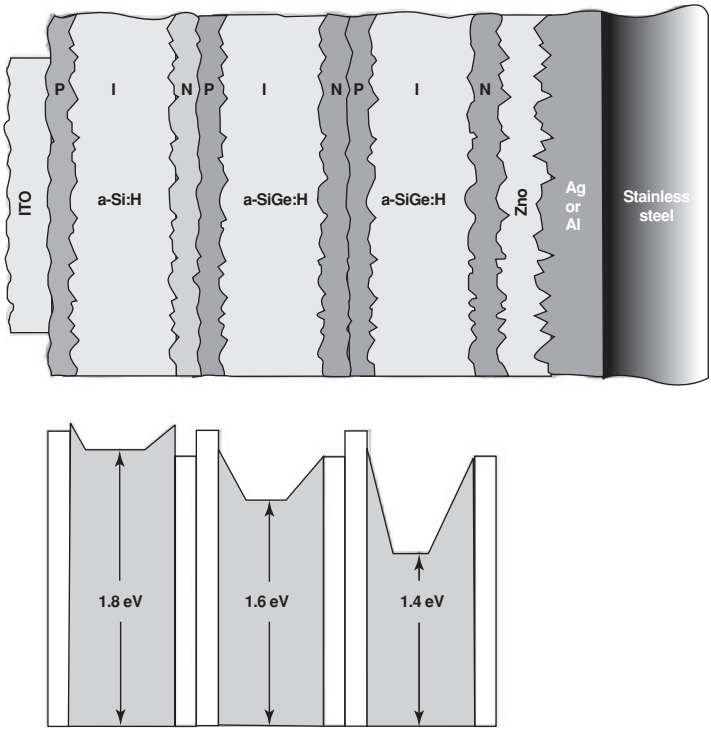

Figure 5.15 A multijunction solar cell structure represented by an a-Si:H/a-SiGe:H/a-SiGe:H triple junction solar cell with a corresponding schematic band diagram.

5.5.6.1 Current matching

The requirement of current matching reflects the fact that component cells function as current sources which are connected in series. The component cell that generates the lowest current determines the net current flowing through the stacked two terminal cell. In order to avoid current losses, each component cell should generate the same current. The current generated by a component cell depends mainly on the absorption in the absorber layer of the cell, which is determined by the thickness of the absorber. Current is matched by adjusting the thickness of the absorber layer of each component cell. To analyze current matching in complex multijunction solar cells and to predict the optimal thickness of the absorber layers, computer modeling is used [108].

5.5.6.2 Tunnel recombination junction

The tunnel recombination junction deals with the interface between the component cells. This interface is in fact an n-p diode which is connected in reverse when the component cells operate in forward conditions. An ohmic contact between the component cells, instead of a rectifying contact, is required for proper operation of the stacked solar cell. The problem of

obtaining the ohmic contact between the component cells can be resolved by fabricating a so-called tunnel recombination junction. This junction ensures that the electrons arriving at the n type layer of the top cell and the holes arriving at the p type layer of the bottom cell fully recombine at this junction. The recombination of the photogenerated carriers at this interface keeps the current flowing through the solar cell. A very high electric field in this reverse biased n-p junction facilitates tunneling of the carriers towards the defect states in the centre of the junction. The effective recombination of the carriers takes place through these defect states. A tunnel recombination junction is usually realized by using microcrystalline silicon for at least one of the doped layers in order to obtain good ohmic contact [121, 122]. Another approach is to incorporate a thin oxide layer at the interface between the two component cells that serves as an efficient recombination layer [123]. When the n-p junction functions as a good ohmic contact, the V_{oc} of the stacked cell is the sum of the open circuit voltages of the component cells. In this case, optimization of the stacked cell reduces to optimization of the component cells [4].

5.5.6.3 Concept of spectrum splitting

An additional advantage of the stacked cell based on a-Si:H is that each component cell can be tailored to a specific part of the solar spectrum. For this wide or low bandgap absorbers, in comparison to the intrinsic a-Si:H, are used, which allow more efficient use of the solar spectrum. A component cell with a high bandgap absorber converts high energy photons and delivers a high V_{oc}, while a component cell with a low bandgap absorber can absorb photons from the red and near infrared part of the solar spectrum. This approach of using absorber layers with different bandgaps in component cells is known as spectrum splitting and leads to a higher conversion efficiency when compared to single junction cells, also often referred to as the multi bandgap approach.

5.5.6.4 Hydrogenated amorphous silicon based tandem solar cells

Several combinations of absorber materials have been used in a-Si:H based stacked cells. The first tandem cells employed the same a-Si:H material for the absorber layers in the component cells. The a-Si:H/a-Si:H tandem cell is called the same bandgap tandem cell. The advantage of a-Si:H/a-Si:H tandem cells is simple fabrication and low cost in comparison with tandem cells using absorbers with different bandgaps. The disadvantage is a relatively lower efficiency. A stabilized efficiency of 10.1 % has been achieved for a-Si:H/a-Si:H tandem cells, both in superstrate [124] and substrate [14] configurations.

For the tandem cell, the highest efficiency is predicted for a combination of absorber materials having a bandgap close to 1.7 eV and 1.1 eV for the top and bottom cell, respectively [125, 23]. In contrast to the wide bandgap intrinsic a-SiC:H, in which the defect density increases with increasing optical bandgap, a wide bandgap a-Si:H material ($E_{opt} \approx 1.80$ eV) prepared at a relatively low deposition temperature and using a high hydrogen dilution of silane has proved to be the most promising absorber material for the top component cells in multijunction solar cells [85, 77].

At present, a-SiGe:H and μc-Si:H are used as low bandgap absorbers. The application of μc-Si:H films is discussed in Chapter 4. The drawback of a-SiGe:H is that its electronic properties

deteriorate with increasing germanium content and no a-SiGe:H has been yet produced with a bandgap lower than 1.4 eV having sufficient optoelectronic properties. With alloying, the defect concentration in a-SiGe:H increases, which results in a lower fill factor of component cells, in which a-SiGe:H absorbers with different bandgaps are incorporated. This feature has to be taken into account in the current matching procedure since a stacked cell has to be matched for the maximum power point in the light soaked state. The short circuit currents of the component cells are therefore only a rough guide for the matching procedure.

Further, a large band offset is introduced at the interfaces between the doped layers and a-SiGe:H. For example, there is a band offset of 0.5 eV between a p type a-SiC:H layer with a typical optical bandgap of 1.95 eV and an a-SiGe:H layer with an optical bandgap of 1.45 eV. These band offsets are believed to obstruct effective collection of photogenerated carriers. In order to overcome the transport barriers, complicated profiling of the germanium concentration is carried out in regions near the interfaces [126, 127]. To denote the concentration profiled region the term graded layer is used.

In a-Si:H/a-SiGe:H tandem cells, the current matching is achieved when the thickness of the a-Si:H absorber in the top cell is between 100 to 150 nm and the thickness of the a-SiGe:H absorber in the bottom component cell is is in the range 120–150 nm. The advantage of using a combination of a-Si:H and a-SiGe:H is that the total thickness of absorber layers is less than 300 nm. The best results obtained with a-Si:H/a-SiGe:H tandem cells for both a superstrate and substrate configurations are presented in Table 5.3. Further improvement is expected from more efficient light confinement, the adjustment of optical bandgaps of the absorber layers, composition control of the a-SiGe:H material and the reduction of optical losses in the TCO and doped layers. By applying these approaches, the short circuit current density of the cell can be increased further although the total thickness of the absorber layers is reduced [12].

5.5.6.5 Hydrogenated amorphous silicon based triple junction solar cells

The addition of a third component cell to the tandem stack leads to a further increase in the conversion efficiency. To date, the highest stabilized efficiency of an a-Si:H based solar cell

Table 5.3 Stabilized efficiencies of a-Si:H based solar cells

Absorber layers	Area [cm^2]	J_{sc} [$mA\,cm^{-2}$]	V_{oc}[V]	FF	η_{stab}[%]	η_{in}[%]	Institution
Superstrate configuration (p-i-n)							
a-Si	1.0	17.5	0.86	0.63	9.47	11.2	IMT-Neuchatel [92]
a-Si/a-Si	1.0	~8.6	~1.73	~0.68	10.1		Fuji [124]
a-Si/a-SiGe	1.0	10.9	1.49	0.65	10.6	11.6	Sanyo [130]
Substrate configuration (n-i-p)							
a-Si	0.25	14.36	0.96	0.67	9.3		USSC [14]
a-Si/a-Si	0.25	7.9	1.83	0.70	10.1		USSC [14]
a-Si/a-SiGe	0.25	10.68	1.71	0.67	12.4		USSC [14]
a-Si/a-SiGe/a-SiGe	0.25	8.27	2.29	0.68	13.0	14.6	USSC [14]

has been achieved with a substrate type triple junction a-Si:H/a-SiGe:H/a-SiGe:H solar cell fabricated by United Solar. This solar cell structure deposited on a stainless steel substrate is shown in Figure 5.15. The top contact is an indium tin oxide (ITO) layer of approximately 70 nm thick and it serves both as the top electrode and as an antireflection coating. The thickness of the ITO layer is not sufficient to achieve a low resistance. In order to reduce contact resistance of the top electrode, a current collecting metal grid is applied on the ITO layer. In order to illustrate the complexity of the solar cell structure, which accommodates the graded layers and different materials for the active layers, Figure 5.15 includes a corresponding schematic band diagram of the cell. The highest stabilized efficiency of the triple cell is reported to be 13.0 %, while the initial efficiency of this cell was 14.6 % [128]. The initial J-V characteristic and quantum efficiency of this cell are presented in Figure 5.16. When comparing the quantum efficiencies of the multibandgap triple cell and the single junction cell (see Figure 5.14), one can clearly see that the multibandgap approach allows the use of a wider spectrum region. An initial efficiency of 15.2 % was reported for a triple cell by United Solar, which indicates that a further increase in stabilized efficiency is feasible [4].

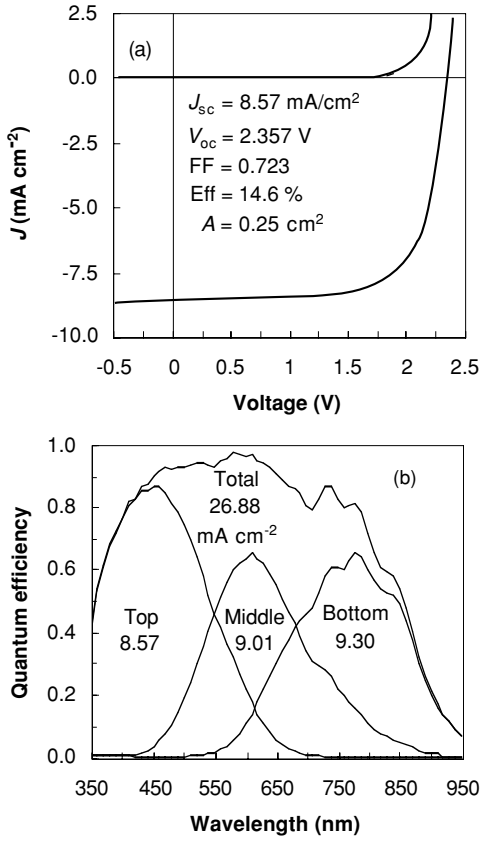

Figure 5.16 (a) Initial AM1.5 J-V characteristic and (b) quantum efficiency of an a-Si:H/a-SiGe:H/a-SiGe:H triple junction solar cell. (Courtesy of Jeff Yang, United Solar Ovonic Corporation).

The advantage of the substrate configuration is that it better suits the optimal deposition temperature of a-Si:H based layers in multijunction cells. In contrast to the superstrate configuration, where the deposition of absorber layers is limited to below 200 °C in order to avoid thermal damage to the p-i interface [75], the n-i-p deposition sequence allows fabrication of low bandgap absorbers at high temperatures.

Further improvement in the performance of the triple cell is expected from applying similar approaches to those for a-Si:H/a-SiGe:H tandem cells. Solar cell manufacturers are carefully evaluating performance enhancement with respect to the increased complexity of the triple-junction cell structure in order to make the best choice for cost-to-performance ratio.

5.5.6.6 External parameters of high efficiency hydrogenated amorphous silicon based solar cells

Table 5.3 presents the best achieved performances of laboratory a-Si:H based solar cells both in superstrate and substrate configurations. The performance degradation of single junction cells is more pronounced than in multijunction cells because of thicker absorber layers and in best cases can be brought down to less than 20 %. The degradation of multijunction cells can be limited to ∼10 %. The V_{oc} rises as the number of stacked junctions increases. For practical applications, the external parameters of multijunction solar cells are advantageous in comparison to single junction cells, because the lower current reduces resistive losses in the electrodes, especially in the TCO, and the higher output voltage allows more flexible design of modules with required voltages.

5.5.6.7 Modeling of hydrogenated amorphous silicon solar cells

Computer simulations have proved to be an indispensable tool for obtaining a better understanding of a-Si:H solar cell performance and for determining trends for optimizing material parameters and solar cell structures. Several computer programs are available for modeling amorphous and microcrystalline silicon solar cells. These programs include sophisticated models describing amorphous silicon electronic properties, but are limited to one-dimensional modeling. Examples are the AMPS program developed at Pennsylvania State University [129] and the ASA program developed at Delft University of Technology [108] which are the most widely used in the amorphous silicon solar cell community. A good overview on modeling issues of amorphous silicon solar cells is given in reference [18].

Although the available programs still have uncertainties in the values of several model parameters, their use already offers some notable advantages over technological development. Using simulations, it is possible to examine the influence of the model parameters, which cannot be determined experimentally, or they can be set independently from each other, so that the impact of small changes in a device configuration can be determined much faster and more reliably. As a result computer programs can deliver external properties of layers or devices that are measurable quantities and/or internal properties that can only be measured indirectly or not at all. The simulation results of the internal parameters of a solar cell presented in Figure 5.12 serve as an example. Moreover, as the computer hardware components are becoming less expensive and more powerful, simulations are getting cheaper compared to the drastically increasing costs of experimental equipment.

5.6 PERFORMANCE AND FABRICATION OF HYDROGENATED AMORPHOUS SILICON BASED MODULES

The electrical power delivered from a small area solar cell is not enough for practical applications. Therefore, solar cells are connected in series and/or parallel to form a module that delivers a required power and voltage. A key step to practical industrial production of a-Si:H solar cells was the development of the monolithically integrated type of a-Si:H solar cell [7]. Monolithic series connection of cells to modules that can be easily implemented in the fabrication process is an attractive feature of a-Si:H solar cell technology. The monolithic series connection of cells is demonstrated in Figure 5.17.

The solar cell performance that is first optimized on a laboratory scale with a cell area ranging from 1 to 100 cm^2 is difficult to obtain on a module level, which has an area of 0.3 m^2 and more. There are inherent and process related effects that reduce the module performance with respect to the laboratory cell performance [130]. The inherent losses result from the transition from individual cells to large area modules of interconnected cells. The monolithic series connection of the cells generates joule losses due to the sheet resistance of the TCO and the contact resistances, and area losses due to the cell interconnection and contact areas. The process related losses originate from economic considerations that determine the trade-off between cost effective production processes and special laboratory processes irrespective of complexity and expense. The process related losses include the use of nonoptimal commercial TCOs and the implementation of large area deposition techniques that lead to nonuniformity of thickness and inhomogeneity in the individual layers. These effects result in statistical effects that average the performances of individual cells and reduce efficiency on the module level. The cumulative effect of the above mentioned reduction factors typically amounts to over 30 %. However, the module manufactures put a lot of effort into minimizing these losses. For example, in the case of triple junction modules fabricated by United Solar, the losses on the module level, related to the nonuniformity, together with an inevitable area loss due to the current carrying grid lines and encapsulation, amount to 16 % [14]. The *J-V* characteristics of the best *substrate type* a-Si:H/a-SiGe:H/a-SiGe:H, fully encapsulated module (905 cm^2) fabricated on a stainless steel substrate with an initial efficiency of 11.2 % and a stable efficiency of 10.5 % [131] is presented in Figure 5.18. The best performance of a single junction superstrate type module on a glass substrate (3917 cm^2) with an initial efficiency of 10.7 % fabricated by Kaneka Corporation is presented in Figure 5.19.

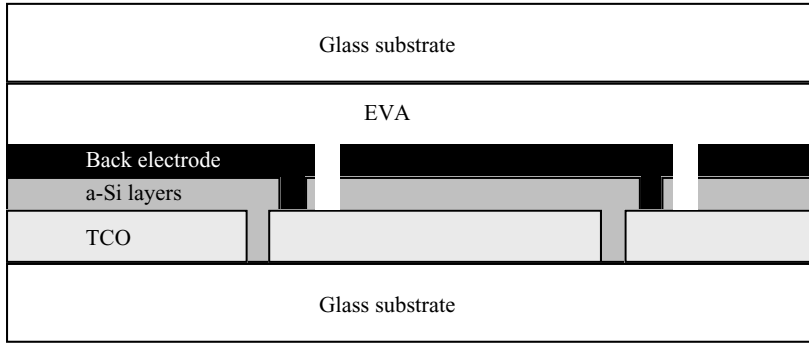

Figure 5.17 The schematic representation of the monolithical series connection of a-Si:H cells on a module.

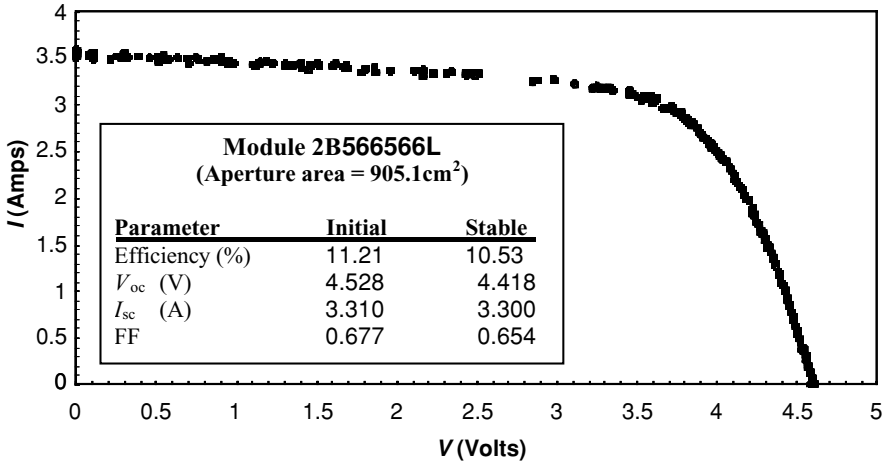

Figure 5.18 Initial and stable NREL AM1.5 Spire measurements on United Solar encapsulated module. (Courtesy of Jeff Yang, United Solar Ovonic Corporation).

Regarding the conversion efficiency, one has to be careful to distinguish among the reported values, because there is a considerable discrepancy between:

- Laboratory record minicells (size below 1 cm^2, no patterning).
- R&D modules, not encapsulated and not produced in large quantities (size of 0.1 m^2).
- Commercial modules.

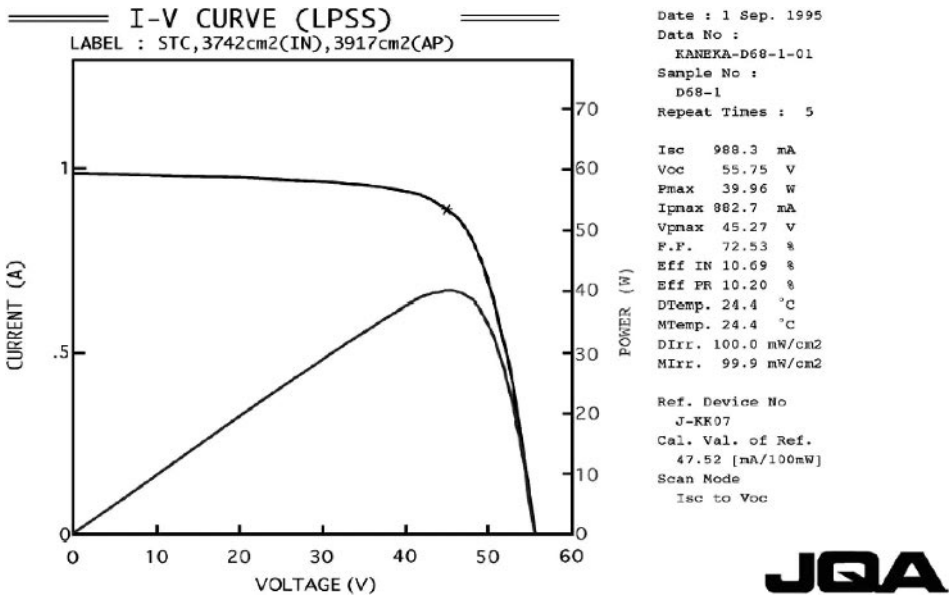

Figure 5.19 The illuminated I-V characteristics of Kaneka single junction a-Si:H module. (Courtesy of Kenji Yamamoto, Kaneka Corporation).

It is important to note that the conversion efficiency is determined from measurements that are carried out under standard test conditions (STC): i.e. with $1\,\mathrm{kW\,m^{-2}}$ irradiation, AM1.5 spectrum and at 25 °C. However, the modules that are installed in the field do not operate at the STC conditions. In order to compare the actual performance of modules based on different technologies, the energy yield per module area under given solar irradiation is used. An excellent discussion on the energy yield of amorphous silicon based modules with respect to other technologies was published recently by Shah *et al*. [132] and the text is reproduced by permission of Wiley & Sons, Ltd in the following section.

5.6.1 Energy yield

Using the energy yield, the user may judge, in a more pragmatic way, the performance of modules in terms of their quantitative benefit, e.g., the real cost return based on electricity feed-in prices. Examples are shown in Table 5.4, where the energy yields of different module types, placed in two locations of substantially different insolation, are compared [133]. Also shown are 'effective' efficiencies. Unlike efficiency values normally referred to STC, they are ratios between the energy yields and the corresponding irradiations, averaged over one year, and thus they include all variations of temperature, solar irradiation intensity and spectral distribution which affect the efficiencies individually and differently for each technology.

Note: the presented compilation only serves to show typical, and practically applicable differences for production modules exposed to the same climatic conditions; it should certainly not be viewed as being generally representative for the technologies listed, nor for the module producers referred to. As one would expect, the energy yields more or less track the STC module efficiencies deduced from the data sheets of the corresponding samples. However, there are a number of notable exceptions. Some of these might be caused by actual STC efficiencies that deviate from data specifications. More interesting are cases that are caused by various power-output dependencies, either individually or in combination, namely on:

- the spectral response relative to the given insolation, both daily and seasonally;
- the temperature;
- the irradiation intensity;
- in case of stacked cells, the current matching, that, in turn, depends on the spectral distribution of the insolation (e.g., due to a higher sensitivity to current matching, the Unisolar US 64 triple-junction generates less energy than the simpler double-junction ASE 30 modules).

In conclusion, the STC efficiencies may be used as a guide to module quality, but the decisive quantity to measure module performance is the energy yield. In this context, an additional quantity has been introduced, the so-called relative performance, defined as the annual energy yield divided by the module power (in $\mathrm{kW_p}$). This quantity basically shows, how well a product performs relative to its specified power; in fact it is equal to the duration (in h/yr) during which the module would deliver its nominal STC power. Owing to the various dependencies mentioned above, thin film silicon modules may even outperform modules based on crystalline silicon (in Table 5.4 compare, e.g., the relative performances of the amorphous silicon tandem module ASE 30 with the single-crystal, wafer-based silicon module BP 585).

Table 5.4 Annual energy yields, relative performances, and total area efficiencies (STC and 'effective') for various module types, exposed in Mallorca and in the UK. The average annual solar irradiation in Mallorca is 1700 kWh m^{-2} yr^{-1} and in Oxford 1022 kWh m^{-2} yr^{-1}. The effective efficiency values are corrected for inverter losses. (The data are provided courtesy of Dr Christian N. Jardine, ECI, University of Oxford)

Product	Cell type	Module efficiency (%) STC[b]	Energy yield (kWh m^{-2} yr^{-1})		Relative performance (kWh kW_p^{-1} yr^{-1})		Effective efficiency (%)	
			Mallorca	Oxford	Mallorca	Oxford	Mallorca	Oxford
Unisolar US 64	a-Si triple	6.3	87.3	54.3	1380.4	858.6	5.67	5.87
ASE 30 DG-UT[a]	a-Si tandem	5.4	88.3	52.9	1655.3	991.8	5.63	5.64
Solarex Millenia	a-Si tandem	5.4	79.8	48.8	1515.5	926.2	5.05	5.22
Intersolar	a-Si single	4.4	38.9	22.3	887.4	557.3	2.45	2.40
Siemens ST 40	CIGS	9.4	150.3	99.2	1553.3	1025.3	9.47	10.53
BP 585	sc-Si	13.6	187.9	117.2	1389.2	871.8	11.6	12.41
ASE 300 DG-UT	mc-Si (EFG)	12.4	155.9	101.8	1340.4	875.1	9.29	10.75
Solarex MSX 64	mc-Si	11.5	143.1	96.2	1368.0	842.0	8.83	10.41
Astropower APX-80	mc-Si (APEX)	8.2	88.1	61.2	1352.9	821.8	5.46	6.47

[a] Now RWE SCHOTT Solar.
[b] data sheet values.

5.6.2 Fabrication of hydrogenated amorphous silicon based modules

In 2004 the total production capacity of a-Si:H based modules was about 75 MW_p, the actual production exceeded 25 MW_p. Among the largest and most advanced producers of a-Si:H based modules are United Solar (USA) with a 30 MW_p production facility, Kaneka Corporation (Japan) with a 20 MW_p plant, and Mitsubishi Heavy Ind. (Japan) having a 10 MW_p production facility. United Solar supplies the market with the new ECO series modules based on the triple junction a-Si:H technology on flexible substrates. The modules are encapsulated with Tefzel fluoropolymers, use no glass, and are fixed with rigid aluminium frames. The modules reach conversion efficiencies of 7.4 %. Kaneka and Mitsubishi Heavy Ind. produce modules based on single junction a-Si:H technology on glass substrates. The modules use glass plate as protection and usually are delivered with aluminium frames. The conversion efficiency of Kaneka modules with a total area of 0.95 m^2 is 6.3 % and the modules of Mitsubishi Heavy Ind. that have a total area of 1.5 m^2 exhibit 6.4 % [134].

The manufacturing of amorphous silicon solar cells is divided into two routes: processing on glass plates [11, 130] and processing on flexible substrates [77]. Both manufacturing approaches include the following main steps:

(1) Substrate conditioning.

(2) Large area deposition of the contact layers, i.e. the TCO as front electrode and the back reflector which is usually a double layer of metal and TCO.

(3) Large area deposition of a-Si:H based layers.

(4) Monolithic series connection of cells (at present applied only for manufacturing on glass) using laser scribing of contact and silicon layers.

(5) Final module assembly including encapsulation, application of electrical connections and framing.

One of the important requirements for a company to stay competitive in the solar cell business is to be technologically independent. This is a driving force for companies to have available technologies for all manufacturing steps. The production scale is very important for economic reasons. A factory with higher production capacity is more efficient regarding the use of energy because processes such as heating up and cooling down contribute relatively less to the overall use of energy. Thin flexible substrates require less energy for heating up to a required temperature than glass plates, which can result in a shorter energy payback time for flexible modules.

5.6.3 Plasma enhanced chemical vapor deposition systems

The central role in module manufacturing is taken by the deposition machine for a-Si:H layers. To date, all module manufactures use the PECVD method and it is the design of the PECVD deposition machine that determines the throughput, flexibility of cell design, quality and uniformity of the layers. The so-called ‘plasma box’ reactor design is widely used in production machines. The plasma box forms an enclosed, separately pumped volume within

the deposition machine, in which plasma is confined between the electrodes and the substrate, the temperature is uniform and the deposition volume is protected from impurities originating from outside the plasma box. It also offers *in situ* cleaning by plasma etching that removes a-Si:H deposited on parts other than the substrate that are exposed to the plasma.

Since several a-Si:H layers have to be deposited on top of each other there are several possibilities for processing of the layers. In general, one can distinguish between in line and batch processing, which determine the design of the PECVD machine. In batch processing, several substrates are processed at the same time. The deposition of all layers takes place in a single reaction chamber, as is the case with the Unaxis KAI machine [21], or the individual layers are deposited in different chambers, multichamber processing in a so-called cluster configuration. In-line processing is, in fact, also multichamber processing that allows deposition on moving substrates. The lengths of the individual reaction chambers have to be carefully designed in order to deposit the required thickness of the individual layers. A special case is continuous roll-to-roll processing, where a roll of flexible substrate is unrolled and transported through a PECVD machine, in which the individual layers are deposited on the moving substrate, and then rolled up again after completion of the deposition. The roll-to-roll process is at present used by United Solar [77]. The different designs of PECVD machines are discussed in detail in reference [18].

Cleaning of deposition chambers is an important part of the manufacturing process. During the deposition the silicon layer is deposited not only on the substrates but also on other parts inside the deposition chamber, such as the electrodes. In continued module production the thickness of this silicon layer increases, until it reaches the critical thickness. Then the undesired silicon deposits can generate particles that are incorporated in solar cell structures causing defects. It is therefore necessary to periodically clean the interior of the PECVD chamber and to remove the deposits from the surfaces. Usually, the deposition chambers are opened to the air and the internal components are subjected to chemical cleaning and shot blasting. Baking is required to remove any atmospheric contaminants that may have adhered to the inner walls of the chamber during the maintenance procedures. These operations substantially decrease the uptime of the PECVD equipment. New approaches that aim to speed up the cleaning process have adopted plasma cleaning methods. However, the gasses that are used in plasma cleaning are usually expensive fluorides, such as SF_6, NF_3, or CF_4. An extensive scrubber is necessary to process these gasses. The gasses are aggressive and lead to corrosion in pumps, lines and scrubbers, which shortens the lifetimes of these parts. The use of these gasses is considered environmentally unfriendly. Since the PECVD production machines represent a substantial capital cost, it is desirable that most of the time they are in operation. Therefore, the most effective way to keep the uptime of the machine high is to have a machine design that enables replacement of fouled parts with clean ones and the cleaning procedure to be carried out away from the machine.

5.6.3.1 Transparent conductive oxide deposition

For modules manufactured on glass substrates, the TCO has become the crucial part to determine the overall performance and lower the cost. Therefore the module producers strive to have their own TCO deposition in order to be independent of the suppliers. Having their own TCO deposition machine enables them to control the quality of the TCO. The challenge is to master the deposition of TCO on a large area ($>1\,m^2$). To date, APCVD is the standard process to

deposit SnO_2:F on large area glass plates [112]. The LPCVD [19] and sputtering [20] processes have been successfully developed for large area ZnO deposition. The conductivity of the TCO top electrode influences the design and cost of the modules. The current that flows through the TCO layer has to be carefully optimized in order to limit the joule losses in the TCO. This is accomplished by optimizing the width of the cells in the module. A higher TCO conductivity allows for a larger cell width and therefore fewer laser scribes.

The use of a stainless steel substrate does not allow monolithic series interconnection and a module fabricated on this substrate is actually a large area solar cell that generates a high current. In order to limit the high resistive losses in the top TCO electrode, the fabrication of a triple junction solar cell is a reasonable choice of United Solar to increase the V_{oc} and lower the J_{sc}.

5.6.3.2 Monolithic integration of cells

The series interconnection on the substrate is achieved during the construction of the solar cell structure. Generally, it includes two or more laser scribing steps of the functional layers, such as TCO, a-Si:H and back contact, after deposition of each of the layers. The laser cutting selectively removes narrow lines (width 50 to 150 μm) of material in order to limit the area losses and at the same time it defines the size of the individual cells. The laser scribing is often a speed limiting step in the module manufacturing. Usually, pulsed Nd:YAG lasers are used for scribing the films. After accomplishing the series interconnection of the cells the module requires only two separate bus bars that connect the first and last cell, respectively, with the external junction box.

5.6.3.3 Shunt repair

Shunts strongly influence the yield of the whole manufacturing process. Shunts created in the device can be the result of several causes, like particles on the substrate during the deposition or locally defective regions in the amorphous silicon film. Shunts can be, to a large extent, prevented by using efficient cleaning procedures, especially after TCO deposition, silicon deposition and scribing steps. When necessary, a shunt repair of modules is used in order to increase the yield. Several methods can be used, such as temperature sensitive etching or reverse bias curing of the cells.

5.6.3.4 Encapsulation and framing

The final product must be well protected against atmospheric influences to prolong its lifetime. Several encapsulation methods are used for protection. The most common method for glass plate module manufacturing is to use polymeric film ethylene vinyl acetate (EVA) as the cover of the module on top of which a glass sheet is placed. However, modules made on glass substrates coated with transparent conductive oxides are susceptible to varying degrees of electrochemical corrosion [135]. Photovoltaic modules can exhibit performance degradation in the field when subjected to high voltages at elevated temperatures in a humid climate. The tin oxide contacts may delaminate from the glass due to a combination of sodium accumulation near the interface

and the ingression of moisture into the PV module from the edges. These corrosion effects can be minimized in thin film PV modules by inhibiting moisture ingression, by limiting module or array voltages, by using low alkali or high resistivity glasses, by increasing the adhesion of the transparent conductive oxide to the glass surface and by using zinc oxide rather than tin oxide as a transparent conductive contact.

In case of flexible substrates usually an EVA/Tefzel combination is used to protect the module. The Tefzel fluoropolymer (copolymer of tetrafluoroethylene and ethylene in the form of a film), which is sometimes applied on both sides of the module, has to be rather thick to guarantee the protection. The encapsulant can considerably increase the material costs of the module.

As a-Si:H solar modules are becoming an attractive element for building applications, increasing attention is being paid to framing in order to facilitate the module building and façade integration and also to give it an esthetical outlook.

5.6.3.5 Temporary superstrate process for roll-to-roll production

A novel approach to fabricate a-Si:H modules has been developed in the Netherlands in the Helianthos project coordinated by the multinational corporation Akzo Nobel [136]. The aim is to demonstrate that flexible thin film silicon PV modules manufactured by means of automated roll-to-roll processes offer a versatile lightweight thin film silicon PV product that will offer competitive kWh costs in a wide range of applications [137]. The production technology is based on a temporary superstrate concept, which combines the advantages of both superstrate and substrate type a-Si:H solar cell technologies. The deposition of a high quality top TCO layer using APCVD and monolithic series integration that offers superstrate technology is combined with roll-to-roll processing that is used in substrate technology. The fabrication process is carried out using the following steps [137]:

(1) Aluminium foil is cleaned, heated to around 500 °C while subsequently a TCO layer of SnO_2:F of 700 nm is deposited on it by means of an APCVD process at a high rate (order 0.1 $\mu m\,s^{-1}$) and with a natural texture enhancing light trapping within the solar cell.

(2) Deposition of the thin film silicon active layer by means of rf PECVD using a device structure equal to those used on a glass//TCO superstrate. Until now the development has focused on single p-i-n a-Si:H devices.

(3) Deposition of a reflective back contact.

(4) Lamination of a commodity polymer carrier foil, e.g. polyethylene terephthalate (PET).

(5) Removal of the temporary superstrate by means of wet etching.

(6) Monolithic series integration by patterning steps between the preceding processes.

(7) Application of contacts and protective encapsulation layers.

In order to demonstrate manufacturability with sufficient yield and uptime, a roll-to-roll pilot line is being constructed for a 35 cm wide web. The pilot line consists of an APCVD machine for the TCO deposition, a PECVD machine with several rf plasma zones for deposition of amorphous silicon layers, a sputter coater for ZnO:Al, Ag and Al, a compression and curing device for lamination, an etching machine with wet etching, neutralization and rinsing baths,

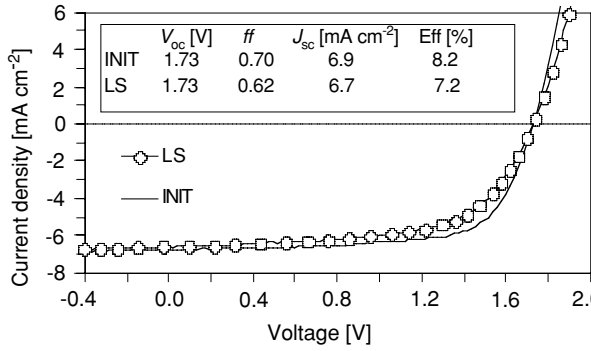

Figure 5.20 The J-V characteristics of a cell on a laboratory tandem module XS0490 in the initial state (INIT) and after 719 hours of light soaking (LS) (Courtesy of Rutger Schlatmann, Akzo Nobel).

roll-to-roll series integration and an encapsulation unit. The laser scribing and printing steps for module series integration is currently the throughput limiting step in the pilot line. Several diagnostic tools have been implemented in the pilot line. For example, in the PECVD machine, apart from monitoring input parameters regarding web handling (tension, speed, run length) and the deposition process (pressures, flows, rf power in-coupling, web temperature), the machine also monitors output parameters allowing direct verification of the film forming process.

Currently, a single junction p-i-n a-Si:H device structure is being implemented in order to demonstrate processing capability. Two types of modules have been fabricated, 'laboratory' modules with an area of 10×10 cm^2, in which eight cells are integrated and 'pilot' modules with an area of 30×30 cm^2, which consist of 26 cells. A typical pilot run yields modules with 6.3 ± 0.2 % aperture area efficiency. The next step planned is to deposit a-Si:H/a-Si:H tandem cells to increase stability against light soaking and to allow the interconnections to be placed further apart. Laboratory tandem modules with an aperture area stabilized efficiency of 7 % have been deposited. The J-V characteristics of a cell in a laboratory tandem module in the initial state (INIT) and after 719 hours of light soaking (LS) is presented in Figure 5.20. An example of a flexible Akzo Nobel pilot module is shown in Figure 5.21.

5.7 APPLICATIONS

Due to the versatility of a-Si:H technology to produce rigid as well as flexible modules and the high energy yield, the application possibilities for a-Si:H based modules are very broad. Modules made from a-Si:H have a substantially lower conversion efficiency temperature coefficient than crystalline silicon modules [130], which results in superior performance at higher operational temperatures. This feature favours the implementation of a-Si:H modules in high temperature conditions.

The applications cover the following market areas:

- Consumer products where small solar cells provide electricity for calculators, watches, etc. Small modules with power ranging from 3 to 50 Wp are used as (portable) battery chargers, in car roofs and a variety of other leisure products.

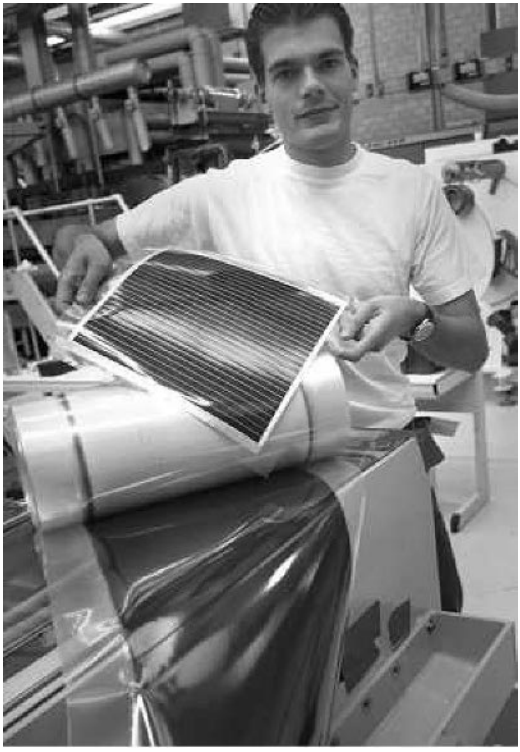

Figure 5.21 A flexible Akzo Nobel 'pilot' module with monolithical series interconnection. (Courtesy of Rutger Schlatmann, Akzo Nobel).

- Residential and commercial grid connected systems that are mainly designed for building integrated photovoltaics (BIPV). The modules usually have a 20 year power output warranty and can be structurally and esthetically integrated as roofing or façade elements. Taking advantage of the laser techniques that are applied during the manufacturing of a-Si:H modules, partly transparent modules can be fabricated. Offering both environmentally friendly performance and a compelling design, these type of products open new possibilities in BIPV applications.
- Several large grid connected systems have been realized with a-Si:H based modules. The largest array of United Solar flexible a-Si:H based modules was installed in California in 2003 to help power oil field operations (500 kW_p installed power). The facility comprises 4800 flexible solar panels, each about 40 cm wide and 540 cm long, mounted on metal frames. The world's largest amorphous silicon solar power plant (installed power of 1 MW_p), employing Mitsubishi Heavy Ind. modules, was completed in the beginning of 2005 in the German city of Buttenwiesen in the suburbs of Munich. The power plant comprises approximately 10 000 amorphous silicon single junction superstrate type modules. The plant, which is shown in Figure 5.22, is annually expected to deliver 1 million kWh.
- Off grid and remote area applications include solar systems with a rated power of 30 to 50 W_p that are mainly designed for lighting in remote homes and construction sites without

Figure 5.22 World's largest 1 MWp amorphous silicon solar power plant in the German city of Buttenwiesen in the suburbs of Munich. (With permission from Phonix SonnenStrom AG).

access to the power grid. Larger systems have been designed to generate power for villages, remote homes, water pumping, telecommunications, traffic control signals, etc.

- Special applications. The lightweight, flexible features of a-Si:H modules in connection with the inherent radiation hardness and superior high temperature performance make the technology a candidate for space PV applications [77].

5.8 OUTLOOK

The flexibility of a-Si:H solar cell technology to deliver modules for a large variety of applications is its most important asset. The technology has a strong potential to produce modules with an attractive cost to performance ratio generating electricity with a price competitive with that of conventional electricity. The cost reduction of a-Si:H modules will be determined by the scaling rate of the production capacity, which does not rise as quickly as in the case of the crystalline silicon solar cell technology. At present, a-Si:H solar cell technology has to concentrate on solving several issues which are discussed in Section 5.25 in order to become a fully mature technology.

Further development of thin film silicon solar cell technology, in general, requires an increase in the performance of a-Si:H solar cells. One has to realize that two thirds of the power generated by a promising micromorph tandem (a-Si:H/μc-Si:H) solar cell comes from the a-Si:H top cell. In the near future, attention will be paid to enhancing light trapping inside the cells, i.e. improving the TCO material quality and optimizing the surface texture. At the same time, research will continue on a-Si:H based materials, which has recently resulted in a completely new class of nanostructured silicon films with a microstructure that exhibits crystalline domains imbedded in an amorphous network.

ACKNOWLEDGMENTS

The author thanks Edward Hamers (Akzo Nobel), Gert Jan Jongerden (Akzo Nobel), Janez Krč (Ljubljana University), Johannes Meier (Unaxis), Wim Metselaar (Delft University of Technology), Vojto Nádaždy (Slovak Academy of Sciences), Paul Peters (Akzo Nobel), Bernd Rech (Research Centre Jülich), Richard van de Sanden (Eindhoven University of Technology), Rutger Schlatmann (Akzo Nobel), Ruud Schropp (Utrecht University), Kenji Yamamoto (Kaneka Corporation), and Jeff Yang (United Solar United Solar Ovonic Corporation) for their help in writing this article.

REFERENCES

[1] H.F. Sterling and R.C.G. Swann, Chemical vapour deposition promoted by r.f. discharge, *Solid-State Electron.,* **8 (8)**, 653 (1965).
[2] W. Spear and P. LeComber, Substitutional doping of amorphous silicon, *Solid State Comm.,* **17 (9)**, 1193 (1975).
[3] D.E. Carlson and C.R. Wronski, Amorphous silicon solar cell, *Appl. Phys. Lett.*, **28 (11)**, 671 (1976).
[4] J. Yang, A. Banerjee, K. Lord, and S. Guha, Correlation of component cells with high efficiency amorphous silicon alloy triple-junction solar cells and modules, in *Proceedings of the 2nd World Conference and Exhibition on Photovoltaic Solar Energy Conversion, Vienna* (1998), 387–390.
[5] P. Maycock, PV market update, *Renewable Energy World*, **7 (4)**, 86 (2004).
[6] Y. Hamakawa, H. Okamoto, Y. Nitta, A new type of amorphous silicon photovoltaic cell generating more than 2.0 V, *Appl. Phys. Lett.,* **35 (2)**, 187 (1979).
[7] Y. Kuwano, T. Imai, M. Ohnishi, and S. Nakano, A horizontal cascade type amorphous Si photovoltaic cell module, in *Proceedings of the 14th IEEE Photovoltaic Specialist Conference* (1980), 1408.
[8] Y. Tawada, H. Okamoto, Y. Hamakawa, a-SiC:H/a-Si:H heterojunction solar cell having more than 7.1 % conversion efficiency, *Appl. Phys. Lett.,* **39 (3)**, 237 (1981).
[9] G. Nakamura, K. Sato, Y. Yukimoto, K. Shirahata, in *Proceedings of the 3rd E.C. Photovoltaic Solar Energy Conference* (1980), p. 835.
[10] H.W. Deckman, C.R. Wronski, H. Witzke, and E. Yablonovitch, Optically enhanced amorphous silicon solar cells, *Appl. Phys. Lett.,* **42 (11)**, 968 (1983).
[11] R.R. Arya and D.E. Carlson, Amorphous silicon PV module manufacturing at BP Solar, *Progr.Photovolt.: Res. Appl.*, **10**, 69–76 (2002).
[12] E. Maruyama, S. Okamoto, A. Terakawa, W. Shinohara, M. Tanaka and S. Kiyama, Toward stabilized 10 % efficiency of large-area (5000 cm^2) a-Si/a-SiGe tandem solar cells using high-rate deposition, *Sol. En. Mat. Sol. Cells*, **74**, 339–349 (2002).
[13] Y. Ichikawa, T. Yoshida, T. Hama, H. Sakai and K. Harashima, Production technology for amorphous silicon-based flexible solar cells, *Sol. En. Mat. Sol.* Cells, **66**, 107–115 (2001).
[14] S. Guha, J. Yang and A. Banerjee, Amorphous silicon alloy photovoltaic research – present and future, *Progr.Photovolt.: Res. Appl.*, **8**, 141–150 (2000).
[15] J. Meier, S. Dubail, R. Flückiger, D. Fischer, H. Keppner, A. Shah, Intrinsic microcrystalline silicon – a promising new thin film solar cell material, in *Proceedings of the 1st World Conference on Photovoltaic Energy Conversion, Hawai* (1994), 409–412.
[16] J. Meier, S. Dubail, J. Cuperus, U. Kroll, R. Platz, P. Torres, J.A. Anna Selvan, P. Pernet, N. Beck, N. Pellaton Vaucher, Ch. Hof, D. Fischer, H. Keppner, A. Shah, Recent progress in micromorph solar cells, *J. Non-Cryst. Solids*, **227–230**, 1250–1256 (1998).

[17] K. Yamamoto, M. Yoshimi, Y. Tawada, Y. Okamoto, A. Nakajima, Thin film Si solar cell fabricated at low temperature, *J. Non-Cryst. Solids*, **266–269**, 1082–1087 (2000).
[18] R.E.I. Schropp and M. Zeman, *Amorphous and Microcrystalline Solar Cells: Modeling, Materials, and Device Technology*, Kluwer Academic Publishers, 1998.
[19] J. Meier, U. Kroll, S. Dubail, S. Golay, S. Fay, J. Dubail, A. Shah, Efficiency enhancement of amorphous silicon p-i-n- solar cells by LP-CVD ZnO, in *Proceedings of the 28th IEEE Photovoltaic Specialist Conference*, (2000), 746–749.
[20] J. Müller, G. Schöpe, O. Kluth, B. Rech, B. Syszka, T. Höing, V. Sittinger, X. Jiang, G. Bräuer, R. Geyer, P. Lechner, H. Schade, M. Ruske, Large area mid-frequency magnetron sputtered ZnO films as substrates for silicon, in *Proceedings of the 17th European Photovoltaic Solar Energy Conference, Munich* (2001), 2876–2879.
[21] J. Meier, U. Kroll, J. Spitznagel, S. Bengagli, T. Roschek, G. Pfanner, Ch. Ellert, G. Androutsopoulos, A. Hügli, G. Büchel, D. Plesa, A. Büchel, A. Shah, Thin film silicon solar cell up-scaling by large-area PECVD KAI systems, in *Proceedings of the 19th European Photovoltaic Solar Energy Conference and Exhibition, Paris* (2004), 3BP1.2.
[22] S. Wieder, J. Liu, T. Repmann, R. Carius, J. Kuske, and U. Stephan, Large area deposition of amorphous and microcrystalline silicon – new tools for industrial applicable mass production, in *Proceedings of the 19th European Photovoltaic Solar Energy Conference and Exhibition, Paris* (2004), 3AO.8.3.
[23] A.V. Shah, M. Vaneček, J. Meier, F. Meillaud, J. Guillet, D. Fischer, C. Droz, X. Niquille, S. Faÿ, E. Vallat-Sauvain, V. Terrazzoni-Daudrix and J. Bailat, Basic efficiency limits, recent experimental results and novel light-trapping schemes in a-Si:H, μc-Si:H and 'micromorph tandem' solar cells, *J. Non-Cryst. Solids*, **338–340**, 639–645 (2004).
[24] D.L. Staebler and C.R. Wronski, Reversible conductivity changes in discharge-produced amorphous Si, *Appl. Phys. Lett.* **31 (4)**, 292–294 (1977).
[25] B. Rech, H. Wagner, Potential of amorphous silicon for solar cells, *Appl. Phys. A*, **69**, 155–167 (199).
[26] R. Street, *Hydrogenated Amorphous Silicon*, Cambridge University Press, Cambridge (1991).
[27] M.H. Brodsky and R.S. Title, Electron spin resonance in amorphous silicon, germanium, and silicon carbide, *Phys. Rev. Lett.*, **23**, 581 (1969).
[28] M. Stutzmann and D.K. Biegelsen, The microscopic structure of defects in a-Si:H and related materials, in *Amorphous Silicon and Related Materials*, H. Fritzsche (Ed.), World Scientific, Singapore (1988).
[29] W. Beyer, Diffusion and evolution of hydrogen in hydrogenated amorphous and microcrystalline silicon, *Sol. En. Mat, Sol. Cells*, **78**, 235–267 (2003).
[30] J.A. Reimer, M.A. Peterich, Structural heterogeneities in device-quality amorphous hydrogenated semiconductors, in *Amorphous Silicon and Related Materials*, H. Fritzsche (Ed.), World Scientific, Singapore (1988).
[31] P.A. Fedders, D.J. Leopold, P.H. Chan, R. Borzi, and R.E. Norberg, Molecular hydrogen in a-Si:H, *Phys. Rev. Lett.*, **85 (2)**, 401 (2000).
[32] M. Stutzmann, Weak bond dangling bond conversion in amorphous silicon, *Phil. Mag. B*, **56 (1)**, 63 (1987).
[33] K. Winer, Defect formation in a-Si:H, *Phys. Rev. B*, **41 (17)**, 12150 (1990).
[34] M.J. Powell and S.C. Deane, Improved defect-pool model for charged defects in amorphous silicon, *Phys. Rev. B*, **48 (15)**, 10815 (1993).
[35] G. Schumm. Chemical equilibrium description of stable and metastable defect structures in a-Si:H, *Phys. Rev. B*, **49 (4)**, 2427 (1994).
[36] W. Shockley and W.T. Read, Statistics of the recombinations of holes and electrons, *Phys. Rev.*, **87 (5)**, 835–842 (1952).
[37] C.T. Sah and W. Shockley, Electron-hole recombination statistics in semiconductors through flaws with many charge conditions, *Phys. Rev.*, **109 (4)**, 1103–1115 (1958).

[38] W.B. Jackson, S.M. Kelso, C. C. Tsai, J. W. Allen, and S.-J. Oh, Energy dependence of the optical matrix element in hydrogenated amorphous and crystalline silicon, *Phys. Rev. Lett.*, **31**, 5187 (1985).

[39] T. Hama, H. Okamoto, Y. Hamakawa and T. Matsubara, Hydrogen content dependence of the optical energy gap in a-Si:H, *J. Non-Cryst. Solids*, **59–60**, 333 (1983).

[40] D. Ritter, E. Zeldov, and K.Weiser, Diffusion length measurements in a-Si:H using the steady state photocarrier grating technique, *J. Non-Cryst. Solids*, **97–98**, 619 (1987); D. Ritter, E. Zeldov, and K.Weiser, Steady state photocarrier grating technique for diffusion length measurement in photoconductive insulators, *Appl. Phys. Lett.*, **49 (13)**, 791 (1986).

[41] I. Balberg and S.Z. Weisz, Accurate determination of the two carriers steady-state mobility-lifetime products in hydrogenated amorphous silicon, *J. Appl. Phys.*, **70**, 2204 (1991). I Balberg, Theory of the small photocarrier grating under the application of an electric field, *Phys. Rev. B*, **44 (4)**, 1628 (1990).

[42] W.B. Jackson and N.M. Amer, Direct measurement of gap-states in hydrogenated amorphous silicon by photothermal deflection spectroscopy, *Phys. Rev. B*, **25 (8)**, 5559 (1982).

[43] M. Vaneček, J. Kočka, J. Stuchlík, Z. Kožíšek, O. Štika, and A. Tříska, Density of the gap states in undoped and doped glow discharge a-Si:H, *Sol. En. Mater.* **8**, 411–423 (1983).

[44] C.R. Wronski, B. Abeles, T. Tiedje, and G.D. Cody, Recombination centers in phosphorous doped hydrogenated amorphous silicon, *Solid State Commun.*, 1423 (1982).

[45] M. Vaneček and A. Poruba, Fourier-transform photocurrent spectroscopy of microcrystalline silicon for solar cells. *Appl. Phys. Lett.*, **80 (5)**, 719 (2002).

[46] M. Vaneček, J. Kočka, A. Poruba, A. Fejfar, Direct measurement of the deep defect density in thin amorphous silicon films with the absolute constant photocurrent method, *J. Appl. Phys.*, **78 (10)**, 6203 (1995).

[47] Z.E. Smith, V. Chu, K. Shephard, S. Aljishi, D. Slobodin, J. Kolodzey, S. Wagner, T.L. Chu, Phototermal and photoconductive determination of surface and bulk defect densities in amorphous silicon films, *Appl. Phys. Lett.*, **50 (21)**, 1521–1523 (1987).

[48] N. Wyrsch, F. Finger, T.J. McMahon, M. Vanecek, How to reach more precise interpretation of subgap absorption spectra in terms of deep defect density in a-Si:H, *J. Non-Cryst. Solids*, **137–138**, 347–350 (1991).

[49] A. Madan, P.G. LeComber and W.E. Spear, Investigation of the density of localized states in a-Si using the field effect technique, *J. Non-Cryst. Solids*, **20**, 239 (1976).

[50] D.V. Lang, J.D. Cohen, and J.P. Harbison, Measurement of the density of gap states in hydrogenated amorphous silicon by space charge spectroscopy, *Phys. Rev. B*, **25**, 5285 (1982).

[51] W. den Boer, Determination of the midgap density of states in a-Si:H using space-charged limited current measurements, *J. de Physique*, **42 (C4)**, 451–454 (1981).

[52] K.D. Mackenzie, P.G. LeComber and W.E. Spear, The density of states in amorphous silicon determined by space-charged limited current measurements, *Phil. Mag. B*, **46**, 377 (1982).

[53] J.D. Cohen and D.V. Lang, Calculation of the dynamic response of Schottky barriers with a continuous distribution of gap states, *Phys. Rev. B*, **25**, 5321 (1982).

[54] V. Nádaždy, R. Durný, and E. Pinčík, Evidence for the improved defect-pool model for gap states in amorphous silicon from charge DLTS experiments on undoped a-Si:H, *Phys. Rev. Lett.*, **78**, 1102 (1997).

[55] V. Nádaždy and M. Zeman, Origin of charged gap states in a-Si:H and their evolution during light soaking, *Phys. Rev. B*, **69**, 165213 (2004).

[56] M. Stutzman, W.B. Jackson, and C.C. Tsai, Light-induced metastable defects in hydrogenated amorphous silicon: A systematic study, *Phys. Rev. B*, **32**, 23 (1985).

[57] H.M. Branz, Hydrogen collision model: quantitative description of metastability in amorphous silicon, *Phys. Rev. B*, **59**, 5498 (1999).

[58] H. Fritzsche, Development in understanding and controlling the Staebler–Wronski effect in a-Si:H, *Annu. Rev. Mater. Res.*, **31**, 47 (2001).

[59] T. Shimizu, Steabler–Wronski effect in hydrogenated amorphous silicon and related alloys, *Jpn. J. Appl. Phys.*, **43 (6A)**, 3257–3268 (2004).
[60] H.R. Park, J.Z. Liu, and S. Wagner, Saturation of the light-induced defect density in hydrogenated amorphous silicon, *Appl. Phys. Lett.*, **55 (25)**, 2658–2661 (1989).
[61] V. Nádaždy, R. Durný, I. Thurzo, E. Pinčík, A. Nishida, J. Shimizu, M. Kumeda, T.Shimizu, Correlation between the results of charge deep-level transient spectroscopy and ESR techniques for undoped hydrogenated amorphous silicon, *Phys. Rev. B*, **66,** 195211 (2002).
[62] R. Biswas, B.C. Pan, and Y.Y. Ye, Metastability of amorphous silicon from silicon network re-bonding, *Phys. Rev. Lett.*, **88**, 205502 (2002).
[63] B.R. Tuttle, Theory of hydrogen-related metastability in disordered silicon, *Phys. Rev. Lett.*, **93 (21)**, 215504 (2004).
[64] L. Yang and L.F. Chen, The effect of H_2 dilution on the stability of a-Si:H based solar cells, in *Amorphous Silicon Technology – 1994, Mater. Res. Soc. Proc.*, **336**, 669–674 (1994).
[65] J. Yang, X. Xu, and S. Guha, Stability studies of hydrogenated amorphous silicon alloy solar cells prepared with hydrogen dilution, in *Amorphous Silicon Technology – 1994, Mater. Res. Soc. Proc.*, **336**, 687–692 (1994).
[66] C.R. Wronski, J.M. Pearce, R.J. Koval, X. Niu, A.S. Ferluato, J. Koh, and R.W. Collins, Light induced defect creation kinetics in thin film protocrystalline silicon materials and their solar cells, in *Amorphous and Heterogeneous Silicon-Based Films – 2002, Mater. Res. Soc. Proc.*, **715**, A13.4 (2002).
[67] R.W. Collins, A.S. Ferluato, Advances in plasma-enhanced chemical vapour deposition of silicon films at low temperatures, *Curr. Opin. Solid State Mat. Sci.*, **6**, 425–437 (2002).
[68] A.H. Mahan, R. Biswas, L.M. Gedvilas, D.L. Williamson, and B.C. Pan, On the influence of short and medium range order on the material bandgap in hydrogenated amorphous silicon, *J. Appl. Phys.*, **96 (7)**, 3818–3826 (2004).
[69] P. Roca i Cabarrocas, A. Fontcuberta i Morral, Y. Poissant, Growth and optoelectronic properties of polymorphous silicon thin films, *Thin Solid Films*, **403–404**, 39–46 (2002).
[70] W. Spear and P. LeComber, Electronic properties of substitutionally doped Si and Ge, *Philos. Mag.*, **33 (6)**, 935 (1976).
[71] N.F. Mott, Conduction in non-crystalline materials. 3. Localized states in a pseudogap and near extremities of conduction and valence bands, *Philos. Mag.*, **19**, 835 (1969).
[72] R.A. Street, Doping and the Fermi energy in amorphous silicon, *Phys. Rev. Lett.*, **49**, 1187–1190 (1982).
[73] M. Stutzmann, R. Street, C. Tsai, J. Boyce, S. Ready, Structural, optical, and spin properties of hydrogenated amorphous silicon-germanium alloys, *J. Appl. Phys.*, **66 (2)**, 569 (1989).
[74] A. Matsuda and K. Tanaka, Guiding principle for preparing highly photosensitive Si-based amorphous alloys, *J. Non-Cryst. Solids*, **97–98**, 1367–1374 (1987).
[75] M. Shima, M. Isomura, E. Maruyama, S. Okamoto, H. Haku, K. Wakisaka, S. Kiyama and S. Tsuda, Investigation of hydrogenated amorphous silicon germanium fabricated under high hydrogen dilution and low deposition temperature conditions for stable solar cells, *Jpn. J. Appl. Phys.*, **37**, 6322–6327 (1998).
[76] S. Guha, Materials considerations for high efficiency and stable amorphous silicon alloy solar cells, in *Proceedings of the International Workshop on Amorphous Semiconductors*, H. Fritsche, D.X. Han, and C.C. Tsai (Eds.), World Scientific Publishing Co., 1987.
[77] S. Guha, Thin film silicon solar cells grown near the edge of amorphous to microcrystalline transition, *So. En.*, **77**, 887–892 (2004).
[78] A. Matsuda, K. Nomoto, Y. Takeuchi, A. Suzuki, A. Yuuki, and J. Perrin, Temperature dependence of the sticking and loss probabilities of silyl radicals on hydrogenated amorphous silicon, *Surf. Sci.*, **227**, 50 (1990).
[79] G. Bruno, P. Capezzuto, and A. Madan, *Plasma deposition of amorphous silicon-based materials*, Academic Press, 1995.

[80] Y. Toyoshima, K. Arai, A. Matsuda and K. Tanaka, In situ characterization of the growing a-Si:H surface by IR spectroscopy, *J. Non-Cryst. Solids*, **137–138**, 765–770 (1991).
[81] E.A.G. Hamers, J. Bezemer, and W. F. van der Weg, Positive ions as growth precursors in plasma enhanced chemical vapor deposition of hydrogenated amorphous silicon, *Appl. Phys. Lett.*, **75 (5)**, 609–611 (1999).
[82] W. Luft, and Y. Simon Tsuo, *Hydrogenated amorphous silicon alloy deposition processes*, Applied Physics Series 1, Marcel Dekker, New York, Basel, Hong Kong, 1993.
[83] T. Takagi, R. Hayashi, G. Ganguly, M. Kondo, A. Matsuda, Gas-phase diagnosis and high-rate growth of stable a-Si:H, *Thin Solid Films*, **345**, 75–79 (1999).
[84] M. Kondo, A. Matsuda, An approach to device grade amorphous and microcrystalline silicon thin films fabricated at high deposition rates, *Curr. Opin. Solid State Mat. Sci.*, **6**, 445–453 (2002).
[85] B. Rech, T. Roschek, J. Müller, S. Wieder, H. Wagner, Amorphous and microcrystalline silicon solar cells prepared at high deposition rates using RF (13.56MHz) plasma excitation frequencies, *Sol. En. Mat. Sol. Cells*, **66**, 267–273 (2001).
[86] H. Curtins, N. Wyrsch, A.V. Shah, High-rate deposition of amorphous hydrogenated silicon – effect of plasma excitation-frequency, *Electron. Lett.*, **23 (5)**, 228–230 (1987).
[87] K. Saito, M. Sano, K. Ogawa and I. Kajita, High efficiency a-Si:H alloy cell deposited at high deposition rate, *J. Non-Cryst. Solids*, **164–166**, 689–692 (1993).
[88] H. Matsumura, Catalytic chemical vapor deposition (CTL-CVD) method producing high quality hydrogenated amorphous silicon, *Jpn. J. Appl. Phys.*, **25**, L949–L951 (1986).
[89] W.M.M. Kessels, R.J. Severens, A.H.M. Smets, B.A. Korevaar, G.J. Adriaenssens, D.C. Schram and M.C.M. van de Sanden, Hydrogenated amorphous silicon deposited at very high growth rates by an expanding Ar-H2-SiH4 plasma, *J. Appl. Phys.*, **89**, 2404 (2001).
[90] A. Shah, J. Dutta, N. Wyrsch, K. Prasad, H. Curtins, F. Finger, A. Howling and Ch. Hollenstein, VHF plasma deposition: A comparative overview, in *Amorphous Silicon Technology – 1992, Mater. Res. Soc. Proc.*, **258**, 15–26 (1992).
[91] J.L. Dorier, C. Hollenstein, A.A. Howling, U. Kroll, Powder dynamics in very-high-frequency silane plasmas, *J. Vac. Sci. Technol. A*, **10 (4)**, 1048–1052 (1992).
[92] J. Meier, J. Spitznagel, U. Kroll, C. Bucher, S. Faÿ, T. Moriarty, A. Shah, High-efficiency amorphous and 'micromorph' silicon solar cells, in *CD Proceedings of the 3rd World Conference on Photovoltaic Energy Conversion, Osaka*, (2003), S20-B9-06.
[93] H. Takatsuka, M. Noda, Y. Yonekura, Y. Takeuchi, Y. Yamauchi, Development of high efficiency large area silicon thin modules using VHF-PECVD, *Sol. En.*, **77**, 951–960 (2004).
[94] A. H. M. Smets, W. M. M. Kessels and M. C. M. van de Sanden, External rf substrate biasing during a-Si:H film growth using the expanding thermal plasma technique, in *Amorphous and Nanocrystalline Science and Technology – 2004, Mater. Res. Soc. Proc.*, **808**, 383 (2004).
[95] A.H.M. Smets, W.M.M. Kessels, M.C.M. van de Sanden, Temperature dependence of the surface roughness evolution during hydrogenated amorphous silicon film growth, *Appl. Phys. Lett.*, **82 (6)**, 865–867 (2003).
[96] W.M.M. Kessels, A.H.M. Smets, D.C. Marra, E.S. Aydil, D.C. Schram, M.C.M. van de Sanden, On the growth mechanism of a-Si:H, *Thin Solid Films*, **383**, 154–160 (2001).
[97] B.A. Korevaar, C. Smit, R.A.C.M.M. van Swaaij, A.H.M. Smets, W.M.M. Kessels, J.W. Metselaar, D.C. Schram, and M.C.M. van de Sanden, Solar cells with intrinsic a-Si:H deposited at rates larger than 5 Å/s by the expanding thermal plasma, in *Proceedings of the 16th European Photovoltaic Solar Energy Conference and Exhibition, Glasgow* (2000), B119.
[98] A. M. H. N. Petit, V. Nádaždy, M. Zeman, R. A. C. M. M. van Swaaij,. H. M. Smets and M. C. M. van de Sanden, Significant improvement of amorphous silicon solar cell by means of rf-biased expanding thermal plasma deposition, submitted to *Appl. Phys. Letts.*
[99] A. H. Mahan, B. P. Nelson, S. Salamon, R.S. Crandall, Deposition of device quality, low H content a-Si:H by hot wire technique, *J. Non-Cryst. Solids*, **137–138 (2)**, 657–660 (1991).

[100] B. Schroeder, Status report: solar cell related research and development using amorphous and microcrystalline silicon deposited by HW(Cat)CVD, *Thin Solid Films*, **430**, 1–6 (2003).
[101] H. Meiling and R.E.I. Schropp, Stable amorphous silicon thin film transistors, *Appl. Phys. Lett.*, **70 (20)**, 2681–2683 (1997).
[102] H. Matsumura, H. Umenoto, A. Masuda, Cat-CVD (hot wire CVD): how different from PECVD in preparing amorphous silicon, *J. Non-Cryst. Solids*, **338–340**, 19–26 (2004).
[103] R.E.I. Schropp, M.K. van Veen, C.H.M. van der Werf, D.L. Williamson, A.H. Mahan, Protocrystalline silicon at high rate from undiluted silane, in *Amorphous and Nanocrystalline Silicon Science and Technology – 2004, Mater. Res. Soc. Proc.*, **808**, A8.4. (2004).
[104] A.H. Mahan, Solar cell research and development using the hot wire CVD process, *Sol. En.*, **77**, 931–938 (2004).
[105] R. H. Franken, C. H. M. van der Werf, J. Löffler, J. K. Rath and R. E. I. Schropp, Beneficial effects of sputtered ZnO:Al protection layer on SnO_2:F for high-deposition rate hot-wire CVD p-i-n solar cells, in *Proceedings of the 3rd International Conference on Hot-Wire CVD Process, Utrecht* (2004) 377, to be published in *Thin Solid Films*.
[106] K. Ishibashi, M. Karasawa, G. Xu, N. Yokokawa, M. Ikemoto, A. Masuda, H. Matsumura, Development of Cat-CVD apparatus for 1-m-size large-area deposition, *Thin Solid Films*, **430**, 58–62 (2003).
[107] R.E.I. Schropp, Present status of micro- and polycrystalline silicon solar cells made by hot-wire chemical vapor deposition, *Thin Solid Films*, **451–452**, 455–465 (2004).
[108] M. Zeman, J.A. Willemen, L.L.A. Vosteen, G. Tao and J.W. Metselaar. Computer modeling of current matching in a-Si:H/a-Si:H tandem solar cells on textured substrates. *Sol. En. Mat. Sol. Cells*, **46**, 81–99 (1997).
[109] X. Deng and E.A. Schiff, Amorphous silicon-based solar cells, in *Handbook of Photovoltaic Science and Engineering*, A. Luque and S. Hegedus (Eds.), John Wiley & Sons, Ltd (2003).
[110] M. Kondo, K. Hayashi, H. Nishio, S. Kurata, A. Ishikawa, A. Takenaka, K. Nishimura, A. Nakajima, H. Yamagishi and Y. Tawada, Development of high efficient large area a-Si solar modules, in *Proceedings of the 13th European Photovoltaic Solar Energy Conference, Nice* (1995), 311–314.
[111] B. Rech, C. Beneking, H. Wagner, Improvement in stabilized efficiency of a-Si:H solar cells through optimized p/i interface layers, *Sol. En. Mat. Sol. Cells*, **41(42)**, 475–483 (1996).
[112] K. Sato, Y. Gotoh, Y. Wakayama, Y. Hayashi, K. Adachi, H. Nishimura, Highly textured SnO_2:F TCO films for a-Si solar cells, *Rep. Res. Lab. Asahi Glass Co. Ltd.*, **42**, 129–137 (1992).
[113] R. Groenen, J. Loffler, P.M. Sommeling, J.L. Linden, E.A.G. Hamers, R.E.I. Schropp, M.C.M. van de Sanden, Surface textured ZnO films for thin film solar cell applications by expanding thermal plasma CVD, *Thin Solid Films*, **392 (2)**, 226–230 (2001).
[114] H. Stiebig, F. Siebke, W. Beyer, C. Beneking, B. Rech and H. Wagner, Interfaces in a-Si: H solar cell structures, *Sol. En. Mat. Sol. Cells*, **48**, 351–363 (1997).
[115] A. Banerjee, J. Yang, K. Hoffman, and S. Guha, Characteristics of hydrogenated amorphous silicon alloy solar cells on a Lambertian back reflector, *Appl. Phys. Lett.*, **65 (4)**, 472–474 (1996).
[116] J. Springer, A. Poruba, L. Mullerova, M. Vanecek, O. Kluth, B. Rech, Absorption loss at nanorough silver back reflector of thin-film silicon solar cells, *J. Appl. Phys.*, **95 (3)**, 1427–1429 (2004).
[117] M. Zeman, R.A.C.M.M. van Swaaij, J.W. Metselaar and R.E.I. Schropp, Optical modeling of a-Si:H solar cells with rough interfaces: Effect of back contact and interface roughness, *J. Appl. Phys.*, **88 (11)**, 6436–6443 (2000).
[118] J. Krč, M. Zeman, F. Smole, and M. Topič, Optical modeling of a-Si:H solar cells deposited on textured glass/SnO_2 substrates, *J. Appl. Phys.*, **92 (2)**, 749–755 (2002).
[119] J. Krč, M. Zeman, O. Kluth, F. Smole, and M. Topič, Light scattering properties of SnO_2 and ZnO surface-textured substrates, in *CD Proceedings of the 3rd World Conference on Photovoltaic Energy Conversion*, *Osaka* (2003), 5P-D4-27.
[120] J. Springer, A. Poruba, and M. Vanecek, Improved three-dimensional optical model for thin-film silicon solar cells, *J. Appl. Phys.*, **96 (9)**, 5329–5337 (2004).

[121] T. Yoshida, K. Maruyama, O. Nabeta, Y. Ichikawa, H. Sakai and Y. Uchida, High efficiency a-Si:H two-stacked tandem solar cell, in *Proceedings of the 19th IEEE Photovoltaic Specialists Conference* (1987), 1095–1100.

[122] A. Banerjee, J. Yang, T. Glatfelter, K. Hoffman, and S. Guha, Experimental study of players in 'tunnel' junctions for high efficiency amorphous silicon alloy multijunction solar cells and modules, *Appl. Phys. Lett.*, **64 (12)**, 1517–1519 (1994).

[123] D. S. Shen, R. E. I. Schropp, H. Chatham, R. E. Hollingsworth, P. K. Bhat, and J. Xi, Improving tunneling junction in amorphous silicon tandem solar cells, *Appl. Phys. Lett.*, **56 (19)**, 1871–1873 (1990).

[124] Y. Ichikawa, S. Fujikake, T. Takayama, S.Saito, H. Ota, T. Yoshida, T. Ihara and H. Sakai, Large-area amorphous silicon solar cells with high stabilized efficiency and their fabrication technology, in *Proceedings of the 23rd IEEE Photovoltaic Specialists Conference* (1993), 27–33.

[125] T.J. Coutts, J.S. Ward, D.L. Young, K.A. Emery, T.A. Gessert, and R. Noufi, Critical issues in the design of polycrystalline, thin-film tandem solar cells, *Progr. Photovolt.: Res. Appl.*, **11 (6)**, 359–375 (2003).

[126] S. Guha, J. Yang, A. Pawlikiewicz, T. Glatfelter, R. Ross, and S. R. Ovshinsky, Band-gap profiling for improving the efficiency of amorphous silicon alloy solar cells, *Appl. Phys. Lett.*, **54 (23)**, 2330–2332 (1989).

[127] R. A. C. M. M. van Swaaij, M. Zeman, S. Arnoult, and J. W. Metselaar, Performance dependence on grading width of a-SiGe:H component solar cells, in *Proceedings of the 28th IEEE Photovoltaic Specialist Conference* (2000), 869–872.

[128] J. Yang, A. Banerjee, and S. Guha, Triple-junction amorphous silicon alloy solar cell with 14.6 % initial and 13.0 % stable conversion efficiencies, *Appl. Phys. Lett.*, **70 (22)**, 2975–2977 (1997).

[129] P. J. McElheny, J. Arch, H. Liu, and S. J. Fonash, Range of validity of the surface-photovoltage diffusion length measurement: A computer simulation, *J. Appl. Phys.*, **64**, 1254–1265 (1998).

[130] P. Lechner and H. Schade, Photovoltaic thin-film technology based on hydrogenated amorphous silicon, Progr.Photovolt.: *Res. Appl.*, **10**, 85–97 (2002).

[131] A. Banerjee, J. Yang, and S. Guha, Optimization of high efficiency amorphous silicon alloy based triple-junction modules, in *Amorphous and Heterogeneous Silicon Thin Films: Fundamentals to Devices – 1999, Mater. Res. Soc. Proc.*, **557**, 743–748 (1999).

[132] A.V. Shah, H. Schade, M. Vaneček, J. Meier, E. Vallat-Sauvain, N. Wyrsch, U. Kroll, C. Droz and J. Bailat, Thin-film silicon solar cell technology, *Progr. Photovolt.: Res. Appl.*, **12**, 113–142 (2004).

[133] C.N. Jardine and K. Lane, PV-COMPARE: relative performance of photovoltaic technologies in northern and southern Europe, *Proceedings of the PV in Europe Conference and Exhibition, Rome* (2002), V8-5.

[134] Market survey on solar modules, *Photon International*, February 2005, 48–67.

[135] D. E. Carlson, R. Romero, F. Willing, D. Meakin, L. Gonzalez, R. Murphy, H. R. Moutinho and M. Al-Jassim, Corrosion effects in thin-film photovoltaic modules, *Progr. Photovolt.: Res. Appl.*, **11**, 377–386 (2003).

[136] E. Middelman, E. van Andel, R.E.I. Schropp, L.V. de Jonge-Meschaninova, P.M.G.M. Peters, R.J. Severens, H. Meiling, M. Zeman, M.C.M. van de Sanden, A. Kuijpers, C.I.M.A. Spee, and G.J. Jongerden, New temporary superstrate process for roll-to-roll production of thin-film solar cells, in *Proceedings of the 2nd World Conference and Exhibition on Photovoltaic Solar Energy Conversion*, **Vol. I**, 816–819 (1998).

[137] G.J. Jongerden, Monolithically series integrated flexible PV modules manufactured on commodity polymer substrates, in *Proceedings of the 3rd World Conference and Exhibition on Photovoltaic Solar Energy Conversion, Osaka* (2003), 6LN-C-05.

[138] Y. Hishikawa, K. Ninomiya, E. Maruyama, S. Kuroda, A. Terakawa, K. Sayama, H. Tarui, M. Sasaki, S. Tsuda and S. Nakano, Approaches for stable multi-junction a-Si solar cells, in *Proceedings of the 1st World Conference on Photovoltaic Energy Conversion, Hawai* (1994), 386–393.

6 Chalcopyrite Based Solar Cells

Renier Klenk, Martha Ch. Lux-Steiner
Hahn-Meitner-Institut Berlin Gleinicker, Berlin

6.1 INTRODUCTION

Chalcopyrite based solar modules uniquely combine advantages of thin film technology with the efficiency and stability of conventional crystalline silicon cells . It is therefore believed that chalcopyrite based modules can take up a large part of the photovoltaic (PV) market growth once true mass production is started.

The most important chalcopyrite compounds for photovoltaic applications are $CuInSe_2$, $CuInS_2$, and $CuGaSe_2$ with bandgaps of 1.0, 1.5, and 1.7 eV, respectively. Together with related materials they offer high optical absorption and a wide range of lattice constants and bandgaps (Figure 6.1). The compounds can be alloyed to obtain intermediate bandgaps. Starting with single crystals [2], chalcopyrite based solar cells have been under investigation since 1974. The first chalcopyrite cells had a $CuInSe_2$ absorber and therefore the technology is most advanced for lower gap materials with a composition close to $CuInSe_2$. Today the efficiency of lab scale thin film devices is close to 20 % [3], an efficiency comparable to the best multicrystalline silicon cells. Many scaling up and manufacturing issues have been resolved. Pilot production lines are operational and modules are commercially available. As of 2005 the market share of chalcopyrite PV modules is not yet significant but major problems that might prevent further commercialization have not been identified.

6.2 POTENTIAL OF CHALCOPYRITE PHOTOVOLTAIC MODULES

The attractive potential of chalcopyrite photovoltaic modules can be summarized by key points which we will briefly illustrate here and assess in more detail in the reminder of the chapter:

- High efficiency.
- Stability.
- Low cost.
- Effective use of raw materials.

Thin Film Solar Cells Edited by J. Poortmans and V. Arkhipov
© 2006 John Wiley & Sons, Ltd

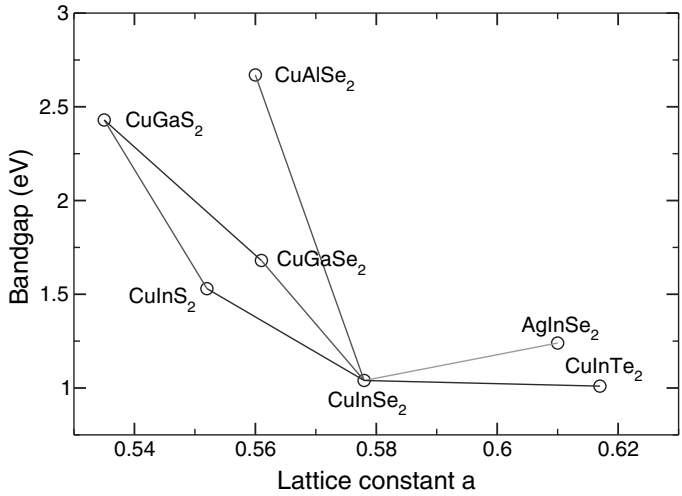

Figure 6.1 Bandgaps and lattice constants of selected chalcopyrites according to data compiled in [1] (lines are a guide to the eye only).

- Short energy payback time.
- Adaptable to various applications.
- Large supporting research and development community.

Chalcopyrites clearly offer the highest efficiency potential among all thin film technologies. The record efficiency for a small, lab scale cell is close to 20 %, using just a single layer antireflective coating and a standard metal grid but none of the complex concepts that have been used to produce record silicon cells. Submodule efficiencies are at almost 17 % [4], and square foot and larger modules range from 14 to 12 % efficiency [5–7]. It is conceivable that the maximum efficiency can be increased further. A significant boost, exceeding even the theoretical limit for silicon, can be expected from the development of multijunction cells . The excellent performance is notable not only under standard reporting conditions but also when assessing monitoring data from outdoor installations.

In contrast to amorphous silicon based cells chalcopyrite devices do not show any degradation under illumination. Outdoor testing indicates that achievable product lifetimes may be comparable to those of conventional photovoltaic modules.

The low cost potential is roughly comparable to that of other thin film technologies and is rooted in the use of inexpensive substrates, effective use of raw materials, high throughput, and large area deposition at low temperatures as well as monolithic interconnection.

Apart from the substrate, the total thickness of a chalcopyrite cell, including all films, is in the range of 2 to 4 μm, which implies that the raw material usage is only a tiny fraction of the material input for a silicon cell. Mass production will not be limited by the availability of raw materials.

The energy payback time (EPBT) is obviously an important parameter when considering how far photovoltaics can contribute to the future energy supply. The much lower thermal budget of thin film preparation (lower process temperatures as well as short process times) leads to a significant benefit.

As we will show in this chapter, there is considerable flexibility concerning the choice of components of a chalcopyrite cell or module as well as concerning the preparation methods for these components. It is therefore possible to design products with an optimum efficiency/cost trade-off for various applications, with power demands ranging from mW to MW and with illumination intensity ranging from indoor, low level to high level under concentration. Chalcopyrite cells can be grown on rigid as well as flexible substrates. They perform well in challenging environments because they are mechanically robust, can operate in a wide temperature range, and can tolerate high radiation levels.

The chalcopyrite technology is supported by a networked international research community comprising universities, research institutes, and companies with experience and long term commitment. This ought to guarantee that any problems surfacing in industrial implementation can be attacked with the necessary background knowledge and that new developments are in the pipeline for future products. The large financial risk of implementing mass production facilities is limiting the production volume. However, the growing involvement of companies developing deposition equipment and fabrication infrastructure provides a solid basis for ongoing commercialization.

6.3 TECHNOLOGY FOR THE PREPARATION OF CHALCOPYRITE SOLAR CELLS AND MODULES

The solar cells consist of a number of films which are deposited onto a rigid or flexible substrate (Figure 6.2). The first film, typically molybdenum, serves as a nontransparent back-contact. It is covered by the actual chalcopyrite film. This p-type film absorbs most of the light and generates the photocurrent (absorber). The heterojunction is formed by depositing a very thin n-type buffer layer (typically CdS) and an n-type wide gap transparent front contact (usually heavily doped ZnO).

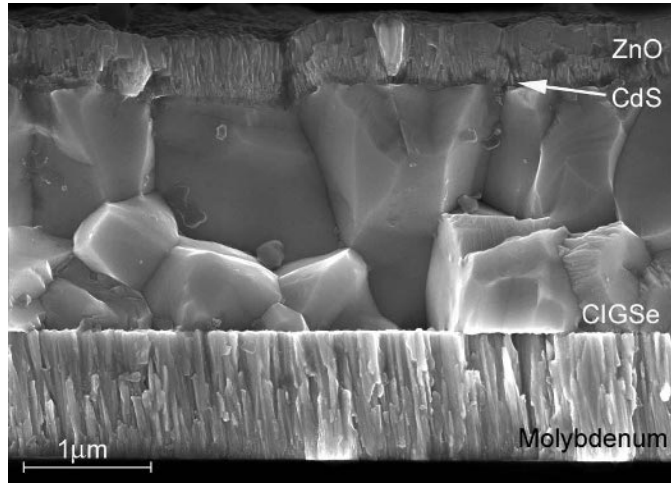

Figure 6.2 Scanning electron micrograph of the cross section of a typical chalcopyrite solar cell with $Cu(In,Ga)Se_2$ (CIGSe) absorber (substrate not shown).

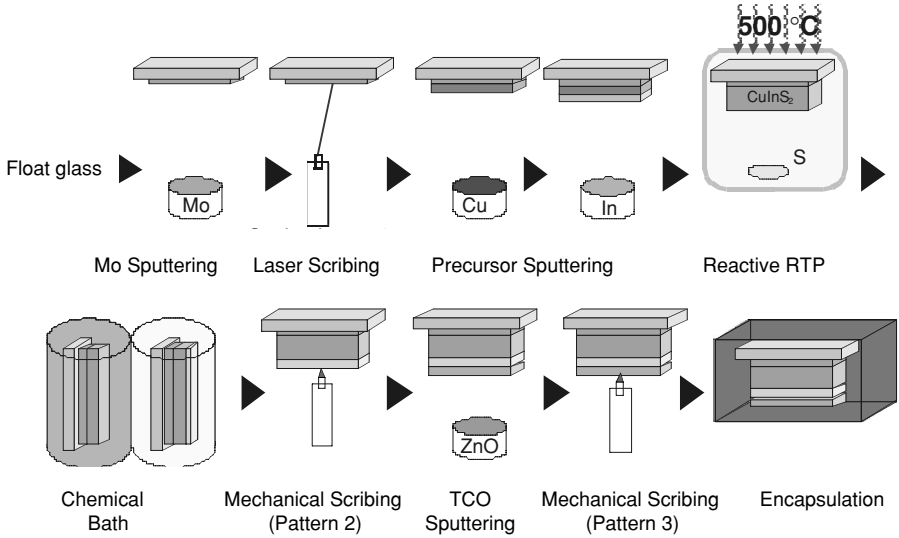

Figure 6.3 Typical sequence of processes to prepare a chalcopyrite photovoltaic module [8]. The sequence shown here is based on the sequential approach (see text) using rapid thermal processing (RTP). Reprinted from Thin Solid Films, 481–482, R. Klenk, J. Klaer, R. Scheer, M. Ch. Lux-Steiner, I. Luck, N. Meyer, U. Rühle, 509, Copyright (2005) with permission from Elsevier.

Thin films with properties suitable for photovoltaic applications can be prepared by a variety of processes. In pilot lines the absorber is grown by multisource evaporation or by a sequential approach (reactive annealing of metal films). To provide just one example, Figure 6.3 shows a sequence of processes necessary to produce a $CuInS_2$ based module using the latter method. In the following paragraphs we will, for each of the films, introduce the most common state-of-the-art methods as they are the basis of today's production lines. Methods still under development and aiming at future significant cost reduction are described in Section 6.6.

6.3.1 Absorber

The most advanced absorber materials are based on $CuInSe_2$ (CISe). Due to its rather low bandgap (1.0 eV) a common practice has evolved where gallium is added to obtain $Cu(In,Ga)Se_2$ with a wider bandgap of approximately 1.15 eV. Due to reasons outlined below, sulfur is incorporated additionally in sequential processes to obtain $Cu(In,Ga)(Se,S)_2$ (CIGSSe). All these absorbers require an optimized sodium concentration for optimum film properties (see Section 6.3.1.3). Another line of development starts from $CuInS_2$ (CIS). In contrast to the other compounds, this base material is grown under copper excess and it also has a higher bandgap ($E_g = 1.5$ eV). Addition of further elements such as sodium or gallium is therefore not strictly necessary. The most commonly used absorber preparation methods are multisource evaporation and sequential processes. Evaporation offers a much more direct control of film formation, including deliberate depth profiles for bandgap engineering as well as making optimum use of the fluxing activity of Cu(S,Se) phases. This is probably the reason

why evaporation still yields the highest cell performance. In particular, unlike evaporation, the sequential processes lead to an aggregation of gallium close to the back contact which causes low gallium content in the active cell region and, consequently, a bandgap below the optimum value. The addition of H_2S to the annealing environment has helped to overcome this problem to a certain degree but it also adds to the overall complexity of the processes and the device. In evaporated films the standard bandgap (in the order of 1.15 eV) can be achieved merely by incorporating sufficient amounts of gallium.

6.3.1.1 Multisource evaporation

Thin films can be grown in a straightforward manner by coevaporating the constituent elements onto a heated substrate. The stoichiometry (concentration of VI element relative to the metals) is handled by a group VI overpressure which has to be maintained in the initial stage of cooling down the substrate. On the other hand, the molecularity (ratio of group I metal versus group III metal concentration) has to be adjusted by tight control of the metal source temperatures. Single crystal substrates with a suitable lattice constant and surface termination can be used and will result in epitaxial growth of the thin film.

The morphology and other properties of the resulting film depend strongly on the molecularity. Copper rich films exhibit larger grains. They are a mixture of chalcopyrite with a close to ideal composition and Cu-VI binary phases, typically found at the surface after cooling down the sample. The chalcopyrite grown under these conditions is characterized by lower defect density and reduced compensational doping in comparison to material grown without Cu excess (Figure 6.4). These observations suggest that the binary phases play an active role in the growth mechanism, also with regard to incorporation of the VI element [9]. Films with an overall molecularity close to unity are often found to be inhomogeneous on a scale of several μm due to localized segregation of Cu-VI binary phases.

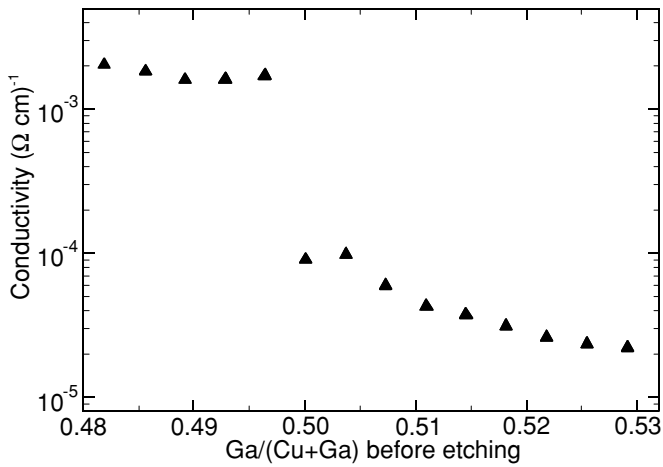

Figure 6.4 Lateral conductivity of $CuGaSe_2$ thin films. Films grown under Cu rich conditions show higher effective doping than those grown under Cu poor conditions. The Cu_xSe segregations were removed by chemical etching prior to the measurement.

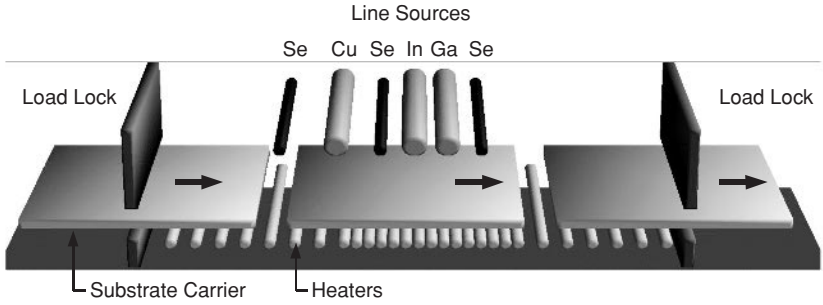

Figure 6.5 Schematic view of an in-line evaporation system. Substrates are supported by a carrier and transferred into the evaporation chamber via a load lock. The substrate temperature is raised by an array of heaters. Before reaching the maximum temperature they pass the copper source and then, after reaching the maximum temperature, the indium and gallium sources. The substrate carriers are gradually cooled down prior to leaving the evaporation chamber via the load lock at the right hand side.

Notwithstanding the small grain size, efficiencies in the order of 14 % are readily achieved with slightly Cu poor Cu(In,Ga)Se_2 films prepared by this simple coevaporation approach. On the other hand, several schemes have been developed to exploit the growth assistance that goes along with excess copper. In the bilayer approach [10], a Cu rich coarse grained seed film is grown first. The Cu rate is then diminished so that the Cu excess present in the seed films is gradually consumed in this second stage, ending up with a slightly Cu deficient film. The idea here is to combine the superior properties of Cu rich films with the absence of second phases in Cu poor films. It is clear, however, that the growth mechanism cannot be sustained once the Cu VI phases have been consumed which may lead to disrupted growth and new nucleation. The advantage of this approach lies in the fact that it can be translated into an industrial inline process where the moving substrate passes first the Cu, then the In and Ga sources (Figure 6.5). Other schemes start from Cu poor films or even films without any copper and add more copper in a second stage (inverted bilayer). If enough copper is delivered in this stage the film becomes Cu rich and recrystallizes. In this case a third stage is needed to again reduce the Cu content and achieve single phase material. This scheme is generally known as the three stage process [11] and has resulted in the highest efficiency of lab scale devices so far (close to 20 %). In principle, there is again the problem of maintaining the growth mechanism after the excess copper has been consumed in the third stage. However, the three stage process enables precise control. The transition points where the film enters and leaves the Cu rich regime are observable through changes in substrate temperature [12] (or power delivered to the heater to maintain a constant temperature) which is often used for *in situ* process control. Monitoring the intensity of light reflected off axis from the substrate is an alternative method for process control (laser light scattering [13]). The three stage process results in a certain depth profile of the Ga/(Ga+In) ratio which is believed to contribute to the excellent performance of cells prepared from these absorbers (bandgap engineering).

6.3.1.2 Sequential processes

Sequential (two step) processes have been developed as an alternative approach to absorber formation [14, 15]. Here, a metallic precursor is typically deposited by sputtering. Sputtering

of pure gallium is problematic due to its low melting point. Copper/gallium alloyed targets are typically used instead. The chalcopyrite is formed in the second step by exposing the precursor to a chalcogen containing atmosphere at elevated temperatures (selenisation/sulfurisation). The method is particularly attractive for production. A process well established in industry is DC sputtering and off-the-shelf equipment is readily available. It is characterized by good reproducibility and large area uniformity of the thicknesses of the individual films. Consequently, the important Cu/III ratio can be tightly controlled in this first step. The high temperature, corrosive environment which is potentially problematic with respect to equipment degradation over time is limited to the second step. Here, it is less critical because this second step mainly affects the chalcogen stoichiometry which is to a great extent self adjusting.

The second step can be carried out in a tube furnace or by rapid thermal processing (RTP). Annealing in a tube furnace (using mixtures of an inert carrier gas and H_2S and/or H_2Se reactive components) is typically a slow batch type process where several substrates are processed simultaneously and where the substrate size is somewhat restricted by the maximum available diameter of the furnace tubes. More recently rapid thermal processing furnaces have been introduced [16, 17]. In one of the processes selenium is evaporated onto the metal precursor (stacked elemental layers) before the high temperature annealing whereas sulfur is still introduced as H_2S during the RTP. Chalcopyrite formation in the two step process depends largely on the thermodynamics and phase formation kinetics of the material system. These fundamental properties have therefore been investigated in detail in order to be able to optimize the processes [18, 19].

In addition to producing low gap $Cu(In,Ga)(S,Se)_2$ absorbers, two step processing has also been found particularly suitable for preparing $CuInS_2$ ($E_g = 1.5\,eV$) [17]. In this case it is possible to simply place pieces or powder of sulfur next to the substrate in the RTP furnace, thereby eliminating the need for chalcogen evaporation in a separate process as well as the use of any toxic gas. Very short annealing periods (a few minutes at top temperature) are achievable due to the growth assistance by Cu_xS using Cu rich (Cu/In = 1.2–1.8) precursors. Films grown under these conditions exhibit high p-type conductivity, therefore the sodium concentration (see Section 6.3.1.3) is not critical [20]. Blocking layers and sodium precursor films are not used. As already mentioned, it is also not necessary to incorporate additional elements for bandgap adjustment.

6.3.1.3 Sodium

Recognizing the important influence of sodium on device performance had been a major breakthrough in the development. Sodium appears to influence the growth mechanism leading to superior morphology as well as higher effective p-type doping. In terms of cell performance the latter seems to be the more important aspect. The observed increase in open circuit voltage is quantitatively consistent with the measured increase in net doping in good cells where recombination in the space charge region is dominant [21]. The fact that an increase in device performance is also achieved by diffusing sodium into an already prepared film is also a strong indication that the electronic effects are more significant than the morphology [22].

Especially in the slower evaporation processes, sodium diffusing from a soda lime glass substrate through the back contact can yield the required sodium concentration in the absorber film. If the substrate does not contain sodium, sodium salts (e.g., NaF) can be coevaporated

or deposited as a precursor film onto the back contact before depositing the absorber. The latter approach, in combination with a diffusion blocking layer underneath the back contact is sometimes also used with soda lime substrates to achieve a more accurate control of sodium concentration, especially in fast sequential processes.

Films prepared with excess copper are characterized by large grains as well as high conductivity and, hence, do not require sodium doping. At the moment, this is technically relevant only for $CuInS_2$ based modules.

6.3.2 Contacts

6.3.2.1 Diffusion barrier and back contact

Sputtered molybdenum is the most frequently used back contact. The inherent stress in the film can be adjusted over a wide range through the pressure of the working gas in the sputter process [23]. Optimized films adhere very well to glass or other substrates and laser or photolithographic patterning is straightforward. A possible alternative to sputtering is e-gun evaporation which so far has been used only in laboratory scale preparation but may also have cost advantages in large scale production.

The actual contact to the chalcopyrite is complex and may involve a Mo–chalcogenide intermediate layer which forms during absorber preparation. At low temperatures the $I(V)$ curve often deviates from that of an ideal diode under forward bias. This bend-over of the curve has been attributed to blocking at the back contact of the cell. However, no voltage drop across the back contact could be found with appropriate test structures [24]. There are other models to explain the $I(V)$ curve bend-over without involvement of a blocking contact [25]. Alternative contact materials for improved optical reflection and novel device configurations are under investigation (Section 6.6).

As already mentioned, diffusion barriers (silicon oxide, silicon nitride) deposited onto the glass substrate before the molybdenum are not strictly necessary but can be used for a more precise control of sodium doping. On the other hand, metal foil substrates often require additional coatings underneath the molybdenum for blocking of impurities as well as substrate planarization and isolation [26].

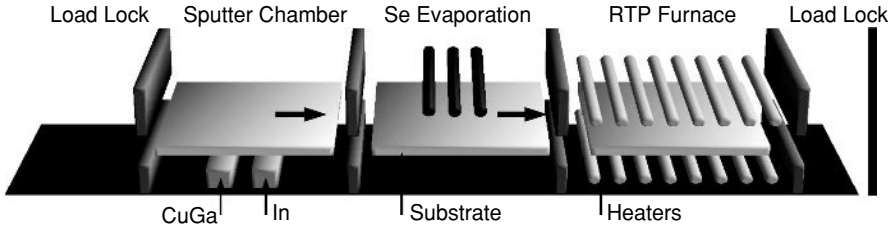

Figure 6.6 Schematic view of an in-line sequential system. Copper and gallium are sputtered from an alloy target. After sputtering indium, the substrate is transferred to an evaporation chamber and coated with selenium. The completed stack is annealed in the rapid thermal processing furnace. No substrate heating is required during metal and selenium deposition.

6.3.2.2 Buffer

The thin (typically 50 nm) buffer layer is grown from a chemical bath [27]. Typical solutions contain a Cd salt, thiourea as a sulfur source and ammonia in an aqueous solution. The substrate is immersed in the cold solution. The solution is then heated to 60–80 °C. The thiourea hydrolyzes and cadmium and sulfur ions recombine to form CdS. The films grow either directly at the substrate or nanoparticles are formed in the solution and deposited onto the substrate. Depending on the deposition conditions, and due to the aqueous environment, the film may contain significant amounts of oxygen and hydrogen. Chemical bath deposition (CBD) of CdS is very reproducible and yields good cell performance on any chalcopyrite absorber.

6.3.2.3 Window

The preferred window or TCO (transparent conductive oxide) film consists of ZnO deposited by sputtering or metal organic chemical vapor deposition (MOCVD). This film needs to have a high lateral conductivity in modules to avoid ohmic losses. It is therefore highly doped with aluminium or gallium (sputtered films) or boron (MOCVD). However, depositing a film with low lateral resistance directly onto the buffer increases the negative influence of local defects (such as pin holes [28]) and local fluctuation of absorber properties (e.g. the bandgap [29]). This can be avoided by first depositing a thin (in the order of 100 nm) ZnO film with lower conductivity, i.e., by sputtering from an undoped target or by adding oxygen to the working gas.

The window layer contributes significantly to the module cost. Low resistivity is therefore desirable to minimize the film thickness. In practice, the resistivity of large area ZnO thin films is in the order of $5 \times 10^{-4}\ \Omega$ cm and cannot be significantly improved because higher doping reduces the electron mobility and causes poor transmission due to free carrier absorption. It has been argued that the film properties are very close to physical limits [30] and that, in the long run, ZnO could be replaced by other materials with higher mobility (lower effective electron mass). Approaches to reduce the cost of ZnO preparation include new methods to fabricate ceramic targets or to use reactive sputtering from metallic targets.

The ZnO film plays an important role for module stability in accelerated lifetime testing under damp heat conditions which forms a part of the EN/IEC 61646 certification. The lateral resistance tends to increase, giving rise to fill factor losses. It is therefore mandatory to optimize ZnO preparation not only with respect to the as-grown properties but also by taking into account the degradation in damp heat.

6.3.2.4 Monolithic integration and encapsulation

Manufacturing of modules adds some process steps to the cell preparation outlined above. The module is divided into cells which are connected in series by monolithic integration. The connection is made from the molybdenum back contact to the TCO during TCO deposition (Figure 6.7). A front metallization has been suggested but is normally not applied. The common scheme requires three patterning steps: an isolation scribe in the molybdenum (P1), scribing the absorber to create a gap which is later filled by TCO (P2), and an isolation scribe of the complete cell structure down to the molybdenum (P3). While the preferred tool for P1 patterning is a

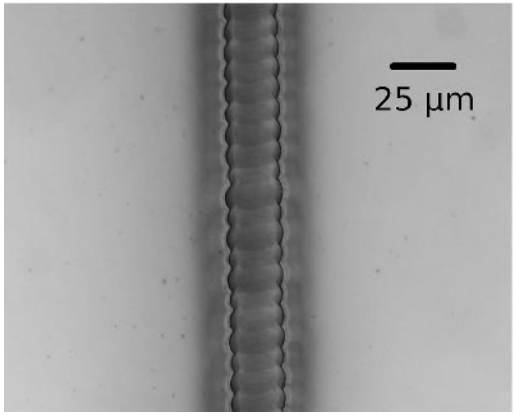

Figure 6.7 Optical microscopy image of a laser scribed line in a molybdenum film on glass. Pulse frequency of the laser and scribing velocity have been adjusted for optimum overlap of pulses.

pulsed Nd-YAG Laser (Figure 6.8), photolithographic patterning is also possible. After laser patterning the substrate is again subject to wet cleaning with rotating brushes to remove loose particles. P2 and P3 patterning are carried out by mechanical scribing. P2 patterning can be carried out before or after deposition of the undoped ZnO layer, the latter method may give a better contact.

The interconnection area constitutes a loss in active area and hence photocurrent. In principle, the scribe lines themselves should be as narrow as possible, the distance between P1, P2 and P3, respectively, should be minimal, whereas the distance between two interconnection areas should be maximal. In practice, a certain width of scribe line has to be maintained for sufficient isolation (P1, P3) and contact resistance (P2). Hence the total width of the interconnection is in the range of 0.5 to 1 mm. In addition, the allowable distance between interconnection areas is limited by the lateral resistance of the ZnO film. The distance can be increased when using a thicker ZnO film. However, a thicker film, apart from being costly, also causes photocurrent losses due do its reduced transparency. Consequently the typical distance is in the range of 5 to 10 mm which results in an area loss due to interconnections of approximately 10 %. Wide gap absorbers offer more flexibility in designing the module due to their reduced current density. Typical photocurrent densities under full illumination are 42 mA/cm^2 at a bandgap of 1 eV

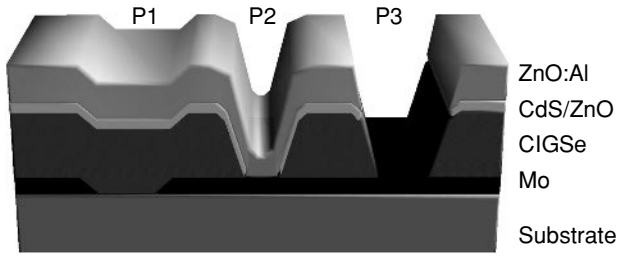

Figure 6.8 Schematic cross section of the cell interconnect in monolithic integration. This figure shows the variant where the P2 scribing is carried out after the deposition of the undoped ZnO.

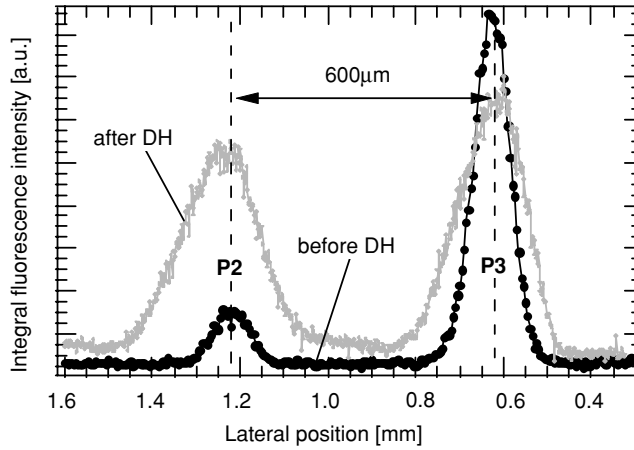

Figure 6.9 Locally resolved sulfur fluorescence (XES) intensity across an interconnect test structure before and after accelerated ageing in damp heat (DH). The position of the scribe lines is indicated (P2, P3) [31].

(CISe) and 22 mA/cm^2 at 1.5 eV (CIS), respectively. A computer simulation has been made available to optimize the module patterning for a given set of film properties [32].

The interconnection appears to play a certain role in module degradation in accelerated aging tests (damp heat). Locally resolved X-ray emission spectroscopy (XES) scans (Figure 6.9) on specially prepared test structures (larger scribe line distance, reduced ZnO thickness) results in a preliminary model of contact degradation. Before damp heat, a large sulfur signal is observed within the P3 scribe line which is due to sulfurisation of the molybdenum surface (which occurs during absorber formation). A smaller signal is observed within the P2 scribe due to the signal being attenuated by the ZnO film. This latter signal increases significantly upon damp heat treatment. The spectra suggest that this is due to the formation of $ZnSO_4$, i.e., damp heat causes a chemical reaction between MoS_2 and ZnO thereby deteriorating the contact in the P2 scribe line.

Concerning the described standard procedures there is still room for improvement because patterning unfortunately interrupts the in-line vacuum processing. Patterning is also critical with respect to the throughput (cycle time).The final glass–glass laminate is produced using EVA foil and standard laminators as in the silicon technology. Encapsulation is critical for passing the accelerated aging tests.

6.4 CHARACTERIZATION AND MODELING

In terms of modeling, the chalcopyrite based solar cell is a quite complex device comprising a number of polycrystalline compound semiconductor films and several heterointerfaces. Nevertheless, tremendous progress has been achieved in measuring, modeling and understanding various aspects of the device. Novel characterization methods specifically adapted to the problems at hand have been developed and introduced. Examples are Kelvin probe force microscopy (KPFM) to measure work functions with submicron lateral resolution (Figure 6.10),

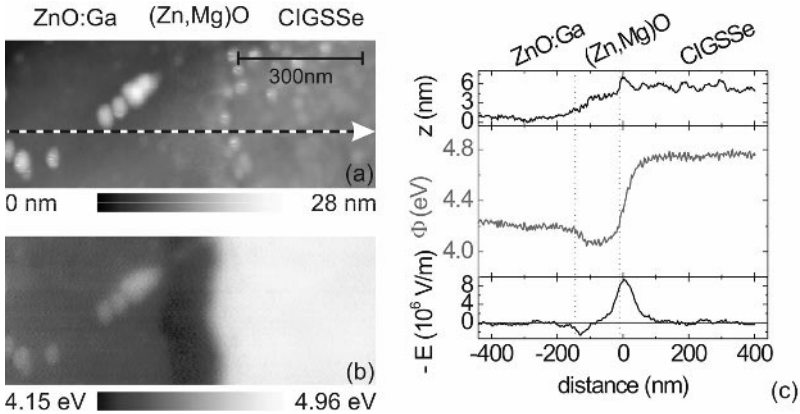

Figure 6.10 KPFM measurement [34] of a mechanically polished cross section of a ZnO:Ga/(Zn,Mg)O/CIGSSe thin-film heterostructure: a) topography, b) work function measured simultaneously with topography. Bright colour corresponds to high work function. c) is a plot of height, work function, and electrical field along the path indicated in a). Reprinted from Thin Solid Films, 481–482, Th. Glatzel, H. Steigert, S. Sadewasser, R. Klenk, M.Ch. Lux-Steiner, 177 , Copyright (2005) with permission from Elsevier.

inverse photoemission spectroscopy (IPES) to directly measure conduction band line ups, and X-ray emission spectroscopy (XES) for the analysis of buried interfaces. In general terms, quantitatively extracting material and device parameters from a measurement result requires a model that describes the correlation between the property assessed by the measurement and the underlying physical parameters. Due to the complexity of compound polycrystalline semiconductor films, the models are often an approximation. The extracted parameters have to be interpreted as *effective* parameters bound to the specific model. They can be useful for comparing different samples quantitatively but can be misleading when used for calculations in a different context. Numerical modeling has emerged as a useful tool for a better understanding of the device. It is important because analytical approximations that can be safely made for other solar cells types are not valid in the chalcopyrite cell. In conclusion, the materials science of chalcopyrites, and solar cells based on them, is a wide field under active development. Here, we have to limit the discussion to a few selected topics and the reader is referred to the literature for more in depth information (the overview given in [33] is a good starting point).

6.4.1 Cell concept

The high optical absorption of the direct semiconductor chalcopyrites makes very thin absorbers feasible. However, it also means that the incident sunlight is absorbed close to the surface. Assuming it would be possible to dope chalcopyrites in a well controlled manner it would still be challenging to reach high efficiency with a homojunction solar cell. Depending on surface passivation, the major part of carriers generated between the surface and the pn junction would be lost due to surface recombination. This problem is avoided by introducing the window/absorber heterojunction concept. Due to the wide bandgap of the window, the absorption is shifted away from the surface to the internal interface. Even assuming no surface

passivation and a very high surface recombination velocity, the losses are nevertheless small because only an insignificant part of the light is absorbed in the window.

On the other hand, the internal heterointerface might itself cause recombination, leading not only to photocurrent loss but also to high bucking currents and consequently low open circuit voltage. But calculations show that interface recombination does not necessarily have a significant impact on cell performance [35]. The severity of interface recombination depends on:

- The density of recombination centers at the interface.
- The doping of absorber and window.
- The type and density of charged interface states.
- The conduction band line-up.

A low density of interface states is always advantageous but may in practice be difficult to achieve because the large area technology cannot be compared to the ultra clean environment required for defect free epitaxial growth. The other, more feasible approach to lowering recombination lies in minimizing the density of either electrons or holes at the interface, which requires appropriate doping, band line-up and interface charge. In terms of bucking current (open circuit voltage) minimizing the density of either type of carrier yields comparable results. Considering the photogenerated carriers it is, however, mandatory that the electrons collected from the absorber are majority carriers at the interface (inverted interface). In conclusion, the structure should be an n^+ window/p absorber heterojunction where the Fermi level (E_F) at the interface is close to the conduction band and where the Fermi level intersects midgap energy at a small distance from the interface in the absorber. The interface charge should be positive (donor like defects) to assist in establishing this structure. Likewise, the energetic position of the absorber conduction band edge (E_C) should be slightly lower than that of the window (spike) because the opposite situation (cliff) tends to push the absorber conduction band away from the Fermi level. Furthermore, in the cliff type band line-up electrons from the window side of the interface could recombine with holes from the absorber side which leads to a reduced barrier.

In the actual chalcopyrite cell these design considerations must be implemented by the buffer layer and its preparation technique. Measurements of the band line-up and Fermi level position at the interface (see [37] for a review of chalcopyrite surface and interface properties) are not straightforward and the results show significant variations [38–41]. The band diagram shown in Figure 6.11 is believed to be a reasonable approximation and shows the type inversion of the interface as required according to the above considerations. There are theories and supporting measurements that indicate an inherent widening of the absorber bandgap towards the surface [39, 42, 43]. It has been speculated that this effect is due to the segregation of distinct Cu poor ordered vacancy compound (OVC) but there is no conclusive evidence concerning the actual structure. If this widening is mainly due to a shift of the valence band edge (as shown in Figure 6.11) this also decreases the hole density at the interface and lowers the interface recombination even further. Obviously, this is only helpful for device performance when the transition from bulk chalcopyrite to surface bandgap widening occurs without introducing a high defect density. However, lattice matching between the bulk and surface phases may be absent in wide gap chalcopyrites [44].

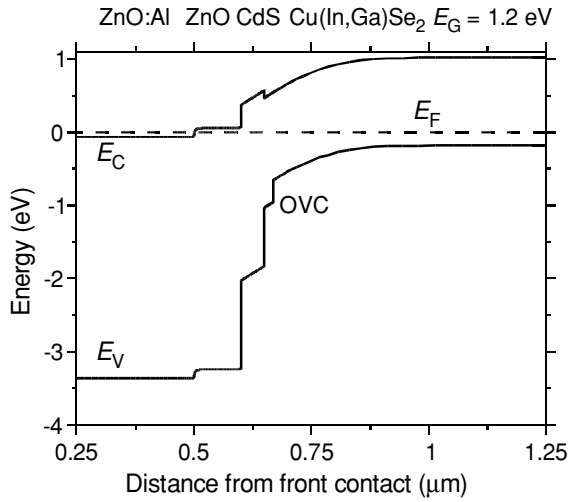

Figure 6.11 Tentative calculated [36] band diagram of a ZnO/CdS/Cu(In,Ga)Se_2 heterojunction assuming a widening of the bandgap at the absorber surface due to an ordered vacancy compound (OVC).

6.4.2 Carrier density and transport

Without deliberate doping, the majority carrier (hole) density in chalcopyrite thin films is usually in the range of 10^{14} –10^{17} cm^{-3} and well suited for the application. Oxygen and sodium are the most common impurities known to influence the carrier density. The density of donors is found to be almost comparable to the acceptor density (compensation, self-compensation [45]). The effective mobility in polycrystalline films at room temperature is in the range 1–100 cm^2/Vs. A complete set of temperature dependent conductivity and Hall effect data including polycrystalline as well as single crystal samples is only available for a certain (prepared with Cu excess) type of $CuGaSe_2$. They are summarized and discussed in [46].

Charge trapped at grain boundaries gives rise to space charge regions extending into the grains. The resulting band bending leads to potential barriers. Hall effect measurements suggest barriers in the order of 50 to 150 meV which can be explained by a charge density in the order of 10^{12} cm^{-2} at the CGSe grain boundary [47]. Kelvin probe force microscopy in ultra high vacuum is a relatively new characterization tool well suited to further clarify the grain boundary models. The high lateral resolution of the microscope allows work function measurements across individual grain boundaries. An average drop in the work function of 110 meV across grain boundaries has been measured in good agreement with the Hall data [48]. The electrical fields in the vicinity of grain boundaries would sweep minority carriers into the grain boundary. However, excessive grain boundary recombination is in contradiction to the high photocurrents which are observed even in fine grained films. Alternative models of the grain boundary have been proposed, based on band structure calculations [49]. A comparison of the impact of either type of grain boundary upon device performance has been performed by two-dimensional numerical calculations [50]. Kelvin probe force microscopy results on the differences in the local variation of the work function with illumination (surface photovoltage) suggest that both aspects, i.e., trapped charge as well as the band structure, play a role in defining the grain boundary properties [51].

There are a number of studies concerning time constants and pathways for radiative recombination as deduced from steady state photoluminescence and photoluminescence decay. Radiative recombination appears to be dominant in good quality polycrystalline films at low (8.5 K) temperature [52]. Free carrier lifetimes in the order of some nanoseconds have been measured. Defect related lifetimes were significantly higher, presumably due to trapping of carriers. Recent photoluminescence investigations [53] reveal a shallow donor (D) and two shallow acceptor levels (A1, A2) which are present throughout the Cu(In, Ga)Se_2 compounds. The levels are found at slightly increasing depth when going from $CuInSe_2$ (D = 10 meV, A1 = 40 meV, A2 = 60 meV) to $CuGaSe_2$. (D = 13 meV, A1 = 60 meV, A2 = 100 meV). The relative concentration of the acceptor level is correlated with Cu/(In+Ga) ratio used during preparation of the film. For $CuGaSe_2$, the same set of shallow defects can explain the photoluminescence as well as the Hall measurement data [54]. It may be tempting to assign these levels to the point defects of a ternary system whose formation energies and depth has been theoretically calculated [55] , but the assignment remains uncertain in view of more complex defects and impurities which might also play a dominant role.

At room temperature the photoluminescence decays with a time constant of several tens of nanoseconds due to nonradiative recombination. The majority of measurements described in the literature and concerning minority carrier transport is assessing the minority carrier diffusion length. The latter can be extracted from electron beam induced current (EBIC) [56] and quantum efficiency measurements [57]. Typical values are in the range of 1–2 μm for good quality films. This implies that the diffusion length and the extension of the space charge region are comparable, which can cause problems in extracting both parameters from a single measurement. The ambiguity can sometimes be resolved by measuring at varied applied bias voltages and using an analytical approximation to calculate the field zone as a function of bias [58].

6.4.3 Loss mechanisms

Depending on absorber material and bandgap, record efficiencies for chalcopyrite based solar cells are in the range of 10 to almost 20 %. Optical [59] and contact related losses are small, at least in small area cells with front contact grids. They need to be considered for modules (without grids [4, 60]) and thin absorbers [57]. In general, close to ideal photocurrent collection is achievable whereas open circuit voltage and fill factor offer room for future improvement. Figure 6.12 shows the external quantum efficiency of a Cu(In,Ga)S_2 ($E_g \approx$ 1.53 eV) solar cell [61] which is close to unity at the maximum with a single layer antireflective coating. The curve is limited by the ZnO and absorber bandgaps at low and high wavelengths, respectively. Holes generated in the CdS buffer layer are not collected which leads to a drop in quantum efficiency for photon energies higher than the bandgap of CdS (the interfaces on both sides are not inverted with respect to the n type CdS which leads to a high recombination probability for holes, nevertheless, partial collection has been reported [62]).

The bucking current is responsible for losses in open circuit voltage. It also leads to losses in fill factor because the diode ideality factor A is higher than unity. In high efficiency CIGSe cells the bucking current is due to bulk recombination in the space charge region of the absorber. The diode ideality factor (between one and two) and its temperature dependence are in agreement with analytical models describing recombination over an exponentially decaying density of

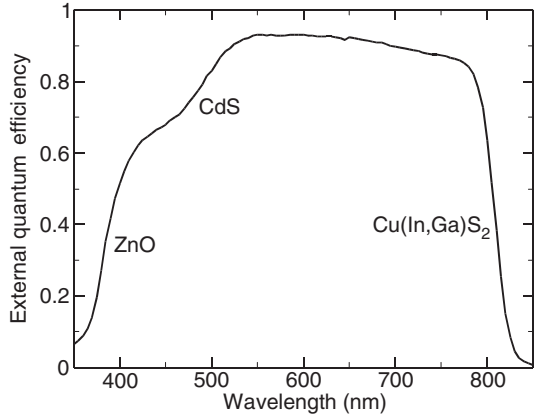

Figure 6.12 External quantum efficiency of a MgF_2/ZnO/CdS/Cu(In,Ga)S_2 solar cell. The blue response is limited by the bandgaps of ZnO and CdS, respectively. The red response is limited by the bandgap of the absorber.

states [63, 64]. Such a defect distribution could be due to band tails and is also observed in optical and admittance spectroscopy [65, 66]. Typical Urbach energies are in the range of 50 to 100 meV.

In addition to the broad defect distribution there also seems to be a narrow defect distribution at 250–300 meV above the valence band [67]. It has been found by several methods and in samples prepared by various methods, including single crystals [25]. This defect maintains its energetic position relative to the valence band within the whole CIGSe system (for varied Ga/(Ga+In) ratios). However, its concentration seems to correlate with the gallium content, with a minimum concentration found at Ga/(Ga+In) ≈ 0.3. Losses in open circuit voltage were found to correlate with the concentration of this defect which suggests its significance as a recombination path [68]. Its concentration is found to increase upon radiation with energetic particles and to decrease with subsequent annealing at moderate temperatures [69]. Other authors have identified a deeper defect at 0.8 eV above the valence band edge [70]. This defect is approaching mid-gap position at high gallium contents and can thus be expected to be an effective recombination center in wide gap CIGSe absorbers.

The saturation current in state-of-the-art low gap cells is mostly thermally activated and the activation energy corresponds to the bandgap of the absorber. The diode ideality factor is only mildly temperature dependent. Measurement of the open circuit voltage is as a function of temperature and extrapolation yield: $V_{oc}(T = 0\ \mathrm{K}) = E_g/q$. Cells with inferior efficiency show a stronger influence of tunneling. Depending on sample and temperature, higher and more temperature dependent diode ideality factors are observed. If the tunneling influence is not too severe, the bucking current mechanism can be described by tunneling assisted recombination via trap states in the space charge region of the absorber [71]. In this case, the activation energy of the saturation current still corresponds to the bandgap after taking into account the temperature dependent diode ideality. Due to a common mistake in the evaluation of measurement results [72] this model may have also been applied to devices where the influence of tunneling is in fact much stronger.

Cells based on wide gap $Cu(In,Ga)S_2$ absorbers exhibit open circuit voltages which are lower than expected, considering the bandgap and the good bulk properties deduced from photocurrent collection. Transport analysis [73] reveals that the dominant bucking current mechanism changes with illumination. The ideal border cases are recombination over a reduced barrier at the interface without major assistance by tunneling (under illumination) and recombination in the space charge region with significant tunnelling assistance (dark). While this change of recombination mechanism with illumination is a unique feature of $Cu(Ga,In)S_2$ based cells [74], reduced thermal barrier and tunneling currents appear to be more general problems and are also observed in wide gap C(I)GSe based solar cells [75, 76]. The achieved development status is illustrated by the exemplary efficiencies listed in Table 6.1.

The findings for the high efficiency cells described so far indicate that a further improvement of efficiency beyond 20 % ought to be feasible by minimizing the bulk defect density. However, it has also been argued that empirical device optimization has already led to an optimum with respect to band edge fluctuations [77, 78]. Such fluctuations (which are also observed in photoluminescence) may assist in charge separation, i.e. photocurrent collection, but are detrimental in terms of bucking current. On the other hand, even if the efficiency of low gap single junction cells is approaching practical limits, wide gap and tandem cells offer a large potential for ultra high efficiency (Section 6.6.7).

Table 6.1 Efficiency of selected small area, laboratory style chalcopyrite based solar cells (partly with antireflective coating)

Lab [Ref]	Substrate	Absorber	Buffer	Efficiency	Remarks
NREL [79]		CISe		15 %	$E_g = 1.04$ eV
NREL [80]		CIGSe		19.5 %	$E_g = 1.15$ eV
NREL [79]		CIGSe		10.2 %	$E_g = 1.64$ eV
NREL [79]	glass	CGSe	CdS	9.5 %	$E_g = 1.68$ eV
HMI [17]		CIS		11.4 %	$E_g = 1.5$ eV
HMI [61]		CIGS		12.3 %	$E_g = 1.53$ eV
HMI [61]		CIGS		10.1 %	$E_g = 1.65$ eV
NREL [81]	steel			17.5 %	flexible
HMI [82]	titanium	CIGSe	CdS	16.2 %	flexible
ETHZ [83]	polyimide			14.1 %	flexible
NREL/Aoyama Gakuin Univ. [84]	glass	CIGSe	Zn(S,O,OH)	18.6 %	Cd free[a] buffer by CBD
Shell Solar/HMI [85]		CIGSSe	In_2S_3	14.7 %	Cd free buffer by ILGAR
Shell Solar/HMI [86]		CIGSSe	(Zn,Mg)O	12.5 %	Cd free buffer by sputtering (dry process)
ZSW/CNRS [87]		CIGSe	In_2S_3	16.4 %	Cd-free buffer by ALCVD (dry process)
Stuttgart Univ. [88]		CIGSe	In_xS	14.8 %	Cd-free buffer by evaporation (dry process)

[a] see [89] for a more complete list of Cd free devices.

Figure 6.13 Partial view of the pilot production line for CIS modules (substrate size 120 × 60 cm^2) at Sulfurcell in Berlin, Germany. Sulfurcell uses the process sequence shown in Figure 6.3. Reproduced with the permission of Dr. Nikolaus Meyer, Hahn-Meitner-Institut Berlin GmbH.

6.5 SCALING UP AND PRODUCTION

Efficient chalcopyrite based photovoltaic modules were demonstrated years ago [90]. Despite this early proof-of-concept, the status has been limited to pilot lines (Figures 6.13 and 6.14), or announcements of such, for a long time. Consequently, chalcopyrites do still not play a significant role in the marketplace. Nevertheless, industrial laboratories have always had a major impact on development and an increasing number of companies world wide is involved in the development of commercial products for the power market as well as niche applications. The first commercial products, announced by Siemens Solar Industries in 1998, were small

Figure 6.14 Large area in-line sputter coater (Von Ardenne Anlagentechnik, Dresden, Germany) for the deposition of molybdenum and zinc oxide at the Wuerth Solar pilot line in Marbach, Germany. Reproduced with the permission of Von Ardenne Anlagebtechnick GmbH.

modules with 5 and 10 W rated output power manufactured on a pilot line in Camarillo, CA. The biggest producers today are Shell Solar and Wuerth Solar. Shell Solar is now operating the production line in Camarillo which has been upgraded with respect to production capacity and product size. The largest Shell Solar modules are rated at 40 W, the Wuerth Solar modules go up to 80 W due to their larger panel size ($60 \times 120\,cm^2$). Both, Shell Solar and Wuerth Solar have also published yield data and efficiency distribution of their (pilot) production which clearly demonstrate the feasibility of mass production of chalcopyrite based modules. Wuerth Solar has announced a new factory with a rated production volume of 15 MWp/a from 2007 onwards [91].

Nevertheless, the transition from laboratory to large scale manufacturing has, in general, been more difficult than expected. According to [92] the main obstacles have been:

- Commercial scale equipment.
- Quality control and *in situ* monitoring.
- Uniformity.
- Low open circuit voltage.
- Throughput.
- Stability.

For some process steps the machines for large area deposition had to be custom designed based on experience with lab scale equipment which is an expensive and error prone process. With the increasing number of installations the equipment manufacturers are gaining experience in manufacturing these systems. The rapid commercialization of other thin film technologies provides synergy effects. Glass companies experienced in very large area thin film coating of glass (low emission coating) are using this experience to offer glass substrates already coated with diffusion blocker and molybdenum. Transparent conductive oxide sputtering machines (Figure 6.14) can be derived from those sold for preparation of TCO coatings for flat panel liquid crystal and organic displays. Equipment manufacturers are now actively participating in the establishment of pilot production lines and it is to be expected that turn-key production facilities with process and product specification will be available in the not too distant future.

Criteria for go/no go classification after each individual process step and methods for quality control by *in situ* monitoring had been neglected for a long time in basic research. However, significant progress has been made in recent years as more research laboratories have also become involved in scaling up activities. Examples include Raman spectroscopy [93] and photoluminescence decay [94] to assess the absorber quality, and X-ray fluorescence [95] for in system stoichiometry measurements. Laser light scattering and substrate temperature monitoring have already been described in Section 6.3.1.

Uniformity or low open circuit voltage appear to be no longer a general problem as indicated by the module efficiencies that have been achieved in practice (Table 6.2).

Throughput in sequential processes has been improved by the development of the rapid thermal annealing processes. For evaporation technology a feasible approach appears to be to scale up the sources for increased width of deposition. Further throughput improvements are desirable for large scale production. Minimizing the required thickness of individual layers

Table 6.2 Efficiency of selected minimodules and full size modules

Company or Institute	Size	Efficiency	Remarks
Hahn-Meitner-Institut [17]	5×5 cm^2	9.7 %	Se free CIS
Uppsala University [4]	5×5 cm^2	16.6 %	With grid
Showa Shell [5]	30×30 cm^2	14.2 %	Cd free
Shell Solar [6]	60×90 cm^2	13.1 %	
Global Solar Energy [108]	7085 cm^2	10.1 %	Not monolithically interconnected, cells on metal foil
Wuerth Solar [7]	60×120 cm^2	12.2 %	

[96], alternative methods for patterning, eliminating the buffer layer from the module structure [86], and high rate reactive TCO sputtering carry potential for such improvement.

Outdoor testing of modules has generally demonstrated excellent stability [98, 99]. Owing to the increasing production volume there is a growing number of installations (Figure 6.15) where the actual performance [100] and long term stability can be assessed (Figure 6.16:). Accelerated lifetime testing, especially the damp heat testing procedure which forms a part of the EN/IEC 61646 certification, has, however, been cumbersome [101, 102]. Partly, this is due to transient effects which occur during stress tests. These can lead to an apparent degradation, however, the efficiency recovers after several days of light soaking. The exact

Figure 6.15 Solar Tower, Training and Technology Center Handwerkskammer Heilbronn, Germany. Wuerth Solar frameless CIS Façade modules with a total nominal power of 8 kWp (STC) were installed in April 2001. The installation comprises 120 modules with the dimensions 60 cm by 120 cm and 40 modules with the dimensions 40 cm by 60 cm. Reproduced with permission of Wurth Solar GmbH & Co.KG.

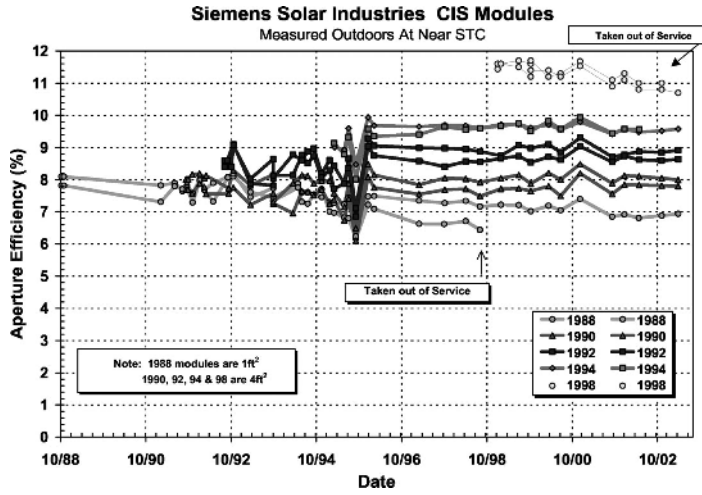

Figure 6.16 Results of long term outdoors measurements of CIGSSe based module prototypes. Modules installed at the National Renewable Energy Lab (NREL) outdoor test facility (OTF) in Golden, Colorado [97]. Reproduced with permission of Shell Solar Industries.

causes for degradation are still under investigation but empirical optimization has already achieved modules which have been independently certified [6, 99].

In conclusion, technical problems have been overcome to a large extent. On the other hand, they still contribute to the financial risk. As long as specialized deposition equipment is produced only in small numbers and turn-key facilities are not available, the technology development has to be taken step by step. This implies a considerable lead time before the production volumes are high enough to achieve competitive production costs in relation to the conventional silicon modules produced in large scale facilities. Innovative niche market products which exploit inherent features of chalcopyrite thin film devices not readily available with silicon can be sold at higher prices. While they can offer a faster return on investment for smaller (start up) companies, the true medium and long term benefit, as acknowledged by independent studies, lies in the cost reduction potential exploitable only through mass production for the power market.

6.5.1 Cost estimations

An early cost study [103] predicted that chalcoypyrite based modules could be manufactured at 0.6 €/Wp in a plant with 60 MWp annual capacity whereas even the most cost effective multicrystalline silicon based technology would require a 500 MWp/a factory to achieve similar costs [104, 105]. Another study [106] comparing the direct module manufacturing costs of single and multicrystalline silicon as well as amorphous silicon, CdTe, and chalcopyrites estimated the cost to be 2.25 $/Wp for a 10 MWp/a chalcopyrite production line. This was lower than the cost for all other technologies, except for multicrystalline silicon estimated at 2.10 $/Wp. The estimation was based on the assumption of 9 % average module efficiency and 65 % production yield for the chalcopyrite modules, numbers that are clearly more favourable in

today's pilot production. It was estimated that a 100 MWp/a production capacity at improved average efficiency and yield could result in costs of 1 \$/Wp, 15 % lower than that of multicrystalline silicon. In general, the study was based on a first generation baseline process and additional cost benefits are expected from current technology updates. A more recent estimation for $CuInS_2$ modules [107] already claims manufacturing costs of 1.5 €/Wp for a small production line (5 MWp/a).

6.5.2 Module performance

It has been pointed out already that chalcopyrite cells offer a very high efficiency potential. Monolithic integration and large area nonuniformity cause only small losses, therefore high efficiencies could also be demonstrated for test structures (minimodules) and even full size modules (Table 6.2).

Considering mass production, the distribution of efficiencies (or power output for a given module size) is much more relevant than the record efficiency of a single module. Wuerth Solar reports [99] an output of 79.9 ± 2.2 Wp for a batch of 306 modules ($60 \times 120\,cm^2$) indicating that a very narrow distribution curve is feasible. In 2004 their production yield was more than 80 % with an average module efficiency slightly higher than 11 % [109]. In 2002 Shell Solar reported [110] an average efficiency of 10.9 % for nearly 16 000 laminates produced in Camarillo (Figure 6.17).

Considering the application the rated power output is an important point. However, the module has to perform well not only at the standard testing conditions applied for measuring the rated power but also at conditions typically encountered in operation, such as lower illumination intensity, varying spectral distribution, partial shading and elevated temperatures (performance ratio). Chalcopyrite modules have shown high power output under these conditions. The typical interconnection scheme with a large number of narrow cells reduces the

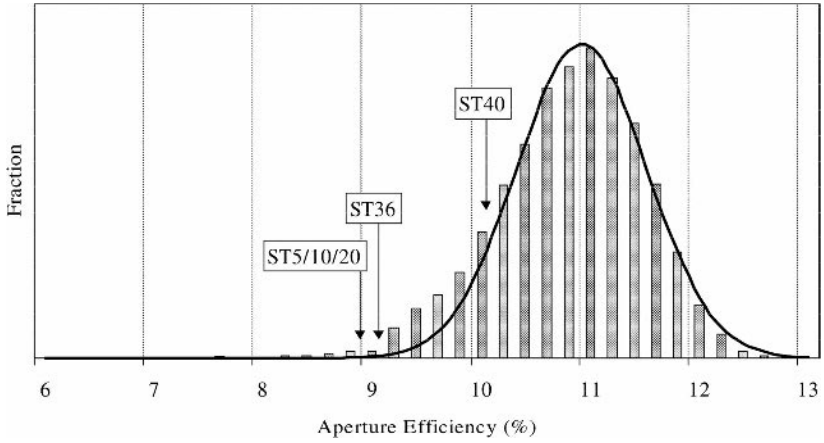

Figure 6.17 Distribution of 1×4 laminates produced in by Shell Solar in 2002. Data includes some 15 785 laminates. Gaussian fit has an average of 10.9 ± 0.6 %. Shown for comparison are the lower specification limits for the product family [110]. Reproduced with permission of Shell Solar Industries.

impact of partial shading. Shunts have been reduced resulting in better performance at low illumination intensity. Higher absorber bandgaps limit the losses with increasing module temperature [100]. Consequently, it has been observed that chalcopyrite modules can outperform silicon modules in terms of the annual energy output on a kWh/kWp basis [99, 109, 111].

6.5.3 Sustainability

Sustainability has many aspects and while not all relevant issues are completely clarified at this point the available data are quite promising (see below). Due to the high efficiency and performance ratio, the long lifetime, the low material consumption, and low thermal budget a chalcopyrite module will have a favourable energy balance. There are a number of research efforts [112] addressing specifically the sustainability of mass production. Like any large scale deployment, mass production of chalcopyrite PV modules will result in production related waste materials, energy consumption, and raw material depletion. Recycling of waste and modules at the end of their lifetime is mandatory for a sustainable technology. In addition, the producer may at some time be legally required to take back modules as is the case already for electronic products in Europe [113].

6.5.3.1 Availability of raw materials and recycling

Thin film technologies make very efficient use of raw materials. While 0.5–1 kg/m^2 of semiconductor grade silicon are required for a conventional module, the material consumption per square meter for the active films of a CISe module is given as: 7–20 g molybdenum, 1.5–4 g copper, 3–9 g indium, 7–20 g selenium, and 1–3 g zinc (depending on the exact module structure and yield [114]). This implies that the total material input is comparable to the material used for just the grid metallization of silicon modules.

Nevertheless, it has been argued that indium is a bottleneck concerning the abundance of raw materials. In 2003 it was used mainly for coatings (65 %), solders and alloys (15 %), and electrical components (10 %) [115]. Indium based coatings are used in the production of flat panel displays where indium tin oxide (ITO) is used as a transparent contact. The annual world production of indium, mainly from zinc ores, is in the order of 300 tons, which translates into chalcopyrite modules with approximately 15 GWp/a in total. On the other hand, indium is about three times more abundant in the Earth's crust than silver, the latter having an annual production of 20 000 tons and a reserve base of 570 000 tons [115]. These numbers imply that the availability of indium is not likely to be an ultimate limiting factor. Moreover, it has already been shown that even thinner active films in a chalcopyrite module are feasible [116]. The flat panel industry may replace ITO by the cheaper ZnO in future and indium recycling will, in addition, contribute to higher availability and lower market prices. Indium free absorbers are under development (see Section 6.6.3). Within the last three decades the prices for indium have been varying over a wide range from below 100 $/Kg to more than 500 $/Kg. However, even the latter price would imply that indium is responsible for only approximately 2 % of the module manufacturing costs.

Waste from the dry processes consists of material that is deposited onto chamber walls, shutters, substrate carriers etc. Recycling should be possible, but the amounts are probably too low to make it attractive unless mass production has started. Sputter targets would presumably

be returned to the manufacturer to reclaim the remaining raw materials. Research has put more emphasis on recycling the waste generated by wet chemical buffer layer deposition [117, 118]. This could be partly done directly at the production site by removing reaction products from the solution then readjusting the concentrations and feeding the solution back to the process.

A complete process sequence for disassembling and recycling of off spec modules and semiproducts has been tested successfully and could also be used for end-of-life modules [119]. The module is heated to 250 °C which softens the EVA encapsulation and allows a mechanical removal of the cover glass. Window and buffer layers are etched away by a mild acidic solution. The chalcopyrite film is scraped from the back contact and finally the latter is dissolved in nitric acid. The test confirms the feasibility of disassembling the module layer by layer which results in low cross contamination. It has been suggested that these relatively clean materials, such as the chalcopyrite powder, could be used directly in adapted preparation processes. It has already been shown that the substrate glass can simply be reused for new modules.

6.5.3.2 Energy payback time

A comparative study on energy payback times has been assisted by the only company that produces silicon as well as chalcopyrite modules [120]. It was concluded that the EPBT for the chalcopyrite module is 1.8 years as compared to 3.3 years for the silicon module. It should be noted that the aluminium frame is responsible for a large fraction of the materials energy content of the chalcopyrite module. The study was also based on first generation chalcopyrite technology and significantly lower EPBT should be feasible.

6.6 DEVELOPING FUTURE CHALCOPYRITE TECHNOLOGY

The chalcopyrite module is still under active international development. Progress in fundamental understanding and preparation technology will result in significant improvements in market potential, module performance, sustainability, and minimized ecological impact of large scale production of next generation modules. We will highlight areas of ongoing development in the following paragraphs.

6.6.1 Lightweight and flexible substrates

Transferring the technology of chalcopyrite based solar cells from rigid glass substrates to flexible, low-mass substrates [26] opens new market segments. Furthermore, flexible substrates are a requirement for roll-to-roll processing which could lower production costs [108]. Such substrates can be plastic or metal foils (Figure 6.18). When combined with foil substrates, the low mass, excellent radiation hardness, and relatively high (compared to other thin film technologies) efficiency make chalcopyrite based technology the leading candidate for thin film cells for space applications [121].

Available plastic foils do not tolerate the high substrate temperatures ordinarily used for chalcopyrite preparation. Common problems at high temperatures are shrinkage, warping, outgassing, and loss of flexibility. Lowering the substrate temperature is possible, but the

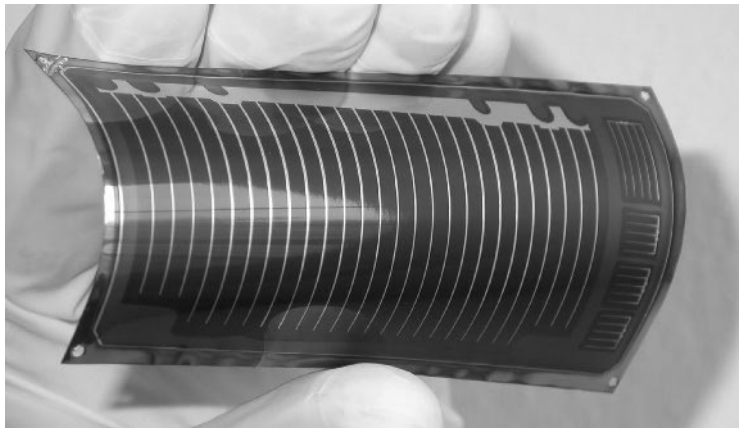

Figure 6.18 Prototype of a flexible CIGSe solar cell for space applications on a thin titanium substrate [121].

efficiencies that can be achieved are, in consequence, somewhat lower. The best results, still below 15 % efficiency, are achieved on polyimide foils [83]. On the other hand, the conductivity of metal foils raises new challenges with respect to pin hole free processing and monolithic integration. Some metals also tend to diffuse into the absorber and cause deterioration of its properties. Isolating and/or diffusion blocking layers are under development to circumvent these problems. In another approach monolithic integration is abandoned altogether. Individual medium sized cells are fabricated and interconnected using a shingling scheme.

Sodium doping is mandatory with any foil substrate and can be carried our through a precursor film, coevaporation or even diffusion after film preparation.

6.6.2 Cadmium free cells

The CdS buffer layer is very thin and contamination of the environment from modules is very unlikely even in extreme conditions. Nevertheless, cadmium is a hazardous material and its elimination from the module may increase the general acceptance of the product and reduce production costs (by avoiding costly safety measures). According to European Union directives [122] several heavy metals (including cadmium) must be not be contained in new electrical and electronic equipment after July 2006. While photovoltaic modules do not currently fall under these regulations [113] they illustrate the general effort to reduce the amount of cadmium in circulation. Owing to the intensive work on cadmium free buffer layers there is a variety of possible alternatives. We will introduce a small selection in this chapter. More information can be found in a recent review article [89].

6.6.2.1 Wet chemical processes

Chemical bath deposition is not restricted to the deposition of CdS. The most common replacements are indium or zinc based sulfides, oxides, hydroxides, or mixtures thereof. The

achievable efficiency is very close to that of the standard device [84]. However, the deposition parameters appear to be more critical and need to be adapted to the specific absorber. Accordingly, it can be challenging to achieve a high reproducibility of cell performance. Cadmium free cells are often found to exhibit metastability effects, e.g., significant improvement with light soaking [123]. It is not yet fully clear how far the long term stability of the cell is also affected by the modified buffer layer. Only one of the current pilot production efforts is known to use a zinc based buffer layer (Table 6.2).

Novel chemical deposition methods such as ILGAR (ion layer gas reaction) have been developed and have been applied successfully mostly to those Cd free alternative buffer layers [124]. There are indications that ZnO deposited by ILGAR can combine the functions of the buffer and the (normally sputtered) undoped part of the window layer [125].

6.6.2.2 Dry processes

Wet chemical deposition is often believed to be significantly cheaper than other deposition methods. However, in a typical processing sequence, buffer layer deposition is the only wet chemical process, which implies that the whole infrastructure has to be implemented for just this single process step. In addition, it prevents true in-line processing. While this is currently not a big issue because the deposition systems are typically not connected and scribing is also carried out in atmosphere, it may be a drawback in view of future large volume production. Dry processes are therefore under investigation. The most successful approaches have been MOCVD [126] and ALCVD (atomic layer chemical vapor deposition [127]). The former has so far produced only small samples, albeit with good efficiency, whereas the latter has been shown to work at least on medium sized substrates ($30 \times 30\,\mathrm{cm}^2$). Atomic layer chemical vapor deposition is, however, an inherently slow process and therefore only cost-effective if carried out in systems that can accommodate a large number of substrates simultaneously, in contradiction to the requirements for an in-line capable process.

Buffer layers can also be evaporated which appears particularly attractive if the absorber is also prepared by evaporation [128]. Efficiencies of almost 15 % can be achieved provided the buffer layer is evaporated *insitu*, i.e., without breaking vacuum after the absorber deposition [88].

Evaporation, MOCVD, and ALCVD, in analogy to CBD, are 'soft' deposition methods and there have been assumptions that this is a major advantage. On the other hand, sputtering of a Cd free buffer layer, if feasible, is clearly a technically very attractive solution. Sputtering is, however, not a soft method and it has been speculated that one of the main functions of the buffer layer consists of protecting the absorber surface from sputter damage during window layer deposition. This assumption is supported by the typically poor device performance observed when simply omitting the buffer layer and sputtering the TCO directly onto the absorber. It was shown, however, that a chemical treatment (partial electrolyte) is, in principle, sufficient to stabilize the absorber surface for window layer sputtering [129]. Only a very thin film is deposited under the conditions of this chemical treatment, which would not be sufficient to prevent sputter damage. More recently it has been shown that an efficiency of more than 12 % can be achieved by a sputtered In_xS buffer layer without chemical treatment [130].

A different novel approach to heterojunction formation originates from the question whether the window layer can be modified in such a way that a buffer layer is no longer necessary. Based on the assumption that the band line up at the chalcopyrite/TCO direct junction is causing the

poor performance, experiments have been carried out using (Zn,Mg)O rather than pure ZnO in the first part of the TCO double layer stack for improved band alignment. Kelvin probe force microscopy measurements of the work function of solar cell cross sections support this model [34]. In terms of cell efficiency (12.5 %), the proof-of-concept could be achieved [131], but further development is necessary to demonstrate long term stability and reproducibility in pilot production. It has been shown that the alloy can be deposited by sputtering from a single mixed target and that its conductivity is comparable to the standard undoped ZnO. Hence, sputtering of (Zn,Mg)O is a simple drop-in replacement and can be integrated easily into existing pilot lines to prepare standard (with CBD buffer) modules and to investigate modules without buffer layers in the same setup.

6.6.3 Indium free absorbers

It is sometimes argued that the lack of abundancy of indium may be limiting the long term perspectives of chalcopyrite based photovoltaics (see Section 6.5.3.1). This has triggered research on In-free absorbers. Compounds such as $Cu_2ZnSn(S,Se)_4$ crystallize in the kesterite structure which can be derived from the chalcopyrite structure by replacing half of the In atoms by Zn and the other half by Sn atoms. It has been shown that the synthesis of crystals and thin films can be carried out using methods well known from chalcopyrite preparation [132, 133]. Also, heterojunction solar cells can be prepared using the established contact layers (molybdenum back contact, CdS buffer etc.). On the other hand, secondary phases are more problematic in this quarternary system as compared to ternary chalcopyrite. Cell efficiencies achieved so far are in the range of 5 % [134] and indicate that research efforts would have to be stepped up significantly to make kesterites a feasible alternative to chalcopyrite absorbers.

6.6.4 Novel back contacts

Molybdenum appears to be an almost ideal contact material at least for current typical cell structures and preparation methods. Corrosion of molybdenum [135] is one of the few known issues and has been reported to contribute to module degradation in accelerated lifetime testing. It is conceivable that the stability could be improved by using molybdenum based alloys instead of pure molybdenum. Another disadvantage of molybdenum is its poor optical reflection which may become relevant in view of efforts to reduce the absorber thickness. The choice of other metals is limited due to their instability under typical absorber deposition conditions. Tungsten seems to yield a good ohmic contact but its optical properties in this respect are poor. Tantalum and niobium have slightly higher reflections and preliminary studies [136] indicate that they may be feasible in terms of contact performance. Transparent conductive oxide coated metal contacts may be an alternative solution to achieve stability, and good electrical as well as optical performance for thin cells. Ohmic TCO/chalcopyrite contacts are also required for novel structures such as bifacial and (semi) transparent cells (see below).

6.6.5 Bifacial cells and superstrate cells

In a variant of the cell structure the nontransparent rear metal contact is replaced by a TCO film [137]. Such a bifacial cell (Figure 6.19) has advantages in certain applications. At the current

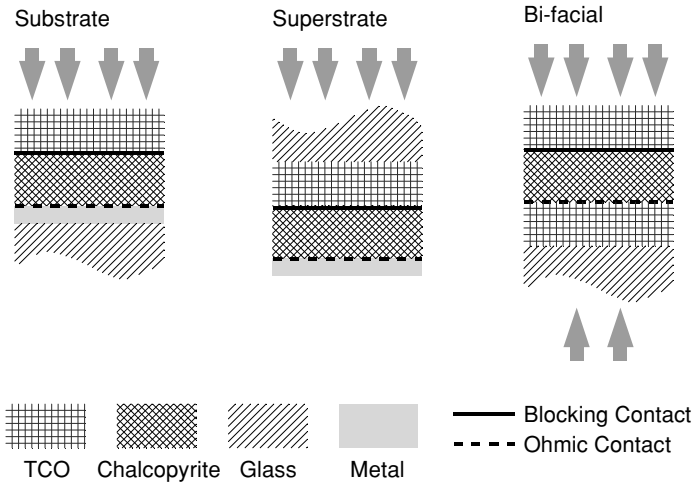

Figure 6.19 Schematic cross sectional views of chalcopyrite solar cell configurations.

development state the efficiency for illumination through the back contact is significantly lower because the carriers are generated outside the field zone in proximity to the poorly passivated contact (poor blue response). Further optimization of absorber thickness, diffusion length, and contact passivation appears to be feasible.

In the conventional module structure the nontransparent back contact is deposited onto the glass substrate. The module is illuminated through the encapsulation material which has to be transparent (usually a second sheet of glass). It is, in principle, possible to reverse the cell structure by starting with the deposition of the transparent contact (Superstrate configuration, Figure 6.19). In this case the TCO/(buffer)/chalcopyrite interface needs to be a blocking junction. The light enters the cell through the superstrate which has the advantage that the module can be encapsulated with nontransparent material of lower mass and lower cost. The efficiency in this structure is reduced due to junction degradation during the high temperature absorber preparation and/or inferior quality of the absorber deposited at lower temperatures. The proof-of-concept is limited to small area cells [138–140].

Heterojunctions can also be prepared on TiO_2 films [141]. This material can be grown so that it is nanostructured (porous) and is better known from its application in dye sensitized cells. Filling the pores of TiO_2 with a chalcopyrite semiconductor has been proposed as a realization of the ETA (extremely thin absorber) concept [142]. The recombination velocity at the TiO_2/chalcopyrite interface must be kept low in view of the very large interface area in this structure. It has been found that blocking or buffer layers are useful in achieving better interface properties [143, 144].

6.6.6 Nonvacuum processing

Nonvacuum processing is being investigated because it may reduce the up front investment required to implement a certain process step. This lowers the initial barrier and financial risk but does not necessarily imply lower overall production costs. The running costs may be actually be higher due to the mix of vacuum and nonvacuum equipment and corresponding

infrastructure requirements, larger amounts of waste generated in wet chemical processing, etc. There is no known vacuum-free alternative for the preparation of the molybdenum back contact, however, metallized glass may be bought from the glass industry and does not have to be prepared on site. Nonvacuum buffer (CBD) and window layer (MOCVD) deposition is already established. Nonvacuum absorber processes are commonly based on sequential processes similar to those described in Section 6.3.1.2 above. They comprise a precursor deposition at room temperature followed by (reactive) annealing at elevated temperature. This second stage of sequential processing, i.e., selenization in mixtures of H_2 Se and inert gas is an already established nonvacuum process. Electrodeposited metal precursors were investigated early in the history of chalcopyrite solar cells [145] and there appears to be a renewed interest [146] in spite of the moderate lab scale efficiencies achieved. Electrodeposition of a metal/Se precursor is the basis of a process developed with strong industrial participation and so far yielding small area cells with 10 % efficiency [147]. Higher efficiencies could be achieved by another group with selenium containing precursors, but only after manipulating the precursor composition by means of conventional evaporation [148].

Another interesting approach is the preparation of inks or slurries which can be deposited by spraying, printing, dip coating, or doctor blading. In one approach [149] the metals are dissolved in acid and hydroxide nanoparticles are precipitated from this solution. The particles are dried, which results in a fine powder of mixed oxides. The powder is dispersed in an aqueous solution to obtain the ink. In this and similar processes the film composition can be controlled precisely and with relative ease by adjusting the relative amounts of material used for particle preparation. The oxide particle precursor needs an additional reduction step prior to selenization carried out in diluted hydrogen. The precursor film can be porous because the volume increase during selenization leads to sufficient densification [150]. In principle it would be possible to include selenium (and/or sulfur) in the precursor particles and to use nonreactive sintering, but results from various approaches were not convincing.

6.6.7 Wide gap and tandem cells

Wide gap cells are interesting for two reasons: better single junction cells and top cells for tandem configuration. A moderate increase of the bandgap to about 1.4 eV for a single junction cell places it at the theoretical maximum of the bandgap/efficiency relation for the solar spectrum [151]. Because of the reduced current density, a higher resistance of the TCO can be tolerated. At the same time the doping of the TCO can be at the upper limit because the absorber cut off wavelength is below the onset of free carrier absorption in the TCO. In consequence the TCO can be made thinner which leads to cost reductions. Compared to low gap absorbers, the loss of performance at higher module temperature is much less severe which leads to improved annual output in terms of kWh/kWp (performance ratio) especially in hot climate. Tandem cells could eventually lead to an efficiency exceeding even the theoretical limit for silicon cells. Low gap CIG(S)Se cells ($E_g \approx 1.1$ eV), such as NREL's 19.5 % efficient cell, are ideally suited as the bottom cell. The top cell absorber should have a bandgap of roughly 1.7 eV [152] and the front as well as the back contacts need to be highly transparent.

Ideally, the top cell would be deposited directly onto the bottom cell (monolithic tandem, Figure 6.20). This, however, requires fundamental changes to the chalcopyrite technology. The top cell, after laying down the window layer, does not tolerate temperatures above 200 °C. This maximum allowable temperature would have to be raised significantly and low temperature

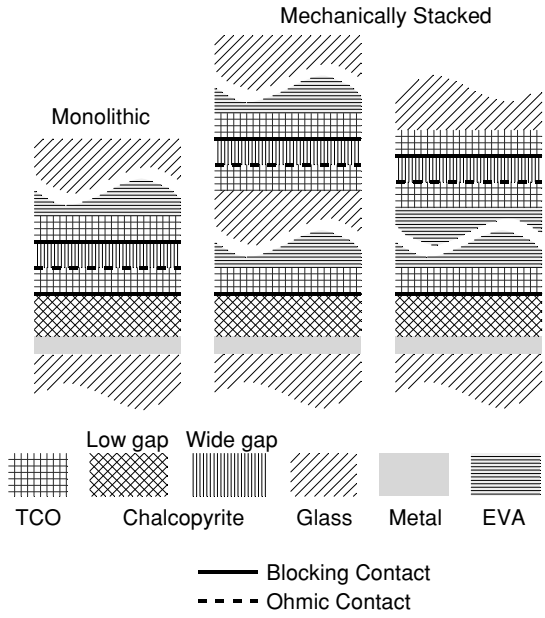

Figure 6.20 Schematic cross sectional views of tandem configurations.

processing would have to be implemented for the deposition of the top cell. It is therefore more likely that the first tandem modules will be mechanically stacked after individual preparation of top and bottom cells, respectively. If the top module were prepared in analogy to the bifacial cell described above this would imply a laminate with three sheets of glass. If the top module had a superstrate structure, top and bottom could be laminated together face-to-face and, like in the conventional single junction module, only two sheets of glass would be necessary for an encapsulated module (Figure 6.20, right hand side).

In practice the realization of highly efficient wide gap cells has not yet been achieved. As pointed out previously, this may have partly historical reasons. On the other hand, significant differences in parameters determining the cell efficiency have been theoretically predicted [153] and are observed in the experiment [154]. It is not fully clear which of these are the most crucial and how they could be resolved. This is expected to change as the development of widegap cells and tandems is one of the focus points of international basic research. Preliminary prototypes of monolithic [155] as well as mechanically stacked [156] tandems are described in the literature. Due to the problems in realizing a highly efficient wide gap chalcopyrite solar cells it has been suggested to use a different material such as amorphous silicon [157] or CdTe [158] for the top cell.

REFERENCES

[1] J. E. Jaffe, A. Zunger, Electronic structure of the ternary chalcopyrite semiconductors $CuAlS_2$, $CuGaS_2$, $CuGaSe_2$ and CuInSe2, *Phys. Rev. B*, **29** (1984) 1882.

[2] S. Wagner, J. L. Shay, P. Migliorato, H. M. Kasper, $CuInSe_2$/CdS heterojunction photovoltaic detectors, *Appl. Phys. Lett.* **25**, (1974) 434.

[3] K. Ramanathan, M. A. Contreras, C. L. Perkins, S. Asher, F. S. Hasoon, J. Keane, D. Young, M. Romero, W. Metzger, R. Noufi, J. Ward, A. Duda, Improved performance in ZnO/CdS/$CuGaSe_2$ Thin-film solar cells, *Prog. Photovolt: Res. Appl*,. **11** (2003) 225.

[4] J. Kessler, J. Wennerberg, M. Bodegård, L. Stolt, Highly efficient Cu(In,Ga)Se_2 mini-modules, *Sol. En. Mat. Sol. Cells*, **75** (2003) 35.

[5] K. Kushiya, Progress in large-area Cu(InGa)Se_2-based thin-film modules with the efficiency of over 13 %, *Proc. 3rd World Conf. Photovoltaic Energy Conversion, Osaka, Japan, 11–18 May 2003*, K. Kurokawa, L. L. Kazmerski, B. McNelis, M. Yamaguchi, C. Wronski, W. C. Sinke (Eds.) (2003) 319.

[6] J. Palm, V. Probst, W. Stetter, R. Toelle, S. Visbeck, H. Calwer, T. Niesen, H. Vogt, O. Hernandez, M. Wendl, F. H. Karg, CIGSSe thin film PV modules: from fundamental investigations to advanced performance and stability, *Thin Solid Films*, **451–452** (2004) 544.

[7] M. Powalla, B. Dimmler, New developments in CIGS thin-film solar cell technology, *Proc. 3rd World Conf. Photovoltaic Energy Conversion, Osaka, Japan, 11–18 May 2003*, K. Kurokawa, L. L. Kazmerski, B. McNelis, M. Yamaguchi, C. Wronski, W. C. Sinke (Eds.) (2003) 313.

[8] R. Klenk, J. Klaer, R. Scheer, M. Ch. Lux-Steiner, I. Luck, N. Meyer, U. Rühle, Solar cells based on $CuInS_2$ – an overview, *Thin Solid Films*, **481–482** (2005) 509.

[9] R. Klenk, T. Walter, H.-W. Schock, D. Cahen, Model for successful growth of polycrystalline films of $CuInSe_2$ by multisource physical vacuum evaporation, *Adv, Mat.*, **5** (1993) 114.

[10] R. A. Mickelsen, W. S. Chen, Apparatus for forming thin-film heterojunction solar cells employing materials selected from the class of I-III-VI_2 chalcopyrite compounds, US Patent 4 392 451 (1983).

[11] A. M. Gabor, J. R. Tuttle, D. S. Albin, M. A. Contreras, R. Noufi, A. M. Hermann, High-efficiency $CuIn_xGa_{1-x}Se_2$ solar cells made from $(In_x,Ga_{1-x})_2Se_3$ precursor films, *Appl. Phys. Lett.*, **65** (1994) 198.

[12] N. Kohara, T. Negami, M. Nishitani, T. Wada, Preparation of device-quality Cu(In,Ga)Se_2 thin films deposited by coevaporation with composition monitor, *Jpn. J. Appl. Phys.*, **34** (1995) L1141.

[13] K. Sakurai, R. Scheer, C. A. Kaufmann, A. Yamada, P. Fons, Y. Kimura, T. Baba, K. Matsubara, S. Niki, Process variants for Cu($In_{1-x}Ga_x$)Se_2 deposition investigated by in situ spectroscopic light scattering, *Proc. 3rd World Conf. Photovoltaic Energy Conversion, Osaka, Japan, 11–18 May 2003*, K. Kurokawa, L. L. Kazmerski, B. McNelis, M. Yamaguchi, C. Wronski, W. C. Sinke (Eds.) (2003) 384.

[14] B. M. Basol, V. J. Kapur, $CuInSe_2$ thin films and high-efficiency solar cells obtained by selenization of metallic layers, *Conf. Rec. 21st IEEE Photovoltaic Specialists Conf., Kissimmee, USA, 21–25 May 1990*, IEEE, New York (1990) 546.

[15] J. Klaer, J. Bruns, R. Henninger, K. Siemer, R. Klenk, K. Ellmer, D. Bräunig, Efficient $CuInS_2$ thin-film solar cells prepared by a sequential process, *Semicond. Sci. Technol.*, **13** (1998) 1456.

[16] F. Karg, V. Probst, H. Harms, J. Rimmasch, W. Riedl, J. Kotschy, J. Holz, R. Treichler, O. Eibl, A. Mitwalsky, A. Kiendl, Novel rapid-thermal-processing for cis thin-film solar cells, *Conf. Rec. 23rd IEEE Photovoltaic Specialists Conf., Louisville, USA, 10–14 May 1993*, IEEE, New York (1993) 441.

[17] K. Siemer, J. Klaer, I. Luck, J. Bruns, R. Klenk, D. Bräunig, Efficient $CuInS_2$ solar cells from a rapid thermal process (RTP), *Sol. En. Mat. Sol. Cells*, **67** (2001) 159.

[18] D. Wolf, G. Müller, Kinetics of CIS-formation studied in-situ by thin film calorimetry, *Thin Solid Films*, **361–362** (2000) 155.

[19] R. Scheer, R. Klenk, J. Klaer, I. Luck, $CuInS_2$ based thin film photovoltaics, *Sol. En.*, **77** (2004) 777.

[20] I. Luck, J. Kneisel, K. Siemer, J. Bruns, R. Scheer, R. Klenk, N. Janke, D. Bräunig, Influence of Na on the properties of Cu-rich prepared $CuInS_2$ thin films and the performance of corresponding $CuInS_2$/CdS/ZnO solar cells, *Sol. En. Mat. Sol. Cells*, **67** (2001) 151.

[21] M. Ruckh, D. Schmid, M. Kaiser, R. Schäffler, T. Walter, H. W. Schock, Influence of substrates on the electrical properties of Cu(In,Ga)Se_2 thin films, *Sol. En. Mat. Sol.Cells*, **41/42** (1996) 335.

[22] D. Rudmann, M. Kaelin, F.-J. Haug, F. Kurdesau, H. Zogg, A. N. Tiwari, Impact of Na on structural properties and interdiffusion of $CuInSe_2$ and $CuGaSe_2$ thin films, *Proc. 3rd World Conf. Photovoltaic Energy Conversion, Osaka, Japan, 11–18 May 2003*, K. Kurokawa, L. L. Kazmerski, B. McNelis, M. Yamaguchi, C. Wronski, W. C. Sinke (Eds.) (2003) 376.

[23] J. H. Scofield, A. Duda, D. Albin, B. L. Ballard, P. K. Predecki, Sputtered molybdenum bilayer back contact for copper indium diselenide-based polycrystalline thin-film solar cells, *Thin Solid Films*, **260** (1995) 26.

[24] W. N. Shafarman, J. E. Phillips, Direct current-voltage measurements of the Mo/$CuInSe_2$ contact on operating solar cells, *Conf. Rec. 25th IEEE Photovoltaic Specialists Conf., Washington, USA, 13–17 May 1996*, IEEE, New York (1996) 917.

[25] M. Burgelman, F. Engelhardt, J. F. Guillemoles, R. Herberholz, M. Igalson, R. Klenk, M. Lampert, T. Meyer, V. Nadenau, A. Niemegeers, J. Parisi, U. Rau, H. W. Schock, M. Schmitt, O. Seifert, T. Walter and S. Zott, Defects in Cu(In,Ga)Se_2 semiconductors and their role in the device performance of thin-film solar cells, *Prog. Photovolt: Res. Appl.*, **5** (1997) 121.

[26] F. Kessler, D. Rudmann, Technological aspects of flexible CIGS solar cells and modules, *Sol. En.*, **77** (2004) 685.

[27] R. H. Mauch, J. Hedstrom, D. Lincot, M. Ruckh, J. Kessler, R. Klinger, L. Stolt, J. Vedel, H. W. Schock, Optimization of windows in ZnO-CdS-$CuInSe_2$ heterojunctions, *Conf. Rec. 22nd IEEE Photovoltaic Specialists Conf., Las Vegas, USA, 7–11 Oct 1991*, IEEE, New York (1991) 898.

[28] U. Rau, M. Schmidt, Electronic properties of ZnO/CdS/Cu(In,Ga)Se_2 solar cells – aspects of heterojunction formation, *Thin Solid Films*, **387** (2001) 141.

[29] U. Rau, P. O. Grabitz, J. H. Werner, Resistive limitations to spatially inhomogeneous losses in solar cells, *Appl. Phys. Lett.*, **85** (2004) 6010.

[30] K. Ellmer, Resistivity of polycrystalline zinc oxide films: current status and physical limit, *J. Phys. D: Appl. Phys.*, **34** (2001) 3097.

[31] Ch.-H. Fischer, M. Bär, A. Grimm, I. Kötschau, I. Lauermann, J. Reichardt, S. Sokoll, M. Aggour, H.-J. Lewerenz, M.C. Lux-Steiner, L. Weinhardt, O. Fuchs, C. Heske, C. Jung, W. Gudat, T. P. Niesen, S. Visbeck, F. Karg, X-rays shed light on the 'hidden' interfaces of solar cells, *BESSY-Highlights 2003* (2004) 14.

[32] M. Burgelman, A. Niemegeers, Calculation of CIS and CdTe module efficiencies, *Sol. En. Mat. Sol. Cells*, **51** (1998) 129.

[33] U. Rau, H. W. Schock, Electronic properties of Cu(In,Ga)Se_2 heterojunctions solar cells-recent achievements, current understanding, and future challenges, *Appl. Phys. A*, **69** (1999) 131.

[34] Th. Glatzel, H. Steigert, S. Sadewasser, R. Klenk, M.Ch. Lux-Steiner, Potential distribution of Cu(In,Ga)$(S,Se)_2$-solar cell cross-sections measured by Kelvin probe force microscopy, *Thin Solid Films*, **481–482** (2005) 177.

[35] R. Klenk, Characterisation and modelling of chalcopyrite solar cells, *Thin Solid Films*, **387** (2001) 135.

[36] M. Burgelman, P. Nollet, S. Degrave, Modelling polycrystalline semiconductor solar cells, *Thin Solid Films*, **361–362** (2000) 527.

[37] R. Scheer, Surface and interface properties of Cu-chalcopyrite semiconductors and devices, *Trends Vac. Sci. Technol.*, **2** (1997) 77.

[38] D. Schmid, M. Ruckh, H.-W. Schock, A comprehensive characterization of the interface in Mo/CIS/CdS/ZnO solar cell structures, *Sol. En. Mat. Sol. Cells*, **41/42** (1996) 281.

[39] M. Morkel, L. Weinhardt, B. Lohmüller, C. Heske, E. Umbach, W. Riedl, S. Zweigart, F. Karg, Flat conduction-band alignment at the CdS/$CuInSe_2$ thin-film solar-cell heterojunction, *Appl. Phys. Lett.* **79** (2001) 4482.

[40] T. Schulmeyer, R. Kniese, R. Hunger, W. Jägermann, M. Powalla, A. Klein, Influence of Cu(In,Ga)Se_2 band gap on the valence band offset with CdS, *Thin Solid Films*, **451–452** (2004) 420.

[41] L. Kronik, L. Burstein, M. Leibovitch, Y. Shapira, D. Gal, E. Moons, J. Beier, G. Hodes, D. Cahen, D. Hariskos, R. Klenk, H.-W. Schock, Band diagram of the polycrystalline CdS/Cu(In,Ga)Se_2 heterojunction, *Appl. Phys. Lett.*, **67** (1995) 1405.
[42] D. Schmid, M. Ruckh, F. Grunwald, H. W. Schock, Chalcopyrite/defect chalcopyrite heterojunctions on the basis of $CuInSe_2$, *J. Appl. Phys.*, **73** (1993) 2902.
[43] I..M. Kötschau, H.W. Schock, Depth profile of the lattice constant of the Cu-poor surface layer in $(Cu_2Se)_{1-x}(In_2Se_3)_x$ evidenced by grazing incidence X-ray diffraction, *J. Phys. Chem. Solids*, **64** (2003) 1559.
[44] M. Contreras, H. Wiesner, J. Tuttle, K. Ramanathan, R. Noufi, Issues on the Chalcopyrite/Defect-Chalcopyrite Junction Model for High-Efficiency Cu(In,Ga)Se_2 Solar Cells, *Sol. En. Mat. Sol. Cells*, **49** (1997) 239.
[45] S. Schuler, S. Siebentritt, S. Nishiwaki, N. Rega, J. Beckmann, S. Brehme, M.Ch. Lux-Steiner, Self-compensation of intrinsic defects in the ternary semiconductor $CuGaSe_2$, *Phys. Rev. B*, **69** (2004) 45210.
[46] S. Siebentritt, Hole transport mechanisms in $CuGaSe_2$, *Thin Solid Films*, **481–482** (2005) 312.
[47] S. Siebentritt, S. Schuler, Defects and transport in the wide gap chalcopyrite $CuGaSe_2$, *J. Phys. Chem. Solids*, **64** (2003) 1621.
[48] S. Sadewasser, Th. Glatzel, S. Schuler, S. Nishiwaki, R. Kaigawa, M.Ch. Lux-Steiner, Kelvin probe force microscopy for the nano scale characterization of chalcopyrite solar cell materials and devices, *Thin Solid Films*, **431–432** (2003) 257.
[49] C. Perrson, A. Zunger, Anomalous grain boundary physics in polycrystalline $CuInSe_2$: the existence of a hole barrier, *Phys. Rev. Lett.*, **91** (2003) 266401.
[50] K. Taretto, U. Rau, J. H. Werner, Numerical simulation of grain boundary effects in Cu(In,Ga)Se_2 thin-film solar cells, *Thin Solid Films*, **481–482** (2005) 8.
[51] D. Fuertes Marrón, S. Sadewasser, A. Meeder, Th. Glatzel, M. Ch. Lux-Steiner, Electrical activity at grain boundaries of Cu(In,Ga)Se_2 thin films, *Phys. Rev. B*, **71** (2005) 033306.
[52] K. Puech, S. Zott, K. Leo, M. Ruckh, H.-W. Schock, Determination of minority carrier lifetimes in $CuInSe_2$ thin films, *Appl. Phys. Lett.*, **69** (1996) 3375.
[53] N. Rega, S. Siebentritt, A. Zajogin, S. Nishiwaki, M. Ch. Lux-Steiner, R. Kniese, M. J. Romero, Excitonic luminescence of Cu(In,Ga)Se_2, *Thin Solid Films*, **481–482** (2005) 286.
[54] S. Siebentritt, I. Beckers, T. Riemann, J. Christen, A. Hoffmann, M. Dworzak, Reconciliation of luminescence and Hall measurements on the ternary semiconductor $CuGaSe_2$, *Appl. Phys. Lett.*, in press.
[55] S. B. Zhang, Su-Huai Wei, A. Zunger, H. Katayama-Yoshida, Defect physics of the $CuInSe_2$ chalcopyrite semiconductor, *Phys. Rev. B*, **57** (1998) 9642.
[56] R. Scheer, M. Wilhelm, V. Nadenau, H. W. Schock, L. Stolt, Collection functions in chalcopyrite heterojunction solar cells: a comparison of Cu(In,Ga)$(S,Se)_2$ absorbers, *Proc. 14th European Photovoltaic Solar Energy Conf., Barcelona, Spain*, H. A. Ossenbrink, P. Helm, H. Ehmann (Eds.), H.S. Stephens, Bedford, UK (1997) 1299.
[57] R. Klenk, H. W. Schock, Photocurrent collection in thin film solar cells - calculation and characterization for $CuGaSe_2$/(Zn,Cd)S, *Proc. 12th European Photovoltaic Solar Energy Conf., Amsterdam, NL*, R. Hill, W. Palz, P. Helm (Eds.), Stephen & Associates, Bedford, UK (1994) 1588.
[58] N. Meyer, T. Dylla, D. Fischer, M. E. Beck, A. Jäger-Waldau, M. Ch. Lux-Steiner, Solar cells based on HCVD grown $CuGaSe_2$ absorbers with high open-circuit voltages, *Proc. 16th European Photvoltaic Solar Energy Conf., Glasgow, UK, 1–5 May 2000*, H. Scheer, B. McNelis, W. Palz, H. A. Ossenbrinck, P. Helm (Eds.), James & James, Glasgow (2000) 429.
[59] K. Orgassa, U. Rau, Quang Nguyen, H. W. Schock, J. H. Werner, Role of the CdS buffer layer as an active optical element in Cu(Ga,In)Se_2 thin-film solar cells, *Prog. Photovolt. Res. Appl.*, **10** (2002) 457.
[60] J. Klaer, I. Luck, A. Boden, R. Klenk, I. Gavilanes Perez, R. Scheer, Mini-modules from a $CuInS_2$ baseline process, *Thin Solid Films*, **431–432** (2003) 534.

[61] R. Kaigawa, A. Neisser, R. Klenk, M. Ch. Lux-Steiner, Improved performance of thin film solar cells based on Cu(In,Ga)S_2, *Thin Solid Films*, **415** (2002) 266.
[62] J. Parisi, D. Hilburger, M. Schmitt, U. Rau, Quantum efficiency and admittance spectroscopy on Cu(In,Ga)Se_2 solar cells, *Sol. En. Mat. Sol. Cells*, **50** (1998) 79.
[63] T. Walter, R. Menner, Ch. Köble, H. W. Schock, Characterization and junction performance of highly efficient Zno/CdS/$CuInS_2$ thin film solar cells, *Proc. 12th European Photovoltaic Solar Energy Conf., Amsterdam, NL*, R. Hill, W. Palz, P. Helm (Eds.), Stephen & Associates, Bedford, UK (1994) 1755.
[64] J. E. Phillips, W. N. Shafarman, E. Shan, Evidence for amorphous like behavior in small grain thin film polycrystalline solar cells, *Proc. 1st World Conf. Photovoltaic Energy Conversion, Hawaii*, IEEE, New York (1994) 303.
[65] R. Herberholz, T. Walter, H. W. Schock, Density of states in $CuIn(S,Se)_2$ thin films from modulated photocurrent measurements, *J. Appl. Phys.*, **76** (1994) 2904.
[66] R. Schäffler, H. W. Schock, Composition dependent optical properties of polycrystalline $CuInSe_2$ thin films, *Solid State Phenomena*, **51–52**, Scitec Publications (1996) 347.
[67] T. Walter, R. Herberholz, C. Müller, H. W. Schock, Determination of defect distributions from admittance measurements and application to Cu(In,Ga)Se_2 based heterojunctions, *J. Appl. Phys.*, **80** (1996) 4411.
[68] G. Hanna, A. Jasenek, U. Rau, H. W. Schock, Influence of the Ga-content on the bulk defect densities of Cu(In,Ga)Se_2, *Thin Solid Films*, **387** (2001) 71.
[69] A. Jasenek, A. Boden, K. Weinert, M. R. Balboul, H. W. Schock, U. Rau, High-energy electron and proton irradiation of Cu(In,Ga)Se_2 heterojunction solar cells, *Mat. Res. Soc. Symp. Proc.*, **668**, Materials Research Society (2001) H3.2.1.
[70] J. T. Heath, J. D. Cohen, W. N. Shafarman, D. X. Liao, A. A. Rockett, Effect of Ga content on defect states in $CuIn_{1-x}Ga_xSe_2$ photovoltaic devices, *Appl. Phys. Lett.*, **80** (2002) 4540.
[71] U. Rau, Tunneling-enhanced recombination in Cu(In,Ga)Se_2 heterojunction solar cells, *J. Appl. Phys.*, **74** (1999) 111.
[72] U. Malm, J. Malmström, C. Platzer-Björkman, L. Stolt, Determination of dominant recombination paths in Cu(In,Ga)Se_2 thin-film solar cells with ALD-ZnO buffer layers, *Thin Solid Films*, **481–482** (2005) 208.
[73] I. Hengel, A. Neisser, R. Klenk, M. Ch. Lux-Steiner, Current transport in $CuInS_2$:Ga/CdS/ZnO Solar Cells, *Thin Solid Films*, **361–362** (2000) 458.
[74] J. Reiß, J. Malmström, A. Werner, I. Hengel, R. Klenk, M. Ch. Lux-Steiner, Current transport in $CuInS_2$ solar cells depending on absorber preparation, *Mat. Res. Soc. Symp. Proc.*, **668**, Materials Research Society (2001) H9.4.1.
[75] V. Nadenau, U. Rau, A. Jasenek, H. W. Schock, Electronic properties of $CuGaSe_2$-based heterojunction solar cells. Part I. Transport analysis, *J. Appl. Phys.*, **87** (2000) 584.
[76] M. Turcu, O. Pakma, U. Rau, Interdependence of absorber composition and recombination mechanism in Cu(In,Ga)$(S,Se)_2$ heterojunction solar cells, *J. Appl. Phys.*, **80** (2002) 2598.
[77] J. H. Werner, J. Mattheis, U. Rau, Efficiency limitations of polycrystalline thin film solar cells: case of Cu(In,Ga)Se_2, *Thin Solid Films*, **481–482** (2005) 399.
[78] U. Rau, J. H. Werner, Radiative efficiency limits of solar cells with lateral band-gap fluctuations, *Appl. Phys. Lett.*, **84** (2004) 3735.
[79] J. AbuShama, R. Noufi, S. Johnston, S. Ward, X. Wu, Improved performance in $CuInSe_2$ and surface-modified $CuGaSe_2$ solar cells, *Proc. 31st IEEE Photovoltaic Specialists Conf., Lake Buena Vista, USA, January 3–7, 2005*, IEEE, New York (2005) 299.
[80] M. A. Green, K. Emery, D. L. King, S. Igari, W. Warta, Solar cell efficiency tables, *Prog. Photovolt: Res. Appl.*, **13** (2005) 49.
[81] B. Egaas, M. A. Contreras, R. Noufi, unpublished result.
[82] C. A. Kaufmann, A. Neisser, R. Scheer, R. Klenk, M. A. Kroon, Cu(In,Ga)Se_2 thin film solar cells on flexible substrates, *Proc. 19th European Photovoltaic Solar Energy Conf., Paris, France,*

7–11 June 2004, W. Hoffman, J.-L. Bal, H. Ossenbrink, W. Palz, P. Helm (Eds.), WIP-Munich and ETA-Florence (2004) 3637.

[83] D. Brémaud, D, Rudmann, G. Bilger, H. Zogg, A. N. Tiwari, Towards the development of flexible CIGS solar cells on polymer films with efficiency exceeding 15 %, *Proc. 31st IEEE Photovoltaic Specialists Conf., Lake Buena Vista, USA, January 3–7, 2005*, IEEE, New York (2005) 223.

[84] M.A. Contreras, T. Nakada, M. Hongo, A.O. Pudov, J.R. Sites, ZnO/ZnS(O,OH)/Cu(In,Ga)Se_2/Mo solar cell with 18.6 % efficiency, *Proc. 3rd World Conf. Photovoltaic Energy Conversion, Osaka, Japan, 11–18 May 2003*, K. Kurokawa, L. L. Kazmerski, B. McNelis, M. Yamaguchi, C. Wronski, W. C. Sinke (Eds.) (2003) 570.

[85] N.A. Allsop, A. Schönmann, H.J. Muffler, M. Bär, M.C. Lux-Steiner, Ch.H. Fischer, Spray-ILGAR indium sulfide buffers for Cu(In, Ga)(S, Se)$_2$ solar cells, *Prog. Photovolt. Res. Appl.*, submitted.

[86] T. Glatzel, H. Steigert, R. Klenk; M. Ch. Lux-Steiner, T. P. Niesen, S. Visbeck, $Zn_{1-x}Mg_xO$ as a window layer in completely Cd-free Cu(In, Ga)(S, Se)$_2$ based thin film solar cells, *Sol. En. Mat. Sol. Cells*, in press.

[87] N. Naghavi, S. Spiering, M. Powalla, B. Cavana, D. Lincot, High-efficiency copper indium gallium diselenide (CIGS) solar cells with indium sulfide buffer layers deposited by atomic layer chemical vapor deposition (ALCVD), *Prog. Photovolt. Res. Appl.*, **11** (2003) 437.

[88] A. Strohm, T. Schlötzer, Q. Nguyen, K. Orgassa, H. Wiesner, H.W. Schock, New approaches for the fabrication of Cd-free Cu(In,Ga)Se_2 heterojunctions, *Proc. 19th European Photovoltaic Solar Energy Conf., Paris, France, 7–11 June 2004*, W. Hoffman, J.-L. Bal, H. Ossenbrink, W. Palz, P. Helm (Eds.), WIP-Munich and ETA-Florence (2004) 1741.

[89] S. Siebentritt, Alternative buffers for chalcopyrite solar cells, *Sol. En.*, **77** (2004) 767.

[90] K. Mitchell, C. Eberspacher, J. Ermer, D. Pier, Single and tandem junction $CuInSe_2$ cell and module technology, *Conf. Rec. 20th IEEE Photovoltaic Specialists Conf., Las Vegas, USA, 26–30 Sept. 1988*, IEEE, New York (1988) 1384.

[91] M. Powalla, B. Dimmler, K.-H. Groß, CIS thin-film solar modules - an example of remarkable progress in PV, *Proc. 20th European Photovoltaic Solar Energy Conf., Barcelona, Spain, June 6–10 2005*, in press.

[92] R. W. Birkmire, Recent progress and critical issues in thin film polycrystalline solar cells and modules, *Conf. Rec. 26th IEEE Photovoltaic Specialists Conf., Anaheim, USA, 29 Sept-3 Oct 1997*, IEEE, New York (1997) 295.

[93] E. Rudigier, I. Luck, R. Scheer, Quality assessment of $CuInS_2$-based solar cells by Raman scattering, *Appl. Phys. Lett.*, **82** (2003) 4370.

[94] J. Palm, V. Probst, A. Brummer, W. Stetter, R. Tölle, T. P. Niesen, S. Visbeck, O. Hernandez, M. Wendl, H. Vogt, H. Calwer, B. Freienstein, F. Karg, CIS module pilot processing applying concurrent rapid selenization and sulfurization of large area thin film precursors, *Thin Solid Films*, **431–432** (2003). 514

[95] M. Powalla, D. Hariskos, E. Lotter, M. Oertel, J. Springer, D. Stellbogen, B. Dimmler, R. Schäffler, Large-area CIGS modules: processes and properties, *Thin Solid Films*, **431–432** (2003) 523.

[96] O. Lundberg, M. Bodegård, J. Malmström, L. Stolt, Influence of the Cu(In,Ga)Se_2 thickness and Ga grading on solar cell performance, *Prog. Photovolt: Res. Appl.*, **11** (2002) 77.

[97] D. E. Tarrant, R. R. Gay, Process R&D for CIS-based thin-film PV, *Annual Technical Report 24 April 2002–23 April 2003*, NREL(SR-520-35684, National Renewable Energy Lab, Golden (2004).

[98] L. Mrig, S. Rummel, Outdoor stability performance of CIS and CdTe photovoltaic modules at SERI, *Conf. Rec. 21st IEEE Photovoltaic Specialists Conf., Kissimmee, USA, 21–25 May 1990*, IEEE, New York (1990) 1038.

[99] M. Powalla, B. Dimmler, R. Schaeffler, G. Voorwinden, U. Stein, H.-D. Mohring, F. Kessler, D. Hariskos, CIGS solar modules: progress in pilot production, new developments and applications, *Proc. 19th European Photovoltaic Solar Energy Conf., Paris, France, 7–11 June 2004*,

W. Hoffman, J.-L. Bal, H. Ossenbrink, W. Palz, P. Helm (Eds.), WIP-Munich and ETA-Florence (2004) 1663.

[100] H.-D. Mohring, D. Stellbogen, R. Schäffler, S. Oelting, R.Gegenwart, P. Konttinen, T. Carlsson, M. Cendagorta, W. Herrmann, Outdoor performance of polycrystalline thin film PV modules in different european climates, *Proc. 19th European Photovoltaic Solar Energy Conf., Paris, France, 7–11 June 2004*, W. Hoffman, J.-L. Bal, H. Ossenbrink, W. Palz, P. Helm (Eds.), WIP-Munich and ETA-Florence (2004) 2098.

[101] J. Malmström, J. Wennerberg, L. Stolt, A study of the influence of the Ga content on the long-term stability of Cu(In,Ga)Se_2 thin film solar cells, *Thin Solid Films*, **431–432** (2003) 436.

[102] J. Klaer, R. Scheer, R. Klenk, A. Boden, Ch. Köble, Stress behaviour of $CuInS_2$ and Cu(In,Ga)Se_2 thin film PV-modules studied by a specific test structure, *Proc. 19th European Photovoltaic Solar Energy Conf., Paris, France, 7–11 June 2004*, W. Hoffman, J.-L. Bal, H. Ossenbrink, W. Palz, P. Helm (Eds.), WIP-Munich and ETA-Florence (2004) 1847.

[103] J. M. Woodcock, H. Schade, H. Maurus, B. Dimmler, J. Springer, A. Ricaud, A study of the upscaling of thin film solar cell manufacture towards 500 MWp per annum, *Proc. 14th European Photovoltaic Solar Energy Conf., Barcelona, Spain*, *30 June–4 July 1997*, H. A. Ossenbrink, P. Helm, H. Ehmann (Eds.), H.S. Stephens, Bedford, UK (1997) 857.

[104] U. Ugalde, J. Alonso, T. Bruton, J. M. Woodcock, K. Roy, K. De Clerq, A general procedure for cost evaluations: application to the MUSIC FM project, *Proc. 14th European Photovoltaic Solar Energy Conf., Barcelona, Spain, 30 June–4 July 1997*, H.A. Ossenbrink, P. Helm, H. Ehmann (Eds.), H.S. Stephens & Associates, Bedford, UK (1997) 897.

[105] T. M. Bruton, MUSIC FM - Five years on fantasy or reality, *Proc. PV in Europe – From PV Technology to Energy Solutions, Rome, Italy, 7–11 October 2002*, WIP Munich, Germany (2002) OA6.1.

[106] L. Frantzis, E. Jones, M. Wood, C. Lee, P. Wormser, Opportunities for Cost Reduction in Photovoltaic Modules, *Proc. 16th European Photvoltaic Solar Energy Conf., Glasgow, UK, 1–5 May 2000*, H. Scheer, B. McNelis, W. Palz, H. A. Ossenbrinck, P. Helm (Eds.), James & James, Glasgow (2000) 2069.

[107] N. Meyer, I. Luck, U. Rühle, J. Klaer, R. Klenk, M. Ch. Lux-Steiner, R. Scheer, Towards thin film module production using a simplified CIS process, *Proc. 19th European Photovoltaic Solar Energy Conf., Paris, France, 7–11 June 2004*, W. Hoffman, J.-L. Bal, H. Ossenbrink, W. Palz, P. Helm (Eds.), WIP-Munich and ETA-Florence (2004) 1698.

[108] M. E. Beck, S. Wiedemann, R. Huntington, J. VanAlsburg, E. Kanto, R. Butcher, J. S. Britt, Advancements in flexible CIGS module manufacturing, *Proc. 31st IEEE Photovoltaic Specialists Conf., Lake Buena Vista, USA, January 3–7, 2005*, IEEE, New York (2005) 211.

[109] B. Dimmler, M. Powalla, R. Schaeffler, CIS solar modules: pilot production at Wuerth Solar, *Proc. 31st IEEE Photovoltaic Specialists Conf., Lake Buena Vista, USA, January 3–7, 2005*, IEEE New York (2005) 189.

[110] D. E. Tarrant, R. R. Gay, V. Probst, F. H. Karg, CIS thin film development and production status at shell solar, *Proc. 3rd World Conf. Photovoltaic Energy Conversion, Osaka, Japan, 11–18 May 2003*, K. Kurokawa, L. L. Kazmerski, B. McNelis, M. Yamaguchi, C. Wronski, W. C. Sinke (Eds.) (2003). 325.

[111] F. H. Karg, D. Kohake, T. Nierhoff, B. Kühne, S. Grosser, M. Ch. Lux-Steiner, Performance of grid coupled pv-arrays based on CIS solar modules, *Proc. 17th European Photovoltaic Solar Energy Conf., Munich, Germany, 22–26 Oct. 2001*, B. McNelis, W. Palz, H.A. Ossenbrink, P. Helm (Eds.), WIP Munich, Germany (2001) 391.

[112] *SENSE – Sustainability evaluation and recycling development for thin-film solar cells*, contract ENK5-CT-2002-00639 (http://www.sense-eu.net/).

[113] M.J de Wild-Scholten, K. Wambach, E.A. Alsema, A. Jäger-Waldau, Implications of European environmental legislation for photovoltaic systems, *Proc. 20th European Photovoltaic Solar Energy Conf., Barcelona, Spain, 6–10 June 2005* W. Palz *et al*. (Eds.), WIP-Munich (2005) 3143.

[114] F. H. Karg, Entwicklung und Fertigung von CIS-Solarmodulen bei Siemens Solar FVS Themen 2000, G. Stadermann (Eds.), Forschungsverbund Sonnenenergie, Berlin, Germany (2000) 145.
[115] US Geological Survey, *Mineral Commodity Summaries*, January 2004.
[116] K. Ramanathan, J.C. Keane, B. To, R.G. Dhere, and R. Noufi, The potential for high performance in CIGS solar cells: a laboratory perspective, *Proc. 20th European Photovoltaic Solar Energy Conf., Barcelona, Spain, June 6–10 2005*, in press.
[117] D. Hariskos, M. Powalla, N. Chevaldonnet, D. Lincot, A. Schindler, B. Dimmler, Chemical bath deposition of CdS buffer layer: prospects of increasing material yield and reducing waste, *Thin Solid Films*, **387** (2001) 179.
[118] B. Malinowska, M. Rakib, G. Durand, Re-use of chemicals in CBD of CdS thin film for CIS solar cells, *Proc. 19th European Photovoltaic Solar Energy Conf., Paris, France, 7–11 June 2004*, W. Hoffman, J.-L. Bal, H. Ossenbrink, W. Palz, P. Helm (Eds.), WIP-Munich and ETA-Florence (2004) 1820.
[119] K. Kushiya, M. Ohshita, M. Tanaka, Development of recycling and reuse technologies for large-area Cu(InGa)Se_2-based thin-film modules, *Proc. 3rd World Conf. Photovoltaic Energy Conversion, Osaka, Japan, 11–18 May 2003*, K. Kurokawa, L. L. Kazmerski, B. McNelis, M. Yamaguchi, C. Wronski, W. C. Sinke (Eds.) (2003) 1892.
[120] K. Knapp, T. Jester, Empirical investigation of the energy payback time for photovoltaic modules, *Sol. En.*, **71** (2001) 165.
[121] A. Neisser, C. A. Kaufmann, R. Klenk, R. Scheer, M. A. Kroon, G. Oomen, H.-W. Schock, Prototype development - flexible Cu(In,Ga)Se_2 thin film solar cells for space applications, *Conf. Rec. 31st IEEE Photovoltaic Specialists Conference and Exhibition, Lake Buena Vista, USA, January 3–7, 2005*, IEEE, New York (2005) 227.
[122] See http://europa.eu.int/comm/environment/waste/weee_index.htm.
[123] K. Kushiya, M. Tachiyuki, T. Kase, Y. Nagoya, T. Miura, D. Okumura, M. Satoh, I. Sugiyama, O. Yamase, Improved FF of CIGS thin-film mini-modules with $Zn(O,S,OH)_x$ buffer by post-deposition light soaking, *Conf. Rec. 26th IEEE Photovoltaic Specialists Conf., Anaheim, USA, 29 Sept–3 Oct 1997*, IEEE, New York (1997) 327.
[124] H. Muffler, M. Bär, C.-H. Fischer, R. Gay, F. Karg, M. C. Lux-Steiner, ILGAR technology, VIII sulfidic buffer layers for Cu(In Ga)$(S,Se)_2$ solar cells prepared by ion layer gas reaction (ILGAR), *Conf. Rec. 28th IEEE Photovoltaic Specialists Conf., Anchorage, USA, 15–22 Sept 2000*, IEEE, New York (2000) 610.
[125] M. Bär, C. H. Fischer, H. J. Muffler, B. Leupolt, T. P. Niesen, F. Kang, M. C. Lux-Steiner, High efficiency chalcopyrite solar cells with ILGAR-ZnO WEL-device characteristics subject to WEL composition, *Conf. Rec. 29th IEEE Photovoltaic Specialists Conf., New Orleans, USA, 19–24 May 2002*, IEEE, New York (2002) 636.
[126] S. Siebentritt, P. Walk, U. Fiedeler, I. Lauermann, K. Rahne, M.Ch. Lux-Steiner, Th.P. Niesen, F.Karg, MOCVD as a dry deposition method of ZnSe buffers for Cu(In,Ga)$(S,Se)_2$ solar cells, *Prog. Photovolt: Res. Appl.*, **12** (2004) 333.
[127] S. Spiering, A. Eicke, D. Hariskos, M. Powalla, N. Naghavi, D. Lincot, Large-area Cd-free CIGS solar modules with In_2S_3 buffer layer deposited by ALCVD, *Thin Solid Films*, **451–452** (2004) 562.
[128] S. Gall, N. Barreau, S. Harel, J. C. Bernède, J. Kessler, Material analysis of PVD-grown indium sulphide buffer layers for Cu(In,Ga)Se_2-based solar cells, *Thin Solid Films*, **481–482** (2005) 138.
[129] K. Ramanathan, F. S. Hasoon, S. Smith, A. Mascarenhas, H. Al-Thani, J. Alleman, H. S. Ullal, J. Keane, Properties of Cd and Zn partial electrolyte treated solar cells, *Conf. Rec. 29th IEEE Photovoltaic Specialists Conf., New Orleans, USA, 19–24 May 2002*, IEEE, New York (2002) 523.
[130] D. Hariskos, R. Menner, S. Spiering, A. Eicke, M. Powalla, K. Ellmer, M. Oertel, B. Dimmler, In_2S_3 buffer layer deposited by magnetron sputtering for Cu(inGa)Se_2 solar cells, *Proc.*

19th European Photovoltaic Solar Energy Conf., Paris, France, 7–11 June 2004, W. Hoffman, J.-L. Bal, H. Ossenbrink, W. Palz, P. Helm (Eds.), WIP-Munich and ETA-Florence (2004) 1894.

[131] Th. Glatzel, H. Steigert, R. Klenk, M. Ch. Lux-Steiner, T. P. Niesen, S. Visbeck, $Zn_{1-x}Mg_xO$ as a window layer in completely Cd-free $Cu(In,Ga)(S,Se)_2$ based thin film solar cells, *Technical Digest Int. PVSEC-14, 707*, accepted for publication in *Sol. En. Mat. Sol. Cells*.

[132] Th. Magorian Friedlmeier, N. Wieser, Th. Walter, H. Dittrich, H.-W. Schock, Heterojunctions based on Cu_2ZnSnS_4 and $Cu_2ZnSnSe_4$ thin films, *Proc. 14th European Photovoltaic Solar Energy Conf., Barcelona, Spain, 30 June–4 July 1997*, H.A. Ossenbrink, P. Helm, H. Ehmann (Eds.), H.S. Stephens & Associates, Bedford, UK (1997) 1242.

[133] H. Katagiri, N. Ishigaki, T. Ishida, K. Saito, Characterization of Cu_2ZnSnS_4 thin films prepared by vapor phase sulfurization, *Jpn. J. Appl. Phys.*, **40** (2001) 500.

[134] H. Katagiri, Cu_2ZnSnS_4 thin film solar cells, *Thin Solid Films*, **481–482** (2005) 426.

[135] J. Wennerberg, J. Kessler, M. Bodegård, L. Stolt, Damp heat testing of high performance CIGS thin film solar cells, *Proc. 2nd World Conf. Photovoltaic Solar Energy Conversion, Vienna, Austria, 6–10 July 1998*, J. Schmid, H. A. Ossenbrink, P. Helm, H. Ehmann, E. D. Dunlop (Eds.), Joint Research Center ISPRA (1998) 1161.

[136] K. Orgassa, H. W. Schock, J. H. Werner, Alternative back contact materials for thin film $Cu(In,Ga)Se_2$ solar cells, *Thin Solid Films*, **431/432** (2003) 387.

[137] T. Nakada, Y. Hirabayashi, T. Tokado, D. Ohmori, $Cu(In_{1-x},Ga_x)Se_2$ thin film solar cells using transparent conducting oxide back contacts for bifcial and tandem solar cells, *Proc. 3rd World Conf. Photovoltaic Energy Conversion, Osaka, Japan, 11–18 May 2003*, K. Kurokawa, L. L. Kazmerski, B. McNelis, M. Yamaguchi, C. Wronski, W. C. Sinke (Eds.) (2003) 2880.

[138] R. Klenk, R. Mauch, R. Schäffler, D. Schmid, Progress in $CuGaSe_2$ based thin film solar cells, *Conf. Rec. 22nd IEEE Photovoltaic Specialists Conf., Las Vegas, USA, 7–11 Oct 1991*, IEEE, Ney York (1991) 1071.

[139] T. Nakada, T. Kume, T. Mise, A. Kunioka, Superstrate-type $Cu(In,Ga)Se_2$ thin film solar cells with ZnO buffer layers, *Jpn. J. Appl. Phys.*, **37** (1998) L499.

[140] F.-J. Haug, D. Rudmann, H. Zogg, A. N. Tiwari, Light soaking effects in $Cu(In,Ga)Se_2$ superstrate solar cells, *Thin Solid Films*, **431–432** (2003) 431.

[141] M. Nanu, L. Reijnen, A. Goossens, J. Schoonman, $CuInS_2/TiO_2$ heterojunction solar cells obtained by atomic layer deposition, *Thin Solid Films*, **431–432** (2003) 492.

[142] I. Kaiser, K. Ernst, Ch.-H. Fischer, C. Rost, I. Sieber, M.-Ch. Lux-Steiner, R. Könenkamp, The EAT-solar cell with $CuInS_2$ a photovoltaic cell concept using an extremely thin absorber (ETA), *Sol. En. Mat. Sol. Cells*, **67** ¨(2001) 89.

[143] F. Lenzmann, M. Nanu, O. Kijatkina, A. Belaidi, Substantial improvement of the photovoltaic characteristics of $TiO_2/CuInS_2$ interfaces by the use of recombination barrier coatings, *Thin Solid Films*, **451–452** (2004) 639.

[144] C. Grasso, M. Burgelman, Theoretical study on the effect of an intermediate layer in CIS-based ETA-solar cells, *Thin Solid Films*, **451–452** (2004) 156.

[145] V. K. Kapur, B. M. Basol, E. S. Tseng, Low cost thin film chalcopyrite solar cells, *Conf. Rec. 18th IEEE Photovoltaic Specialists Conf., Las Vegas, USA, 21–25 Oct 1985*, IEEE, New York (1985) 1429.

[146] J. Rechid, R. Thyen, A. Raitzig, S. Wulff, M. Mihhailova, K. Kalberlah, A. Kampmann, 9 % efficiency: CIGS on Cu substrate, *Proc. 3rd World Conf. Photovoltaic Energy Conversion, Osaka, Japan, 11–18 May 2003*, K. Kurokawa, L. L. Kazmerski, B. McNelis, M. Yamaguchi, C. Wronski, W. C. Sinke (Eds.) (2003) 559.

[147] J.-F. Guillemoles, O. Roussel, O. Ramdani, M. Benosman, C. Hubert, J. P. Fauvarque, A. Chomont, N. Bodereau, P. Panheleux, P. Fanouillère, J. Kurdi, N. Naghavi, P. P. Grand, L. Parissi, M. Ben-Farah, J. Connolly, S. Taunier, P. Mogensen, D. Lincot, O. Kerrec, The CISEL project: recent achievements, *Proc. 19th European Photovoltaic Solar Energy Conf., Paris, France, 7–11 June*

2004, W. Hoffman, J.-L. Bal, H. Ossenbrink, W. Palz, P. Helm (Eds.), WIP-Munich and ETA-Florence (2004) 1669.

[148] R. N. Bhattacharya, W. Batchelor, K. Ramanathan, M. A. Contreras, T. Moriarty, The performance of $CuIn_{1-x}Ga_xSe_2$-based photovoltaic cells prepared from low-cost precursor films, *Sol. En. Mat. Sol. Cells*, **63** (2000) 367.

[149] Vijay K. Kapur, Ashish Bansal, Phucan Le, Omar I. Asensio, Non-vacuum processing of $CuIn_{1-x}Ga_xSe_2$ solar cells on rigid and flexible substrates using nanoparticle precursor inks, *Thin Solid Films*, **431/432** (2003) 53.

[150] C. Eberspacher, C. Fredric, K. Pauls, J. Serra, Thin-film CIS alloy PV materials fabricvated using non-vacuum, particles-based techniques, *Thin Solid Films*, **387** (2001) 18.

[151] R. Klenk, S. Bakehe, R. Kaigawa, A. Neisser, J. Reiß, M. Ch. Lux-Steiner, Optimising the open-circuit voltage of $Cu(In,Ga)S_2$ solar cells – design and analysis, *Thin Solid Films*, **451–452** (2004) 424.

[152] T. J. Coutts, K. A. Emery, J. S. Ward, Modeled performance of polycrystalline thin-film tandem solar cells, *Prog. Photovolt. Res. Appl.*, **10** (2002) 192.

[153] S.-H. Wei, S. B. Zhang, A. Zunger, Effects of Ga addition to $CuInSe_2$ on its electronic, structural, and defect properties, *Appl. Phys. Lett.*, **72** (1998) 3199.

[154] S. Siebentritt, Wide gap chalcopyrites: material properties and solar cells, *Thin Solid Films*, **403–404** (2002) 1.

[155] W. N. Shafarman, P. D. Paulson, Losses in $CuInSe_2$-based thin film monolithic tandem solar cells, *Proc. 31st IEEE Photovoltaic Specialists Conf., Lake Buena Vista, USA, January 3–7, 2005*, IEEE, New York (2005) 231.

[156] S. Nishiwaki, S. Siebentritt, P. Walk, M. Ch. Lux-Steiner, A stacked chalcopyrite thin-film tandem solar cell with 1.2 V open-circuit voltage, *Prog. Photovolt. Res. Appl.*, **11** (2003) 243.

[157] K. Mitchell, C. Eberspacher, J. Ermer, D. Pier, Single and tandem junction $CuInSe_2$ cell and module technology, *Conf. Rec. 20th IEEE Photovoltaic Specialists Conf., Las Vegas, USA, 26–30 Sept. 1988*, IEEE, New York (1988) 1387.

[158] M. Symko-Davies, Status of high performance PV: polycrystalline thin-film tandems, *Proc. 31st IEEE Photovoltaic Specialists Conf., Lake Buena Vista, USA, January 3–7, 2005*, IEEE, New York (2005) 410.

7 Cadmium Telluride Thin Film Solar Cells: Characterization, Fabrication and Modeling

Marc Burgelman
University of Gent

7.1 INTRODUCTION

The development of thin film solar cells based on cadmium telluride (CdTe) has come a long and successful way from the introduction of a 6 % efficient CdS/CdTe cell in 1972 by Bonnet and Rabenhorst [1] to the present champion efficiency of 16.5 % obtained by researchers at NREL in 2002 [2]. During these three decades, our insight in the cell physics and operation principles has steadily grown, together with our mastering of deposition and fabrication technologies. Presently, two major manufacturers are producing CdTe based photovoltaic modules commercially: Antec Solar in Germany [3–5] and First Solar in the US [6]. The progress of CdTe cells and modules has been reviewed regularly [7–11], and an overview of the historical evolution of the CdTe cell and module technology has been given recently [12]. In this chapter, we will review thin film CdTe photovoltaics with some emphasis on the physics and modeling of the cell operation.

The commercial photovoltaic scene is now largely dominated by crystalline bulk silicon devices. There is presently no real alternative for single and multicrystalline silicon panels for terrestrial applications, when it comes to high performance. However, if photovoltaic electricity is to become a significant energy source, then the production of PV modules has to increase substantially in volume and to decrease in cost. Thin film solar cells have basic advantages over their crystalline counterparts concerning materials utilization, mass production and integrated module fabrication: this has been the driving force for their development since the early sixties. Of the many materials and cells studied, three material families have emerged and reached a mature status, and their commercial production has started up: (i) cells based on a CdTe absorber; (ii) cells based on absorbers of the Cu(In,Ga)Se_2 family and (iii) cells with amorphous silicon (a-Si) and microcrystalline silicon (μc-Si) or Si:Ge and Si:C alloys. Other cell materials and technologies are rapidly evolving, and constitute a third PV wave: thin film silicon, and various kinds of nanostructured solar cells, among which are photoelectrochemical solar cells and organic solar cells.

Cadmium telluride is a material that is particularly well suited for thin film photovoltaics [10, 13]. It has a direct bandgap $E_g = 1.45$ eV, which is well within the optimum range of

Thin Film Solar Cells Edited by J. Poortmans and V. Arkhipov
© 2006 John Wiley & Sons, Ltd

1.2 eV to 1.5 eV for maximum photovoltaic energy conversion (e.g. [14–18]). The bandgap of crystalline silicon and $CuInSe_2$ is at the low side; $Cu(In,Ga)Se_2$, CdTe, $CuInS_2$ and GaAs have an optimum bandgap; $CuGaSe_2$ and amorphous silicon have too high an E_g. Because of the high optical absorption coefficient (higher than a-Si, much higher than crystalline silicon), a few micrometers of CdTe is sufficient to absorb all the incident sunlight. As a consequence, a minority carrier diffusion length of the order of one μm is sufficient to allow all the generated carriers to be collected at the contacts: this greatly relaxes the materials quality requirements, so that polycrystalline layers with grains of the order of one μm can do the job. Also, nature has been benevolent to CdTe and other II–VI and related materials, e.g. $Cu(In,Ga)Se_2$, since the grain boundaries in the polycrystalline layers are not very electrically active, even without technological passivation steps.

Cadmium telluride is the only stable Cd–Te compound in the Cd–Te phase diagram, and it melts congruently. This advantageous property allows deposition of near stoichiometric CdTe films of device quality with a multitude of deposition technologies. On the other hand, CdTe does not lend itself to tailoring of the bandgap profile in the device, as can be done with $Cu(In,Ga)Se_2$ and with amorphous Si alloys. The high energies of the Cd–Te and the Cd–S bond, the extremely low solubility of CdTe and CdS compounds in water and the low vapor pressure of these compounds are advantages from the environmental point of view.

Other materials properties are less advantageous. Being a binary compound, the occurrence of native defects renders a precise control of the doping density difficult. This is *a fortiori* the case for ternary and quaternary compounds such as $Cu(In,Ga)Se_2$ and for amorphous materials. The interactions between these native defects and foreign elements can trigger self compensation reactions, and this renders impurity doping of CdTe difficult. These effects are more pronounced in CdTe than in e.g. $Cu(In,Ga)Se_2$. The difficulty to obtain a strong p doping in thin CdTe films is a distinct disadvantage of this material. The problem has to be relieved by special 'activation treatments' and by clever contacting schemes: these two issues are main subjects in CdTe solar cell research.

In this chapter we will treat: (i) the materials and cell concepts for CdTe based solar cells; (ii) the research areas and trends in CdTe solar cell research; (iii) the accomplishments and technology of CdTe solar cells and modules and (iv) the characterization and modeling of CdTe solar cells.

7.2 MATERIALS AND CELL CONCEPTS FOR CADMIUM TELLURIDE BASED SOLAR CELLS

In all common CdTe technologies, the deposition temperature or the annealing temperature is rather high (400 °C and above). As a consequence, all kinds of material interactions between the CdTe absorber and the other cell materials (substrate, window, buffer, contact) are possible. The material properties thus come only about after completion of the whole cell. This has two important consequences: (i) materials properties measured on a single CdTe layer on an inert substrate are possibly not relevant for a CdS/CdTe solar cell and (ii) it is difficult to measure the CdTe material properties on a complete cell, because the presence of the other layers will influence the standard characterization measurements, or even render them impossible. We will discuss here some properties of the materials used in CdTe photovoltaics. In view of the above remark, some criticism about the precise numerical values is in order.

7.2.1 Optical properties of cadmium telluride

There is some scatter in the value of the room temperature (300 K) bandgap energy E_g of CdTe reported in the literature: $E_g = 1.44$ eV [16–19]; $E_g = 1.464$ eV [20]; $E_g = 1.50$ eV [17, 21, 22]; $E_g = 1.51$ eV [20] and $E_g = 1.56$ eV [14]. A careful analysis of the absorption data by Mathew and Enriquez [23] shows that the optical absorption is due to a direct bandgap transition with $E_g^d = 1.487$ eV and an indirect transition between the band and a shallow localized level with $E_g^i = 1.408$ eV; a phonon energy $E_p = 21$ meV is involved in this indirect transition. Only the direct transition generates a free electron hole pair and thus is relevant for the photovoltaic operation. The direct bandgap varies almost linearly with temperature, and extrapolates to $E_g^d(0\,\mathrm{K}) = 1.61$ eV at zero Kelvin, so $\partial E_g/\partial T \cong -0.41$ meV/K [23].

In Figure 7.1, some absorption curves $\alpha(\lambda)$ of CdTe are shown. The curves from the standard data books of Adachi [21] and Palik [24] almost coincide. The peak seen in the Adachi curve around $\lambda = 820$ nm is due to the generation of an exciton; it is a matter of discussion whether this absorption contributes to the photovoltaic action at room temperature [25]. In cell modelling we adopt a $\alpha(\lambda)$ curve based on Adachi's data, but adapted around the band edge; the adaptations are based on measurements by Albin [26] and on Palik's data. Toušek *et al.* [27] have accurately measured the subbandgap absorption of chemical bath deposited CdTe layers with the constant photocurrent method (CPM). The resolution of this method is very high, but the results are specific for the sample they studied. Wood *et al.* [28] have given a series expansion of the complex refraction index $n^* = n + ik$ in powers of the wavelength λ. The curve in Figure 7.1 has been calculated from the given series for $k(\lambda)$ and from $\alpha(\lambda) = 4\pi k(\lambda)/\lambda$.

In an ideal solar cell of thickness d, all absorbed photons contribute to the light current. For each wavelength, this is a fraction $1 - \exp(-\alpha(\lambda) \cdot d)$ of the incident photons. Only photons

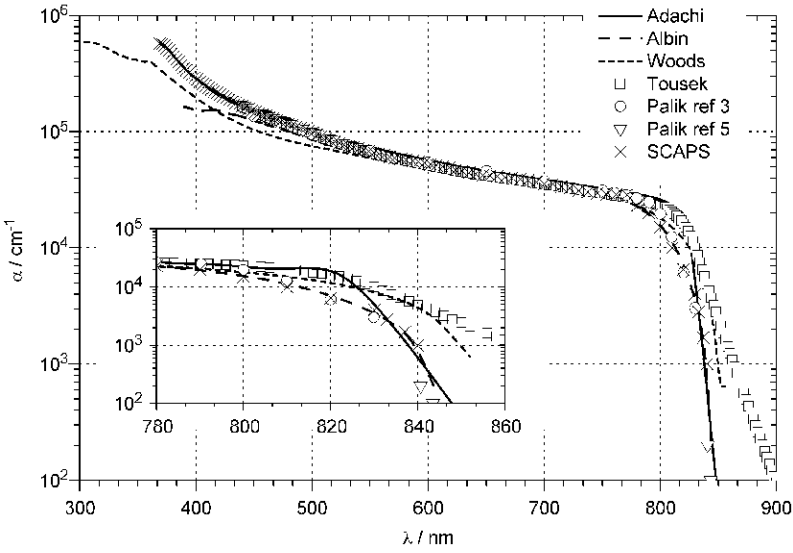

Figure 7.1 The optical absorption coefficient $\alpha(\lambda)$ of CdTe: some data from the literature. In the inset, a detail around the cut-off wavelength λ_g is given.

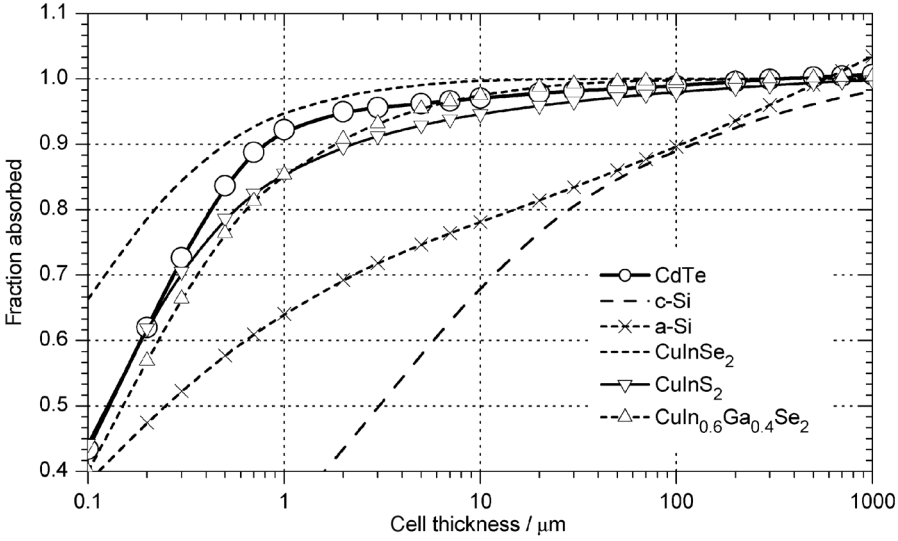

Figure 7.2 Fraction f of the useful photons that are converted to electrical current.

with $h\nu > E_g$ or $\lambda < \lambda_g \cong 1240\,\text{nm eV}/E_g$ can contribute to the current. Hence a cell can only convert a fraction f of the useful photons into electrical current:

$$f(d) = \frac{\int_0^\infty \left[1 - \exp\left(-\alpha(\lambda) \cdot d\right)\right] N_{ph}(\lambda)\ \mathrm{d}\lambda}{\int_0^{\lambda_g} N_{ph}(\lambda)\ \mathrm{d}\lambda} \tag{7.1}$$

Here $N_{ph}(\lambda)$ is the incoming photon flux with wavelength around λ (e.g. expressed in number of photons $\text{cm}^{-2}\,\text{s}^{-1}\,\text{nm}^{-1}$). In Figure 7.2 this fraction $f(d)$ has been calculated for illumination with the AM1.5G spectrum, and for some photovoltaic materials. It is clear that CdTe is very well suited for a thin solar cell absorber: a thickness of only 1 μm is sufficient to convert 92 % of the useful sunlight. A crystalline silicon solar cell needs to be 200 μm thick to reach the same value.

At the junction with CdS, mixed CdTe–CdS phases can be formed: a sulfur rich CdTe phase, $CdTe_{1-x}S_x$ with $x << 1$, in the CdTe absorber, and a tellurium rich CdS phase, $CdS_{1-y}Te_y$ with $y << 1$, in the CdS window. The bandgap $E_g(x)$ of the mixed phases depends parabolically on the composition x or y, and has a minimum value $E_g = 1.40\,\text{eV}$ at a composition of around 25 % (atomic) CdS in CdTe [26, 29]. This effect shifts the quantum efficiency of CdTe/CdS cells to longer wavelengths with a few tens of nm: around $\lambda = 520\,\text{nm}$, the $CdS_{1-y}Te_y$ mixed phase enhances the window absorption (this is a loss), and around $\lambda = 860\,\text{nm}$, there is enhanced absorption due to the $CdTe_{1-x}S_x$ mixed phase (this is a gain). Normally, the gain in the infrared does not compensate for the loss in the green region. Bandgap data on alloys of CdTe with other II–VI compounds, such as ZnTe, are found e.g. in [20, 28, 30].

7.2.2 Electrical properties of cadmium telluride

Some properties of CdTe relevant for the operation and modeling of the CdS/CdTe solar cells are shown in Table 7.1. There is a considerable scattering in the literature data on almost all electrical material properties, and the parameters in Table 7.1 should be considered as a guide only. The parameters which deal with doping and recombination are not real material properties, but they are specific for each deposition technology, if not for each individual sample. Some general properties and trends, relevant for the operation of CdTe photovoltaics are discussed below.

The rules of thumb for shallow dopants also apply to CdTe (Table 2): group III elements substituting Cd or group VII elements substituting Te act as shallow donors, whilst group I elements substituting Cd and group V elements substituting Te act as shallow acceptors [32–34]. The ionization energies of shallow acceptors increase with increasing atomic number: from 58 meV for Li to 263 eV for Au and from 56 meV for N to 92 meV for As. The donors in

Table 7.1 Some material properties of CdTe and CdS

Property	Symbol	Unit	Value CdTe	Ref.	Value	Ref.
Melting point	T_m	°C	1092		1750 (at 100 atm)	
Sublimation point	T_s	°C			980	
Density	ρ	$g\,cm^{-3}$	5.85		4.82	
Molecular mass	M	$g\,mol^{-1}$	240.01		144.47	
Crystal lattice			fcc (zincblende)		hexagonal (wurzite)	
	a	Å	6.480	[18]	4.136	[18]
	c	Å			6.713	[18]
Bandgap (300 K)	E_g	eV	1.45		2.42	
Electron affinity	χ	eV	4.28–4.5	[16]	4.5	[16]
Electron effective mass (relative)	m_e^*		0.09–0.11		0.165–0.25	
			0.14	[16]	0.15	[16]
					0.35	[18]
Hole effective mass (relative)	m_h^*		0.4–0.63		0.7 ||, 2.45–253 ⊥	
			0.37	[16]	0.8	[16]
					0.07	[18]
Effective density of states	N_C	cm^{-3}	$7.9\ 10^{17}$	[17]	$2.24\ 10^{18}$	
	N_V	cm^{-3}	$1.3\ 10^{19}$	[17]	$1.8\ 10^{19}$	
Electron mobility	μ_n	$cm^2\,V^{-1}\,s^{-1}$	1000–1200	[21]	400	[21]
Hole mobility	μ_p	$cm^2\,V^{-1}\,s^{-1}$	50–80	[21]	50	
Static dielectric constant (relative)	ε_s		10.2–10.5	[21]	10.21 E||c, 8.99 $E\perp$c	[21]
			10.36	[31]		
Optical dielectric constant (relative)	ε_∞		7.1–7.3	[21]	5.38E||c, 5.31	
			7.18	[31]	$E\perp c$	[21]
Refractive index	n		3.106 (550 nm)	[21]	2.57 (550 nm)	[21]
			2.996 (850 nm)		2.38 (850 nm)	

Table 7.2 Shallow dopants in CdTe

	Dopant	Site	Class
Donors	Al, Ga, In	Cd site	Group III elements
	F, Cl, Br, I	Te site	Group VII elements
	V_{Te}, Cd_i		Native defects
Acceptors	Li, Na, Cu, Ag, Au	Cd site	Group I and Ia elements
	N, P, As, Sb	Te site	Group V elements
	V_{Cd}		Native defects

Table 7.2 are shallower than the acceptors: their ionization energy is about 13 to 15 meV [33]. Divalent Cd and Te vacancies act as a shallow acceptor and donor, respectively.

Isoelectric elements, e.g. Zn at a Cd site, and S or Se at a Te site, do not seem to introduce an impurity level [33]. Other impurity elements act as deep donor or acceptor centers. Some data can be found in the literature [32, 33, 35].

The doping situation in CdTe is further complicated by the ability of native defects to form complexes, which can act as doping centers themselves, and possibly compensate for the impurity doping. The most prominent example in CdTe solar cells is the action of chlorine, which is usually introduced in the CdTe layer during the '$CdCl_2$ treatment'. A chlorine atom substituting a Te atom acts as a shallow donor, and hence becomes positively charged. It forms, however, a complex with a doubly negatively charged cadmium vacancy, and this negatively charged $\left(Cl_{Te}^{+} - V_{Cd}^{2-}\right)^{-}$ complex acts as a single acceptor. The effects of treating CdTe in a chlorine containing environment will be further discussed in Section 7.3.1. Another example relevant for CdTe photovoltaics is copper. When introduced in low concentrations, it occupies a Cd site, and this Cu_{Cd} acts as a shallow acceptor. When introduced in larger quantities, however, part of the copper will occupy an interstitial place, and this Cu_i acts as a donor, partially compensating the Cu_{Cd} acceptors. The compensation of a shallow acceptor by the creation of a shallow donor (or vice versa) releases an amount of energy almost equal to the bandgap E_g. Since CdTe has a larger bandgap than $CuInSe_2$ or $Cu(In,Ga)Se_2$, the tendency for self compensation is more pronounced in CdTe. Although high active doping densities, exceeding $10^{17}\,cm^{-3}$, were reported in the literature for impurity doping in CdTe crystals, it seems that a doping density of a few $10^{15}\,cm^{-3}$ is a practical limit in thin film CdTe solar cells. For a further treatment of self compensation and impurity doping in CdTe, we refer to the literature [36–40].

The recombination properties of CdTe also strongly depend on the preparation method, and can vary from sample to sample. For photovoltaic operation, the recombination of minority carriers in the absorber is relevant. Thus, in CdTe based solar cells, the electron life time τ_n and the electron diffusion length L_n are the relevant parameters. The lifetime τ_n can be estimated from e.g. photoluminescent (PL) decay measurements and from decay of the open circuit voltage V_{oc} after shutting down the illumination. The diffusion length L_n can be estimated from electron beam induced current (EBIC) measurements, or from an analysis of the measured spectral response $QE(\lambda)$ (e.g. [41]). There are however difficulties in interpreting τ_n and L_n data from the literature. In some measurements, the excitation conditions (e.g. high injection in PL and EBIC) greatly differ from the normal operation conditions in a solar cell (low injection). Also the interpretation of measurements in solar cells is difficult, as the measurement can be

influenced by two-dimensional effects in the grains of the polycrystalline material [42]. In that sense, it is better to speak of the 'apparent diffusion length' L_{napp}. Values for L_{napp} in the range 0.2 to 4 μm have been reported, corresponding to a lifetime in the nanosecond range or below.

7.2.3 The Buffer material: cadmium sulfide

The partner of choice for the cadmium telluride absorber is cadmium sulfide (CdS). In early CdS/CdTe solar cells, the CdS layer was the only transparent layer, and consequently was called the 'window layer' (that is, for wavelengths longer than about 520 nm). In all present CdS/CdTe cells, the window layer is a transparent conductive oxide (TCO), e.g. SnO_x, and the CdS layer is made much thinner; it is now commonly named the 'buffer layer'.

The buffer has to fulfil several requirements:

1. Crystallography/morphology: the buffer or the window/buffer structure serves as an underlayer for absorber growth. This begs for a rather thick buffer with large grains. Also, the buffer layer should be compact, as voids can cause a shunt between the absorber and the front contact. A minimum thickness of a few tens of a nanometer seems to be required for this.

2. During the CdTe deposition or postdeposition treatment at high temperature, interdiffusion between CdS and CdTe occurs. The buffer should be thick enough so as not to be completely consumed. Interdiffusion is promoted by the $CdCl_2$ treatment (see Section 7.3.1). It has both positive and negative effects to the cell's operation. When the interdiffusion is strong enough (penetration a μm or more), the light current is decreased (Section 7.2.1). In screen printed CdTe cells, the $CdTe_{1-x}S_x$ formed by interdiffusion is compact, and has better crystallographic properties than the porous pure CdTe layer on top of it [43]. Another projected advantage is connected with interface states, see next item.

3. Electrical/Crystallography: the lattice mismatch between the CdS buffer and the CdTe absorber gives rise to interface states with density N_i, which can adversely affect the cell performance: $N_i \propto \frac{1}{d^2_{\mathrm{CdS}}} - \frac{1}{d^2_{\mathrm{CdTe}}} = \frac{1}{a^2_{\mathrm{CdS}}} - \frac{2}{a^2_{\mathrm{CdTe}}}$, where d is the distance between two adjacent atoms in the interface plane. In the hexagonal CdS, this is the (0,0,1) plane, and $d = a$; in the cubic CdTe, this is the (1,1,1) plane, and $d = a/\sqrt{2}$. With the values in Table 7.1, $N_i \cong 4\,10^{13}\ \mathrm{cm}^{-2}$. In spite of the large lattice mismatch, the CdS/CdTe combination performs well without any interface passivation steps. Therefore there have been hardly any explorations for a better matched buffer material. It has been claimed that a narrow interdiffusion range (e.g. 100 nm) between CdS and CdTe allows for a smoother transition between both lattices, which should relax the surface states. However, the same number of bulk recombination states will appear, distributed in the 100 nm transition region. It depends on the details of the recombination profile in the near interface region whether the net effect will be advantageous or not.

4. Electrical: the energy bands of the buffer and the absorber should be more or less matched. The misalignment of the conduction bands (CB) is determined by the electron affinity χ of both materials (Figure 7.3): $\Delta E_{\mathrm{C}} = E_{\mathrm{C}}^{\mathrm{CdTe}} - E_{\mathrm{C}}^{\mathrm{CdS}} = \chi^{\mathrm{CdS}} - \chi^{\mathrm{CdTe}}$. If ΔE_{C} is too positive, there is a 'cliff' in the band diagram: the CB of CdTe is above the CB of CdS at the junction; this decreases the open circuit voltage V_{oc}. If ΔE_{C} is too negative, there is a 'spike' in the band diagram: the CB of CdS is above the CB of CdTe at the junction; this decreases the short-circuit current density J_{sc}. The mismatch, however, is not critical: a value of $|\Delta E_{\mathrm{C}}| < 0.3\,\mathrm{eV}$

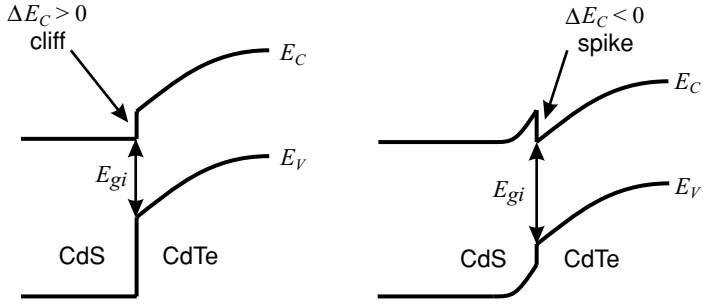

Figure 7.3 Definition of a cliff ($\Delta E_C > 0$, left) and a spike ($\Delta E_C < 0$, right) in the alignment of the conduction band at the CdS/CdTe interface. The interface bandgap E_{gi} is also indicated (see Section 7.5.2).

can be tolerated [44]. Common values of the electron affinity of the pure materials are $\chi^{CdS} = 4.5$ eV and $\chi^{CdTe} = 4.28$ eV, giving rise to an allowable small cliff of 0.22 eV. There is, however, much scatter in the χ values reported in the literature. Recent work by the group at Darmstadt University [45] reports a small $\Delta E_C \cong 0.03$ eV in real CdS/CdTe structures.

5. Electrical: if the hole diffusion length L_p in CdS were of the order of the buffer layer thickness, the light absorbed in the CdS layer could contribute to the light current. It is still a matter of debate whether this is the case or not. Commonly one assumes that L_p is very small, and that light absorbed in the CdS is lost. Some other electrical properties of CdS are listed in Table 7.1.

6. Electrical: in the older screen printed cells by Matsushita [46], no TCO layer was applied: the CdS layer is the only window layer, and should be conductive enough to draw the current laterally away to the contacts. The sheet resistance of the CdS layer should not exceed a few tens of $\Omega_{\square}$. This calls for a rather thick layer (screen printed and sintered CdS layers are typically 30 μm thick), and for doping the CdS with In or Ga. If a TCO window is present, the requirements on the lateral conductivity of CdS are almost completely relaxed. Hence, the TCO/CdS/CdTe structure now is generally adopted.

7. Optical: absorption in the buffer layer is to be avoided. The buffer should be as thin as possible, or a wider bandgap material should be chosen. However, replacing the CdS layer by CdZnS, ZnS, ZnSe, SnO_2 and other wide gap n type materials has not been successful. A CdZnS/CdS bilayer buffer is studied in [47].

In Figure 7.4 the optical absorption coefficient $\alpha(\lambda)$ of the materials forming a CdTe solar cell is plotted in the short wavelength region. From this, the optical loss in the buffer layer can be calculated from:

$$QE_{\text{ideal}}(\lambda) = \exp(-\alpha_{TCO} d_{TCO}) \cdot \exp(-\alpha_{CdS} d_{CdS}) \cdot (1 - \exp(-\alpha_{CdTe} d_{CdTe})) \qquad (7.2)$$

Equation (7.2) expresses that the light absorbed in the TCO and in the CdS buffer is completely lost, and that the light absorbed in the CdTe is completely converted to electric current. Closed CdS layers with thicknesses down to 20 nm can be made with chemical bath deposition (CBD). This is the technique of choice for the buffer of $Cu(In,Ga)Se_2$ cells. However, CdTe cells need a thicker CdS layer, as explained above. This is a direct consequence of the cell concept: in CdTe

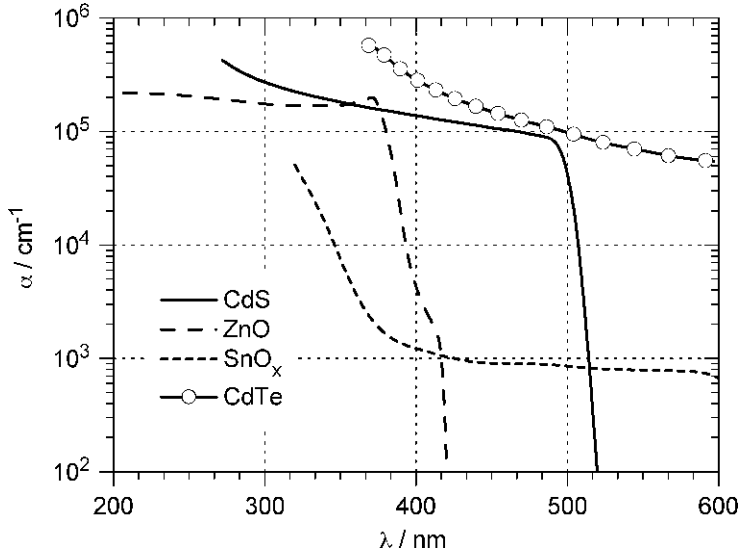

Figure 7.4 Optical absorption coefficient of the absorber, buffer and window layers in a CdTe solar cell. The data for CdTe, CdS and ZnO are from [21], the data for SnO_x are from [48].

cells, the buffer is exposed to high temperatures during the deposition of the absorber, whereas in Cu(In,Ga)Se_2 cells, the buffer is deposited at low temperature on top of the absorber. For compatibility with the CdTe deposition technique, a rather thick layer of CdS (100–300 nm) is deposited with close space sublimation (CSS). Figure 7.5 shows that this technological choice causes a reduced response in the 350–500 nm wavelength region, corresponding to a light current loss of a few mA/cm^2 [49]. A comparison of CBD CdS with CSS CdS was given by Albin [50]: CBD CdS has smaller grains, lower absorption, are less crystalline, show a range of E_g values, contain more oxygen and better prevent interdiffusion for the same thickness.

7.2.4 Window materials for cadmium telluride based solar cells

The role of the window is evidently to transmit light to be absorbed in the CdTe layer. Therefore a wide bandgap, low scattering material is preferred. All TCOs show reduced transmittance in the infrared, due to free carrier absorption. In CdTe cells, only light with $\lambda < 860$ nm is converted, and free carrier absorption is not an issue. This is, however, the case in narrow bandgap solar cells such as $CuInSe_2$ and Cu(In,Ga)Se_2, where longer wavelengths have to be transmitted through the window.

To draw the light current laterally to the contacts, the sheet resistance of the TCO should be around 10 Ω, or smaller. The thickness of the TCO is thus a trade-off between high transparency and low resistance. Normally, the TCO should be doped. The TCO layer also should be thick enough to constitute a barrier against diffusion of unwanted species from the substrate (e.g. Na from soda-lime glass) or from the TCO itself. For this reason, the TCO is often implemented as a bilayer system: a doped, conductive layer, separated by a diffusion barrier from the CdS buffer. The diffusion barrier can consist of the same TCO, but not intentionally doped, or a

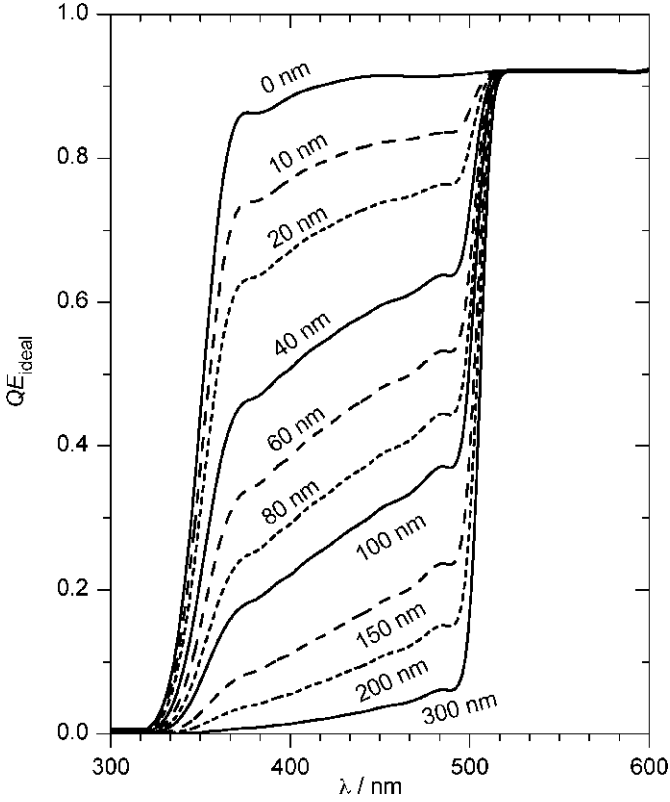

Figure 7.5 Ideal spectral response $QE_{ideal}(\lambda)$ of a CdTe solar cell as a function of the CdS buffer layer thickness, calculated with Equation (7.2). The other layers have thickness $d_{TCO} = d_{CdTe} = 1$ μm. The TCO is SnO_x.

different TCO. In Table 7.3 some properties of popular TCO materials are listed: indium tin oxide (ITO) possibly doped with fluorine (F) or antimony (Sb), tin oxide (SnO_2 or SnO_x) possibly doped with F or Sb, zinc oxide (ZnO) possibly doped with boron (B) or aluminium (Al), and cadmium stannate (Cd_2SnO_4, sometimes also written as $CdSnO_3$). A commonly used system is soda-lime glass/ITO/SnO_2/CdS [10]. The window structure of the record CdTe cell was borosilicate glass/Cd_2SnO_4/Zn_2SnO_4/CdS [2].

7.3 RESEARCH AREAS AND TRENDS IN CADMIUM TELLURIDE SOLAR CELLS

7.3.1 The activation treatment of cadmium telluride

The treatment of CdTe and other II–VI materials with chlorine containing species has been studied for a long time. In the late eighties, this treatment, with $CdCl_2$ as the chlorine source, was applied to CdTe based solar cells [55] and was quickly adopted by the research community as an indispensable and somehow magic recipe for the fabrication of CdTe solar cells [56].

Table 7.3 Some properties of window materials

Property	Symbol	Unit	ITO	SnO_x	ZnO	Cd_2SnO4
Bandgap	E_g	eV	3.7 [22] 3.6 [16]	3.7 3.5 [22] 3.8 [18]	3.35 [14, 22] 3.2 [16]	2.9 [18]
Electron affinity	χ	eV	4.2–4.5 [22] 4.1 [16] 4.3–4.4 [18]	4.4–4.5 [2] 4.8 [22] 4.8–4.9 [18]	4.8 [22] 4.2 [16, 18]	4.55 [18]
Dopants			F	Sb, F [18]	B, Al, In	H, Li, Zn [18]
Sheet resistance	R_{sq}	Ω	3–5 [54]	3–8 [2] 7–10 [51] 6–15 [54]	6–15 [54]	2.6 [2] 16 [53]
Resistivity	ρ	Ω cm	$2\ 10^{-4}$ [52]	$3–8\ 10^{-4}$ [2] $3.5–5\ 10^{-4}$[51]		$1.3\ 10^{-4}$ [2] $3\ 10^{-4}$ [53]
Transparency	T	%	95 [54]	90 [51, 54]	90 [54]	80 [53]

In its original form, the $CdCl_2$ treatment consisted [55] of dripping a solution of $CdCl_2$ in methanol onto the glass/TCO/CdS/CdTe substrate, letting the methanol solvent volatilize and heat treating for a short time (e.g. 15 min) at moderate temperature (e.g. 450 °C) in air. Meanwhile, the technique has been improved and made more suitable for mass production, by using a thin solid $CdCl_2$ film, applied by evaporation [57] or by CSS [3], as the source of chlorine. Other variants have been studied, including the use of gaseous $CdCl_2$, of other Cl containing gases (Cl_2, HCl [58, 59]), other cadmium halogenides ($CdBr_2$, CdI_2), and other Cl containing salts ($MnCl_2$ [60] NaCl [61]), other ambient gasses for the heat treatment (vacuum, inert gas, varying oxygen content [62]). The effects of this treatment has been investigated intensely, see e.g. [63]. We briefly summarize:

1. Grain growth occurs when the initial grains are small (of the order of 1 μm) but not when the initial grains are large (> 1 μm). As CdTe produced with CSS, has fairly large grains as-deposited, usually no further grain growth is observed upon $CdCl_2$ treatment, though it has been reported occasionally [64].
2. The internal crystallographic structure of the grains improves in all cases (disappearance of subgrain structure).
3. Intermixing between CdS and CdTe at the interface can be promoted. This effect of the $CdCl_2$ treatment has been documented extensively, e.g. [65–68].
4. The p type doping is established (type conversion) or improved; the minority carrier lifetime τ_n is improved.
5. The density of deep electronic states in the bulk or at the interface can be reduced [64], but other deep states can be introduced [69, 70]. The mechanisms of introducing or annealing out deep states are related with the creation of Cd vacancies during treatment, and interaction with chlorine and oxygen.
6. Overtreatment can cause a V_{oc} loss due to the introduction of deep recombination centers [69, 71]. It can also result in loss of adhesion [2].

The precise mechanisms of the $CdCl_2$ treatment are not yet fully clear. A eutectic mixture of CdTe and $CdCl_2$is formedwith a melting point of 505 °C, well below that of pure $CdCl_2$ (568 °C). The presence of a liquid phase and the mechanisms of liquid phase sintering cannot be invoked for a normal treatment temperature lower than 500 °C. Gas phase material transport has been postulated instead, possibly facilitated by an intermediate volatility compound such as $TeCl_2$ [72]. Recently, Hiie [73] found that the presence of the oxidised species $CdTeO_3$ lowers the melting point of the CdTe–$CdCl_2$ eutectic down to 455–480 °C. It is now commonly agreed that the administering of chlorine to the CdTe solar cell is indispensable. If it is not during a post deposition 'activation treatment', it is during CdTe deposition (e.g. $CdCl_2$ particulates added to the CdTe slurry in screen printing; use of chlorine salts as a source in electrodeposition).

It is clear that these effects more or less thoroughly modify the set of input parameters to be used in numerical simulations of $CdCl_2$ treated solar cells. The doping and recombination properties of the cell, especially, are affected by the activation treatment. Hence, a detailed characterization of the shallow and deep states is needed: doping type, concentration profile, energy levels or distributionand capture cross-sections.

7.3.2 The back contact structure

There are fundamental material reasons why finding a stable, ohmic contact to the CdTe layer in a CdTe–CdS thin film solar cell constitutes a scientific and technological challenge: CdTe is a p type material with a rather large bandgap of $E_g = 1.45$ eV, and it is difficult to give it a high doping density. The property that determines the contact behaviour is the contact barrier Φ_b for holes; it is measured between the hole Fermi level and the valence band edge at the contact. The standard metal semiconductor theory [14, 74] calculates the contact barrier when a very narrow native oxide of thickness d_i and dielectric constant ε_i is inserted between the metal and the semiconductor; surface states with energy density D_{ss} are present in the interface gap, with a spread in energy between $E_V + \Phi_0$ and E_C; the parameter Φ_0 is a fitting parameter, whose physical significance will become clear later. If the doping density is not too high, the barrier is given by:

$$\Phi_b = \left(\chi + E_g - \Phi_m\right) \frac{C_i}{C_i + C_{ss}} + \Phi_0 \frac{C_{ss}}{C_i + C_{ss}} \tag{7.3}$$

Here C_i is the capacitance per unit area of the native oxide $C_i = \varepsilon_i \varepsilon_s / d_i$, and C_{ss} is the capacitance of the surface states $C_{ss} = q^2 D_{ss}$. When no such native oxide are present ($d_i \to 0$ or $C_i \to \infty$), or if no surface states are present ($C_{ss} \to 0$), this leads to the ideal approximation:

$$\Phi_b = \chi + E_g - \Phi_m \quad \text{if} \quad C_i \to \infty \text{ or } C_{ss} \to 0 \tag{7.4}$$

Even with a quite common value of 4.3 to 4.5 eV for the CdTe electron affinity χ, obtaining a contact barrier lower than 0.5 eV would require a contact metal with a high work function Φ_m exceeding 5.5 eV, which cannot be reached if one excludes noble metals for economic reasons.

The other extreme approximation is valid when $C_{ss} \to \infty$ or $C_i \to 0$: the contact barrier is then only determined by Fermi level pinning at the lowest interface states level, thus at $E_V + \Phi_0$:

$$\Phi_b = \Phi_0 \quad \text{if} \quad C_i \to 0 \text{ or } C_{ss} \to \infty \tag{7.5}$$

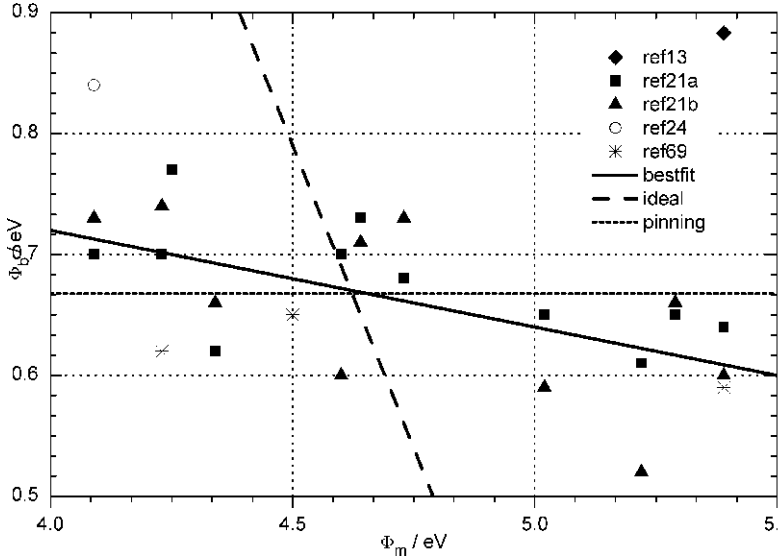

Figure 7.6 Contact barrier of various metals to n and p type materials (source: Ponpon [75]; the reference numbers in the legend refer to [75]). The solid line represents the model from Equation (7.3), with $C_i/(C_i + C_{ss}) = 0.08$ and $\Phi_0 = 0.63$ eV; the dotted line represents the ideal model from Equation (7.4); the dashed line represents the ideal approximation from Equation (7.5), with $\Phi_0 = 0.67$ eV.

In many materials, Φ_0 is between one third and one half of the bandgap. This Fermi level pinning mechanism thus gives rise to a rather high contact barrier, independent of the contact material. The contact barrier of various metals on n and p CdTe was studied by Ponpon [75], and is shown in Figure 7.6 for p CdTe. Recently, contact barriers on CdTe and ZnTe thin films were determined by Kraft *et al.* [76]. As is obvious from Figure 7.6, the barrier to p CdTe is always rather high, and it can be influenced only to a limited extend by a proper choice of contact material. Also, the contact barrier can only roughly be predicted from Equation (7.3) with proper constants. An accurate value should be determined for each contact experimentally.

The material properties of CdTe do not favour a large choice of acceptable contact metals. The contact properties can be improved if the CdTe layer is heavily doped. However, obtaining a doping density exceeding $10^{16}\,\mathrm{cm}^{-3}$ in CdTe also is a problem, since CdTe is prone to self compensation. This is related to the rather high value of the bandgap, to the introduction of chlorine by the activation treatment and to many possible interactions and complex formations between impurities and native defects in CdTe (see sections 7.2.2 and 7.3.1).

The contact should not only be low resistive, it should also be stable. That means that no impurities should diffuse from the contact to the cell during the cell's operation (only diffusion at high temperature during the cell fabrication can be tolerated), and the contact material should not chemically interact with the CdTe absorber. When a bilayer or multilayer structure is used, no layer should interact with its neighbors.

Thus, making a good, stable contact to CdTe is an art in itself, and it comprises several steps: surface pretreatment (e.g. etching in bromine–methanol or in nitric–phosphoric acids), control of diffusion of extrinsic dopants from the contact or buffer layer to the CdTe layer, the application of buffer layers to prevent unwanted diffusion or reactions. Copper containing contacts initially perform well (copper forms a shallow acceptor in CdTe), but their long

term performance can be a problem [77], as the copper under certain circumstances diffuses through the CdTe layer and accumulates at the CdS junction and in the CdS layer. Diffusion of impurities, copper and otherwise, from graphite contacts and its effect on cell doping and stability, was studied e.g. in [78–83]. Stable contact structures containing no intentional copper were extensively explored. The chemical stability between CdTe, several buffer layers and contact materials was studied e.g. in [11] and [84]. Finally, a stable copperless contact structure was defined in [85]: CdTe/etching/Sb_2Te_3/Mo.

The presence of a contact barrier affects the I-V characteristics of a CdTe thin film solar cell in a characteristic way (see further, Figure 7.11): the I-V curves show a kink in the forward biased quadrant, which is commonly called 'roll over' of the I-V curves [86]. The main effects on the cell performance are a decrease in fill factor FF when Φ_b exceeds about 0.45 eV, and the associated efficiency loss [86, 87]. A useful approximate formula for the efficiency loss was given in [87]:

$$\eta = \eta_0 \left(1 - \frac{kT}{qV_{oc}} \ln\left(1 + \frac{J_L}{J_c}\right)\right) \tag{7.6}$$

where η_0 is the efficiency if no contact barrier were present, J_L is the light current density, and J_c is the saturation current density of the contact Schottky barrier; J_c is thermally activated with energy Φ_b. There is hardly any efficiency loss to fear as long as the contact saturation current is lower than the light current.

Several secondary effects are reported:

(1) A minority carrier (electron) current can be present at the CdTe back contact, giving rise to 'cross over' of the I-V curves [87]; in special cases, all I-V curves of a set of experiments can cross over in one single point [88]; these effects are favoured by red light illumination, by thin cells (< 5 μm) [89] and by a large apparent electron diffusion length, which can be caused by two-dimensional effects [88].

(2) When the CdTe doping at the back contact is sufficiently high, the hole current through the contact is described by drift and diffusion (e.g. [14] p 258) through the space charge layer (SCL); this effects weakens the aspect of the roll over, and eventually the room temperature I-V curve looks as if there is only a weak barrier, or even no barrier at all [90].

(3) Also, high doping at the contact makes the apparent barrier dependent on bias voltage and illumination [90]. Though these effects render the determination of the barrier from room temperature I-V measurements doubtful, they generally influence the fill factor and the efficiency in a positive way.

7.3.3 Environmental issues

A treatment of cadmium telluride solar cells cannot be complete without a paragraph on health and environmental issues. This is true for any thin film or bulk solar cell [91], as it is for any new industrial product. Due to some sensitivity of the general public, the subject has been studied intensively, and we strongly recommend the interested reader to consult [92] and the references therein. A few facts constitute the leitmotiv: cadmium is a by-product of zinc production, and as such is present in huge quantities and has many large scale industrial applications; cadmium is toxic, however insoluble Cd compounds are much less toxic; all measures should be

taken – and are taken – to prevent cadmium entering in the ecosystem, and expose humans to ingestion or inhalation. The risk assessment and prevention distinguishes between four stages in the life-cycle of potentially hazardous materials in the industrial product [93–98]: (i) the mining and production of the CdTe and CdS material; (ii) the production of solar modules; (iii) the active life (>20 year) of the solar module in a PV installation; (iv) the dismantling, disposal, recycling of the modules after their lifetime.

The toxicity of some solar cell materials is reviewed in [99]. As little information is available on the compound CdTe, the toxicity of CdTe is inferred from the parent element Cd. It is accepted that insoluble, low volatility compounds such as CdS and CdTe are less harmful by ingestion. Therefore the US National Renewable Energy Laboratory (NREL) and the Brookhaven National Laboratory BNL) argue for a toxicological investigation of the CdTe compound itself [100]. The major zinc ores contain about 0.25 % Cd, hence a few tens of thousands of tons of Cd are produced annually [92]. If this Cd is not industrially processed, it has to be disposed of as hazardous waste. More than half of the Cd is used in rechargeable batteries, the rest is applied in pigments, plastic stabilizers, plating, soldering, etc. A GW/yr scale CdTe PV production would take up about 1 % of the Cd consumption only.

The health and environmental aspects of CdTe PV production were well documented by the leading production companies First Solar [101] and Antec [4]. Handling and processing potentially hazardous materials is not an uncommon industrial activity at all. As with all other industrial activities, CdTe PV is subject to safety laws and regulations. Careful design of the plant and tight control of the production equipment, permanent monitoring of the workers environment and possibly medical monitoring of the personnel are key points. Though not legally required for the exposure levels occurring in the plant, First Solar has carried out medical monitoring of the personnel [101], and all blood and urine Cd levels measured were way below the threshold concern levels. It appears to be technically and economically possible to design and operate a factory with zero Cd emissions [10].

The main perceived risks during the active lifetime of a solar panel are leaching out of broken modules and fire hazards. First results are that in typical residential fires, where a temperature of 800–1000 °C is reached, no Cd compound is released, due to the low vapour pressure of CdTe and CdS at these temperatures, but that these compounds are encapsulated in the molten glass instead [102]. Leaching of hazardous materials from crushed CdTe and CIGS modules was also investigated [103], however, the concentrations measured in all scenarios were below the limit or tolerable concentrations.

According to current laws, end-of-life or broken modules pass the leaching criteria for nonhazardous waste. However, disposal of such modules (CdTe as well as others) in landfills is not a scenario that is promoted by any PV actor. Instead, recycling schemes have been set up for used PV modules, including broken modules or fragments from manufacturing. These schemes include scraping, crushing, melting and regeneration of materials that will reenter in the production lines [10].

7.3.4 Other research areas and trends

7.3.4.1 Purity: ‘just pure enough’

Impurities are always present, even if not intended. They can originate from the source materials, from processing, e.g. contamination with evaporation sources, vacuum chamber walls or

components, (electro)chemical deposition baths, handling and storage in general and from the other solar cell materials (substrate, cell layers and encapsulation materials). So even if most labs use a CdTe source material of nominally 5N or 6N purity (that means a relative amount of impurities below 10^{-5} or 10^{-6}), it is not guaranteed that the CdTe layer in the final cell is anywhere near as pure. Usually one finds contaminants in huge quantities, in the 10^{17}–10^{19} cm^{-3} range [11]. These concentrations are far above the electrically active concentrations; this can be due to self compensation. There is as yet no black and white list of malign and benign impurities. Impurity is a substantial element of production cost and control. The goal 'just pure enough' is worth devoting substantial research to.

7.3.4.2 Cell thickness: thinner cells

In present production, CdTe is too thick: 5 to 10 μm, whereas 1–2 μm should suffice for the cell operation, though really thin cells are expected to suffer a little bit from reduced response in the infrared. The actual cell thickness is a disadvantage for materials usage and deposition speed, thus production cost. Also, the environmental cost is higher than necessary. Unfortunately, thin or porous films tend to decrease the production yield, especially when wet etching processes or treatments are present. Thus when the production technique does not yield compact, closed films, a minimum thickness is required for technological reasons. Some experimental work on thin absorber films has been done [62, 104]. The influence of CdTe thickness for ideal, compact cells has also been addressed by modeling, e.g. [89].

When the CdTe thickness is further reduced to the 100 nm range and below, a planar cell concept does not allow absorbing a substantial part of the light in the CdTe. Cells with an extremely thin absorber (ETA cells) use a porous window material, usually TiO_2, and an extremely thin CdTe layer penetrating into the TiO_2 [105–107].

7.3.4.3 Grain boundaries

A general account of possible grain boundary effects is given e.g. in [17]. The grain size in polycrystalline CdTe solar cells depends on technology, but is of the order of 1 μm. It is thus comparable to the various characteristic lengths of a solar cell: absorption depth $1/\alpha$, diffusion length L_n, depletion width W. Hence, an influence of the grain structure on the cell performance is to be anticipated. The quantitative influence of the polycrystalline nature of CdTe cells was estimated by Sites *et al.* [108], who compared single crystalline GaAs with polycrystalline CdTe. Both materials have the same band gap $E_g = 1.45$ eV, and have thus, in principle, the same photovoltaic potential. However, the efficiency span between the best GaAs cell (25.7 %) and the best CdTe cell (16.5 %) is 9.2 %, and between half and two thirds of that difference is ascribed to polycrystallinity. On the other hand, polycrystalline CdTe cells perform remarkably well when compared to their single crystalline counterparts (they are even better). These intriguing observations have motivated ample research on the subject, which was recently boosted with a dedicated Workshop [109].

Several effects can cause distortions in the energy band diagram around a grain boundary (GB): charged interface states, reduced or enhanced doping in the interior of the grain close to the GB, diffusion to and segregation at the GBs of impurities, material modifications at the GB. It is not surprising that there is quite some scatter in the literature reports, as there can be a

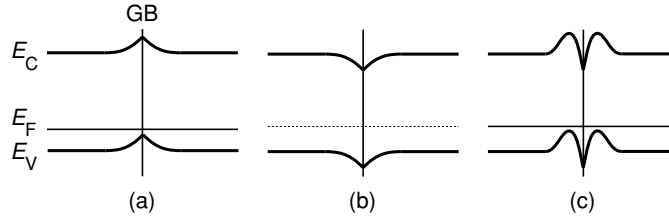

Figure 7.7 Energy bands crossing a grain boundary (GB) in CdTe: some possible situations. (a) Barrier for electrons, accumulation of holes at barrier; (b) barrier for holes: depletion of holes at barrier; (c) double barrier: barrier for electron and for holes, depletion of holes at barrier.

very large sample-to-sample variation due to technological details. Grain boundaries can under certain circumstances be preferred paths for diffusion of all kind of species, including Na from the substrate, In from the TCO window, S from the CdS bufferand Te, Cu and Sb from the contact structure (see previous sections, and [110, 111]). The discussion of the electrical effect of the GBs on the final cell characteristics is schematized in the energy diagrams of Figure 7.7. In Figure 7.7a, the GB constitutes a barrier for the minority carriers, and accumules majorities. As a consequence, there is enhanced hole conduction and decreased electron recombination in the GB. Such band structure was inferred in [112–115]. However, the structure of Figure 7.7b, with depleted GBs, which form a barrier for the majority holes, has been inferred from R-EBIC measurements in undoped CdTe; near to Te inclusions, the band diagram was as in Figure 7.7a [116]. Direct evidence for depleted grains (Figure 7.7b) was found by capacitance scanning microscopy [117]. Both opposing viewpoints are reconciled by Woods *et al.* [112, 113] who postulated a double barrier, one for holes and one for electrons, from frequency dependent conductance measurements (Figure 7.7c). Structures where the GB is constituted of another material, and hence has a bandgap differing from the bulk E_g are not considered in Figure 7.7. Applying simple rules of thumb, the structures in Figure 7.7 a and c are thought to be beneficial for photovoltaic operation, as they 'passivate' the GB against electron recombination. The structure in Figure 7.7b would lead to enhanced GB recombination, and thus be unfavorable. However, the details of electron and hole density, recombination and transport are very complicated, and strongly depend on the GB barrier height and the two-dimensional geometry (transverse or longitudinal GB). An original view of Visoly-Fisher [118], where the GBs in Figure 7.7b (but with a stronger band bending) are low recombination pathways of enhanced electron transport, needs quantitative verification.

7.3.4.4 Advanced cell structures and applications

The CdTe solar cells discussed so far have the 'superstrate configuration' (Figure 7.8). For applications in space, the power-to-weight ratio becomes an important figure of merit, and the massive glass substrate should be replaced by a thin foil. The superstrate configuration can be maintained when a transparent plastic foil is used; however, the plastic material is then exposed to the high CdTe processing temperature. A metal foil can be used in a 'substrate configuration'. The problems with the plastic superstrate were solved by the group at ETH-Zürich by using a 10 μm thin spin coated polyimide film, combined with a lift off technique from a reusable glass substrate; an efficiency of 11.4 % was obtained [129, 130]. This advanced cell concept

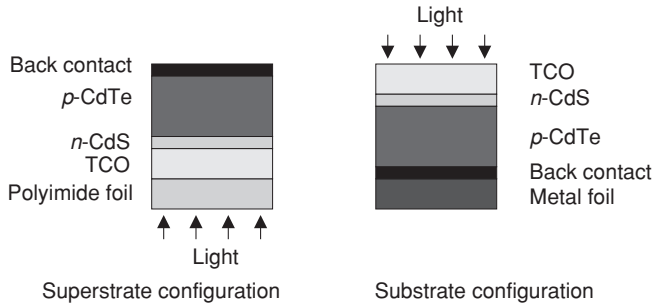

Figure 7.8 CdTe solar cells with a superstrate configuration (left) and with a substrate configuration (right).

was developed and tested for applications in space; also applications in building integrations are possible.

Thin film CdTe cells are very radiation resistant [131, 132]: somewhat better than CIGS, and significantly better than crystalline GaAs or Si bulk cells. A simple explanation for this is that defects introduced by the electron and proton radiation only start degrading the cell's performance when they begin outnumbering the defects already present in the as-made cells. The performance of bulk crystalline cells relies on a very high minority carrier diffusion length: it should be a factor of 100 higher than in thin- film cells, thus the trap concentration should be 10^3 to 10^4 times lower than tolerable in thin film cells. As a consequence, thin film cells only begin to degrade at a total fluence which is orders of magnitude higher than crystalline Si or GaAs cells. A comparison of the radiation degradation of different materials is given in Figure 7of [132].

Further technological development of the back contact is underway. By special CdTe surface treatments, an ohmic contact of an n^+-type TCO on p type CdTe could be realized [133]. This cell structure has two transparent contacts; applications as a bifacial cell or as a component of a tandem cell are envisaged. Other work aims to replace the wet etching step in the present cell technology (the CdTe surface treatment before depositing the contact structure) by dry, vacuum based processing [134]. Completely 'dry' cells were realized recently [135].

7.4 FABRICATION OF CADMIUM TELLURIDE CELLS AND MODULES

7.4.1 Deposition methods for cadmium telluride based solar cells

7.4.1.1 Close spaced sublimation and related techniques

Today's two leading CdTe PV manufacturers, Antec and First Solar, use a sublimation technique for the deposition of the CdTe absorber. Antec uses close spaced sublimation (CSS) to deposit about 0.1–0.2 μm of CdS and about 5–10 μm of CdTe sequentially [10]. In the CSS technique, the source and the substrate are placed at a short distance of each other (1 mm to a few cm, depending on the size) in a rough vacuum (0.1 to 1 Pa or 10^{-3} to 10^{-2} mbar). The source and the substrate are heated to a high temperature (in the 500 °C range), the source being at a slightly higher temperature than the substrate. As a source, one can use the CdTe compound

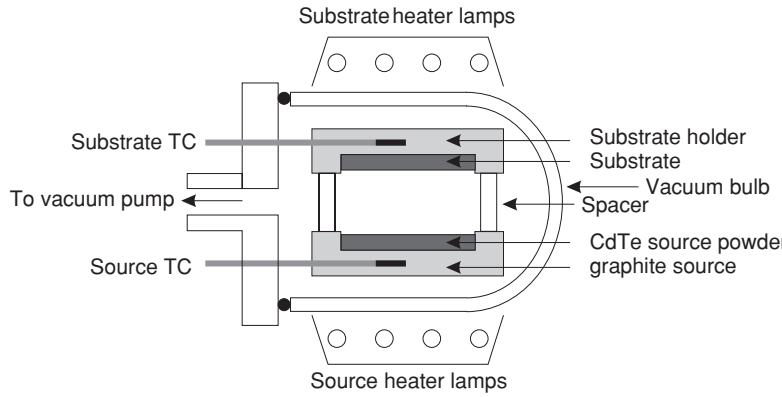

Figure 7.9 Schematics of CdTe deposition by close spaced sublimation (CSS). TC means thermocouple.

in the form of a pressed tablet, or in granulate or powder form. A stoichiometric mixture of Cd and Te powder can also be used. The driving force for the deposition is the source to substrate temperature difference, and the surface energy at the substrate, which can depend on the substrate composition, crystallography and morphology.

In Figure 7.9 a sketch of a batch CSS deposition apparatus is given. The technique has many variants. An inert carrier gas, Ar or N_2, can be used at pressure of e.g. 100 Pa or 1 mbar, or even at atmospheric pressure. This form of the sublimation technique is sometimes called close spaced vapour transport (CVT or CSVT). The technique can be used for both CdS and CdTe.

7.4.1.2 Other deposition techniques, vacuum and nonvacuum

As explained in the introduction, CdTe is a tolerant material. Device quality CdTe layers have been fabricated by a multitude of deposition techniques. It seems that the final CdTe material properties are determined more by the $CdCl_2$ after-treatment than by the deposition itself. This has triggered much research on cheap deposition techniques, including quite a few nonvacuum techniques. We give here a nonexhaustive summary:

(1) Other vacuum techniques

(1) Evaporation and stacked elemental layers: conventional vacuum evaporation has been used by the group at Delaware to fabricate CdS/CdTe cells with efficiencies above 10 % [119]. In the technique of stacked elemental layers (SEL), a succession of thin Cd and Te layers are evaporated, and annealed to CdTe afterwards [120].

(2) Atomic layer deposition (ALD): when the successive elemental layers in SEL are effectively limited to a monoatomic layer, the technique was originally called atomic layer epitaxy (ALE); now the name ALD has become established. The monoatomic elemental Cd and Te layers are deposited by periodically switching a gas flow between a Cd containing and a Te containing inert carrier gas. Inorganic precursors are used (e.g. Te and Cd or $CdCl_2$). This technique allows excellent control of the CdS/CdTe intermixing region, which can be limited to any number of atomic layers, e.g. 100. High efficiency ($\eta = 14\,\%$) CdS/CdTe solar cells were made with this technique [121].

(3) Metal organic chemical vapor deposition (MOCVD): now the precursors for the gas phase deposition of CdTe are metal organic compounds, e.g. dimethyl cadmium and diisopropyl tellurium. Both gases are applied simultaneously to the substrate, and the CdTe film properties are controlled by the process parameters (gas temperature, flow and concentration, substrate temperature) [71].

(4) Sputtering: this technique is well suited for industrial large scale production, and it has been applied successfully to CdS/CdTe [122, 123] and to the back contact structure (Section 7.3.2 and references therein).

(2) Nonvacuum Techniques:

(1) Electrodeposition: this technique has been developed up to industrialization by BP solar [124]. The deposition of CdS and CdTe is at low temperature, and a thermal treatment above 400 °C is applied afterwards.

(2) Chemical bath deposition (CBD) for CdS: dipping in an aqueous solution containing Cd^{2+} ions and S^{2-} ions is the preferred technique for depositing the CdS buffer layer in $Cu(In,Ga)Se_2$ solar cells. It has also been used for CdS/CdTe cells [50]. The technique yields very thin, closed layers. However, only films of limited thickness can be deposited and hence the technique is not used for CdTe.

(3) Solution spray: an aqueous solution containing a Cd precursor (e.g. $CdCl_2$) and a Te precursor (TeO_2 or an organic Te compound) can be sprayed onto a heated substrate. The CdTe compound is formed on the substrate, and the residues are volatilized. This technique was developed by Photon Energy, later Golden Photon, to yield highly efficient cells (12.7 %) and modules [125, 126].

(4) Screen printing and sintering: This technique has also been developed to an advanced industrial level by Matsushita Batteries [46, 127]. The Universities of Seoul [128] and Gent [43, 78] also contributed to this technique. The screen printing slurry consists of CdS or CdTe (or Cd and Te) powder, with some percentage of $CdCl_2$ powder as a flux. After screen printing and drying, the substrates are sintered at a high temperature (500–600 °C) in ambient nitrogen. The obtained films are rather thick (10–30 μm), and have large grains. Efficiencies up to 12 % were obtained.

7.4.2 Design of series integrated cadmium telluride modules

An essential advantage of thin film solar cells is the possibility of automated series connection of cells in a module. This is illustrated in Figure 7.10. All layers are deposited at the full module size. After deposition, the TCO layer(s) are patterned by laser or mechanical scribing over the entire width of the substrate. The cuts have to be as narrow as possible (100 μm range) and leave no TCO material which could shunt the structure; their mutual spacing follows from an optimization design and is of the order of 5–10 mm (see Section 7.5.3.6). After deposition of the CdS and the CdTe layer and the activation treatment, a second scribe is given which leaves the TCO layer; this is possible because the TCO layer is usually much harder and adherent than the semiconductor layers. In this second cut, the metallization layer(s) form an interconnection between the left hand and the right hand cell. A third scribe then isolates the

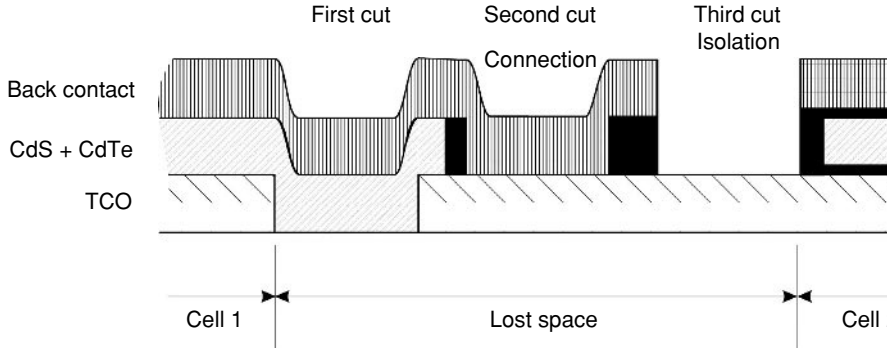

Figure 7.10 Series interconnection of two adjacent cells in a module by laser scribing. The black parts indicate possible damage to the CdTe layer during the laser scribing.

back contacts of the two cells from each other. This integrated series connection technology can be automated to handle a full 60 × 120 cm^2 module at high throughput (e.g. 2 minutes) [6, 12].

7.4.3 Production of cadmium telluride solar modules

Presently CdTe solar modules are produced in two major plants: Antec Solar Energy [136] and First Solar [137].

In the Antec plant [4, 5, 136], the TCO is applied by sputtering, and the CdS and CdTe are deposited by CSS. These steps, together with the activation of CdTe, the contact treatment, the sputter deposition of the contact buffer and contact metal, and the laser scribing for the series connection, are integrated in one production line. The size of the panels is 60 × 120 cm^2, the throughput is 2 minutes per module. This gives a production capacity of 100 000 m^2/yr, corresponding to 8 MWp/yr with the present module efficiency of 8 %. In a second production line, the glass plates are encapsulated and sealed to finished modules. The actual production costs below 2 £/Wp, and the energy payback time is less than one year under central European insolation conditions.

First Solar [6, 137] uses the same module size. The CdS and CdTe layers are deposited with high rate vapor transport deposition (HRVTD), where the vapors of subliming CdS or CdTe are brought over the substrate plates (this is a variant of the CSS technique). The production was 3 MWp in 2003, and a plant extension with a capacity of 25 MWp is planned to be in operation in 2005.

Matsushita Battery in Japan has produced screen printed and sintered CdTe solar cells for the indoor market, e.g. for Panasonic calculators [46, 127]. Although the technical status was well developed, the activity was stopped in 2002. BP Solar also reached an advanced technical status with their electrodeposited CdTe modules [124], illustrated by a large area panel with efficiency exceeding 10 %. A 10 MWp plant was set up in Fairfield, California, but the activity was stopped in 2002.

As in every industrial activity, the landscape of the companies is a very dynamic one, with players emerging, reemerging, associating or withdrawing. For an overview of the actual status and the historic evolution, we refer to [12].

7.5 ADVANCED CHARACTERIZATION AND MODELING OF CADMIUM TELLURIDE SOLAR CELLS

7.5.1 Characterization and modeling: introduction

Modern polycrystalline cells are complicated structures and the effects of some particular phenomenon, mechanism or material parameter are often beyond intuition or simple rules of thumb. Modeling then can be used to provide insight, to interpret measurements and to asses the potential merits of a cell structure. Only under certain assumptions and simplifications are analytical descriptions possible. Numerical modeling is a necessity for the realistic description of thin-film PV devices. The large quantity of parameters needed for numerical simulation (50 seems to be a minimum) is, however, a real concern. An exhaustive exploration of a 50-dimensional parameter space is definitely out of reach. This means that numerical modeling needs input from specialized measurements of layers and specially prepared structures to fix as many as possible parameters with some level of confidence. In that respect one can truly say that characterization and modeling go together like a horse and carriage. Also, choosing a parameter set to simulate a measurement is not a blind job which can be left to a computer, but it requires physical insight and feeling. Simple, analytical or numerical "'submodels'", which describe the gross action of (a small) part of the parameters (e.g. at the back contact of a CdTe cell), are of great help in acquiring such physical insight and feeling. We will first briefly discuss some advanced characterization methods that can help to shine some light in the jungle of parameters. Afterwards, we will start our discussion of modeling with the analytical 'two diode' model which is particularly successful for the CdTe back contact.

7.5.2 Characterization methods for cadmium telluride materials and cells

7.5.2.1 Electrical characterization

Routine I-V in light and dark learn us the four basic photovoltaic parameters: the efficiency η, the short-circuit current density J_{sc}, the open circuit voltage V_{oc}, and the fill factor FF. Phenomena typical for CdTe thin film solar cells are immediately displayed by the I-V curves: 'roll over', which is ascribed to a contact phenomenon, and 'cross over', which can have a variety of causes (see further Figure 7.11).

Dark I-V measurements as a function of temperature are almost routine measurements. When the log I-V plot shows a linear region, extrapolation to $V = 0$ yields the dark diode saturation current J_s, whilst the slope yields the diode ideality factor n. When done as a function of temperature, a plot of log J_s versus $1/T$ yields the activation energy ΔE, if it shows a straight part and if n does not depend on T. The restrictions means that the I-$V(T)$ curves should be decently described by a Shockley law:

$$J(V,T) = J_s(T)\left(\exp\left(\frac{qV}{nkT}\right) - 1\right) - J_L \quad \text{with} \quad J_s(T) = J_{s0}\exp\left(-\frac{\Delta E}{kT}\right) \tag{7.7}$$

at least in some voltage and temperature ranges. Several current mechanisms can give rise to a Schockley like I-V law (see below). When one finds that the diode ideality factor n is larger

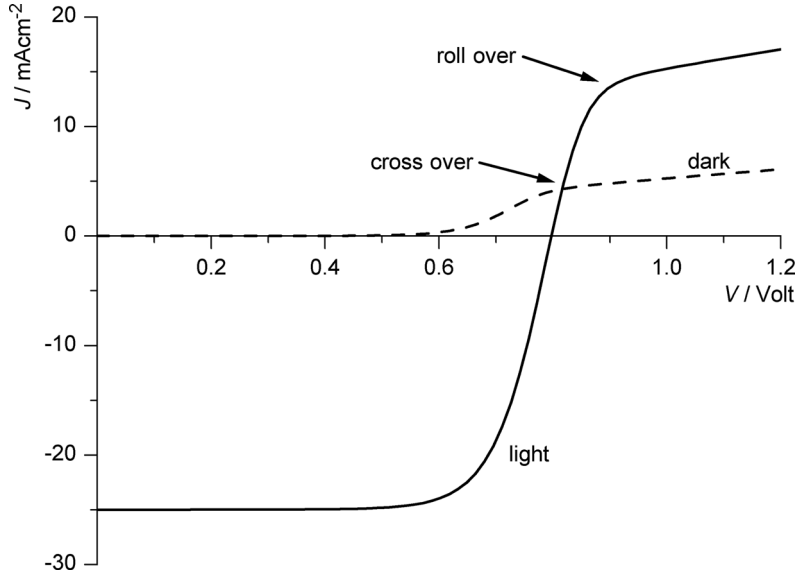

Figure 7.11 Dark (dashed line) and illuminated (solid line) J-V characteristics of a thin film CdTe/CdS solar cell. Definition of terms: 'roll over' and 'cross over'.

than two and decreases with increasing temperature, tunneling could be the current mechanism. An analytical expression that can be used for combined emission over and tunnelling though a Schottky barrier is [74]:

$$J = J_s \exp\left(\frac{V}{E_0}\right) \quad \text{with} \quad E_0 = E_{00} \coth\left(\frac{qE_{00}}{kT}\right) \quad \text{and} \quad E_{00} = q\frac{\hbar}{2}\sqrt{\frac{N_A}{m^*\varepsilon_s\varepsilon_0}} \tag{7.8}$$

where J_s is a complicated function of the temperature, barrier height and semiconductor properties; J_s is only weakly dependent on bias voltage [138]. If displayed in a standard ln J-V plot, the apparent ideality factor $n(T)$ depends on temperature and can be quite large ($n > 2$).

The dark I-V measurement can be severely disturbed by a series resistance R_s and/or a shunt conductance G_{sh}. Equation (7.7) should then be replaced by:

$$J(V,T) = J_s\left[\exp\left(\frac{q(V - R_s AJ)}{kT}\right) - 1\right] - J_L + (V - R_s AJ)\frac{G_{sh}}{A} \tag{7.9}$$

where A is the cell area. Curve fitting should be used to extract the parameters J_L, J_s, n, R_s and G_{sh} for each temperature. When a series resistance is the only dominating effect, it is easier to vary, at each temperature, the illumination intensity and to record J_{sc} and V_{oc}. Then one can construct the $J_{sc} - V_{oc}(T)$ curves. Unless the series resistance is very high, J_{sc} and V_{oc} are not affected by it, and the $J_{sc} - V_{oc}(T)$ curves contain, in principle, the same information as the dark $J - V(T)$ curves without series resistance. However, in CdTe and other thin film solar cells, the light current is not a simple translation of the dark current, as it is in crystalline cells. Hence J_s, n and ΔE derived from the $J_{sc} - V_{oc}$ measurement can differ from the same parameters derived from a dark J-V measurement. This explains the somewhat mysterious

Table 7.4 Dark current parameters J_s, ΔE, n and $V_{oc}(0\,K)$ for some common current mechanisms. The p region (CdTe) is assumed to be the lower doped region. QNR is the quasi neutral region and SCL is the space charge layer in the CdTe; E_{gi} is the interface bandgap defined in Figure 7.3; N_i and S_i are the interface states density and recombination velocity. The other symbols have their usual meaning

	n	$J_s(N_A, \tau)$	ΔE of $J_s(T)$	$qV_{oc}(0\,K)$
Recombination in QNR	1	$\propto \frac{1}{N_A\sqrt{\tau}}$	E_g	E_g
Recombination in SCL (midgap defect)	2	$\propto \frac{1}{\tau\sqrt{N_A}}$	$\frac{E_g}{2}$	E_g
Recombination in SCL (nonmidgap defect at $E_i + E_t$)	low V: $n = 1$	$\propto \frac{1}{\tau\sqrt{N_A}}$	$\frac{E_g}{2} + E_t$	$\frac{E_g}{2} + E_t$
	high V: $n = 2$	$\propto \frac{1}{\tau\sqrt{N_A}}$	$\frac{E_g}{2}$	E_g
Interface recombination	$1 + \frac{N_A}{N_D} \approx 1$ for n^+p-junction	$\propto S_i\, n(0)$	$E_{gi} = E_g - \Delta E_C$ if $\Delta E_C > 0$	
			$E_{gi} = E_g$	if $\Delta E_C < 0$
Tunneling through and emission over barrier	$n = \frac{E_{00}}{kT}\coth\left(\frac{E_{00}}{kT}\right) \approx 1 + \frac{E_{00}^2}{3k^2T^2}$ if $E_{00} \ll kT$			
Tunneling trough barrier	$n.kT = E_{00}$ $(n > 1)$			

formulation 'dark diode current parameters measured under illumination' which is sometimes used in the literature. In ideal cells, the open circuit voltage decays linearly with temperature. Extrapolation of the (straight part of the) $V_{oc} - T$ plot to 0 K also gives an indication about the current mechanism. An overview of the parameters J_s, ΔE, n and $V_{oc}(0\,K)$ for some common current mechanisms is given in Table 7.4 (compiled from several sources, e.g. [16, 139, 140]). This table can serve as a guide for interpreting dark J-V or J_{sc}-V_{oc} curves. It is important that the interpretation be checked for self consistency, since the values of n, ΔE and $V_{oc}(0\,K)$ are interrelated.

Capacitance-voltage measurements (C-V measurements) are routinely applied to assess the doping density. The procedure is simple: one constructs a $1/C^2$-V plot (Mott–Schottky plot); the local slope of that plot is inversely proportional to the doping density at a position x away from the junction [41]. For a one sided n^+p junction (that is: the n region is much more heavily doped than the p region), one obtains:

$$N_A(x) = -\frac{2}{A^2 q \varepsilon_s \varepsilon_0} \frac{dV}{d\left(1/C^2\right)} \quad \text{where} \quad x = A\frac{\varepsilon_s \varepsilon_0}{C} \tag{7.10}$$

Several remarks are in order: the doping density $N_A(x)$probed in Equation 7.(10) is relevant to the least doped region, which is not always known *a priory*. It is generally assumed that CdS/CdTe is an n^+p type solar cell, and that thus the doping density in the CdTe layer is probed. In polycrystalline materials, it can be difficult to determine the precise area A due to texture and two-dimensional effects; when one underestimates the area by a factor two, a measurement point is erroneously positioned too close to the interface, and the doping density

is overestimated by a factor four. The extrapolated intercept of the Mott–Schottky curve with the V-axis equals V_{bi}–kT/q for a uniformly doped one sided junction. The value of V_{bi} obtained from C-V measurements should be checked for self consistency with the dark J-V parameter ΔE. The presence of deep traps complicates the C-V behaviour; also the capacitance C becomes dependent on the measurement frequency [41]. Nevertheless, the simple Equation (7.10) is still often used to derive the 'apparent doping density'. The presence of a Schottky barrier at the back contact has a thorough influence on the C-V behaviour (see Section 7.5.3.1).

Measurement of the complex impedance versus frequency yields the C-f (T) and G-$f(T)$ curves. Several mechanisms can give rise to a frequency dependent capacitance, including: dielectric relaxation in the CdTe layer, deep traps in CdTe (single level and distributed levels), the back contact, an inversion layer at the CdS/CdTe junction, interface states. The characteristic parameters (low frequency value C_{LF}, high frequency value C_{HF}, time constant τ and activation energy ΔE_τ of τ) of these mechanisms have been analyzed in [141]. When deep levels are supposed to cause the dispersion of the C-f curves, their density and energy distributions can be estimated from an analysis of log C-f plots measured at different temperatures [142].

To interpret the quantum efficiency, one should first calculate the internal quantum efficiency $QE_{int}(\lambda)$ from the measured external quantum efficiency $QE_{ext}(\lambda)$. In a simple optical structure, with a front side reflection $R(\lambda)$ and transmission $T(\lambda)$ of the total cell, the calculation is simple:

$$QE_{int}(\lambda) = \frac{QE_{ext}(\lambda)}{1 - R(\lambda) - T(\lambda)} \tag{7.11}$$

The relationship between QE_{int} and QE_{ext} is more complicated when more optical phenomena are taken into account. The long wavelength region of $QE_{int}(\lambda)$ gives information about the back region. Some popular methods to derive the diffusion length L_n from $QE_{int}(\lambda)$ rely on an approximation of the ideal Shockley solar cell [14, 17]:

$$QE(\lambda) \approx \left[1 - \exp(-\alpha W)\right] + \exp(-\alpha W)\,\frac{\alpha L_n}{\alpha L_n + 1} \tag{7.12}$$

Two approximations are in order:

$$QE(\lambda) \to \frac{\alpha L_n}{\alpha L_n + 1} \quad \text{or} \quad \frac{1}{1 - QE(\lambda)} \to \alpha L_n + 1 \quad \text{when} \quad \alpha W < 1 \quad \text{and} \quad L_n > W$$
$$QE(\lambda) \to \frac{\alpha (L_n + W)}{\alpha L_n + 1} \approx \alpha (L_n + W) \quad \text{when} \quad \alpha W < 1 \quad \text{and} \quad W > L_n \tag{7.13}$$

The first approximation is valid in silicon cells; when the absorption coefficient $\alpha(\lambda)$ is precisely known, the inverse of $1 - QE$ is plotted versus α in the long wavelength region, and L_n is derived from the slope, when a straight line is obtained. The second approximation can be used for CdTe solar cells [90]. The QE is measured for varying reverse voltage at a fixed long wavelength ($820\,\text{nm} < \lambda < 860\,\text{nm}$), and the depletion width follows from a C-V measurement; knowledge of $\alpha(\lambda)$ is not required. In a QE versus W plot, the extrapolation of the straight part (if any) to the W axis yields $-L_n$. A critique on the validity of these and related techniques to determine the diffusion length is given in [42].

Deep level transient spectroscopy (DLTS) and related techniques cannot be considered as routine techniques [41]. A cell is biased at a quiescent reverse voltage. Then a short excitation is given to the cell: a voltage pulse which still stays in reverse bias (standard DLTS), or a voltage pulse which gives the cell a forward bias for a short time (injection DLTS), or a short laser pulse (optical DLTS). The cell then returns to its quiescent state, and during that transient, the capacitance (measured at a high frequency, typically 1 MHz) is recorded. This is done at several temperatures. Several methods can be used to process the measured $C(t)$ transients at each temperature, to obtain information about deep states present in the cell: their energy levels, concentration and capture cross-sections. For DLTS results on CdTe solar cells, we refer to the literature [143–147].

7.5.2.2 Structural, physical and chemical characterization

All kinds of standard spectroscopy (XPS, Auger, EDS, SIMS) and microscopy (SEM, TEM) have been applied to CdTe layers and CdTe/CdS solar cells. We discuss here a few specialized techniques in some more detail.

A direct measure of the response of the solar cell on a microscopic scale is obtained by electron beam induced current (EBIC) and optical beam induced current (OBIC). The excitation is a focused electron or optical beam, and the measured output is the electrical current in the cell. An electron beam can be better focused than a laser beam, and hence EBIC has a higher spatial resolution. The photocurrent or induced current can be probed at the same position as the incident beam (direct EBIC, OBIC), or by an electrode which remains at some fixed distance from the incident beam during scanning (remote EBIC, OBIC). The technique can be applied to the surface of the cell (plane EBIC) or to a cross-section (transverse EBIC). The information gained is the lateral homogeneity, and, with some assumptions, the diffusion length. Electron beam induced current and related measurements have been extensively used in CdTe solar cell research [11, 111, 114–116]. Nonuniformity of the output of CdTe/CdS solar cells has also been studied with lock-in thermography, where the near infrared radiation from the cell surface is scanned and converted to a temperature image [148].

Emission measurements such as photoluminescence (PL) or cathodoluminescence (CL) can give information about the bandgap, the excitonic structure, deep states and recombination properties. Here the excitation is a laser or electron beam, and the output is light emitted at a longer wavelength. Applications on CdTe thin film solar cells are found e.g. in [149–153].

In ultraviolet photon spectroscopy (UPS) and X-ray photon spectroscopy (XPS) the excitation is radiation with energy in the order of 10 eV (UPS) to some hundreds of eV (XPS). The energy of the emitted electrons is measured. The method gives information about the energetic position of the Fermi level and of the valence band edge at the surface. Combined with the knowledge of the band gap E_g, the position of the conduction band edge and hence the complete band alignment at the surface is probed [45, 76, 154, 155]. The position of the conduction band can be probed directly with photoelectron spectroscopy (PES) [156]. The question how the band alignment at the surface of a partial structure relates to the band alignment in the interior of a complete cell has to be approached by other considerations.

Advanced scanning techniques are derived from atomic force microscopy (AFM) and scanning tunneling microscopy (STM). They can probe the surface potential (surface photovoltage, SPV [157]), work function (Kelvin probe force microscopy, KPFM [158]) and electrical current or surface capacitance with submicrometer resolution [117, 118]. Advanced optical

measurements can be used for an accurate determination of the optical absorption $\alpha(\lambda)$ in the subbandgap region. We refer to the work of the Prague University group [27].

7.5.3 Modeling of thin film cadmium telluride solar cells

7.5.3.1 The analytical two diode model for cadmium telluride solar cells

The contact energy barrier Φ_b at the CdTe back contact structure gives rise to a Schottky diode pointing in the opposite direction to the main CdS/CdTe solar cell junction. The analytical description of a CdTe solar cell with this 'two diode model' shown in Figure 7.12 is remarkably successful because it gives a simple semiquantitative description of some effects particular to the CdTe solar cell. The model was brought up by Stollwerck and Sites to explain the gross effects on the illuminated I-V characteristics [86], and was refined at the University of Gent to describe also the ac behaviour, the influence of minority current at the back contact, the voltage and illumination dependence at the back contact [87, 88, 90, 159].

The dc model states that the current $J_j - J_L$ through the CdS/CdTe junction and the current J_c through the contact is the same, whilst the voltages are summed (Figure 7.12). For the solar cell junction, an ideal Shockley law is assumed with an ideality constant n, and for the contact

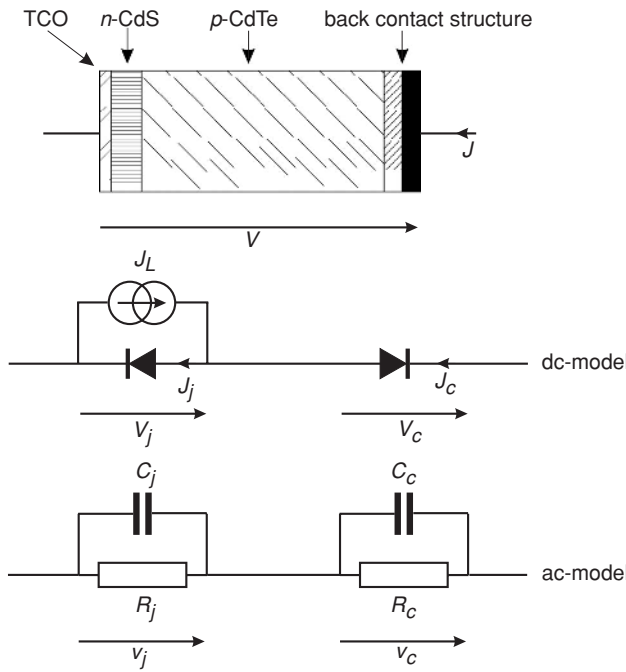

Figure 7.12 The two diode model for the CdS/CdTe junction and the back contact structure. Reprinted from Thin Solid Films,403–404, M. Kontges, R. Reineke-Koch, P. Nollet, J. Beier, R. Schaffler, J. Parisi, Light induced changes in the electrical behaviour of CdTe and Cu(In,Ga) Se2 solar cells, p. 280–286. Copyright (2002) with permission from Elsevier.

a thermionic emission law. With a correct treatment of the signs, one obtains:

$$
\begin{aligned}
J &= J_s \left(\exp\left(\frac{qV_j}{nkT} \right) - 1 \right) - J_L \qquad \text{CdS / CdTe junction} \\
&= -qN_V v_r \exp\left(-\frac{\Phi_b}{kT} \right) \left(\exp\left(-\frac{qV_c}{kT} \right) - 1 \right) \quad \text{contact} \\
V &= V_j + V_c
\end{aligned}
\tag{7.14}
$$

where v_r is the emission velocity of holes over the contact barrier. As a first refinement, v_r can be replaced by the drift velocity v_d at the contact, which depends on the doping density and the voltage V_c over the contact, or by an effective velocity v_{eff} describing the combined effects of thermionic emission, drift and diffusion [14, 74]. This simple model already explains the roll off of the I-V curves, and its dependence on the contact barrier Φ_b. It gives a first estimate of the dependence of the fill factor FF and the efficiency η on Φ_b [86]. The simple formula Equation (7.6) was derived from these Equations (7.14) in [87].

Only a few extensions to this model are required to also describe the cross over of the I-V curves [160]. An empirical approach is to assume that one or more of the parameters in Equations (7.14) depend on illumination: the diode saturation current J_s or the contact saturation current J_c, possibly caused by a light dependence of the barrier Φ_b. Also light dependent shunt and series resistances have been invoked. Although all those empirical assumptions can almost perfectly explain the cross over of one I-V curve, they do not give a physical explanation of *why* and *how* a given parameter depends on illumination intensity and wavelength: not surprisingly, they most often fail in explaining other measurements than the one I-V curve they were conceived for. Physical approaches within the analytical two diode model, and corroborated with measurements and numerical simulations, are:

(1) The back contact junction is photovoltaic [160]: a current source has to be placed in parallel over the contact diode in the dc circuit in Figure 7.12. This current source has the opposite direction to the source J_L over the solar cell junction, and responds only to long wavelength light ($\lambda > 820\,\text{nm}$).

(2) Not only holes, but also minority electrons contribute to the current through the contact [87, 88]. A term describing the electron current has to be added to the second equation of Equations (7.14), and an estimate of the electron density at the edge of the contact space charge layer has to be made. It turns out that this mechanism can only be important when the diffusion length L_n is large, or the cell is thin, or two-dimensional effects at the contact decrease the effective thickness. The source of a nonnegligible electron concentration at the contact SCL can be direct optical generation (then this model is equivalent to (1) or a sufficiently large forward bias voltage over the solar cell junction. The model explains the single point cross over of a set of I-V curves observed under certain conditions [88].

(3) The energy barrier depends on illumination in an indirect way [90]: long wavelength illumination changes the occupation of deep acceptor states near the contact; this, in turn, changes their charge state, and hence the electrostatic potential profile and the energy

barrier in the device. This makes the majority (hole) current passing the contact illumination dependent.

(4) Several mechanisms analogous to (3) were invoked at the front contact to explain the short wavelength effects at forward bias [161–165]: at forward V and for $\lambda < 520\,\text{nm}$, the apparent quantum efficiency becomes negative and (in magnitude) larger than unity. Though these models differ in details, they have a common starting point: deep acceptor states (in the CdS or at an interface) compensate or overcompensate for the shallow donor doping of CdS. Under illumination, and when a suitable ratio $\sigma_p/\sigma_n > 1$ is assumed, these acceptors become uncharged, the effective doping density in the CdS changes and hence the potential profile over the CdS. This can have a severe influence on the current transport to the rest of the solar cell. In [161, 162] ovecompensation is assumed, which results in a hump like potential profile over the CdS: this layer acts as a modulated barrier photodiode (MBP). In [163–165] more or less complete compensation is assumed; the details of the rather complicated behavior of the cell (both *QE* and *I-V*) at forward voltage and short wavelengths could be explained. These high V/short λ effects are reviewed in [166, 167]. It should be remarked that all models in this paragraph (4) exceed the analytical two diode model, and intensively use numerical simulation. Only the MBP model could be treated analytically with simplifying assumptions [161, 162].

The ac behaviour can also be explained quite well with the two diode model. In the equivalent circuit in Figure 7.12, all network elements depend on the dc bias value of the voltage over the element: R_j and R_c depend exponentially on the dc values V_j and V_c (a strong dependence), respectively; C_j and C_c show the usual square root dependence of bias voltage: $C_j \propto \sqrt{V_{bij} - V_j}$ and $C_c \propto \sqrt{V_{bic} + V_c}$ where V_{bij} and V_{bic} are appropriate built-in voltages (a weak dependence). From elementary circuit theory one can calculate the measured capacitance C. We confine ourselves here to the low and the high frequency limits:

$$C_{LF} = \frac{R_j^2 C_j + R_c^2 C_c}{\left(R_j + R_c\right)^2} \qquad C_{HF} = \frac{C_j C_c}{C_j + C_c} \tag{7.15}$$

At negative up to moderate positive applied voltage, the current is lower than the contact saturation current, and hence the contact does not limit the current: $R_j >> R_c$ and hence $C_{LF} \cong C_j$. Since V_j increases with the applied voltage V, $C_{LF} \cong C_j$ increases with increasing V. From analysis of the Mott–Schottky plot one then deduces the doping density in the CdTe layer close to the CdS junction. At high forward voltage, however, the contact is limiting the current, and $R_c >> R_j$ and $C_{LF} \cong C_c$. Also V_c increases with V, but V_c is the reverse voltage for the contact (Figure 7.12), hence $C_{LF} \cong C_c$ decreases with increasing applied voltage. From analysis of the Mott–Schottky plot one then deduces the doping density in the CdTe layer close to the contact. One can show easily from Equations (7.15) that at an intermediate voltage, where $R_j C_j = R_c C_c$, one measures the series capacitance $C_{LF} = C_j C_c/(C_j + C_c)$, which is lower than both C_j and C_c. This explains the characteristic shape of the low frequency *C-V* measurements of a CdTe solar cell with a back contact barrier: it has a minimum in between two maxima (Figure 7.13). These results of the two-diode model allow one to determine the CdTe doping separately in the junction and in the contact region [87, 159]; this has become a standard procedure for CdTe solar cells with a contact barrier.

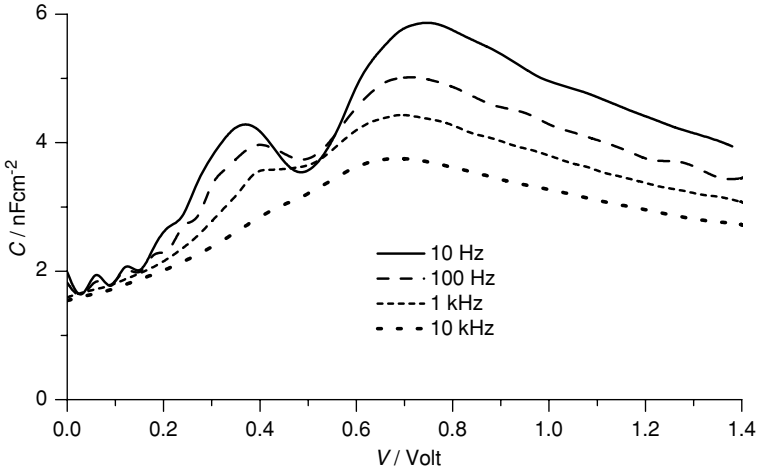

Figure 7.13 Measured C-V characteristics at forward bias of a CdTe cell without $CdCl_2$ activation. The measurement frequencies are 10, 20, 40 and 100 kHz. Reproduced with permission from *Sol. Energy Mater. Sol. Cells*, **63**, V. Singh, D. Linam, D. Dils, J. McClure and G. Lush, Electro-optical characterization and modeling of thin films CdS-CdTe heterojunction solar cells, pp 445–466. Copyright (2000) Elsevier.

7.5.3.2 Numerical modeling tools

A numerical solar cell simulator is a computer programme that numerically solves the 'semiconductor equations' for a given solar cell structure. The dc semiconductor equations (in one dimension) are the Poisson equation that relates the electrostatic potential ψ to the total charge density:

$$\frac{\mathrm{d}^2\Psi}{\mathrm{d}x^2} = -\frac{q}{\varepsilon_s\varepsilon_0}\left[p(x) - n(x) + N_\mathrm{D}^+ - N_\mathrm{A}^- + \rho_\mathrm{ds}(n, p)\right] \quad \text{Poisson} \tag{7.16}$$

and the continuity equations that relate the electron and hole current with recombination and generation of carriers:

$$\begin{aligned} \frac{\mathrm{d}J_n}{\mathrm{d}x} &= G(x) - R(n, p) \qquad \text{electron continuity} \\ \frac{\mathrm{d}J_p}{\mathrm{d}x} &= G(x) - R(n, p) \qquad \text{hole continuity} \end{aligned} \tag{7.17}$$

In Equation. (716), N_D^+ and $N_\mathrm{A}^-$are the densities of the ionized shallow donors and acceptors, respectively; ρ_ds is the charge density contained in the deep states, which generally depends in a nonlinear way on the electron and hole concentrations. In Equation 7.(17), G is the generation by the illumination; it depends on the wavelength λ and the position x. The term R in Equation (7.17) is the total recombination in the deep states, which also nonlinearly depends on the carrier concentrations. The currents J_n and J_p are composed of a diffusion term and a drift term.

There are thus three differential equations for three unknown functions $\psi(x)$, $n(x)$ and $p(x)$. With suitable boundary conditions, this system can be solved. In a computer algorithm, the solar cell structure is first divided into slices, typically some tens to more than a hundred per semiconductor layer. For a five layer system, the number of slices can be e.g. $N = 500$. Each differential equation is approximated by a system of N nolinear algebraic equations. The resulting system of $3N = 1500$ equations with $3N$ unknowns (ψ, n and p in each slice) are solved numerically. The program will need input for each of the five layers: thickness and semiconductor properties, including recombination information for all shallow and deep levels present. A large number of input parameters (50 to 100) is thus to be expected.

Solar cell simulation programmes differ in their numerical capabilities (number of layers, number of deep levels per layer, speed of calculation, etc.), in the physical mechanisms implemented (different recombination mechanisms, tunnelling, etc.), in their ease of operation (the users interface) and in their availability and price. An overview of numerical simulators used for thin film solar cells is given in [168]. The results discussed below were obtained with the programme SCAPS developed at the University of Gent [169–171].

7.5.3.3 Finding a consistent parameter set

A starting parameter set for simulating the most marked features of a broad class of CdS/CdTe thin film solar cells is the 'baseline set' given by Gloeckler and Sites [48]. When our aim is predictive numerical simulation, it is a prerequisite to find a consistent parameter set. This means a single parameter set for one cell, which describes all measured effects. By this we mean that no *ad hoc* assumptions are made (e.g. an assumed voltage or illumination dependence of some parameter, e.g. a barrier), that no numerical tricks are used (e.g. 'neutral levels' in which there is recombination, but no charge – though this idealization does not correspond to a physical reality, it is a feature implemented in SCAPS and other simulation programmes), and that use is made of all measurements, including DLTS if available. Because the determination of the trap density and capture cross-sections is by no means a simple routine, and can lead to substantial errors, we consider the parameters N_t, σ_n and σ_p as fitting parameters. On the contrary, we use all defects with their energy levels E_t as determined by DLTS in the parameter set. Finding such a consistent parameter set is a laborious task. A first set was given by fitting the forward V/short λ effects [164, 165]. This set was refined in sequential stages to also include a fit of the dark and illuminated J-V, the J_{sc}-V_{oc}, the C-V and the C-f measurements, all as a function of temperature, and the $QE(\lambda, V)$ measurement [172, 173]. This was done for two particular series of Antec cells: one with $CdCl_2$ activation treatment in air, the other in vacuum. The defect related parameters of our baseline set are shown in Table 7.5; the other parameters values are taken from Table 7.1.

7.5.3.4 Modeling results

This parameter set was used as a baseline for parameter variation, where each time one single parameter was varied, the others retaining their baseline values [174]. The simulations were carried out with SCAPS.

Table 7.5 Parameter set for typical vacuum and air activated cells. Trap energies are measured from the valence band edge; positions are measured from the CdS/CdTe junction (source: [173]).

	Air activated cell	Vacuum activated cell
CdS		
Thickness [nm]	70	70
Shallow N_D [cm^{-3}]	$5\ 10^{16}$	$5\ 10^{16}$
Defect 1	Function: light dependence of CdS	
Type	acceptor	acceptor
E_t [eV]	$E_V + 1.97$	$E_V + 1.97$
N_t [cm^{-3}]	$4.9\ 10^{16}$	$3\ 10^{16}$
σ_n [cm^2]	10^{-20}	10^{-20}
σ_p [cm^2]	10^{-11}	10^{-11}
Defect 2	Function: recombination in CdS	
CdTe		
Thickness [μm]	5	8.7
Shallow N_A [cm^{-3}]	$1.5\ 10^{15}$(0–3 μm) $1.0\ 10^{16}$ (3–5 μm)	$2.0\ 10^{15}$ (0–0.55 μm) $3.0\ 10^{13}$ (0.55–8.2 μm) $4\ 10^{14}$ (8.2–8.7 μm)
μ_n [$cm^2\ V^{-1}\ s^{-1}$]	110	110
μ_p [$cm^2\ V^{-1}\ s^{-1}$]	70 (0–3 μm) 1 (3–5 μm)	70 (0–8.2 μm) 1 (8.2–8.7 μm)
Defect 1	Function: dark J-V, recombination, V_{oc}	
Type	Acceptor	Acceptor
Range [μm]	0–3.0 μm	0–8.2 μm
E_t [eV]	$E_V + 0.72$	$E_V + 0.74$
N_t [cm^{-3}]	$1.0\ 10^{15}$	$1.0\ 10^{15}$(0–0.1 μm) $5.0\ 10^{14}$(0.1–0.55 μm) $7.7\ 10^{14}$(0.55–8.2 μm)
σ_n [cm^2]	$1.0\ 10^{-13}$	$3.0\ 10^{-14}$
σ_p [cm^2]	$1.0\ 10^{-12}$	$4.0\ 10^{-12}$
Defect 2	Function: shape of dark J-V, / recombination, V_{oc}	
Type	Acceptor	Acceptor
Range [μm]	0–0.1 μm	0–0.1 μm
E_t [eV]	$E_V + 1.03$	$E_V + 1.03$
N_t [cm^{-3}]	$8.0\ 10^{14}$	$8.0\ 10^{14}$
σ_n [cm^2]	$1.2\ 10^{-11}$	$1.2\ 10^{-11}$
σ_p [cm^2]	$1.0\ 10^{-11}$	$1.0\ 10^{-11}$
Defect 3	Function: C-V at low $T < 250$ K	
Type	Donor	Donor
Range [μm]	0.1–3.0 μm	0.55–8.2 μm
E_t [eV]	$E_V + 0.2$	$E_V + 0.3$
N_t [cm^{-3}]	$1.0\ 10^{15}$	$2.7\ 10^{13}$
σ_n [cm^2]	10^{-20}	10^{-20}
σ_p [cm^2]	10^{-20}	10^{-20}
Back contact		
Φ_b [eV]	0.42	0.55

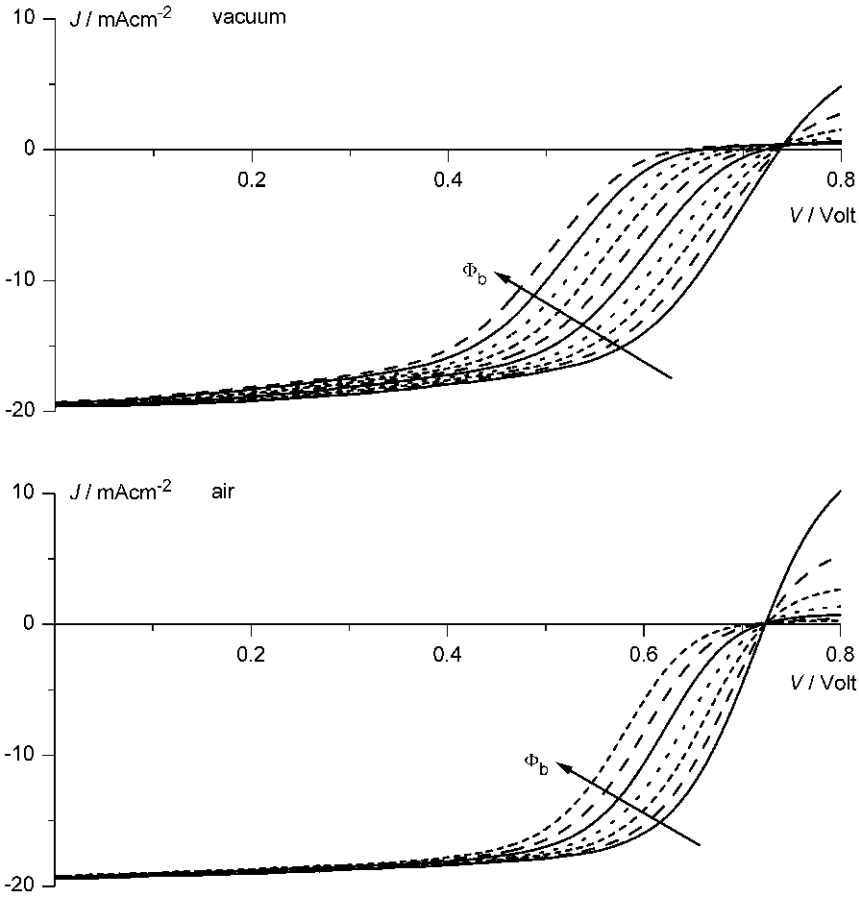

Figure 7.14 Variation of the I-V characteristics with the energy barrier Φ_b at the CdTe back contact. The other parameters have their baseline values. Top: a vacuum activated cell; Φ_b varies from 0.42 eV to 0.60 eV (step 0.02 eV). Bottom: an air activated cell; Φ_b varies from 0.40 eV to 0.52 eV (step 0.02 eV). Reproduced with permission from *Sol. Energy Mater. Sol. Cells*, **63**, V. Singh, D. Linam, D. Dils, J. McClure and G. Lush, Electro-optical characterization and modeling of thin films CdS-CdTe heterojunction solar cells, pp 445–466. Copyright (2000) Elsevier.

(1) The Contact Barrier

In Figure 7.14, the simulated I-V curves of vacuum and air activated cells are shown when the contact barrier Φ_b is varied. The effects illustrate what is commonly known. When Φ_b increases, the I-V curves start to roll over in the forward biased quadrant from about $\Phi_b \geq 0.4$ eV at room temperature, then FF decreases, and finally an S shaped I-V curve in the active quadrant develops. The associated efficiency loss is shown in Figure 7.15. The lower efficiency for the vacuum activated cells is due to the overall lower doping density, as we will show.

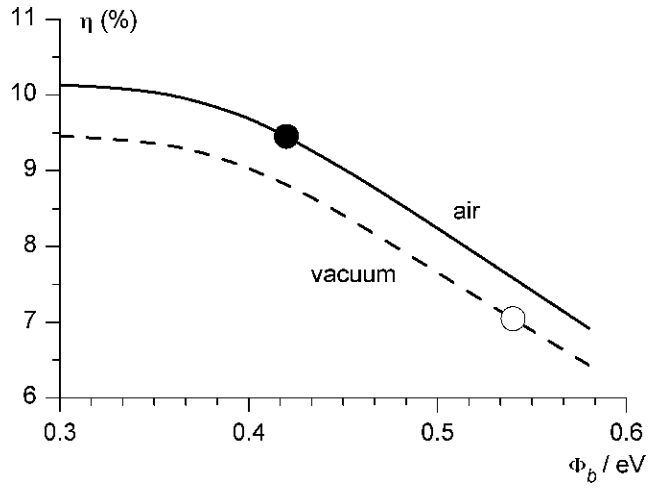

Figure 7.15 Efficiency of a vacuum (dashed line) and an air activated (solid line) cell as a function of the contact energy barrier Φ_b. The baseline values for both are indicated. Reproduced with permission from *Sol. Energy Mater. Sol. Cells*, **63**, V. Singh, D. Linam, D. Dils, J. McClure and G. Lush, Electro-optical characterization and modeling of thin films CdS-CdTe heterojunction solar cells, pp 445–466. Copyright (2000) Elsevier.

(2) The Doping Profile

When the doping density at the CdTe contact is varied, the other parameters having their baseline value for each cell, the I-V curves in Figure 7.16 are obtained. The resemblance to Figure 7.14, where Φ_b was varied, is striking. This illustrates that the effects of contact doping can be mistakenly interpreted as an effect of contact barrier. In particular, a high doping density at the CdTe contact can effectively mask the effects of a contact barrier. This result has been presented before (e.g.[90]), but it is often overlooked. The influence of the other shallow and deep doping and trap profiles in Table 7.5 is also studied. This is summarized in Figure 7.17 for air activated cells and Figure 7.18 for vacuum activated cells. In both cases, a high shallow doping at the contact N_{Acontact} is favourable. If N_{Acontact} could be increased beyond $10^{16}\,\text{cm}^{-3}$, an efficiency gain of 0.5 % (absolute) could still be expected. The deep acceptors at $\cong E_V + 0.72\,\text{eV}$ only contribute to the doping at reverse bias voltage, but they enhance the recombination in the SCL in the bias active voltage bias range ($0 < V < V_{\text{oc}}$): therefore, their concentration should be limited to about $10^{15}\,\text{cm}^{-3}$ (Figure 7.17). Also the bulk doping should be as high as possible, though the gain is only marginal for $N_{\text{Abulk}} > 5\,10^{15}\,\text{cm}^{-3}$. A low shallow CdTe bulk doping density deteriorates FF and hence η; this is illustrated for vacuum activated cells in Figure 7.18. This has been ascribed to too low an electric field in the SCL [159].

The efficiency does not depend entirely on the doping density $N_{\text{Ajunction}}$ near the CdS/CdTe junction, as several effects are simultaneously present. At high $N_{\text{Ajunction}}$, V_{oc} is high because of the higher built-in voltage, but the long wavelength current response decreases because of the small SCL width; at low $N_{\text{Ajunction}}$, the current collection is poor because of the electric field in the SCL is too weak; J_{sc} is maximal for intermediate $N_{\text{Ajunction}} \cong 2\,10^{15}\,\text{cm}^{-3}$, the maximum being broader for air activated cells; for higher value $N_{\text{Ajunction}} \cong 5$ to $8\,10^{15}\,\text{cm}^{-3}$, V_{oc} is

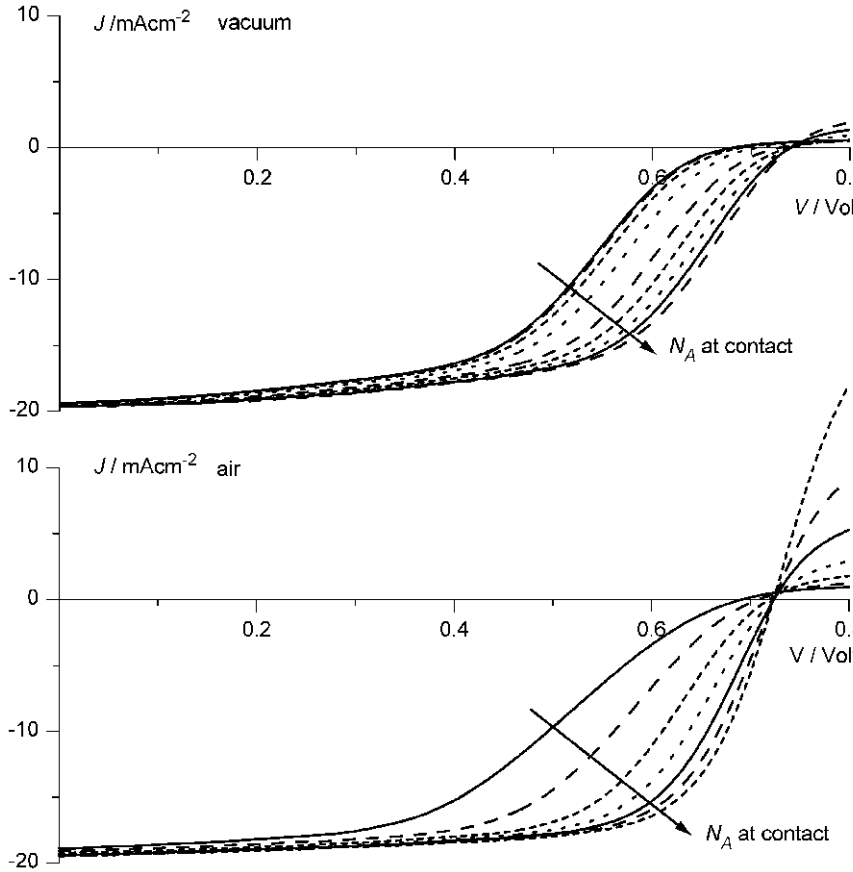

Figure 7.16 Variation of the *I*-*V* characteristics of a vacuum activated cell (top) and an air activated cell (bottom) with the doping density N_{Acontact} at the CdTe back contact. The other parameters have their baseline values (thus $\Phi_b = 0.42$ eV (air) and 0.55 eV (vacuum)). Top: a vacuum activated cell; the N_{Acontact} values are 10^{13}, 3 10^{13}, $10^{14}, \ldots, 10^{17}$ cm^{-3}. Bottom: an air activated cell; the N_{Acontact} values are 10^{14}, 3 10^{14}, $10^{15}, \ldots, 10^{17}$ cm^{-3}. Reproduced with permission from *Sol. Energy Mater. Sol. Cells*, **63**, V. Singh, D. Linam, D. Dils, J. McClure and G. Lush, Electro-optical characterization and modeling of thin films CdS-CdTe heterojunction solar cells, pp 445–466. Copyright (2000) Elsevier.

decreased because the roll over of the *I*-*V* curves already starts in the active quadrant. This complicated behaviour makes the CdTe doping near the junction the most critical parameter to adjust. Especially for vacuum activated cells, this parameter should be in a rather narrow range. The simulation results obtained here may explain the sometimes contradictory effects reported for introducing copper as a dopant from the back contact into the CdTe layer. It definitely diffuses easily through the CdTe layer, and accumulates at the CdTe/CdS junction and in the CdS layer [77]. We showed here, however, that the resulting cell behaviour is very sensitive to variations in the doping profile near the junction. Hence, technologies which rely on establishing a well tuned profile of copper related acceptors may bear a risk in terms of producibility and stability.

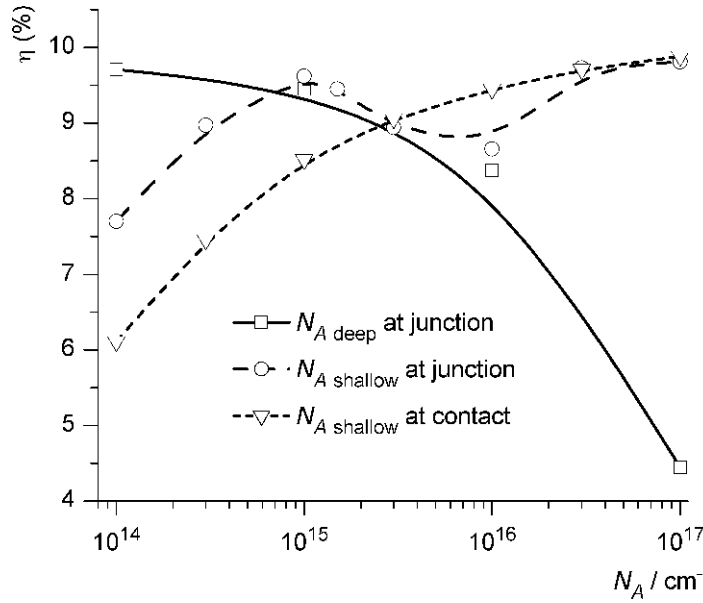

Figure 7.17 Efficiency of an air activated cell as a function of the density of the shallow doping at the contact and at the CdS junction, and of the deep acceptor density at the junction (level at $E_V + 0.72$ eV). The other parameters have their baseline values. Reproduced with permission from *Sol. Energy Mater. Sol. Cells*, **63**, V. Singh, D. Linam, D. Dils, J. McClure and G. Lush, Electro-optical characterization and modeling of thin films CdS-CdTe heterojunction solar cells, pp 445–466. Copyright (2000) Elsevier.

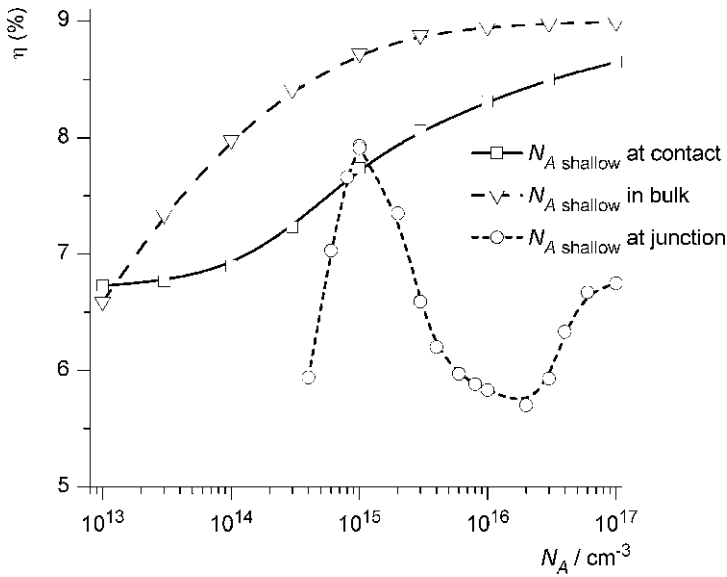

Figure 7.18 Efficiency of a vacuum activated cell as a function of the density of the shallow CdTe doping, at the contact, in the bulk, and at the CdS junction. The other parameters have their baseline values. Reprinted from Thin Solid Films, 480–481. M. Burgelman, J. Verschraegen, S. Degrave and P. Nollet, Analysis of CdTe and CIGS Solar Cells in relation to materials issues p. 392–398, Copyright (2005) with permission from Elsevier.

Other components of deep levels were investigated in literature. It was e.g. pointed out that deep donors close to the back contact cause a loss of V_{oc} due to compensation of the shallow acceptor doping in CdTe close to the back contact [89]. This is consistent with our results shown in Figure 7.16, though a loss of FF seems to be a more dominant effect for cells described by our parameter set.

The profile of shallow doping density in our cells is high–low–high, when going from the back contact to the junction. Such a profile has been invoked before to explain a set of measurements on cells of other fabrication [175]. The variations in such a high–low–high profile have been used to explain the behaviour of CdTe cells upon ageing [176]. Other profiles of shallow doping have also been reported, e.g. a doping density increasing steadily from the junction to the contact [89]. The simulations shown here demonstrate that all components of the shallow and the deep doping profile have their influence on the final I-V characteristics of a thin CdTe solar cell.

7.5.3.5 Modeling results: other subjects

We should mention here the early work of the group at Purdue University [177–182]. Other aspects of the CdTe cell that have been simulated extensively are: the effects in the QE and J-V measurements at forward voltage and short wavelengths (see Section 7.5.2.1), the C-V and C-f behaviour [141, 183–185] and various other parameter studies [186, 187].

7.5.3.6 Modeling results: (pseudo) two-dimensional modeling

Polycrystalline thin film solar cells properly require the use of two-dimensional or even three-dimensional programs because of grain boundaries and nonplanar interfaces. Grain boundary effects seem to be more prominent in CdTe cells than in CIGS cells. Although one-dimensional problems effectively average the effect of grain boundary states over the bulk, they have been surprisingly successful. Also, transition to two or three dimensions will increase substantially the number of input parameters, many of which are presently not well known.

In a simpler approach, pseudo two-dimensional simulation is obtained by combining one-dimensional physical simulation, e.g. with SCAPS, with network like treatment (e.g. SPICE) of the other dimensions. A useful application of this is the monolithic series integration of thin film cells in a module (Section 7.4.2), which is treated e.g. by the module design simulator [188]. In this programme, all the physics of the 'elementary unit cell' are lumped in one exponential diode law, to be specified by the user. All two-dimensional aspects of the series integration are treated as a network of such unit cells and resistors. While the direct link with cell physics is lost in this way, there is a tremendous gain in speed and interactivity when it comes to designing the series integration. A similar network approach, combined with an analytical effective medium model, was used by Shvydka, Karpov *et al*. to simulate the effect of nonuniformities and small area defects [189–191]. The effects of nonuniform illumination or small area contacts have also been treated in this way, e.g. [192].

As specialized, nanoscale characterization tools for the physical and chemical properties at the grain boundaries have been developed recently (Section 7.3.4.3), it is to be expected that these pseudo two-dimensional and full two-dimensional numerical simulations will be

applied for a quantitative description of the influence of grain boundary effects on the cell's photovoltaic output.

7.6 CONCLUSIONS

In this chapter, we described the photovoltaic achievements of CdTe solar cells and modules. The important summary for the general PV community is that CdTe solar modules are now being produced, and are on the market. This was however not the main emphasis of this chapter: rather it was the long scientific and technological chain from material properties to the final cell performance.

Cadmium telluride is reputed as a forgiving material, in the sense that the solar cell properties do not suffer too much from the rather poor crystalline quality of the layers constituting the cell. This is illustrated by the fact that good CdTe cells have been made with a multitude of different techniques: it seems that, regardless of the deposition technology, a more or less universal recipe – activation treatment with $CdCl_2$– leads to decent cells. This seeming simplicity of the fabrication technology, however, hides the complexity that exists in the cell structure and operation. Excellent scientists and skilled technicians have brought CdTe solar cell technology to the high level where it stands now, largely on an empirical basis, thereby combining technological mastery with a remarkable intuition for materials technology. For further developments and achievements our knowledge of *how* to do it will have to be complemented by our insight into *why* things work as they do. And our general, qualitative understanding of the main working principles will have to evolve to a detailed quantitative understanding of all materials and phenomena involved. Recent developments in advanced characterization tools and in physical modeling, and a mature, active and multidisciplinary research community are the pillars that further CdTe cell and module development can built on. We are confident that, in the moving scene of PV and other energy developments, CdTe photovoltaics will continue to contribute to that shared dream of humanity – clean, affordable energy from the Sun, for all.

ACKNOWLEDGMENTS

This work is supported by the Research Fund of the University of Gent (BOF-GOA). It also contains work carried out in the European research projects CADBACK (contract JOR3-CT98-0218) and EUROCAD (contract JOU-CT92-0243).

REFERENCES

[1] D. Bonnet and H. Rabenhorst, New results on the development of a thin film *p*-CdTe/*n*-CdS heterojunction solar cell, *Proc. 9th IEEE Photovoltaic Specialists Conference* (Silver Springs, MD, May 1972), 129–131, IEEE, New York (1972).

[2] X. Wu, J. Keane, R. Dhere, C. DeHart, A. Duda, T. Gessert, S. Asher, D. Levi and P. Sheldon, 16.5 %-efficient CdS/CdTe polycrystalline thin film solar cell, *Proc. 17th European Photovoltaic Solar Energy Conference* (Munich, Germany, October 2001), 995–1000, WIP, Munich (2002).

[3] D. Bonnet, H. Richter and K.H. Jäger, The CTS thin film solar module – closer to production, *Proc. 13th European Photovoltaic Solar Energy Conference* (Nice, France, Oct. 1995), 1456–1460, Stephens & Associates, UK (1996).
[4] D. Bonnet and M. Harr, Manufacturing of CdTe solar cells, *Proc. 2nd World Conference on Photovoltaic Energy Conversion* (Vienna, Austria, July 1998), 397–402, JRC, European Commission (1998).
[5] M. Harr and D. Bonnet, Production of advanced thin film solar modules, *Proc. 17th European Photovoltaic Solar Energy Conference* (Munich, Germany, October 2001), 1001–1004, WIP, Munich (2002).
[6] D. Rose, R. Powell, U. Jayamaha, M. Maltby, D. Giolando, A. McMaster, K. Kormanyos, G. Faykosh, J, Klopping and G. Dorer, R&D of CdTe-absorber photovoltaic cells, modules, and manufacturing equipment: plan and progress 10 100 MW/yr, *Proc. 28th IEEE Photovoltaic Specialists Conference* (Anchorage, AL, September 2000), 428–431, IEEE, New York (2000).
[7] D. Bonnet, The CdTe thin film solar cell – an overview, *Int. J. Solar Energy*, **12**, 1–14 (1992).
[8] T. Chu and S. Chu, Recent progress in thin film cadmium telluride solar cells, *Prog. Photovolt. Res. Appl.*, **1**, 31–42 (1993).
[9] P.Meyers and S. Albright, Technical and economic opportunities for CdTe PV at the turn of the millennium, *Prog. Photovolt. Res. Appl.*, **8**, 161–169 (2000).
[10] D. Bonnet, Cadmium telluride solar cells, in *Clean Electricity from Photovoltaics*, M. Archer and R. Hill (Eds.), Imperial College Press, London (2001).
[11] K. Durose, D. Boyle, A. Abken, C. Ottley, P. Nollet, S. Degrave, M. Burgelman, R. Wendt, J. Beier and D. Bonnet, Key aspects of CdTe/CdS solar cells, *Physica Status Solidi a*, **229,** 1055–1064 (2002).
[12] D. Bonnet, The evolution of the CdTe thin film solar cell, *Proc. 19th European Photovoltaic Solar Energy Conference* (Paris, France, June 2004), 1657–1662, WIP, Munich (2004).
[13] D. Bonnet and P. Meyers, Cadmium telluride – material for thin film solar cells, *J. Mater. Res.*, **13**, 2740–2753 (1998).
[14] S. M. Sze, *Physics of semiconductor devices* (2nd edn.), John Wiley & Sons Inc., New York (1981).
[15] M. Green, *Solar Cells – Operating Principles, Technology and System Applications*, The University of South Wales (1998).
[16] S. J. Fonash, *Solar Cell Device Physics*, Academic Press, New York (1977).
[17] A. L. Fahrenbruch and R. H. Bube, *Fundamentals of Solar Cells*, Academic Press, New York (1983).
[18] K. L. Chopra and S. R. Das, *Thin Film Solar Cells*, Plenum Press, New York (1983).
[19] A. Milnes and D. Feucht, *Heterojunctions and Metal-semiconductor Junctions*, Academic Press, New York (1972).
[20] R. Granger, Optical absorption of Cd/Zn/Te/Se compounds, in *Narrow Gap Cadmium Based Compounds*, Peter Capper (Ed.), EMIS Datareview Series, INSPEC, London, 427–432 (1994).
[21] S. Adachi, *Optical Constants of Crystalline and Amorphous Semiconductors*, Kluwer Academic Publishers, Boston (1999).
[22] H. J. Möller, *Semiconductors for Solar Cells*, Artech House, London (1993).
[23] X. Mathew and J. Pantoja Enriquez, Temperature dependence of the optical transitions in CdTe thin film – investigation with photoresponse spectra, *Sol. Energy Mater. Sol. Cells*, **63**, 347–354 (2000).
[24] E. Palik, Cadmium telluride (CdTe), in *Handbook of Optical Constants of Solids,* E. Palik (Ed.), Academic Press, New York, 409–427 (1985).
[25] M. Green, *Silicon Solar Cells – Advanced Principles &Practice*, The University of South Wales (1995).
[26] D. Albin, N. Dhere, A. Mason and A. Compaan, Optical bandgap data at room temperature for the $CdTe_{1-x}S_x$ alloy system, unpublished results (9-9-1997). Private communication by D. Albin (2005).

[27] J. Toušek, D. Kindl, J. Toušková, S. Dolhov and A. Poruba, Diffusion length in CdTe by measurement of photovoltage spectra in CdTS/CdTe solar cells, *J. Appl. Phys.*, **89**, 460–465 (2001).
[28] D. Wood, K. Rogers, D. Lane and J. Coath, Optical and structural characterization of CdS_xTe_{1-x} thin films for solar cell applications, *J. of Phys.: Condensed Matter*, **12**, 4433–4450 (2000).
[29] K. Ohata, J. Saraie and T. Tanaka, *Jpn. J. Appl. Phys.*, **12**, 1641 (1973).
[30] G. Gordillo, F. Rojas and C. Calderón, Optical characterization of $Cd(S_xTe_{1-x})$ thin films deposited by evaporation, *Superficies y Vacio*, **16**, 30–33 (2003).
[31] R. Granger, Dielectric constants of Cd/Zn/Te/Se compounds, in *Narrow Gap Cadmium Based Compounds*, Peter Capper (Ed.), EMIS Datareview Series, INSPEC, London, 433–435 (1994).
[32] K. Zanio, *Semiconductors and Semimetals*, **13**, Academic Press, New York (1978).
[33] J. Pautrat and N. Magnea, Shallow and deep levels in Zn/Cd/Te/Se compounds, in *Narrow Gap Cadmium Based Compounds*, Peter Capper (Ed.), EMIS Datareview Series, INSPEC, London, 546–554 (1994).
[34] E. Molva, J. Chamonal and J. Pautrat, Shallow acceptors in cadmium telluride, *Physica Status Solidi B*, **109**, 635–644 (1982).
[35] M. Astles, Impurity doping in CdTe, in *Narrow Gap Cadmium Based Compounds*, Peter Capper (Ed.), EMIS Datareview Series, INSPEC, London, 494–500 (1994).
[36] Y. Marfaing, Impurity doping and compensation mechanisms in CdTe, *Thin Solid Films*, **387**, 123–128 (2001).
[37] Y. Marfaing, Models of doping impurity compensation in cadmium telluride, *Revue de Physique Appliquée*, **12**, 211–217 (2001).
[38] X. Mathew, J. Arizmendi, J. Campos, P. Sebastian, N. Mathews, C. Jiménez, M. Jiménez, R. Silva-González, M. Hernández-Torres and R. Dhere, Shallow levels in the band gap of CdTe films deposited on metallic substrates, *Sol. Energy Mater. Sol. Cells*, **70**, 379–393 (2001).
[39] V. Lyahovitskaya, L. Cherniak, J. Greenberg, L. Kaplan and D. Cahen, Low temperature, post-growth self-doping of CdTe single crystals due to controlled deviation from stoiciometry, *J. Appl. Phys.*, **88**, 3976–3981 (2000).
[40] V. Lyahovitskaya, L. Cherniak, J. Greenberg, L. Kaplan and D. Cahen, *n*- And *p*-type post-growth self-doping of CdTe single crystals, *J. Cryst. Growth*, **214–215**, 1155–1157 (2000).
[41] D. Schroder, *Semiconductor Material and Device Characterization*, 2nd ed., John Wiley & Sons Inc., Toronto (1998).
[42] G. Agostinelli and E. Dunlop, Artefacts in the measurement of effective diffusion lengths in CdTe solar cells, *Proc. 17th European Photovoltaic Solar Energy Conference* (Munich, Germany, October 2001), 1054–1057, WIP, Munich (2002).
[43] I. Clemminck, M. Burgelman, M. Casteleyn and B. Depuydt, Screen printed and sintered CdTe-CdS solar cells, *Int. J. Solar Energy*, **12**, 67–78 (1992).
[44] A. Niemegeers, M. Burgelman and A. De Vos, On the $CdS/CuInSe_2$ conduction band discontinuity, *App. Phys. Lett.*, **67(6)**, 843–845 (1995).
[45] J. Fritsche, T. Schulmeyer, D. Kraft, A. Thißen, A. Klein and W. Jägermann, Utilisation of sputter depth profiling for the determination of band alignment at polycrystalline CdTe/CdS heterointerfaces, *Appl. Phys. Lett.*, **81**, 2297–2299 (2002).
[46] H. Matsumoto, K. Kuribayashi, H. Uda, Y. Komatsu, A. Nakano and S. Ikegami, Screen-printed CdS/CdTe solar cell of 12.8 % efficiency for an active area of 0.78 cm^2, *Solar Cells*, **11**, 367–373 (1984).
[47] I. Oladeji, L. Chow, C. Ferekides, V. Viswanathan, Zhiyong Zhao, Metal/CdTe/CdS/$Cd_{1-x}Zn_x$/TCO/glass: a new CdTe thin film solar cell structure, *Sol. Energy Mater. Sol. Cells*, **61**, 203–211 (2000).
[48] M. Gloeckler, A.Fahrenbruch and J.Sites, Numerical modelling of CIGS and CdTe solar cells: setting the baseline, *Proc. 3rd World Conference on Photovoltaic Energy* Conversion (Osaka, Japan, May 2003), 491–494, WCPEC-3, Osaka (2003).

[49] J. Sites, Chalcogenide solar cells: choosing the window, presented (invited) at the European Materials Research Society Conference (Symposium O: Thin film chalcogenide photovoltaic materials), E-MRS, Strasbourg, France, 24–28 May 2004; accepted for publication in *Thin Solid Films*.

[50] D. Albin, Y. Yan amd M. Al-Jassim, The effect of oxygen on interface and microstructure evolution in CdTe/CdS solar cells, *Prog. Photovolt. Res. Appl.*, **10**, 309–322 (2002).

[51] J. Britt and C. Ferekides, Thin-film CdS/CdTe solar cell with 15.8 % efficiency, *Appl. Phys. Lett.*, **62**, 2851–2852 (1993).

[52] N. Romeo, A. Bosio, V. Canavari, M. Terheggen and L. Vaillant Roca, Comparison of different conducting oxides as substrates for CdS/CdTe thin film solar cells, *Thin Solid Films*, **431–432**, 364–368 (2003).

[53] K. Oehlstrom, V. Sittinger, S. Friedmann, A. Abken, R. Reineke-Koch and J. Parisi, Cd_2SnO_4 as front contact for CdS/CdTe solar cells, *Proc. 17th European Photovoltaic Solar Energy Conference* (munich, Germany, October 2001), 1172–1175, WIP, Munich (2002).

[54] R. Schropp and M. Zeman, *Amorphous and Microcrystalline Silicon Solar Cells: Modelling, Materials and Device Technology*, Kluwer Academic Publishers, Boston (1998).

[55] B. McCandles, L. Moulton and R. Birkmire, Recrystallisation and sulphur diffusion in $CdCl_2$-treated CdTe/CdS thin films, *Prog. Photovolt. Res. Appl.*, **5**, 249–260 (1997).

[56] B. Başol, Processing high efficiency CdTe solar cells, *Int. J. Solar Energy*, **12**, 25–35 (1992).

[57] N. Romeo, A. Bosio and V. Canevari, A new method to prepare efficient CdTe/CdS thin film solar cells, *Proc. 11th European Photovoltaic Solar Energy Conference* (Montreux, Switzerland, October 1992), 972–974, Harwood, CH (1993).

[58] T. Zhou, N. Reiter, R. Powell, R. Sasala and P. Meyers, Vapor chloride treatment of polycrystalline CdTe/CdS films, *Proc. 1st World Conference on Photovoltaic Energy Conversion* (Hawaii, 1994), 103–106, IEEE, New York (1995).

[59] B. McCandless, I. Youm and W. Birkmire, Optimization of vapour post-deposition processing for evaporated CdS/CdTe solar cells, *Prog. Photovolt. Res. Appl.*, **7**, 21–30 (1999).

[60] T. Potlog, L. Ghimpu, P. Gashin, A. Pudov, T. Nagle and J. Sites, Influence of annealing in different chlorides on the photovoltaic parameters of CdS/CdTe solar cells, *Sol. Energy Mater. Sol. Cells*, **80**, 327–334 (2003).

[61] Marc Köntges, *Beleuchtungsabhängiger Ladungstransport durch tiefe kompensierende Störstellen in CdTe und Cu(In,Ga)Se_2-Solarzellen*, PhD thesis, University of Oldenburg / IFSH (2002) (in German).

[62] K. Nakamura, T. Fujihara, T. Toyama and H. Okamoto, Influence of $CdCl_2$ treatment on the structural and electrical properties of highly efficient 2-μm thick CdS/CdTe thin film solar cells, *Jpn. J. Appl. Phys.*, **41**, 4474–4480 (2002).

[63] K. Krishna and V. Dutta, Effect of *in situ* $CdCl_2$ treatment on spray deposited CdTe/CdS heterostructure, *J. Appl. Phys.*, **96**, 3962–3971 (2004).

[64] P. Paulson, V. Dutta, Study of *in situ* $CdCl_2$ treatment on CSAS deposited CdTe films and CdS/CdTe solar cells, *Thin Solid Films*, **370**, 299–306 (2000).

[65] I. Clemminck, M. Burgelman, M. Casteleyn, J. De Poortere and A. Vervaet, Interdiffusion of CdS and CdTe in screenprinted and sintered CdS-CdTe solar cells, *Proc. 22nd IEEE Photovoltaic Specialists Conference* (Las Vegas, NV, 1991), 1114–1119, IEEE, New York (1992).

[66] B. McCandless, M. Engelmann and R. Birkmire, Interdiffusion of CdS/CdTe thin films: modelling and x-ray diffraction line profiles, *J. Appl. Phys.*, **89**, 988–994 (2001).

[67] P. Gibson, M. Baker and M. Özsan, Investigation of sulphur interdiffusion at the CdS/CdTe interface of thin-film solar cells, *Surface and Interface Analysis*, **33**, 825–829 (2002).

[68] U. Jahn, T. Okamoto, A, Yamada and M. Konagai, Doping and intermixing in CdS/CdTe solar cells fabricated under different conditions, *J. Appl. Phys.*, **90**, 2553–2558 (2001).

[69] S. Ringel, A. Smith, M. McDougal and A. Rohatgi, The effects of the $CdCl_2$ on the electronic properties of molecular-beam epitaxially grown CdTe/CdS heterojunction solar cells, *J. Appl. Phys.,* **70**, 881– 889 (1991).

[70] A. Niemegeers, M. Burgelman, H. Richter and D. Bonnet, A model for the effects of the $CdCl_2$ treatment on the performance of CdTe/CdS solar cells, *Proc. 14th European Photovoltaic Solar Energy Conference* (Barcelona, Spain, July 1997), 2079–2082, Stephens & Associates, UK (1998).

[71] A. Rohatgi, A study of efficiency limiting defects in polycrystalline CdTe/CdS solar cells, *Int. J. Solar Energy*, **12**, 37–49 (1992).

[72] N. Romeo, A. Bosio, V. Canevari and T. Kuku, Crystallisation of CdTe thin films by $CdCl_2$ treatment at high temperature, *Proc. 12th European Photovoltaic Solar Energy Conference* (Amsterdam, the Nederlands, April 1994), 662–663, Stephens & Associates, UK (1994).

[73] J. Hiie, CdTe:$CdCl_2$:O_2 annealing process, *Thin Solid Films*, **431–432**, 90–93 (2003).

[74] E. H. Rhoderick, *Metal-semiconductor Contacts*, Clarendon, Oxford (1978).

[75] J. P. Ponpon, A review of ohmic and rectifying contacts on cadmium telluride, *Solid-State Electronics*, **28**, 689–706 (1985).

[76] D. Kraft, B. Späth, J. Fritsche, A. Thißen, A. Klein and W. Jaegermann, Metal contacts to CdTe and ZnTe, presented at the European Materials Research Society Conference (Symposium O: Thin film chalcogenide photovoltaic materials), E-MRS, Strasbourg, France, 24–28 May 2004; accepted for publication in *Thin Solid Films*.

[77] K. Dobson, I. Visoly-Fisher, G. Hodes and D. Cahen, Stabilizing CdTe/CdS solar cells with Cu-containing contacts to p-CdTe, *Adv. Mat.*, **13**, 1495–1499 (2001).

[78] B. Depuydt, M. Burgelman, M. Casteleyn, A. Vervaet and A. Niemegeers, The effects of diffusion of impurities from graphite back contacts on CdS/CdTe cells, *Proc. 13th European Photovoltaic Solar Energy Conference* (Nice, France, October 1995), 593–596, Stephens & Associates, UK (1996).

[79] V. Singh, O. Erikson and J. Chao, Analysis of contact degradation at the CdTe-electrode interface in thin film CdTe-CdS solar cells, *J. Appl. Phys.*, **78**, 4538–4542 (1995).

[80] Y. Soo, S. Huang, S. Kim, G. Kioseoglou, Y. Kao, A. Compaan, D. Grecu and D. Albin, Effects of heat treatment on diffusion of Cu atoms into CdTe single crystals, *Appl. Phys. Lett.*, **76**, 3729–3731 (2000).

[81] C. Corwine, A. Pudov, M. Gloeckler, S. Demtsu and J. Sites, Copper inclusion and migration from the back contact in CdTe solar cells, *Sol. Energy Mater. Sol. Cells*, **82**, 481–489 (2004).

[82] M. Soliman, The effect of annealing on the junction properties of CdTe/CdS cells with carbon contacts, *Renewable Energy*, **23**, 355–360 (2001).

[83] A. Hanafusa, T. Aramoto and A. Morita, Performance of graphite pastes doped with various materials as back contact for CdS/CdTe solar cell, *Jpn. J. Appl. Phys.*, **40**, 6764–6769 (2001).

[84] A. Abken, Chemical stability of sputtered Mo/Sb_2Te_3 and Ni/Sb_2Te_3 layers in view of stable back contacts for CdTe/CdS thin film solar cells, *Sol. Energy Mater. Sol. Cells*, **73**, 391–409 (2002).

[85] D. Bätzner, A. Romeo, M. Terheggen, M. Döbeli, H. Zogg and A. Tiwari, Stability aspects in CdTe/CdS solar cells, *Thin Solid Films*, **451-452**, 536–543 (2004).

[86] G. Stollwerck and J. Sites, Analysis of the CdTe back contact barriers, *Proc. 13th European Photovoltaic Solar Energy Conference* (Nice, France, 1995) Stephens & Associates, UK (1996).

[87] A. Niemegeers and M. Burgelman, Effects of the Au/CdTe back contact on *IV*- and *CV*-characteristics of Au/CdTe/CdS/TCO solar cells, *J. Appl. Phys.*, **81**, 2881–2886 (1997).

[88] M. Burgelman, P. Nollet, S. Degrave and J. Beier, Modelling the cross-over of the *I*-*V* characteristics of thin film CdTe solar cells, *Proc. 28th IEEE Photovoltaic Specialists Conference* (Anchorage, AL, September 2000), 551–554, IEEE, New York (2000).

[89] T. McMahon and A. Fahrenbruch**,** Insights into the nonideal behavior of CdS/CdTe solar cells, *Proc. 28th IEEE Photovoltaic Specialists Conference* (Anchorage, AL, September 2000), 539–542, IEEE, New–York (2000).

[90] J. Beier, M. Köntges, P. Nollet, S. Degrave and M. Burgelman, Importance of electron current in *p*-type CdTe in CdS/CdTe thin film solar cells at forward bias, *Mat. Res. Soc. Symp. Proc.*, **668**, H9.5.1–H9.5.6 (2001).

[91] V. Fthenakis, Overview of potential hazards, in *Practical Handbook of Photovoltaics: Fundamentals and Applications*, T. Markvart and L. Castañer, Elsevier, Amsterdam, 857–868 (2003).

[92] K. Zweibel and V. Fthenakis, Cadmium facts and handy comparisons, revision 26-12-2002, Report of NREL (National Renewable Energy Laboratory) and BNL (Brookhaven National Laboratory), available at http://www.nrel.gov/cdte/pdfs/cdte_factsheet.pdf . See also http://www.nrel.gov/cdte/ref_res.html .

[93] E. Alsema and B. van Engelenburg, Environmental risk of CdTe and CIS solar cell modules, *Proc. 11th European Photovoltaic Solar Energy Conference* (Montreux, Switzerland, October 1992), 995–998, Harwood, CH (1993).

[94] V. Fthenakis, Life cycle impact analysis of cadmium in CdTe PV production, *Renew. & Sustain. En. Rev.*, **8**, 303–334 (2004).

[95] P. Moskowitz, Environmental, health and safety issues related to the production and use of CdTe photovoltaic modules, *Int. J. Solar Energy*, **12**, 259–281 (1992).

[96] V. Fthenakis and P. Moskowitz, Thin-film photovoltaic cells: health and environmental issues in their manufacture, use and disposal, *Prog. Photovolt. Res. Appl.*, **3**, 295–306 (1995).

[97] P. Moskowitz and V. Fthenakis, Environmental, health and safety issues associated with the manufacture and use of II-VI photovoltaic device, *Solar Cells*¸ **30**, 89–99 (1991).

[98] V. Fthenakis and P. Moskowitz, Photovoltaics: Environment, health and safety issues and perspectives, *Prog. Photovolt. Res. Appl.*, **8**, 27–38 (2000).

[99] V. Fthenakis, S. Morris, P. Moskowitz and D. Morgan, Toxicity of cadmium telluride, copper indium diselenide, and copper gallium diselenide, *Prog. Photovolt. Res. Appl.*, **7**, 489–497 (1999).

[100] Nomination of cadmium telluride to the national toxicology program, memorandum of the US National Renewables Energy Laboratory (NREL) and the Brookhaven National Laboratory (BNL), 2003.

[101] J. Bohland and K. Smigielski, First Solar's CdTe module manufacturing experience; environmental, health and safety results, *Proc. 28th IEEE Photovoltaic Specialists Conference* (Anchorage, AL, September 2000), 575–578, IEEE, New York (2000).

[102] P. Moskowitz and V. Fthenakis, Toxic materials released from photovoltaic modules during fires; health risks, *Solar Cells*, **29**, 63–71 (1990).

[103] H. Steinberger, Health, safety and environmental risks from the operation of CdTe and CIS thin-film modules, *Prog. Photovolt. Res. Appl.*, **6**, 99–103 (1998).

[104] T. Toyama, T. Suzuki, M. Gotoh, K. Nakamura, H. Okamoto, Reduction of infrared response of CdS/CdTe thin-film solar cell with decreased thickness of photoactive layer, *Sol. Energy Mater. Sol. Cells*, **67**, 41–47 (2001).

[105] K. Ernst, A. Balaidi, R. Könenkamp, Solar cell with extremely thin absorber on highly structured substrate, *Semiconductor Science and Technology*, **18**, 475–479 (2003).

[106] C. Grasso, K. Ernst, R. Könenkamp, M. Burgelman, M.-C. Lux-Steiner, Photoelectrical characterization and modeling of the eta-solar cell, *Proceedings of the 17th European Photovoltaic Conference* (munich, Germany, Ooctober 2001), 211–214, WIP, Munich (2002).

[107] S. Irvine, V. Barrioz, A. Stafford and K. Durose, Materials issues in very thin film CdTe for photovoltaics, presented at the European Materials Research Society Conference (Symposium O: Thin film chalcogenide photovoltaic materials), E-MRS, Strasbourg, France, 24–28 May 2004; accepted for publication in *Thin Solid Films* (December 2004).

[108] J. Sites, J. Granata and J. Hiltner, Losses due to polycrystallinity in thin-film solar cells, *Sol. Energy Mater. Sol. Cells*, **55**, 43–50 (1998).

[109] U. Rau, R. Noufi, and L. Stolt (organizers), Workshop on Polycrystallinity in CIGS Thin-Film Solar Cells, Strasbourg, France, 29 May 2004. Contributions on CdTe were presented by A. Compaan

(A10), W. Jägermann (B01), I. Visoly-Fischer (C03) and M. Burgelman (C12). No Workshop Records were published.

[110] Y. Yan, D. Albin and M. Al-Jassim, Do grain boundaries assist S diffusion in polycrystalline CdS/CdTe heterojunctions?, *Appl. Phys. Lett.*, **81**, 171–173 (2002).

[111] K. Durose, M. Cousins, D. Boyle, J. Beier and D. Bonnet, Grain boundaries and impurities in CdTe/CdS solar cells, *Thin Solid Films*, **403–404**, 396–404 (2002).

[112] L. Woods, D. Levi, V. Kaydanov, G. Robinson and R. Ahrenkiel, Electrical characterization of CdTe grain boundary properties from as processed CdTe/CdS solar cells, *Proc. 2nd World Conference on Photovoltaic Energy Conversion* (Vienna, Austra, July 1998), 1043–1046, JRC, European Commission (1998).

[113] L. Woods, G. Robinson and D. Levi, The effects of $CdCl_2$ on CdTe electrical properties using a new theory for grain boundary conduction, *Proc. 28th IEEE Photovoltaic Specialists Conference* (Anchorage, AL, September 2000), 603–606, IEEE, New York (2000).

[114] P. Edwards, S. Galloway and K. Durose, Erratum to EBIC and luminescence mapping of CdTe/CdS solar cells, *Thin Solid Films*, **372**, 284–291 (2000).

[115] S. Galloway, P. Edwards and K. Durose, Characterisation of thin film CdS/CdTe solar cells using and optical beam induced current, *Sol. Energy Mater. Sol. Cells*, **57**, 61–74 (1999).

[116] K. Durose, J. R. E. Sadler, A. Yates, A. Szczerbakow, R-EBIC study of the electrical activity of grain boundaries in CdTe and Cd(S,Te), *Proc. 28th IEEE Photovoltaic Specialists Conference* (Anchorage, AL, September 2000), 487–490, IEEE, New York (2000).

[117] I. Visoly-Fisher, S. Cohen and D. Cahen, Direct evidence for grain-boundary depletion in polycrystalline CdTe from nanoscale-resolved measurements, *Appl. Phys. Lett.*, **82**, 556–568 (2003).

[118] I. Visoly-Fisher, S. Cohen, A. Ruzin and D. Cahen, How polycrystalline devices can outperform single crystal ones: thin film CdTe solar cells, *Adv. Mat.*, **76**, 879–883 (2004).

[119] R. Birkmire, B. McCandles and S. Hegedus, Effects of processing on CdTe/CdS materials and devices, *Int. J. Solar Energy*, **12**, 145–154 (1992).

[120] M. Bhatti, K. Hynes, R. Miles and R. Hill, Thin films of cadmium telluride produced using stacked elemental layer (SEL) processing for use in thin film solar cells, *Int. J. Solar Energy*, **12**, 171–182 (1992).

[121] J. Skarp, E. Anttila, A. Rautiainen and T. Suntola, ALE-CdS/CdTe-PV-cells, *Int. J. Solar Energy*, **12**, 137–142 (1992).

[122] F. Abou-Elfotouh and T. Coutts, RF magnetron sputtering of polycrystalline CdTe thin film solar cells, *Int. J. Solar Energy*, **12**, 223–246 (1992).

[123] A. Compaan, Ch. Tabory, Y. Li, Z. Feng and A. Fisher, CdS/CdTe solar cells by RF sputtering and by laser physical vapour deposition, *Proc. 23nd IEEE Photovoltaic Specialists Conference* (Louisville, KY, May 1993), 394–399, IEEE, New York (1993).

[124] D. Cunningham, M. Rubcich and D. Skinner, Cadmium telluride PV module manufacturing at BP Solar, *Prog. Photovolt. Res. Appl.*, **10**, 159–168 (2004).

[125] S. Albright, B. Ackerman, J. Jordan, Efficient CdTe/CdS solar cells and modules by spray processing, *IEEE Trans. Electron Dev.*, **37**, 434–437 (1990).

[126] S. Albright, R. Chamberlin, B. Ackerman and J. Jordan, Performance measurement irregularities on CdS/CdTe devices and modules, *Int. J. Solar Energy*, **12**, 109–120 (1992).

[127] S. Ikegami and A. Nakano, Effect of oxygen on photovoltaic properties of screen-printed CdS/CdTe solar cell and module, *Int. J. Solar Energy*, **12**, 53–65 (1992).

[128] J. Park, B. Ahn, H. B. Im *et al*., Photovoltaic properties of sintered CdS.CdTe solar cells doped with Cu, *J. Electrochem. Soc.*, **139**, 3351–3356 (1992).

[129] A. Tiwari, A. Romeo, D. Bätzner and H. Zogg, Flexible CdTe solar cells on polymer films, *Prog. Photovolt. Res. Appl.*, **9**, 211–215 (2001).

[130] A. Romeo, M. Arnold, D. Bätzner, H. Zogg and A. Tiwari, Development of high efficiency flexible CdTe solar cells, *Conference Records of PV in Europe, from PV technology to energy solutions* (Rome, Italy, October 2002), 377–381 (2002).

[131] A. Romeo, D. Bätzner, H. Zogg and A. Tiwari, Influence of proton irradiation and development of flexible CdTe solar cells on polyimide, *Mat. Res. Soc. Symp. Proc.*, **668**, H3.3.1–H3.3.6 (2001).
[132] D. Bätzner, A. Romeo, M. Döbeli, K. Weinert, H. Zogg and A. Tiwari, High energy irradiation properties of CdTe/CdS solar cells, *Proc. 29th IEEE Photovoltaic Specialists Conference* (New Orleans, LA, 20–24 May 2002), 982–985, IEEE, New York (2002).
[133] A. Tiwari, G. Khrypunov, F. Kurdzesau, D. Bätzner, A. Romeo and H. Zogg, CdTe solar cell in a novel configuration, *Prog. Photovolt. Res. Appl.*, **12**, 33–38 (2004).
[134] D. Niles, X. Li, D. Albin, D. Rose, T. Gessert and P. Sheldon, Evaporated Te on CdTe : a vacuum-compatible approach to making back contact to CdTe solar cell devices, *Prog. Photovolt. Res. Appl.*, **4**, 225–229 (1996).
[135] N. Romeo, A. Bosio, V. Canevari, A. Podestà, S. Mazzamuto and G. Guadalupi, High efficiency CdTe/CdS thin film solar cells with Sb_2Te_3 back contact by a thoroughly dry process, *Proc. 19th European Photovoltaic Solar Energy Conference* (Paris, France, June 2004), 1718–1720, WIP, Munich (2004).
[136] ANTEC Solar Energy AG, Emil-Paßburgstraße 1, D-99310 Arnstadt, Germany. See: http://www.antec-solar.de/
[137] First Solar, LLC, 28101 Cedar Park Blvd., Perrysburg, OH 43551, USA See: http://www.firstsolar.com/
[138] F. Padovani and R. Stratton, Field and thermionic-field emission in Schottky barriers, *Solid-State Electr.*, **9**, 695-707 (1966).
[139] Thomas Walter, *Herstellung und optoelektronische Charakterisierung polykristaliner I-III-VI_2-Verbindungshalbleiter und darauf basierender Heteroübergänge für Dünnschichtsolarzellen*, PhD thesis, University of Stuttgart, Institut für Physikalische Elektronik (IPE) (1994) (in German).
[140] M. Burgelman, A. De Vos and A. Niemegeers, Device simulation of polycrystalline heterojunction solar cells, *Proc. 12th European Photovoltaic Solar Energy Conference* (Amsterdam, the Nederlands, April 1994), 1557–1560, Stephens & Associates, UK (1994).
[141] A. Niemegeers, S. Gillis and M. Burgelman, Interpretation of capacitance spectra in the special case of novel thin film CdTe/CdS and CIGS/CdS solar cell device structures, *Proc. 2nd World Conference on Photovoltaic Energy Conversion* (Vienne, Austria, July 1998), 1071–1074, JRC, European Commission (1998).
[142] T. Walter, R. Herberholz, C. Müller and H.-W**.** Schock, Determination of defect distributions from admittance measurements and application to Cu(In,Ga)Se_2 based heterojunctions, *J.Appl. Phys.*, **80**, 4411–4420 (1996).
[143] W. Lee, N. Taskar, S. Ghandi and J. Borrego, Deep level transient spectroscopy studies of n-CdTe and p-CdTe, presented at the 8th Photovoltaic Research and Development Project Review Meeting, Denver, CO, USA, November 15–18 (1987).
[144] A. Balcioglu, R. Ahrenkiel and F. Hasoon, Deep-level impurities in CdTe/CdS thin-film solar cells, *J. Appl. Phys.*, **88**, 7175–7178 (2000).
[145] V. Komin, B. Tetali, V. Viswanathan, S. Yu, D. Morel and C. Ferekides, The effect of $CdCl_2$ treatment on CdTe/CdS thin film solar cells studied using deep level transient spectroscopy, *Thin Solid Films*, **431–432**, 143–147 (2003).
[146] J. Versluys, P. Clauws, P. Nollet, S. Degrave and M. Burgelman, DLTS and admittance measurements on CdTe/CdS solar cells, *Thin Solid Films*, **431–432**, 148–152 (2003).
[147] J. Versluys, P. Clauws, P. Nollet, S. Degrave and M. Burgelman, Characterisation of deep defects in CdS/CdTe thin film solar cells using deep level transient spectroscopy, *Thin Solid Films*, **451–452**, 434–438 (2004).
[148] D. Shvydka, J. Rakotoniaina and O. Breitenstein, Lock-in thermography and non-uniformity modeling of thin-film CdTe solar cells, *App. Phys. Lett.*, **84**, 729–731 (2004).
[149] C. Bridge, P. Dawson, P. Buckle and E. Özsan, Photoluminescence spectroscopy and decay time measurements of polycrystalline thin film CdTe/CdS solar cells, *J. Appl. Phys.*, **88**, 6451–6456 (2000).

[150] T. Okamoto, A. Yamada, M. Konagai, Optical and electrical characterizations of highly efficient CdTe thin film solar cells prepared by close-spaced sublimation, *J. Crystal Growth*, **214/215**, 1148–1151 (2000).

[151] D. Halliday, M. Potter, D. Boyle and K. Durose, Photoluminescence characterization of ion implanted CdTe, *Mat. Res. Soc. Symp. Proc.*, **668**, H1.8.1–H1.8.6 (2001).

[152] K. Nakamura, M. Gotoh, T. Fujihara, T. Toyama and H. Okamoto, Electromodulated photoluminescence study of CdS/CdTe thin-film solar cell, *Jpn. J. Appl. Phys.*, **40**, 4508–4511 (2001).

[153] M. Romero, D. Albin, M. Al-Jassim, X. Wu, H. Moutinho and R. Dhere, Cathodoluminescence of Cu diffusion in CdTe thin films for CdTe/CdS solar cells, *Appl. Phys. Lett.*, **81**, 2962–2964 (2002).

[154] J. Fritsche, S. Gunst, A. Thißen, R. Gegenwart, A. Klein and W. Jaegermann, CdTe thin film solar cells: the CdS/SnO_2 front contact, *Mat. Res. Soc. Symp. Proc.*, **668**, H5.1.1–H5.1.6 (2001).

[155] J. Fritsche, T. Schulmeyer, A. Thißen, A. Klein and W. Jaegermann, Interface modification of CdTe thin film solar cells by $CdCl_2$-activation, *Thin Solid Films*, **431–432**, 267–271 (2003).

[156] L. Weinhardt, C. Heske, E. Umbach, T.P. Niesen, S. Visbeck, and F. Karg,, Band alignment at the i-ZnO/CdS interface in Cu(In,Ga)(S,Se)$_2$ thin film solar cells, *Appl. Phys. Lett.*, **84**, 3175–3177 (2004).

[157] R. Chakrabarti, J. Dutta, S. Bandyopadhyay, D. Bhattacharyya, S. Chaudhuri and A. Pal, Surface photovoltage measurement in CdTS/CdTe solar cell: grain boundary effect, *Sol. Energy Mater. Sol. Cells*, **61**, 113–126 (2000).

[158] Th. Glatzel, H. Steigert, S. Sadewasser, R. Klenk and M-Ch. Lux-Steiner, Potential distribution of Cu(In,Ga)(S,Se)$_2$-solar cell cross sections measured by Kelvin probe force microscopy, presented at the European Materials Research Society Conference (Symposium O: Thin film chalcogenide photovoltaic materials), E-MRS, Strasbourg, France, 24–28 May 2004; accepted for publication in *Thin Solid Films*.

[159] M. Burgelman, P. Nollet and S. Degrave, Electronic behaviour of thin film CdTe solar cells, *Appl. Phys. A*, **A69**, 149–153 (1999).

[160] Guido Agostinelli, *Photocurrent analysis of CdTe solar cells*, PhD thesis, University of Gent / ELIS (2002).

[161] G. Agostinelli, D.L. Bätzner and M. Burgelman, An alternative model for V, G and T dependence of CdTe solar cells IV characteristics, *Proc. 29th IEEE Photovoltaic Specialists Conference* (New Orleans, LA, 20–24 May 2002), 744–747, IEEE, New York (2002).

[162] G. Agostinelli, D. Bätzner and M. Burgelman, A theoretical model for the front region of CdTe Solar Cells, *Thin Solid Films*, **431–432**, 407–413 (2003).

[163] G. Agostinelli, E. Dunlop, D. Bätzner, A. Tiwari, P. Nollet, M. Burgelman and M. Köntges, Light dependent current transport mechanisms in chalcogenide solar cells, *Proc. 3rd World Conference on Photovoltaic Energy* Conversion (Osaka, Japan, May 2003), 356–359, WCPEC-3, Osaka (2003).

[164] M. Köntges, R. Reineke-Koch, P. Nollet, J. Beier, R. Schäffler, J. Parisi, Light induced changes in the electrical behavior of CdTe and Cu(In,Ga)Se_2 solar cells, *Thin Solid Films*, **403–404**, 280–286 (2002).

[165] P. Nollet, M. Köntges, M. Burgelman, S. Degrave, and R. Reineke-Koch, Indications for presence and importance of interface states in CdTe/CdS solar cells, *Thin Solid Films*, **431–432**, 414–420 (2003).

[166] M. Gloeckler and J. Sites, Apparent quantum efficiency effects in CdTe solar cells, *J. Appl. Phys.*, **95**, 4438–4445 (2004).

[167] M. Gloeckler and J. Sites, Quantum efficiency of CdTe solar cells in forward bias *Proc. 19th European Photovoltaic Solar Energy Conference* (Paris, France, June 2004), 1863-1866, WIP, Munich (2004).

[168] M. Burgelman, J. Verschraegen, S. Degrave and P. Nollet, Modeling thin film PV devices, *Prog. Photovolt. Res. Appl.*, **12**, 143–153 (2004).

[169] M. Burgelman, P. Nollet and S. Degrave, Modelling polycrystalline semiconductor solar cells, *Thin Solid Films*, **361–362**, 527–532 (2000).

[170] A. Niemegeers, S. Gillis and M. Burgelman, A user program for realistic simulation of polycrystalline heterojunction solar cells: SCAPS-1D, *Proc. 2nd World Conference on Photovoltaic Energy Conversion* (Vienne, Austrai, July 1998), 672–675, JRC, European Commission (1998).

[171] S. Degrave, M. Burgelman, P. Nollet, Modelling of polycrystalline thin film solar cells: new features in SCAPS version 2.3, *Proceedings of the 3rd World Conference on Photovoltaic Energy* Conversion (Osaka, Japan, May 2003), 487–490, WCPEC-3, Osaka (2003).

[172] P. Nollet and M. Burgelman, Results of consistent numerical simulation of CdTe thin film solar cells, *Proc. 19th European Photovoltaic Solar Energy Conference* (Paris, France, June 2004), 1725–1728, WIP, Munich (2004).

[173] Peter Nollet, *Karakterisatie en modellering van CdTe/CdS dunne-filmzonnecellen*, PhD thesis, University of Gent / ELIS (2004) (in Dutch).

[174] M. Burgelman, J. Verschraegen, S. Degrave and P. Nollet, Analysis of CdTe and CIGS solar cells in relation to materials issues, Thin Solid Films, **480–481**, 392–398 (2005).

[175] V. Singh, D. Linam, D. Dils, J. McClure and G. Lush, Electro-optical characterization and modeling of thin film CdS-CdTe heterojunction solar cells, *Sol. Energy Mater. Sol. Cells*, **63**, 445–466 (2000).

[176] S. Degrave, P. Nollet, G. Stojanoska, M. Burgelman and K. Durose, Interpretation of ageing experiments on CdTe/CdS solar cells, *Proc. 17th European Photovoltaic Solar Energy Conference* (munich, Germany, October 2001), 1058–1061, WIP, Munich (2002).

[177] Y. Lee and J. Gray, Numerical modeling of the temperature and illumination intensity dependent performance of CIS solar cells, *Proc. 12th European Photovoltaic Solar Energy Conference* (Amsterdam, the Nederlands, April 1994), 1561–1564, Stephens & Associates, UK (1994).

[178] Y.-J. Lee and J. L. Gray, Numerical modeling of CdS/CdTe solar cells: a parameter study, *Proc. 22nd IEEE Photovoltaic Specialists Conference* (Las Vegas, NV, October 1991), 1151–1155, IEEE, New York (1991).

[179] Y.-J. Lee and J. L. Gray. Numerical modeling of polycrystalline CdTe and CIS solar cells, *Proc. 23nd IEEE Photovoltaic Specialists Conference* (Louisville, KY, May 1993), 586–591, IEEE, New York (1993).

[180] Y.-J. Lee and J. Gray, The effects of the band bending caused by interface states in CdTe/CdS solar cells, *Proc. 1st World Conference on Photovoltaic Energy Conversion* (Hawaii, 1994), 287–290, IEEE, New York (1995).

[181] S. Durbin and J. Gray, Considerations for modelling heterojunction transport in solar cells, *Proc. 1st World Conference on Photovoltaic Energy Conversion* (Hawaii, 1994), 1746–1749, IEEE, New York (1995).

[182] J.L. Gray, ADEPT: a general purpose device simulator for modeling solar cells in one- two and three dimensions, *Proc. 25nd IEEE Photovoltaic Specialists Conference* (Washington D.C., April 1996), 436–438, IEEE, New York (1996). Also see http://www.ece.purdue.edu/∼grayj/ADEPT/adept.htm

[183] J. Gray, Interpretation of capacitance-voltage characteristics in thin-film solar cells using a detailed numerical model, *Proc. 25nd IEEE Photovoltaic Specialists Conference* (Washington D.C., April 1996), 905–908, IEEE, New York (1996).

[184] G. Friesen, M. Özsan and E. Dunlop, Impedance model for CdTe solar cells exhibiting constant phase element behaviour, *Thin Solid Films*, **361–362**, 303–308 (2000).

[185] D. Shvydka, U. Jayamaha, V. Karpov and D. Compaan, Capacitance-frequency analysis of CdTe photovoltaics, *Proc. 29th IEEE Photovoltaic Specialists Conference* (New Orleans, LA, 20–24 May 2002), 752–755, IEEE, New York (2002).

[186] A. Fahrenbruch, Modeling results for CdS/CdTe solar cells, Colorado State University Report, March 2000, 2020–2022.

[187] D. Linam, V. Singh, J. McClure, G. Lush, X. Matthew and P. Sebastian, Light and voltage dependence of the junction transport properties of CdTe/CdS photovoltaics, *Sol. Energy Mater. Sol. Cells*, **70**, 335–344 (2001).

[188] M. Burgelman and A. Niemegeers, Calculation of CIS and CdTe module efficiencies, *Sol. Energy Mater. Sol. Cells*, **51**, 129–143 (1998).

[189] V. Karpov, R. Harju and G. Dorer, Nonuniform power generation in polycrystalline thin film photovoltaics, *Proc. 28th IEEE Photovoltaic Specialists Conference* (Anchorage, AL, September 2000), 547–550, IEEE, New York (2000).

[190] D. Shvydka, A. Compaan and V. Karpov, Nonlocal response in CdTe photovoltaics, *J. Appl. Phys.*, **91**, 9059–9065 (2002).

[191] V. Karpov, A. Compaan and D. Shvydka, Random diode arrays and mesoscale physics of large-area semiconductor devices, *Phys. Rev. B*, **69**, Art. No. 045325 (2004).

[192] S. Degrave, M. Burgelman and P. Nollet, Quantitative study of solar cells based on Cu-In-S based absorber layers grown by the CISCuT-process, *Opto-Electron. Rev.*, **8**, 295–298, (2000).

8 Charge Carrier Photogeneration in Doped and Blended Organic Semiconductors

V. I. Arkhipov[1], and H. Bässler[2]
[1]IMEC, Leuven, Belgium
[2]Institute of Physical, Nuclear and Macromolecular Chemistry, Philipps-Universität Marburg, Germany

8.1 INTRODUCTION

Made from cheaper materials, organic solar cells promise to open up new markets for solar energy, potentially powering everything from watches and calculators to laptop computers. Their flexibility and minimal weight will allow them to be placed on almost anything from tents that would provide power to those inside, to clothing that would power personal electronic devices. Advantages of organic materials and polymers for photovoltaic applications are obvious [1–3] but these materials have several serious drawbacks.

At variance with conventional crystalline semiconductors like Si, Ge, GaAs, etc., photoexcitation of an organic material does not immediately create free charge carriers. Primary optical excitations in organic materials, both crystalline and amorphous, are Frenkel type molecular singlet excitons with a binding energy of around 0.5 eV or larger. It should be stressed that an increase in photon energy beyond the absorption edge cannot change the nature of primary photoexcitations. The reason is that, due to weak Van der Waals interactions between constituents in a molecular solid, the oscillator strength is very small for direct photoionization even at high excess photon energies beyond the $S_1 \leftarrow S_0$ 0–0 transition. Energetic photons rather generate highly excited Franck–Condon states that dissipate their excess vibronic energy on a timescale of around 100 fs. Therefore, the first and major problem of organic photovoltaics is how to make excitons dissociate into free charge carriers.

The next problem, common in both organic and inorganic solar cells, is full collection of photogenerated charges. In organic, especially disordered, materials, carrier mobility is several orders of magnitude smaller than in crystalline inorganic semiconductors like silicon. This imposes severe restrictions on the maximum thickness of organic photovoltaic devices. Furthermore, it is very difficult to get appreciable mobilities of both electrons and holes in the same organic material. Accumulation of less mobile carriers in the bulk will hamper charge collection at the electrodes and thereby dramatically reduce the solar cell efficiency.

Thin Film Solar Cells Edited by J. Poortmans and V. Arkhipov
© 2006 John Wiley & Sons, Ltd

Another problem is efficient harvesting of excitons. Since, owing to a large binding energy, intrinsic dissociation of relaxed excitons into free carriers is virtually impossible, diffusion of excitons towards either charge transfer centers or donor/acceptor interfaces is a prerequisite for charge photogeneration. Typical exciton diffusion length in disordered organics is not larger than 10–20 nm which restricts the size of the donor phase to 20–40 nm only. A 40 nm organic film is still too thin to provide full light absorption. A solution could be either multiplayer planar or bulk heterojunction solar cells. The former approach is more relevant for small molecule materials that can be vacuum deposited with well controlled thicknesses and morphologies of individual layers. The major problems of such devices remain exciton harvesting and charge collection at the electrodes.

Fabrication of polymer based planar heterojunction devices by spin coating or screen printing is problematic because it requires the use of solvents, which can dissolve the donor polymer but not the acceptor material and vice versa. Semiconducting polymers are used in so-called bulk heterojunction solar cells. These devices exploit the phase separation that occurs in polymer donor/acceptor blends on the scale of a few nanometers to a few tens of nanometers. In principle, this scale matches almost perfectly the exciton diffusion length, which provides conditions for efficient exciton harvesting via dissociation at the donor/acceptor interface. However, the dissociation mechanism is not yet fully understood. Furthermore, while full phase separation is proven on the acceptor (typically, C_{60} based) side, it is not yet clear if pure donor polymer phase is formed on the scale of $\sim$10 nm or if the polymer is homogeneously mixed with the acceptor. On the more technological side, the major problems to be solved in bulk heterojunction devices are: (i) full light absorption in a typically 100 nm thick device, (ii) the decrease of opencircuit voltage upon blending of a donor polymer with a strong electron acceptor, and (iii) charge transport via random interpenetrating percolation networks for electrons and holes.

The present review is focused on the processes and mechanisms related to charge photogeneration in pristine, weakly, and heavily doped conjugated polymers rather than on technological aspects. We discuss exciton quenching and dissociation into geminate pairs of charge carriers at charge transfer (CT) centers, the role of energetic disorder in the Onsager type dissociation of geminate pairs, interfacial exciton dissociation and geminate recombination in polymer donor/acceptor blends, etc. The center of gravity will be shifted to recent experimental and theoretical advances. Detailed discussion of more traditional issues like the excitonic nature of optical excitations in conjugated polymers, the exciton binding energy, exciton energy relaxation and site-selective spectroscopy, etc. can be found elsewhere [4–7].

8.2 EXCITON DISSOCIATION IN NEAT AND HOMOGENEOUSLY DOPED RANDOM ORGANIC SEMICONDUCTORS

8.2.1 Intrinsic photogeneration in conjugated polymers

It is well established that in conjugated polymers the primary optical excitations are neutral singlet or triplet excitons. A direct spectroscopic proof of this notion is the observation of an energy gap between singlet and triplet states of about 0.7 eV [8–12]. Since this quantity is a measure of the strength of the exchange interaction between the electron and the hole comprising the exciton, it proves that the excitons are tightly bound. In the singlet state the root mean square (rms) electron–hole seperation is about 1 nm as inferred from the electroabsorption data and quantum chemical calculations [13–15]. This implies that the dissociation of a singlet

excitation should require an energy of $\gg kT$ at room temperature. Unfortunately, the exciton binding energy, E_b, is not amenable to direct spectroscopic probing except in the case of crystalline polydiacetylenes. In these materials E_b is known to be ≈ 0.5 eV [16].

Because of E_b being 0.5 eV or larger, one would expect that photoconduction starts at a photon energy $h\nu = E(S_1) + E_b$ where $E(S_1)$ is the energy of the singlet excitation. Action spectra of cw photoconduction in films of various conjugated polymers, such as substituted polyphenylenevinylenes (PPVs) [17], ladder type poly (paraphenylenes) [18], or polythiophenes [19], do, in fact, bear out a pronounced increase well above the absorption edge set by the spectroscopic $S_1 \leftarrow S_0$ 0–0 transition. This increase is an indication of the onset of intrinsic photogeneration, very much like in conventional molecular crystals [4]. It is generally agreed that there it is the signature of autoionization from a nonrelaxed higher energy Franck–Condon state [20]. It generates coulombically bound electron–hole pairs that can either recombine geminately or dissociate fully in the course of a temperature and/or electric field assisted diffusive random walk. A similar phenomenon occurs in conjugated polymers. The extra energy needed to form a coulombically unbound electron hole pair relative to the energy of a relaxed singlet exciton can also be delivered via a two quantum process, such as a two photon absorption, a sequential photoionization of a relaxed S_1 excitation or via a bimolecular encounter of two excitons [21–23].

The only way to dissociate a relaxed singlet excitation, i.e. a singlet excitation after any vibrational excess energy has been dissipated, in a neat system is to apply a high electric field. It should compensate for the loss of coulombic binding energy required to expand the electron–hole pair. In a molecular crystal of the anthracene type this process is beyond the range of accessible electric fields because E_b is too large. In a 100 nm thick film of a conjugated polymer it does occur and commences at an electric field of typically 10^6 V/cm, i.e. well below breakdown fields. A signature of field assisted dissociation of S_1 excitons is fluorescence quenching at high electric fields [24, 25]. This phenomenon is well known for inorganic semiconductors like GaAs but, owing to the low exciton binding energy, it already occurs at fields in the 10 kV/cm range.

The occurrence of field assisted dissociation of singlet excitons can be monitored directly via transient absorption. There are several reports in the literature testifying that, upon exciting with 100 fs laser pulses, a polymer film generates a transient absorption signal near 2 eV, i.e. well below the optical gap of the film [26, 27]. This is due to the generation of radical cations and anions, conventionally termed polarons. From the temporal growth of that signal one can conclude that: (i) dissociation occurs within the entire intrinsic lifetime of the vibrationally relaxed S_1 excitons, typically 300 ps, and (ii) it does not occur at a well defined rate, but follows dispersive kinetics [27]. This is a characteristic feature of an energetically random system featuring inhomogeneously broadened absorption spectra [28, 29]. The condition for dissociation is that there must be a nearby charge accepting state whose energy, dependent on the electric field, is comparable to the energy of the exciton. It is obvious that energetic disorder must translate into a distribution of reaction distances and, concomitantly, reaction rates.

The reaction product is a metastable coulombically bound electron—hole pair (e–h pair), i.e. a geminate e–h pair that has the options of subsequent complete dissociation or geminate recombination. There is abundant evidence for this notion:

1. Upon turning off the stimulating electric field, delayed fluorescence is emitted from the sample. It decays in a power law fashion, $I_{DF}(t) \propto t^{-n}$ with $n \approx 1$ [24] and reflects the monomolecular recombination of the geminate pair that leads to a fluorescent S_1 state [30].

2. In a delayed field collection experiment, in which the sample is excited at a certain electric field, one measures a photoconductive response after some delay time well after the prompt fluorescence has decayed. The result proves that exciton dissociation produces metastable e–h pairs that decay in a power law fashion.
3. Thermally stimulated luminescence emitted from conjugated polymers upon photoexcitation at low temperatures can be observed hours after excitation and must originate from e–h pairs that can have a very long lifetime depending on temperature [31].

8.2.2 Sensitized photogeneration of charge carriers in homogenously doped conjugated polymers

8.2.2.1 Experiments

According to results outlined in Section 8.2.1 there should be no photogeneration of charge carriers in single component conjugated polymers at low to moderate electric fields because dissociation of a singlet excitation is impeded by a large coulombic binding energy. Nevertheless, it is well established that there is, indeed, photoconduction near the absorption edge at moderate electric fields [17–19]. However, the yield is orders of magnitude less than unity, strongly field dependent but only weakly temperature dependent. This is clearly at variance with what a semiconductor band model would predict. Action spectra bear out a plateau within a photon energy range of almost 1 eV. Obviously, some of the S_1 excitations are liable to subsequent dissociation although the energy needed to overcome the coulombic attraction is not fully revealed in the temperature dependence of the effect.

The pioneering work by Lee *et al.* [32] on photoconduction in poly(2-methoxy, 5-(2′-ethyl-hexoxy)-1,4-phenylenevinytene (MEH-PPV) doped by C_{60} raised the suspicion that dissociation is aided by inadvertent dopants that act as sensitizers. Controlled doping is the method of choice to check this hypothesis. Representative data will be described below. A copolymer of phenylenevinylene type with phenyl alkoxy substituents (PhPPV), manufactured by the Covion Organic Semiconductor Company, with a high degree of purity was chosen as a host material. Dopants were either trinitrofluorenone (TNF) or perylenediimide (PdI). Both are strong electron acceptors. Figure 8.1 shows the absorption and photoluminescence spectra of a pristine PhPPV film and a film containing 1 % (per weight) of TNF [33]. Since TNF absorbs in the UV its presence does not alter the absorption spectrum of the doped film while the fluorescence of the host material is strongly quenched. There is a concomitant shortening of the lifetime of the S_1 excitations of the PhPPV. Time resolved fluorescence measurements indicate that the S_1 lifetime of a PhPPV chain, isolated in a solid 5.10-methenyltetrahydrofolate (MTHF) poly(2-methoxy, 5-(2′-ethyl-hexoxy)-1,4-phenylenevinytene) matrix, is about 700 ps while in a neat film it drops to 350 ps. This lifetime shortening effect can be ascribed to exciton quenching by unidentified impurities with a concentration of 0.04 %. The concentration dependence of the fluorescence can be explained in terms of incoherent exciton diffusion towards dopants [29]. Since there is no spectral overlap between the polymer emission and the absorption of the dopants the quenching event has to be identified as CT, more specifically electron transfer from an excited PhPPV segment to a nearby dopant molecule.

Photocurrent action spectra, measured under stationary conditions upon shining light through a semitransparent Al electrode in a symmetric Al/film/Al diode are presented in Figure 8.2. The quantum yield turns out to be almost constant up to a photon energy of about 3.5 eV.

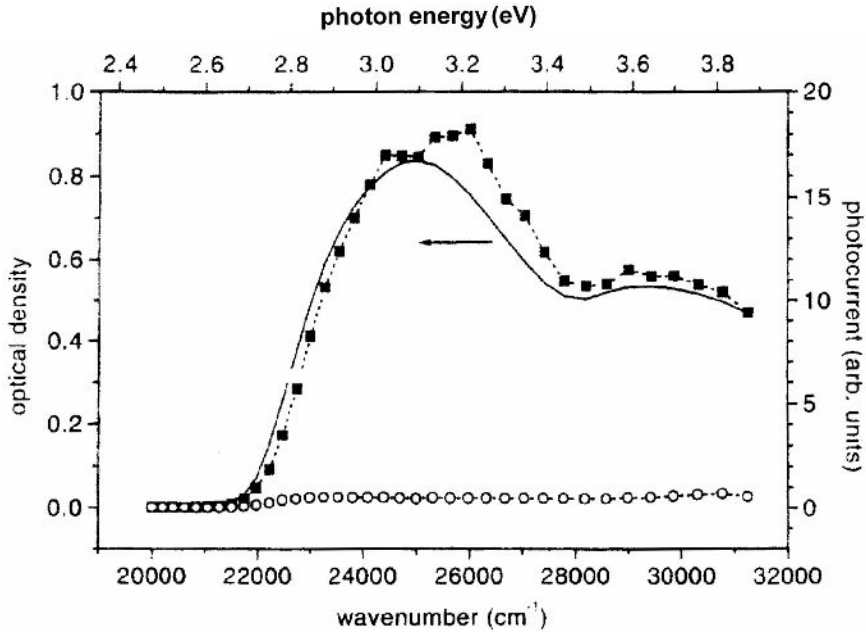

Figure 8.1 Photoluminescence (PL) and absorption (OD) spectra of PhPPV (dashed line: PL spectrum of pure PhPPV; solid line: PL spectrum of TNF doped PhPPV; solid line with squares: OD spectrum of pure PhPPV). The normalized PL spectra are shown in the inset. Reproduced with permission from C. Im, E. V. Emelianova, H. Bässler, H. Spreitzer, and H. Becker, *J. Chem. Phys.* **117**, 2961 (2002). Copyright (2002) American Institute of Physics.

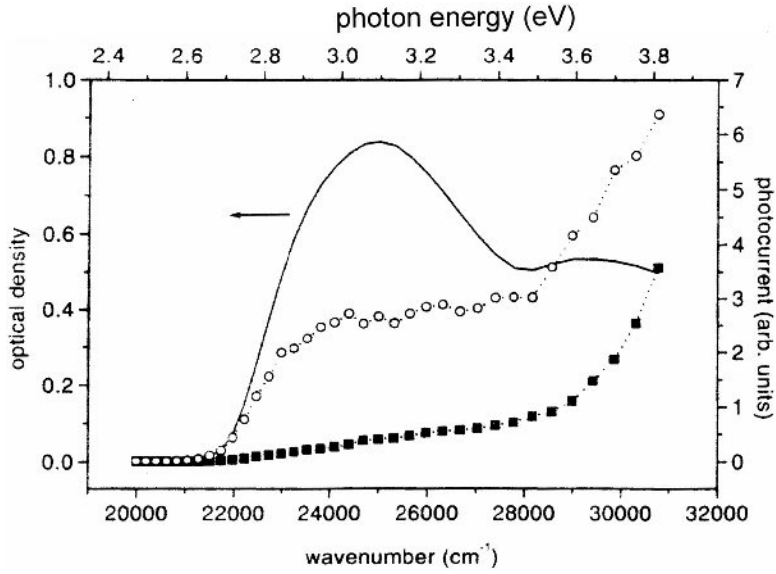

Figure 8.2 Spectral dependences of the charge carrier photogeneration quantum yield η in Al/PhPPV/Al configuration at 293 K. The electric field was 2.7×10^5 V/cm in the doped film and 2.5×10^5 V/cm in the undoped film. The yield was calculated by normalizing current to number of photons absorbed in the bulk. Reproduced with permission from C. Im, E. V. Emelianova, H. Bässler, H. Spreitzer, and H. Becker, *J. Chem. Phys.* **117**, 2961 (2002). Copyright (2002) American Institute of Physics.

Remarkably, in the spectral range covering the $S_1 \leftarrow S_0$ absorption band, the addition of 1 % of the dopant increases the photoresponse by not more than about a factor of two although the host fluorescence is reduced by more than a factor of ten. At first glance this result is intriguing. However, it can be readily explained by considering that even in the neat PhPPV film, about 50 % of all S_1 excitations are already quenched by 0.04 % of unidentified impurities. Therefore, the photoresponse cannot increase by more than a factor of two.

Since the field and temperature dependencies of the photocurrent in the neat and the doped film are virtually identical (see below) one can go one step further and conclude that the ubiquitously measured photocurrents within the spectral range of the $S_1 \leftarrow S_0$ transition at moderate electric fields are, in fact, sensitized by predominantly electron accepting impurities. Evidence for the presence of impurities with high electron affinity, like oxidation products of the polymers or dissolved oxygen, is inferred from the absence of electron signals in studies of the mobility of charge carriers in conjugated polymers with low ionization potentials. Since in a defect free matrix isolated polymer the hole and electron mobilities are comparable [34], this proves that in a bulk film electron motion is trap limited. Note that in p type materials the lowest unoccupied molecular orbital (LUMO) is usually well above that of common impurities. Therefore, impurities such as oxidation products of polymer chains act as deep electron traps yet not as hole traps.

Figure 8.3 shows the field dependences of the photocurrent in a neat PhPPV film and in a PhPPV film doped with 1 % TNF. These data were recorded using pulsed excitation because under these conditions the experiments can be extended to higher fields without the risk of spurious prebreakdown effects [35]. Within the overlapping field range, transient and cw data

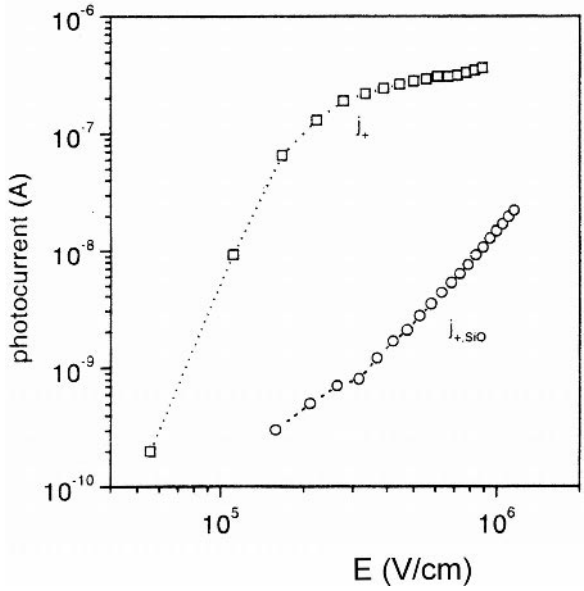

Figure 8.3 Field dependence of the charge photogeneration yield in PhPPV and PhPPV doped with 1 % TNF at low photon dose (filled symbols: ITO positive bias; open symbols: ITO negative bias). The data on MeLPPP are shown for comparison. Reproduced with permission from M. Weiter, V. I. Arkhipov, and H. Bässler, *Synth. Met.* **141**, 165 (2004). Copyright (2004) Elsevier.

were mutually consistent. The quantum yield has been calculated by integrating the transient photocurrent normalized to the number of absorbed photons. In the calculation, bimolecular electron–hole recombination has been neglected because the photocurrent turned out to be strictly linear in light intensity. The quantum yield of photogeneration is a strong function of the electric field. If one had analyzed the data in terms of the three-dimensional version of Onsager's theory for geminate electron–hole recombination one would have ended up with initial pair separations of ≈ 1.4 nm and 1.55 nm for the pristine and doped films, respectively.

It is a common observation that in conjugated polymers the temperature dependence of photocurrents is weak. Data for PhPPV confirm this fact (Figure 8.4). They pertain to an undoped sample but the results for a doped film were no different. The maximal value of the activation energy, inferred from the high temperature slope of an Arrhenius plot at a moderate

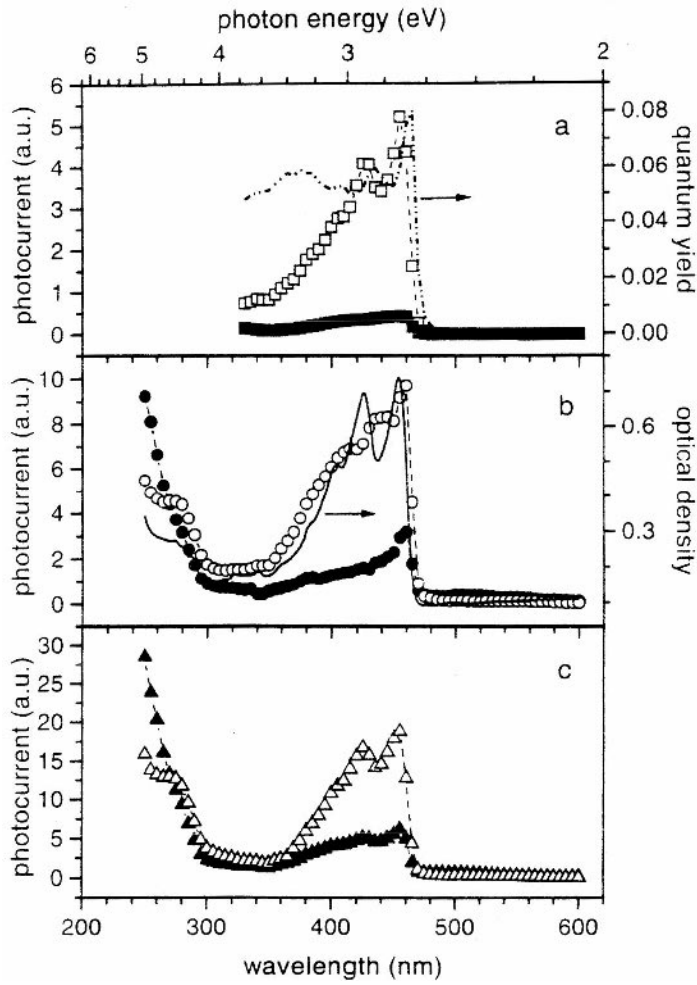

Figure 8.4 Temperature dependence of the quantum yield in a PhPPV film at different electric fields as a function of temperature. Reproduced with permission from M. Weiter, V. I. Arkhipov, and H. Bässler, *Synth. Met.* **141**, 165 (2004). Copyright (2004) Elsevier.

electric field, is ≈ 70 meV. Note that in a medium with a dielectric constant of 3.5, the coulombic binding energy of an e–h pair with 1.4 nm separation would be 0.33 eV. An extreme case appears to be the ladder type poly (paraphenylene). At a field of 10^5 V/cm the quantum yield of photocarrier generation is $\approx 10^{-4}$ only, virtually independent of temperature [18].

Replacement of TNF as a dopant by PdI at moderate concentration does not alter the phenomenology of photogeneration although PdI acts both as an electron acceptor and as an acceptor of singlet excitations of the polymer host [36]. The flat photocurrent action spectrum indicates that energy transfer does not fully quench excitons and that photogeneration must involve excited PdI molecules. Since both the yield as well as the field dependence are comparable to those in the TNF doped system, the charge delivering process must be identical, i.e. the precursor entity must be a coulombically bound pair of a PhPPV cation and a PdI anion that requires field assistance for further dissociation. However, at high dopant concentrations a remarkable threshold effect has been observed. Beyond 10 % dopant, the field dependence of the yield is shifted to lower fields and saturates at moderate fields (Figure 8.5). Concomitantly, the yield, measured at a given moderate electric field, say 5×10^5 V/cm, bears out a strong increase between 1 % and 10 % doping (Figure 8.5). Obviously, the probability of geminate pair dissociation in that particular system increases by more than two orders of magnitude. Since the implications of this observation for photovoltaics are obvious (see Section 8.2.3) it would be rewarding to measure the sensitizer concentration dependence of the photogeneration yield in e.g. systems doped with C_{60} [32] covering a large concentration range in order to establish criteria for that threshold effect.

8.2.2.2 Monte Carlo simulation

The experimental results on sensitized photogeneration in doped conjugated polymers cannot be simply rationalized in terms of Braun's amendment [37] (see Section 8.3.1) of Onsager's theory of optically generated geminate electron–hole pairs [38]. The key problem is the weak temperature dependence of the yield, which is incompatible with its strong field dependence. A straightforward conjecture has been that this is a signature of disorder associated with any random system. It is well established that in systems in which charge transport occurs via hopping among an energetically dispersed manifold of sites with a Gaussian density-of-states (DOS) distribution, the charge carrier mobility features a super Arrhenius type of temperature dependence. This is caused by thermally activated jumps of carriers localized in tail states of the DOS to states close to a so-called transport energy [39, 40]. Since under quasiequilibrium the energy of the former decreases with decreasing temperature, the activation energy itself is proportional to $1/T$. This has important implications not only for charge carrier motion but also for their initial generation.

A well tested example is charge carrier injection from a metallic electrode into a random dielectric [41–43]. Since the transport energy decreases with decreasing temperature (assuming that the carriers are negative) the energy required for injection also decreases with T. As a consequence the temperature dependence of the injection current is weaker than expected if disorder were absent. By analogy, one would also expect that the liberation of one of the charge carriers comprising a geminately bound e–h pair, i.e. the 'injection' into states close to the transport energy of the DOS, costs less energy and the temperature dependence is lowered.

The above conjecture was tested by computer simulation [44]. In a hopping system with a Gaussian DOS of variance σ from 0.05 eV to 0.15 eV and a dielectric constant of 3.5, pairs of a

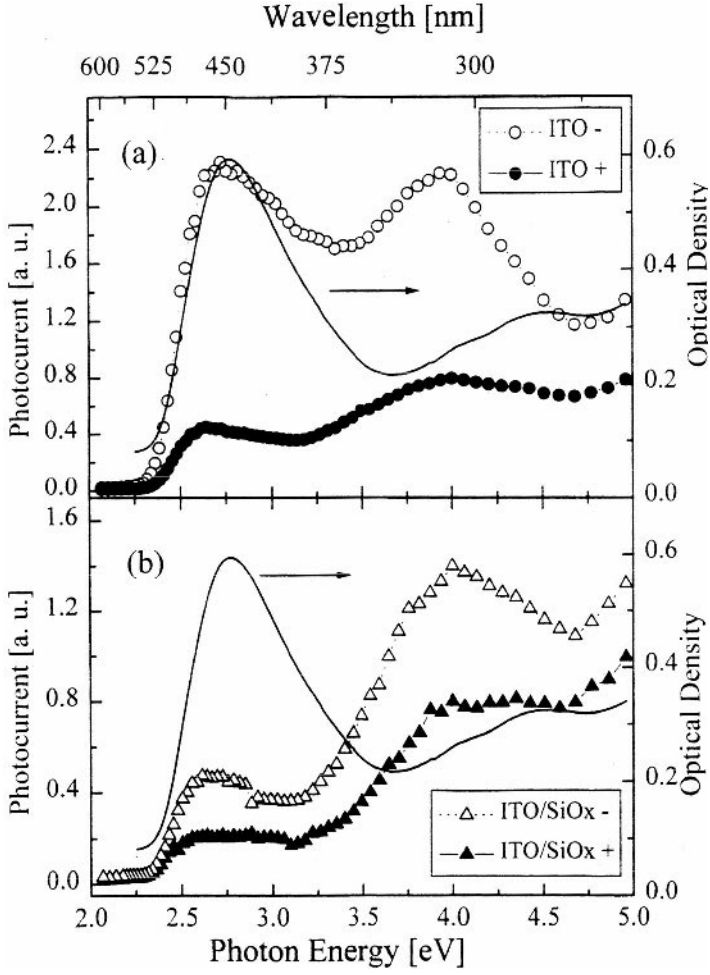

Figure 8.5 Dependence of the charge carrier photogeneration quantum yield η at 293 K on the dopant concentration for various sample configurations. Reprinted with permission from C. Im, W. Tian, H. Bässler, A. Fechtenkötter, M. D. Watson, and K. Müllen, *J. Chem. Phys*. **119**, 3952 (2003). Copyright (2003) American Institute of Physics.

stationary positive and a mobile negative charge with variable e–h separation were generated. A Miller–Abrahams type hopping rate was assumed. The rate for the final recombination event was taken as the rate for a downhill jump in energy. Figure 8.6 demonstrates that disorder, indeed, has a major influence on e–h pair dissociation. The data pertain to an e–h pair with initial pair separation of 2.4 nm in a material with a Gaussian DOS variance of 0.1 eV in an applied electric field of 10^4 V/cm. While at high temperatures the yield η approaches the expected Arrhenius behavior with an activation of 0.168 eV, the $\eta(T)$ dependence flattens and becomes almost constant at lower temperatures. The latter effect is retained even if the initial pair separation was decreased from 2.4 nm to 1.2 nm. The inset to Figure 8.6 shows that the enhancement of the yield relative to the value expected for a fully ordered system scales exponentially with the degree of disorder, quantified in terms of the DOS variance.

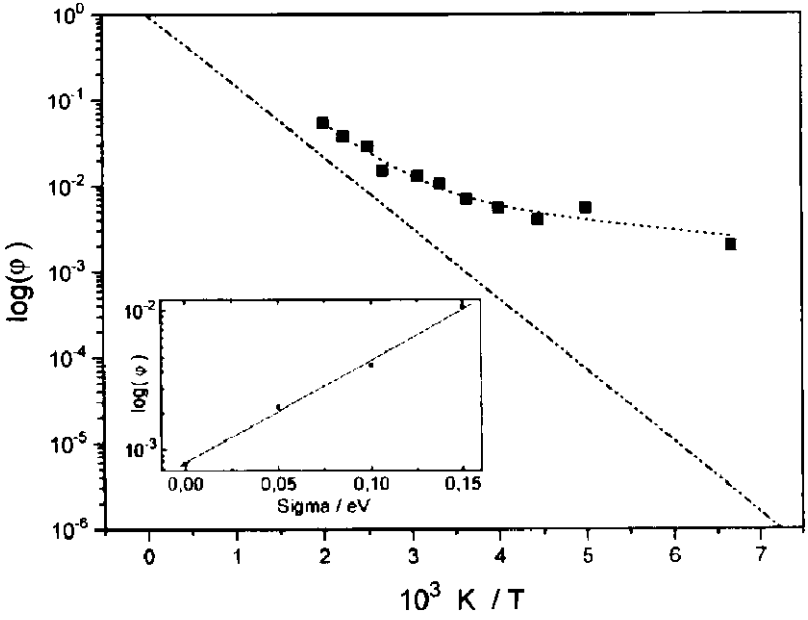

Figure 8.6 Temperature dependence of escape probability φ of a charge carrier started at a distance of $r_0 = 24$ Å from its counter charge in a hopping system characterized by a Gaussian DOS of variance $\sigma = 0.1$ eV ($\varepsilon = 3.55$, $E = 10^6$ V/m). The dash-dotted line is the prediction of three-dimensional Onsager theory for geminate pair dissociation. The inset shows the variation of φ with increasing σ at $T = 250$ K. The data point for $\sigma = 0$ is the theoretical value obtained from Onsager's theory. Reproduced with permission from U. Albrecht and H. Bässler, *Chem. Phys. Lett.* **235**, 389 (1995). Copyright (1995) Elsevier.

Operationally, the field dependence of the yield (Figure 8.7) can be fitted by the three-dimensional version of Onsager's theory assuming an apparent pair separation of 3.1 nm instead of 2.4 nm. At this stage it is worth recalling that the field and temperature dependences of a stationary photocurrent are solely determined by carrier generation rather than by transport because eventually all carriers must reach the electrode(s) unless bimolecular recombination or trapping at 'infinitely' deep traps is occurring. This notion has an important bearing on the efficiency of a photovoltaic cell.

It is obvious that by taking into account disorder, one can at least qualitatively recover both the field and temperature dependencies of photogeneration in conjugated polymers doped with sensitizers at low to moderate concentrations [45]. It is an open question, though, whether or not disorder effects alone can explain the experimental results. There is at least one system in which disorder is insufficient in explaining the temperature dependence of the yield. It is a film of methyl-substituted ladder-type poly(p-phenylene) (MeLPPP). Due to the rigidity of the polymer backbone it is the polymer with the lowest degree of disorder. Nevertheless the photocurrent measured within the region of the $S_1 \leftarrow S_0$ transition decreases by a factor of two only upon lowering the temperature from 295 K to 120 K [18]. Alternative mechanisms to explain the results are: (i) optical release of the mobile charge carriers, i.e. the hole, of the geminate pair by triplet excitons [46] and (ii) the consideration of zero point oscillations of the mobile charge carrier on the polymer chain [47]. The latter idea will be elaborated further in Section 8.3.1.

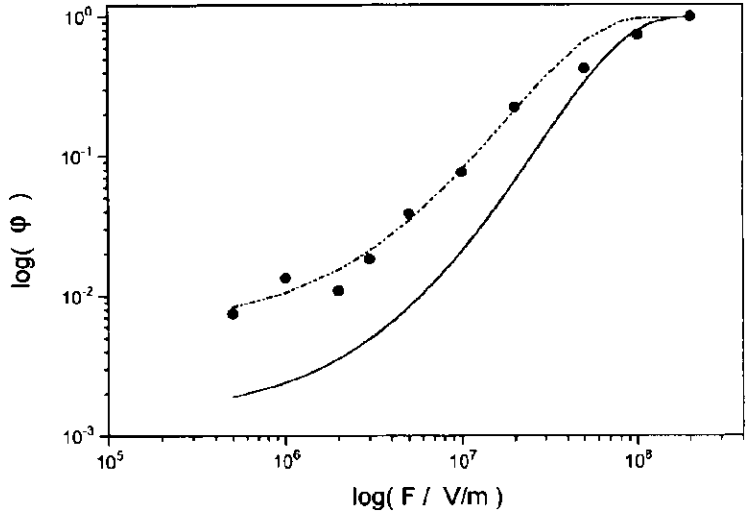

Figure 8.7 Field dependence of φ ($r_0 = 24$ Å, $T = 300$ K, $\sigma = 0.1$ eV). The dashed and solid curves are the prediction of three-dimensional Onsager theory for $r_0 = 31$ Å and $r_0 = 24$ Å, respectively, calculated under the premise that all carriers are started in down field direction from the counter charge. Reproduced with permission from U. Albrecht and H. Bässler, *Chem. Phys. Lett.* **235**, 389 (1995). Copyright (1995) Elsevier.

8.2.3 Photogeneration of charge carriers at a donor–acceptor interface

In the previous section, photogeneration of charge carriers in random organic dielectrics, notably conjugated polymers, homogeneously doped with an electronegative sensitizer has been discussed. It has been demonstrated that even at moderate dopant concentration, i.e. 0.1 % to 1 % by weight, virtually all absorbed photons are converted to geminately bound electron–hole pairs via efficient energy transfer followed by CT from the excited donor to the acceptor [33]. However, the fraction of pairs that escape geminate recombination is strongly dependent on the collecting electric field. At moderate fields, e.g. 10^5 V/cm, the yield is typically 10^{-3} only [33]. This is detrimental for using such a system in a photovoltaic cell.

In a particular system, i.e. a copolymer of PPV (PhPPV) doped with PdI it has been observed, however, that the quantum yield increases drastically as the concentration of the electron accepting PdI reaches ≈ 20 % [36]. On the other hand, it was found that practically all optical excitations are already harvested by the dopants at much lower doping levels. Consequently, one has to conclude that this increase is solely due to improved dissociation of the geminate e–h pairs. Evidence for this notion comes from the field dependence of the photocurrent at different dopant concentrations. Beyond a critical concentration of 30 % the yield saturates at $\approx 3 \times 10^5$ V/cm (Figure 8.8). This shift of the saturation field as a function of the electric field is a clear indication that at higher acceptor concentrations the initially generated e–h pair is more expanded. This is of paramount importance for the operation of a photovoltaic cell. In the following section this effect will be discussed together with other pertinent aspects of photovoltaics such as: (i) the distinction between dopants that act as energy or as CT centers, (ii) the generation of free charge carriers, and (iii) their recombination.

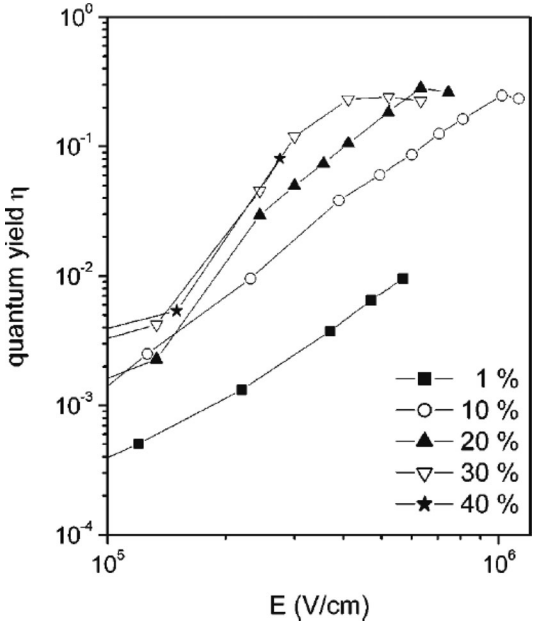

Figure 8.8 Field dependencies of the charge carrier photogeneration quantum yield η in the ITO/PhPPV:PdI/Al configuration at 293 K for various PdI dopant concentrations. Excitation wavelength was 550 nm (2.25 eV). Reprinted with permission from C. Im, W. Tian, H. Bässler, A. Fechtenkötter, M. D. Watson, and K. Müllen, *J. Chem. Phys.* **119**, 3952 (2003). Copyright (2003) American Institute of Physics.

8.2.3.1 Energetics at donor–acceptor interfaces

The key requirement for the optically generated e–h pair at a donor–acceptor pair is that its energy be lower than the energy of the lowest excited singlet state of either the donor or acceptor. Otherwise, energy transfer would populate the lowest lying singlet state that can decay radiatively. This is a prerequisite for efficient electroluminescence in light emitting diodes (LEDs). Conceptually, this is straightforward. However, predicting which system is suitable for either an LED or a photovoltaic device is not at all straightforward. The ambiguity is related to the lack of precise knowledge of the energy levels of the e–h pair. This energy is the difference between the energy of a radical cation of the donor, i.e. its ionization energy or, equivalently, the energy of the highest occupied molecular orbital (HOMO), and that of a radical anion as set by its electron affinity or, equivalently, the energy of the lowest unoccupied molecular orbital (LUMO), albeit diminished by the coulombic binding energy of the pair.

In practice, one often makes the estimate that the energy of the pair is solely determined by the oxidation and reduction potentials of both components as measures of the HOMO and LUMO levels and ignores the coulombic binding energy of the pair. Even worse, often only one of the potentials of the components is available via cyclic voltammetry and the missing potential is inferred from the optical $S_1 \leftarrow S_0$ 0–0 transitions. This ignores the coulombic binding energy of the excited singlet state that is usually $\gtrsim$ 0.5 eV. On the other hand, even if one can measure the oxidation and reduction potentials of the components simultaneously

via cyclic voltammetry, a systematic error is encountered because these data measure CT from an electrode to a molecule/polymer. However, a in polar solution the solvation energy of the cation/anion is increased relative to that in a solid dielectric because reorganization within the solvation shell is absent in the latter case. A conclusive test of whether energy or CT prevails in a donor–acceptor system, had to be complemented by spectroscopy. Only a simultaneous measurement of the donor fluorescence quenching and either the onset of acceptor fluorescence or the appearance of transient absorption of the radical anion/cation [48] would be a stringent test of energy transfer and vice versa. The above ambiguity becomes irrelevant if the dopant is highly electronegative, such as C_{60} or TNF because their LUMOs are at least 1 eV below those of common donors such as PPV or polyfluorene type systems. In these cases CT is always favored.

An interesting situation is encountered when the level off-sets between donors and acceptors are only a few 0.1 eV. In this case an exciplex may be formed. An exciplex is the equivalent to an excimer that involves two chemically identical chromophors. It has a repulsive ground state and its wavefunction is composed of polar and nonpolar contributions. The intermolecular character implies a reduced oscillator strength in emission and a rather broad and featureless emission spectrum. The fluorescence decay time is typically >10 ns, i.e. appreciably longer than that of singlet excitations of uncoupled chromophores whose fluorescence lifetimes are usually on a sub-ns time scale. The exciplex should not be confused with a CT state or a geminately bound electron hole pair in which CT is complete. It is an open question whether or not transition from an exciplex to a tightly bound e–h pair is an exothermic or an endothermic process because two opposing effects are involved. On the one hand, the spatial expansion of the exciplex to form an e–h pair costs coulombic binding energy; on the other hand, there is a gain of electronic polarization energy when a state with only partial CT is converted to a fully charge separated state embedded in a polar organic solid.

The importance of exciplexes in donor–acceptor type photovoltaic cells has already been recognized [49]. The recent spectroscopic work of the Cambridge group elaborates on this phenomenon on a more quantitative way. The system is a blend of poly(9,9-dioctylfluorene-co-benzohiadiazole) (F8BT) with either poly(9,9-dioctylfluorene-co-bis-N,N-(4-butylphenyl)-bis-N,N-phenyl-1,4-phenylenediamine (PFB) or poly(9,9-dioctylfluorene-co-N-(4-butylphenyl)diphenylamine (TFB) [50, 51]. Upon spin coating the blend under rapid drying conditions the usual demixing of both polymers is diminished and a film is formed with a large interfacial area between the two polymers. It turns out that a PFB:F8BT blend displays a high charge separation yield (4 % photocurrent external quantum efficiency) and low electroluminescence efficiency (<0.64 lm/W) whereas in TFB:F8BT the electrolumiescence is efficient (19.4 lm/W) and photovoltaic response weak. Fluorescence studies indicate that in both systems an interfacial exciplex is formed as evidenced by the broad emission, bathochromatically shifted relative to the superimposed emission of the noncomplexed emission of the F8BT. The different behavior illustrates the importance of fine tuning of the energy levels of both components. In the PFB:F8BT system, the monomer fluorescence near 530 nm is weak and associated with an activation energy of 200 ± 50 meV while in the TFB:F8BT system, monomer and exciplex emissions are comparable and the activation energy for the population of the monomer emissions is 100 ± 30 meV only (Figure 8.9). Since the lifetime of the exciplex is as large as 40 ± 5 ns it serves as a reservoir of excitations with longer lifetimes that can either regenerate the monomer singlet state of F8BT or fully dissociate. If the temperature activated regeneration of the exciton prevails, the system features electroluminescence. Otherwise the system can serve as a photovoltaic device.

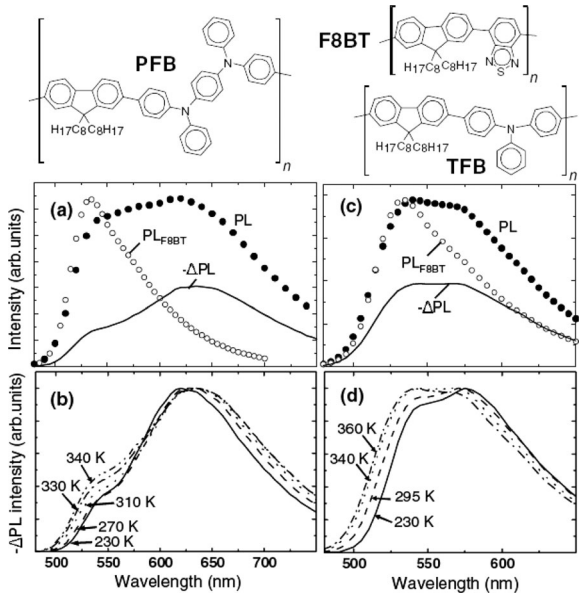

Figure 8.9 (a) Photoluminescence intensity (PL, filled circles) and reduction of photoluminescence intensity due to an applied reverse bias of 10 V (ΔPL, solid line) for a PFB:F8BT blend device at 340 K. PL and ΔPL are plotted in the same scale and reflect their relative intensities. (b) ΔPL spectra (at 10 V) from the same device as in (a) at different temperatures. (c) PL (filled circles) and ΔPL at a reverse bias of 15 V (solid line) for a TFB:F8BT blend device at 340 K. (d) ΔPL spectra from the same device as in (c) at different temperatures. For comparison, the PL spectrum from an F8BT only device (open circles) is plotted in both parts (a) and (c). The structures of PFB, F8BT, and TFB are also shown. Reproduced with permission from A. C. Morteani, P. Sreearunothai, L. M. Herz, R. H. Friend, and C. Silva, *Phys. Rev. Lett.* **92**, 247402 (2004). Copyright (2004) American Physical Society.

Another system in which exciplex formation has been detected spectroscopically is a blend of electron donating poly(2-methoxy-5-(3,7-dimethyloctyloxy)-1,4-phenylenevinylene) (MDMO-PPV) and electron accepting poly(oxa-1,4-phenylene-(1-cyano-1,2-vinylene)-(2-methoxy-5-(3,5-dimethyloctyloxy)-1,4-phenylene)-1, 1-(2-cyanovinylene)-1,4-phenylene) (PCNEPV) [52]. Figure 8.10 demonstrates that while the absorption spectrum of the blend is a superposition of the absorption of the components, its emission is red shifted relative to the parent fluorescence spectra featuring a peak at 1.85 eV. It was assigned to emission from the exciplex. Astonishingly, its initial lifetime is only 1.6 ns, intermediate to the fluorescence lifetimes of MDMO-PPV (0.36 ns) and PCNEPV (14 ns). Consistent with a low radiative yield – note that in Figure 8.10 the exciplex emission is enlarged by a factor of 34 relative to that of PCNEPV – this suggests that it is controlled by a nonradiative channel. One might conjecture that this is dissociation to a coulombically bound electron–hole pair, i.e. a genuine CT state, in which the loss of some coulombic binding energy is overcompensated by an increase in the electronic stabilization energy as mentioned above. However, this is inconsistent with the observation that the yield of exciplex emission decreases upon applying an external electric field. It suggests that the transition from exciplex to CT state is weakly endothermic rather than exothermic as illustrated by Figure 8.11. So far, the origin of the low exciplex yield,

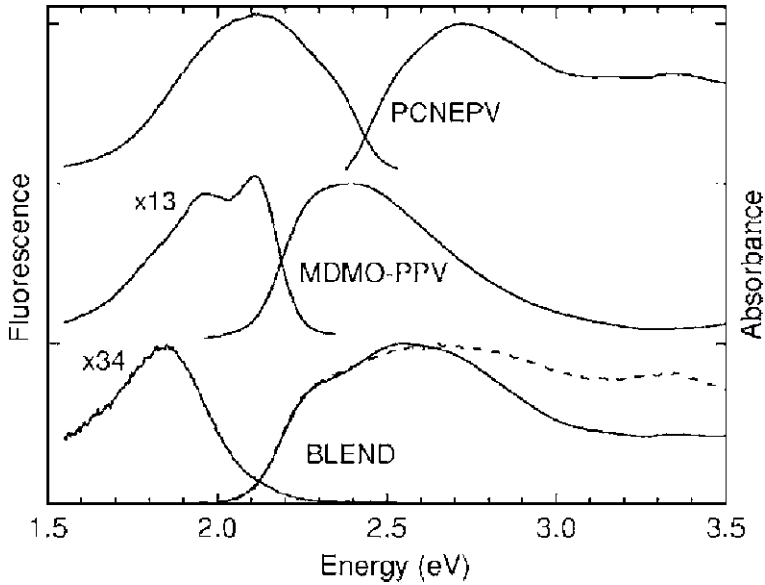

Figure 8.10 Normalized UV-vis absorption and emission spectra of films of PCNEPV, MDMO-PPV, and the 1:1 wt % blend at room temperature (excitation at 2.29 eV). The excitation spectrum of the emission at 1.85 eV for the blend is shown by the dashed line. Reproduced with permission from T. Offermans, P. A. van Hal, S. C. J. Meskers, M. M. Koetse, and R. A. J. Janssen, *Phys. Rev. B* **72**, 045213 (2005). Copyright (2005) American Physical Society.

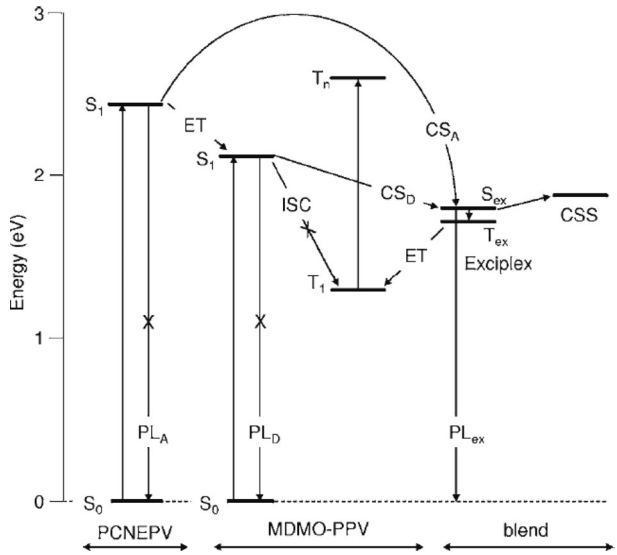

Figure 8.11 State energy diagram of the various singlet (S), triplet (T), exciplex (ex), and charge-separated (CS) states in the donor (D)—acceptor (A) blend of MDMO-PPV and PCNEPV; and transitions (ET = energy transfer; CS = charge separation; PL = photoluminescence; ISC = intersystem crossing) between these states. Crosses indicate processes that do occur in the pure materials, but that are quenched in the blend. Reproduced with permission from T. Offermans, P. A. van Hal, S. C. J. Meskers, M. M. Koetse, and R. A. J. Janssen, *Phys. Rev. B* **72**, 045213 (2005). Copyright (2005) American Physical Society.

which, by the way, is complemented by a comparably low photovoltaic efficiency, remains unclear. From these results one would agree that the formation of an exciplex at the interface of a donor–acceptor blend is rather unfavorable for the efficiency of a photovoltaic cell, particularly if the energy of the exciplex exceeds the triplet state energy of either the donor or acceptor. If the exciplex and CT states are close in energy there can be frequent charge exchange and, accordingly, efficient generation of the triplet state of the exciplex. The latter can readily decay to a lower triplet state of one of the components and be lost for either photocarrier generation or electroluminescence [52].

8.2.3.2 Generation of charge carriers

An obvious requirement for efficient solar power conversion in a photovoltaic cell is that all photons should generate electron–hole pairs that may subsequently dissociate completely. This condition can be met in two or multicomponent donor–acceptor systems only because in a single component system the large exciton binding energy prevents dissociation. Since the initially generated excited state is the singlet exciton in either the donor or the acceptor phase it has to diffuse towards a reaction center. Although in conjugated polymers exciton diffusions lengths are as large as 10–20 nm [29, 53], this precludes the use of, say, 100 nm thick bilayer assemblies and calls for blend systems in which exciton dissociation occurs throughout the entire sample.

If both components are polymers, phase separation occurs because of the low entropy of mixing and excitons have to diffuse towards an internal interface between the components. Studies of fluorescence quenching as a function of composition within the range 1:5 to 5:1 in the PFB:F8BT system [54] (for compounds see Section 8.2.3.1) indicate, however, that all excitons reach the internal interface regardless of composition. Any dependence of the photovoltaic efficiency has, therefore, to be associated with the subsequent fate of the geminate e–h pair. It turns out that once an exciton has diffused towards a reaction center or if absorption occurred next to it already, CT is an ultrafast process. By monitoring the rise of the transient absorption it has been proven that transfer of an electron from a MEH-PPV chain to a nearby C_{60} molecule only takes 45 fs [3, 55].

In a two component donor–acceptor system the photovoltaic efficiency, monitored, for instance, by photocurrent measurements, depends on both the concentration of the acceptor and the morphology of the sample. It is determined by the dissociation efficiency of a photon induced e–h pair at a CT center under the action of either an external electric field or the built-in field in the diode. There are several key observations pertaining to this fact (often made on different systems, though):

1. Varying the concentration of the acceptor in the PhPPV:PdI system between 0.1 % and $> \approx 30$ % shows that the dissociation yield increases by more than two orders of magnitude as the PdI concentration increases. This correlates with the observation that the $\eta(F)$ dependence saturates at lower fields (see Figure 8.8).
2. Improvement of the phase structure in blend systems has a positive effect on the efficiency. It can be accomplished by thermal annealing, for instance, in the MDMO:PCNEPV system, or by varying the composition as in the PFB:F8BT system (for components see Section 8.2.3.1).

3. Studying the external photogeneration quantum yield in a photovoltaic cell containing a blend of poly(2-methoxy-5-(3-7-dimethyl-octyloxy)-1,4-phenylenevinylene ($0C_1C_{10}$-PPV) and the soluble fullerene derivative (6,6)-phenyl-C_{61}-butyric acid methyl ester (PCBM) sandwiched between poly(3,4-ethylene dioxythiophene (PEDOT) and Al electrodes as a function of light intensity, temperature, and applied voltage shows that the yield is almost constant when the light intensity varies between 0.02 and 100 mW/cm^2. Within a temperature range of 120 to 325 K it is weakly temperature dependent with an activation energy of 50 meV.
4. Transient optical studies of charge recombination dynamics in an MDMO-PPV polymer blended with PCBM features a power law time dependence extending into the millisecond range [52].

The essential question raised is which properties are responsible for the observation that the yield increases dramatically as the concentration of the acceptor phase exceeds 20 %. Is it: (i) the ultimate monomolecular recombination of a donor radical cation and the acceptor radical anion, (ii) that the e-h hole pair is more liable to subsequent escape from the coulombic potential because charge transport is facilitated when the percolation limit for transport is reached, or (iii) that the coulombic attraction is not relevant at all and the finite yield is caused by carrier recombination at traps and by low charge carrier mobility because of imperfect morphology of the active layers?

The charge carrier mobility must certainly affect the performance of a photovoltaic cell. At low concentrations of electron acceptor the generated electron will be deeply trapped. Eventually, a space charge will be built up that will have a feedback effect on charge generation and will give rise to bimolecular charge recombination. Opening a percolative path for the motion of the minority carriers alleviates this problem. On the other hand, even beyond the percolation threshold there is usually an asymmetry regarding electron and hole motion. It is dictated by the energies of the intrinsic HOMO and LUMO levels of the components because they determine whether an impurity acts as a trap or not. For instance, in a blend of a methanofullerene and a PPV derivative (OC_1C_{10}-PPV) [56] the electron is more mobile than the hole because the extremely low lying LUMO of C_{60} prevents electron trapping at any possible impurity. The situation may be different with electron acceptors that are less electronegative than C_{60}, such as F8BT. Nevertheless, it has been argued that in the PFB:F8BT system, efficient collection of charges at the electrodes requires the presence of a conduction path in the minority phase. In fact, the charge collection efficiency is found to scale with the surface area of the interface between the mesoscale PFB rich and the F8BT rich phases formed via phase separation (Figure 8.12). This requirement is satisfied when charge generation occurs close to the interface between both phases. It has been suggested that a mesoscale phase separation of the order of the thickness of the film could optimize the morphology of such polymer blend devices. This will maximize the interfacial area between the phases and establishes a network for charge carrier motion towards the collecting electrodes [54].

Experimentally, it has been established that the charge photogeneration yield in these systems normally reaches maximum at a acceptor/donor ratio as high as 3:1 [57] which is apparently much larger than the thresholds of both electron percolation and phase separation. Furthermore, it has been recently shown that the most efficient 3:1 polymer/C_{60} derivative blends do not reveal full phase separation on the polymer side: such blends consist of pure C_{60} derivative phase and approximately 1:1 polymer/C_{60} mixture as 'donor' phase [58]. Although

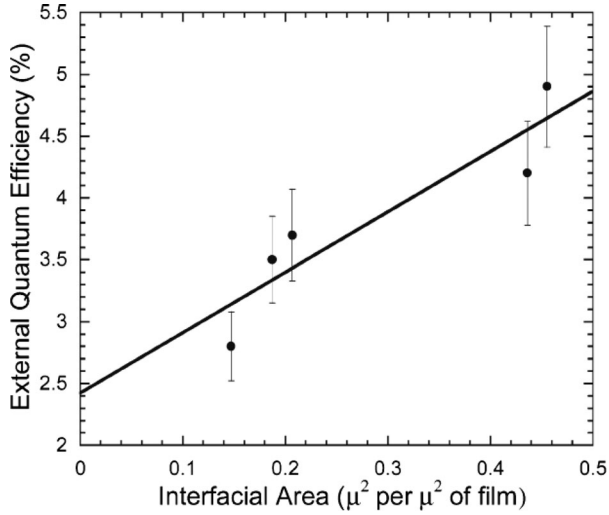

Figure 8.12 External quantum efficiency at 400 nm illumination for devices of blend ratios 1:1, 4:5, 3:5, 2:5, and 1:5 PFB/F8BT, (from left to right on graph), versus interfacial area between the mesoscale phases. The line is the best fit straight line. Reproduced with permission from H. J. Snaith, A. C. Arias, A. C. Morteani, C. Silva, and R. H. Friend, *Nano Lett*. **2**, 1353 (2002). Copyright (2002) American Chemical Society.

it is not yet clear whether or not this mixture is really homogeneous on the 2–5 nm scale, a high density of strong electron acceptors should dramatically reduce the exciton lifetime anyway and, concomitantly, the exciton diffusion length.

Improved morphology of devices, be it accomplished by thermal annealing or by changing the composition of the blend, could also affect the properties of the initially generated geminate e–h pair. It could even be the key factor for the increase of the device efficiency [52]. This notion implies that the initially generated entity is a coulombically bound rather an entirely free electron–hole pair. The former assumption is supported by the facts that: (i) in organic systems with dielectric constants ranging between three and four, coulombic interactions have got to be important and (ii) the photovoltaic efficiency is linearly dependent on light intensity, indicating that charge carrier recombination is kinetically a first rather than a second order process. Note that geminate recombination of an e–h pair is a strictly monomolecular process.

The observation that in the PhPPV:PdI system, the field dependence of the efficiency of photocarrier generation is shifted towards lower fields at higher concentrations of PdI provides a strong argument in favor of the conjecture that, indeed, primary CT is the process that changes at higher concentrations of the acceptor. This field dependence is controlled by the diffusive escape of the e–h pair from its mutual coulombic potential. It is described by Onsager's theory if modified by the disorder effects (see Section 8.2.2.2). The field dependence, notably the field at which the yield saturates, is determined by the initial separation of the e–h pair. The fact that the saturation field shifts to lower values (see Figure 8.8) proves that e–h pairs generated at higher PdI concentrations are more loosely bound than those at lower acceptor loading. Since the dissociation of an e–h pair with separation of 2.4 nm saturates near 10^6 V/cm, a saturation field of 3×10^5 V/cm, observed with Pd concentrations of $\gtrsim 30\,\%$, indicates the initial pair separation is as large as ≈ 7 nm. In Figure 8.13 the saturation fields are translated into the

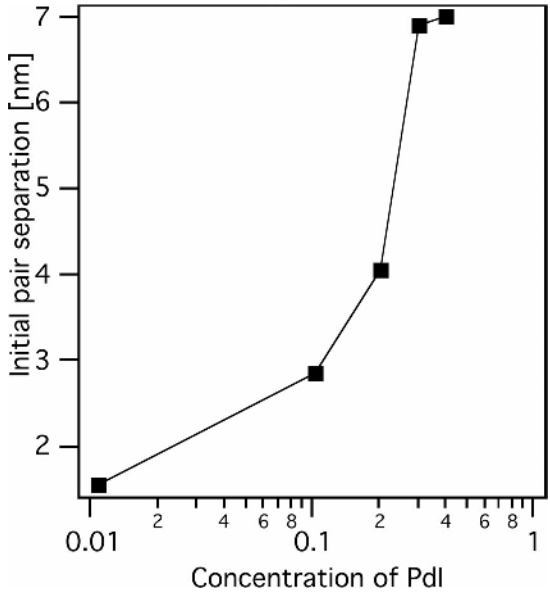

Figure 8.13 Initial separation between charges in e–h pairs as a function of PdI content in the PhPPV:PdI blend. The data shown in Figure 8.4 were recalculated to the initial separation on the basis of the Onsager model of geminate recombination.

initial e–h separation as a function of PdI concentration. Note that in a system with a dielectric constant of 3.5 an e–h pair of separation of 7 nm has a coulombic binding energy of 60 meV. This is comparable to the activation energy reported for a 0C1C10-PPV:PCBM blend [59].

Although it may not be legitimate to generalize the above conclusion, it is obvious that at least in the PhPPV:PdI system, the rate limiting factor is the so-called thermalization length of the e–h pair formed in a system above a critical acceptor concentration. The origin of this phemonenon is still open to conjecture. Advances regarding conceptual understanding are discussed in Section 8.3.2, but not until recent results on the kinetics of geminate pair recombination have been discussed.

8.2.3.3 Kinetics of geminate electron–hole pairs

The most recent study of the recombination and dissociation kinetics of geminately bound e–h pairs at a donor–acceptor interface is the simulation work of Offermans *et al.* [60]. The key assumption is that an optical excitation generates a nearest neighbor e–h pair, the electron/hole being located at the acceptor/donor phase, respectively. Both phases have dielectric constants of four and are represented by cubic lattices with lattice constant of 1 nm. The hopping sites form a Gaussian DOS distribution characterized by different variances of $\sigma_e = 70$ meV and $\sigma_h = 120$ meV. A variable electric field acts perpendicular to the interface and hopping obeys Miller–Abrahams rates. Different from the earlier simulation of the Marburg group [30, 44] it was assumed that the rate of the nonradiative ultimate e–h recombination event is 1 ns^{-1} while the prefactor rate for intersite hopping is 10 ps^{-1}. In the simulations one monitors independently

the fraction of holes and electrons near the interface as well as their distance from the interface for low and high electric fields and their average energies within the DOS as a function of time. For $F \geq 2 \times 10^5$ V/cm the dissociation yield increases strongly and saturates at a field of 2×10^6 V/cm. If one would replot the original data on the temperature dependence in Ref. [60] on an Arrhenius scale one would end up with a similar dependence as that shown in Figure 8.6, i.e. at high temperatures the yield approaches activated behavior with an activation energy of 50 meV while at lower temperatures the dependence becomes weaker.

The simulation results can be rationalized in terms of stochastic motion of particles in a disordered lattice. Initially, the carriers are bound coulombically and localized at adjacent donor–acceptor sites. A carrier can readily move away from its sibling of opposite polarity only if the loss of coulombic binding energy is compensated by the energy gained by hopping to a site with lower energy. In a system with the dielectric constant $\varepsilon = 4$ and a lattice spacing of 1 nm this energy is as large as 0.18 eV. For holes this is easy to accomplish since 0.18 eV is only $1.5\sigma_h$, σ_h being 120 meV. The situation is difficult for an electron since for $\sigma_e = 070$ meV the probability of finding a site 0.18 eV deep below the center of the DOS is much lower. The process is facilitated if the hole has already jumped away from the interface because then the electron feels a reduced coulombic attraction. However, this simulation is unable to recover the experimental observation that in the PhPPV:PdI system, the carrier yield saturates at lower electric fields at acceptor concentrations around and above 10 %.

This reasoning leads to a step model of geminate pair dissociation at the interface. In the first step, the hole jumps to a low energy site, away from the interface. Afterwards the probability for recombination of electron and hole will be strongly suppressed and the expanded pair may be considered to be metastable. In the second step, this expanded pair can dissociate via diffusive motion of the electron in the potential well created by the coulombic attraction exerted by the more distant hole. At the same time the hole may jump back to the interface, allowing for fast geminate recombination.

This simulation reflects how a complex system behaves under the imposed premises. Accordingly, deviations from this behavior in a real world sample indicate in which aspect the model system differs from it. Particularly, one can compare the above simulation results with the properties of an ITO:PEDOT/MDMO-PPV:PCBM/LiF/Al photovoltaic cell studied by Dyakonov [59] and the photoconductivity data for the 70 % PhPPV:PdI system. It turns out that in both cases the photoconductive yield already saturates at lower electric fields. In the first case the collection efficiency per absorbed photon is ≈50 % at an internal electric field of about 2×10^5 V/cm, assuming a built-in voltage of 2 V across a 10 nm thick sample. This is comparable to the yield reported in Figure 8.5. We conjecture that the main difference between the real world sample and the simulation sample is the increase of the e–h separation at the internal interface. The effect is believed to be due to the ultrafast motion of the hole inside a conjugated polymer chain. However, this effect can profitably be exploited only if the slower carrier, i.e. the electron, can move away from the interface quickly. This requires the establishment of a percolative network. This, in turn, requires sample architectures that favor charge transport.

Transient absorption provides access to the kinetics of optical charge carrier generation at a donor–acceptor interface. As mentioned in Section 8.2.3.1 the formation of an interfacial geminate e–h pair is an ultrafast process occurring on a <100 fs timescale. Any retardation of it must be caused by diffusion of the primary excitation towards the interface. Transient absorption recorded at longer timescales monitors the subsequent decay of the charges. Operationally it is unimportant if the recombination kinetics is measured as the temporal decay

of the absorption of the generated charge carriers, usually that of the radical cation, or of the spectral hole burnt into the $S_1 \leftarrow S_0$ transition of the neutral donor phase, as the latter becomes charged and, therefore, the transition is removed from the original spectral position. Unfortunately, those spectral features do not allow one to conclude whether or not a charge is coulombically bound to a sibling or not, because a coulombic electric field would cause only a marginal spectral shift. Those spectral features are intramolecular properties associated with considerable inhomogeneous broadening. This is a serious handicap in the interpretation of experimental data. For instance, Montanari *et al.* [61, 62] interpreted the temporal decay of the positive MDMO-PPV polarons, i.e. the radical cation, in an MDMO-PPV:PCBM composite, in terms of recombination of localized charges, ignoring their coulombic interaction. Their decay features an algebraic $t^{-1/2}$ law, assigned to the recombination of holes that relax towards tail states of the density of states distribution. In the same system, Offermans *et al.* [63] measured the decay of the spectral hole burnt into the tail of the $S_1 \leftarrow S_0$ 0–0 transition of the MDMO-PPV after it had been excited by 2.76 eV photons (see Figure 8.14). The temporal decay features a similar algebraic $t^{-1/2}$ law (Figure 8.15), consistent with Ref. [61], and carries useful information on the spectral relaxation of the localized holes. The authors of Ref. [63]were able to interpret their results by simulating the recombination of were able to interpret their results by simulating the recombination of geminate e–h pairs. On the other hand, the Montanari results [61] have also been analyzed successfully, based upon a simulation in which geminate recombination is ignored altogether with the shape of the DOS being exponential. Obviously, the results of the simulation are not unique and additional criteria have to be invoked in order to conclude on the importance of geminate versus nongeminate recombination. The reason for this ambiguity is that an algebraic decay law of reactant in a disordered material is quite insensitive to the exact shape of the DOS and the superposition of a coulombic potential. Earlier simulation results on geminate pair recombination in a single component system with a Gaussian DOS also revealed that the decay of the reactants obeys a similar law while the reaction rate follows, more or less, a t^{-1} law [30]. The latter result has been confirmed by the decay of delayed fluorescence emitted from a single component ladder type poly(para-phenylene) [64]. The conclusion that, in this case, delayed fluorescence is, indeed, due to geminate recombination of an e–h pair rather than bimolecular annihilation of two triplet excitons was proven by experiments in an electric field, which acts on charges yet not on neutral excitons.

8.2.3.4 Nongeminate recombination of electron–hole pairs

It is obvious that an efficient solar cell requires that all charge carriers, escaped from their initial coulombic potential wells, must reach the electrodes in order to be collected without any further loss. This establishes a criterion on the efficiency of bimolecular, i.e. nongeminate, recombination indicating that the transit time of a carrier must be less than the bimolecular recombination time [65, 66]. In the simplest case of equal mobilities $\mu_+ = \mu_- = \mu$ and concentrations $n_+ = n_- = n$ of electrons and holes, the rate equation for generation and loss of carriers is given by:

$$\frac{dn}{dt} = G - \frac{n}{\tau_{tr}} - \beta n^2 \tag{8.1}$$

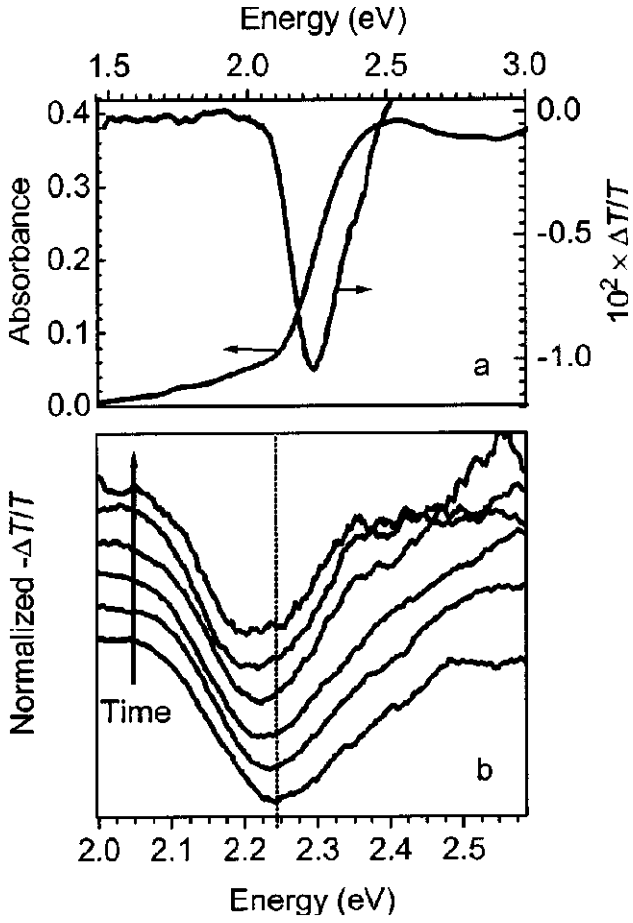

Figure 8.14 (a) Absorption spectrum of spectral holes (excitation at 2.76 eV, acquisition delay 33 ns, gate width 10 ns, $T = 80$ K) in a MDMOPPV:PCBM blend. (b) Time dependence of spectral holes. Spectra were recorded at delay time/gate width combinations of: 10 ns/2 ns; 33 ns/10 ns; 233 ns/30 ns; 1 ms/100 s, 3 ms/300 ns; and 10 ms/300 ns. Spectra were recorded with excitation at 2.76 eV (fluence 2.0 mJ/cm^2) at $T = 80$ K and are shifted upward in successive steps for clarity. Reprinted with permission from T. Offermans, S. C. J. Meskers, and R. A. J. Janssen, *J. Chem. Phys.* **119**, 10924 (2003). Copyright (2003) American Institute of Physics.

where β is the constant of bimolecular recombination, G the yield of coulombically decoupled electron–hole pairs, $\tau_{tr} = d/\mu F$ the transit time, and d the electrode separation in a sandwich cell. The condition that monomolecular recombination, i.e. discharge at the electrodes, dominates over bimolecular recombination is $\beta n < \tau_{tr}^{-1}$ which yields:

$$n < \frac{\mu F}{\beta d} \tag{8.2}$$

The general notion is that, in molecular solids, bimolecular electron–hole recombination is of the Langevin type, i.e. it occurs once the charge carriers enter their mutual coulombic potential defined by the capture radius $r_c = e^2/4\pi\varepsilon_0\varepsilon kT$ where ε_0 is the permittivity of free space and

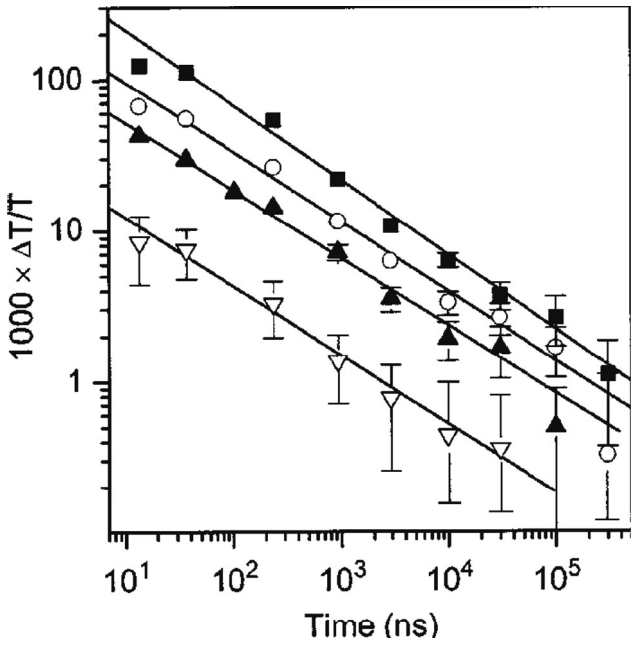

Figure 8.15 Decay of the depth of the spectral hole in MDMO-PPV:PCBM as a function of time. Excitation 2.76 eV, pump fluences: (□) ∼2 mJ/cm^2; (○) ∼1 mJ/cm^2; (▲) ∼0.5 mJ/cm^2; and (♡) ∼ 0.05 mJ/cm^2. Solid lines represent fits of $\Delta T \sim t^{-\alpha}$ to the data with (■) $\alpha = 50 \pm 0.01$; (○) $d = 0.46 \pm 0.02$; (▲) $\alpha = 0.45 \pm 0.03$; and (▽) $\alpha = 0.46 \pm 0.16$. Reprinted with permission rom T. Offermans, S. C. J. Meskers, and R. A. J. Janssen, *J. Chem. Phys.* **119**, 10924 (2003). Copyright (2003) American Institute of Physics.

ε the relative dielectric constant. The Langevin model predicts that:

$$\frac{\beta}{\mu} = \frac{e}{\varepsilon_0 \varepsilon} \tag{8.3}$$

It is well established that the Langevin relationship between the mobility and recombination constant should be correct irrespective of whether or not the sample is crystalline or amorphous, such as an organic light emitting diode [67]. Substituting Equation (8.3) into Equation (8.2) yields:

$$n < \frac{\varepsilon_0 \varepsilon F}{ed} \tag{8.4}$$

Since $\varepsilon_0 \varepsilon F/e$ is the surface density of charge carriers on the plates of a capacitor, Inequality (8.4) implies that bimolecular recombination becomes important if the total charge inside a diode of thickness d is comparable to the capacitor charge. This sets a limit on the linear regime of the stationary photocurrent generated in a solar cell. Suppose that in a 300 nm thick cell, a photon flux of 100 mW/cm^2 is completely absorbed and generates pairs of free electrons and holes at an external efficiency of 10 % yielding a generation rate of 4×10^{20} carriers/cm^{3}s. If the built-in voltage is $V_{bi} = 0.5$ V, the capacitor charge carrier density in the bulk is 10^{15} cm^{-3}.

The meet inequality (8.4) the carrier transit time must be $\leq 2.5 \times 10^{-6}$ s implying a carrier mobility as high as $\mu \geq 8 \times 10^{-4}$ cm^2/Vs.

The above requirement becomes even more stringent if one sort of carrier has a significantly lower mobility. In that case the stationary concentration of the less mobile carriers, say the electrons, is $n_- = (\mu_+/\mu_-)n_+$. Therefore, the critical stationary concentration of the more mobile carriers is controlled by the motion of the less mobile carriers:

$$n_+ < \frac{\mu_-}{\mu_+}\frac{\varepsilon_0 \varepsilon F}{ed} \tag{8.5}$$

Inequalities (8.4) and (8.5) confirm the general notion that the charge carrier mobilities should be as high as possible and symmetric. Otherwise the mobility of the slower carriers controls the onset of bimolecular recombination of carriers that have escaped geminate recombination.

Recently, the time dependent mobility and recombination of the photoinduced charge carriers in a solar cell in which the active element was a spin coated blend of poly[2-methoxy-5-(3,7-dimethyloctyloxy)-phenylenevinylene] (MDMO-PPV) acting as a hole acceptor and 1-(3-methoxycarbonyl)propyl-1-phenyl-(6,6)-C_{61} (PCBM) being the electron acceptor have been studied employing the CELIV (charge extraction in a linearly increasing voltage) technique [68]. Originally, this technique was developed to measure transport of charge carriers present in a sample in the dark, by extracting them upon applying a linearly rising voltage [69]. In Ref. [68] charge carriers were photoinjected by a strongly absorbed 3 ns laser flash. The temperature range was from 120 to 300 K. In order to avoid injection from the electrodes, a reverse bias voltage pulse was applied after an adjustable delay time $t_{\rm del}$ ranging from 1 μs to 1 s. Within this time interval those carriers that had already escaped geminate recombination and avoided bimolecular recombination were probed, up to $t = t_{\rm del}$. It turned out that the carrier mobility was time dependent featuring an algebraic power law, which is a signature of carrier energy relaxation towards the tail states of a Gaussian distribution of states in an energetically disordered organic hopping system. The bimolecular rate 'constant' $\beta(t)$ was also time dependent following the same power law as expected because $\beta(t)$ is controlled by carrier diffusion. One message extracted from the results is that the ratio $\beta(t)/\mu(t)$ is independent of time and close to the value that Langevin's theory predicts – see Equation (8.3).

However, a 1:2 blend of regioregular poly(3-hexyl-thiophene) (RRP3HT) [70] and PCBM behaves very differently as far as bimolecular recombination of photogenerated charges is concerned [66]. The sample had a thickness of 80–100 nm and an optical density OD = 1.9(αd = 4.4, where α is the absorption coefficient). Transient photocarrier response was measured upon exciting the sample by 3 ns laser pulses with a maximal energy of 0.3 mJ/pulse under the condition that the Resistance-Capacitance (RC) time constant was much larger than the carrier transit time. From the extracted charge normalized to the capacitor charge, which approaches 30 at the highest light intensity, and the extraction time, the bimolecular recombination coefficient was calculated as $\beta = 2 \times 10^{-13}$ cm^3/s. Combined with a mobility of the fastest carriers of $\mu = 4 \times 10^{-3}$ cm^2/Vs, measured independently, but on the same solar cell employing the time-of-flight technique, this yields $\beta/\mu = 5 \times 10^{-11}$ Vcm, i.e. about four orders of magnitude smaller than the value $e/\varepsilon_0\varepsilon$ predicted by Langevin's theory. This is a remarkable result that demonstrates the enormous impact of the morphology of the donor–acceptor blend. Obviously, the self alignment of the polythiophene chains imposed by regioregularly arranged substituents reduces bimolecular recombination greatly because it creates a continuous

interpenetrating network that helps to establish independent pathways of electrons and holes. It is open to conjecture if this phenomenon is related to the reduced rate of geminate recombination of initially generated e–h pairs at appropriate compositions of the blend. In any event, this testifies to the crucial role of mesoscopic ordering in blended organic solar cells.

8.3 MODELS OF EXCITON DISSOCIATION IN HOMOGENEOUSLY DOPED CONJUGATED POLYMERS AND IN POLYMER BASED DONOR/ACCEPTOR BLENDS

Before embarking on a discussion of the theoretical aspects of research into organic solar cells, experimental results will be briefly summarized. The excitonic approach to photophysics of conjugated polymers suggests the following scenario for free carrier photogeneration. Excitation of a conjugated polymer by light within the absorption band creates Frenkel type singlet excitons with the binding energy E_b of around 0.5 eV. Photon absorption generates Franck–Condon states that can be either vibronically relaxed or 'hot', the latter being the case if the energy of incident photons is in excess of the absorption edge. Upon relaxation of a hot Franck–Condon state through a vibronic progression, the excess photon energy is transferred into intrasegmental vibronic excitations and the exciton occupies a hot segment. Fast dissociation of such excitons into pairs of free carriers is feasible even at moderate external electric fields [71–73], while the field assisted intrinsic dissociation of a relaxed exciton would require fields in the MV/cm range. However, a relaxed singlet exciton can be quenched and dissociate into a (geminate) pair of charges at a CT center. A typical CT center in a conjugated polymer consists of a conjugated segment and an adjacent electron scavenger (deep electron trap). Exciton dissociation at a CT center is possible if the electron affinity of the scavenger is large enough in order to compensate for the exciton binding energy.

However, exciton quenching at a CT center does not yet yield free carriers. Instead, a strongly coulombically bound geminate pair of charges is generated. The respective Coulomb binding energy can be estimated as 0.5 eV for a distance between the conjugated segment and electron scavenger of 1 nm and the dielectric constant of three. This estimate shows that the charges in a geminate pair are bound no more weakly than in a vibronically relaxed singlet exciton. This notion explains the notorious difference between the photoluminescence (PL) quenching efficiency and the carrier photogeneration yield in doped conjugated polymers [33, 36]. While the PL intensity drops to almost zero at a quencher concentration of 1 % the onset of efficient charge generation typically requires a doping level in excess of 10 % [31] i.e. photogeneration of free carriers is possible in donor/acceptor blends rather than in homogeneously doped polymers.

8.3.1 The Onsager–Braun model

It seems straightforward to try to rationalize the experimental results on photocarrier generation in donor—acceptor type organic solar cells in terms of Braun's extension of Onsager's theory of geminate pair dissociation. Recall that in 1934 Onsager formulated a theory for the dissociation of infinite lifetime ions in a weak electrolyte [74]. In 1938 he treated the case of a radiatively induced pair of charges that recombine instantaneously once having collided (infinite sink

approach) [38]. In 1984 Braun [37] considered the case that the pair has a finite lifetime. It implies multiple excursions of a pair that can eventually fully escape its mutual coulombic potential or ultimately recombine. This should be relevant for blended organic solar cells because efficient photogeneration is premised upon the lowest energy state of the system being an electron–hole pair located at a pair of donor and acceptor moieties that has a finite lifetime. Any prolongation of its lifetime by multiple excursions within the cycle exciton–exciplex–CT state would inevitably increase the yield of complete pair dissociation $\eta(F, T)$ that is given by:

$$\eta\left(F, T\right) = \frac{k_{\mathrm{d}}\left(F, T\right)}{k_{\mathrm{d}}\left(F, T\right) + k_{\mathrm{rec}}} \tag{8.6}$$

where k_{d} is the rate constant of complete dissociation of a geminate pair and k_{rec} the rate of its monomolecular recombination. According to Braun [37], k_{d} is given by:

$$k_{\mathrm{d}}\left(F, T\right) = \frac{3\beta}{4\pi a^3} \exp\left(-\frac{E_{\mathrm{eh}}}{kT}\right)\left(1 + b + \frac{b^2}{3} + \frac{b^3}{18} + \frac{b^4}{180} + \cdots\right) \tag{8.7}$$

where a is the initial separation of the carriers bound in an e-h pair at a donor-acceptor interface with the binding energy E_{eh}, $b = e^3 F/8\pi\varepsilon_0 \langle\varepsilon\rangle (kT)^2$, $\langle\varepsilon\rangle$ being the spatially averaged relative dielectric constant, and β is the rate constant for Langevin-type electron-hole recombination, i.e. $\beta = e\langle\mu\rangle/\varepsilon_0\langle\varepsilon\rangle$, with $\langle\mu\rangle$ being the sum of the spatially averaged electron and hole mobilities. In a disordered system, one has also to consider that the intra-pair separation is associated with a distribution. It is often parameterized by a distribution function of the form $\rho(r) = r^2 \exp(-r^2/a^2)$. Accordingly, Equations (8.6) and (8.7) should be integrated over the distribution of r and Equation (8.6) becomes:

$$\eta\left(F, T\right) = \frac{4}{\sqrt{\pi a^3}} \int_0^\infty \mathrm{d}r \rho\left(r\right) \eta\left(r, F, T\right) \tag{8.8}$$

Michailetchi *et al.* [75] used Equation (8.8) in order to rationalize photocurrent data of a bulk heterojunction device using poly(2-methoxy-5-(3′,7′-dimethyloctyloxy)-p-phenylene-vinylene) (OC_1C_{10}-PPV) and PCBM with a 20:80 composition. Using $\langle\varepsilon\rangle = 3.4$, $a = 1.3$ nm, and a pair lifetime of 1 μs, the experimental field dependence could be reproduced. From the temperature dependence, measured at very low applied voltage (0.01 V) and at the built-in voltage, the activation energies were estimated as 94.1 and 35.4 meV, respectively. They would translate to e–h separations of 4.5 and 12 nm, i.e. considerably larger than the average mean value of 1.5 nm based on $a = 1.3$ nm. This discrepancy is ubiquitously observed in random organic systems and might be attributed to disorder (see Section 8.2.2.2). Another question relates to the chosen value for the lifetime of the geminate e–h pair or an exciplex as a precursor which should be controlled by nonradiative coupling of the pair to molecular vibrations. It is plausible that the lifetime of a charge transfer state exceeds that of an exciplex, which is typically in a 1–50 ns range, but this notion requires experimental verification.

The Onsager–Braun formalism including disorder effects provides a plausible, if consistent regarding parameterization, explanation of charge photogeneration in bulk heterojunction organic solar cells but, is it compelling? It certainly can neither account for the sudden increase in the generation yield at critical dopant concentration beyond the limit at which photon harvesting and primary e–h pair generation are complete, nor explain the increase of the yield in

morphologically optimized systems. In the following section a theoretical concept is advanced that might offer an explanation of the abovementioned problems.

8.3.2 Exciton dissociation in conjugated polymers homogeneously doped with electron scavengers

Two effects can be responsible for the steep increase in charge photogeneration yield at high dopant concentrations: (i) the formation of interpenetrating percolation networks for (hopping) transport of both electrons and holes as well as (ii) the onset of full or partial separation of donor and acceptor phases which allows for exciton dissociation at the developed donor/acceptor interface. Bipolar transport is obviously a must for full charge collection, but it cannot provide high photovoltaic yield without efficient exciton dissociation as a first step in light harvesting. Full harvesting of excitons at the interface is essential for efficient carrier photogeneration, which is possible only if the exciton diffusion length is larger than or, at least, comparable with the maximum distance an exciton has to cross in order to reach the nearest interface. This condition can be fulfilled in optimized planar multilayer photovoltaic devices by controllable deposition of individual layers. The control of morphology in bulk heterojunction donor/acceptor systems is much more difficult.

From the energy conservation point of view, dissociation of a relaxed exciton into a free hole and a localized electron at a CT center is, in principle, feasible if the difference Δ between energies of the host and guest LUMOs is larger than the exciton binding energy. However, this general notion does not provide answers to some important questions raised in experimental studies of this process:

1. If no intermediate states are involved charge generation at a CT center has to be described as an adiabatic quantum mechanical transition from the initial state of two carriers bound in an on-chain singlet exciton to the final state in which the electron is localized in the LUMO of the nearby acceptor and the hole occupies an on-chain state at a distance larger than the Onsager radius, which is around 20 nm at room temperature. It is unlikely that the respective matrix element is large enough for the typical time of exciton dissociation to be shorter than 100 fs.
2. Provided that the energetic requirements are fulfilled, the yield of direct exciton dissociation into free charge carriers should depend neither upon external electric field nor upon temperature. However, measurements do reveal a strong field dependence of the yield although its temperature dependence turns out to be rather weak, especially at low temperatures.
3. Since CT has to be an adiabatic process, the excess energy should afterwards be released and dissipated within the acceptor molecule occupied by the transferred electron. Since the energy dissipation time is typically shorter than 100 fs it is fairly unlikely that, over such a short time, the electron could escape from the Coulomb potential well by hopping, even if the concentration of acceptor molecules is close to 50 % or larger. Therefore, full separation of charges is feasible only due to motion of the on-chain hole, but then it is not clear how the excess energy, released upon deep trapping of the electron, can be transferred back to the on-chain hole.

After exciton dissociation into a (short) geminate pair the on-chain hole is still coulombically bound to the trapped electron. The respective potential $U(x)$ can be described as a modified one-dimensional Coulomb well:

$$U(x) = -\frac{e}{4\pi\varepsilon_0\varepsilon(x^2 + a^2)^{1/2}} \tag{8.9}$$

where a is the distance from the chain to the electron scavenger. Since the hole is free within the polymer chain (or within a conjugated segment thereof) its ground state energy must include the energy of the on-chain zero point oscillations. Unfortunately, the respective Schrödinger equation cannot be solved analytically for the potential given by Equation (8.9). However, the ground state energy E_0 can be estimated if this potential distribution is approximated by a parabolic potential $U_{\text{osc}}(x)$, calculated by expanding $U(x)$ into a power series at $x = 0$. The result reads:

$$U_{\text{osc}}(x) = -\frac{e^2}{4\pi\varepsilon_0\varepsilon a}\left(1 - \frac{x^2}{2a^2}\right), \quad E_0 = -\frac{e^2}{4\pi\varepsilon_0\varepsilon a} + \frac{e\hbar}{4\sqrt{\pi\varepsilon_0\varepsilon a^3 m_{\text{eff}}}} \tag{8.10}$$

where m_{eff} is the effective on-chain hole mass. This parameter virtually determines the effective binding energy $E_{\text{b}} = -E_0$ of the geminate pair and, therefore, plays a key role in the process of free carrier photogeneration.

The value of m_{eff} in conjugated polymers is still subject of controversy. Quantum chemical calculations performed for several polymers [14] showed that m_{eff} is around $(0.03–0.08)m_{\text{e}}$, where m_{e} is the free electron mass. The use of such values of m_{eff} in Equation (8.10) yields zero or almost zero binding energy of geminate pairs, implying their immediate dissociation into free carriers even without an external electric field. However, experimental studies of the dopant assisted exciton dissociation did reveal a strong field dependence of the yield [33, 35, 36]. Another indication in favor of larger values of the effective on-chain carrier mass, came from the study of microwave conductivity in conjugated polymers [76]. It turned out that the on-chain mobility of relaxed polarons is still not higher than 0.1–1 cm^2/Vs indicating an effective carrier mass of $(1–2)m_{\text{e}}$ while the mobility of freshly generated carriers can be as large as 1500 cm^2/Vs [76].

This apparent contradiction between theoretical calculations and experimental data can be explained if one bears in mind the difference between the timescales of exciton dissociation and on-chain charge transport. The former is a quasiinstantaneous process and its immediate result is an on-chain hole that is not yet embedded into a structurally and, possibly, electronically relaxed molecular environment. Its effective mass can indeed be as small as predicted by the calculations of Ref. [14]. It is worth noting that electroreflection experiments, done on single crystalline polydiacetylenes [77] did reveal an on-chain carrier mass much smaller than m_{e} and close to its calculated value. Since both polaronic and vibrational relaxations in conjugated polymers occur on the timescale, shorter than 100 fs, one can expect that conductivity measurements on a longer timescale would reveal a contribution of only relaxed polarons.

Another indication of a large difference between effective masses of 'freshly generated' and relaxed carriers comes from the comparison between charge transfer rate in photogeneration experiments and jump rate estimated from charge transport measurements. On the one hand, electron transfer from a photoexcited PPV segment to C_{60} occurs on a timescale of 50 fs [55]. On the other hand, the prefactor of carrier mobility, inferred from μ versus $1/T^2$ plots at $T \to \infty$, is usually 10^{-2} cm^2/Vs. By assuming $eD = kT\mu$ and $D = a^2\nu/6$ this translates into

a disorder free interchain jump time of $1/\nu = 1$ ps. A plausible explanation for this difference could be that the latter time corresponds to an adiabatic transfer of a relaxed charge carrier having an effective mass of $>2m_e$ while the former is the time of a 'vertical' transition into a state with a low effective mass.

Based on these facts, the following scenario of exciton dissociation at a CT center can be envisaged. Immediately after transfer of the negative charge from a polymer chain to a nearby electron scavenger, the nonrelaxed light on-chain hole occupies the ground state or one of the excited states within the potential well formed by the negative charge of the trapped electron. Since the effective mass of the hole is still small prior to polaronic relaxation, the energy of its zero point oscillations must be relatively large and, therefore, sharing in the excess energy released upon deep trapping of the electron, has to be in favor of the on-chain hole. In the course of fast (<100 fs) polaronic and vibronic relaxations, the effective mass of the on-chain hole increases up to (1–2)m_e, which leads to a concomitant decrease ΔE of the zero point oscillation energy. From Equation (8.10), the value of ΔE can be estimated as:

$$\Delta E = \frac{e\hbar}{4\sqrt{\pi\varepsilon_0\varepsilon a^3}}\left(\frac{1}{\sqrt{m_{\text{eff}}^{(\text{inst})}}} - \frac{1}{\sqrt{m_{\text{eff}}^{(\text{rel})}}}\right) \tag{8.11}$$

where $m_{\text{eff}}^{(\text{inst})}$ and $m_{\text{eff}}^{(\text{rel})}$ are the instantaneous effective mass and the effective mass of the relaxed hole, respectively. For $m_{\text{eff}}^{(\text{inst})} = 0.03m_e$, $m_{\text{eff}}^{(\text{rel})} = 2m_e$, and $a = 0.5$ nm, Equation (8.11) yields $\Delta E \approx 1.2$ eV. This excess energy has to be funneled into the local vibrational bath making the segment temporarily hot. As has been previously suggested in the model of hot exciton dissociation [71, 72], this energy can be used by the on-chain hole in order to escape from the Coulomb potential well of its negative twin via a Boltzmann like thermally activated release process. Since the initially occupied conjugated segment is hot, the escape probability only weakly depends upon the ambient temperature [72]. However, the field dependence of the yield remains strong because the external field determines the height of the potential barrier that the hole has to cross in order to become free.

Remarkably, the above estimate for the excess energy released upon polaronic relaxation of the on-chain hole, favorably agrees with both the excess photon energy typically required for the onset of intrinsic hot exciton dissociation [18, 78, 79] and the electron affinity of those acceptor materials that provide efficient exciton dissociation in organic donor/acceptor blends. Particularly, if the gain of energy upon electron transfer is not large enough to provide sufficient energy for zero point oscillations of the temporarily light hole, one should expect a much slower CT process that directly creates a relaxed on-chain hole or an exciplex state, both being unfavorable for the eventual full charge separation. In principle, this notion can explain a low exciplex yield in the MDMO-PPV/PCNEPV blend discussed in Section 8.2.3.1.

8.3.3 Exciton dissociation at a polymer donor/acceptor interface

It has been shown in the previous section that, in conjugated polymers strongly doped with electron acceptors, i.e. in polymer donor/acceptor blends, the yield of intrinsic charge carrier photogeneration can increase up to almost 100 % provided that the morphological demands are met [36, 57]. Moreover, such efficient exciton dissociation can be achieved even at moderate electric fields and low temperatures. This indicates a really efficient mechanism preventing

geminate pairs from recombination at a polymer/acceptor interface. A strong difference between exciton dissociation in weakly and strongly doped polymers is also supported by the fact that e–h pairs can be detected at small concentrations of acceptors while in polymer/acceptor blends mostly free charges and/or loosely bound long pairs have been observed [80]. The fast and efficient dissociation of geminate pairs suggests that a bottleneck for geminate recombination must exist at a polymer/acceptor interface. Below, we describe a model of interfacial exciton dissociation in donor/acceptor blends that shows how this bottleneck could be formed [81].

The model rests on the notion that a dipolar layer can exist at a polymer/acceptor interface, as testified by the observation of a vacuum level shift of 0.25 eV at the interface between the five ring conjugated oligomer p-bis [(p-styryl)styryl]benzene and C_{60} [82]. An optical excitation, generated in a conjugated polymer, can diffuse towards the interface and dissociate into an e–h pair. Immediately after dissociation, the electron will be localized at the electron acceptor molecule while the hole remains on the polymer chain next to the interface. The potential energy of the on-chain hole, E_p, is determined by its interaction with the negatively charged nearest electron acceptor and partial charges of dark dipoles as shown in Figure 8.16. By neglecting contributions of all partial charges except for the four nearest ones, the coordinate dependence of the potential energy along the chain can be estimated as:

$$E_p(x) = \frac{e^2}{4\pi\varepsilon_0\varepsilon}\left(-\frac{1}{\sqrt{x^2+b^2}} + \frac{\alpha}{a+x} + \frac{\alpha}{a-x} - \frac{\alpha}{\sqrt{(a+x)^2+b^2}} - \frac{\alpha}{\sqrt{(a-x)^2+b^2}}\right) \tag{8.12}$$

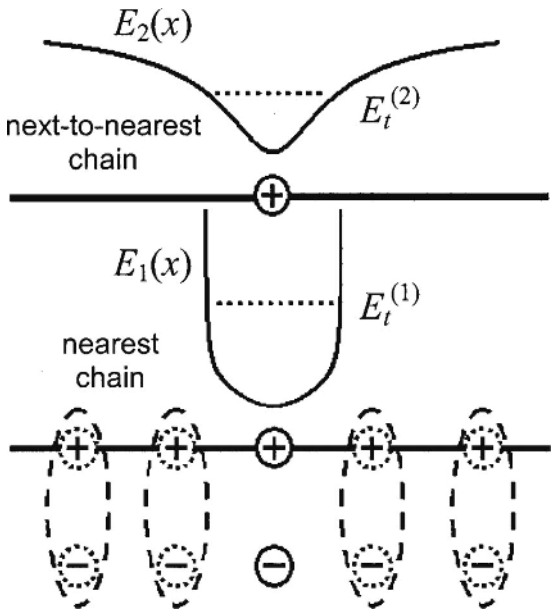

Figure 8.16 Potential energy distribution and total energy of a hole occupying a polymer chain either nearest or next-to-nearest to a polymer/acceptor interface. The potential distributions are caused by dark interfacial dipoles and the sibling electron trapped at an acceptor next to the interface. From V. I. Arkhipov, P. Heremans, and H. Bässler, *Appl. Phys. Lett.* **82**, 4605 (2003).

where a is the distance between electron acceptors, b the distance between the chain and electron acceptors, and α the share of elementary charge transferred from the chain to an acceptor in the dark.

Although an on-chain hole is supposed to occupy an extended state it cannot move freely along the chain mainly because of positive partial dipole charges residing on the same chain to the right and to the left of the hole. Together with negatively charged acceptors, these charges form an on-chain potential well for the hole and restrict its otherwise free motion along the chain. In order to estimate the energy of zero point oscillations within this potential well, one can approximate the real potential distribution given by Equation (8.12) by the parabolic oscillatory potential as:

$$E(x) \approx \frac{e^2}{4\pi\varepsilon_0\varepsilon}\left(-\frac{1}{b}+\frac{2\alpha}{a}-\frac{2\alpha}{\sqrt{a^2+b^2}}\right)+\frac{e^2}{8\pi\varepsilon_0\varepsilon}\left[\frac{1}{b^3}+\frac{4\alpha}{a^3}-\frac{6\alpha a^2}{(a^2+b^2)^{5/2}}\right]x^2 \tag{8.13}$$

The total energy $E_t^{(1)}$ of a hole, occupying the ground state on the chain nearest to the interface, is a sum of the minimum potential energy $E_p(x=0)$ and the kinetic energy of zero point oscillations:

$$E_t^{(1)} = \frac{e^2}{4\pi\varepsilon_0\varepsilon}\left(-\frac{1}{b}+\frac{2\alpha}{a}-\frac{2\alpha}{\sqrt{a^2+b^2}}\right) + \frac{\hbar}{2}\sqrt{\frac{e^2}{4\pi\varepsilon_0\varepsilon m_{\text{eff}}}\left[\frac{1}{b^3}+\frac{4\alpha}{a^3}+\frac{2\alpha}{(a^2+b^2)^{3/2}}-\frac{6\alpha a^2}{(a^2+b^2)^{5/2}}\right]} \tag{8.14}$$

If the hole has been transferred from the chain nearest to the interface to the next nearest one, its coulombic potential energy increases but, at the same time, its kinetic energy drops significantly because the caging effect is eroded. The calculation, similar to that described above, leads to the following expression for the total energy $E_t^{(2)}$ of such a hole:

$$E_t^{(2)} = \frac{e^2}{4\pi\varepsilon_0\varepsilon}\left[-\frac{1}{(b+d)}+\frac{2\alpha}{\sqrt{a^2+d^2}}-\frac{2\alpha}{\sqrt{a^2+(b+d)^2}}\right] + \frac{\hbar}{2}\sqrt{\frac{e^2}{4\pi\,\varepsilon_0\varepsilon m_{\text{eff}}}\left\{\frac{1}{(b+d)^3}-\frac{2\alpha}{\left(a^2+d^2\right)^{3/2}}+\frac{6\alpha a^2}{\left(a^2+d^2\right)^{5/2}}+\frac{2\alpha}{\left[a^2+(b+d)^2\right]^{3/2}}-\frac{6\alpha a^2}{\left[a^2+(b+d)^2\right]^{5/2}}\right\}} \tag{8.15}$$

where d is the distance between polymer chains. The energy difference $E_t^{(1)} - E_t^{(2)}$ is shown in Figure 8.17 as a function of the effective carrier mass for different values of the dark charge transfer parameter α. Remarkably, this energy difference is positive at sufficiently small values of the effective carrier mass, i.e. a repulsive potential barrier separating a negatively charged acceptor, and a hole, occupying a segment of a chain next nearest to the interface, is established. This prevents geminate recombination and stabilizes the interfacial geminate pairs provided that the effective mass is $\sim 0.2\, m_e$ or less. However, even if on-chain holes are heavier and the total energy of holes increases upon their transfer from nearest to next nearest chains, this increase is weaker than it would be without the cage effect. From the Onsager theory of geminate recombination it is known that even a small reduction in the attraction potential, especially at short distances, leads to a strong increase in the dissociation probability. This

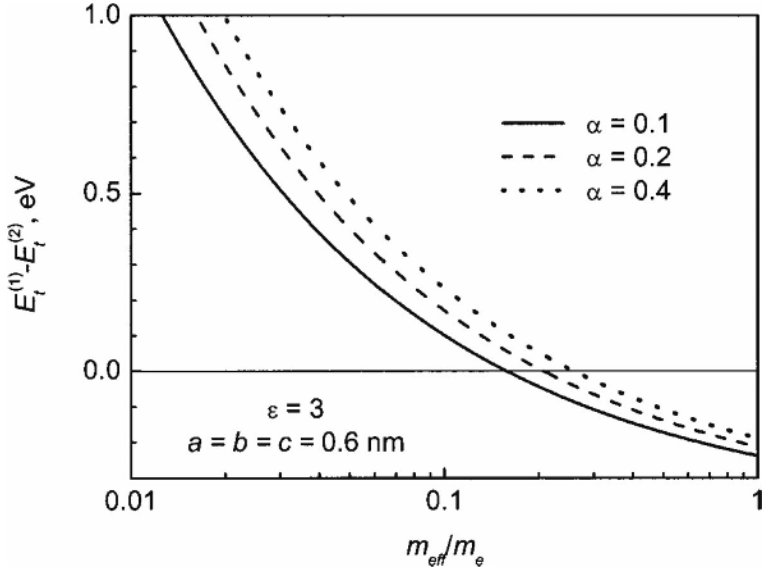

Figure 8.17 Dependence of the repulsive barrier height upon the effective on-chain carrier mass for different values of the dark charge transfer parameter α. From V. I. Arkhipov, P. Heremans, and H. Bässler, *Appl. Phys. Lett.* **82**, 4605 (2003).

can explain the apparent increase of the e–h pair separation in the PhPPV:PdI system beyond the threshold concentration of the acceptor. Therefore, the cage effect should also strongly enhance dissociation of geminate pairs into free carriers at larger values of the effective carrier mass.

Since the model requires polymer chains to be fully parallel to the interface within, at least, the two molecular layers nearest to the interface, and the array of acceptor molecules to be ordered, it readily explains why the molecular ordering near the internal donor/acceptor interface combined with a sufficiently high concentration of acceptors is crucial for attaining a high photovoltaic efficiency. Because of the importance of the on-chain zero point oscillations it is also obvious why polymeric photovoltaic cells are normally more efficient than small molecular devices.

This model explains the increase of the photogeneration efficiency at higher acceptor concentrations in terms of the increase of the Geminate Pair (GP) dissociation rates. Alternatively, one could invoke the onset of percolative motion of the electron across the array of acceptor molecules. However, any change of the carrier diffusivity without an independent increase in the dissociation rate constant could not affect the trade-off between dissociation and recombination of geminate pairs. The model also has several practical implications:

(1) The interface morphology must strongly affect the exciton dissociation yield as experimentally verified. Any structural disorder at the interface is counterproductive because it will diminish the energy of zero point oscillations and, therefore, destroy the bottleneck for geminate recombination.

(2) The existence of a dipolar layer at the donor/acceptor interface facilitates dissociation. Although, as evidenced by the data plotted in Figure 8.17, the degree of dark charge transfer has a relatively minor effect on the exciton dissociation yield, the latter must increase with increasing α especially in weak electric fields.

(3) Efficient dissociation of excitons is possible at moderate fields only if carriers within e–h pairs are separated by potential barriers, which prevents geminate recombination. This is not the case for so-called 'double-cable' polymers with acceptor moieties directly attached to the main donor chain [83].

Therefore, the present model of interfacial dissociation predicts a relatively low efficiency of photovoltaic devices based on the double cables.

8.4 CONCLUSIONS

Efficient power conversion in an organic solar cell requires: (i) that all primary optical excitations reach a CT center and generate metastable geminate electron–hole pairs, (ii) that such a pair must escape easily from its mutual coulombic potential and avoid geminate recombination, and (iii) that the liberated charge carriers are collected by the built-in electric field without suffering bimolecular recombination and/or deep trapping. Owing to the large exciton binding energy in a single component organic solid, the first condition can only be fulfilled in two component systems in which the energy of the charge transfer state is lower that of the singlet excitations of either donor or acceptor. Efficient light harvesting also requires that the exciton diffusion length is at least comparable to the length scale of donor and acceptor phases. Since the former are <10 nm this sets an upper limit on the structural dimensions of blend systems in which phase separation occurs. Organized interpenetrating networks can fulfill these requirements.

What is still open to debate, however, is the detailed mechanism by which a geminate electron–hole pair, generated at the internal donor/acceptor interface, escapes from its mutual coulombic potential. One possibility to interpret experimental results is to apply the Onsager–Braun model for dissociation of an e–h pair with finite lifetime. However, in order to explain the notoriously weak temperature dependence of the yield, one has to assume that the ultimate lifetime of the pair is 1 μs or assure that the rate constants for geminate recombination and dissociation are comparable (see Equation (8.6)). Otherwise, the dissociation would be strictly proportional to the rate constant for dissociation, which is determined by the coulombic binding energy of the e–h pair. This would imply unrealistically large e–h separations. Invoking disorder effects would alleviate this problem to some extent.

Nevertheless there is an urgent need to prove or disprove the assumption of a long lifetime of the e–h pair via experimental studies of the dynamics of photogenerated geminate pairs as a function of in the concentration of the electron acceptors. The Onsager–Braun model contains only two adjustable parameters, i.e. the pair lifetime and its separation, yet not the acceptor concentration. On the other hand, it is known that the yield depends strongly on acceptor concentration. For one particular system, i.e. PhPPV:PdI, an increase of the photocarrier yield by more than two orders of magnitude has indeed been observed. It is an open question if this is an indication that primary charge transfer is facilitated by donor–acceptor blending or if

this simply due to opening of a transport path for electrons thus alleviating recombination and space charge effects.

Another question that calls for experimental clarification is whether or not the excess energy dissipated upon dissociation of an exciton into a geminate e–h pair facilitates the generation of e–h pairs with larger intrapair distances. At first sight this might explain why systems containing C_{60}, which is one of the strongest electron acceptors because of its low lying LUMO, are preferred candidates for efficient organic solar cells. On the other hand, it has been observed that in the PhPPV:PdI system the quantum efficiency of photogeneration reaches 20 %. Remarkably, the spectrally resolved yield of that process is constant within the entire absorption spectrum of the blend, whose optical gap is set by the PdI absorption. Evidently, is makes no difference if the PdI is excited via a energy dissipating Förster type energy transfer or by direct excitation. This proves that it is the excited singlet state of PdI that dissociates into a PhPPV/PdI pair regardless of how it has been excited. Since the energy of the singlet state of PdI is 2.2 eV only, the excess energy relative to that of the e–h pair has got to be small. The same argument applies to the PFB:F8BT system (see Section 8.2.3.1). This is clearly at variance with the notion that the magnitude of the excess energy is a key parameter in the design of an efficient organic cell. Nevertheless, a systematic study of the possible influence of the excess energy would shed light on the mechanism of the e–h pair formation.

Recently, a model has been advanced aiming at understanding efficient photogeneration in donor–acceptor blends in which at least one component is a π-conjugated polymer. The essential idea is that at the first moment when a charge carrier is generated on a polymer chain, its mobility is determined by strong electronic intrachain coupling. It can reach a value on the order of 10^3 cm^2/Vs [76] and the effective mass is about 0.05 m_e [14]. Although a carrier will relax quickly on a sub-ps timescale because of scattering at chain imperfections, molecular vibrations and phonons, this ultrafast motion guarantees that the initial separation of the e–h pair can be a multiple of the length of a repeat unit of the chain. The pair will certainly suffer geminate recombination unless the coulombic potential is screened, for instance, by a dipole layer that is established at the internal interface of the donor–acceptor heterojunction and/or at potential fluctuations. This would have a concomitant effect on nongeminate recombination because the latter is also determined by the attractive coulombic potential. This illustrates the crucial role of morphology and its control in organic solar cells.

REFERENCES

[1] J. J. M. Halls, C. A. Walsh, N. C. Greenham, E. A. Marseglia, R. H. Friend, S. C. Moratti, and A. B. Holmes, Efficient photodiodes from interpenetrating polymer networks, *Nature* **376**, 498 (1995).

[2] G. Yu, J. Gao, J. C. Hummelen, F. Wudl, and A. J. Heeger, Polymer photovoltaic cells – enhanced efficiencies via a network of internal donor-acceptor heterojunctions, *Science* **270**, 1789 (1995).

[3] B. Kraabel, J. C. Hummelen, D. Vacar, D. Moses, N. S. Sariciftci, A. J. Heeger, and F. Wudl, Sub-picosecond photoinduced electron transfer from conjugated polymers to functionalized fullerenes, *J. Chem. Phys*. **104**, 4267 (1996).

[4] H. Pope and C. E. Swenberg, *Electronic Processes in Organic Crystals and Polymers*, 2nd ed. (Oxford, Univ. Press, 1999).

[5] H. Bässler, Excitons in conjugated polymers, in *Primary photoexcitations in conjugated polymers: Molecular excitons versus semiconductor band model*, N. S. Sariciftci (ed.), (World Scientific, Singapore, 1997).

[6] V. I. Arkhipov and H. Bässler, Exciton Dissociation in Conjugated Polymers, in *Handbook of Luminescence, Display Materials and Devices*, H. S. Nalwa and L. S. Rohwer (eds.), (American Scientific Publishers, Los Angeles 2003), v. 1, p. 279.

[7] V. I. Arkhipov and H. Bässler, Exciton dissociation and charge photogeneration in pristine and doped conjugated polymers, *Phys. Stat. Sol. (a)* **201**, 1152 (2004).

[8] Y. V. Romanovskii, A. Gerhard, B. Schweitzer, U. Scherf, R. I. Personov, and H. Bässler, Phosphorescence of pi-conjugated oligomers and polymers, *Phys. Rev. Lett.* 84, 1027 (2000).

[9] D. Hertel, S. Setayesh, H. G. Nothofer, U. Scherf, K. Müllen, and H. Bässler, Phosphorescence in conjugated poly(para-phenylene)-derivatives, *Advanced Mater.* **13**, 65 (2001).

[10] A. P. Monkman, H. D. Burrows, I. Hamblett, S. Navaratnam, U. Scherf, and C. Schmitt, The triplet state of the ladder-type methyl-poly(p-phenylene) as seen by pulse radiolysis-energy transfer, *Chem. Phys. Lett.* **327**, 111 (2000).

[11] A. P. Monkman, H. D. Burrows, L. J. Hartwell, L. E. Horsburgh, I. Hamblett, and S. Navaratnam, Triplet energies of pi-conjugated polymers, *Phys. Rev. Lett.* **86**, 1358 (2001).

[12] A. Köhler, J. S. Wilson, R. H. Friend, M. K. Al-Suti, M. S. Khan, A. Gerhard, and H. Bässler, The singlet-triplet energy gap in organic and Pt-containing phenylene ethynylene polymers and monomers, *J. Chem. Phys*. **116**, 9457 (2002).

[13] M. G. Harrison, S. Möller, G. Weiser, G. Urbasch, R. F. Mahrt, H. Bässler, and U. Scherf, Electro-optical studies of a soluble conjugated polymer with particularly low intrachain disorder, *Phys. Rev. B* **60**, 8650 (1999).

[14] J.-W. van der Horst, P. A. Bobbert, M. A. J. Michels, and H. Bässler, Calculation of excitonic properties of conjugated polymers using the Bethe-Salpeter equation, *J. Chem. Phys.* **114**, 6950 (2001).

[15] J. Rissler, H. Bässler, F. Gebhard, and P. Schwerdtfeger, Excited states of ladder-type poly-p-phenylene oligomers, *Phys. Rev. B* **64,** 045122 (2001).

[16] G. Weiser, Stark-effect of one-dimensional wannier excitons in polydiacetylene single-crystals, *Phys. Rev. B* **45,** 14076 (1992).

[17] M. Chandross, S. Mazumdar, S. Jeglinski, X. Wei, Z. V. Vardeny, E. W. Kwock, and T. M. Miller, Excitons in poly(para-phenylenevinylene), *Phys. Rev. B* **50**, 14702 (1994).

[18] S. Barth, H. Bässler, U. Scherf, and K. Müllen, Photoconduction in thin films of a ladder-type poly-para-phenylene, *Chem. Phys. Lett.* **288** (1), 147, (1998).

[19] G. Dicker, M. P. de Haas, L. D. A. Siebbeles, and J. M. Warman, Electrodeless time-resolved microwave conductivity study of charge-carrier photogeneration in regioregular poly(3-hexylthiophene) thin films, *Phys. Rev. B* **70** (4), 045203, (2004).

[20] N. E. Geacintov and M. Pope, Generation of Charge Carriers in Anthracene with Polarized Light' *J. Chem. Phys.* **47**, 1194 (1967).

[21] C. Silva, A. S. Dhoot, D. M. Russell, M. A. Stevens, A. C. Arias, J. D. MacKenzie, N. C. Greenham, R. H. Friend, S. Setayesh, and K. Müllen, Efficient exciton dissociation via two-step photoexcitation in polymeric semiconductors *Phys. Rev. B* **64**, 125211, (2001).

[22] G. Lanzani, G. Cerullo, D. Polli, A. Gambetta, M. Zavelani-Rossi, and C. Gadermaier, Photophysics of conjugated polymers: the contribution of ultrafast spectroscopy, *Phys. Stat. Sol. (a)* **201**, 1116, May (2004).

[23] D. Hertel, Y. V. Romanovskii, B. Schweitzer, U. Scherf, and H. Bässler, The origin of the delayed emission in films of a ladder-type poly(para-phenylene) *Synth. Met.* **116** (1-3)**,** 139, (2001).

[24] B. Schweitzer, V. I. Arkhipov, and H. Bässler, Field-induced delayed photoluminescence in a conjugated polymer, *Chem. Phys. Lett.* **304**, 365 (1999).

[25] D. Hertel, E. V. Soh, H. Bässler, and L. J. Rothberg, Electric field dependent generation of geminate electron-hole pairs in a ladder-type pi-conjugated polymer probed by fluorescence quenching and delayed field collection of charge carriers *Chem. Phys. Lett.* 361, 99 (2002).

[26] W. Graupner, G. Cerullo, G. Lanzani, M. Nisoli, E. J. W. List, G. Leising, and S. De Silvestri, Direct observation of ultrafast field-induced charge generation in ladder-type poly(para-phenylene), *Phys. Rev. Lett.* **81**, 3259 (1998).

[27] V. Gulbinas, Y. Zaushitsyn, V. Sundström, D. Hertel, H. Bässler, and A. Yartsev, Dynamics of the electric field-assisted charge carrier photogeneration in ladder-type poly(para-phenylene) at a low excitation intensity, *Phys. Rev. Lett.* **89**, 107401 (2002).

[28] S. C. J. Meskers, J. Hübner, M. Oestreich, and H. Bässler, Dispersive relaxation dynamics of photoexcitations in a polyfluorene film involving energy transfer: Experiment and Monte Carlo simulations, *J. Phys. Chem. B* **105**, 9139 (2001).

[29] V. I. Arkhipov, E. V. Emelianova, and H. Bässler, Quenching of excitons in doped disordered organic semiconductors, *Phys. Rev. B* **70**, 205205 (2004).

[30] B. Ries and H. Bässler, Monte-carlo study of dispersive charge-carrier transport in spatially random-systems with and without energetic disorder, *J. Mol. Electron.* **3**, 15 (1987).

[31] A. Kadashchuk, Yu. Skryshevskii, A. Vakhnin, N. Ostapenko, V. I. Arkhipov, E. V. Emelianova, and H. Bässler, Thermally stimulated photoluminescence in disordered organic materials, *Phys. Rev. B* **63**, 115205 (2001).

[32] C. H. Lee, G. Yu, D. Moses, K. Pakbaz, C. Zhang, N. S. Sariciftci, A. J. Heeger, and F. Wudl, Sensitization of the photoconductivity of conducting polymers by C60 - photoinduced electron-transfer, *Phys. Rev. B* **48**, 15425 (1993).

[33] C. Im, E. V. Emelianova, H. Bässler, H. Spreitzer, and H. Becker, Intrinsic and extrinsic charge carrier photogeneration in phenyl-substituted polyphenylenevinylene- trinitrofluorenone blend systems, *J. Chem. Phys.* **117**, 2961 (2002).

[34] P. Prins, L. P. Candeias, A. J. J. M. van Breemen, J. Sweelssen, P. T. Herwig, H. F. M. Schoo, and L. D. A. Siebbeles, Electron and hole dynamics on isolated chains of a solution-processable poly(thienylenevinylene) derivative in dilute solution, *Advanced Mater.* **17**, 718 (2005).

[35] M. Weiter, V. I. Arkhipov, and H. Bässler, Transient photoconductivity in a thin film of a poly-phenylenevinylene-type conjugated polymer, *Synth. Met.* **141**, 165 (2004).

[36] C. Im, W. Tian, H. Bässler, A. Fechtenkötter, M. D. Watson, and K. Müllen, J. Photoconduction in organic donor-acceptor systems, *Chem. Phys.* **119**, 3952 (2003).

[37] C. L. Braun, Electric-field assisted dissociation of charge-transfer states as a mechanism of photo-carrier production, *J. Chem. Phys.* **80**, 4157 (1984).

[38] L. Onsager, Initial recombination of ions, *Phys. Rev.* **54**, 554 (1938).

[39] M. Grünewald and P. Thomas, Hopping model for activated charge transport in amorphous silicon, *Phys. Stat. Sol. (b)* **94**, 125 (1979).

[40] V. I. Arkhipov, E. V. Emelianova, and G. J. Adriaenssens, Effective transport energy versus the energy of most probable jumps in disordered hopping systems, *Phys. Rev. B* **64**, 125125 (2001).

[41] U. Wolf, V. I. Arkhipov, and H. Bässler, Current injection from a metal to a disordered hopping system. I. Monte Carlo simulation, *Phys. Rev. B* **59**, 7507 (1999).

[42] V. I. Arkhipov, U. Wolf, and H. Bässler, Current injection from a metal to a disordered hopping system. II. Comparison between analytic theory and simulation, *Phys. Rev. B* **59**, 7514 (1999).

[43] T. van Woudenbergh, P. W. M. Blom, M. C. J. M. Vissenberg, and J. N. Huilberts, Temperature dependence of the charge injection in poly-dialkoxy-p-phenylene vinylene, *Appl. Phys. Lett.* **79**, 1697 (2001).

[44] U. Albrecht and H. Bässler, Yield of geminate pair dissociation in an energetically random hopping system, *Chem. Phys. Lett.* **235**, 389 (1995).

[45] S. Barth, D. Hertel, Y.-H. Tak, H. Bässler, and H. H. Hörhold, Geminate pair dissociation in random organic systems, *Chem. Phys. Lett.* **274**, 165 (1997).

[46] V. I. Arkhipov, E. V. Emelianova, and H. Bässler, A tandem mechanism of charge-carrier photo-generation in disordered organic materials, *Chem. Phys. Lett.* **340**, 517 (2001).

[47] V. I. Arkhipov, E. V. Emelianova, and H. Bässler, Dopant-assisted charge carrier photogeneration in conjugated polymers, *Chem. Phys. Lett.* **372**, 886 (2003).
[48] I. Riedel, M. Pientka, and V. Dyakonov, Charge Carrier Photogeneration and Transport in Polymer-fullerene Bulk-heterojunction Solar Cells, in *Physics of Organic Semiconductors*, W. Brütting (ed.) (Wiley VCH, Weinheim, 2005).
[49] M. Cocchi, D. Virgili, G. Giro, V. Fattori, P. Di Marco, J. Kalinowski, and Y. Shirota, Efficient exciplex emitting organic electroluminescent devices, *Appl. Phys. Lett.* **80**, 2401 (2002).
[50] A. C. Morteani, P. Sreearunothai, L. M. Herz, R. H. Friend, and C. Silva, Exciton regeneration at polymeric semiconductor heterojunctions, *Phys. Rev. Lett.* **92**, 247402 (2004).
[51] A. C. Morteani, R. H. Friend, and C. Silva, Endothermic exciplex-exciton energy-transfer in a blue-emitting polymeric heterojunction system, *Chem. Phys. Lett.* **391**, 81 (2004).
[52] T. Offermans, P. A. van Hal, S. C. J. Meskers, M. M. Koetse, and R. A. J. Janssen, Exciplex dynamics in a blend of pi-conjugated polymers with electron donating and accepting properties: MDMO-PPV and PCNEPV, *Phys. Rev. B* **72**, 045213 (2005).
[53] B. Kannan, K. Castelino, and A. Majumdar, Design of nanostructured heterojunction polymer photovoltaic devices, *Nano Lett.* **3**, 1729 (2003).
[54] H. J. Snaith, A. C. Arias, A. C. Morteani, C. Silva, and R. H. Friend, Charge generation kinetics and transport mechanisms in blended polyfluorene photovoltaic devices, *Nano Lett.* **2**, 1353 (2002).
[55] C. J. Brabec, G. Zerza, G. Cerullo, S. De Silvestri, S. Luzzati, J. C. Hummelen, and S. Sariciftci, Tracing photoinduced electron transfer process in conjugated polymer/fullerene bulk heterojunctions in real time, *Chem. Phys. Lett.* **340**, 232 (2001).
[56] V. D. Mihailetchi, J. K. J. van Duren, P. W. M. Blom, J. C. Hummelen, R. A. J. Janssen, J. M. Kroon, M. T. Rispens, W. J. H. Verhees, and M. M. Wienk, Electron transport in a methanofullerene, *Adv. Funct. Mater.* **13**, 43 (2003).
[57] S. E. Shaheen, C. J. Brabec, N. S. Sariciftci, F. Padinger, T. Fromherz, and J. C. Hummelen, 2.5 % efficient organic plastic solar cells, *Appl. Phys. Lett.* **78**, 841 (2001).
[58] J. K. J. van Duren, X. N. Yang, J. Loos, C. W. T. Bulle-Lieuwma, A. B. Sieval, J. C. Hummelen, and R. A. J. Janssen, Relating the morphology of poly(p-phenylene vinylene)/methanofullerene blends to solar-cell performance, *Adv. Funct. Mat.* **14**, 425 (2004).
[59] V. Dyakonov, Title: Mechanisms controlling the efficiency of polymer solar cells, *Appl. Phys. A* **79**, 21 (2004).
[60] T. Offermans, S. C. J. Meskers, and R. A. J. Janssen, Monte-Carlo simulations of geminate electron-hole pair dissociation in a molecular heterojunction: a two-step dissociation mechanism, *Chem. Phys.* **308**, 125 (2005).
[61] I. Montanari, A. F. Nogueira, J. Nelson, J. R. Durrant, C. Winder, M. A. Loi, N. S. Sariciftci, and C. Brabec, Transient optical studies of charge recombination dynamics in a polymer/fullerene composite at room temperature, *Appl. Phys. Lett.* **81**, 3001 (2002).
[62] J. Nelson, Diffusion-limited recombination in polymer-fullerene blends and its influence on photocurrent collection, *Phys. Rev. B* **67**, 155209 (2003).
[63] T. Offermans, S. C. J. Meskers, and R. A. J. Janssen, Charge recombination in a poly(para-phenylene vinylene)-fullerene derivative composite film studied by transient, nonresonant, hole-burning spectroscopy, *J. Chem. Phys.* **119**, 10924 (2003).
[64] B. Schweitzer, V. I. Arkhipov, U. Scherf, and H. Bässler, Geminate pair recombination in a conjugated polymer, *Chem. Phys. Lett.* **313**, 57 (1999).
[65] U. Albrecht and H. Bässler, Efficiency of charge recombination in organic light-emitting-diodes, *Chem. Phys.* **199**, 207 (1995).
[66] A. Pivrikas, G. Juška, A. J. Mozer, M. Scharber, K. Arlauskas, N. S. Sariciftci, H. Stubb, and R. Österbacka, Bimolecular recombination coefficient as a sensitive testing parameter for low-mobility solar-cell materials, *Phys. Rev. Lett.* **94**, 176806 (2005).
[67] U. Albrecht and H. Bässler, Langevin-type charge-carrier recombination in a disordered hopping system, *Phys. Stat. Sol. (b)* **191**, 455 (1995).

[68] A. J. Mozer, G. Dennler, N. S. Sariciftci, M. Westerling, A. Pivrikas, R. Österbacka, and G. Juška, Time-dependent mobility and recombination of the photoinduced charge carriers in conjugated polymer/fullerene bulk heterojunction solar cells, *Phys. Rev. B* **72**, 035217 (2005).
[69] G. Juška, K. Arlauskas, M. Vilinas, and J. Kočka, Extraction current transients: New method of study of charge transport in microcrystalline silicon, *Phys. Rev. Lett.* **84**, 4946 (2000).
[70] H. Sirringhaus, P. J. Brown, R. H. Friend, M. M. Nielsen, K. Bechgaard, B. M. W. Langeveld-Voss, A. J. H. Spiering, R. A. J. Janssen, E. W. Meijer, P. Herwig, and de D. M. Leeuw, Two-dimensional charge transport in self-organized, high-mobility conjugated polymers, *Nature* **401**, 685 (1999).
[71] V. I. Arkhipov, E. V. Emelianova, and H. Bässler, Hot exciton dissociation in a conjugated polymer, *Phys. Rev. Lett.* **82**, 1321 (1999).
[72] V. I. Arkhipov, E. V. Emelianova, S. Barth, and H. Bässler, Ultrafast on-chain dissociation of hot excitons in conjugated polymers, *Phys. Rev. B* **61**, 8207 (2000).
[73] D. M. Basko and E. M. Conwell, Hot exciton dissociation in conjugated polymers, *Phys. Rev. B* **66**, 155210 (2002).
[74] L. Onsager, Deviations from Ohm's Law in Weak Electrolytes, *J. Chem. Phys.* **2**, 599 (1934).
[75] V. D. Mihailetchi, L. J. A. Koster, J. C. Hummelen, and P. W. M. Blom, Photocurrent generation in polymer-fullerene bulk heterojunctions, *Phys. Rev. Lett.* **93**, 216601 (2004).
[76] E. Hendry, M. Koeberg, J. M. Schins, L. D. A. Siebbeles, and M. Bonn, Ultrafast charge generation in a semiconducting polymer studied with THz emission spectroscopy, *Phys. Rev. B* **70**, 033202 (2004).
[77] G. Weiser, A. Horvàth, Variation with disorder of absorption and electroabsorption spectra of a pi-conjugated polymer: 4BCMU, *Chem. Phys.* **227**, 153 (1998).
[78] S. Barth, H. Bässler, Intrinsic photoconduction in PPV-type conjugated polymers, *Phys. Rev. Lett.* **79**, 4445 (1997).
[79] S. Barth, H. Bässler, H. Rost, and H. H. Hörhold, Extrinsic and intrinsic dc photoconductivity in a conjugated polymer, *Phys. Rev. B* **56**, 3844 (1997).
[80] M. C. Scharber, N. A. Schultz, N. S. Sariciftci, and C. J. Brabec, Optical- and photocurrent-detected magnetic resonance studies on conjugated polymer/fullerene composites, *Phys. Rev. B* **67**, 085202 (2003).
[81] V. I. Arkhipov, P. Heremans, and H. Bässler, Why is exciton dissociation so efficient at the interface between a conjugated polymer and an electron acceptor?, *Appl. Phys. Lett.* **82**, 4605 (2003).
[82] S. C. Veenstra and H. T. Jonkman, Energy-level alignment at metal-organic and organic-organic interfaces, *J. Polym. Sci. B: Polym. Phys.* **41**, 2549 (2003).
[83] A. Cravino and N. S. Sariciftci, Double-cable polymers for fullerene based organic optoelectronic applications, *J. Mater. Chem.* **12**, 1931 (2002).

9 Nanocrystalline Injection Solar Cells

Michael Grätzel
Laboratory of Photonics and Interfaces, Ecole Polytechnique Fédérale de Lausanne, Switzerland

9.1 INTRODUCTION

Thin film photovoltaic cells have been dominated so far by amorphous silicon, cadmium telluride (CdTe) and copper indium gallium diselenide (CIGS) p-n junction devices, profiting from the experience and material availability of the semiconductor industry. However, there is an increasing awareness of the possible advantages of devices based on mesoscopic inorganic or organic semiconductors commonly referred to as 'bulk' junctions due to their interconnected three-dimensional structure. These are formed, for example, from nanocrystalline inorganic oxides, ionic liquids and organic hole conductor or conducting polymer devices, which offer the prospect of very low cost fabrication without expensive and energy intensive high temperature and high vacuum processes. They are compatible with flexible substrates and a variety of embodiments and appearances to facilitate market entry, both for domestic devices and in architectural or decorative applications. It is now possible to depart completely from the classical solid state cells, which are replaced by devices based on interpenetrating network junctions. The mesoscopic morphology produces an interface with a huge area, endowing these systems with intriguing optoelectronic properties. Contrary to expectation, devices based on interpenetrating networks of semiconductors have shown strikingly high conversion efficiencies, which compete with those of conventional devices. The prototype of this family of devices is the dye sensitized solar cell (DSC), invented in the author's laboratory at the *Ecole Polytechnique Fédérale de Lausanne* [1]. This accomplishes the separation of the optical absorption and the charge separation processes by the association of a sensitizer as light absorbing material with a wide bandgap semiconductor of mesoporous or nanocrystalline morphology [1, 2]. The DSC currently reaches $>11\,\%$ energy conversion efficiencies under standard reporting conditions (AM1.5 global sunlight at 1000 W/m^2 intensity, 298 K temperature) in liquid junction devices [3] rendering it a credible alternative to conventional p-n junction photovoltaic devices. Solid state equivalents using organic hole conductors have exceeded 4 % efficiency [4] whereas nanocomposite films composed of inorganic materials, such a TiO_2 and $CuInS_2$ have achieved efficiencies between 5 and 6 % [5, 6]. New dyes showing increased optical cross-sections and capable of absorbing longer wavelengths are currently under development. Similarly, the performance of mesoscopic TiO_2 films employed as electron collectors is benefiting greatly from

Thin Film Solar Cells Edited by J. Poortmans and V. Arkhipov
© 2006 John Wiley & Sons, Ltd

recent advances in nanomaterial research. Taking advantage of the highly transparent nature of the sensitized nanocrystalline oxide film a tandem structre employing a DSC and CIGS top and bottom cell having a conversion efficiency $>15\,\%$ has been realized [7].

Obtaining long term stability for DSCs at temperatures of 80–85 °C had remained a major challenge for over 10 years and has only recently been achieved [8]. Solvent free electrolytes such as ionic liquids or solid polymers as hole conductors have been introduced to provide solutions for practical applications. Stabilization of the interface by using self assembly of hydrophobic sensitizers in conjunction with amphiphilic coadsorbents has been particularly rewarding. Stable operating performance under both prolonged thermal stress (at 85 °C) and AM1.5 light soaking conditions (at 60 °C) has been achieved [9]. These devices retained 98 % of their initial power conversion efficiency after 1000 h of high temperature aging. Long term accelerated testing shows that DSCs can function in a stable manner for over 20 years, if the interfacial engineering issues are properly addressed. The present review gives an overview of the state-of-the-art of the academic and industrial development of this new solar cell, emphasis being placed on the work performed in the author's laboratory.

9.2 BAND DIAGRAM AND OPERATIONAL PRINCIPLE OF THE DYE SENSITIZED SOLAR CELL

Figure 9.1 shows a band diagram of the DSC explaining its operational principle. In contrast to silicon or other p-n junction thin film PV cells, the DSC separates the light absorption process from the transport of charge carriers. Sunlight is harvested by a sensitizer that is attached to the surface of a large bandgap semiconductor, typically an oxide such as TiO_2 film. Photoexcitation

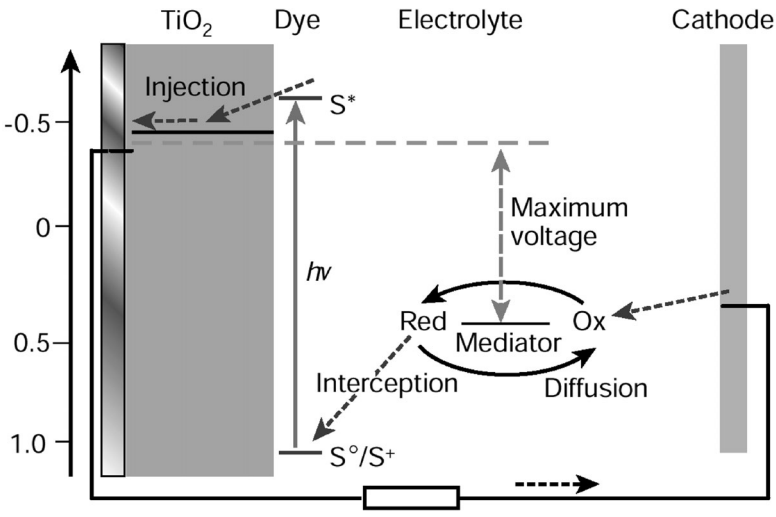

Figure 9.1 Energy band diagram of the DSC. Light absorption by the dye (S) produces an excited state (S*) that injects an electron into the conduction band of a wide bandgap semiconducting oxide, such as TiO_2. The electrons diffuse across the oxide to the transparent current collector made of conducting glass. From there they pass through the external circuit performing electrical work and reenter the cell through the back contact (cathode) by reducing a redox mediator (ox). The reduced form of the mediator (red) regenerates the sensitizer closing the cyclic conversion of light to electricity.

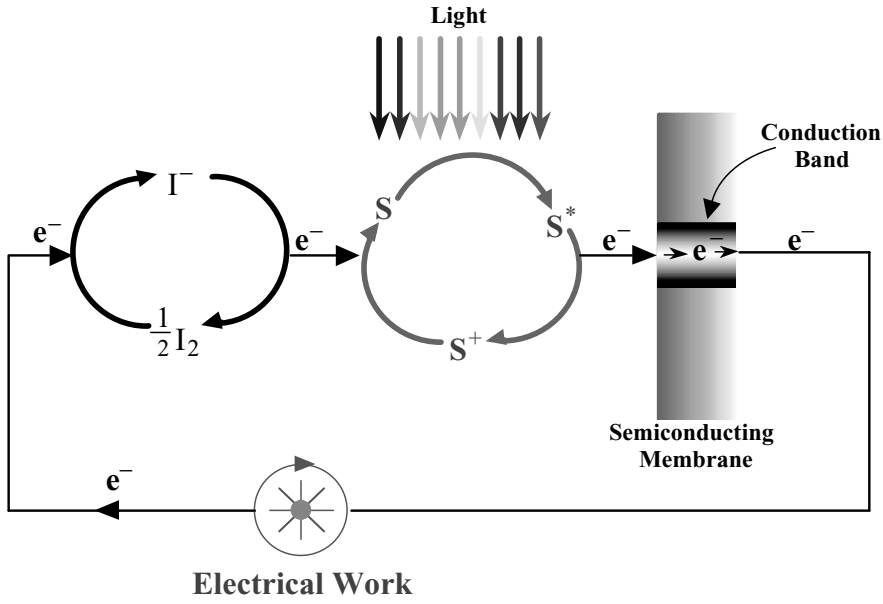

Figure 9.2 The two coupled redox cycles involved in the generation of electricity from light in a dye sensitized solar cell.

of the dye results in the injection of electrons into the conduction band of the oxide. The dye is regenerated by electron donation from the electrolyte, usually an organic hole conductor or an electrolyte, such as an ionic liquid containing most frequently the iodide/triiodide couple as a redox system. This intercepts the recapture of the conduction band electron by the oxidized state of the sensitizer S^+. The iodide is regenerated in turn by the reduction of triiodide at the counterelectrode, where the circuit is completed via electron migration through the external load. The voltage generated under illumination corresponds to the difference between the quasi-Fermi level of the electron in the solid and the redox potential of the electrolyte, or the work function of the hole conductor. Thus the device is regenerative, producing electricity from light without any permanent chemical transformation.

Figure 9.2 shows the coupling of redox cycles involved in the solar energy conversion process. In analogy to natural photosynthesis, light acts as an electron pump initiating charge flow from the sensitizer via the conduction band of the oxide semiconductor to the external circuit. The dye is regenerated by electron donation from iodide producing iodine or triiodide. The latter diffuses to the counter electrode where the electrons injected into the circuit by the sensitizer reduce it back to iodide thus closing the two redox cycles involved in the energy conversion process. The turnover frequency of the sensitizer is 25 s^{-1} in full sunshine and during 20 years of outdoor service it must support 100 million turnovers.

9.3 THE IMPORTANCE OF THE NANOSTRUCTURE

The nanocrystalline morphology of the semiconductor oxide film is essential for the efficient operation of the device. On a flat surface, a monolayer of dye absorbs at most a few %t of the light because it occupies an area that is several hundred times larger than its optical

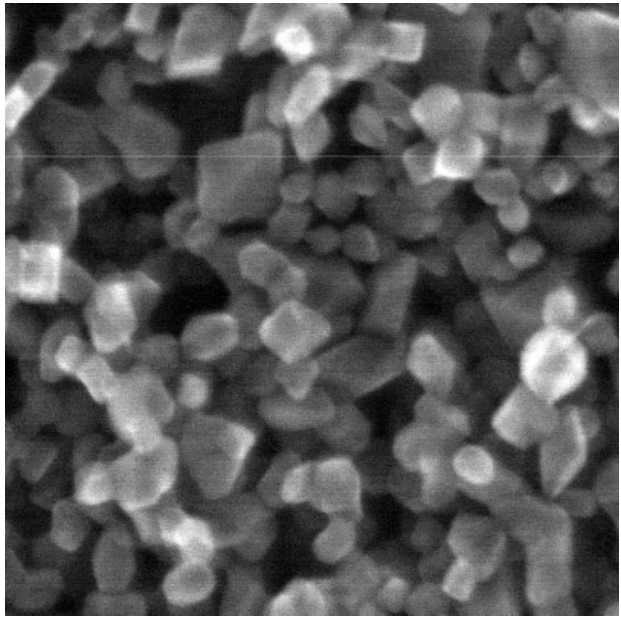

Figure 9.3 Transmission electron microscope picture of a mesoscopic TiO_2 (anatase) film. Note the bipyramidal shape of the particles having (101) oriented facets exposed. The average particle size is 20 nm.

cross-section. Using multilayers of sensitizer does not offer a viable solution to this problem. Only the molecules that are in direct contact with the oxide surface would be photoactive, the remainder merely filtering the light. Apart from poor light harvesting, a compact semiconductor film would need to be n-doped to conduct electrons. In this case energy transfer quenching of the excited sensitizer by the electrons in the semiconductor would inevitably reduce the photovoltaic conversion efficiency.

Figure 9.3 is a scanning electron microscopy picture of a mesoscopic TiO_2 (anatase) layer. The particles have an average size of 20 nm and the facets exposed have mainly (101) orientation, corresponding to the anatase crystal planes with the lowest surface energy. Employing such oxide nanocrystals covered by a monolayer of sensitizer as light harvesting units allows one to overcome the notorious inefficiency problems, which have haunted all solar energy conversion devices based on the sensitization of wide bandgap semiconductors.

9.3.1 Light harvesting by a sensitizer monolayer adsorbed on a mesoscopic semiconductor film

Consider a 10 μm thick mesoscopic oxide film composed of 20 nm sized particles whose real surface area is over 1000 times greater than the projected one. Due to the small size of the particle, such films show high transparency and negligible light scattering. Lambert Beer's law can be applied to describe the light absorption yielding for the reciprocal absorption length:

$$\alpha = \sigma c \tag{9.1}$$

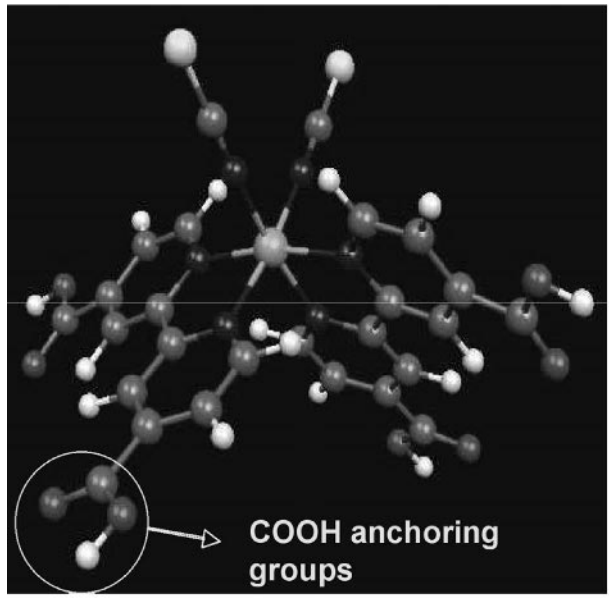

Figure 9.4 Structure of the N3 dye cis–$RuL_2(SCN)_2$ (L = 2,2-bipyridyl-4,4′dicarboxylate).

here σ and c are the optical absorption cross-section of the sensitizer and its concentration in the mesoporous film, respectively. The value of σ can be derived from the decadic extinction coefficient ε of the sensitizer using the relation:

$$\sigma = \varepsilon \, 1000 \, [\mathrm{cm}^2/\mathrm{mole}] \tag{9.2}$$

Figure 9.4 shows the structure of the widely used N3 dye cis–$RuL_2(SCN)_2$ (L = 2,2-bipyridyl-4,4′dicarboxylate). The optical cross-section of this sensitizer at 530 nm, where it has an absorption maximum, is 1.4×10^7 cm^2/mole and its concentration in the nanocrystalline film at full monolayer coverage is typically 2×10^{-4} mole/cm^3. Hence $\alpha = 2.8 \times 10^3$ cm^{-1} and the absorption length $1/\alpha$ is 3.6 μm for 530 nm light. The light harvesting efficiency (LHE) is derived from the reciprocal absorption length via:

$$\mathrm{LHE}(\lambda) = 1 - 10^{-\alpha d} \tag{9.3}$$

where d is the thickness of the nanocrystalline film. Using $d = 10$ μm and $\alpha = 2.8 \times 10^3$ cm^{-1}, one obtains LHE = 99.8 %. This explains the deep coloration of the nanocrystalline TiO_2 layers despite the fact that they are covered only by a monolayer of sensitizer. A film exhibiting ordered mesoporous structure, such as shown in Figure 9.5 has a significantly higher internal surface area than one that is composed of randomly associated nanoparticles [10]. Because more sensitizer is adsorbed for the same film thickness the absorption length is reduced enhancing the absorption of solar light and hence the conversion yield.

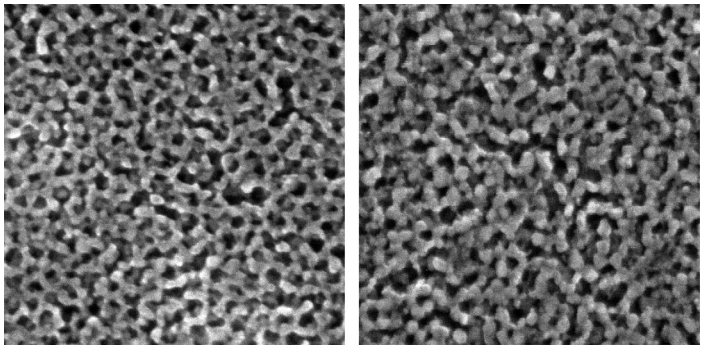

Figure 9.5 Top view of an ordered mesoporous TiO_2 (anatase) film produced by a block copolymer templating method [10].

9.3.2 Enhanced red and near infrared response by light containment

The light harvesting by the surface adsorbed sensitizer can be further improved by exploiting light localization and optical enhancement effects. For example, incorporating 100–400 nm sized anatase particles enhances significantly the absorption of red or near infrared photons by the film. A scanning electron micrograph of such particles is shown in Figure 9.6. These light management strategies employ scattering and photonic bandgap effects [11–13] to localize light in the mesoporous structure, augmenting the optical pathway significantly beyond the film thickness and enhancing the harvesting of photons in a spectral region where the optical cross-section of the sensitizer is small. The benefits from using such a light management strategy are clearly visible below, where the light scattering layer is shown to enhance the photocurrent response of the DSC in the near infrared and visible regions of the solar spectrum. The gain in short circuit photocurrent through these optical containment effects can be as high as 30 %.

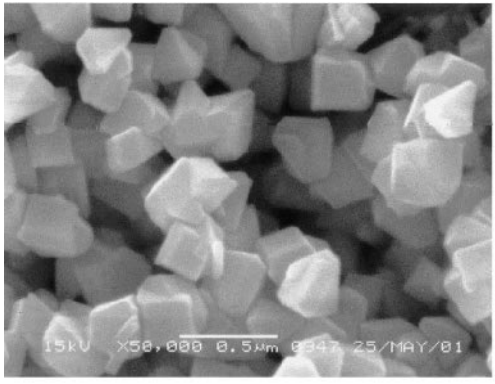

Figure 9.6 Scanning electron micrograph showing anatase crystals of ca. 400 nm size, employed as light scattering centers to enhance the red response of the DSC. (Courtesy of Dr. Tsuguo Koyanagi, Catalysts & Chemicals Ind. Co. Ltd., Japan).

9.3.3 Light induced charge separation and conversion of photons to electric current

The incident photon to current conversion efficiency (IPCE) sometimes referred to also as 'external quantum efficiency' (EQE) corresponds to the number of electrons measured as photocurrent in the external circuit divided by the monochromatic photon flux that strikes the cell. The flowing product can express this key parameter:

$$\mathrm{IPCE}(\lambda) = \mathrm{LHE}(\lambda)\, \phi_{\mathrm{inj}}\, \eta_{\mathrm{coll}} \tag{9.4}$$

Here LHE(λ) is the light harvesting efficiency for photons of wavelength λ, ϕ_{inj} is the quantum yield for electron injection from the excited sensitizer in the conduction band of the semiconductor oxide and η_{coll} is the electron collection efficiency. Having analyzed the light harvesting efficiency of dye loaded mesoscopic films above we discuss now the other two parameters.

The quantum yield of charge injection (ϕ_{inj}) denotes the fraction of the photons absorbed by the dye that are converted into conduction band electrons. Charge injection from the electronically excited sensitizer into the conduction band of the semiconductor is in competition with other radiative or radiationless deactivation channels. Taking the sum of the rate constants of these nonproductive channels together as k_{deact} gives:

$$(\phi_{\mathrm{inj}}) = k_{\mathrm{inj}}/(k_{\mathrm{deact}} + k_{\mathrm{inj}}) \tag{9.5}$$

Typical k_{deact} values lie in the range 10^3 to $10^{10}\ \mathrm{s}^{-1}$. Hence injection rates in the ps range have to be attained in order to obtain ϕ_{inj} values close to one. The currently used sensitizers satisfy this requirement. These dyes incorporate functional groups, for example carboxylate, hydroxamate or phosphonate moieties [14], that anchor the sensitizer to the oxide surface. By forming a strong coordinative bond with the titanium surface ions, these groups enhance electronic coupling of the sensitizer LUMO with the conduction band of the semiconductor. The lowest energy electronic transition for ruthenium polypyridyl complexes such the N3 dye is of MLCT (metal to ligand charge transfer) character.

Thus, upon excitation, the electron density shifts from the ruthenium metal to the surface attached ligand from where very rapid electron injection into the semiconductor takes place, Figure 9.7. With molecularly engineered sensitizers like these, the injection times are in the ps or fs range [15–18] and the quantum yield of charge injection generally exceeds 90 %. In fact, for several sensitizers the electron transfer into the conduction band of the oxide is so rapid that it occurs from vibrationally hot excited states [16–18].

Shown in Figure 9.8 is the transient absorption signal following fs laser excitation of the N-719 dye (cis–$\mathrm{RuL_2(SCN)_2}$ (L = 2,2-bipyridyl-4,4′dicarboxylate)) adsorbed on the surface of nanocrystalline titania [19]. The formation of the oxidized sensitizer and conduction band electrons due to heterogeneous charge transfer from the excited ruthenium complex into the conduction band of the oxide occurs on a fs timescale. Figure 9.8 indicates that the reaction is completed within the fs laser excitation pulse. Fitted data provide a cross-correlation time of 57 fs that is consistent with the instrument response measured by Kerr gating in a thin glass window. This temporal resolution does not allow determination of the rate of the injection process accurately, but its time constant can be estimated as being definitely shorter than 20 fs corresponding to a rate constant $k_{\mathrm{inj}} > 5{\cdot}10^{13}\ \mathrm{s}^{-1}$. Such a high rate can be rationalized in terms of electronic coupling of the π^* sensitizer LUMO with the t_{2g} wavefunction of the Ti(3d)

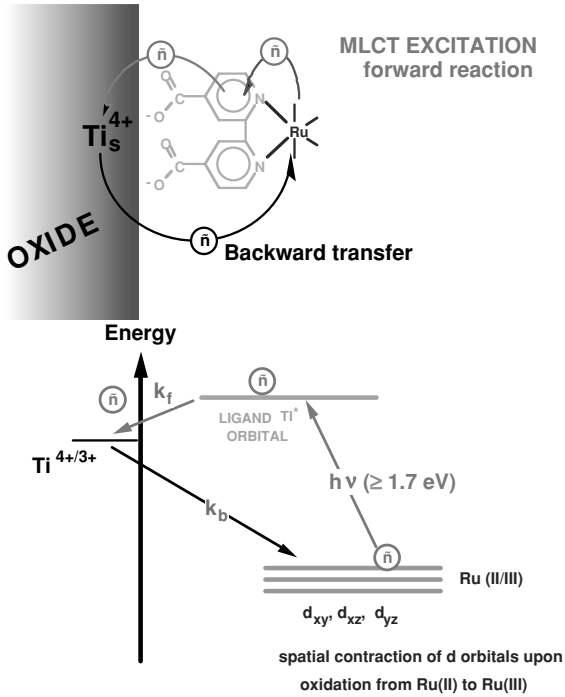

Figure 9.7 Interfacial electron transfer involving a ruthenium complex bound to the surface of TiO_2 via a carboxylated bipyridyl ligand. Orbital diagram for the forward electron injection (rate constant $k_{(f)}$ from the π^* orbital of the bipyridyl ligand into the empty t_{2g} orbitals forming the TiO_2 conduction band and the backward electron transfer from the conduction band of the oxide into the Ru(III) d orbitals.

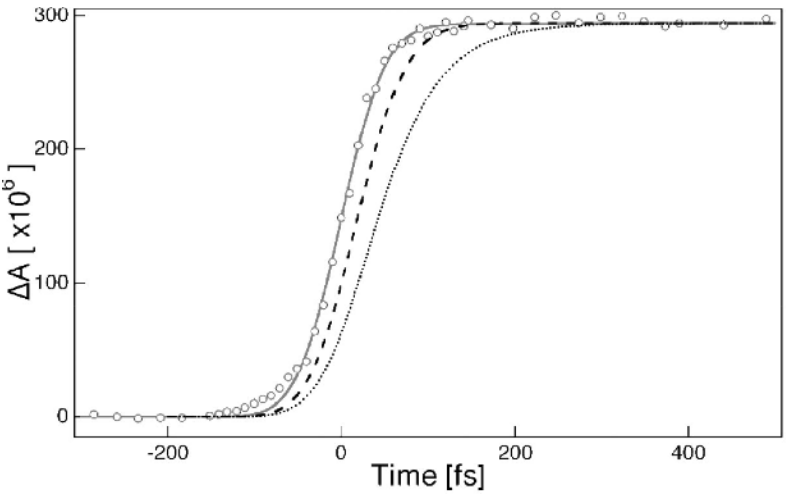

Figure 9.8 Transient absorption signal for N719 adsorbed on nanocrystalline titania (ℓ) (pump wavelength 535 nm, probe 860 nm). Fitted instrument response is 57 fs (———). Simulated exponential rises with time constants of 20 fs (——) and 50 fs (· · · · · · ·) and convoluted with the same instrument response are shown.

conduction manifold and a large density of acceptor states in the semiconductor. Since nuclear motion in the molecule and its environment takes place within a time frame of at least 20 fs, the observed charge injection dynamics are certainly beyond the scope of vibration mediated electron transfer models [20]. The process rate is therefore likely to be limited only by the electron dephasing in the solid. Interestingly, much slower injection kinetics extending into the ps time domain were observed when the sensitizer was present in an aggregated form at the surface of the titania films [19].

As the next step in the conversion of light into electrical current, a complete charge separation must be achieved. On thermodynamic grounds, the preferred process for the electron injected into the conduction band of the titanium dioxide films is the back reaction with the oxidized sensitizer. Naturally this reaction is undesirable, since instead of electrical current it merely generates heat. For the characterization of the recombination rate, an important kinetic parameter is the rate constant k_b. It is of great interest to develop sensitizer systems for which the value of k_{inj} is high and that of k_b low.

While for the N3 type sensitizer the forward injection is a very rapid process occurring in the fs time domain, the back reaction of the electrons with the oxidized ruthenium complex occurs on a much longer timescale of μs to ms. One of the reasons for this striking behaviour is that the electronic coupling element for the back reaction is one to two orders of magnitude smaller for the back electron transfer. As the recapture of the electrons involves a d-orbital localized on the ruthenium metal, the electronic overlap with the TiO_2 conduction band is small and is further reduced by the spatial contraction of the wavefunction upon oxidation of Ru(II) to Ru(III).

A second important contribution to the kinetic retardation of charge recombination arises from the fact that this process is characterized by a large driving force and small reorganization energy, the respective values for N-719 being 1.5 and 0.3 eV, respectively. This places the electron recapture clearly in the inverted Marcus region reducing its rate by several orders of magnitude. For the same reason the interfacial redox process is almost independent of temperature and is surprisingly insensitive to the ambient that is in contact with the film [21].

Charge recombination is furthermore inhibited by the existence of an electric field at the surface of the titanium dioxide film. While the depletion layer field within the oxide is negligible due to the small size of the particles and their low doping level, a dipole layer is established at the surface by proton transfer from the carboxylic acid groups of the ruthenium complex to the oxide surface In aprotic media, Li^+ or Mg^{2+} are potential determining ions for TiO_2 [22] and they may also be used to charge the surface positively. The local potential gradient from the negatively charged sensitizer to the positively charged oxide drives the injection in the desired direction and inhibits the electrons from reexiting the solid.

Finally, the back reaction dynamics are strongly influenced by the trapping of the conduction band in the mesoscopic film. If the diffusion of trapped electrons to the particle surface is rate determining, the time law for the back reaction is a stretched exponential [23]. If, by contrast, the interfacial back electron transfer is so slow that it becomes rate determining, then the back reaction follows first order kinetics.

9.3.4 Charge carrier collection

The question of charge carrier percolation over the mesoscopic particle network is presently attracting a great deal of attention. This important process leads to nearly quantitative collection

of electrons injected by the sensitizer. These large bandgap semiconductor oxide films are insulating in the dark, however, a single electron injected into a 20 nm sized particle produces an electron concentration of 2.4×10^{17} cm^{-3}. This corresponds to a specific conductivity of 1.6×10^{-4} S cm^{-1} if a value of 10^{-4} cm^2/s is used for the electron diffusion coefficient [24]. In reality the situation is more complex as the transport of charge carriers in these films involves trapping, unless the Fermi level of the electron is so close to the conduction band that all the traps are filled and the electrons are moving freely. Therefore the depth of the traps that participate in the electron motion affects the value of the diffusion coefficient. This explains the observation [25, 26] that the diffusion coefficient increases with light intensity. Recent Monte Carlo modeling gives an excellent description of the intricacies of the electron transport in such mesoscopic semiconductor films [27]. Of great importance for the operation of the DSC is the fact that charges injected in the nanoparticles can be screened on the mesoscopic scale by the surrounding electrolyte, greatly facilitating electron percolation [28]. The electron charge is screened by the cations in the electrolyte, which eliminates the internal field, so no drift term appears in the transport equation. Figure 9.9 illustrates this local screening effect.

The electron motion in the conduction band of the mesoscopic oxide film is coupled with an interfacial electron transfer reaction and with ion diffusion in the electrolyte. Bisquert [29] has used an infinite transmission line description to model these processes. The mesoscopic film is thought to be composed of a string of oxide nanoparticles, Figure 9.9. Apart from recapture by the oxidized dye, the electrons can be lost to the electrolyte by the reaction with the oxidized form of the redox mediator, e.g. triiodide ions:

$$I_3^- + 2e_{cb}^-(TiO_2) \rightarrow 3I^- \tag{9.6}$$

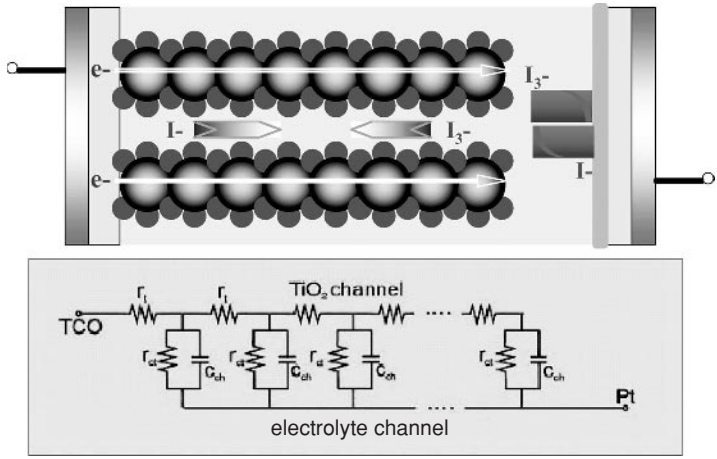

Figure 9.9 Transmission line description of the conduction band electron motion trough a network of mesoscopic semiconductor particles. The electrical equivalent circuit treats each particle as a resistive element. Interfacial electron transfer to the triodide is modeled by a charge transfer resistance connected in parallel with the capacitance of the particle–electrolyte interface. The red dots present cations from the electrolyte.

The equivalent electrical circuit shown in the lower part of the figure treats each particle as a resistive element coupled to the electrolyte through the interface. The latter is presented by the electric double layer capacitor (C) connected in parallel with the resistance (r_{ct}) for interfacial electron transfer. The red dots denote electrolyte cations.

It is clear from Figure 9.9 that the movement of electrons in the conduction band of the mesoscopic films must be accompanied by the diffusion of charge compensating cations in the electrolyte layer close to the nanoparticle surface. The cations screen the Coulomb potential of the electrons avoiding the formation of uncompensated local space charge, which would impair their motion through the film. This justifies using an 'ambipolar' or effective diffusion coefficient, which contains contributions from both the electrons and charge compensating cations [30, 31] to describe charge transport in such mesoscopic interpenetrating network solar cells. Impedance spectroscopy gives useful clues to rationalize the intriguing findings made with these films under bandgap illumination [32].

Figure 9.10 illustrates the injection and recombination processes. Mastering the interface to impair the unwanted back reactions remains a key target of current research [33]. The efficient interception of recombination by the electron donor, e.g. iodide:

$$2S^{+} + 3I^{-} \longrightarrow 2S + I_3^{-} \tag{9.7}$$

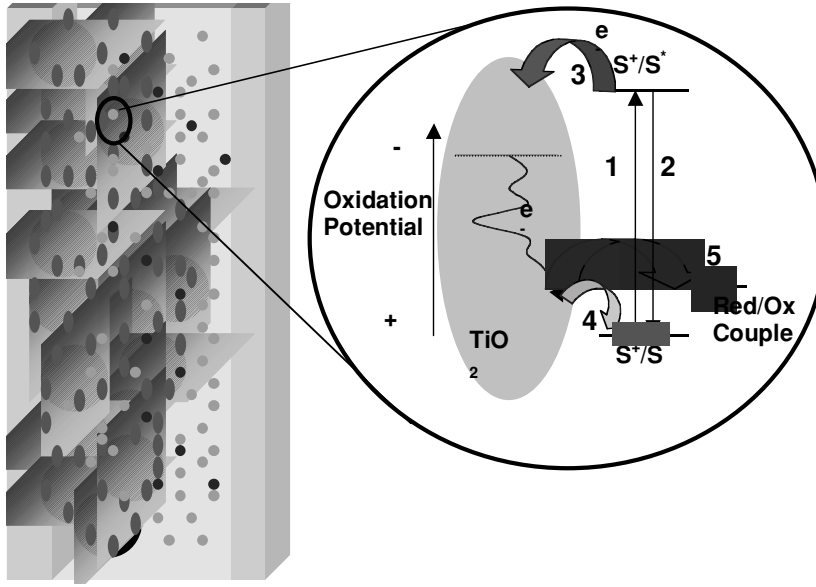

Figure 9.10 Photoinduced processes occurring during photovoltaic energy conversion at the surface of the nanocrystalline titania films. 1: sensitizer (S) excitation by light, 2: radiative and nonradiative deactivation of the sensitizer, 3: electron injection in the conduction band followed by electron traping and diffusion to the particle surface, 4: recapture of the conduction band electron by the oxidized sensitizer (S^{+}), 5: recombination of the conduction band electrons with the oxidized form of the redox couple regenerating the sensitizer and transporting the positive charge to the counterelectrode. Grey spheres: titania nanoparticles, red dots: sensitizer, green and blue dots: oxidized and reduced form of the redox couple.

is crucial for obtaining good collection yields and high cycle life of the sensitizer. In the case of N3 or its amphiphilic analogue Z-907, time resolved laser experiments have shown the interception to take place with a rate constant of about $10^5 - 10^7\ s^{-1}$ at the iodide concentrations that are typically applied in the solar cell [34]. This is more than a hundred times faster than the recombination rate and $>10^8$ times faster than the intrinsic lifetime of the oxidized sensitizer in the electrolyte in the absence of iodide.

In order to reach IPCE values close to 100 %, provisions must be made to collect all photogenerated charge carriers. A key parameter is the electron diffusion length:

$$L_n = \sqrt{D_e \tau_r} \tag{9.8}$$

where D_e and t_r are the diffusion coefficient and lifetime of the electron, respectively. Collection of charge carriers is quantitative if the electron diffusion length exceeds the film thickness (d):

$$L_n > d \tag{9.9}$$

The film in turn needs to be significantly thicker than the light absorption length ($1/\alpha$) in order to ascertain nearly quantitative harvesting of the light in the spectral absorption range of the quantum dot or the molecular sensitizer:

$$d > 1/\alpha \tag{9.10}$$

The thickness of the nanocrystalline layer required to satisfy the last conditions is typically of the order of a few μm depending on the optical cross-section of the sensitizer and its concentration in the film as discussed above.

9.3.5 Quantum dot sensitizers

Semiconductor quantum dots (QDs) can replace dyes as light harvesting units in the DSC [35, 36]. Light absorption produces excitons or electron–hole pairs in the QD. The electron is subsequently injected into the semiconducting oxide support while the hole is transferred to a hole conductor or an electrolyte present in the pores of the nanocrystalline oxide film. Efficient and rapid hole injection from PbS quantum dots into triarylamine hole conductors has already been demonstrated and IPCE values exceeding 50 % have been reached without attempting to optimize the collector structure and retard interfacial electron hole recombination [35]. Quantum dots have much higher optical cross-sections than molecular sensitizers, depending on the their size. However, they also occupy a larger area on the surface of the mesoporous electrode decreasing the QD concentration in the film. As a result, the value of the absorption length is similar to that observed for the dye loaded films.

A recent exciting discovery shows that multiple excitons can be produced from the absorption of a single photon by a quantum dot via impact ionization (IMI) if the photon energy is three times higher than its bandgap [36, 37]. The challenge is now to find ways to collect the excitons before they recombine. As recombination occurs on a fs timescale, the use of mesoporous oxide collector electrodes to remove the electrons presents a promising strategy, opening up research avenues that ultimately may lead to photovoltaic converters reaching IPCE values of over 100 %.

9.4 PHOTOVOLTAIC PERFORMANCE OF THE DYE SENSITIZED SOLAR CELL

Having dealt with the fundamental features of operation of a DSC we present now recent performance data obtained with this new type of thin film photovoltaic cell. A cross-sectional view of the cell structure used in these experiments is shown in Figure 9.11. Both the front and back contact are made of soda-lime float glass covered by a transparent conducting oxide. The latter material is fluorine doped tin dioxide (FTO) having a sheet resistance of 10–15 Ohm/square and an optical transmission of 80–90 % in the visible, including reflection losses. The back contact is coated with a small amount of Pt to catalyze the interfacial electron transfer from the SnO_2 electrode to triiodide, the typical loading being 50 mg/m^2. The nanocrystalline TiO_2 film is deposited by screen printing onto the FTO glass serving as the front electrode followed by a brief sintering in air at 450 °C to remove organic impurities and enhance the interconnection between the nanoparticles. Adsorption of the sensitizer monolayer occurs from solution by self assembly. The cell is sealed using a Bynel (Dupont) hotmelt. Redox electrolyte is introduced by injection through a hole on the back contact.

9.4.1 Photocurrent action spectra

Mesoscopic TiO_2 films are currently prepared mainly by hydrothermal methods, which have been standardized to yield films composed of 15 to 20 nm sized anatase. The mesoscopic morphology has a dramatic effect on the performance of a dye sensitized solar cell. Figure 9.12 compares the photocurrent action spectrum obtained from a single crystal of anatase to that of a nanocrystalline film, both being sensitized by the standard N-719 ruthenium dye. i.e. cis–$RuL_2(SCN)_2$ (L = 2,2-bipyridyl-4,4′dicarboxylate). The incident photon-to-current conversion efficiency (IPCE) or external quantum efficiency is plotted as a function of wavelength. The IPCE value obtained with the single crystal electrode is only 0.13 % near 530 nm, where the N-719 sensitizer has an absorption maximum, while it reaches 88 % with the nanocrystalline

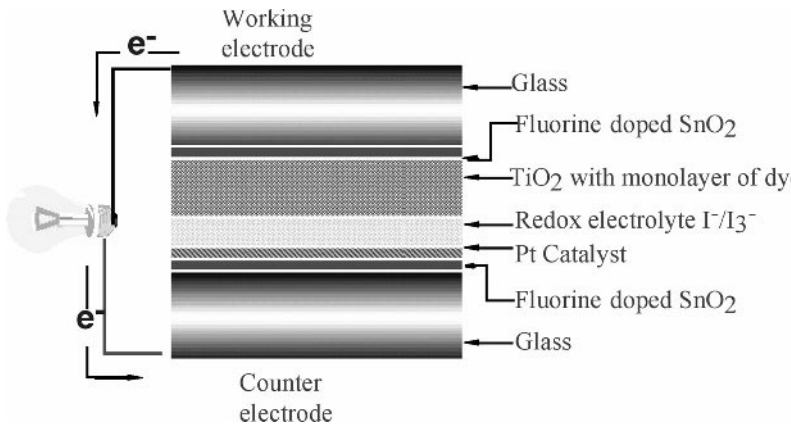

Figure 9.11 Cross-sectional view of the embodiment of DSC used in the laboratory for photovoltaic performance measurements.

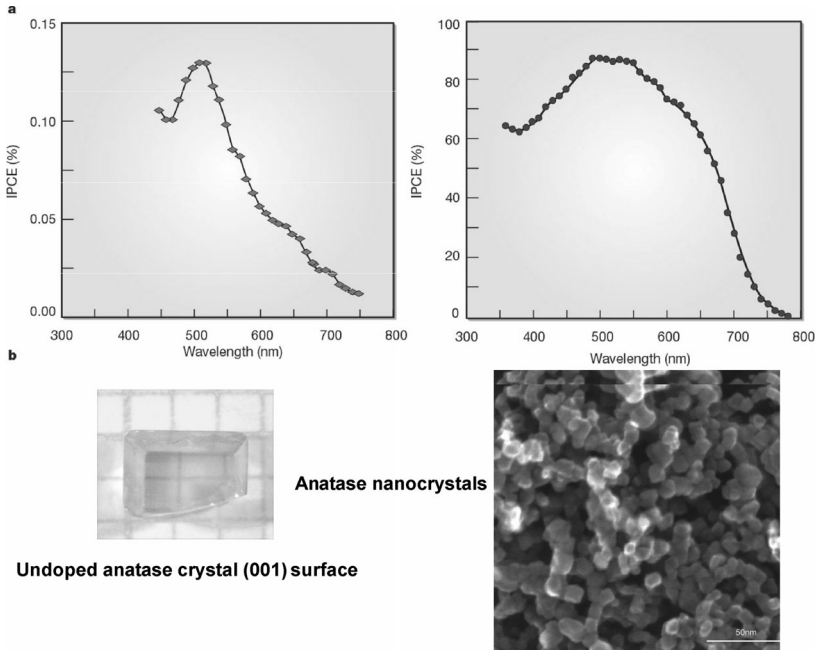

Figure 9.12 Conversion of light to electric current by dye sensitized solar cells. The incident photon to current conversion efficiency is plotted as a function of the excitation wavelength. Left: single crystal anatase cut in the (001) plane. Right: nanocrystalline anatase film. Pictures of the two electrodes used as current collectors are also presented. The electrolyte consisted of a solution of 0.3M LiI and 0.03 M I_2 in acetonitrile.

electrode. As a consequence, in sunlight the photocurrent augments more than 1000 times when passing from a single crystal to a nanocrystalline electrode. This striking improvement defies expectation as such large area junctions should fare poorly in photovoltaic energy conversion, the presence of defects at the disordered surface enhancing recombination of photogenerated charge carriers.

Taking into account the optical losses in the FTO glass that serves as a front contact, the conversion of incident photons is practically quantitative in the 500–600 nm range were the sensitizer has an absorption maximum. It is apparent from Equation 9.4 that the light harvesting, electron injection and charge carrier collection efficiency must be close to unity to achieve this result. Impedance studies have shown the diffusion length of the conduction band electrons in the DSC to be typically in the 20–100 μm range. This exceeds the thickness of the nanocrystalline TiO_2 film explaining why all photoinduced charge carriers can be collected.

9.4.2 Overall conversion efficiency under global AM1.5 standard reporting conditions

The overall conversion efficiency of the dye sensitized cell is determined by the photocurrent density measured at short circuit (J_{sc}), the open circuit photovoltage (V_{oc}), the fill factor of the

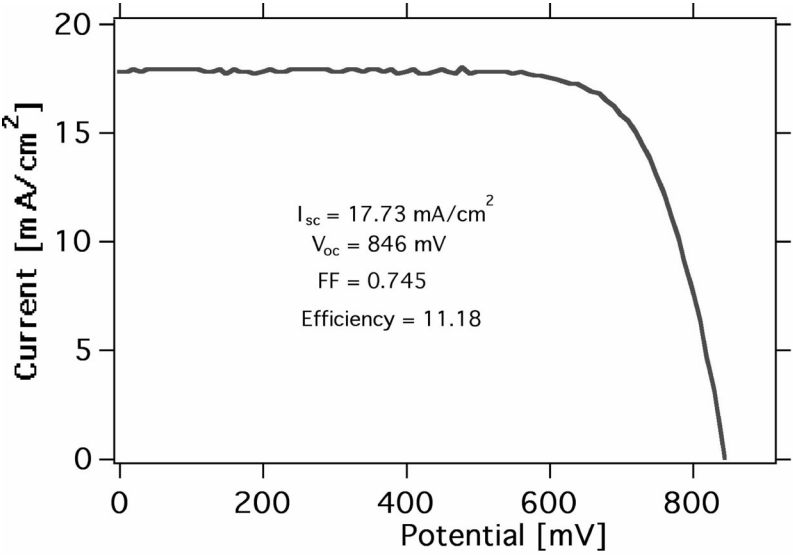

Figure 9.13 Photocurrent density versus voltage curve for a DSC employing the N-719 dye adsorbed on a double layer of nanocrystalline TiO_2 (Figure 9.4) and scattering particles. (Figure 9.6). The iodide//triiodide based redox electrolyte employed a mixture of acetonitirel and valeronitrile as a solvent. The conversion efficiency in AM 1.5 sunlight was 11.18 %.

cell (FF) and the intensity of the incident light (I_s)

$$\eta_{\text{global}} = J_{sc} \times V_{oc} \times \text{FF}/I_s \tag{9.11}$$

Under full sunlight (AM1.5 global, intensity $I_s = 1000\,\text{Watt/cm}^2$), short circuit photocurrents ranging from 16–22 mA/cm^2 are reached with state-of-the-art ruthenium sensitizers, while V_{oc} is 0.7 to 0.86 V and FF values 0. 65–0.8. A certified overall power conversion efficiency of 10.4 % was attained [38] in 2001. A new record efficiency over 11.2 % was achieved recently [4] and Figure 9.13 shows the current voltage curve obtained with this cell.

9.4.3 Increasing the open circuit photovoltage

We have identified additives, such as guanidinium ions, which are able to suppress the dark current at the titania–electrolyte junction. Although these effects remain yet to be fully understood it appears that these ions assist the self assembly of dye molecules at the TiO_2 surface, rendering it more impermeable and reducing in this fashion the dark current of the cell. In addition guanidinium butyric acid was found to suppress the number of surface states acting as a recombination centers [39].

The ruthenium dye N-719 is adsorbed at the TiO_2 surface via two of the four carboxylate groups. The spatial configuration of the adsorbed dye at the (111) oriented surface of the TiO_2 nanocrystals has been assessed by FTIR analysis and molecular dynamics calculation. The dye monolayer is disordered and the lateral repulsion of the negatively charged dye molecules is attenuated by spontaneous coadsorption of cations. It is desirable to increase the order of

the dye monolayer at the interface and render it denser. The goal here is to make the dye layer insulating in order to block the dark current across the interface. The resulting gain in open-circuit voltage can be calculated from the diode equation:

$$V_{oc} = (nRT/F)\ln[(i_{sc}/i_o) - 1], \tag{9.12}$$

where n is the ideality factor, whose value is between 1 and 2; i_o is the reverse saturation current and R and F are the ideal gas and Faraday's constant, respectively. Increasing the injection and lowering the recombination rates are critical for maximizing the open circuit voltage of a cell as shown by Equation (9.12). Using 1.5 as a value for the ideality factor in DSC, the reduction of the dark current by a factor of ten would result in a voltage increase of 90 mV, boosting the conversion efficiency of the cell by at least 15 %. The fact that the dye itself blocks the dark current of the DSC has been confirmed recently [38].

9.5 DEVELOPMENT OF NEW SENSITIZERS AND REDOX SYSTEMS

While the improvements in DSC performance obtained recently are remarkable, it would be very difficult to reach much higher efficiencies with the standard N-719 sensitizer unless the redox system was changed. Due to the mismatch of the redox levels of the N-719 and the iodide/triiodide couple, the regeneration reaction of the sensitizer consumes too large a fraction of the absorbed photon energy as is apparent from the band diagram shown in Figure 9.1. Work on alternative redox systems whose Nernst potentials are better adapted to that of the N-719 dye are currently being developed [40] and should ultimately lead to DSCs exhibiting V_{oc} values above 1 V.

Alternatively, if the present iodide based redox system is maintained, introducing panchromatic sensitizers or dye mixtures can boost the efficiency of cells further. To give 15 % conversion efficiency, these should be designed to yield at least 24 mA/cm^2 short circuit current under full sunlight and fill factor as well as open circuit voltage values similar to those that are presently obtained. To achieve such photocurrents the light harvesting in the 650 to 900 nm range needs to be significantly improved.

Scheme 9.1 shows the structure of a heteroleptic ruthenium complex coded K-19 which due to the extension of the π-system in one of its ligands has an enhanced absorption coefficient. An analogue of this dye with long alkyl side chains on the bipyridyl group, named Z-907, showed excellent light conversion performance and cell stability [8]. These dyes of Z-series have proved themselves to be very useful to solid state DSC, where their hydrophobic nature indeed

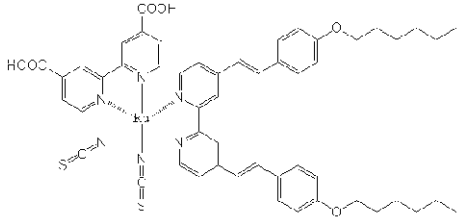

Scheme 9.1 K-19 sensitizer with an extended p system in one of its ligands.

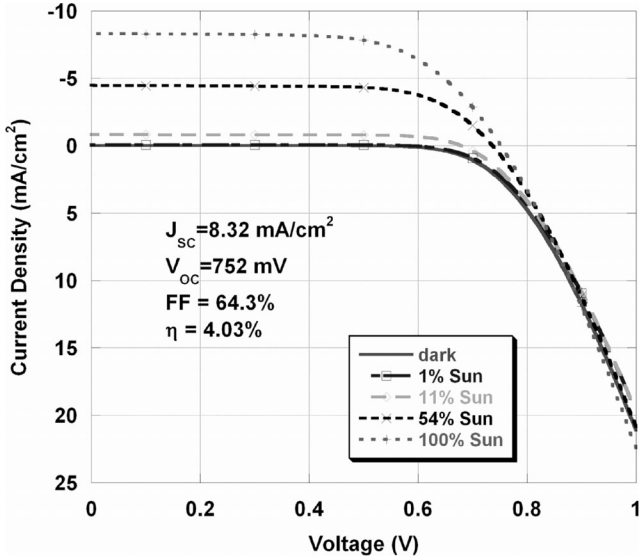

Figure 9.14 J-V data for a 4 % efficient solid state DSC [4].

became a helpful factor. Subsequently, they enhanced the performance of systems containing ionic electrolytes and hole conductors. The K-19 dye also exhibits excellent conversion yield and stability [9].

9.6 SOLID STATE DYE SENSITIZED SOLAR CELLS

Solid state DSCs employing the hydrophobic Z-907 dye and the hole conductor spiro-OMeTAD [41] in conjunction with additives such as $Li(CF_3SO_2)_2N$, t-butyl pyridine and $N(PhBr)_3SbCl_6$ as a p dopant have shown >4 % energy conversion efficiency under AM1.5 global illumination [4]. The data is shown in Figure 9.14. Here again the self assembly of the dye molecules to a dense layer on the TiO_2 surface plays an important role, the COOH groups serving as anchors and the hydrophobic chains as a blocking layer between the hole conductor and TiO_2.

9.7 DYE SENSITIZED SOLAR CELL STABILITY

While long term accelerated light soaking tests have confirmed the intrinsic stability of current DSC embodiments [42], stable operation under high temperature stress 80–85 °C has been achieved only recently by judicious molecular engineering of the sensitizer used in conjunction with a robust and nonvolatile electrolyte.

9.7.1 Criteria for long term stability of the dye

Scheme 9.2 illustrates the catalytic cycle that the sensitizer performs during cell operation. Critical for stability are any side reactions that may occur from the excited state S* or the

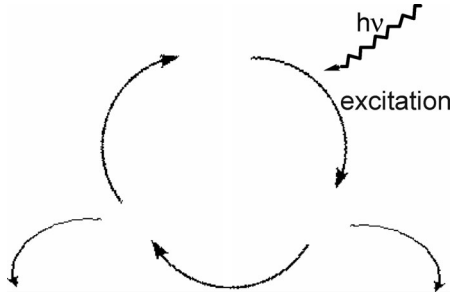

Scheme 9.2 The catalytic cycle of the sensitizer during cell operation.

oxidized state of the dye (S^+), which would compete with electron injection from the excited dye into the conduction band of the mesoscopic oxide and with the regeneration of the sensitizer. These destructive channels are assumed to follow first or pseudo-first order kinetics and are assigned the rate constants k_1 and k_2. By introducing the two branching ratios, $P_1 = k_{inj}/(k_1 + k_{inj})$ and $P_2 = k_{reg}/(k_2 + k_{reg})$ where k_{inj} and k_{reg} are the first order or pseudo-first order rate constants for the injection and regeneration processes, respectively, the fraction of the sensitizer molecules that survives one cycle can be calculated as the product $P_1 \times P_2$. Also, the upper limit for the sum of the two branching ratios can be calculated for a cell operation of 20 years and is shown to be 1×10^{-8}. The turnover frequency, averaged over seasons and day–nighttime, of the dye has been derived as 0.155 s^{-1}.

9.7.2 Kinetic measurements

As indicated above, for most of the common sensitizers the rate constant for electron injection from the excited state to the conduction band of the TiO_2 particles is in the fs range. Assuming $k_{inj} = 1 \times 10^{13}$ /s, a destructive side reaction with $k_1 < 10^5/s^1$ could be tolerated. Ruthenium sensitizers of the N3 type readily satisfy this condition. They can undergo photoinduced loss or exchange of the thiocyanate ligand, which, however, occurs at a much lower rate than the 10^5 /s limit. It is also debatable whether this pathway is destructive, as the product formed still acts as a charge transfer sensitizer. In ethanolic solution prolonged photolysis of N3 dye leads to sulfur loss and formation of the cyanato-ruthenium complex probably via photoxidation by oxygen. However this reaction is not observed when the dye is adsorbed on oxide surfaces.

Precise kinetic information has also been gathered for the second destructive channel involving the oxidized state of the sensitizer, the key parameter being the ratio k_2/k_{reg} of the rate constants for the degradation of the oxidized form of the sensitizer and its regeneration. The S^+ state of the sensitizer can be readily produced by chemical or electrochemical oxidation and its lifetime determined independently by absorption spectroscopy. Data from a recent study of Z-907 shows that the formation of its oxidized form occurs over the first 8–10 min after the addition of an oxidant. The subsequent decay occurs with a lifetime of 75 minutes corresponding to $k_2 = 2.2 \times 10^{-4}\ s^{-1}$. The regeneration rate constant for this sensitizer in a typical iodide/triiodide redox electrolyte is at least 2×10^5 /s. Hence the branching ratio is about 10^{-9}, which is well below the limit of 10^{-8} admitted to achieve the 100 million turnovers and a 20 year lifetime for the sensitizer.

9.7.3 Recent experimental results on dye sensitized solar cell stability

Many long term tests have been performed with the N3 type ruthenium complexes confirming the extraordinary stability of these charge transfer sensitizers. For example, a European consortium financed under the Joule program [42] has confirmed cell photocurrent stability over 10 000 hours of light soaking at 2.5 sun equivalents corresponding to ca. 56 million turnovers of the dye without any significant degradation. These results corroborate the projections from the kinetic considerations made above. A more difficult task has been to reach stability under prolonged stress at higher temperatures, i.e. 80–85 °C. Recent stabilization of the interface by using self assembly of sensitizers in conjunction with amphiphilic coadsorbents has been particularly rewarding by allowing the DSC to meet, for the first time, the specifications laid out for outdoor applications of silicon photovoltaic cells. For example, the new amphiphlic sensitizer K-19, shows increased extinction coefficients due to extension of the π conjugation of the hydrophobic bipyridyl and the presence of electron donating alkoxy groups. Taking advantage of the enhanced optical absorption of this new sensitizer and using it in conjunction with decylphoshponic acid (DPA) as coadsorbent and a novel electrolyte formulation, a $\geq$8 % efficiency DSC has been realized showing strikingly stable performance under both prolonged thermal stress and light soaking [9].

Hermetically sealed cells were used for long term thermal stress tests of cells stored in the oven at 80 °C. As shown in Figure 9.15, the V_{oc} of such a device drops only by 25 mV over 1 000 hours aging at 80 °C, while there is a ~70 mV decline (not shown) for device B in the case of film stained with the K-19 sensitizer alone. The stabilizing effect of the DPA is attributed to the formation of a robust and compact molecular monolayer at the mesoscopic TiO_2 surface, reducing the amount of adsorbed water and other interfering impurities. This stabilization of the V_{oc} allows device A to sustain the high conversion efficiency during extended heat exposure. Figure 9.15 shows that this device maintained over 98 % of its initial conversion efficiency after 1000 hours aging at 80 °C. While no change was observed for the fill factor, after 1000 hours aging, the measured J_{sc} of 15.38 mA/cm^2 was even higher than its initial value of 15.16 mA/cm^2. The opposing changes of J_{sc} and V_{oc} probably reflect a small positive

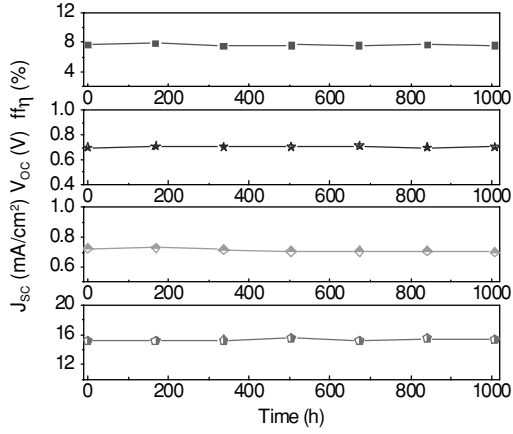

Figure 9.15 Temporal evolution of photovoltaic parameters (AM1.5 full sunlight) of device A during continued thermal aging at 80 °C in the dark.

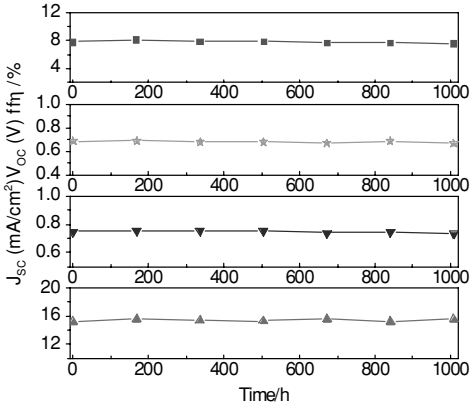

Figure 9.16 Temporal evolution of photovoltaic parameters (AM1.5 full sunlight) of device A during continued one sun equivalent visible light soaking at 60 °C.

shift of flat band potential of the mesoporous titania film under the thermal stress, which can result in a net enhancement of photoinduced charge separation efficiency in DSC.

Cells covered with a 50 μm thick polyester film (Preservation Equipment Ltd, UK), as a UV cut-off filter (up to 400 nm), were irradiated at open circuit and 60 °C in a Suntest CPS plus lamp (ATLAS GmbH, 100 mW/cm^2). As shown in Figure 9.16, device A showed an excellent stability under the dual stress of heating and visible light soaking, retaining 97.7 % of its initial power conversion efficiency. Impressively, the measured J_{sc} of 15.53 mA/cm2 after 1000 hours aging was still higher than the initial value of 15.15 mA/cm^2 while a 16 mV drop in V_{oc} and less than 3 % decrease in fill factor were observed. This confirms again the photochemical inertness of the styryl unit attached to the bipyridyl ligand to prolonged visible light soaking [9].

9.7.4 First large scale field tests and commercial developments

Over recent years industrial interest in the dye sensitized solar cell has surged and the development of commercial products is progressing rapidly. A number of industrial corporations, such as Konarka (www.konarkatech.com) in the USA, Aisin Seiki in Japan, and well as RWE in Germany and Solaronix in Switzerland are actively pursuing the development of modules, both flexible and glass based. Particularly interesting are applications in building integrated photovoltaic elements such as electric power producing glass tiles. The Australian company Sustainable Technologies International (www.sta.com.au) has produced such tiles on a large scale for field testing and several buildings have been equipped with a wall of this type. Aisin Seiki in Japan in collaboration with Toyota has started DSC prototype production. The layout of these modules is shown in Figure 9.17. Note the monolithic design is using carbon as interconnection and cathode material in order to keep the cost down.

These DSC pannels have been installed in the walls of the Toyota Dream House shown in Figure 9.18, house offering a building intergrated source of solar power to the inhabitants.

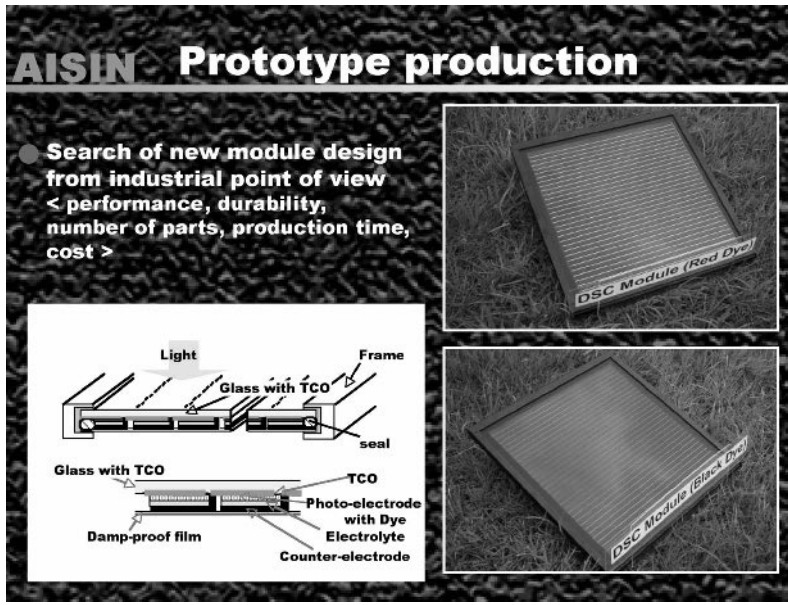

Figure 9.17 Production of DSC prototypes by Aisin Seiki in Japan. Note the monolithic design of the PV modules and the use of carbon as interconnection and counter electrode material. The red dye is related to N-719 while the black dye has the structure $RuL'(NCS)_3$ where $L' = 2, 2', 2''$-terpyridyl4,4,′4′′ tricarboxylic acid.

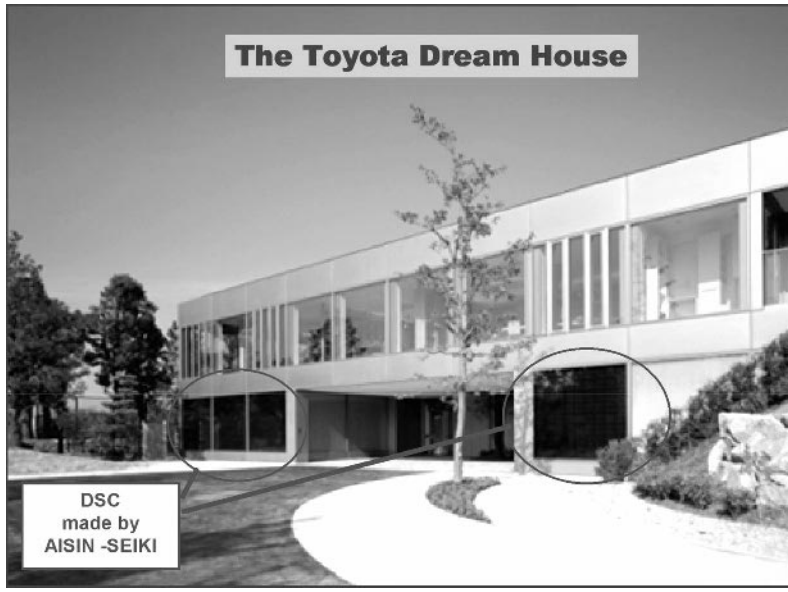

Figure 9.18 The Toyota Dream House featuring DSC panels made by Aisin Seiki. For details see web announcment http://www.toyota.co.jp/jp/news/04/Dec/nt04_1204.html.

9.8 FUTURE PROSPECTS

Reaching much beyond 12 % conversion efficiency for DSC, by relying mainly on panchromatic and IR absorbing dyes or surface modifications, will require enhanced light collection in the 700–900 nm region. An alternative and promising approach will be the use of a tandem concept, where the top and bottom cells are judiciously chosen to absorb complimentary components of the available light including the infrared region. Such a device was recently tried in our laboratory and obtained 15 % conversion efficiency. A preliminary report on this work was given at the 2005 European conference in Barcelona and we shall disclose further details shortly.

ACKNOWLEDGEMENTS

Financial support from EU and Swiss (ENK6-CT2001-575 and SES6-CT-2003-502783), and USAF (contract No. FA8655-03-13068) is acknowledged.

REFERENCES

[1] B. O'Regan and M. Grätzel, Low cost and highly efficient solar cells based on the sensitization of colloidal titanium dioxide, *Nature* **335**, 7377 (1991).
[2] M. Grätzel, Photoelectrochemical cells, *Nature* **414**, 338–344 (2001).
[3] M. Grätzel, Mesoscopic solar cells for electricity and hydrogen production from sunlight, *Chem. Lett.* **34**, 8–13 (2005).
[4] L. Schmidt-Mende, U. Bach, R. Humphry-Baker, T. Horiuchi, H. Miura, S. Ito, S. Uchida and M. Grätzel, Organic dye for highly efficient solid-state dye-sensitized solar cells, *Adv. Mater.* **17**, 813–815 (2005).
[5] M. Nanu, J. Schoonman, and A. Goossens, *Adv. Mat.* **16**, 453 (2004).
[6] M. Nanu, J. Schoonman, and A. Goossens, *Adv. Func. Mat.* **15**, 95 (2005).
[7] P. Liska, R. Thampi, D. Brémaud, D. Rudmann, H. M. Upadhyaya, A. N. Tiwari and M. Grätzel, Nanocrystalline dye-sensitized solar cell //copper indium gallium selenide thin film tandem showing greater than 15 % conversion efficiency *Appl. Phys. Lett.* Submitted.
[8] P. Wang, S. M. Zakeeruddin, J. E. Moser, M. K. Nazeeruddin, T. Sekiguchi and M. Grätzel, *Nature Mat.* **2**, 402 (2003).
[9] P. Wang, C. Klein, R. Humphry-Baker, S. M. Zakeeruddin, and M. Grätzel, *Appl. Phys. Lett.* **86**, 123508 (2005).
[10] M. Zoukalova, A. Zoukal, L. Kavan, M. K. Nazeeruddin, P. Liska, and M. Grätzel, Organized mesoporous TiO_2 films exhibiting greatly enhanced performance in dye solar cells, *Nanolett.* **5**, 1789–1792 (2005).
[11] S. Nishimura, N. Abrams, B. Lewis, L. I. Halaoui, Th. E. Mallouk, K. D. Benkstein, J. van de Lagemaat and A. J. J. Frank, *Am. Chem. Soc.* **125**, 6306 (2003).
[12] L. I. Halaoui, N. M. Abrams, and T. E. Mallouk, *J. Phys. Chem.* **109**, 6334 (2005).
[13] S. Hore, P. Nitz, C. Vetter, C. Prahl, M. Niggemann, and R. Kern, *Chem. Comm.* **15**, 2011 (2005).
[14] A. Hagfeldt and M. Grätzel, *Acc. Chem. Res.* **33**, 269–277 (2000).
[15] Y. Tachibana, J. E. Moser M. Grätzel, D. R. Klug, and J. R. Durrant, *J. Phys. Chem.* **100**, 20056 (1996).
[16] J. E. Moser and M. Grätzel, *Chimia* **52**, 160 (1998).
[17] a) G. Benkö, J. Kallioinen, J. E. I. Korppi-Tommola, A. P. Yartsev, and V. Sundström, *J. Am. Chem. Soc.* **124**, 489 (2002). b) J. Kallioinen, G. Benkö, V. Sundström, J. E. I. Korppi-Tommola and

A. P. Yartsev, A. P. *J. Phys. Chem. B* **106**, 4396 (2002). c) G. Benkö, J. Kallioinen, P. Myllyperkiö, F. Trif, J. E. I. Korppi-Tommola, A. P. Yartsev and V. Sundström, *J. Phys. Chem. B* **108**, 2862 (2004).
[18] Schwarzburg, K.; Ernstorfer, R.; Felber, S.; Willig, F. *Coord. Chem. Rev.* **2004**, 248(13-14), 1259–1270.
[19] B. Wenger, M. Grätzel and J. E. Moser, *Am. Chem. Soc. 127*, 12150–12151 (2005).
[20] a) J. M. Lanzafame, R. J. D. Miller, A. A. Muenter and B. A. Parkinson, *J. Phys. Chem.* **96**, 2820 (1992). b) R. Huber, J. E. Moser, M. Grätzel and J. Wachtveitl, *Proc. SPIE* **5223**, 121 (2003).
[21] J. E. Moser and M. Grätzel, *Chem. Phys.* **176**, 493 (1993).
[22] G. Redmond and D. Fitzmaurice, *J. Phys. Chem.* **97**, 11081 (1993).
[23] J. Nelson and R. E. Chandler, *Coord. Chem. Rev.* **248**, 1181–1194 (2004).
[24] H. G. Agrell, G. Boschloo and A. Hagfeldt, *J. Phys. Chem. B*, **108**, 12388 (2004).
[25] M. J. Cass, A. B. Walker, D. Martinez and L. M. Peter, *J. Phys. Chem. B*, **109**, 5100 (2005).
[26] A. J. Frank, N. Kopidakis and J. van de Lagemaat, *Coord. Chem. Rev.* **248**, 1165 (2004).
[27] M. J. Cass, F. L. Qiu, Alison B. Walker, A. C. Fisher and L. M. Peter *J.Phys. Chem. B*, **107 (1)**, 113–119 (2003).
[28] W. Kubo, T. Kitamura, K. Hanabusa, Y. Wada and S. Yanagida, *Chem. Comm*, 374–375 (2002).
[29] J. Bisquert, *J. Phys. Chem. B*, **106**, 325–33 (2002).
[30] F. Fabregat-Santiago, J. Bisquert, G. Garcia-Belmonte, G. Boschloo and A. Hagfeldt, *Sol. En. Mat. Sol. Cells* **87**, 117 (2005).
[31] S. Nakade, W. Kubo, Y. Saito, T. Kanzaki, T. Kitamura, Y. Wada and S. Yanagida, S. *J. Phys. Chem. B* **107** **page (2003).
[32] F. Fabregat-Santiago, J. Bisquert, G. Garcia-Belmonte, G. Boschloo and A. Hagfeldt, *Sol. En. Mat. Sol. Cells* **87**, 117 (2005).
[33] P. Wang, S. M. Zakeeruddin, J. E. Moser, R. Humphry-Baker, P. Comte, V. Aranyos, A. Hagfeldt, M. K. Nazeeruddin and M. Grätzel, *Adv. Mat.* **16**, 1806 (2004).
[34] P. Wang, B. Wenger, R. Humphry-Baker, J. E. Moser, J. Teuscher, W. Kantlehner, J. Mezger, E. V. Stoyanov, S. M. Zakeeruddin and M. Grätzel, *J. Am. Chem. Soc.* **127**, 18 (2005).
[35] R. Plass, S. Pelet, J. Krüger, M. Grätzel and U. Bach. *J. Phys. Chem. B*, **106**, 7578–7580 (2002).
[36] A. J. Nozik, Quantum dot solar cells, *Next Gen. Photovolt.* 196–222 (2004).
[37] R. Schaller and V. I. Klimov, *Phys. Rev. Lett.* **92**, 186601 (2004).
[38] M. K. Nazeeruddin, A. Kay, I. Rodicio, R. Humphrey-Baker, E. Müller, P. Liska, N. Vlachopoulos and M. Grätzel, *J. Am. Chem. Soc.* **115**, 6382 (1993).
[39] Z. Zhang, S. M. Zakeeruddin, B C. O'Regan, R. Humphry-Baker, and M. Grätzel, Influence of 4-guanidinobutyric acid as coadsorbent in reducing recombination in dye-sensitized solar cells, *J. Phys. Chem. B. **vol, page* 2005.
[40] H. Nusbaumer, S. M. Zakeeruddin, J. E. Moser and M. Grätzel, *Euro. J. Chem.* **9**, 3756 (2003).
[41] U. Bach, D. Lupo, P. Comte, J. E. Moser, F. Weissörtel, J. Salbeck, H. Spreitzert and M. Grätzel, *Nature* **395**, 550 (1998).
[42] A. Hinsch, J. M. Kroon, J. M. R. Kern, I. Uhlendorf, J. Holzbock, A. Meyer and J. Ferber, *Progr. Photovolt.* **9**, 425–438 (2001).

10 Charge Transport and Recombination in Donor–Acceptor Bulk Heterojunction Solar Cells

A. J. Mozer and N. S. Sariciftci
Linz Institute for Organic Solar Cells (LIOS), Johannes Kepler University, Linz, Austria

10.1 INTRODUCTION

The idea of utilizing organic materials for solar energy conversion has been the subject of fascinating research for several decades. Organic materials are typically inexpensive, easily processable and their functionality can be tailored by molecular design and chemical synthesis. The most important functionality is the highly polarizable π electron systems of organic molecules. Although the electronic structure of organic materials is different from typical inorganic crystalline materials, the delocalized π electron systems assign material properties that are traditionally assigned to inorganic semiconductors, e.g., light absorption and emission in the visible and the near infrared spectral range, the wide range of conductivity from insulator to metallic, and the ability to transport charges over macroscopic distances.

In 1985 Tang [1] first demonstrated an organic solar cell exhibiting power conversion efficiency around 1 %. This cell was based on a bilayer structure of two known photoconductors Me-Ptcdi (N, N'-dimethyl-perylene-3,4,9,10-dicarboximide)/ZnPc (zinc-phtalocyanine), both of which are rather inefficient photovoltaic materials when used in a single layer structure. This is because charge generation efficiency in organic materials is typically low, attributed to the small mean free path (low mobility) of charge carriers, which is smaller than the Coulomb radius $r_c = e^2/4\pi\varepsilon_0\,\mathrm{k}T$ (small dielectric constant) [2]. Therefore the primary photoexcitations are bound neutral excited states (binding energies of 0.04 eV up to 1 eV) [3, 4], and the generation of free charge carriers requires excess energy gained by e.g., electron transfer from the donor containing the excitation to lower lying molecular orbitals of the electron acceptor moieties or to interfaces. The device concept of multilayer small molecule photovoltaic devices has been pursued until today, and power conversion efficiencies in excess of 3.5 % in laboratory scale have been presented [5].

Since their initial discovery in 1977 [6], conductive polymers gained interest due to their metallic or semiconducting properties accompanied by the easy processing and flexibility of common plastics [7]. The fabrication of the first diodes in 1987 based on a soluble

Thin Film Solar Cells Edited by J. Poortmans and V. Arkhipov
© 2006 John Wiley & Sons, Ltd

poly(3-hexylthiophene) sandwiched between a transparent conductive oxide and evaporated aluminum contacts marked the beginning of the field of plastic electronics [8]. It is expected that several electronic devices, such as displays based on polymer light emitting diodes [9], integrated electronic circuits based on polymer field effect transistors [10], and plastic solar cells [11] will enter the market in applications where inexpensive material and fabrication costs accompanied by flexibility and light weight are desirable ('throw away electronics').

The most promising candidates for flexible plastic solar cells are based on the bulk heterojunction concept, which consists of an interpenetrating network of a conjugated polymer and a fullerene. The current state of this rapidly expanding field is discussed here, focusing on novel materials and advanced characterization techniques.

The review is organized as follows: in Section 10.2, the photogeneration mechanism, namely ultrafast photoinduced electron transfer [12] between a photoexcited conjugated polymer and buckminsterfullerene observed by various optical techniques will be reviewed, and early device work will be summarized. In Section 10.3, the operational principles of state-of-the-art bulk heterojunction solar cells is discussed, focusing on two main issues of nanomorphology optimization and improving the spectral sensitivity of bulk heterojunction solar cells. In Section 10.4, the charge carrier mobility and recombination is studied using novel transient conductivity techniques. First, the intercorrelated properties of the chemical structure, morphology and charge carrier mobility are emphasized in regioregular MDMO-PPVs (poly(2-methoxy-5-(3,7-dimethyloctyloxy)-1,4-phenylenevinylene). Next, the mobility of photogenerated and doping induced charge carriers is compared in the same samples of a regioregular poly(3-hexylthiophene) using the time of flight (ToF) and charge carrier extraction by linearly increasing voltage (CELIV) techniques. This comparative study shows that the principally different techniques of ToF and CELIV deliver a mutually consistent picture of charge carrier mobility. Finally, the photoinduced charge extraction by linearly increasing voltage (photo-CELIV) technique is introduced to simultaneously determine charge carrier mobility and lifetime in bulk heterojunction solar cells. The determined mobility and lifetime values are then compared to the current density versus voltage curves of bulk heterojunction solar cells with varying active layer thicknesses. Finally, a short summary and a brief outlook for further developments is given.

10.2 DEVELOPMENT OF BULK HETEROJUNCTION SOLAR CELLS

In π conjugated polymers, the semiconducting properties are accompanied by the attractive mechanical properties and processing advantages of conventional polymers [7]. Fullerenes [13] as new forms of carbon are another interesting class of functional materials. Buckminsterfullerene (C_{60}) is a strong electron acceptor capable of taking as many as six electrons, and forms charge transfer salts with a variety of strong donors.

Mixing C_{60} with semiconducting polymers, no significant ground state interaction is observed. Upon photoexcitation of the conjugated polymer donor, a cascade of reactions is initiated leading to charge separation as schematically illustrated by the following equations [14]:

$$D + A \rightarrow {}^{1,3}D^* + A \quad \text{(excitation on donor)} \tag{10.1}$$

$${}^{1,3}D^* + A \rightarrow {}^{1,3}(D \cdots A)^* \quad \text{(excitation delocalized on the donor–acceptor complex)} \tag{10.2}$$

$$^{1,3}(D\cdots A)^{*} \rightarrow {}^{1,3}\left(D^{\delta+}\cdots A^{\delta-}\right)^{*} \quad \text{(partial charge transfer)} \tag{10.3}$$

$$^{1,3}\left(D^{\delta+}\cdots A^{\delta-}\right)^{*} \rightarrow {}^{1,3}\left(D^{+\bullet}\cdots A^{-\bullet}\right) \quad \text{(ion radical pair formed)} \tag{10.4}$$

$$^{1,3}\left(D^{+\bullet}\cdots A^{-\bullet}\right)^{*} \rightarrow {}^{1,3}\left(D^{+\bullet}+A^{-\bullet}\right) \quad \text{(charge separation)} \tag{10.5}$$

The photophysical process described above (—Equations 10.1–10.5) is a photoinduced electron transfer, and the experimental evidence for its occurrence between nondegenerate conjugated polymers and C_{60} by various optical probes is summarized as follows:

(1) The optical absorption spectrum of the (2'-ethyl-hexyloxy)-p-phenylene vinylene (MEH-PPV):C_{60} blend is a simple superposition of the two components and no indication of ground state interaction is observed [14].

(2) Instead of the triplet–triplet absorption band centered around 1.35 eV in the photoinduced absorption (PIA) spectrum of pristine MEH-PPV, a sharp PIA edge at 1.1 eV and a plateau at 1.6–2.0 eV is observed in the PIA spectrum of the MEH-PPV:C60 blend (Figure 10.1) [15].

(3) From photoinduced absorption detected magnetic resonance (PIADMR) [16], the 1.35 eV peak in the pristine polymer has been attributed to triplet–triplet absorption, which is completely quenched in the blends with C_{60}. The photoinduced charge transfer is sufficiently fast to quench singlet to triplet intersystem crossing in MEH-PPV resulting in absorption features attributed to positive radical cations (photodoping) [14].

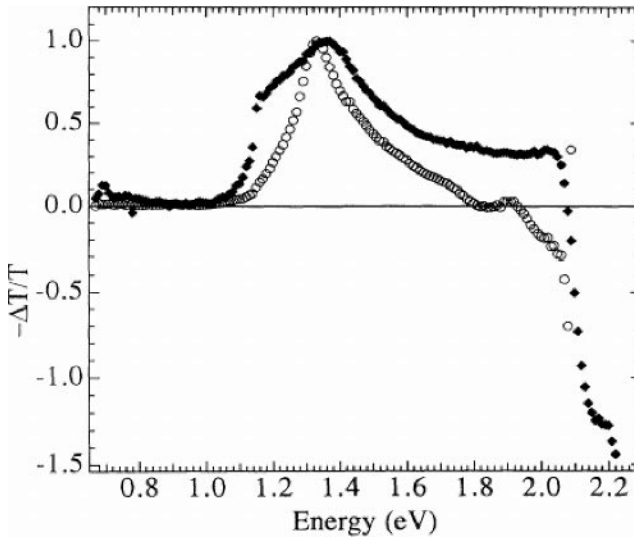

Figure 10.1 Photoinduced absorption spectra of MEH-PPV (○) and MEH-PPV/C_{60} composite (●) at 80 K obtained by pumping with an argon ion laser at 2.41 eV with 50 mW. Reprinted Figure 3 with permission from Smilowitz *et al.*, *Physical Review B* **47**, 13835, 1993. Copyright (1993) by the American Physical Society.

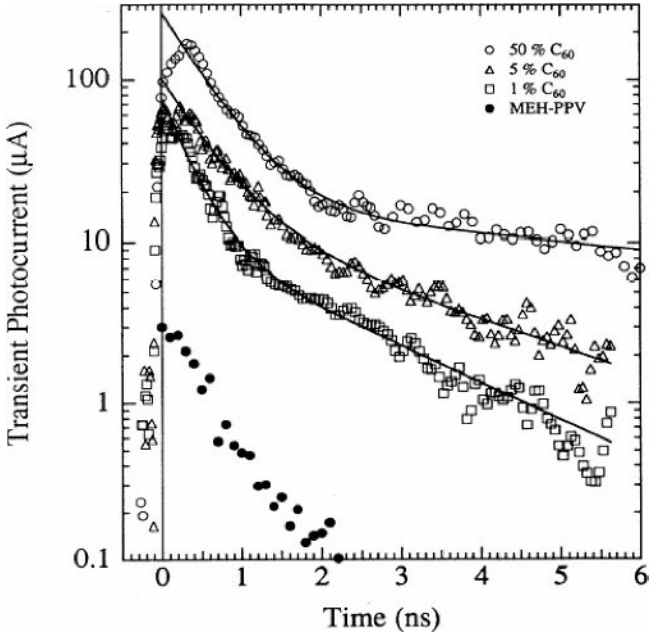

Figure 10.2 Transient photoconductivity of pristine MEH-PPV (•) and its various blends with C_{60}. Reprinted figure 2 with permission from Lee *et al.*, *Physical Review B* **48**, 15425, 1993. Copyright (1993) by the American Physical Society.

(4) Subpicosecond transient absorption studies [17] have revealed that the photoinduced charge transfer happens within 40 fs of photoexcitation, quenching even the coherent vibrational excitations of the conjugated polymer [18]. This ultrafast timescale of charge transfer ensures a nearly 100 % quantum yield for photoinduced charge separation.

(5) Steady state photoconductivity (PC) experiments showed that blending conjugated polymers with only 1 % C_{60} can increase the PC by orders of magnitude. From time resolved photoconductivity experiments it was concluded that the increased steady state photoconductivity is the cumulative effect of increased charge generation and increased charge carrier lifetime (Figure 10.2) [19].

(6) Definitive evidence for the occurrence of photoinduced charge transfer was obtained by light induced electron spin resonance (LESR) studies [12, 20]. Upon photoexcitation of the MEH-PPV:C_{60} mixture with energy larger than the $\pi - \pi^*$ gap of the conjugated polymer, two LESR signals are detected. The signal around $g < 2$ is characteristic of a C_{60}^- radical anion alongside with the $g \sim 2.002$ value, which is typical of a conjugated polymer radical cation. Time resolved LESR studies also showed that the signature of the charges at liquid helium temperatures may remain detectable for hours indicating persistent photoconductivity at low temperatures [21].

(7) Transient absorption studies in the ns–ms time regime showed that the photogenerated charges are long living with a power law relaxation kinetics indicating that some portion of the charge carriers might be deeply trapped [22].

The above experimental observations are consistent with an ultrafast photoinduced electron transfer between the photoexcited state of the conjugated polymer and fullerene with a quantum yield of charge generation approaching unity. The photogenerated charge carriers are metastable with lifetimes up to milliseconds. An immediate realization was that by the application of selective electrical contacts to the above described system, a photovoltaic device may be fabricated. First, bilayer devices of a spin coated MEH-PPV layer and an evaporated C_{60} layer sandwiched between indium tin oxide (ITO) coated glass and aluminum have been presented [23]. These flat heterojunction devices exhibited four orders of magnitude rectification in the current versus voltage curves in the dark, and a few $\mu A\,cm^{-2}$ short circuit current and 0.5 V open circuit voltage under $\sim$1 $mW\,cm^{-2}$ monochromatic (514 nm) illumination through the ITO side. The spectral response of the diodes showed that the majority of the photocurrent in such bilayer devices is generated within the thin interface between the MEH-PPV and C_{60} heterojunction. The real breakthrough was achieved by creating an interpenetrating network of the electron donor and electron acceptor materials extending the interface area over the whole photoactive layer resulting in a device architecture often referred to as the bulk heterojunction [11].

10.3 BULK HETEROJUNCTION SOLAR CELLS

10.3.1 Operational principles

The concept of a bulk heterojunction is shown in Figure 10.3 together with a band structure displaying the highest occupied molecular orbital (HOMO) and the lowest unoccupied molecular orbital (LUMO) of the electron donor and electron acceptor, and the work function of the electrodes. The chemical structure of some of the materials commonly used in organic solar cells is shown in Figure 10.4.

The charge carriers are generated by photoinduced electron transfer. For efficient charge generation, an exciton photogenerated anywhere in the blend has to reach an acceptor interface within its lifetime; therefore the magnitude of the maximum allowed phase separation is determined by the exciton diffusion length. For intimately mixed blends, experiment has shown

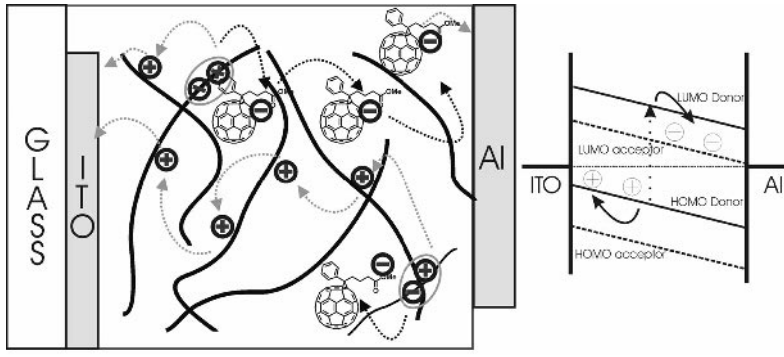

Figure 10.3 Schematic illustration of a bulk heterojunction based on the interpenetrating network of a conjugated polymer and PCBM. The electronic levels relevant to the device performance are also displayed.

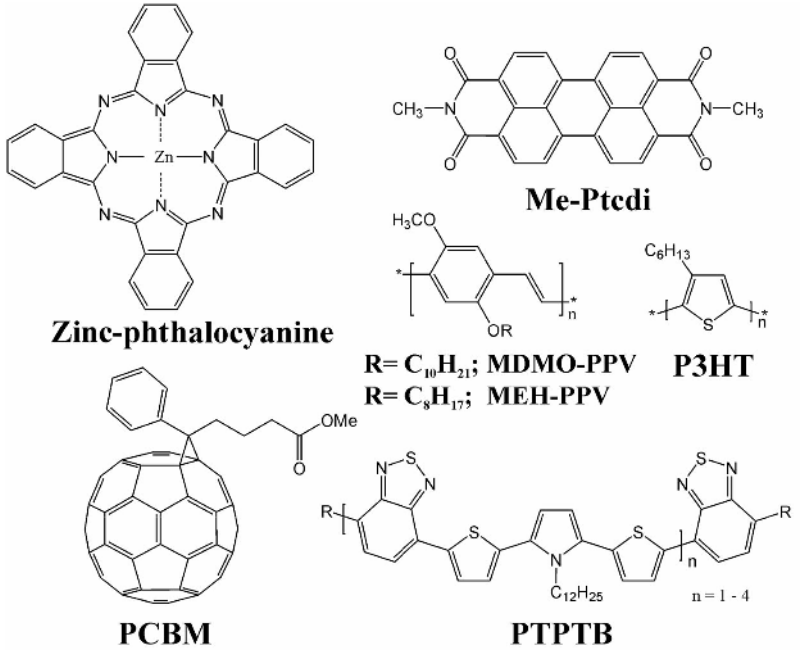

Figure 10.4 Chemical structures of materials used in the Tang solar cells: zinc phthalocyanine and Me-Ptcdi (perylene-3,4,9,10-tetracarboxylic-N, N'-dimethyl-diimide); and in plastic solar cells: MDMO-PPV (poly-[2-(3,7-dimethyloctyloxy)-5-methyloxy]-p-phenylene vinylene); MEH-PPV (2'-ethylhexyloxy)-p-phenylene vinylene); PTPTB (poly-N-dodecyl-2,5-bis(2'-thienyl)pyrrole-2,1,3-benzothiadiazole); P3HT (poly(3-hexylthiophene-2,5-diyl); and PCBM (1-(3-methoxycarbonyl)propyl-1-phenyl[6,6]C_{61}).

that only a few weight % of the electron acceptor is sufficient to quench virtually all excitations (Figure 10.5) [14]. For efficient photovoltaic devices, however, the created charge carriers need to be transported to the corresponding electrodes within their respective lifetimes, which will depend on the charge carrier mobility. The ability to transport both charges in a blend of donor and acceptor materials will be also a sensitive function of the blend nanomorphology, i.e. details of the interpenetrating, bicontinuous network of both materials. For obtaining a significant photocurrent, a nearly 20 mol % load of 1-(3-methoxycarbonyl)propyl-1-phenyl[6,6]C_{61} (PCBM) is necessary (Figure 10.5).

As a last step, charge carriers are extracted from the device through two contacts. A transparent ITO coated glass matching the HOMO level of the conjugated polymer (hole contact) is used on the illumination side, and an evaporated thin lithium fluoride/aluminum metal contact matching the LUMO of PCBM (electron contact) is used on the other side. In the state-of-the-art devices, a thin (100 nm) hole injection layer, a highly doped poly(3,4-ethylenedioxythiophene)-poly(4-styrenesulfonate) (PEDOT-PSS) interfacial film, is used, which also serves to smoothen the surface of the ITO and to increase device stability.

The active layers of bulk heterojunction solar cells can be formed by various solution processing techniques, such as spin coating [24], doctor blading[25], screen printing [26], and spray coating [27]. Spin coating can be conveniently used in laboratory scale academic research;

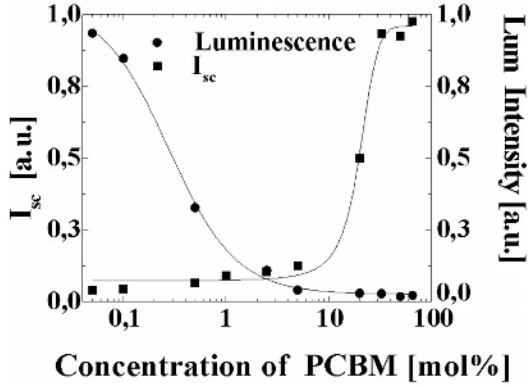

Figure 10.5 Photoluminescence quenching (●) and short circuit photocurrent (■) of a blend of MEH-PPV: PCBM as a function of the concentration of PCBM in the blend.

meanwhile the various printing techniques enable the production of large scale prototype plastic solar cells [28].

The main parameters determining the power conversion efficiency of solar cells is the open circuit voltage (V_{oc}), the short circuit current (I_{sc}) and the fill factor (FF) according to Equation 10.6:

$$\eta\,(\%) = \left(\frac{P_{out}}{P_{in}}\right) \times 100 = \frac{FFV_{oc}J_{sc}}{P_{in}} \times 100 \tag{10.6}$$

where P_{out} is the output electrical power of the device under illumination and P_{in} is the incident light power.

In single layer polymer diodes the open circuit voltage (V_{oc}) corresponds to the difference between the work functions of the anode and cathode materials (metal–insulator–metal, MIM diode) [29, 30]. The open circuit voltage of an MDMO-PPV:PCBM device is ~0.8 V at room temperature, and increases slightly to ~0.9 V at lower temperatures [31]. The open circuit voltage is proposed to correspond to the energy level difference between the LUMO of PCBM (4.1 eV [32] or 4.3 eV [33]), and the HOMO of MDMO-PPV (5.3 eV) [34]. Moreover, the open circuit voltage only weakly depends on the work function of the cathode material used, but exhibits a strong dependence on the LUMO of the electron acceptor [35]. These observations indicate that a simple MIM picture cannot account for the built-in field of bulk heterojunction solar cells. An open circuit voltage of + 0.6 V is observed in a device using Au as the cathode even though the work function of Au is very similar to the work function of the ITO/PEDOT-PSS anode; therefore the built-in field in a simple MIM picture should be close to 0 V. It has been proposed that the cathode work function is aligned with the LUMO of PCBM via a mechanism often referred to as 'Fermi level pinning.' [36] Mihailetchi *et al.* [37] showed that the relatively insensitive V_{oc} of bulk heterojunction solar cells with a cathode of higher work function material than the LUMO of PCBM, e.g., (LiF/Al and Ca) may be attributed to the formation of an ohmic contact to PCBM.

The work of Gadisa *et al.* [38] examined the V_{oc} dependence of bulk heterojunction solar cells based on polythiophenes with varying HOMO levels. The authors observed an almost

linear dependence of V_{oc} by changing the HOMO of the conjugated polymer, which confirms that the maximum V_{oc} is also influenced by the HOMO of the polymer.

The I_{sc} depends on the spectral sensitivity of the photoactive materials (the fraction of incident light absorbed by the photoactive layer), the efficiency of charge generation and the efficiency of charge collection. The charge generation and collection efficiency for certain material combinations depends strongly on the phase separated nanomorhology of the photoactive blend, which is discussed in Section 10.3.2.

The limited photon harvesting of bulk heterojunction solar cells can only be overcome using novel materials with light absorption in the longer wavelength range (low bandgap materials). Some of the recent developments in improving light harvesting in bulk heterojunction solar cells are discussed in Section 10.3.3.

Finally, the fill factor is strongly influenced by the product of the mobility (μ) and lifetime (τ) of the charge carriers. A viable way to improve the charge carrier mobility of conjugated polymers and therefore improve the fill factor of bulk heterojunction solar cells is using regioregular polymers as demonstrated in Section 10.4.

10.3.2 Nanomorphology–property relations

10.3.2.1 Investigation of the nanomorphology

The power conversion efficiency of bulk heterojunction solar cells based on an MDMO-PPV:PCBM mixture of 1:4 weight % is improved from approximately 1 % (AM1.5) to 2.5 % by simply changing the solvent from which the active layer has been cast [24]. Atomic force microscopy (AFM) investigations showed that rather large (i.e., 100–200 nm) clusters are formed in toluene cast films, while a smooth surface morphology was observed for chlorobenzene cast films. Transmission electron microscopy (TEM) and AFM studies [39] assigned the large clusters to a PCBM rich phase. In a more detailed study, the phase separation in MDMO-PPV:PCBM blends with increasing PCBM content spin coated from chlorobenzene, was followed in three dimensions by a combination of AFM, TEM, and depth profiling experiments using dynamic time of flight secondary ion mass spectrometry (TOF-SIMS) [40]. The study showed very smooth films by AFM and no observable contrast in the TEM experiments up to 50–60 % PCBM content. The film surface was increasingly uneven at higher PCBM loads (>67 %), and correspondingly, two phases in the TEM images could be identified. The darker phase, which was growing with increasing PCBM content, was identified as a rather pure PCBM phase similarly to [39]. The distribution of a deuterated PCBM-derivative (d5-PCBM) over the film thickness was studied using ToF-SIMS, and a uniform distribution was observed for all d5-PCBM concentrations and film thicknesses. The electronic properties of the various MDMO-PPV:PCBM blends under illumination and dark was also studied, and an increasing photocurrent and power conversion efficiency between 50—and 70 % PCBM load was observed. In summary, the optimum device performance around 80 % PCBM loading into the polymer matrix arises from improved electron transport and reduced bimolecular recombination, and is closely related to the observed nanoscale phase separation.

Fine details of the nanoscale morphology in the photoactive layer using AFM and scanning electron microscopy (SEM) has been recently reported by Hoppe *et al*. [41]. The SEM images obtained for chlorobenzene cast films at 1:2, 1:4, and 1:6 MDMO-PPV:PCBM ratios by weight are compared in Figure 10.6 a, b, and c, respectively. In all cases, small (20–30 nm) bright nanospheres embedded in a rather uniform matrix are observed, except for the 1:6 film, in

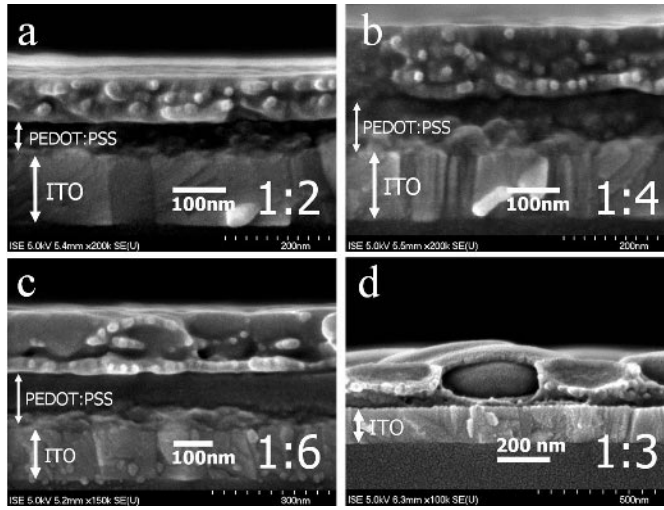

Figure 10.6 a, b, and c: Cross-section SEM images of films prepared by spin coating of MDMO-PPV:PCBM 1:2, 1:4, and 1:6 weight ratios from chlorobenzene solution; and d, 1:3 weight ratio MDMO-PPV:PCBM from toluene solution. Reprinted with permission from Hoppe *et al*., *Adv. Funct. Mater.*, **14**, 1005, Nanoscale morphology of conjugated polymer/fullerene-based bulk-heterojunction solar cells. Copyright (2004) by Wiley-VCH.

which larger clusters are also observed. These large clusters are clearly visible, and their size is dependent on the PCBM load, in films cast from toluene (Figure 10.6 d), therefore being assigned to the PCBM phase similarly to [39, 40]. The small, bright nanospheres, however, can be found in all films studied, e.g., in the 'thin skin' surrounding the large clusters in the toluene cast films, or uniformly distributed in the chlorobenze cast films. Their size seems to be independent of the solvent type and the PCBM content. The authors attribute these bright nanospheres to an MDMO-PPV phase, in which the polymer chains attain coiled conformation. This notion is supported by annealing experiments, in which the contrast between the different phases is improved due to the tendency of PCBM to diffuse and crystallize. Large holes appear instead of the PCBM clusters indicating the diffusive motion of PCBM towards crystallization centers. Interestingly, however, the small spheres remain at the same position. Consequently, the PL of the MDMO-PPV reappears upon annealing, which strongly supports the assignment of the small nanospheres to the MDMO-PPV polymer.

Figure 10.7 shows AFM images of MDMO-PPV:PCBM 1:4 weight ratio films cast from toluene with varying MDMO-PPV concentrations from 0.1 to 0.3 %. Clearly, larger scale phase separation is observed using more concentrated solutions, which is attributed to the longer drying times of thicker films. The effect of drying conditions on the morphology has been observed earlier [42], and can influence the results of spectroscopic investigations.

10.3.2.2 Donor–acceptor 'double cable' polymers

The above morphology studies demonstrated that although the preparation of bulk heterojunction solar cells is very simple, the proper control of the processing parameters is complex, and involves detailed studies of the influence of many factors, incl., the choice of solvent, the

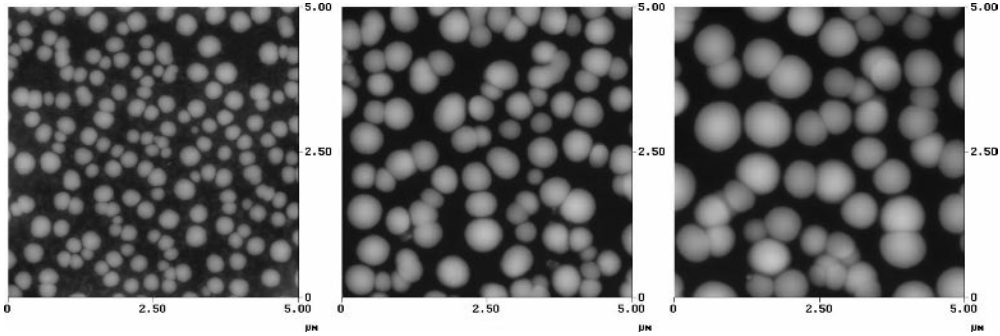

Figure 10.7 AFM images of MDMO-PPV:PCBM 1:4 ratio films cast from toluene solutions with increasing poymer content. Reprinted with permission from Hoppe *et al*., *Adv. Funct. Mater.*, **14**, 1005, Nanoscale morphology of conjugated polymer/fullerene-based bulk-heterojunction solar cells. Copyright (2004) by Wiley-VCH.

concentration of the solution, the weight ratio of the active components, etc. The optimum set of parameters may obviously change with different material combinations. In order to achieve control of the morphology at the molecular level, the concept of 'double cable' polymers has been introduced (Figure 10.8) [43]. These are electron donor conjugated polymers carrying a number of adjacent electron acceptor moieties as covalently linked substituents. It is expected that an electron created by photoinduced electron transfer will travel by hopping between the acceptor moieties; meanwhile the rather high on-chain hole mobility as well as subsequent interchain hopping will transport the positive charge. Ideally, phase separation in these materials is prevented, or, in other words, the interface between the electron acceptor (n-type) and the electron donor (p-type) materials is brought down to the molecular level. As such, 'double cable' polymers can be viewed as molecular heterojunctions (Figure 10.8). Major criterion for the application of these materials in photovoltaic elements is the absence of ground state interaction between the electron donor and acceptor moieties (the 'cables' must not short). This can be achieved by introducing an insulating spacer between the n-type and p-type 'cable.' The spacer may also increase the solubility of the macromolecule; however, its length must be appropriate so as not to hinder photoinduced electron transfer.

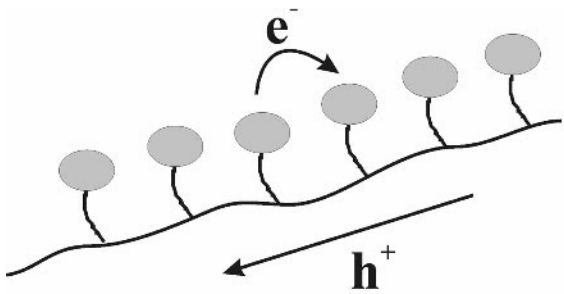

Figure 10.8 Ideal representation of 'double cable' polymers. The charge carriers generated by photoinduced charge transfer can be transported within one molecule, therefore viewed as a 'molecular heterojunction'.

Due to the rather low solubility of donor–acceptor dyads, the first 'double cables' were prepared by electropolymerization. The bipolar character of the macromolecules was clearly observed using electrochemical techniques. Soluble 'double cable' polymers have also been chemically synthesized, and preliminary work in photovoltaic elements of 'double cable' materials have been published. Barriers to overcome for higher power conversion efficiency are the rather low percentage of the fullerene load limiting charge transport, and the still rather low solubility of 'double cable' polymers [44].

10.3.3 Improving the photon harvesting

The absorption of the MDMO-PPV:PCBM blend is compared to the terrestrial total photon flux at AM1.5 conditions in Figure 10.9. The absorption of the MDMO-PPV:PCBM blend is limited in spectral regions around <1.8 eV [45]. To improve the spectral sensitivity of bulk heterojunction solar cells, conjugated polymers with lower π–π^* bandgaps are required (i.e. low bandgap materials). The need to tune the emission color of conjugated polymer based light emitting diodes (LEDs) has triggered the development of several synthetic strategies to influence the band- gap of conjugated polymers. Today a detailed understanding of the molecular structure–bandgap correlation has been reached ('bandgap engineering') [46].

An alternating electron rich N-dodecyl-2,5-bis(2'-thienyl)pyrrole and an electron-deficient 2,1,3-benzothiadiazole unit (PTPTB) (see Figure 10.4), has received attention as a low bandgap polymer showing promising characteristics in bulk heterojunction solar cells. The onset of the absorption of PTPTB is around 780 nm (Figure 10.9), corresponding to an optical bandgap of $\sim$1.6 eV. This polymer exhibits efficient photo- and electroluminescence in the near infrared part of the spectra (maximum around 800 nm). When PTPTB is mixed with PCBM, the PL is quenched and the typical absorption features of the photoinduced charges (polarons) are

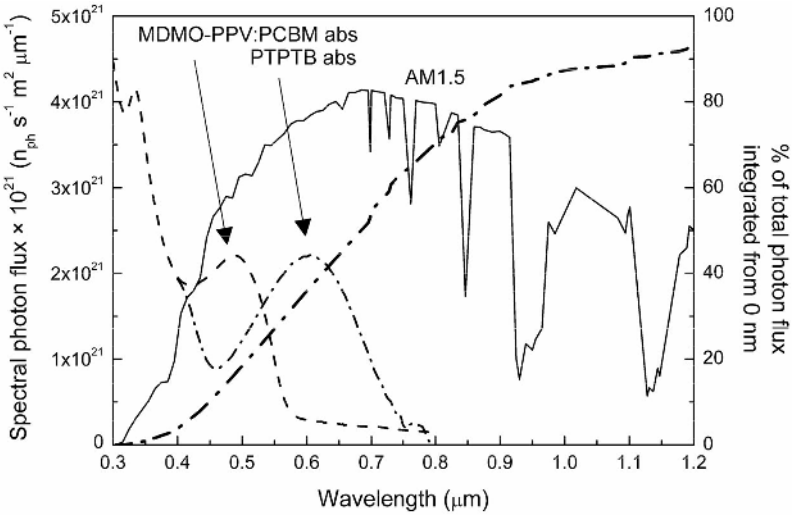

Figure 10.9 Spectral photon flux and integrated total photon flux of AM1.5 solar spectra. The absorption of the MDMO-PPV:PCBM blend and the low bandgap polymer PTPTB are displayed for comparison.

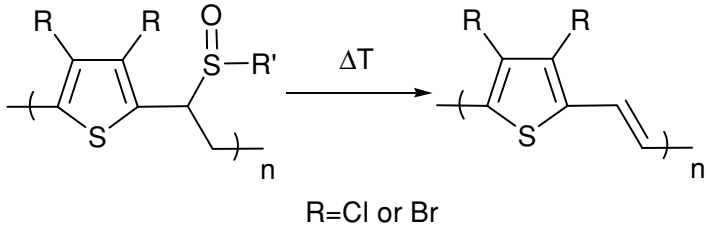

Scheme 10.1 Conversion of the precursor polymer to the conjugated poymer poly(thieneylene vinylene) via the sulfinyl route.

detected in a PIA experiment. Bulk heterojunction solar cells based on a PTPTB:PCBM blend with power conversion efficiency around 1 % have been fabricated. The spectrally resolved photocurrent measured under short circuit conditions (incident photon to converted electron, IPCE) follows closely the absorption of the conjugated polymer. The spectral sensitivity of the PTPTB:PCBM blend is extended to longer wavelengths by almost 200 nm as compared to the MDMO-PPV:PCBM blend, where the solar photon flux is more intense. The rather low fill factor is mainly responsible for the limited overall performance of these devices.

Another interesting class of low bandgap polymers is poly(thienylene vinylene)s (PTVs) [47]. They exhibit one of the highest charge carrier mobilities in a field effect transistor (FET) structure [48]. On the other hand, PTVs are generally insoluble. To overcome problems with solubility, Vanderzande *et al*. have recently developed a precursor approach to bulk heterojunction solar cells based on 3,4-dichloro and 3,4-dibromo derivatives of poly(thienylene vinylene)s. A precursor polymer is synthesized via the sulfinyl route, which is converted to the conjugated polymer PTV by mild heat treatment according to Scheme 10.1. The bandgap of the resulting PTV derivative is 1.55 eV. The precursor polymer is very soluble, and can be deposited using the usual solution processing techniques. For the fabrication of bulk heterojunction solar cells, films containing a mixture of the precursor polymer and PCBM are converted at temperatures where PCBM is still stable. The power conversion efficiency of bulk heterojunction solar cells based on a PTV derivative and PCBM prepared via such a precursor route is around 0.2 %, and mainly limited by the small open circuit voltage and the fill factor. Initial studies showed that optimizing the thermal conversion process is the key to further improvements. It was also demonstrated that a subsequent post production treatment of the diodes can improve the V_{oc} and FF of the diodes, possibly due to reducing shunts and pinholes in the films of the photoactive layer.

Another problem associated with the limited spectral sensitivity of conjugated polymer/C_{60} solar cells is the low absorption coefficients of fullerenes in the visible region of the spectrum. This is because the lowest energy electronic transitions (440–640 nm) of C_{60} are symmetry forbidden [49]. Therefore, the main component of the photovoltaic blend currently used in bulk heterojunction solar cells is mostly optically inactive. Wienk *et al*. have demonstrated that by using less symmetrical fullerenes, such as a C_{70} derivative of PCBM (70-PCBM), the short circuit current of bulk heterojunction solar cells can be improved due to the significantly increased visible absorption of the C_{70} derivate. Moreover, the increased (lower energy) absorption of the C_{70} derivative does not overlap with the absorption of the conjugated polymer MDMO-PPV and therefore the 70-PCBM could be selectively photoexcited within the

blend . Upon photoexcitation of the fullerene, the optical signatures of the positive charges on MDMO-PPV were clearly observed by photoinduced absorption experiments, which indicates that a photoinduced hole transfer from the photoexcited state of the fullerene to the conjugated polymer occurs. Such a charge generation mechanism was previously assumed, but this is the first time it has been clearly demonstrated. The power conversion efficiency of the MDMO-PPV:70-PCBM solar cell is around 3 %, which is limited by the slightly smaller V_{oc} (0.77 V) and FF (0.51) of these devices as compared to the standard MDMO-PPV:PCBM solar cells.

The above examples showed that optimizing one parameter (morphology or bandgap) may deteriorate other properties, such as charge carrier mobility, or the film forming properties. In order to improve the power conversion efficiency of bulk hetereojunction solar cells, materials that perform all the necessary functions are required. One of the important functions is to efficiently transport the photogenerated charges over macroscopic distances. The experimental methods to determine and synthetic strategies to improve charge carrier mobility in bulk heterojunction solar cells will be summarized in the next Section.

10.4 CHARGE CARRIER MOBILITY AND RECOMBINATION

10.4.1 Measurement techniques

The drift distance of charge carriers photogenerated anywhere within the active layer of the solar cell is given by $l_d = \mu \times \tau \times E$, where μ is the mobility, τ is charge carrier lifetime and E is the electric field. This equation assumes that the charge carriers are electric field driven [50]. Due to the rather low mobility of organic materials, high concentrations of photogenerated charge carriers are required to reach a short circuit current density of $\sim$10 mA cm^{-2}, e.g, $n \sim 10^{16}$cm^{-3} if $\mu = 10^{-4}$ cm^2 V^{-1}s^{-1}. High charge carrier concentration generally leads to increased bimolecular recombination resulting in short lifetimes ($\tau(t) = [\beta n(t)]^{-1}$ and consequently, short drift and diffusion distances.

Charge carrier mobility and the lifetime of the charge carriers are not independent in most organic materials. The bimolecular recombination coefficient of a Langevin type recombination typical for low mobility organic materials is written as $\beta_L = e(\mu_e + \mu_h)/\varepsilon\varepsilon_0$, where μ_e (μ_h) is the electron (hole) mobility and e, ε, ε_0 are the elementary charge and dielectric constants of the material and vacuum, respectively. The important questions are, therefore, how to measure charge carrier mobility (μ) and lifetime (τ) in bulk heterojunction solar cells, and how μ and τ are correlated within the interpenetrating network of the electron donor and electron acceptor materials.

First it will be demonstrated that improving the charge carrier mobility of conjugated polymers is a viable way to improve the power conversion efficiency of bulk heterojunction solar cells. The charge transport properties of regioregular MDMO-PPV is compared to its regiorandom counterpart, and the importance of molecular structure–morphology–charge carrier mobility is emphasized. Next, the principally different techniques of time of flight (ToF) and charge carrier extraction by linearly increasing voltage (CELIV) are compared in samples of regioregular poly(3-hexylthiophene). Finally, it will be demonstrated how to determine the charge carrier mobility and lifetime of the charge carriers simultaneously in bulk heterojunction solar cells using the novel photo-CELIV technique.

10.4.1.1 Transient conductivity techniques: ToF, CELIV and photo-CELIV

The measurement principles and the schematic responses of the ToF, CELIV and photo-CELIV techniques are illustrated in Figure 10.10. In the time of flight technique, the transit time (t_{tr}) of a two-dimensional sheet of photogenerated charge carriers drifting through a sample of known thickness (d) is determined under an applied external electric field ($E = U/d$). The ToF mobility is then calculated as $\mu = d^2/(U \times t_{tr})$. The condition of surface photogeneration in a ToF technique requires large film thicknesses with high optical density (OD $>$ 10). Photocurrent transients can be characterized as nondispersive exhibiting a well developed plateau, in which case the transit time is defined as the intersection of the plateau with the tail of the photocurrent transient as shown in Figure 10.10. In the presence of strong dispersion, the recorded photocurrent transients do not exhibit a plateau, but decrease constantly. In this dispersive case the transit time is defined as the intersection of the two linear regimes in the log photocurrent versus log time plots [51]. The electric field is assumed to be uniformly distributed over the sample, a condition which is maintained by: (i) limiting the number of photogenerated charge carriers to less than 10 % of the capacitive charge (CU), (ii) the dielectric relaxation time (τ_σ)being larger than the transit time $\tau_\sigma = \varepsilon_0/\sigma_c > t_{tr} = d^2/\mu U$, where σ_c is the conductivity in $\Omega\,\mathrm{cm}^{-1}$ units. Otherwise the number of equilibrium or doping induced charge carriers (ep_0d, where p_0 is the charge carrier concentration) are sufficient to screen and redistribute the electric field prior to the arrival of the photoexcited charge carriers at the electrodes [52].

In conductive samples with short τ_σ, the complementary technique of CELIV can be used. In the CELIV technique, the equilibrium charge carriers are extracted from a dielectric under a reverse bias voltage ramp ($A = \mathrm{d}U_{max}/\mathrm{d}t_{pulse}$) [53]. The mobility of extracted charge carriers is calculated from the time when the extraction current reaches its maximum (t_{max}). The CELIV measurement is most conveniently performed when the current due to the capacitance

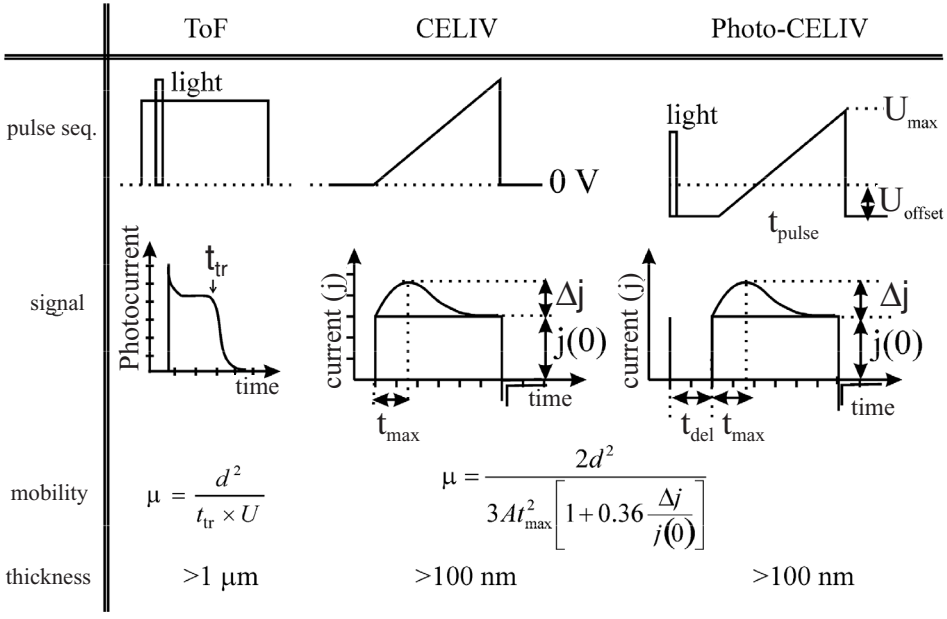

Figure 10.10 The pulse sequence and schematic response of the ToF, CELIV, and photo-CELIV techniques. The calculation of mobility and typical device thicknesses are also displayed.

displacement current ($j(0) = A \times \varepsilon_0/d$), equals the extraction current at its maximum Δj. This experimental condition is achieved by e.g. selecting an appropriate thickness of the sample. In contrast to ToF, the CELIV technique can be used to determine charge carrier mobility in samples of only a few hundred nm thickness.

Due to the rather large bandgap of most organic materials, the amount of equilibrium charge carriers is too low to be determined by CELIV, and needs to be increased by e.g., chemical doping. Alternatively, charge carriers can be photogenerated by a short laser flash. The photogenerated charge carriers undergo recombination or are extracted under the built-in field through the external circuit (short circuit conditions). The built-in field can be compensated by applying a DC offset bias (U_{offset}) leading to flat band conditions, in which case the photogenerated charge carriers are forced to meet and recombine. The remaining charge carriers can be extracted under a reverse bias voltage ramp after an adjustable delay time (t_{del}) determining their lifetime (photo-CELIV). The calculation of the mobility using the photo-CELIV technique shown in Figure 10.10 assumes bulk generation of charge carriers, which limits the active layer thickness to approximately 300–400 nm depending on the absorption coefficient at the excitation wavelength.

10.4.2 Charge transport in conjugated polymers

Conjugated polymers can be viewed as one-dimensional semiconductors, in which the semiconducting properties are attributed to the extended π electron systems formed by the π_z electrons of the σ-conjugated backbone. Although microwave conductivity techniques [54, 55], showed that the on-chain mobility of conjugated polymers can reach very high values, the macroscopic transport properties are controlled by orders of magnitude slower interchain hopping processes. The solubility and processability of conjugated polymers are achieved by attaching side chains to the conjugated backbone. Naturally, the length of the insulating side chain affects the interchain electronic coupling, thereby influencing mobility, as is evidenced by the decreasing charge carrier mobility in a series of regioregular polyalkylthiophenes with increasing side chain length [56]. Furthermore, the regularity of the side chain attachment plays an important role in the solid state morphology and ordering. For example, regioregular poly(3-hexylthiophene), in which the solubilizing side chains are attached in a regular pattern, forms crystalline phases [57], while regiorandom poly(3-hexylthiophene-2,5-diyl (P3HT) is typically amorphous. The electronic properties of these two materials are also quite different. Regioregular P3HT exhibits one of the highest mobilities among conjugated polymers in the FET structure, meanwhile mobility in regiorandom P3HT is three to four orders of magnitude lower [58, 59].

The effect of side chain substitution on charge carrier mobility was investigated for a series of alkoxy-PPVs in the work of Martens *et al.* [60]. The charge carrier mobility measured by space charge limited current measurements of the symmetrically substituted $OC_{10}C_{10}$-PPV is one order of magnitude higher than the asymmetrically substituted, regiorandom OC_1C_{10}-PPV (also known as MDMO-PPV). From the temperature and electric field dependence of the mobility studies it was concluded that increased on-chain and interchain disorder is mainly responsible for the lower mobility of regiorandom MDMO-PPV.

Based on the above arguments, it is expected that increasing the regioregularity of conjugated polymers is viable way to improve their charge carrier mobility. Lutsen *et al.* [61] have recently synthesized a soluble regioregular MDMO-PPV polymer based on the sulfinyl precursor route [62]. The charge transport properties of this regioregular polymer were compared to the commercially available regiorandom MDMO-PPV using the ToF technique.

10.4.2.1 Regioregular MDMO-PPVs

A series of MDMO-PPV copolymers has been synthesized by mixing two stereoisomers of the same monomer (monomer A) and (monomer B) via the sulfinyl precursor route as illustrated Scheme 10.2. The solubility of the MDMO-PPV copolymers is greatly reduced as the ratio of either of the isomers is increased above 80 %, which is attributed to aggregation of the conjugated chains in solution. The improved tendency for aggregation is further supported by X-ray power diffraction (XRD) measurements, which showed a clearly distinguished reflection peak in the MDMO-PPV powders at around 3 ° as the regioregularity increases [63]. The exact position of this peak was determined by small angle X-ray scattering measurements, and it corresponds to the repeating distance between the polymer backbones separated by the side chains (∼28 Å).

Since the preparation of devices for mobility measurements requires very soluble materials, the conjugated polymer resulting from the polymerization of the 70:30 weight % mixture of monomer A and monomer B (referred to as '70:30 MDMO-PPV') was selected, and its charge transport and photovoltaic properties were compared to regiorandom MDMO-PPV (referred to as 'RRa-MDMO-PPV').

Figure 10.11 shows the room temperature mobility values determined by the ToF technique for both polymers with various film thicknesses. The mobility of 70:30 MDMO-PPV is approx. 3.5 times larger at all measured electric fields for all film thicknesses as compared to RRa-MDMO-PPV. The electric field dependence of the mobility has been determined for 70:30 MDMO-PPV and RRa-MDMO-PPV at various temperatures, and analyzed in the framework of disorder formalism developed by Bässler and coworkers to describe the temperature and electric field dependence of mobility in a charge transport medium with superimposed energetic and positional disorder [64]:

$$\mu(T, E) = \mu_0 \exp\left[-\frac{2}{3}\left(\frac{\sigma}{kT}\right)^2\right] \exp\left\{C\left[\left(\frac{\sigma}{kT}\right)^2 - \Sigma^2\right]E^{1/2}\right\} \tag{10.7}$$

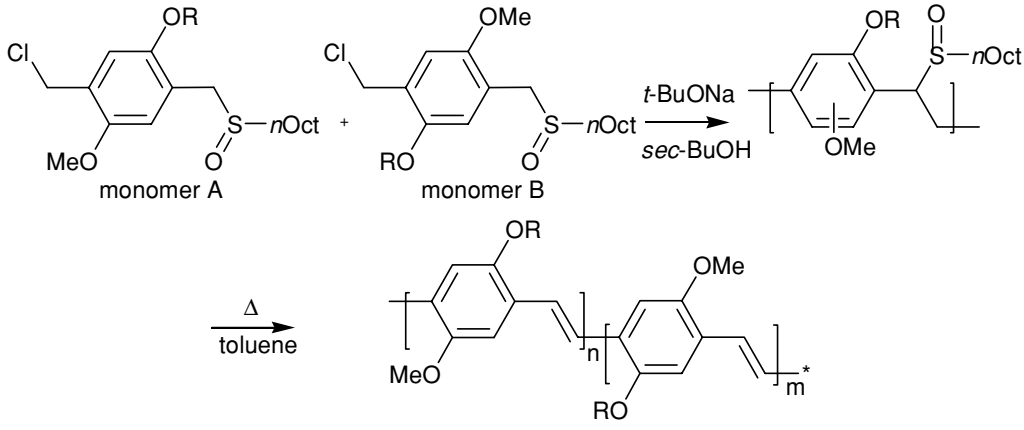

Scheme 10.2 Synthesis of the regioregular MDMO-PPV copolymers via the sulfinyl precursor route.

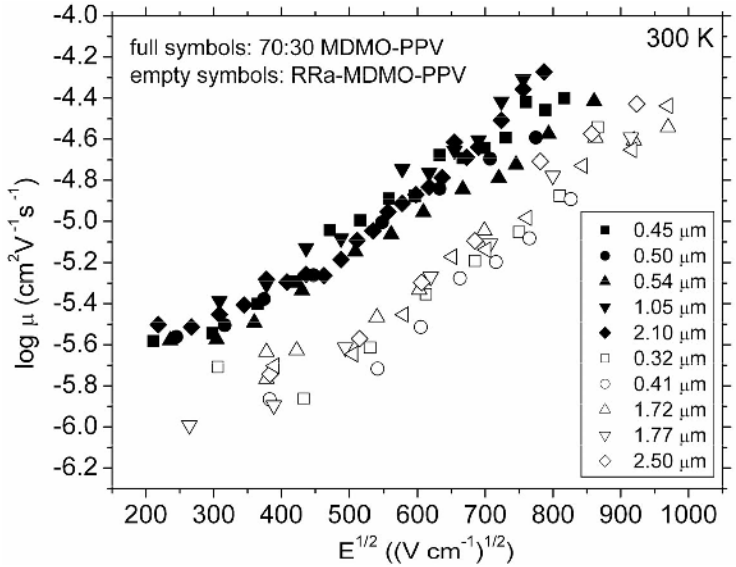

Figure 10.11 Charge carrier mobility determined by the ToF technique for various thicknesses of 70:30 MDMO-PPV (solid symbols) and RRa-MDMO-PPV (empty symbols) at room temperature. Reprinted from Figure 2 with permission from A.J. Mozer *et al.*, *J. Phys. Chem. B*, **108**, 5235, Novel regiospecific MDMO-PPV copolymer with improved charge transport for bulk heterojunction solar cells. Copyright (2004) by the American Chemical Society.

where σ [eV] is the width of the Gaussian density of states, Σ is a parameter characterizing positional disorder, μ_0 [$cm^2\ V^{-1}\ s^{-1}$] is a prefactor mobility in the energetically disorder free system, E [$V\ cm^{-1}$] is the electric field, and C is a fit parameter.

The logarithm of the mobility extrapolated to zero electric field (log $\mu(E = 0)$) is plotted versus inverse temperature squared in Figure 10.12. The ordinate intercepts of the lines determine the value of the prefactor mobility (μ_0), while the slope is related to the width of the Gaussian distribution of density of states (σ). The parameters μ_0, σ, and C of Equation (10.7) have been calculated, and are summarized in Table 10.1. The fitting constant C was calculated from the slope of the field dependence of mobility versus $(\sigma/kT)^2$. The prefactor mobility is one order of magnitude higher for 70:30 MDMO-PPV and σ also increases slightly. Interestingly, the zero field mobility of 70:30 MDMO-PPV in Figure 10.12 is only higher above ~ 230 K, but decreases faster due to the larger energetic disorder, and eventually becomes lower than that of RRa-MDMO-PPV below 230 K. Furthermore, the field dependence of mobility characterized by parameter C is slightly larger for 70:30 MDMO-PPV. The determined value of C agrees well within a factor of only two with the theoretically calculated value ($C = 2.9 \times 10^{-4}$ [$(cm\ V^{-1})^{1/2}$]).

The prefactor mobility is primarily governed by the amount of electronic coupling between neighboring transport sites, which is a sensitive function (exponential) of the intersite distance. The slight increase in the energetic disorder of 70:30 MDMO-PPV may originate from lower lying energy states of ordered nanoaggregates as compared to the amorphous matrix acting as energetic deep traps for overall charge transport. The above model is schematically illustrated in

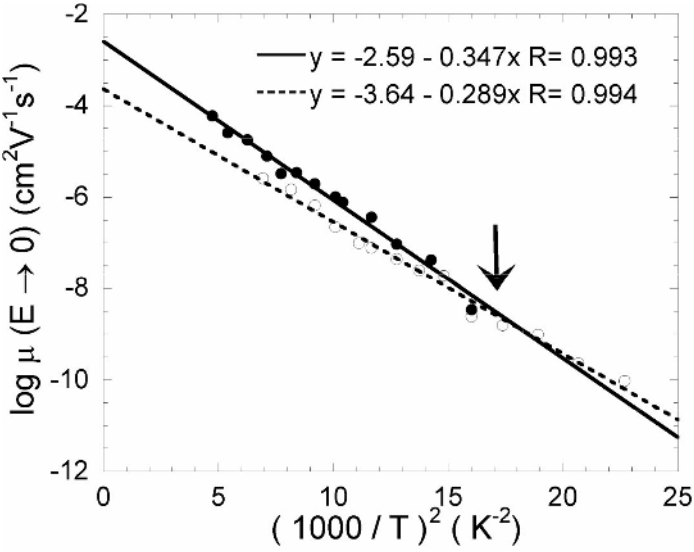

Figure 10.12 Logarithm of the zero field mobility versus $(1000/T)^2$ for 70:30 MDMO-PPV (solid symbols) and RRA-MDMO-PPV (empty symbols). The lines represent linear fit of the data. Reprinted from Figure 5 with permission from A.J. Mozer *et al.*, *J. Phys. Chem. B*, **108**, 5235, Novel regiospecific MDMO-PPV copolymer with improved charge transport for bulk heterojunction solar cells. Copyright (2004) by the American Chemical Society.

Figure 10.13. The first diagram illustrates charge motion in the amorphous regions of the films, in which the energy of the transport sites experience a statistically varying environment. The second diagram, on the other hand, depicts regions where the conjugated chains are partially aligned with better interchain interactions. These regions are expected to create preferential paths ('highways') for the charge carriers, therefore increasing the mobility. Since the more extended electronic wavefunctions of the ordered regions are thought to be more polarizable, the extent of the dipole induced interactions are expected to be higher in the ordered regions of the films, which lowers the site energy. Since the ordered regions in our model are embedded in an amorphous matrix, these lower lying energy states may act as traps and broaden the distribution of the density of states. Charge hopping at the end of these 'highways' (indicated by the large arrow in Figure 10.13) requires sufficient thermal energy and/or tilting of the barrier by an external electric field. Therefore, at high temperatures and high electric fields,

Table 10.1 Determined values of μ_{RT} (room temperature mobility), and parameters μ_0 (prefactor mobility), σ (energetic disorder) and C of the disorder formalism (Equation 10.7)

Sample	$\mu_{RT}[cm^2V^{-1}s^{-1}]$	$\mu_0[cm^2V^{-1}s^{-1}]$	σ[meV]	$C[(cmV^{-2})^{1/2}]$
70:30 MDMO-PPV	2.8×10^{-5}	2.6×10^{-3}	115	1.54×10^{-4}
RRa-MDMO-PPV	0.85×10^{-5}	0.22×10^{-3}	105	1.35×10^{-4}

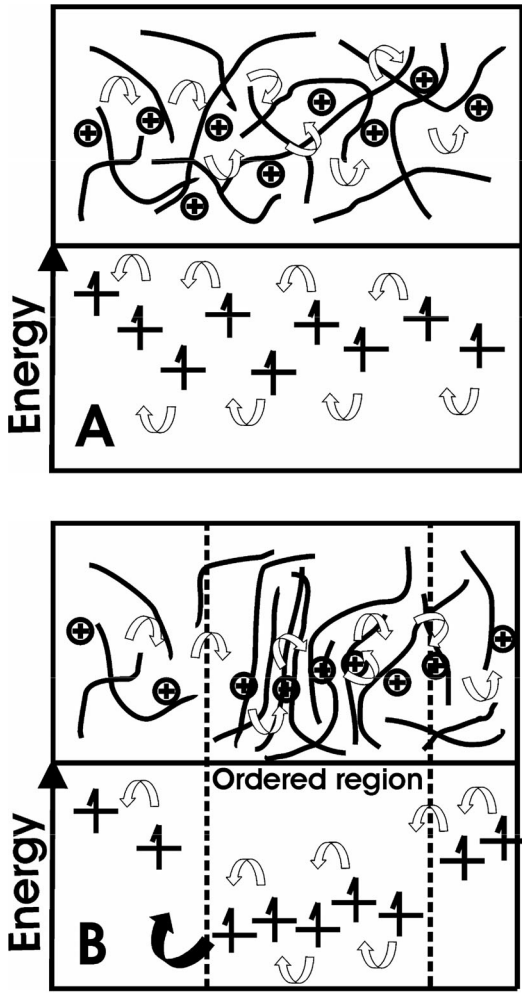

Figure 10.13 Schematic illustration of charge motion and the energy of hopping sites in cases where the conjugated chains are randomly oriented (top) and where local ordering of the conjugated chains takes place (bottom). Reprinted from Scheme 2 with permission from A.J. Mozer *et al*., *J. Phys. Chem. B*, **108**, 5235, Novel regiospecific MDMO-PPV copolymer with improved charge transport for bulk heterojunction solar cells. Copyright (2004) by the American Chemical Society.

films of 70:30 MDMO-PPV with better interchain packing show higher charge carrier mobility. At low temperatures and low electric fields, however, charges might be trapped at the lower lying energy sites of the aligned regions hence causing stronger temperature and electric field dependence of mobility.

The proposed increased interchain interactions between the conjugated chains of the regioregular MDMO-PPV is supported by the increased tendency to aggregate as the regioregularity increases. Further indication is given by recent thermally stimulated luminescence (TSL) studies [63].

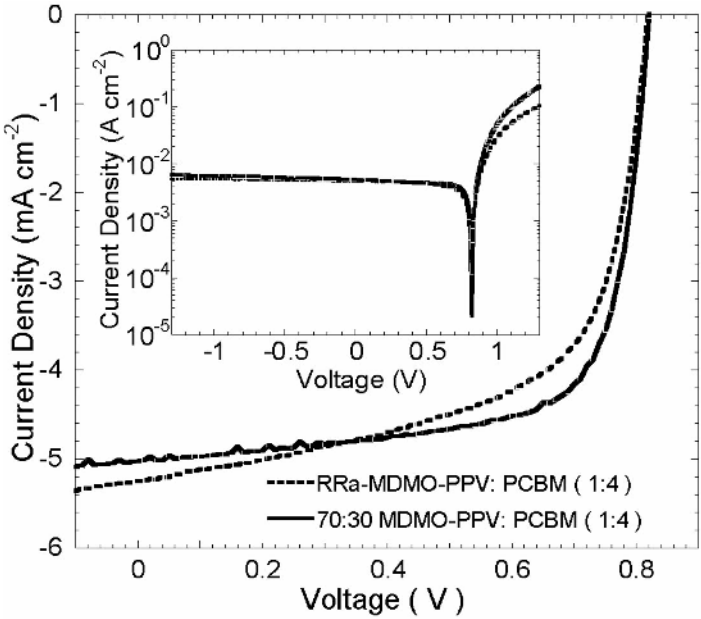

Figure 10.14 Current density versus voltage curves for bulk heterojunction solar cells based on the 1:4 ratio of 70:30 MDMO-PPV (solid line) or RRa-MDMO-PPV (broken line) and PCBM under simulated AM1.5 conditions. Reprinted from Figure 8 with permission from A.J. Mozer *et al.*, *J. Phys. Chem. B*, **108**, 5235, Novel regiospecific MDMO-PPV copolymer with improved charge transport for bulk heterojunction solar cells. Copyright (2004) by the American Chemical Society.

Bulk heterojunction solar cells based on the 1:4 weight ratio mixture of 70:30 MDMO-PPV:PCBM have been fabricated and compared to RRa-MDMO-PPV in Figure 10.14. Although the short-circuit current and open-circuit voltage are quite similar for the two devices, 70:30 MDMO-PPV shows a slightly increased power conversion efficiency due to the very high (0.7) FF. The current density versus voltage curves have been analyzed using a simple one diode model according to Equation (10.8). The equivalent circuit of the one diode model is displayed in Figure 10.15.

$$j = j_0 \left[\exp\left(\frac{V - jR_{\mathrm{rs}}}{n\mathrm{k}T} \right) - 1 \right] + \frac{V - jR_{\mathrm{rs}}}{R_{\mathrm{p}}} - j_{\mathrm{sc}} \tag{10.8}$$

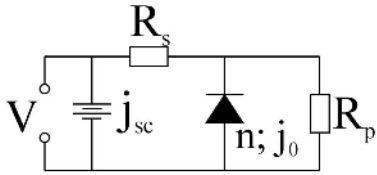

Figure 10.15 Equivalent circuit model of a heterojunction solar cell. The short circuit current is represented by a current source.

Table 10.2 Photovoltaic performance of bulk heterojunction solar cells and the parameters of Equation (10.8) obtained by numerical calculation

	J_{sc} mA cm^{-2}	V_{oc} V	FF	$\eta_{AM1.5}$ %	J_0 mA cm^{-2}	R_s Ω cm^{-2}	R_P Ω cm^{-2}	n
70:30 MDMO-PPV	5.0	0.8	0.71	2.65	6×10^{-7}	1.3	2150	1.9
RRa-MDMO-PPV	5.25	0.82	0.61	2.5	6×10^{-7}	3	950	2

where j [A cm^{-2}] and V [V] are the current density and voltage values, j_0 [A cm^{-2}] is the reverse bias dark current, R_s [Ω cm^{-2}] is the series resistance, R_p [Ω cm^{-2}] is the parallel resistance and j_{sc} [A cm^{-2}] is the short circuit current density under illumination. The equation 10.8 has been numerically solved, and the parameters obtained by the best fit are summarized in Table 10.2. The series resistance of the bulk heterojunction photovoltaic devices based on 70:30 MDMO-PPV is reduced by a factor of 2.3 as compared to RRa-MDMO-PPV, which may be attributed to the improved charge carrier mobility of the photogenerated charge carriers as is suggested by the ToF mobility studies.

10.4.2.2 Regioregular poly(3-hexylthiophene)

A more drastic improvement of the performance of bulk heterojunction solar cells was recently achieved using regioregular poly(3-hexylthiophene) (P3HT) as an electron donor [65, 66]. These devices show incident photon to converted electron efficiency (IPCE) close to 75 % at the absorption maximum, which indicates nearly 100 % collection of the photogenerated charges at the electrodes in a thin 100–200 nm device. Charge carrier mobility in P3HT is often investigated in an FET structure; however detailed temperature and electric field dependence of mobility studies by ToF was not available. This is partially due to the large dark conductivity of poly(alkylthiophenes) attributed to oxygen [67, 68] or moisture [69] doping when exposed to air, which generally limits the applicability of ToF due to the screening of the electric field.

We have investigated the temperature and electric field dependence of mobility in low conductivity, purified samples of P3HT by the ToF technique. The low conductivity of the samples is achieved by the purification procedure described in [70]. In addition, the devices were prepared, stored and characterized in a dry, inert atmosphere. The photocurrent transients recorded at 293 and 180 K in regioregular P3HT are shown at various applied voltages in Figure 10.16. The 3.6 μm thick sample sandwiched between ITO and Al electrodes was illuminated by 3 ns laser pulses at 532 nm excitation wavelength through the aluminum side. The transit time of charge carriers indicated by the arrows decreases at every temperature as the voltage increases. Moreover, the photocurrent transients are nondispersive with a plateau and a rather short post transit time tail at around room temperature. At lower temperatures (<180 K) the plateau region gradually disappears and the post transient tail is inhomogenously broadened. Dispersive transients indicate that the relaxation of the charge carriers photogenerated at random energies towards quasi-equilibrium is not completed prior to arrival at the exit electrode, or correspondingly, the spatial inhomogenous spreading of the packet of charge carriers is comparable to the device thickness.

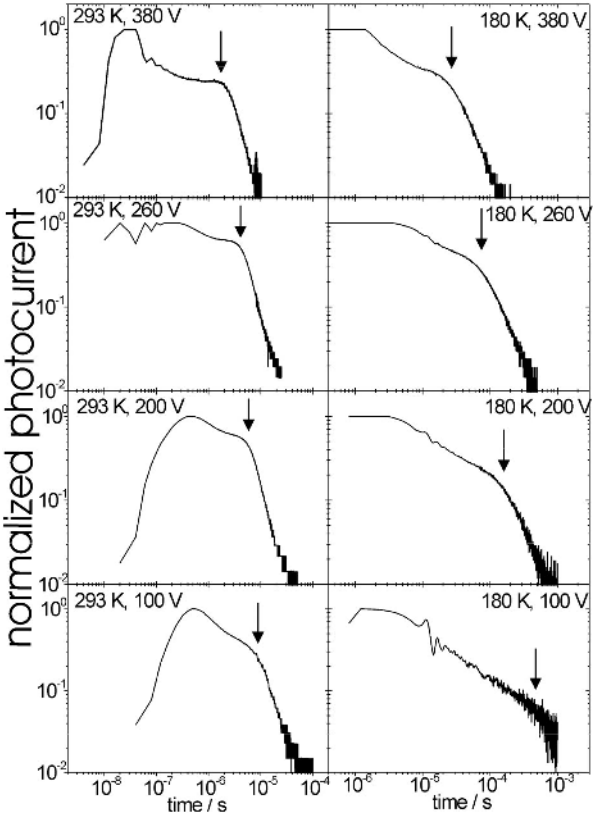

Figure 10.16 ToF transients of a low dark conductivity, 3.6 μm thick P3HT sample sandwiched between ITO and Al recorded at various applied voltages and at 293 and 180 K. The transit time is indicated by the arrows.

The calculated mobility versus the electric field squared is plotted in Figure 10.17. The mobility follows a $\log \mu \propto \beta E^{1/2}$ Poole–Frenkel like dependence at lower temperatures, but β turns to negative at higher temperatures (>250 K). Such negative electric field dependence of mobility at higher temperatures has been observed in various organic semiconductors, such as molecularly doped polymers [71, 72], molecular glasses [73] and a polysilane derivative [74], yet this is the first time it has been clearly observed in a conjugated, semiconducting polymer [75]. The occurrence of negative electric field dependence of mobility is understood to be the effect of superimposed energetic and positional disorder as expressed by Equation 10.7. With increasing temperature Σ exceeds σ/kT, and the sign of the field dependence ($(\sigma/kT)^2 - \Sigma^2$) is reversed. The slope of the field dependence versus $(\sigma/kT)^2$ is plotted in Figure 10.18. Clearly, β turns to negative at a $(\sigma/kT)^2$ value of 10, and $\Sigma = 3.3$ is calculated. The σ value was determined from the linear regime in the logarithm mobility extrapolated to zero electric field versus inverse temperature squared ($\log \mu(E = 0)$ versus T^{-2}) plot as shown in the inset of Figure 10.18. The deviation from the predicted linear dependence at lower temperatures may be attributed to a nondispersive to dispersive transition, since Equation 10.7 is considered valid only for charge transport under quasi-equilibrium conditions. Since the time to reach the quasi-equilibrium level during transport is increasing faster (as $t_{rel}/t_0 = 10\exp(1.07(\sigma/kT))^2$)

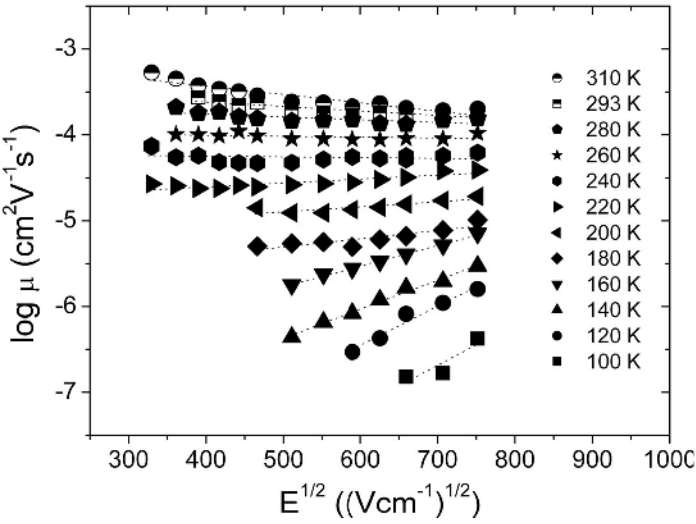

Figure 10.17 Electric field dependence of ToF mobility at various temperatures. The lines represent linear fits of the data. Reprinted from *Chemical Physics Letters*, **389**, A. Mozer and N. Sariciftci, Negative electric field dependence of charge carrier drift mobility in conjugated, semiconducting polymers, 438–442. Copyright (2004) with permission from Elsevier.

than the transit time with decreasing temperature, a nondispersive to dispersive (ND→D) transition is predicted [76]. The occurrence of an ND→D transition is also indicated by the change in the shape of the photocurrent transients in Figure 10.16.

The ND→D transition is intrinsic to the ToF technique, in which the charge carriers are photogenerated at random energies by the strongly absorbed laser flash. On the other hand, an ND→D transition should be absent in the CELIV technique, in which the charge carriers are in thermodynamic equilibrium prior to extraction due to the principally different mode of charge

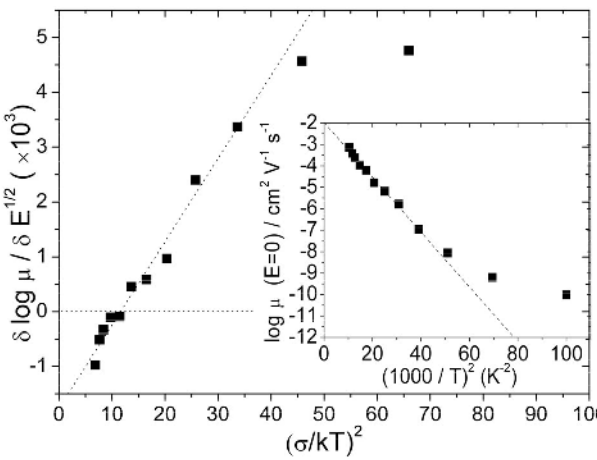

Figure 10.18 Slope of the electric field dependence of mobility ($\delta \log \mu / \delta E^{1/2}$) versus $(\sigma/kT)^2$. The lines represent linear fits between 310 and 180 K.

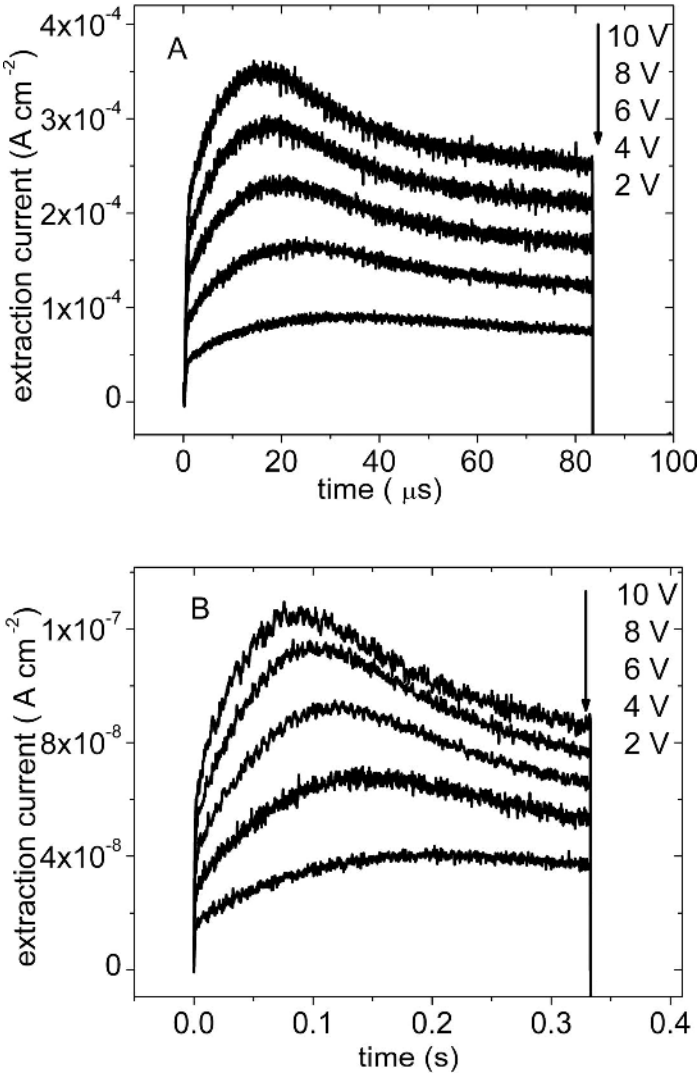

Figure 10.19 Recorded CELIV curves of a 1.3 μm P3HT sample sandwiched between ITO and Al at various maximum applied voltages and at (A) 293 K and (B) 130 K. Reprinted Figure 7 with permission from A. Mozer, N. Sariciftci, A. Pivrikas, R. Osterbacka, G. Juska, L. Brassat and H. Bässler, *Phys. Rev. B*, 71, Charge carrier mobility in regioregular poly (3-hexylthiophene) probed by transient conductivity techniques: A comparative study, 035214, 2005. Copyright (2004) by the American Physical Society.

generation. The reversible oxygen or moisture doping observed in regioregular P3HT provides the opportunity to determine the temperature and electric field dependence of mobility using the CELIV technique in the same P3HT samples exposed to air [77].

Figure 10.19 shows CELIV transients measured for a 1.3 μm P3HT sample sandwiched between ITO and Al electrodes by applying reverse bias voltage pulses with varying U_{max} A, 293 K, and B, 130 K. The time to reach the maximum of the extraction current (t_{max})

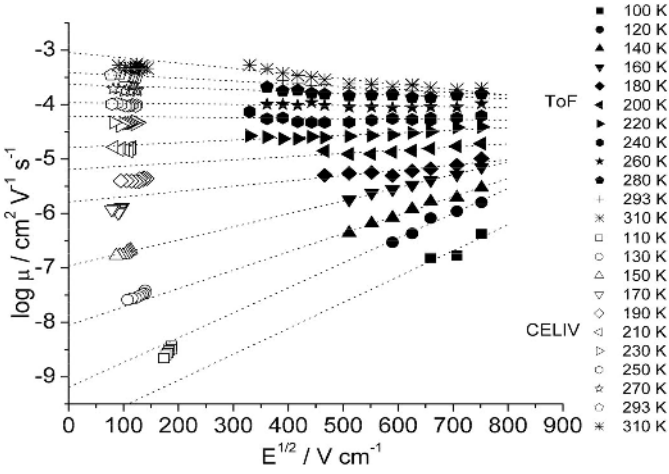

Figure 10.20 Electric field dependence of mobility of doping induced carriers (samples exposed to air, CELIV technique) and photogenerated charge carriers (low conductivity samples, ToF technique). Reprinted Figure 9 with permission from A. Mozer, N. Sariciftci, A. Pivrikas, R. Osterbacka, G. Juska, L. Brassat and H. Bässler, *Phys. Rev. B*, **BT9158**, Charge carrier mobility in regioregular poly (3-hexylthiophen) probed by transient conductivity techniques: A comparative study, 2004. Copyright (2004) by the American Physical Society.

shifts to shorter times by increasing the maximum of the voltage pulses, and features a strong temperature dependence. The electric field varies constantly during extraction, and it can be averaged as $E = (A \times t_{\max})/d$. The temperature and electric field dependence of mobility values determined by the CELIV technique as well ToF technique is plotted versus $E^{1/2}$ in Figure 10.20. The overall agreement obtained by these principally different techniques, and particularly, the negative electric field dependence of mobility at temperatures above ~250 K implies that it is not an experimental artifact of the ToF technique caused by either dark conductivity or the effect of charge carrier diffusion. The latter effect was claimed to cause negative electric field dependence in a ToF experiment at weak electric fields due to the diffusive motion of charge carriers [78], which is absent in the CELIV technique due to the equilibrium distribution of charge carriers before extraction. The observed negative electric field dependence, therefore, is presumed to be intrinsic to the P3HT samples studied, and can be explained as the influence of positional disorder on the motion of charge carriers.

Simulations showed that fluctuation of the intersite electronic coupling creates faster routes as well dead ends for charge carriers executing their random walk. At high electric fields, detour routes around a difficult site are gradually eliminated forcing the carriers to make difficult jumps, therefore decreasing mobility.

In Figure 10.21, $\log \mu(E = 0)$ versus $(1000/T)^2$ is plotted for ToF and CELIV measurements for samples with various thicknesses. The CELIV mobility follows the prediction of Equation 10.7 over the entire measured temperature range. The ToF technique, on the other hand, tends to yield higher values at lower temperatures, which may be attributed to the above mentioned ND→D transition at around 180 K. The mobility values measured by both techniques correspond well at higher temperatures indicating that the mode of charge generation does not alter the charge transport properties, at least in this small charge concentration regime [77].

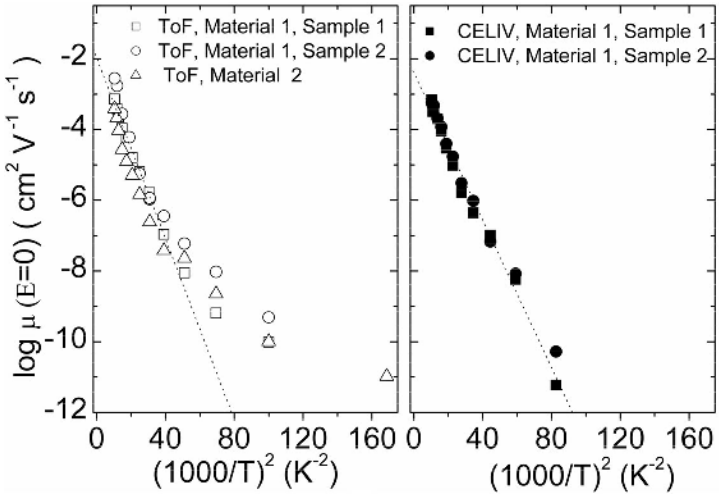

Figure 10.21 Temperature dependence of the mobility extrapolated to zero electric field for several samples determined by the CELIV technique (solid symbols) and the ToF technique (empty symbols). Reprinted Figure 11 with permission from A. Mozer, N. Sariciftci, A. Pivrikas, R. Osterbacka, G. Juska, L. Brassat and H. Bässler, *Phys. Rev. B*, 71, Charge carrier mobility in regioregular poly (3-hexyltiophene) probed by transient conductivity techniques: A comparative study, 035214, 2005. Copyright (2004) by the American Physical Society.

10.4.3 Charge transport and recombination in bulk heterojunction solar cells

10.4.3.1 Photo-CELIV technique

Charge carrier mobility in bulk heterojunction solar cells has been studied using a ToF technique [79], or calculated from the transfer characteristics of an FET [80]. These experiments showed that the electron mobility (PCBM phase) and the hole mobility (conjugated polymer phase) in the photoactive blend is fairly balanced, which is counterintuitive to experiments performed on the pristine materials. Space charge limited current measurements showed that the mobility of injected holes in the pure MDMO-PPV thin films is several orders of magnitude lower than injected electrons in PCBM thin films [81]. Recent ToF studies performed on MDMO-PPV:PCBM 1:2 blends concluded that the mobility is unbalanced, the electron mobility being at least two orders of magnitude higher than the hole mobility [82]. The apparent discrepancy between the above examples shows that the straightforward experimental determination of mobility using currently available methods is problematic.

The ToF technique is limited to a rather thick sample ($\sim$1 μm at the absorption maximum), which is at least 3–10 times higher than the optimum thickness of bulk heterojunction solar cells requires. Both mobility and solar cell performance may exhibit strong morphology dependence. The morphology may vary depending on the film preparation conditions, e.g. concentration of the solution, drying time, etc. In addition, the concentration of charge carriers in a ToF technique is limited to 10 % of the capacitive charge, which limits the concentration in a typical device configuration to $n \sim 10^{14}$ cm^{-3}. This concentration is at least 2–3 orders of magnitude lower than the charge carrier concentration in a solar cell under AM1.5 illumination conditions.

Mobility values obtained by FET measurements seem to fit better the predictions of numerical simulations of current density and voltage curves of bulk heterojunction solar cells [83]. Nevertheless, the FET technique, in which the motion of electric field induced charge carriers is monitored near the surface of an insulator, also has serious limitations. First of all, the mobility obtained by the FET technique may also be strongly dependent on the morphology of the film. The morphology of the phase separated network near the insulator may be altogether different to the bulk. Moreover, the direction of the motion of charges in an FET is perpendicular to the direction of motion in a sandwich type photodiode, and the presence of anisotropy of mobility, such as observed in [84] could not be distinguished *a priori*.

The recombination dynamics of the photogenerated charge carriers in a blend of electron donor and electron acceptor materials have been studied by various optical techniques, such as light induced electron spin resonance (LESR) [20], photoinduced absorption (PIA) [85], photoinduced reflection/absorption (PIRA) [86] and transient absorption (TA) [22]. In these optical techniques, the charge carrier induced changes of the absorption of the films ($-\Delta T$) is monitored either by a modulation technique (PIA) or followed in a time resolved experiment (TA). The recorded signals are often very dispersive, especially at low temperatures and low frequencies or long timescales. Although the nature of these long lived photoexcitations is of practical importance, optical techniques cannot directly distinguish between mobile or deeply trapped, immobile charge carriers. For example, transient absorption experiments on the blend MDMO-PPV:PCBM showed power law decay of the $-\Delta T/T$ signal with an exponent of $\alpha = 0.4$ in the μs to ms timescale [87]. Power law decay indicates a broad distribution of lifetimes due to strong dispersion. Moreover, optical techniques are typically applied on films without electrodes; therefore operational devices cannot be easily studied.

Information on the recombination processes in operational bulk heterojunction solar cells is often obtained indirectly by the incident light intensity dependence of the short circuit current [31]. Scaling factors close to one indicate that the short circuit current is not limited by second order recombination processes, such as bimolecular (nongeminate) recombination. In the latter case, an exponent close to 0.5 is expected. Unfortunately, this experiment provides little information on any first order recombination processes, which scale linearly with light intensity. Examples of such first order recombination processes are trap mediated (quasi-) monomolecular recombination or recombination due to accumulated space charge.

Both the charge carrier mobility (μ) and the lifetime (τ) can be determined *simultaneously* in operational bulk heterojunction solar cells using the photo-CELIV technique. In this technique, charge carriers are photogenerated by a short laser flash, followed by either extraction of the charge carriers under the intrinsic electric field and/or recombination. The intrinsic field may be compensated by the application of a forward bias offset voltage minimizing the external photocurrent and forcing recombination (flat band conditions). The remaining charge carriers can be extracted by a linearly increasing voltage pulse after a certain delay time (t_{del}).

The three different stages of the photo-CELIV technique are illustrated in Figure 10.22. Initially (stage 1), charge carriers are photogenerated via photoinduced charge transfer. During the second, equilibration, stage, the charge carriers recombine under zero electric field conditions. The zero field condition is achieved by compensating the built-in field of the device by the application of a forward bias offset voltage (U_{offset}). Simultaneously, the charge carriers may relax towards the tail states of the distribution. In stage 3, the remaining charge carriers are extracted by a reverse bias voltage pulse. From the time the extraction current reaches its maximum, the mobility is calculated, and by calculating the concentration of extracted charge carriers versus delay time, the recombination kinetics are studied.

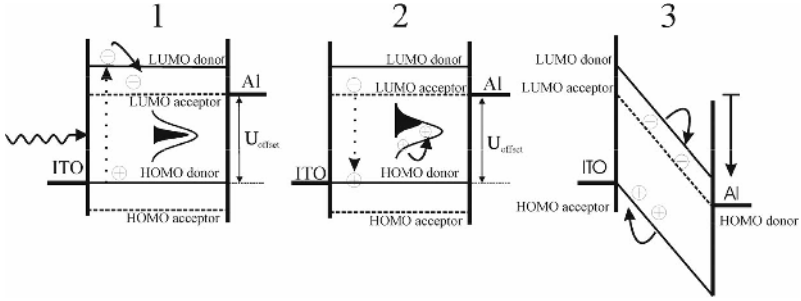

Figure 10.22 The three main stages of the photo-CELIV technique: (1) charge generation, (2) charge recombination and energy relaxation, (3) charge extraction.

The effect of U_{offset} on the recorded photo-CELIV curves is shown in Figure 10.23. The sandwich type device used for this study is a typical of a bulk heterojunction solar cell (ITO/PEDOT-PSS/MDMO-PPV:PCBM 1:4/Al). The MDMO-PPV was prepared by the sulfinyl precursor route according to Scheme 10.2. The device (active layer thickness 265 nm) exhibited a power conversion efficiency of 1.8 % as determined using a calibrated solar simulator unit. The absorption coefficient of the photoactive layer at 532 nm excitation wavelength is $4 \times 10^4\ \text{cm}^{-1}$, corresponding to OD $\sim$1, and thus bulk generation of charge carriers. The delay time (t_{del}) between the light pulse and the linearly increasing voltage ramp ($A = 4$ V/10 μs) was 5μs.

Under short-circuit conditions (0 V applied voltage), most of the photogenerated carriers exit the device prior to the reverse bias voltage pulse under the influence of the built-in field of the device (photoconductivity). Applying 0.9 V, the photocurrent upon photoexcitation is minimal (flat band conditions), and the extraction current due to the reverse bias voltage pulse is increased. Finally, the photocurrent turns to negative when $U_{\text{offset}} > 0.9$ V, which indicates that the charge carrier motion is electric field driven. In addition, significant injection current flows, shown by the nonzero offset current, and the injected charge carriers are also extracted under the CELIV pulse together with the photogenerated ones. Experimentally, U_{offset} is chosen close to the built-in field of the device, yet slightly smaller in order to avoid dark injection, which complicates the evaluation of the photo-CELIV curves. It is worth mentioning that the built-in field could be more precisely compensated in devices without PEDOT-PSS hole

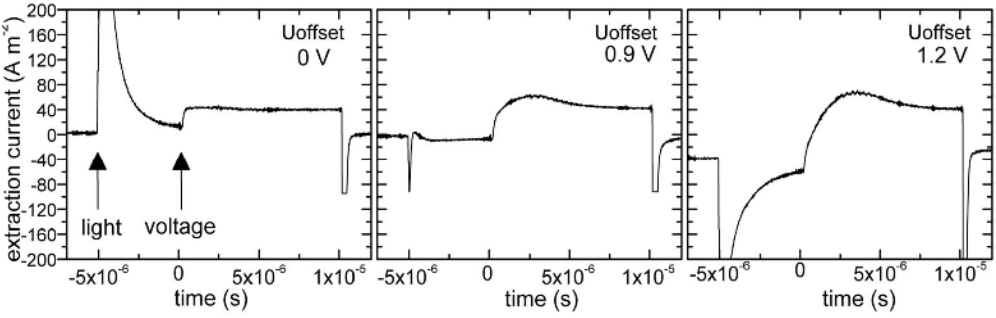

Figure 10.23 The effect of U_{offset} on the recorded photo-CELIV curves at 5 μs fixed delay time.

injection layers. Nevertheless, no significant difference in the mobility values and its time and concentration dependence has been observed between devices with and without PEDOT-PSS.

Figure 10.24 A, shows recorded photo-CELIV curves as a function of delay time. The U_{offset} during these measurements was 0.75 V. The maximum of the extraction current decreases with increasing delay time, indicative of charge carrier recombination, and $t_{\max}$ shifts slightly to longer times [88]. The extraction current at all applied delay times decreases till the capacitance current step value, which shows that the majority of the photoinduced charge carriers are extracted in these photo-CELIV experiments. In Figure 10.24 B, the photo-CELIV transients recorded at varying light intensities and at fixed 5 μs delay time are shown. The maximum of the extraction current is constant until the threshold light intensity of $\sim 1\ \mu\text{J cm}^{-2}\ \text{pulse}^{-1}$ and decreases constantly at lower light intensities. In contrast to the results obtained by the delay time dependent measurements, $t_{\max}$ at various light intensities remains almost constant. Finally, in Figure 10.24 C, the photo-CELIV curves recorded as a function of the maximum of the applied voltage pulse ($U_{\max}$) at fixed 15 μs delay time and fixed light intensity are shown. The $t_{\max}$ value is shorter when the maximum of the voltage pulses is increased indicating the voltage (field) dependence of the mean charge carrier velocity.

The obtained mobility values are plotted versus delay time in Figure 10.25 A. The mobility decreases with t_{del} until 10 μs, and remains almost unchanged for longer delays. In Figure 10.25 B, the mobility is plotted as a function of the concentration of charge carriers obtained by the intensity dependent photo-CELIV measurement. Clearly, the rather strongly increasing mobility at short time delays in Figure 10.25 A, does not correspond to the weak concentration dependence of the mobility. Figure 10.25 C shows the voltage (field) dependence of the mobility for two different delay times: (i) 5 μs and (ii) 15 μs. The electric field dependence of the mobility at longer delay times is a typical positive dependence, as expected for an amorphous semiconductor, yet at short delays it shows an anomalous negative dependence. This comparison shows that the time dependent mobility at shorter time delays is not related to the charge carrier concentration (occupational density) dependence of the mobility alone, which is expected to play a role in disordered semiconductors due to e.g., trap filling effects. It may be related to time dependent energy relaxation of the charge carriers at short timescales.

The number of extracted charge carriers is calculated by integrating the extraction current transients, and plotted versus the delay time in Figure 10.26. The concentration decay is fitted using a time dependent (dispersive) recombination as [89]:

$$\frac{\mathrm{d}n}{\mathrm{d}t} = -\beta(t)n^2 \tag{10.9}$$

where $\beta(t)$ is the time dependent recombination coefficient. The time dependence of $\beta(t)$ can be directly calculated using the data shown in Figure 10.26 as:

$$\beta(t) = -\frac{\mathrm{d}n/\mathrm{d}t}{n^2} \tag{10.10}$$

and the values are shown in the inset of Figure 10.26. A power law time decay following $\beta(t) = \beta_0 t^{-(1-\gamma)}$, where γ characterizes dispersion, is found. The solution to Equation 10.9 by substituting $\beta(t) = \beta_0 t^{-(1-\gamma)}$ yields

$$n(t) = \frac{n(0)}{1 + (t/\tau^{\gamma})} \tag{10.11}$$

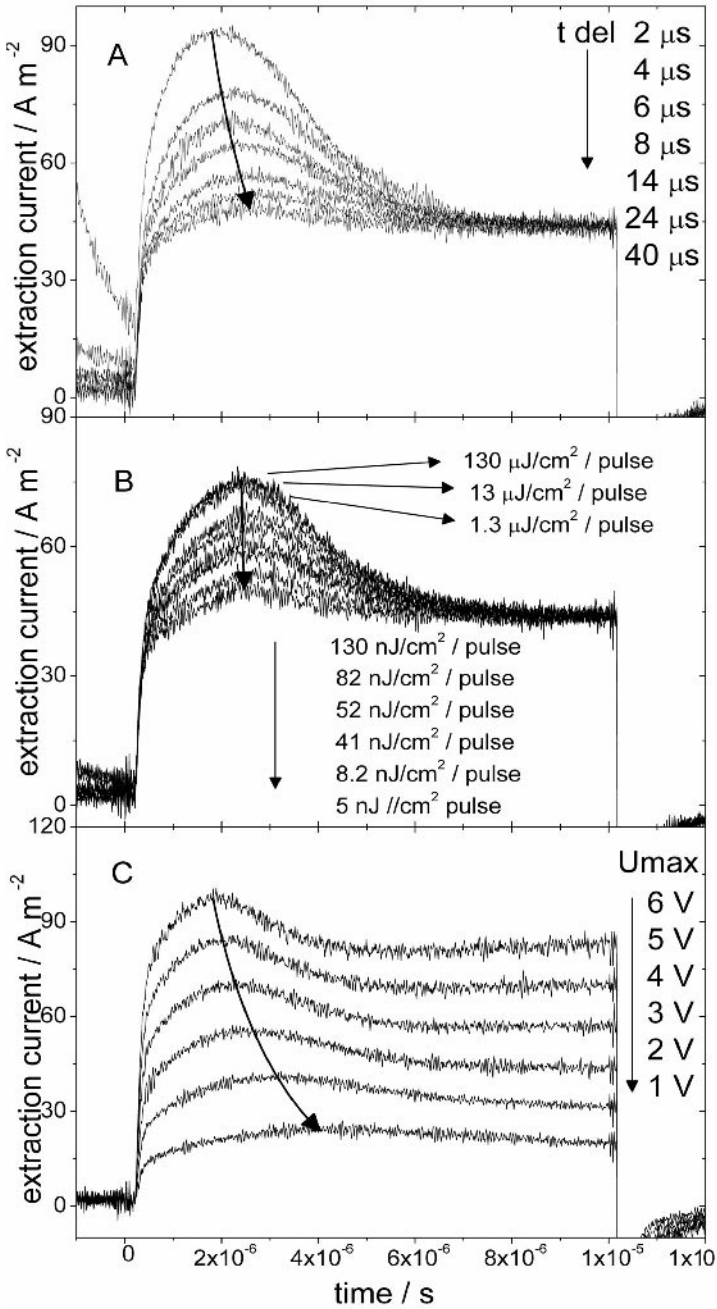

Figure 10.24 Recorded photo-CELIV curves as a function of (A) delay time, (B) incoming light intensity at fixed 5 μs delay time, and (C) applied maximum voltage (U_{max}) at fixed 15 μs delay time and fixed light intensity. Reprinted with permission from Figure 1, A. Mozer *et al*., *Applied Physics Letters*, **86**, 112104, Charge transport and recombination in bulk heterojunction solar cells studied by the photoinduced charge extraction in linearly increasing voltage technique. Copyright (2005), American Institute of Physics.

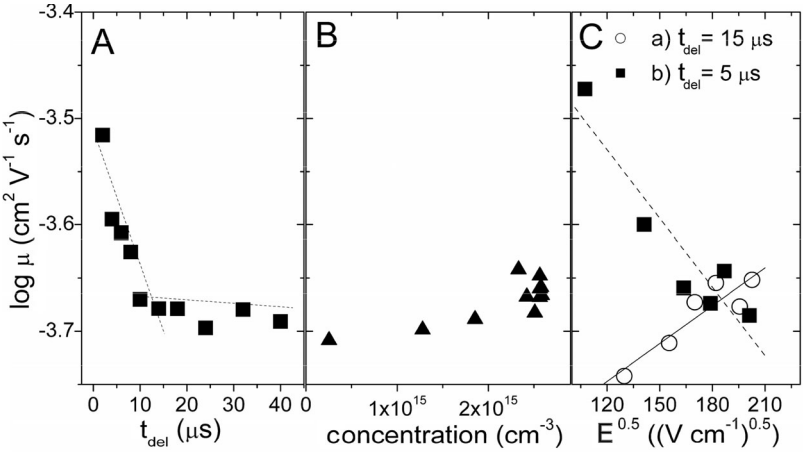

Figure 10.25 The mobility values versus (A) delay time, (B) charge carrier concentration determined from intensity dependent measurement, and (C) square root of the electric field at (a) 15 μs delay time and (b) 5 μs delay time.

where $n(0)$ is the initial ($t = 0$) concentration of photogenerated charge carriers and $\tau_B = (\gamma/(\mathrm{n}(0)\beta_0))^{1/\gamma}$ is an 'effective' bimolecular lifetime. The obtained fitting parameters are $\beta(0) = 6 \times 10^{-11}\,\mathrm{cm}^3\,\mathrm{s}^{-1}$, $\tau_B = 1.7 \times 10^{-6}\,\mathrm{s}$, $n(0) = 9 \times 10^{15}\,\mathrm{cm}^{-3}$ and $\gamma = 0.99$, the latter indicating a nondispersive (time independent) bimolecular recombination at room temperature. Temperature dependent photo-CELIV studies showed that the nondispersive bimolecular recombination law observed at room temperature ($\gamma = 0.99$) changes significantly when the temperature is decreased, e.g., $\gamma = 0.47$ at 120 K indicative of a highly dispersive (time

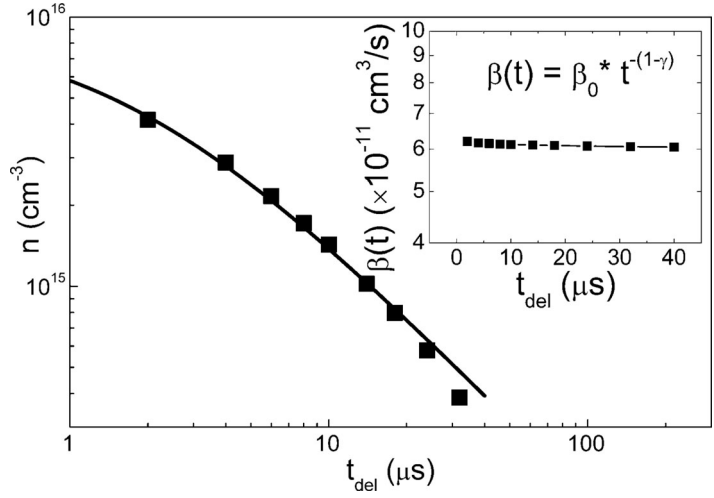

Figure 10.26 Concentration of the charge carriers calculated from delay time dependent photo-CELIV curves versus t_{del}. The inset shows $\beta(t)$ versus t_{del} calculated according to Equation (10.5).

dependent) recombination process. Moreover, the 'effective' bimolecular lifetime τ_B decreases with increasing temperature, ($\sim$319 μs at 120 K) clearly showing that the recombination is a thermally activated process with calculated activation energy of $\sim$80 meV.

The simultaneous determination of mobility (μ) and lifetime (τ) using the photo-CELIV technique gives surprising results when compared to previous transient absorption (TA) studies. The different recombination law calculated from delay time dependent photo-CELIV as compared to the TA measurement of Refs. [22, 87] might arise from the fact that the concentration decay of all the charge carriers including the immobile ones is probed in the transient absorption experiment. On the other hand, only charge carriers with reasonable mobility are extracted in the photo-CELIV experiment. From the end of the extraction pulse extraction current it is estimated that the number of unextracted, deeply trapped charge carriers is minimal at room temperature. The important question, therefore, is whether these long living charge carriers can also be extracted under operational conditions in bulk heterojunction solar cells, or in other words, whether the $\mu\tau$ product determined by the photo-CELIV technique can properly describe the measured current density versus voltage curves of bulk heterojunction solar cells.

10.4.3.2 Thickness dependence of MDMO-PPV/PCBM solar cells

It is expected that the short circuit current of bulk heterojunction solar cells will rise with increasing active layer thickness due to increased absorption. According to $d \geq l_d = \mu \times \tau \times E$, on the other hand, electrical losses due to recombination are expected when the thickness of the active layer exceeds the drift distance of the charge carriers, where $E = V_{oc}/d$ is the electric field. Based on these arguments, the thickness dependence of the short circuit current of bulk heterojunction solar cells should give an estimate of the drift distance of the charge carriers, which can then be compared to the $\mu\tau$ product determined by the photo-CELIV technique.

As has been emphasized, the performance of bulk heterojunction solar cells is morphology dependent; therefore the proposed comparative study can only be meaningful if the morphology of the active layer is unchanged by changing the thickness of the active layer. The same solution of MDMO-PPV:PCBM 1:4 by weight (chloroform, 0.5 mg polymer /ml solution^{-1}) was used to prepare all the active layers of bulk heterojunction solar cells with varying thickness by varying the spin speed during the spin coating between 1000 and 6000 rpm. It was expected that this procedure would be more suitable for the proposed thickness dependent experiment as compared to e.g. varying the total concentration, or the type of solvent. The thickness of the active layer was around 125 nm at 6000 rpm, and increased nonlinearly to 280 nm at 1000 rpm. The films prepared at lower spin speeds were somewhat less uniform, therefore eight devices were measured, and the results averaged. The average power conversion efficiency of the bulk heterojunction solar cells versus the film thickness of bulk heterojunction solar cells is shown in Figure 10.27. It is around 2.5 % using a thickness of 125 nm, which drops to approx. 1.7 % when the thickness is increased to 280 nm.

The parameters I_{sc}, V_{oc}, FF, and the injection current density at +2 V are shown in Figure 10.28 for comparison. The average short circuit current density increases slightly as the thickness of the active layer is increased. It is maximal at 225 nm ($\sim$6 mA cm^{-2}), and drops slightly when at 280 nm. The measured V_{oc} is constant $\sim$800 mV for all active thickness. The fill factor, on the other hand, drops constantly from 0.6 to 0.4 as the thickness of the active layer is increased, which corresponds nicely to the reduced injection current density at +2 V. From

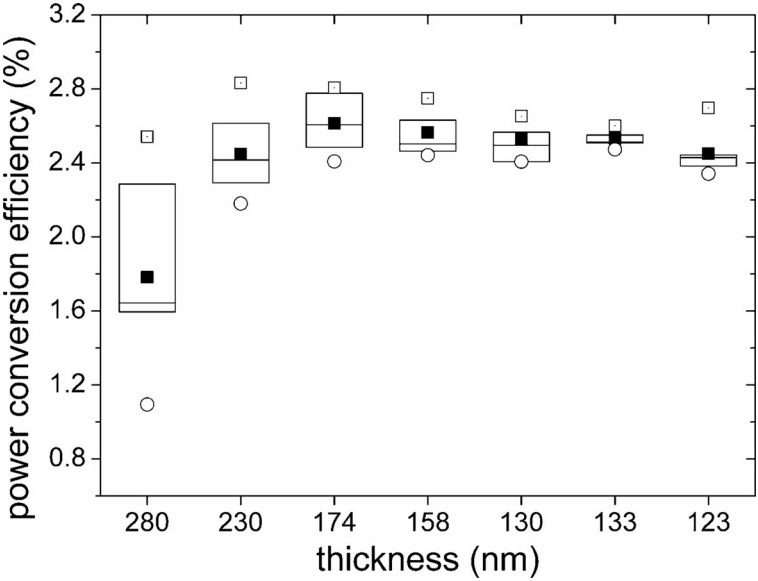

Figure 10.27 The average power conversion efficiency versus the thickness of MDMO-PPV:PCBM bulk heterojunction solar cells.

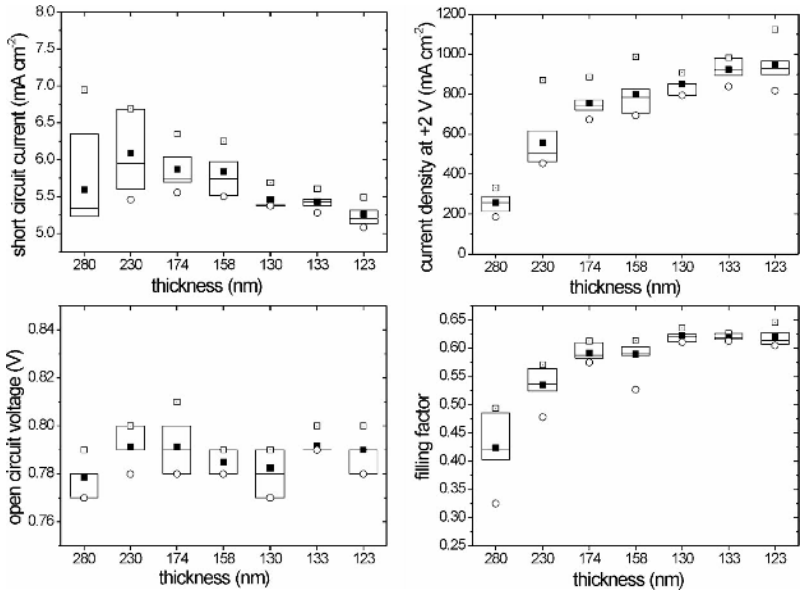

Figure 10.28 The average short circuit current density, injection current density at +2 V, open circuit voltage, and fill factor of MDMO-PPV:PCBM bulk heterojunction solar cells versus the spin speed during spin coating.

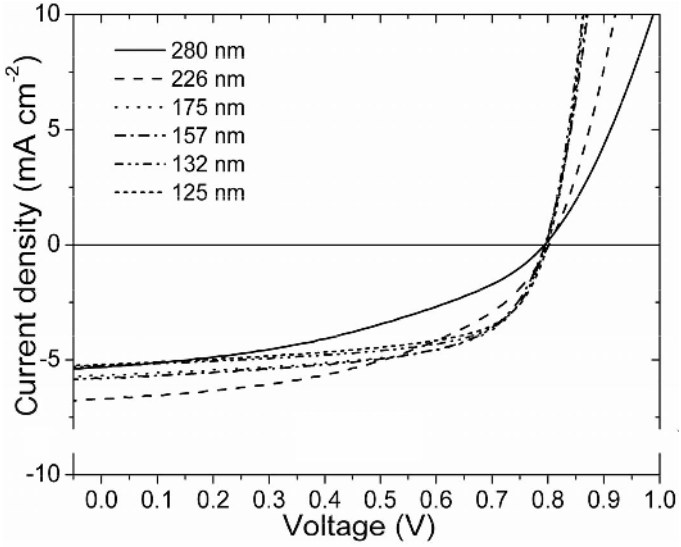

Figure 10.29 The current density versus voltage curves of bulk heterojunction solar cells with varying active layer thicknesses under illumination.

this data it is evident that the drop in the power conversion efficiency at 280 nm is attributed mainly to the reduced fill factor, which decreases more strongly than the slight increase in the short circuit current.

The current density versus voltage curves under illumination are shown in Figure 10.29 for various active layer thicknesses. The *J-V* curves are analyzed by a modified version of a simple one diode model shown in Figure 10.15, which has been introduced by Schilinsky *et al*. to explain the illumination intensity dependent *J-V* curves of bulk heterojunction solar cells based on P3HT:PCBM blends [83]. The model takes into account the applied voltage (V_{ext}) dependent reduction of the charge collection of the photogenerated charge carriers at the electrodes. As the external voltage is increased towards flat band conditions, the electric field in the device is reduced. Accordingly, only charge carriers created within the reduced drift distance $l_d = \mu \times \tau \times (V_{oc} - V_{ext})/d$ will contribute to the short circuit photocurrent. In other words, the photocurrent (j_{sc}) in Equation 10.8 is not constant, but depends on the applied voltage (V_{ext}).

Important predictions from that model are that the sign of the photocurrent changes when $V_{ext} > V_{oc}$, and that the short circuit current is reduced when V_{ext} is raised towards V_{oc}. Moreover, the high fill factor of devices with 125 nm thickness indicates that only a small electric field $(V_{oc} - V_{ext})/d$ is sufficient to collect most of the photogenerated charge carriers from the whole device (the photocurrent reaches $\sim$5 mA cm^{-2} at 0.6 V, corresponding to 0.2 V/125 nm electric field). On the other hand, the photocurrent density steadily increases to $\sim$0.1 V (corresponding to a field of 0.7 V/226 nm) when the device thickness is increased to 226 nm.

The $\mu\tau$ product of the long lived charge carriers can be calculated using the values determined by the photo-CELIV technique as:

$$\mu \times \tau_B = 2 \times 10^{-4}\,\mathrm{cm^2\,V^{-1}\,s^{-1}} \times 2 \times 10^{-6}\,\mathrm{s} = 4 \times 10^{-8}\,\mathrm{cm^2 V^{-1}} \qquad (10.12)$$

The maximum thickness of the active layer ($d < l_d$) can be calculated as:

$$d = \sqrt{\mu \times \tau \times V_{oc}} = \sqrt{8 \times 10^{-10}\,\mathrm{cm^2\,V^{-1}} \times 0.8\,\mathrm{V}} = 180\,\mathrm{nm} \tag{10.13}$$

According to this result, the majority of the long lived charge carriers can be collected at external electrodes in photovoltaic devices not exceeding 180 nm active layer thickness, or in other words, bimolecular recombination of the charge carriers should not limit the short circuit current of the device. The calculated drift distance of the long lived (μs–ms) charge carriers is in accordance with experimental observations shown in Figure 10. 28, which implies that the majority of long lived charge carriers can be collected in operational bulk heterojunction solar cells. These conclusions are also supported by observed light intensity dependence of the short circuit photocurrent density [31]. Scaling factors close to one are typically observed, which indicates that the short circuit current is not limited by second order recombination processes, such as bimolecular recombination.

10.5 SUMMARY

The science and technology of bulk heterojunction solar cells has been reviewed focusing on advanced characterization techniques and novel materials. The various microscopic (AFM, SEM, TEM) tools are used to study the correlation between the nanomorphology of the interpenetrating phase separated network and the efficiency of the bulk heterojunction solar cells. The various mobility techniques (FET, space charge limited current measurements, and ToF) are used to determine the charge carrier mobility within the bicontinous interpenetrating network of the electron and hole transporting phases. It has been demonstrated that the novel technique of photoinduced charge carrier extraction by linearly increasing voltage (photo-CELIV) can be used to simultaneously determine the charge carrier mobility (μ) and lifetime (τ) in bulk heterojunction solar cells. The obtained $\mu\tau$ values are in accordance with the observed performance of bulk heterojunction solar cells with varying active layer thicknesses. The major limitation of bulk heterojunction solar cells is their limited absorption in the lower energy part of the solar spectra. Recent developments including low bandgap polymers and light absorbing fullerenes have been summarized.

ACKNOWLEDGMENTS

The authors acknowledge the financial support of the European Commission within the framework of Research and Training Network (RTN) project EUROMAP (Contract No. HPRN-CT-2000-00127). A. J. M. thanks the group of D. Vanderzande for the MDMO-PPV polymers, and R. Österbacka, G. Juska, and A. Pivrikas for their valuable help with the mobility setups. H. Bässler and V. Arkhipov are gratefully acknowledged for their help with charge transport studies. Finally, we thank A. Cravino, C. Winder, and H. Hoppe for their suggestions during preparation of this manuscript.

REFERENCES

[1] C. W. Tang, Two-layer organic photovoltaic cell, *Appl. Phys. Lett.*, **48**, 183 (1986).

[2] M. Pope and C. E. Swenberg, *Electronic Processes in Organic Crystals and Polymers*, 2nd edn, Oxford University Press, New York, 1999.

[3] *Primary photoexcitations in conjugated polymers: Molecular excitons versus semiconductor band model*, N. S. Sariciftci (Ed.), World Scientific, Singapore, 1997.

[4] V. I. Arkhipov and H. Bässler, Exciton dissociation and charge photogeneration in pristine and doped conjugated polymers, *Phys. Stat. Sol. (a)*, **201**, 1152 (2004).

[5] P. Peumans, A. Yakimov, and S. R. Forrest, Small molecular weight organic thin film photodetectors and solar cells, *J. Appl. Phys.*, **93**, 93 (2003).

[6] H. Shirakawa, E. J. Louis, A. G. MacDiarmid, C. K. Chiang, and A. J. Heeger, Synthesis of electrically conducting organic polymers: halogen derivatives of polyacetylene (CH)x, *J. Chem. Soc. Chem. Comm.*, **16**, 578 (1977).

[7] A. J. Heeger, S. Kivelson, J. R. Schrieffer, and W. P. Su, Solitons in Conductive Polymers, *Rev. Mod. Phys.*, **60**, 781 (1988).

[8] H. Tomozawa, D. Braun. S. Phillips, and A. J. Heeger, Metal-polymer Schottky barriers on cast films of soluble poly(3-alkylthiophenes), *Synth. c. Metals*, **22**, 63 (1987).

[9] R. H. Friend, R. W. Gymer, A. B. Holmes, J. H. Burroughes, R. N. Marks, C. Taliani, D. D. C. Bradley, D. A. Dos Santos, J. L. Brédas, M. Lögdlund, and W. R. Salaneck, Electroluminescence in conjugated polymers, *Nature*, **121**, 397 (1999).

[10] Z. Bao, A. Dodabalapur, and A. J. Lovinger, Soluble and processable poly(3-hexylthiophene) for thin films field-effect applications with high mobility, *Appl. Phys. Lett.*, **69**, 4108 (1996).

[11] C. J. Brabec, N. S. Sariciftci, and J. C. Hummelen, Plastic Solar Cells, *Adv. Funct. Mater.*, **11**, 15 (2001).

[12] N. S. Sariciftci, L. Smilowitz, A. J. Heeger, and F. Wudl, Photoinduced electron transfer from a conducting polymer to buckminsterfullerene, *Science*, **258**, 1474 (1992).

[13] H. W. Kroto, A. W. Allaf, and S. P. Balm, C_{60}: Buckminsterfullerene, *Chem. Rev.*, **91**, 1213 (1991) and refs. therein.

[14] N. S. Sariciftci and A. J. Heeger, Photophysics, charge separation and device applications of conjugated polymer/fullerene composites in *Handbook of Conductive Molecules and Polymers*, H. S. Nalwa (Ed.), Vol. 1, John Wiley & Sons Ltd, 1997.

[15] L. Smilowitz, N. S. Sariciftci, R. Wu, C. Gettinger, A. J. Heeger, and F. Wudl, Photoexcitation spectroscopy of conducting-polymer-C_{60} composites: photoinduced electron transfer, *Phys. Rev. B*, **47**, 13835 (1993).

[16] X. Wei, Z. V. Vardeny, N. S. Sariciftci, and A. J. Heeger, Absorption-detected magnetic-resonance studies of photoexcitations in conjugated-polymer/C_{60} composites, *Phys. Rev. B*, **53**, 2187 (1996).

[17] B. Kraabel, D. McBranch, N. S. Sariciftci, D. Moses, and A. J. Heeger, Ultrafast spectroscopic studies of photoinduced electron transfer from semiconducting polymer to C_{60}, *Phys. Rev. B*, **50**, 1854 (1994).

[18] C. J. Brabec, G. Zerza, G. Cerullo, S. De Silvestri, S. Luzzati, J. C. Hummelen, and N. S. Sariciftci, Tracing photoinduced electron transfer process in conjugated polymer/fullerene bulk heterojunctions in real time, *Chem. Phys. Lett.*, **340**, 232 (2001).

[19] C. H. Lee, G. Yu, D. Moses, K. Pakbaz, C. Zhang, N. S. Sariciftci, A. J. Heeger, and F. Wudl, Sensitization of the photoconductivity of conducting polymers by C_{60}: photoinduced electron transfer, *Phys. Rev. B*, **48**, 15425 (1993).

[20] V. Dyakonov, G. Zoriniants, M. Scharber, C. J. Brabec, R. A. J. Janssen, J. C. Hummelen, and N. S. Sariciftci, Photoinduced charge carriers in conjugated polymer–fullerene composites studied with light-induced electron-spin resonance, *Phys. Rev. B*, **59**, 8019 (1999).

[21] N. A. Schultz, M. C. Scharber, C. J. Brabec, and N. S. Sariciftci, Low-temperature recombination

kinetics of photoexcited persistent charge carriers in conjugated polymer/fullerene composite films, *Phys. Rev. B*, **64**, 245210 (2001).
[22] I. Montanari, A. F. Nogueira, J. Nelson, J. R. Durrant, C. Winder, M. A. Loi, and N. S. Sariciftci, Transient optical studies of charge recombination dynamics in a polymer/fullerene composite at room temperature, *Appl. Phys. Lett.*, **81**, 3001 (2002).
[23] N. S. Sariciftci, D. Braun, C. Zhang, V. I. Srdanov, A. J. Heeger, G. Stucky, and F. Wudl, Semiconducting polymer-buckminsterfullerene hererojunctions: diodes, photodiodes, and photovoltaic cells, *Appl. Phys. Lett.*, **62**, 585 (1993).
[24] S. E. Shaheen, C. J. Brabec, N. S. Sariciftci, F. Padinger, T. Fromherz, and J. C. Hummelen, 2.5 % efficient organic plastic solar cells, *Appl. Phys. Lett.*, **78**, 841 (2001).
[25] C. J. Brabec, F. Padinger, J. C. Hummelen, R. A. J. Janssen, and N. S. Sariciftci, Realization of large area flexible fullerene – conjugated polymer photocells: a route to plastic solar cells, *Synth. Metals*, **102**, 861 (1999).
[26] S. E. Shaheen, R. Radspinner, N. Peyghambarian, and G. E. Jabbour, Fabrication of bulk heterojunction plastic solar cells by screen printing, *Appl. Phys. Lett.*, **79**, 2996 (2001).
[27] T. Ishikawa, M. Nakamura, K. Fujita, and T. Tsutsui, Preparation of organic bulk heterojunction photovoltaic cells by evaporative spray deposition from ultradilute solution, *Appl. Phys. Lett.*, **84**, 2424 (2004).
[28] M. Al-Ibrahim, H. K. Roth, and S. Sensfuss, Efficient large area polymer solar cells on flexible substrates, *Appl. Phys. Lett.*, **85**, 1481 (2004).
[29] I. D. Parker, Carrier tunneling and device characteristics in polymer light-emitting diodes, *J. Appl. Phys.*, **75**, 1656 (1994).
[30] I. H. Campbell, T. W. Hagler, D. L. Smith, and J. P. Ferraris, Direct measurement of conjugated polymer electronic excitation energies using metal–polymer–metal structures, *Phys. Rev. Lett.*, **76**, 1900 (1996).
[31] I. Riedel, J. Parisi, V. Dyakonov, L. Lutsen, D. Vanderzande, and J. C. Hummelen, Effect of temperature and illumination on the electrical characteristics of polymer-fullerene bulk-heterojunction solar cells, *Adv. Func. Mater.*, **14**, 38 (2004).
[32] 4.1 eV determined by cyclic voltammetry (CV) in solution, see ref. 34.
[33] 4.3 eV determined by Electrochemical Voltage Spectroscopy (EVS) in solid films, see ref. 34.
[34] David Mühlbacher, Comparative study of the electrochemical and the optical band gap of organic semiconductors, MSc Thesis, Johannes Kepler University Linz, Austria (2003).
[35] C. J. Brabec, A. Cravino, D. Meissner, N. S. Sariciftci, T. Fromherz, M. T. Rispens, L. Sanchez, and J. C. Hummelen, Origin of the open circuit voltage of plastic solar cells, *Adv. Func. Mater.*, **11**, 374 (2001).
[36] C. M. Heller, I. H. Campbell, D. L. Smith, N. N. Barashkov, and J. P. Ferraris, Chemical potential pinning due to equilibrium electron transfer at metal–C60-doped polymer interfaces, *J. Appl. Phys.*, **81**, 3227 (1997).
[37] V. D. Mihailetchi, P. W. M. Blom, J. C. Hummelen, and M. T. Rispens, Cathode dependence of the open circuit voltage of polymer: fullerene bulk heterojunction solar cells, *J. Appl. Phys.*, **94**, 6849 (2003).
[38] A. Gadisa, M. Svensson, M. R. Anderson, and O. Inganäs, Correlation between oxidation potential and open-circuit voltage of composite solar cells based on blends of polythiophenes–fullerene derivative, *Appl. Phys. Lett.*, **84**, 1609 (2004).
[39] T. Martens, J. D'Haen, T. Munters, Z. Beelen, L. Goris, J. Manca, M. D'Olieslaeger, D. Vanderzande, L. De Schepper, and R. Andriessen, Disclosure of the nanostructure of MDMO-PPV:PCBM bulk hetero-junction organic solar cells by a combination of SPM and TEM, *Synth. Metals*, **138**, 243 (2003).
[40] J. K. J. van Duren, X. Yang, J. Loos, C. W. T. Bulle-Lieuwma, A. B. Sieval, J. C. Hummelen, and R. A. J. Janssen, Relating the morphology of poly(p-phenylene vinylene)–methanofullerene blends to solar-cell performance, *Adv. Funct. Mater.*, **14**, 425 (2004).

[41] H. Hoppe, M. Niggemann, C. Winder, J. Kraut, R. Hiesgen, A. Hinsch, D. Meissner, and N. S. Sariciftci, Nanoscale morphology of conjugated polymer–fullerene-based bulk-heterojunction solar cells, *Adv. Funct. Mater.*, **14**, 1005 (2004).
[42] T. Martens, Z. Beelen, J. D'Haen, T. Munters, L. Goris, J. Manca, M. D'Olieslaeger, D. Vanderzande, L. De Schepper, and R. Andriesssen, Morphology of MDMO-PPV:PCBM bulk heterojunction organic solar cells studied by AFM, KFM, and TEM, *Proc. of SPIE*, Vol. 4801 (2002).
[43] A. Cravino and N. S. Sariciftci, Double-cable polymers for fullerene based organic optoelectronic applications, *J. Mater. Chem.*, **12**, 1931 (2002), and refs. therein.
[44] A. Cravino and N. S. Sariciftci, Molecules as bipolar conductors, *Nature Mat.*, **2**, 360 (2003).
[45] C. Winder and N. S. Sariciftci, Low bandgap polymers for photon harvesting in bulk heterojunction solar cells, *J. Mater. Chem.*, **14**, 1077 (2004).
[46] J. Roncali, Synthetic principles for bandgap control in linear conjugated systems, *Chem. Rev.*, **97**, 173 (1997).
[47] M. M. Murray and A. B. Holmes, Poly(arylene vinylene)s – synthesis and applications in semiconducting devices, in *Semiconducting Polymers: Chemistry, Physics and Engineering*, G. Hadziioannou and P. F. van Hutten (Eds.), Wiley VCH, Weinheim 2000.
[48] H. Fuchigami, A. Tsumura, and H. Koezuka, Polythienylenevinylene thin film transistor with high carrier mobility, *Appl. Phys. Lett.*, **63**, 1372 (1993).
[49] M. S. Dresselhaus, G. Dresselhaus, and P. C. Eklund, *Science of Fullerenes and Carbon Nanotubes*, Academic Press, USA (1996).
[50] C. Waldauf, P. Schilinsky, J. Hauch, and C. J. Brabec, Material and device concepts for organic photovoltaics: towards competitive efficiencies, *Thin Solid Films*, **451–452**, 503 (2004).
[51] H. Scher and E. W. Montroll, Anomalous transit-time dispersion in amorphous solids, *Phys. Rev. B*, **12**, 2455 (1975).
[52] G. Juška, K. Genevičius, K. Arlauskas, R. Österbacka, and H. Stubb, Charge transport at low electric fields in π-conjugated polymers, *Phys. Rev. B*, **65**, 233208 (2002).
[53] G. Juška, K. Arlauskas, M. Viliūnas, and J. Kočka, Extraction current transients: a new method of study of charge transport in microcrystalline silicon, *Phys. Rev. Lett.*, **84**, 4946 (2000).
[54] G. H. Gelinck, J. M. Warman, and G. J. Staring, Polaron pair formation, migration, and decay on photoexcited poly(phenylenevinylene) chains, *J. Phys. Chem.*, **100**, 5485 (1996).
[55] H. Bässler, Charge transport in random organic semiconductors, in *Semiconducting Polymers: Chemistry, Physics and Engineering*, G. Hadziioannou and P. F. van Hutten, (Eds.), Wiley VCH, Weinheim 2000.
[56] S. Nagamatsu, S. S. Pandey, W. Takashima, T. Endo, M. Rikukawa, and K. Kaneto, Photocurrent transport in processable poly(3-alkylthiophene), *Synth. Metals*, **121**, 1563 (2001).
[57] T.-A. Chen, X. Wu, and R. D. Rieke, Regiocontrolled synthesis of poly(3-alkylthiophenes) mediated by zinc: their characterization and solid-state properties, *J. Am. Chem. Soc.*, **117**, 233 (1995).
[58] H. Sirringhaus, P. J. Brown, R. H. Friend, M. M. Nielsen, K. Bechgaard, B. M. W. Langeveld-Voss, A. J. H. Spiering, R. A. J. Janssen, E. W. Meijer, P. Herwig, and D. M. de Leeuw, Two-dimensional charge transport in self-organized, high mobility conjugated polymers, *Nature*, **401**, 685 (1999).
[59] Z. Bao, A. Dodabalapur, and A. J. Lovinger, Soluble and processable poly(3-hexylthiophene) for thin films field-effect applications with high mobility, *Appl. Phys. Lett.*, **69**, 4108 (1996).
[60] H. C. F. Martens, P. W. M. Blom, and H. F. M. Schoo, Comparative study of hole transport in poly(p-phenylene vinylene) derivatives, *Phys. Rev. B*, **61**, 7489 (2000).
[61] L. Lutsen, P. Adriaensens, H. Becker, A. J. van Breemen, D. Vanderzande, and J. Gelan, New synthesis of a soluble high molecular weight poly(arylene vinylene): poly[2-methoxy-5-(3,7-dimethyloctyloxy)-p-phenylene vinylene]. Polymerization and device Properties, *Macromolecules*, **32**, 6517 (1999).
[62] A. J. Mozer, P. Denk, M. C. Scharber, H. Neugebauer, N. S. Sariciftci, P. Wagner, L. Lutsen, and D. Vanderzande, Novel regiospecific MDMO-PPV copolymer with improved charge transport for bulk heterojunction solar cells, *J. Phys. Chem. B*, **108**, 5235 (2004).

[63] A. J. Mozer, P. Denk, M. C. Scharber, H. Neugebauer, N. S. Sariciftci, P. Wagner, L. Lutsen, D. Vanderzande, A. Kadashchuk, R. Staneva, and R. Resel, Novel regiospecific MDMO-PPV polymers with improved charge transport properties for bulk heterojunction solar cells, *Synth. Metals*, **153**, 81 2005.

[64] H. Bässler, Charge transport in disordered organic photoconductors, *Phys. Stat. Sol. (b)*, **175**, 15 (1993).

[65] F. Padinger, R. S. Rittberger, and N. S. Sariciftci, Effects of postproduction treatment on plastic solar cells, *Adv. Funct. Mater.*, **13**, 1 (2003).

[66] P. Schilinsky, C. Waldauf, and C. J. Brabec, Recombination and loss analysis in polythiophene based bulk hererojunction photodetectors, *Appl. Phys. Lett.*, **81**, 3885 (2002).

[67] Z. Bao, A. Dodabalapur, and A. J. Lovinger, Soluble and processable regioregular poly(3-hexylthiophene) for thin film field-effect transistor applications with high mobility, *Appl. Phys. Lett.*, **69**, 4108 (1996).

[68] M. S. A. Abdou, F. P. Orfino, Z. W. Xie, M. J. Deen, and S. Holdcroft, Reversible charge transfer complexes between molecular oxygen and poly(3-alkylthiophene)s, *Adv. Mater.*, **6**, 838 (1994).

[69] S. Hoshino, M. Yoshida, S. Uemura, T. Kodzasa, N. Takada, T. Kamata, and K. Yase, Influence of moisture on device characteristics of polythiophene-based field-effect transistors, *J. Appl. Phys.*, **95**, 5088 (2004).

[70] M. M. Erwin, J. McBride, A. V. Kadavanich, and S. J. Rosenthal, Effects of impurities on the optical properties of poly-3-hexylthiophene thin films, *Thin Solid Films*, **409**, 198 (2002).

[71] A. Peled and L. B. Schein, Hole mobilities that decrease with increasing electric fields in a molecularly doped polymer, *Chem. Phys. Lett.*, **153**, 422 (1988).

[72] M. Novo, M. van der Auweraer, F. C. DeSchyver, P. M. Borsenberger, and H. Bässler, Anomalous field dependence of the hole mobility in a molecular doped polymer, *Phys. Stat. Sol. (b)*, **177**, 223 (1993).

[73] H. Kageyama, K. Ohnishi, S. Nomura, and Y. Shirota, Negative electric-field dependence of hole mobility for a molecular glass of tri(o-terphenyl-4-yl) amine, *Chem. Phys. Lett.*, **277**, 137 (1997).

[74] I. I. Fishchuk, A. Kadashchuk, H. Bässler and M. Abkowitz, Low field charge-carrier hopping transport in energetically and positionally disordered organic materials, *Phys. Rev. B*, **70**, 245212 2004.

[75] A. J. Mozer and N. S. Sariciftci, Negative electric field dependence of charge carrier drift mobility in conjugated, semiconducting polymers, *Chem. Phys. Lett.*, **389**, 438 (2004).

[76] P. M. Borsenberger, R. Richert, and H. Bässler, Dispersive and nondispersive charge transport in a molecularly doped polymer with superimposed energetic and positional disorder, *Phys. Rev. B*, **47**, 4289 (1993).

[77] A. J. Mozer, N. S. Sariciftci, A. Pivrikas, R. Österbacka, G. Juška, L. Brassat, and H. Bässler, Charge carrier mobility in regioregular poly(3-hexylthiophene) probed by transient conductivity techniques: a comparative study, *Phys. Rev. B*, **71**, 035214 (2005).

[78] A. Hirao, H. Nishizawa, and M. Sugiuchi, Diffusion and drift of charge carriers in molecularly doped polymers, *Phys. Rev. Lett.*, **75**, 1787 (1995).

[79] S. A. Choulis, J. Nelson, Y. Kim, D. Poplavskyy, T. Kreouzis, J. R. Durrant, and D. D. C. Bradley, Investigation of transport properties in polymer–fullerene blends using time-of-flight photocurrent measurements, *Appl. Phys. Lett.*, **83**, 3812 (2003).

[80] W. Geens, T. Martens, J. Poortmans, T. Aernouts, J. Manca, L. Lutsen, P. Heremans, S. Borghs, R. Mertens, and D. Vanderzande, Modelling the short-circuit current of bulk heteojunction solar cells, *Thin Solid Films*, **451–452**, 498 (2004).

[81] V. D. Mihailetchi, J. K. J. van Duren, P. W. M. Blom, J. C. Hummelen, R. A. J. Janssen, J. M. Kroon, M. T. Rispens, W. J. H. Verhees, and M. M. Wienk, Electron transport in a methanofullerene, *Adv. Func. Mater.*, **13**, 43 (2003).

[82] S. A. Choulis, J. Nelson, S. M. Tuladhar, S. Cook, Y. Kim, J. R. Durrant, and D. D. C. Bradley, Transport and recombination dynamics studies of polymer–fullerene based solar cells, *Macromol. Symph.*, **205**, 1 (2004).

[83] P. Schilinsky, C. Waldauf, J. Hauch, and C. J. Brabec, Simulation of light intensity dependent current characteristics of polymer solar cells, *J. Appl. Phys.*, **95**, 2816 (2004).

[84] H. Sirringhaus, P. J. Brown, R. H. Friend, M. M. Nielsen, K. Bechgaard, B. M. W. Langeveld-Voss, A. J. H. Spiering, R. A. J. Janssen, E. W. Meijer, P. Herwig, and D. M. de Leeuw, Two-dimensional charge transport in self-organized, high mobility conjugated polymers, *Nature*, **401**, 685 (1999).

[85] M. C. Scharber, C. Winder, H. Neugebauer, and N. S. Sariciftci, Anomalous photoinduced absorption of conjugated polymer–fullerene mixtures at low temperatures and high frequencies, *Synth. Metals*, **141**, 109 (2004).

[86] C. Arndt, U. Zhokhavets, G. Bobsch, C. Winder, C. Lungenschmied, and N. S. Sariciftci, Investigation of excited states in polymer–fullerene solar cells by means of photoinduced reflection-absorption spectroscopy, *Thin Solid films*, **451–452**, 60 (2004).

[87] A. F. Nogueira, I. Montanari, J. Nelson, J. R. Durrant, C. Winder, N. S. Sariciftci, and C. J. Brabec, Charge recombination in conjugated polymer–fullerene blended films studied by transient absorption spectroscopy, *J. Phys. Chem. B*, **107**, 1567 (2003).

[88] A. J. Mozer, N. S. Sariciftci, L. Lutsen, D. Vanderzande, R. Österbacka, M. Westerling, and G. Juška, Charge transport and recombination in bulk heterojunction solar cells studied by the photoinduced charge extraction in a linearly increasing voltage technique, *App. Phys. Lett.*, **86**, 112104 (2004).

[89] A. J. Mozer, G. Dennler, N. S. Saricitfci, M. Westerling, A. Pivrikas, R. Österbacka, and G. Juška, Time-dependent mobility and recombination of the photoinduced charge carriers in conjugated polymer/fullerene bulk heterojunction solar cells, *Phys. Rev.* B, **72**, 035217 (2005).

11 The Terawatt Challenge for Thin Film Photovoltaics

Ken Zweibel
NREL, Golden, CO, USA

11.1 PROLOGUE

It is critical to understand what this report purports to do and what it cannot do. It cannot analyze either company or technology specific information about thin film manufacturing. It cannot give any current actual prices, because they depend on volume and varying specifications. Thin film photovoltaic (PV) manufacturing is changing quickly, and most crucial details are confidential.

So what can this report do? It can assemble in one place a set of technology options, process choices, and device designs and attempt to give a rough estimate of their status and potential. There are long lists of these attributes (e.g., Tables 11.1 and 11.4) that seem to indicate actual costs. But this is not the case. The lists are long to assure that as much as practical is included – missing process steps or major materials components would be a serious shortfall. But the actual costs estimated under each category are simply educated guesses. With time, they will change. This is a snapshot of what the author believes is a fair picture of the landscape of thin film PV. One cannot do more; it is really rather a question of whether one should simply do less, and not publish at all. But in the interest of addressing a bigger question – 'Can thin film PV meet the Terawatt Challenge?' – it seems worthwhile to make the effort, especially considering the critical importance of solar (covered in the next section) in terms of climate change and oil depletion. Solar is 'the only big number out there' (in the sense of the size of the resource available to meet climate change without carbon dioxide emissions) and this matters. This report should suffice to give a sense of the progress in thin films; their potential; and what remain as major challenges.

Tables 11.16–11.19 summarize the results of the rough, but methodologically consistent cost estimates. They show that a number of thin film module options have system price potentials in the range of \$1–\$1.2/Wp DC. This translates (in an average US solar location like Kansas City) to about 5–7 ¢/kWh AC electricity. Such electricity should be inexpensive enough to: (i) provide intermittent, daytime electricity from grid tied systems and (ii) split water and make hydrogen for portable fuels. If PV is to be used for dispatchable electricity, other aspects of system design and cost must be addressed through long distance transmission and storage.

This study was conservative. There are a number of clear avenues for further PV cost reduction (e.g., through less expensive encapsulation) that could take PV prices substantially lower.

Thin Film Solar Cells Edited by J. Poortmans and V. Arkhipov
© 2006 John Wiley & Sons, Ltd

In addition to the cost estimates, other topics associated with the 'Terawatt (TW) Challenge' include materials availability, land area needs, and energy payback. These were examined as well. In some cases there may be materials availability issues (e.g., indium and tellurium supply), while in others only the prospect of steady growth (e.g., glass). Due to the diversity of PV module options, no supply issue is critical. Land issues turn out to be a red herring – land use is actually a strength of PV since: PV can be used on roofs and other structures, it is the most efficient means of converting primary solar energy to usable form, sunlight is ubiquitously available in sufficient quantities, and only tiny amounts of land (on a relative basis) are in question (about 1 % of land area). Energy payback is also found to be a nonissue, as it falls toward about 1–2 years today, and below that with further technical progress.

The evolution of PV into one of the world's largest industries is not going to happen without major unforeseen problems. However, this study attempts to address the obvious ones, so that we can put aside the mythology of PV (for example, that it is only 'boutique power' or that one must pave the world with it to be useful) and get on with changing the world's energy infrastructure. With the years of rapid market growth now underway in PV, the author is sure this will not be the last effort to understand the real potential and pitfalls of meeting the TW Challenge.

11.2 'THE ONLY BIG NUMBER OUT THERE – 125 000 TW' (QUOTE, NATE LEWIS, 2004)

The world uses about 10 terawatt (TW) of energy (the US, about 3 TW) and by 2050 is projected to need about 30 TW. Thus the world will need about 20 TW of nonCO_2 energy to stabilize CO_2 in the atmosphere by mid century. For details about non CO_2 energy needs for meeting climate change, see Hoffert *et al*., 1998. Hoffert (NYU), Rick Smalley (Rice Nobel Laureate), and Nate Lewis (CalTech) call this the 'Terawatt (TW) Challenge,' and whether thin film PV can meet the challenge is the subject of this study. Shockingly, it turns out that among the nonCO_2 options, it is possible that solar is the only one that can (discussed below).

The primary barrier to TWscale use of PV is cost, and that will be the main focus of this study. Secondary barriers, including feedstock availability, land use, and energy payback, will also be covered. A final barrier, only touched on here, is system related: how do we use intermittent PV electricity to provide dispatchable electricity and fuel? This is described in outline, but deserves a separate in depth study.

But why is it crucial that PV be able to meet the TW Challenge? Why not other sources of nonCO_2 energy? This is an important question that most policy makers do not yet agree on, and the public is another step removed from such a consensus.

In recent presentations and publications, CalTech's Nate Lewis, 2004 has emphasized that among the renewables, only solar has a large enough resource base to meet a major fraction of the world's energy needs. The rest of the renewables (wind, biomass, geothermal, hydro) do not have adequate global resources to do so – although they can meet a fraction of a TW each (still a very significant contribution, when one realizes that the US now uses 3 TW). But this means that solar (with about 125 000 TW of global incident sunlight) has both a huge opportunity and a huge *responsibility*.

To state clearly: any technology that can produce at least a TW of annual energy should be considered having met the TW Challenge and contribute to the reduction of climate change. But we go further here; we want to know how many TWs thin film PV could provide by mid century.

Key scenarios for stabilizing CO_2 in the atmosphere during the 21st century turn on the viability of CO_2 sequestration. Sequestration is capturing CO_2 during, e.g., coal burning, piping it to a storage location, and then pumping it into special underground storage, e.g., aquifers, where it would presumably stay without leakage for millennia. This approach is unproven but important. Much work is being done to demonstrate it.

If sequestration does *not* work, it is almost certain that the world will need at least 10 TW of nonCO_2 producing energy by mid century, and perhaps as much as 20 TW, to stabilize CO_2 in the atmosphere. Even nuclear power would have difficulty meeting this without breeder reactors, due to the lack of uranium fuel for present designs. But this means that nuclear has multiple problems: proliferation of breeder reactors with plutonium fuel (with concomitant global tensions and terror issues), waste disposal, and accidents. Let us put aside nuclear as possibly too dangerous. Then the simplest scenario to stabilize CO_2 by mid century is one in which PV and other renewables are used for electricity (10 TW) and to make hydrogen for transportation (10 TW); and fossil fuels (coal, natural gas, oil) are used to make residential and industrial heat (10 TW). Departures from this strategy include using coal to make gasoline; but this would mean more CO_2. The challenges facing solar are: (i) economic (can renewables be cheap enough? Can storage of hydrogen on vehicles be cheap enough?) and (ii) infrastructure (we pump gasoline, not hydrogen; we use gasoline engines, not fuel cells or turbines). Under this scenario, and given the vastness of the solar resource, there could be a huge 10–20 TW demand for PV by mid century. (Recall that we only use about 10 TW worldwide today, so this is a huge amount of energy.)

But what if sequestration works? Would the need for solar be eliminated or much reduced? Perhaps not as much as one might think. Why? Let us look a little more closely at the coal/sequestration approach.

People are excited about the potential of sequestration, because if it works, coal could be used to meet most electricity demand. Everyone knows there's plenty of cheap coal. The cost of sequestration and rising demand might add about 50–150 % to the price of coal generated electricity, but it wouldn't make coal use untenable. Still, even under this scenario, some renewables would be used simply because they would be cost competitive at these higher prices.

What about transportation?

Princeton's Bob Williams has presented a unique scenario based on *biomass CO_2 sequestration* in which coal and biomass could be used for liquid fuels and still stabilize CO_2 in the atmosphere. How? *Biomass-produced CO_2 sequestration* could be adopted to actually *remove* significant CO_2 from the atmosphere. This is even better than biomass being CO_2 neutral; it provides a sink that can be played off against fossil fuels. Biomass used as energy or used as feedstock along with coal could make liquid fuels (e.g., gasoline). By effectively removing some CO_2 from the atmosphere via the biomass, the net CO_2 produced in the transportation sector (where CO_2 cannot be captured) would be low enough to allow CO_2 stabilization despite using a lot more coal.

Under the coal and biomass CO_2 sequestration scenario, no other renewables would appear to be needed for a major fraction of the world's energy, at least until mid century (when biomass resources would become inadequate to the task).

But this is not the last word on this key question.

Williams and Lewis have proposed an innovative idea for using solar energy to make carbon fuels, i.e., as an alternative to biomass in the sequestration scenario. If successful, such an approach would significantly increase the demand for PV *despite sequestration's success*.

How could PV produce carbon fuels? Lewis suggests an *in situ*, electrochemical approach mimicking photosynthesis. An electrochemical solar cell would be used to combine CO_2 taken from the air with hydrogen from water splitting, producing a hydrocarbon liquid fuel. His suggested *in situ* approach, similar to but more complex than existing efforts to split water electrochemically with *in situ* PV, would require long term research and one or more major breakthroughs.

Perhaps we could afford the wait. Under Williams' plan for biomass sequestration, analysis suggests that biomass resources would become inadequate about mid century. Thus development of *in situ* PV synthesis of carbon fuels could take until then and still play a major role.

However, there may be simpler and shorter term ways to harness PV to remove some CO_2 from the atmosphere and make hydrocarbons. Just as there is a way to use any PV electricity to split water using an (*ex situ*) electrolyzer, there may be ways to simply use flat plate PV electricity to make carbon fuels. How? Carbon dioxide may be absorbed from the atmosphere (as it is by leaves in photosynthesis) or taken from the emissions of coal plants, and hydrogen from water can be combined with it to make hydrocarbons. Because concentrating atmospheric CO_2 takes too much energy, the large area of a leaf or of flat plate PV can be used to capture CO_2 from the air economically. Physical and chemical processes would have to be developed to capture the CO_2. But the rest of the processes are already being done: splitting the water with an electrolyzer; chemically synthesizing the hydrocarbon fuel from the CO_2 and the resulting hydrogen (e.g., running a methanol fuel cell backwards), and the DC PV energy. On the PV side, the challenge is purely economic: can PV be inexpensive enough? But it would not have to be directly competitive with gasoline prices; it would compete (under the sequestration scenario) with biomass, instead.

Thus *even under the sequestration scenario*, many TW of PV might be of value. Of course, without sequestration (which seems more probable), solar would be *essential*. And under either scenario, sequestration or not, we should establish that PV can meet the TW Challenge from an economic and materials availability standpoint.

It may be that developing PV to produce hydrocarbons (instead of hydrogen) will be important for transportation, even if sequestration fails. The cost of using PV to make a liquid fuel instead of hydrogen is approximately only the added cost of the CO_2 processing, since splitting water is part of both approaches. But some of this added cost would be offset by the ease with which liquid fuels can be transported and stored (versus hydrogen) and the presence of the whole liquid fuel infrastructure in transportation. Then there would be further cost savings during use in vehicles, as the weight advantage of liquid fuels is significant. In fact, many policy makers are skeptical about whether the use of hydrogen for transportation is feasible at all, due to these factors. One way or another, PV as the source of nonCO_2 energy for making hydrocarbons or hydrogen could play a critical role in the transportation sector.

There is another collateral value to making hydrogen or hydrocarbons – storage. Photovoltaic is intermittent. Measures must be taken to smooth the delivery of solar energy to meet fluctuating demand, especially at night, during cloudy periods, or for seasonal extremes. Two methods of doing this exist: storage and long distance transmission. Storage could be accomplished by making hydrogen or hydrocarbons for conversion back to electricity. Other supply and demand mismatches could be minimized by improving long distance transmission. National and supranational grids could be upgraded to support large proportions of intermittent PV and wind; and to best use fossil fuels, storage, and other renewables. And multicontinent (even multihemispheric) transmission (e.g., Colbert and Smalley, 2002) could also fill gaps. Some of these infrastructure adjustments will be necessary to bring on the solar age.

As always, the bottom line is PV cost. Solar can meet energy needs globally from a resource standpoint. What would it have to cost to do it cost effectively? Each market has a different system cost and competitive price. And competitive prices will change with time, especially in a carbon constrained world, or if oil becomes more expensive. This study will establish that thin film PV costs can be brought down to about 5 ¢/kWh. (There are pathways that would take these costs even lower, but they are more speculative.) A cost of 5 ¢/kWh seems adequate to provide energy (electricity and transportation fuel) at prices not-too-different from today's prices.

The need for solar by mid century could be 10–20 TW. 'Solar is the only big number out there,' as Lewis would say. We have to find ways to use that resource. Thus it is incumbent on the PV community to rethink how it can meet the challenge, including facing issues such as reaching ultralow costs; managing explosive growth (with any materials bottlenecks that might occur); and producing, deploying, and using PV systems on an unheard of scale.

There may be other ways to make low cost PV than thin films (e.g., wafer silicon or concentrating PV), but thin films are paradigmatically designed for low cost; and they are the focus of this study.

11.3 LOW COST AND THE IDEA OF THIN FILMS

The idea of thin films is simple: use mostly low cost material (glass, metal, plastic) and very little high cost semiconductor. A micron or so of semiconductor is about 2–6 g/m^2; even ultraexpensive material (say, $1000/kg) only costs pennies per watt at this level. This idea has been around as long as PV, but the difficulty has been developing semiconductors that would work well enough (have high enough conversion efficiency) and then finding ways to actually make them cheaply at high yield. And thin films have their own peculiar stability issues, both intrinsically and at the module level, which have also added to the challenge. However, throughout, the idea of thin films has maintained its power, so that no single failure or long, costly delay has destroyed thin film development. But setbacks have taught us something about what is needed. Fortunately, thin films today are approaching technical readiness (Zweibel *et al*., 2004), achieving measurable and growing market share, and may finally show that they have an excellent chance of reaching truly low cost. This study makes an attempt to explain why thin films are likely to be successful for meeting large scale PV electricity demands.

11.4 A BOTTOM UP ANALYSIS OF THIN FILM MODULE COSTS

Almost all thin film PV devices have a great deal in common. They attempt to minimize material costs by using ultrathin semiconductors to convert sunlight to electricity; they attempt to reach adequate sunlight-to-electricity conversion efficiencies; and they require excellent outdoor reliability. In this sense, thin films are a direct response to the high materials costs of wafer silicon PV modules.

However, thin film modules share most functional aspects with wafer silicon modules. That is, they require top and bottom protection from the outdoor environment, so that they can last outdoors about thirty years. They need top and bottom contacts, bus bars, and a connection to an external circuit to carry away current. They need ways to connect the cells together to provide the right balance of voltage and current. They need some sort of mounting scheme, or at least the ability to be mounted if none is explicitly included. They may need edge seals and edge

protection, such as an edge delete. All in all, there is a great deal that thin film modules have in common with crystalline silicon modules; and with each other, no matter what the semiconductor converter is. These commonalities can be called the balance of module, or BOM. Importantly, they turn out to be a significant portion of module cost. (See tables below for particulars.)

The presence of substantial BOM means that: (i) reaching the highest possible efficiencies and (ii) reducing the manufacturing costs of the active elements of thin film modules are essential if they are to be competitive in the PV marketplace – not to mention (the real goal of all PV development), to be able to be competitive with fossil fuels. Cost reductions must come from reducing semiconductor materials costs, energy costs, capital costs, maintenance costs; and intending to use the largest substrate areas possible with easily connected cells to allow for the fullest automation. This must all be done while also optimizing conversion efficiencies, yield, and stability.

This simple comparison with crystalline silicon sets the stage for what follows (a comparison among thin films in greater depth) and is a caution against the idea that all thin films are automatically cheaper at the system level than wafer x-Si technologies. Such a system cost advantage can be tenuous or absent, and only a full exploitation of the potential advantages of thin films in real designs can lead to success in the marketplace; and more importantly, to a cost low enough to meet climate change and fossil fuel depletion needs on a global scale. Fortunately, several thin films (CdTe and a-Si products) are already competitive in the marketplace, so many challenges have been overcome.

Thin films share enough costs in common (BOM from encapsulation, contacting, and other shared costs; balance of system costs extrinsic to them) that efficiency is a very important parameter for defraying these shared costs (Von Roedern I 2005).

11.4.1 Approach

A spreadsheet was developed for the *estimated* component costs of thin film modules of various types. This was done in two parts – so-called commonalities or BOM of most thin film modules; and the unique aspects of each design, being mostly the semiconductors that convert sunlight to electricity (nonBOM). An initial production level of 25 MWp/yr was assumed, which is like the capacity of existing facilities or those that are planned by new start-ups. Then similar estimates were developed for future, larger scale production levels, in which both economies of scale and technical progress were estimated.

In most cases, thin film manufacturing bifurcates into: (i) approaches that take advantage of high quality processes that cost more but produce the best films or (ii) less expensive processes that produce less efficient devices. Another bifurcation is between glass and flexible substrates, and this can have implications at the system cost level (discussed below). In addition, some technologies have low semiconductor materials costs almost independent of how wasteful the approach; others are very sensitive to materials utilization rates. List 11.1 shows the primary set of thin film approaches examined here and the breakdown along these lines, with some simplifications where possible. We do not know which of these various strategies will be the best. Nor will any of them with only current technology meet the TW Challenge – significant R&D still needs to be done. But many of them have the potential if fully developed.

The technologies will be analyzed in these broad categories to capture the impacts of each difference in cost and efficiency. In no cases are actual company costs used, since these are not known and could not be used if they were. In addition, by retaining some flexibility, more

List 11.1 Characteristic thin film designs

Technology	Selected example companies
Batch amorphous silicon on glass	EPV
In-line or clustered amorphous silicon or thin film-Si on glass	Mitsubishi, Kaneka, Sharp
In-line a-Si or thin x-Si on flexible substrates	UniSolar, Iowa Thin Films
CdTe on glass	Antec, AVA Technologies, Solar Fields, First Solar
CIS/glass, good materials use, moderate-high capital	ISET
CIS/glass, poor materials use, moderate-high capital	Wurth, Shell Solar, Showa Shell, Honda
CIS/glass, good materials use, low capital	
CIS/glass, poor materials use, low capital	
CIS/flexible, good materials use, moderate-high capital	
CIS/flexible, poor materials use, moderate-high capital	Global Solar
CIS/flexible, good materials use, low capital	Several startups: e.g., Miasole, Daystar, Nanosolar
CIS/flexible, poor materials use, low capital	

present and *future* variations could be examined rather than being limited to actual process lines and device designs. It will be established that this approach does not much affect the accuracy or ruggedness of the estimates. In fact, in all cases, there is substantial overlap that underpins comparisons, e.g., efficiency, substrates, and BOM. The differences can be smaller than the similarities.

In addition to the above, some newer thin film technologies were also investigated, but in a more rudimentary fashion. These technologies are 5–20 years behind developmentally those in Table 11.1, and the purpose of examining them is to see if they have potential to be even better if all research challenges are overcome. However, meeting the TW Challenge does not require that any technologies beyond those given in Table 11.1 (and existing x-Si) be developed (but no doubt, some will be, reducing risks even further).

Various sources were used for these estimates. The most critical challenge was to get the right process steps and the right set of materials. If process steps or materials are missing, then the analysis can be off substantially. Literature, presentations, parallel work at NREL, and private communications were the source of the process steps. However, it is almost certain that a few, idiosyncratic processes were missed, as these are the least likely to be publicly discussed. Shunt curing and photolithography are examples of processes that may be overlooked (but actually, were not). Steps like these are not major costs, and they vary among approaches. To capture this type of missing information, a small additional 'miscellaneous' category was included for all options.

There is a further check on near term cost analysis: both the amorphous silicon and CdTe technologies are in production at the 25 MWp/yr level, and several companies publicly announced that they are profitable (e.g., First Solar and UniSolar, May 2005). Thus one can deduce that their costs are within a reasonable range of those of x-Si for existing production. Similarly, many companies publish partial accounting of their costs (e.g., total capital

investment for new plants). Both First Solar and UniSolar did this recently ($2.5/Wp for UniSolar and $1.2/Wp for First Solar, from press releases). Others have as well. Another example of an 'easy' cost to estimate is semiconductor materials. The feedstock costs can be found (e.g., Appendix 1 of Keshner and Arya 2004) and the layer thicknesses estimated from published articles on cells. The fraction of material wasted is important, since this can vary greatly. All in all, many aspects of production can be estimated in a like manner.

Estimates included processing equipment and the materials, and other associated costs such as labor, energy, and rent. The BOM costs were easiest, since they are usually commodity materials such as glass, metal, plastic, or ethylene vinyl acetate (EVA). In those cases, quotes were taken from the internet, from vendors, or from private communications. In many cases, common sense estimates were made based on these inputs. No number represents an absolute, since vendors vary, prices vary with volume, and costs change. They are educated estimates, and that's all they should be viewed as. Where they are cost drivers, care was taken to assure that they are reasonable.

The nonBOM portion was more challenging, but estimates are possible from publications; and trends are relatively easy to discern. Handling and other miscellany were included. Maintenance was taken as 4 % of the initial capital cost for all technologies. Capital cost per unit output was assumed to be based on a capital recovery factor of 15 % per year.

Analysis was also done of future costs, based on expected technical progress. For example, costs can be adjusted for thinner layers and improved process waste percentages. Based on an increase in throughput (from faster film fabrication, from thinner layers, and wider substrates, etc.), capital, maintenance, energy, rent and other costs can be adjusted. This type of analysis was done to project future cost trajectories.

In several cases the author received private communications of in depth breakdowns of entire thin film processes from private sector sources. But these were always given within a framework of confidentiality, to be used in a generic, nonattributable way. That is why they cannot be referenced; and the particulars of processes are not broken down in parallel to any single company's approach. Yet detailed numbers exist that back up the results given here, and often the author's estimates agree quite closely or are higher than numbers mentioned in various venues (conferences, workshops, group conversations).

In all cases, some common sense had to be used. No single cost number is usable alone; experience and insight must be applied. A synthesis was made.

Are the estimates off? Definitely, but likely within reason. Are the process sequences off? Probably not much, except for the proprietary aspects. It is the author's belief that the estimates in this chapter for Table 11.1 thin films will track real world costs within about 20 %. For others (so-called third generation (3G) thin films), the uncertainty is much greater and will be noted where possible.

A simple, but important arithmetic relationship underlies the analysis. Most PV costs are given in dollars per watt peak ($/Wp). This is fine for the end user (especially if it is a system price), but it hides the nature of the technical challenges, especially in thin films. Two components go into a cost in $/Wp: the output or efficiency of the device, and its manufacturing cost per unit area. By combining them you get a cost in $/Wp. However, costs and efficiency vary greatly among thin films. There are many thin film options with very low potential costs (especially, potentially low *nonBOM* costs), but often they have inadequate efficiencies, resulting in high $/Wp costs. Their challenge is to raise their performance. But this is often overlooked when people merely highlight their low nonBOM manufacturing cost. Conversely, there might be thin films with high efficiency that have high area costs, and the balance determines their competitiveness.

The actual relationship is very simple: the dollars per watt cost can be found simply by dividing the manufacturing costs per unit area (say $\$/m^2$) by the output of the same area (which for $1\,m^2$ is $1000\,Wp/m^2$ times the efficiency). The same relationship works at the module level: the module cost (in \$/module) divided by its output (Wp/module) is its \$/Wp cost. Obviously, the same relationships show how to go the other way: if one knows the \$/Wp cost and either the efficiency (or unit output) or the area cost, one can calculate the missing parameter. The simple relationship is as follows:

$$\$/\text{Wp} = (\text{Cost/unit area})/(\text{output/unit area}) \tag{11.1}$$

Unit area can be the module area; or, as in this chapter, the cost per square meter. Output per square meter is $1000\,Wp/m^2$ times the efficiency (or it is the module's nameplate rating at **STC). Thus a $\$10/m^2$ area cost for a 10 % module is \$0.1/Wp; and for a 5 % module, it is \$0.2/Wp. A \$1/Wp cost for an 8 % module implies an $\$80/m^2$ manufacturing area cost; but for a 12 % module, it's $\$120/m^2$. This is all arithmetic using the relation above. Because thin film technologies vary across a wide spectrum in both cost and efficiency, this is the way the analysis must be done to reveal underlying issues.

11.4.2 Results

For the commonalities (BOM) among all thin film modules, a set of distinct substrates were chosen: glass, stainless steel, and polyimide. Only those substrates and encapsulation schemes that are already in common use were chosen (e.g., glass/EVA, Tefzel/EVA), and this could be viewed as a limitation of the study (since they are all rather expensive). However, since encapsulation is crucial for reliability, it seemed the proper choice. To first order, any cost breakthrough in encapsulation is likely to benefit all thin films (and x-Si), and could be treated independently. (If individual technologies have uniquely lower cost options for encapsulation, they should try to develop and implement them as fast as possible to gain a competitive advantage over those given here. More likely, they have specific problems that require somewhat more robust encapsulation and incrementally higher cost.)

Then estimates of the rest of the functional aspects of the BOM were added to the three substrate options (see Table 11.1 for a detailed example with glass), except for sales, marketing, management, R&D, warranty, shipping, taxes, and profit. (These are actually added later at the system price level.) Each BOM design had a top and bottom contact (including transparent concutive oxide, TCO); each had bus bars and wires out; each had adhesive where needed. All cost categories were included: materials, equipment and maintenance, labor, facilities. Where materials were the same between designs (e.g., EVA adhesive or Tefzel or TCO, back contact metals) the same assumptions were used throughout, but adjusted if there were differences of thickness or processes. Cell interconnection monolithically or by soldering was also included.

Note that this means that the only aspects of the design that will vary for the nonBOM portion of the thin film device will be between the two contacts (where those contacts include the top TCO and the bottom metal). This approach makes the analysis quite generic, but it does sacrifice some aspects of specificity.

Table 11.1 shows the estimated breakdown of BOM commonalities for the simplest of all thin film designs: a glass-to-glass superstrate with tin oxide TCO on top; and EVA adhesive and glass on the bottom. The second case, last column of Table 11.1, is where a substrate glass is used and the TCO is added before the top piece of glass is added. (The slightly higher cost

Table 11.1 Estimated BOM commonalities of glass/TCO/glass module designs; direct manufacturing cost @ 25 MWp/yr[a,b]

Unit	Component	Detail	Buy glass w/TCO	(Substrate glass version)
$/m^2	Front contact or TCO capital cost	CVD or sputtering	N/a	2
$/m^2	Laminator		2	2
$/m^2	Scriber//cell interconnection	scriber	2	2
$/m^2	Back contact capital cost	sputtering	2	2
$/m^2	Substrate and preparation	soda lime glass	10	7
$/m^2	Front contact materials	target or gas	N/a	5
$/m^2	Back contact materials	target	0.6	0.5
$/m^2	Maintenance		2	2.7
$/m^2	Misc. handling costs	glass	1.5	1.5
$/m^2	Packaging and shipping		1.5	1.5
$/m^2	Adhesive	EVA	3.7	3.7
$/m^2	Encapsulating layer and prep	Soda lime glass	7	7
$/m^2 equivalent	Bus bars		2	2
$/m^2 equivalent	Wires and 'jbox'		4	4
$/m^2 equivalent	Edge seals materials and capital		1	1
$/m^2 equivalent	Frame or mounting scheme		3	3
$/m^2 equivalent	Specialty chemicals		0.5	0.6
$/m^2 equivalent	Utilities (BOM only)		2	3
$/m^2 equivalent	Rent (BOM only)		2	2
$/m^2 equivalent	Labor (BOM only)		5	6
$/m^2	Subtotal		51	58
%	Yield on BOM		0.95	0.95
$/m^2	Total of BOM commonalities		54	62

[a] For perspective: if a module is 10 % efficient (100 W/m^2), \$1/m^2 is \$0.01/Wp; and if annual output is 25 MW, \$1/m^2 is equivalent to \$250 000 of annual costs (about 2 % of total BOM costs). The total BOM (about \$60/m^2) would then be equivalent to about \$15M/yr, or \$0.6/Wp. However, at 5 % module efficiency, the BOM by itself would be \$1/Wp.

[b] The following are not included in Table 11.1: sales, marketing, management, R&D, warranty, shipping, insurance, taxes, and profit.

for this second case reflects the volume advantage of buying glass/TCO from a glassmaker instead of making it in small volumes.) It should be emphasized that all numbers in this chapter are estimates and will likely change over time due to design changes, volume purchases, or innovations. Some of that is built into later tables.

But the classic glass-to-glass module is not the only possible encapsulation design. Tables 11.2 and 11.3 provide a summary of the entire spectrum of BOM combinations at current cost and production levels. As such, they provide a lower cost 'floor' for almost all thin films today (since each thin film has one of these BOM); and that floor tends to be in the \$60–\$75/m^2 range, *without a single active conversion element being added to the design*. This is an important result, since, for example, the long term **DOE goal for thin film modules is under \$50/m^2, including all aspects. However, recall that these BOM estimates are a snapshot of *current* costs. They do not include any improved designs or economies of scale. These can

Table 11.2 Summary of estimated BOM commonalities at 25 MWp/yr level, near term

Glass/TCO/EVA/glass or Glass/EVA/metal/glass	Tefzel/EVA/stainless steel/EVA/tefzel	Tefzel/EVA/polyimide/EVA/tefzel
54–62 $/m^2	67–79 $/m^2	70 $/m^2

be expected to be significant. In fact, one may expect BOM costs to drop by about 25–50 % in some future, steady state, high volume scenario, without significant design changes (see Table 11.5, and discussion below). With design changes (such as replacing the back encapsulation with a thin film barrier layer, or with other radical changes that somehow maintain reliability), the reduction could be even greater. However, a stubborn BOM debit of about \$20–\$40/m^2 (perhaps less with design changes), even in the future, is important to include in planning for thin film research. It tends to keep efficiency high on the research priority list.

A few observations about Table 11.2:

- The use of stainless steel or polyimide today engenders the need for a second, bottom encapsulation barrier, in this case EVA//Tefzel (or EVA//glass), which adds significant expense (for comparison, glass does double duty as a substrate and encapsulant).
- However, flexible modules laminated on roofs have significant balance of system (BOS) advantages for that application, which can more than offset this extra module cost. This will be discussed later.
- Future designs to use less expensive substitutes for any of these materials will demand substantial reliability testing.
- However, volume production and on-site manufacturing (e.g., for EVA, Tefzel, glass) would affect these costs positively. To be conservative, these are not taken into account in this study.

BOM commonalities were also developed for nonstandard designs, e.g., for twojunction thin films both as two and four terminal devices. These required different BOM choices for scribing, for contacts between the top and bottom junctions, and for external wiring. A summary is given in Table 11.3.

Observations about Table 11.3:

- The two terminal design is essentially the same as the basic glass/EVA/glass design for a single junction (i.e., this is like some existing two junction a-Si designs – only a small debit for a tunnel junction is added to the BOM);

Table 11.3 Summary of estimated BOM commonalities at 25 MWp/yr level, near term, for multijunctions (all glass/EVA/glass design)

Two terminal design	Four terminal design
56 $/m^2	73 $/m^2

- The about \$15/m^2 added BOM cost of the four-terminal design implies about 1 % in efficiency debit (depending on module efficiency) versus a single junction or a two terminal BOM design, before any additional cost for the semiconductors themselves is added. Obviously, these added costs must be offset by greater efficiency to make this choice cost effective versus the two terminal approach or versus a single junction competitor.
- The payoff for multijunctions is in potentially higher efficiencies, which help offset BOM and area related BOS costs.

To find *total module cost*, designs for the active semiconductor portions (nonBOM) of each thin film technology were developed, including multiple designs (such as in CIS) where warranted by different processing schemes. In other words, physical vapor deposition (PVD) approaches, chemical vapor deposition (CVD) approaches, precursors and selenization approaches – all the recognized ways that thin films such as CIS, a-Si, and CdTe are made – were estimated. However, no effort was made to exactly replicate any company's specific approach, for obvious and numerous reasons (e.g., it can't be done; and it shouldn't be done for confidentiality purposes). So in that sense, even at the most detailed level, there were some limitations on precision. However, every effort was made to make the numbers true to a current best estimate of costs for plants of the sizes given in some steady state (i.e., without first time design costs). For a look at various cell and module designs and process sequences, see: e.g., Wieting, 2005; Basore, 2004; Delahoy *et al.*, 2004; Guha and Yang, 2003; Enzenroth *et al.*, 2004; Powell, 2004, Jansen *et al.* (2005). However, this is not an all inclusive list of resources, as pointed out in the introduction.

Table 11.4 shows the nonBOM breakdown of one technology (superstrate batch process a-Si/a-Si on TCO/glass) with the various process steps and other inputs (parallel to Table 11.1 for BOM). Notice that it does not include anything for either top or bottom contacts. It is just the 'difference' appropriate to this approach.

Table 11.4 shows the categories used to break down each of the technologies, as well as a sense of what cost estimates were made. The resulting \$1.56/Wp direct manufacturing cost for a-Si/a-Si modules at 6 % efficiency seems quite reasonable in comparison to sales prices (about \$2.25/Wp in some markets) in today's low volume, high overhead marketplace (at production levels that are not yet at 25 MWp/yr). At 6 % module efficiency, 1 \$/m^2 is 2 ¢/Wp (@ 85 % yield), so (for example), nonBOM capital equipment and related maintenance contribute only ten times this, or about 20 ¢/Wp. This is the advantage of the a-Si batch process and some other similarly low-capital cost approaches (e.g., CdTe). It also means the initial capital investment is low (subtracting maintenance): only \$1.8/Wp of capacity (or about \$45M for 25 MWp/yr capacity). Note that at higher efficiencies, these same dollar per square meter costs would yield much lower dollar per watt costs and initial investments. This is the flip side for a-Si batch processing – the efficiencies are low.

As already stated, in the case of dye sensitized, plastic cells, and quantum dots, which are not yet in prototype production, estimates were less secure. In fact, this is a well known problem with all cost projections: numbers that are further from being reduced to practice are fuzziest and prone to the largest mistakes and biases. In this study, some liberalism was used in estimating the costs of the nonBOM portions of these so-called 3G thin films (because such costs are considered their unique strength); but a more moderate liberalism was used regarding their projected efficiencies (since this is their greatest challenge). However, they were all taken to be stable long term. This is quite optimistic. But the choice was made for a simple

Table 11.4 Estimated nonBOM (active materials) breakdown for a-Si double junction made on TCO–glass using the batch process (many substrates at once) @ 25 MWp/yr

NonBOM only	Level 1: 1–3 years (25 MW/yr)	Batch
		a-Si
$/m^2	Absorber capital	6
$/m^2	Absorber material	1.5
$/m^2	Junction partner capital	1
$/m^2	Junction partner material	0.1
$/m^2	Buffer capital	0.5
$/m^2	Buffer material	0.2
$/m^2	Back reflector	3
$/m^2	Extra tunnel junctions	0.5
$/m^2	Cell testing and binning	1
$/m^2	Coatings to protect layers	0.2
$/m^2	Specialty chemicals	1
$/m^2	Misc. treatments capital and materials	1
$/m^2	Rent	3
$/m^2	Labor	4
$/m^2	Maintenance	2
$/m^2	Utilities	6
$/m^2	Subtotal	31
%	Yield on active materials	0.85
%	Module efficiency, total area	6
$/m^2	Total nonBOM	37
$/Wp	Total nonBOM @ 6 % module efficiency	0.61
$/m^2	Proper BOM for Glass/TCO/glass	54
$/m^2	ES&H	3
$/m^2	Total module	93
$/Wp	Total module @ 6 %	1.56

reason: any major instability problem would probably make these technologies totally noncompetitive (except for unique but small niche markets). In summary: the second generation (2G) thin films (CIS, CdTe, a-Si) were treated rather conservatively (because they are more mature and there is more data); BOM was treated rather conservatively, with no assumptions about large economies of scale; 3G thin films were given the 'benefit of the doubt' simply to show their potential value. Predictions for 2G thin films should be seen as 'realistic'; predictions for 3G thin films as 'optimistic.'

To allow parametric studies of the technologies near term and at several levels of future development and manufacturing capacity, the source spreadsheet was expanded to provide estimates of future developments in thin films. Both BOM commonalities and noncommonalities (nonBOM) were varied with levels of technical maturity and throughput.

In terms of BOM commonalities, an assumed cost reduction of 10 % was applied at each level of increased single plant throughput. The first level of production was assumed to be about 25 MWp; and subsequent levels were increased to 50, 200 and 1000 MWp/yr, with concomitant

Table 11.5 A summary of the possible cost evolution of BOM commonalities at different throughput/maturity levels ($/m^2); BOM reduced 10 % at each larger production level

Annual single plant production	Glass/ EVA/glass	Tefzel/EVA/ stainless steel/ EVA/Tefzel	Tefzel/EVA/ polyimide/ EVA/Tefzel	Two terminal Glass/ EVA/glass	Four terminal Glass/ EVA/glass
Soon (25 MWp)	54	67	70	56	73
50 MWp	49	60	63	50	66
200 MWp	44	54	57	45	59
1 GWp	39	49	51	41	53

BOM cost reductions. In the end, the final level of BOM costs was reduced by about 25 % from the original value for each BOM design. This is less aggressive than an 80 % learning curve would imply from these volumes, which would have led to a reduction of about 60 %; but BOM volume production is already being achieved through the existing x-Si volume increases, so BOM cost reductions will likely take a more modest slope with time than nonBOM reductions in thin films.

In a recent study (Keshner and Arya, 2004), a bottom up approach was taken with BOM, showing that volume purchases and make-buy decisions could contribute substantially to cost reductions; as could design alternatives. Their glass/TCO BOM costs were 50 % lower than those assumed here for the long term (about 10–20 $/m^2). Part of the reason was more aggressive design assumptions (they replaced the back glass with a plastic barrier layer, although this is technically unproven); and they assumed even greater volumes and resulting cost reductions via, e.g., strategies like a front end glass plant at 3 GWp/yr plant size. In other words, the cost of the BOM assumed here should be considered conservative. For perspective: at 10 % efficiency, Table 11.4 is a BOM cost reduction from 55 ¢/Wp today to about 40 ¢/Wp; but Keshner and Arya imply about 12 ¢/Wp. That is a very large difference, and it would drive large differences in system cost for module technologies with different manufacturing cost/efficiency ratios. Future studies focused on BOM might be able to refine these results.

Next, the technology specific (nonBOM) aspects of each approach were looked at, and a timeline was developed using a bottom up approach. Expected technical improvements were delineated and their impacts assigned. Where possible, clear pathways and mechanistic cost reduction assumptions were used. For example, if layer thickness could be reduced from 3 microns to 1 micron for ultimate, practical (efficient) devices, equal improvement increments were chosen for the various production levels. Other projected improvements included faster semiconductor deposition speeds; better materials use; more uniform layers; higher quality layers; wider substrates; and incorporating a higher fraction of today's best cell efficiencies into future typical commercial modules. In addition, some volume economies were also assumed (e.g., in the capital equipment costs), though not as aggressively as in Keshner and Arya, 2004. These projections were seeded into the spreadsheet at various levels of maturity and throughput for each of the major cases. The results were costs for the nonBOM of the technologies that varied as follows (Table 11.6). Note the spread in projected cost reductions from the '25 MWp/yr' level to the '1 GWp/yr' level. The amount for a-Si is least (and thus perhaps most conservative); CdTe in the middle; and CIS much larger. This relates to the assumed reduction in capital costs for the CIS; and the reduction in semiconductor materials costs (from thinner

Table 11.6 Possible evolution of technology specific (nonBOM) costs ($//m^2) by technology

Annual output	CIS/SS (high capital, poor materials)	CIS/glass (high capital, poor materials)	CIS/glass (moderate capital, poor materials)	CdTe	a-Si/a-Si batch on glass	a-Si in-line on flexible (SS)
25 MWp	140	140	106	45	36	59
50 MWp	87	104	81	34	28	48
200 MWp	71	72	64	28	24	40
1 GWp	36	41	32	16	15	24
% reduction	74	71	70	65	58	59

layers and better utilization) for the CdTe and CIS. However, it also means that the amorphous silicon projections could be viewed as less uncertain.

To get total module costs, these nonBOM costs were added to appropriate BOM commonalities for the different packaging and substrate designs; and then an ES&H cost estimate for in-plant costs (and recycling for CdTe) was added (this was also in Table 11.4). The total module costs in $/m^2 are shown in Table 11.7.

Again, the cost reduction for CIS appears more optimistic (as a percentage change) than those for the other thin films, and this can be attributed to projected capital and materials cost reductions, especially for the evaporation approaches. It could also be attributed to the fact that the nonCIS technologies are all more mature and already in production.

But manufacturing cost is only half the story. The other half is module efficiency, and in many cases it has driven a bifurcation in approaches between optimizing manufacturing costs and optimizing efficiency.

Table 11.8 shows a projection of the evolution of commercial module efficiencies. It should be borne in mind that efficiency affects both the module cost and the system cost; it applies at both these levels to get the final value of a module in terms of the end user (system cost, which is given below in Table 11.13). It can also have an impact in terms of specific applications: e.g., rooftop arrays are often area limited, favoring higher efficiencies. Two rows at the end of Table 11.8 show the relative increase in module efficiency from today's levels; and a comparison between the projected long term module efficiency and the best laboratory cell today.

Table 11.7 Possible evolution of total module costs by technology ($//m^2)

Annual output	CIS/SS (high capital, poor materials)	CIS/glass (high capital, poor materials)	CIS/glass (moderate capital, poor materials)	CdTe	a-Si/a-Si batch on glass	a-Si in-line on flexible (SS)
25 MWp	230	210	170	110	94	130
50 MWp	170	160	140	93	80	110
200 MWp	140	130	120	82	70	99
1 GWp	100	91	82	65	57	77
% reduction	57	57	52	41	39	41

Table 11.8 Estimated commercial module efficiency evolution (total area, STC; stabilized a-Si)a

Annual output	CIS/SS (high capital, poor materials)	CIS/glass (high capital, poor materials)	CIS/glass (moderate capital, poor materials)	CdTe	a-Si/a-Si batch on glass	a-Si in-line on flexible (SS)
25 MWp	8.5 %	11 %	10 %	8.5 %	6 %	7 %
50 MWp	10 %	12 %	11.5 %	10 %	7 %	8 %
200 MWp	11.25 %	14 %	12.75 %	11.5 %	7.5 %	9 %
1 GWp	14 %	16 %	15.5 %	14 %	8.5 %	10.5 %
% increase	65 %	45 %	55 %	65 %	42 %	50 %
% of today's best cell	72 % (of 19.5 %)	82 %	79 % (of 19.5 %)	85 % (of 16.5 %)	68 % (of 12.5 %)	84 % (of 12.5 %)

[a]An up-to-date table of module efficiencies taken from websites is provided in Appendix 11.2. In some cases, numbers differ slightly from those in Table 11.8.

The technologies highlighted in Tables 11.1–11.8 are those in first time or prototype production. But they were not the only technology options studied. Studying others brings up a whole new level of uncertainty, and estimates for these must be viewed with increased skepticism. Not only is uncertainty greater, but the choices needed to make the technologies cost-effective at all are much riskier technically. For example, are any of the new technologies stable? Since we can't say, we assume they are, just to get a start at comparison. But if they are not, then these comparisons are unusable and even misleading if used out of context. (To a lesser degree there remain reliability issues in the 2G thin films, too, and even in newly modified x-Si products.) There are numerous favorable assumptions made to make cost estimates of emerging 3G thin films. It is crucial that the reader not compare them directly to more mature technologies without this in mind.

The newer technologies share the BOM of the other technologies. This is a helpful grounding that can result in insights. The first obvious question: can a new technology even come close to being cost competitive with those already examined? If not, why should we try to develop them?

There were basically two categories of alternate technologies: further variations on the classic 2G thin films (CIS, CdTe, and thin-Si) but not yet in pilot production (e.g., CIS precursor inks, microcrystalline Si); and so-called 3G thin films such as dye sensitized cells, plastics, quantum dots, and tandem CIS/CdTe like cells.

Table 11.9 shows a summary of the estimated cost evolution of these less mature approaches, for just the nonBOM portions (the BOM was assumed to be the same as the others, depending on designs). Since all of these will start production later than current options, they were assumed to be introduced at larger throughput levels just to be competitive. However, this may not be their actual development path. Note the very low nonBOM cost estimates for the 3G thin films – this is their presumed strength. Complications from unknown process requirements or future large scale production problems were not included and may raise these estimates to much higher levels. Such complications may also exist for the other technologies, but with a reduced probability (since they are better known and more mature). Thus all these estimates make the key assumption that everything on the cost side will go well for these new technologies.

Table 11.10 shows the efficiency assumptions for these alternate technologies, which are certainly open to debate. Notice the radically greater spread in future module efficiency estimates

Table 11.9 Alternative thin film module options, estimated cost evolution of nonBOM only ($/m^2)

Annual output	CIS/glass moderate capital, good materials	CIS on foil low capital, moderate materials	Thin x-Si (in-line) on glass	Dye cells on glass	Plastic or quantum dots on plastic	Four terminal CdTe/ CIS[a]	Two terminal CdTe/ CIS[a]	Two terminal CdTe/ quantum dots
25 MWp	N/a	N/a	N/a	N/a	N/a	N/a	N/a	N/a
50 MWp	47	41	59	34	N/a	N/a	N/a	N/a
200 MWp	35	30	42	23	20	N/a	N/a	N/a
1 GWp	22	17	23	13	9	49	53	28

[a]The 'CdTe/CIS' nomenclature is used to indicate a future, successful combination of high gap CdTe and low gap CIS; however, this is unproven and not optimized at this juncture and should be considered high risk (see Table 11.10).

versus current status. But this is unavoidable, as any new technology will always start out very low; and without great progress, it will simply disappear.

Table 11.11 shows a qualitative assessment of relative risk among the technologies. It is based on the gap between current efficiency levels and the long-term efficiencies needed for success; and on technical challenges to scale up, pilot production, or commercial success, including stability issues. These risks need to be borne in mind when assessing real status and potential. Due to similar challenges, many early thin film options have already fallen by the wayside despite high hopes, and this is the way the higher risk options should be viewed until proven otherwise.

For the long term scenario (1 GWp/yr production), a breakdown of the module manufacturing costs by materials; labor; utilities and rent; maintenance; and capital is given in the

Table 11.10 Alternative thin film module options, estimated efficiency (%) evolution

Annual output	CIS/glass moderate capital, good materials	CIS foil low capital, moderate materials	Thin x-Si (in-line) on glass	Tandem dye cells on glass	Plastic or quantum dots on plastic	Four terminal 'CdTe/ CIS'	Two terminal 'CdTe/ CIS'	Two terminal CdTe/ quantum dots
25 MWp	N/a	N/a	N/a	N/a	N/a	N/a	N/a	N/a
50 MWp	8	7	6.5	6	N/a	N/a	N/a	N/a
200 MWp	10	10	8	7	5	N/a	N/a	N/a
1 GWp	14	14	11	10	8	20	19	17
% of today's best cell	72 % (of 19.5 %)	72 % (of 19.5 %)	91 % (of 11 %)	83 % (of 12 %)	160 % (of 5 %)	137 % (of 15 %)	N/a	N/a
Comment on assumed efficiency levels	13 % cell today	11 % cell today	11 % cell today	12 % cell today	5 % cell today	15 % cell today	Just starting	Not yet tried

Table 11.11 Estimated relative technical risks of the thin film technologies (1 is lowest risk) to reach their ultimate cost goals (at 1 GW/yr production)

Technology	Relative risk	Comments on major risks
a-Si/a-Si/glass batch	1.5 (least)	Commercial
a-Si/flexible in line	1.5	Commercial
CdTe	1.5	Commercial
CIS/glass moderate–high capital poor materials	2.5	A few MW
CIS/glass moderate capital good materials	3.5	A few MW
CIS/foil good capital moderate materials	3.5	A few MW
In-line x-Si/glass	3.5	a-Si/x-Si phase control, higher efficiency and rates, larger areas
Dye sensitized/glass	4.5	Stability, module design, higher efficiencies
Four terminal 'CdTe/CIS' (glass)	7	High efficiency top cell at 1.7eV, top cell transparency
Two terminal 'CdTe/CIS' (glass)	8	High efficiency top cell at 1.7eV, not killing first cell while making 2nd top cell transparency
Quantum dots plastic	10	Stability, efficiency
Two terminal CdTe & quantum dots glass	10 (worst)	Current matched quantum dot cell, stability, top cell transparency

following figures. Note that this is only the active (nonBOM) portion of the cost, and as such must be combined with BOM, module efficiency, ES&H, and final BOS costs to reach system costs. For example, this picture gives the most favorable picture of the 3G thin films.

Note that the utilities are rather high. Even though thin film modules have energy paybacks of about a year, a year outside is about 170 kWh/m^2 in an average location. At a nickel a kWh, that's about \$8.5/m^2 in electricity cost. But this is shared with the BOM (especially its embedded energy) and will be lower with time (especially for thinner layers, where cost can come down more than half). But even 60 kWh (3 \$/m^2) is a large cost in Figure 11.1. This also shows how low the other nonBOM costs are.

From Figure 11.1, it would appear that batch a-Si has a major advantage over in-line a-Si (from having lower capital costs). However, once all the other factors (BOM, BOS, module efficiency are included; see Table 11.14) this apparent major advantage almost completely disappears. Then when the advantages of flexible modules show up at the system level, the advantage is reversed: the a-Si flexible module is a more competitive product. This pattern occurs over and over in thin films: apparent advantages at one level of cost or efficiency can be misleading if other factors are not included in the judgment. In fact, this is the general give and take throughout PV technologies: cost on one side, efficiency on the other (and stability as a general requirement). Each technology makes its 'bet' on its strength; but in the end, a combination of strengths is required; e.g., CdTe may not be the best in every category, but it is nearly the best in all of them, leading to the lowest system costs among the thin films examined (see Table 11.14).

The CIS approaches (Figure 11.2) run the gamut from high cost, high efficiency to low cost, low efficiency, and everything in between. The higher capital cost technologies are in

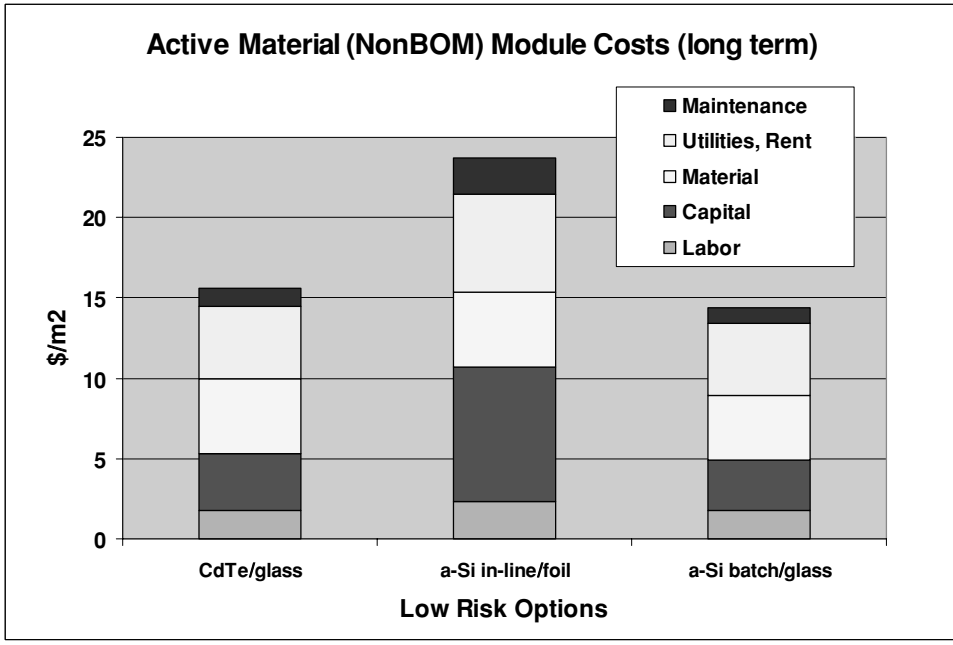

Figure 11.1 For low risk options, a breakdown of module manufacturing costs ($/m^2) for the active junctions layers (nonBOM) for the long term scenario (1 GW/yr).

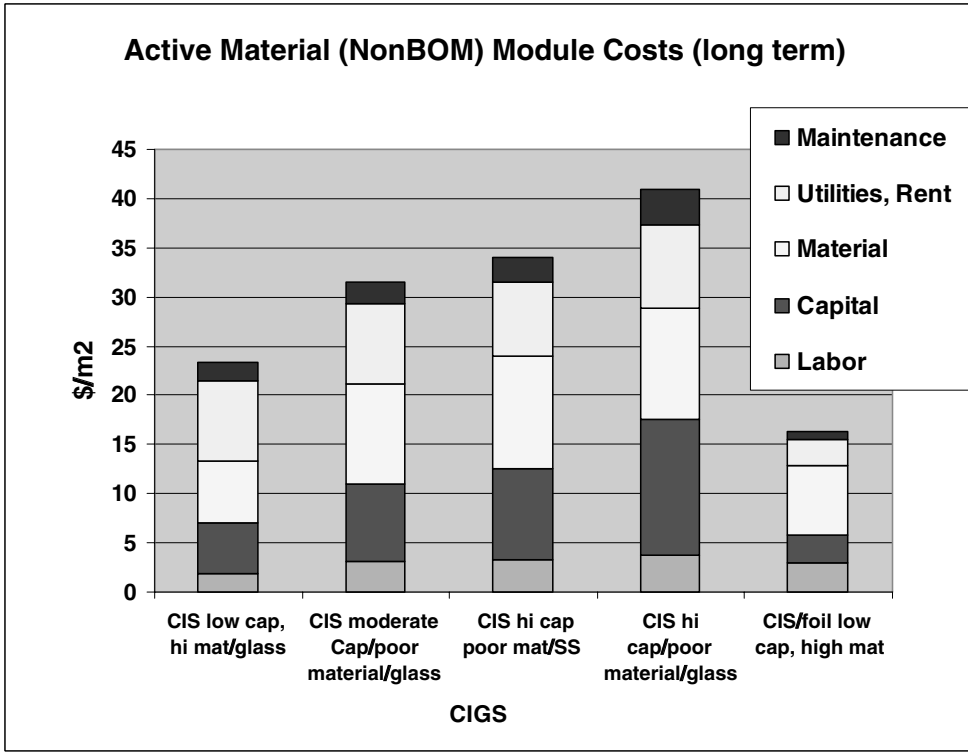

Figure 11.2 For CIS–alloy options, a breakdown of module manufacturing costs ($/m^2) for the active junctions layers (nonBOM) for the long term scenario (1 GW/yr).

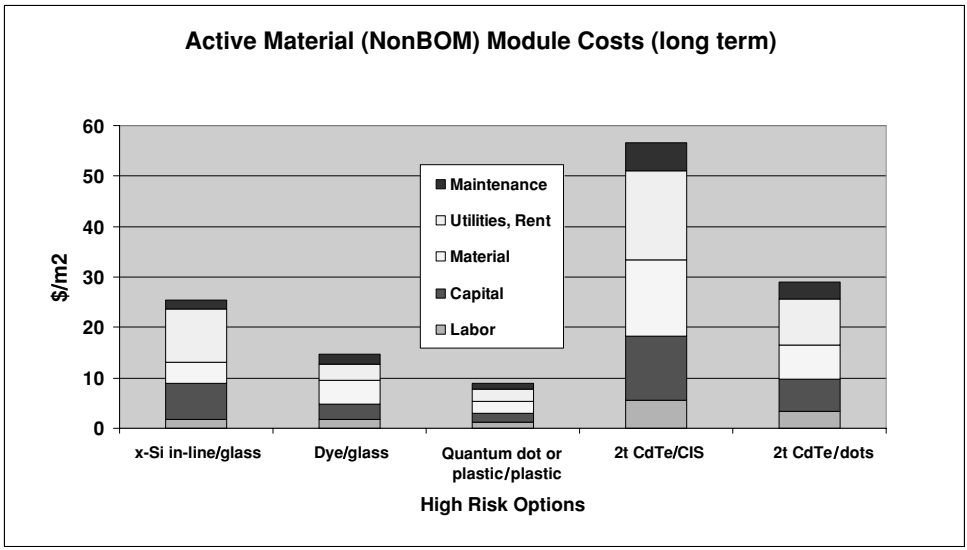

Figure 11.3 For high risk options, a breakdown of module manufacturing costs ($/m^2) for the active junctions layers (nonBOM) for the long term scenario (1 GW/yr).

pilot production. Others are just demonstrating cells. Although most of the costs for the CIS approaches are higher than those in Figure 11.1, CIS is known for its high efficiencies, thus making the potential of the options in Figure 11.2 attractive.

The thin film x-Si (in Figure 11.3) is betting on the strength of crystalline silicon as a known technology to surpass a-Si in efficiency, though this may be difficult (due to the indirect bandgap of x-Si). Similarly, there are substantial variations in approaches to thin film x-Si; some choose higher temperatures and may incur extra substrate costs; others at lower temperatures might not be able to make as efficient devices. These are the type of cost uncertainties implicit in the less well developed options. The dye sensitized approach is a radically different PV technology that has the potential for low nonBOM, while maintaining efficiency. However, a minor shortfall in the dye cell's relative efficiency or some special design requirement in the modules would easily consume this apparent cost advantage, even at the module level. Stability is also an issue, since little is known now about actual dye cell modules outdoors.

It is interesting to contemplate how options with very different nonBOM expenses (e.g., the 'CdTe/CIS' two-terminal multijunction versus the quantum dot module, which is over six times lower) can be about the same cost at the system level (see Table 11.14). That is, when BOM is added to both, and then the relative efficiency of the multijunction is assumed to be more than double that of the quantum dot module, the system results actually favor the multijunction. Yet without considering the BOM, BOS, and relative efficiencies, one would miss this.

As can be seen from Table 11.16 (below), the high risk alternatives (except one hybrid version that has never been tried) are hard pressed to approach the potential of the simpler, low and moderate risk single junction CdTe and CIS options. This brings into question their value as research paths. Why work on them if they do not even provide an advantage over lower risk choices? Perhaps this is too harsh. Perhaps as part of buildings and avoiding most BOM and BOS, the lower cost options could do well; but of course, such applications are open to the less risky ones, too. In the end, some of the high risk technologies may find a home as special

Table 11.12 Projected module cost evolution of thin films ($/Wp)[a]

	25 MWp	50 MWp	200 MWp	1 GWp
CdTe/glass	1.28	0.94	0.73	0.47
Two terminal CdTe & quantum dots	N/a	N/a	N/a	0.47
CIS/glass moderate capital, good materials use	N/a	1.32	0.89	0.51
CIS/glass moderate capital, poor materials use	1.73	1.24	0.93	0.53
Two terminal 'CdTe/CIS'	N/a	N/a	N/a	0.53
CIS on glass hi capital, poor materials use	1.87	1.37	0.91	0.57
Four terminal 'CdTe/CIS'	N/a	N/a	N/a	0.57
Dye sensitized/glass	N/a	1.4	0.96	0.58
CIS on SS low capital, high materials use	N/a	1.71	1	0.59
In-line x-Si/glass	N/a	1.62	1.06	0.59
a-Si batch/glass	1.56	1.21	0.97	0.67
CIS on SS, hi capital poor materials use	2.67	1.68	1.27	0.71
a-Si in-line/SS	1.88	1.44	1.13	0.73
Quantum dots or plastic/plastic	N/a	N/a	1.6	0.8

[a]BOM, nonBOM, and ES&H are included; sales, marketing, management, R&D, warranty, shipping, taxes, insurance, and profit are not included in these direct manufacturing costs.

aspects of the other technologies, e.g., the quantum dot technology as a low cost bottom cell to scavenge wasted long wavelength photons at minimal cost. Why might this work when the quantum dot design by itself might not? Because very little extra BOM cost is incurred for the two terminal design; whereas by itself, the low efficiency quantum dot technology would have to carry the entire BOM. And the nonBOM cost of the quantum dot cell may be very small.

Combining all the above derived and assumed numbers, it is possible to summarize the resulting evolution in module cost (in dollars per watt) for each technology (Table 11.12) and then rank them by system price (Table 11.14) the final arbiter of PV module value.

The system level comparison requires including both BOS costs and a mark up for all the missing marketing, management, other sundries, and profit.

Balance of system costs vary with application. For this analysis, large systems that contribute to CO_2 reduction were chosen as most apt. Two such systems are large, commercial roofs; and ground mounted systems. Table 11.13 shows the BOS assumptions for large, ground mounted systems. A system today that might be considered an example of such designs is the Springerville, AZ, installation managed by Tucson Electric Power (private communication, Hansen, 2005; and Mason, 2004). It is important to note that low module efficiencies incur a large, area related penalty (more modules are needed to make the same output) in ground mounted systems. (We will see later that this is usually, but not universally, true for commercial rooftop systems.)

Tables 11.14–11.15 show the same evolution of assumptions for large, commercial rooftop systems. However in this case, two kinds of modules and designs are assumed: glass modules with racks, and flexible laminates without racks. The difference is that the area related costs for the flexible modules is much lower due to the absence of racks and also simpler set up and installation. The reduced area related costs allow lower efficiency, flexible laminates to still be competitive with x-Si modules on glass. It also reveals that thin films made on glass modules are not as competitive as those made on flexible substrates for this application.

Table 11.13 Assumed BOS cost evolution for large, ground mounted systems

	Hardware		Nonhardware (design, prep, install, ship...)		BOS total		Indirect: profit & marketing	O&M ¢//kWh
	Area related	Power related	Area related	Power related	Area related	Power related	Dollar related multiplier	
25 MW	60	0.4	30	0.1	90	0.5	25 %	0.3
50 MW	50	0.35	20	0.09	70	0.44	20 %	0.2
200 MW	40	0.3	15	0.08	55	0.38	15 %	0.1
1 GW	30	0.2	10	0.07	40	0.27	10 %	0.05

Table 11.14 Assumed BOS cost evolution of large, commercial rooftop systems (glass modules)

	Hardware		Nonhardware (design, prep, install, ship...)		BOS total		Indirect: profit & marketing	O&M ¢//kWh
	Area related	Power related	Area related	Power related	Area related	Power related	Dollar related multiplier	
25 MW	90	0.6	45	0.15	135	0.77	40 %	0.9
50 MW	80	0.525	30	0.13	110	0.66	32 %	0.6
200 MW	70	0.45	23	0.11	93	0.56	24 %	0.3
1 GW	60	0.3	15	0.09	75	0.39	16 %	0.15

Table 11.15 Assumed BOS cost evolution of large, commercial rooftop systems (flexible laminates)

	Hardware		Nonhardware (design, prep, install, ship...)		BOS total		Indirect: profit & marketing	O&M ¢//kWh
	Area related	Power related	Area related	Power related	Area related	Power related	Dollar related multiplier	
25 MW	63	0.6	36	0.15	99	0.75	40 %	0.6
50 MW	56	0.5325	24	0.13	80	0.66	32 %	0.4
200 MW	49	0.45	18	0.11	67	0.56	24 %	0.2
1 GW	42	0.3	12	0.09	54	0.39	16 %	0.1

Table 11.16 Comparison of thin film system prices for ground mounted, large systems ($//Wp DC) based on the above data and assumptions

	25 MWp	50 MWp	200 MWp	1 GWp	Relative risk
Two terminal CdTe & quantum dots	N/a	N/a	N/a	1.08	High
Two terminal 'CdTe/CIS'	N/a	N/a	N/a	1.11	High
CdTe/glass	3.55	2.5	1.83	1.12	Low
Four terminal 'CdTe/CIS'	N/a	N/a	N/a	1.14	High
CIS/glass moderate cap, poor material	3.9	2.76	2	1.16	Moderate
CIS/glass moderate cap, good material	N/a	3.17	2.09	1.18	Moderate
CIS/glass hi cap, poor material	4	2.87	1.93	1.2	Moderate
CIS/SS low cap, good material	N/a	3.78	2.23	1.26	Moderate
In-line x-Si/glass	N/a	3.77	2.45	1.34	Moderate
Dyesensitized/glass	N/a	3.55	2.39	1.37	Moderate
CIS/SS moderate cap, poor material	5.28	3.39	2.46	1.4	Moderate
a-Si/SS in-line	4.58	3.32	2.46	1.52	Low
a-Si/glass batch	4.45	3.24	2.42	1.55	Low
Quantum dots or plastic on plastic	N/a	N/a	3.5	1.7	High
Possible x-Si wafer	4.59	3.84	3.22	2.62	Low

Table 11.16 compares technologies at the system level in $/Wp for a large, ground mounted system. For this purpose, an estimated price has been developed from the various costs. The price includes everything: module, BOS, sales, marketing, management, R&D, warranty, shipping, taxes, insurance, profit, and O&M. The assumed margin for the systems is reduced with time and size, and becomes quite low, as one might believe that at the desired multi-100s-of-GWp/yr level for the large volume estimates (and that is the point of this analysis), overheads, for example, will be tiny, as they are in other energy commodity industries like coal.

A comment on Table 11.16. Why aren't systems selling for the low prices seen here? First, of all the options that are lower than x-Si (at $4.59/Wp), only CdTe is in manufacturing. The price of systems is also 'what the market will bear'. However, the CdTe system price does seem low, given current experience. This may indicate a flaw in the analysis (perhaps the area related BOS is higher than assumed here) or larger margins for these systems than taken into account here. But also recall that no single company's approach is the basis of these estimates. Also, perhaps existing CdTe manufacturing is not quite as optimized for 25 MWp/yr production as assumed here.

Table 11.18 shows the comparison of thin films for large, commercial rooftop systems, in this case including the BOS advantage of flexible modules.

Some observations about the tables and figures:

- Although CIS and CdTe dominate the lowest, long term costs by about 30 %, inherent issues with indium and tellurium availability mean that thinner cells (about 0.5–1 micron) would help maximize their contribution to the TW Challenge (see next section). It is not clear they can reach the efficiencies of Table 11.8 at reduced thicknesses. The CIS and CdTe cells alone are probably not going to be the only surviving PV options. But they may be the most economical.

Table 11.17 Comparison of thin film system prices for ground mounted, large systems ($/Wp DC) with risks and barriers

	25 MWp	1 GWp	Projected improvement from today's price (%)	Comments and barriers
Two terminal CdTe & quantum dots	N/a	1.08	100 %	Never been tried; totally unproven; quantum dot or plastic cell unproven
Two terminal 'CdTe/CIS'	N/a	1.11	100 %	Probably not worth it for this application (if either subcell works they will be used instead)
CdTe/glass	3.6	1.12	67 %	Thinner CdTe, manufacturability of thin CdS design; best combination of least risk, most reward for this application
Four terminal 'CdTe/CIS'	N/a	1.14	100 %	Not worth it for this application (if either subcell works they will be used instead)
CIS/glass moderate cap, poor material	3.96	1.16	70 %	Lower capital costs; thinner CIS; unproven manufacturing
CIS/glass moderate cap, good material	n/A	1.18	100 %	Unproven efficiency; unproven manufacturing
CIS/glass hi cap, poor material	4.03	1.2	70 %	Lower capital; thinner CIS; unproven manufacturing
CIS/SS low cap, good material	N/a	1.26	100 %	Better for rooftops; efficiency unproven; thinner CIS; unproven manufacturing
In-line x-Si/glass	N/a	1.34	100 %	Higher efficiency, lower capital; unproven manufacturing
Dye sensitized/glass	N/a	1.37	100 %	Unproven efficiency and stability; unproven manufacturing; encapsulation issues
CIS/SS moderate cap, poor material	5.35	1.4	75 %	Better for rooftops; lower capital, higher efficiency, thinner CIS; unproven manufacturing
a-Si/SS in-line	4.66	1.52	66 %	Better for rooftops; lower capital
a-Si/glass batch	4.53	1.55	65 %	Higher efficiency
Quantum dots or plastic on plastic	N/a	1.7	100 %	Completely unproven efficiency and stability
Possible x-Si wafer	4.59	2.62	43 %	Better for rooftops because of efficiency; technically more mature (less improvement expected)

Table 11.18 Comparison of thin film system prices for large, commercial rooftop systems ($//Wp DC)

	25 MWp	50 MWp	200 MWp	1 GWp	Relative risk
Two terminal CdTe & quantum dots	N/a	N/a	N/a	1.51	High
Two terminal 'CdTe/CIS'	N/a	N/a	N/a	1.52	High
Four terminal 'CdTe/CIS'	N/a	N/a	N/a	1.54	High
CIS/SS low cap, good material	N/a	4.63	2.78	1.58	Moderate
CdTe/glass	5.07	3.58	2.61	1.61	Low
CIS/glass moderate cap, poor material	5.36	3.78	2.75	1.63	Moderate
CIS/glass hi cap, poor material	5.39	3.88	2.64	1.66	Moderate
CIS/glass moderate cap, good material	N/a	4.43	2.94	1.67	Moderate
CIS/SS moderate cap, poor material	6.41	4.15	3	1.73	Moderate
a-Si//SS in-line	5.66	4.1	3.04	1.9	Low
In-line x-Si/glass	N/a	5.25	3.44	1.92	Moderate
Dyesensitized/glass	N/a	5.04	3.42	1.99	Moderate
Quantum dots or plastic on plastic	N/a	N/a	4.36	2.16	High
a-Si/glass batch	6.38	4.65	3.48	2.5	Low
Possible x-Si wafer	5.96	4.88	4.0	3.16	Low

- Cadmium telluride has the opportunity to dominate all markets, but is especially attractive for ground mounted systems. For residential roof top systems, especially small ones, x-Si may still be more attractive due to its higher efficiency.
- Long term, CIS is as attractive as CdTe, but it is about a 'generation' in factory size behind CdTe and a-Si. This lag may make it hard for CIS to fully realize its potential. Risks are also higher with CIS, and not all key challenges may have been overcome (first time manufacturing at the 25 MWp/yr level does not exist). Thus long term comparisons that seem to show equality with CdTe are not complete without this risk assessment.
- Despite good potential, the CIS/CdTe multijunction may *not* play a role long term, because it would have about the same system price as the separate single junctions but would use more rare indium and tellurium per output watt (while also increasing manufacturability complexity, offset somewhat by higher efficiencies). Intermediate term, it might find a niche where efficiency outweighs system cost, e.g., on small roofs, but this is not a key market.
- The 'top cell CdTe/quantum dot bottom cell' (current matched, two terminal approach) provides some minor, potential cost and efficiency advantages over the single junction CdTe or CIS separately; though counter intuitive, it is a potentially sensible way to scavenge low energy photons if the bottom cell can be added cheaply (e.g., using quantum dots, plastic, or dye cells), without damaging the CdTe top cell. This is an ultrahigh risk, speculative option that has never even been fabricated in the lab.
- Thin film silicon approaches (including both amorphous and nanocrystalline silicon) separate into two categories: those on glass and those that are flexible. The ones on glass all have system prices between traditional x-Si itself and the CIS–CdTe complex. However, near term, the thin Si technologies on glass have a hard time competing because they are not leaders in any category, trailing both x-Si and CdTe. However, flexible thin Si (e.g., amorphous silicon on stainless steel) is competitive at the system level versus x-Si for large, metal roofs – an important market.

Table 11.19 Comparison of thin film system prices for large, commercial systems ($//Wp DC) with risks and barriers

	25 MWp	1 GWp	Projected improvement from today's price (%)	Comments and barriers
Two terminal CdTe & quantum dots	N/a	1.51	100 %	Never been tried; totally unproven; quantum dot or plastic cell unproven
Two terminal 'CdTe/CIS'	N/a	1.52	100 %	Probably not worth it for this application (if either subcell works they will be used instead)
Four terminal 'CdTe/CIS'	N/a	1.54	100 %	Not worth it for this application (if either subcell works they will be used instead)
CIS/SS low cap, good material	N/a	1.58	100 %	Better for rooftops; efficiency unproven; thinner CIS; unproven manufacturing
CdTe/glass	5.07	1.61	66 %	Thinner CdTe, manufacturability of thin CdS design; best combination of least risk, most reward for this application
CIS/glass moderate cap, poor material	5.36	1.63	69 %	Lower capital costs; thinner CIS; unproven manufacturing
CIS/glass hi cap, poor material	5.39	1.66	100 %	Lower capital; thinner CIS; unproven manufacturing
CIS/glass moderate cap, good material	N/a	1.67	100 %	Unproven efficiency; unproven manufacturing
CIS/SS moderate cap, poor material	6.41	1.73	74 %	Better for rooftops; lower capital, higher efficiency, thinner CIS; unproven manufacturing
a-Si/SS in-line	5.66	1.9	66 %	Better for rooftops; lower capital
In-line x-Si/glass	N/a	1.92	100 %	Higher efficiency, lower capital; unproven manufacturing
Dye sensitized/glass	N/a	1.99	100 %	Unproven efficiency and stability; unproven manufacturing; encapsulation issues
Quantum dots or plastic on plastic	N/a	2.16	100 %	Completely unproven efficiency and stability
a-Si/glass batch	6.38	2.5	65 %	Higher efficiency
Possible x-Si wafer	5.96	3.16	47 %	Better for rooftops because of efficiency; technically more mature (less improvement expected)

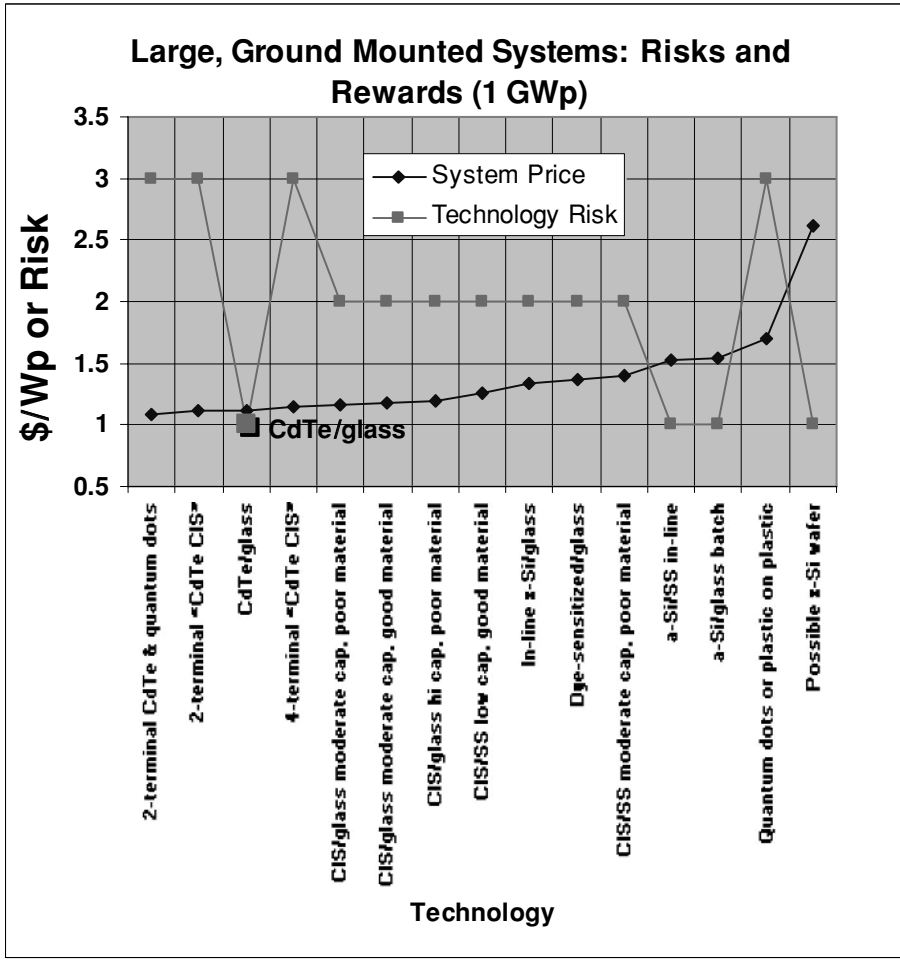

Figure 11.4 Risk and reward by technology for large, ground mounted systems (1 GWp); the CdTe technology stands out for low cost and low risk.

- Dye cells on glass have many aspects in common with thin silicon, except they seem to have lower capital costs. However, dye cells have not been manufactured, and skepticism remains about their reliability outdoors. Aspects of module design to overcome stability issues may lead to added costs.
- The other 3G thin films (quantum dots, plastics) are hampered by severely low efficiencies. They simply may be too inefficient to ever be usable except for specialty applications indoors. Even if they progress in terms of efficiency, they are so immature that they may completely disappear due to technical risks of scale up and outdoor reliability. To be competitive, these type of thin films need efficiencies almost as high as the others, and proven stability.
- It is unclear if any of the more exotic 3G options have materials availability issues at this point (ruthenium dye is a clear issue, but future designs may eliminate it; this should be studied).

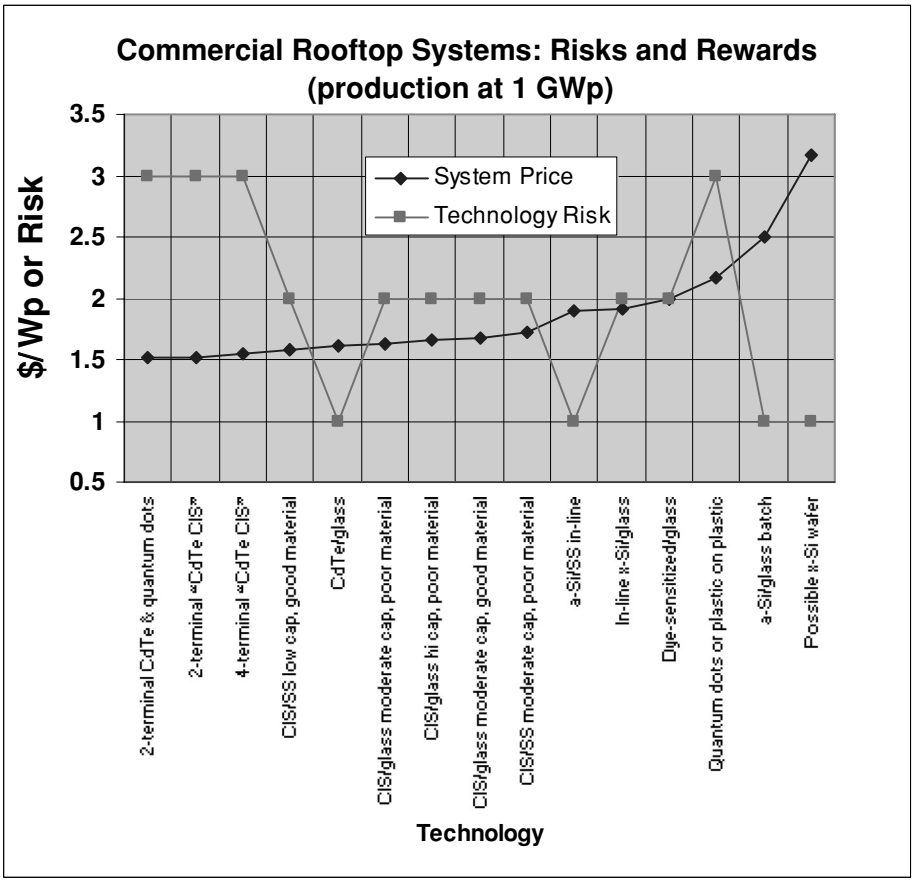

Figure 11.5 Risks and rewards for commercial rooftops (1 GWp).

- For comparison (and a sanity check), an 15.6 % traditional x-Si module costing \$1.85/Wp, based on the most aggressive BOS case above, would have a long term system cost of \$2.62/Wp – which, given the current leadership of x-Si in PV, means that x-Si will likely be around as a competitor for the entire projected period. Only thin films truly executing the above scenarios might change this. In practice, with expected vastly expanding markets for the foreseeable future, x-Si and thin films will likely share the marketplace.
- For the most part, there are some critical issues in each thin film that could seriously hamper success; and those who are involved will have to tackle them while also maintaining explosive manufacturing growth. There is no certainty this will happen successfully, and some 'skepticism' factor should probably be added to the above cost projections (e.g., in comparison with the crystalline silicon technologies, with their lower risk) to reflect this.
- On the other hand, anything that would move the goals of a technology in a much more positive direction (e.g., a major efficiency advance over the stated levels) would also affect the leadership among thin films and in PV. Certainly, the predicted long term efficiencies of the technologies are something that could change and be very important.

- Any new, lower cost packaging designs beyond those assumed in this study would probably reduce the cost of *all* modules for which they could be used, assuming reliability could be maintained for any of them (but see next bullet).
- Given their lack of competitive advantage in conventional applications, the 3G options should rededicate themselves to much higher efficiency strategies (e.g., creative multijunction structures) and to seeing whether their specific designs (e.g., lower processing temperatures) allow a *unique* potential for simpler, less costly BOM than other thin films. The hurdle of outdoor reliability also remains very challenging.
- This analysis shows groupings of technologies, with single junction CIS and CdTe looking the best because of their combination of high efficiency and low manufacturing cost. However, within groupings, it would be premature to use the results to decide that one approach is clearly better than another, given the inherent uncertainties and the need for successful execution. Indeed, there is a similarity of long term potential prices if different approaches are well executed – and the message may not be their potential similarity of cost, but the similarity of the hurdles needed to get there.

For an average US solar location like Kansas City, \$1/Wp DC is equivalent to about 6 ¢/kWh (see Appendix 11.1 for levelized energy calculations). Thus the range of costs in Tables 11.16 and 11.18 (about \$1.1 for ground mounted; \$1.5 for rooftop) implies about 6–9 ¢/kWh AC PV electricity. Especially for larger systems, it might be expected that the sunnier locations would predominate, and in that case costs would be more favorable. Overall, these costs appear within the range needed to meet the TW Challenge for PV, especially when it is recalled that rather conservative assumptions were made for the BOM aspects of the modules and BOS for systems.

11.5 OTHER ASPECTS OF THE 'TERAWATT CHALLENGE'

So far, the potential to achieve very low cost has been emphasized. That is critical to making PV cost effective enough to be used economically. But there are other factors to the 'TW Challenge.' The main one is materials availability. To have 10–20 TW of PV energy installed by mid century, we need about 50–100 TW *peak*, due to the 15–25 % capacity factor of PV. To accomplish this by 2065, for example, would require very high initial growth, resulting in about 4000 GWp of annual PV production in 2065. This means that about 15 TW (not peak) of PV would be installed and producing electricity in 2065 (given an assumed average lifespan of 30 years). Figure 11.6 shows a growth rate for PV to reach 75 TWp installed in 2065.

The materials requirements to meet this challenge have been studied in an NREL FAQ (NREL, 2005 http://www.nrel.gov/ncpv/pvmenu.cgi?site+ncpv&idx=3&body=faq.html) by this author, which is summarized here.

We do not expect shortages of most basic materials (glass, steel, aluminum, and plastic) except perhaps copper if its current extraction growth rate falls. If this happens, the problem might be alleviated by changes in BOS design to use other conductors.

We do foresee possible availability issues for a few of the semiconductor materials. NREL, 2005 shows that only the CdTe and CIS technologies might be affected; the thin film silicon technologies are not limited, even those with germanium (there are major amounts of unused byproduct Ge in aluminum, coal, and zinc ore). Newer, 3G, technologies need to be studied and are not included in the FAQ or this discussion.

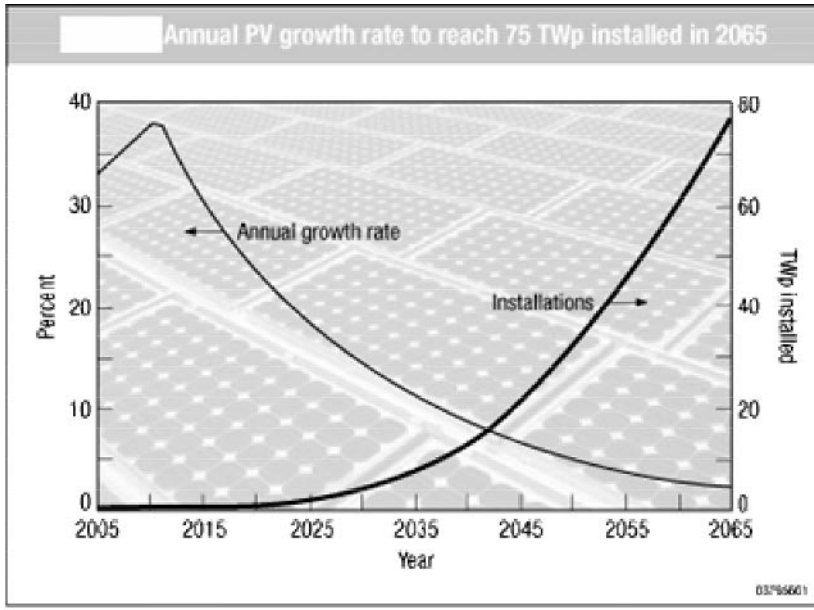

Figure 11.6 A physically reasonable world annual PV sales growth rate that would reach 75 TWp installed in 2065. PV has grown at over 30 % per year over the last six years (and over 50 % in 2004).

Given that CdTe and CIS are important low cost technologies, Table 11.20 summarizes the potential installed volumes of CIS and CdTe given an optimistic scenario of complete recycling and thinner layers (0.5 micron). Note that the thickness of today's CIS and CdTe PV is about 1–3 microns. Record efficiencies in these materials (at 2–3 micron thicknesses or more) are 16.5 % for CdTe and 19.5 % for CIS. So far, nonoptimized 1 micron CIS cells have reached about 17 % at NREL (Ramanathan *et al*., 2005); and 0.9 micron CdTe cells have reached about 11 % at U. Toledo (Gupta, 2001; Gupta and Compaan, 2005); submicron cells are planned (even down to 0.25 micron), and some work is already being done (Ernst *et al*., 2003). To date this has not been an area of much research, because current module costs have not yet been optimized for semiconductor materials costs. However, as thickness has now been identified as a key criterion for TW production, NREL has recently shifted some funding into this area.

Table 11.20 gives CIS and CdTe production by 2065 by assuming: (i) all existing amounts (beyond current nonPV demand, itself assumed growing at 1 %/yr) are available for use, and within PV, (ii) there is 100 % materials use, and (iii) complete recycling. Photovoltaic materials are not used up the way fuels are; they can be fully reused in new devices. Most data in Table 11.20 is derived from Andersson, 2000 and Sanden, 2003 and USGS, 2003. The final amount in TWp (right column) is found by dividing the total cumulative amount of feedstock available between now and 2065 by the amount needed per TWp.

Amounts of tellurium or indium that could be mined as primary materials (not as byproducts) have not been included in Table 11.20. We do not know the potential size of such deposits. Especially for tellurium, a material with very small markets to date, it seems possible there could be significant unexploited deposits. Such deposits could change the whole picture of materials availability for the CIS and CdTe technologies.

Table 11.20 Potential installed TWp of CIS and CdTe in 2065 (with complete recycling)

	Primary metal and its assumed growth	Percent byproduct currently unused in primary metal[a]	Cumulative amount in 2065 (MT) using assumed extraction growth rates	MT required per TWp	Maximum installed in 2065 (TWp)
Indium	Zn, 1 %//yr	77 %	100 000	5600[b]	17 TWp
Selenium	Cu & coal, 1 %/yr	87 %	2 900 000	9000	300 TWp
Tellurium	Cu, 1 %/yr	96 %	330 000	11 000	30 TWp

[a] In all cases, most of the current byproduct is unused (Sanden, 2003); assumes 15 % efficiency, 0.5 micron layers. Future research may allow reducing layer thickness further, as well as higher efficiencies, both of which would reduce materials demand. No feedstock sources beyond those given in the table are considered (e.g., tellurium mines).

[b] Indium required in devices is reduced by 20 % replacement by Ga (as in existing devices); future designs may include even larger substitutions. Assumes 15 % module efficiency and 0.5 micron thick layers. Future research may further reduce layer thickness and increase efficiencies, reducing materials demand.

Notes: The amounts in the table assume steady growth along historical lines in Cu and Zn extraction. Of these, Cu seems more vulnerable to slowing over the next few decades. Also, the unused byproduct amounts are very uncertain: they are based on extrapolating average Te and In levels in the primary ores. However, actually processing this material to extract a high percentage of Te and In will be an economic challenge. For example, only 60 %–80 % of the base metal content is extracted. In addition, the available byproduct will be unused early in the growth of PV but must remain available for future processing as demand increases; this is currently not a normal procedure in the mining industry.

Because such possibilities are unknown, we limit ourselves to the values in Table 11.20. Using a factor of five to reduce to TW (not peak) on the amounts in Table 11.20, CIS could contribute as much as 3.4 TW, and CdTe, as much as 6 TW by 2065. This means that these technologies can each be considered capable of meeting the TW Challenge and effectively contribute to the reduction of climate change. The amounts are also a substantial fraction of the desired 10–20 TW amount (and of course, huge by any other measure; e.g., the size of US energy consumption is 3 TW). Possible additions from primary materials are not counted in this sum, so perhaps even more could be made. Further, a steady state should be attained around 2065 in which recycled modules and ongoing PV device improvements (thinner cells, higher performance) would stabilize the need for newly extracted materials after 2065. The need could actually decline. But to be prudent, we should not assume that CdTe and CIS will carry the entire load, alone, despite their potential economic leadership (and especially because CIS is still unproven in manufacturing).

The use of certain materials used to make thin film modules deserve a brief discussion. Although *perceived* as a problem by some, many studies show that no danger exists from making, using, or disposing/recycling CdTe modules (http://www.nrel.gov/cdte/; and especially Fthenakis, 2004). There also apparently are no issues in terms of market acceptance. The biggest market for CdTe has been Germany, a country sensitive to environmental and heavy metal issues.

The CIS technology has an echo of this problem due to the presence of selenium, also an element that is viewed with concern (though its recent use as a food supplement has ameliorated

perceptions greatly). Other PV technologies usually have smaller, parallel problems that are less obvious – e.g., the Pb solder in x-Si technology, or the toxic/explosive gasses in thin film silicon. In fact, it is well accepted that no energy option, no matter how 'green', is totally without environmental impacts, especially on the TW scale. The best known and perhaps most rational measures of environmental impact, energy and CO_2 paybacks, are favorable for thin films (NREL, 2005a) – about one year for the kind of large, thin film systems we are examining.

One other barrier often cited is the land area needed to supply TWs of PV. Actually, using the original Nate Lewis number of 125 000 TW of sunlight on the Earth's surface can easily dissuade us of this concern. Assuming that this falls evenly on land and sea, this is about 36 000 TW falling on land. Assuming we need 20 TW of PV, and the PV systems only averaged 10 % sunlight-to-electricity conversion, that would be 0.55 % of the Earth's land area for modules. Assuming a (module–system area) packing factor of 40 %, this requires 2.5 times more land, or 1.4 % of the land area. Today, 1.1 % of the US land area is used for national defense (bases and bombing ranges) and 0.04 % is used to raise Christmas trees. Not only is the use of 1.4 % of land for PV not a serious burden for converting our energy infrastructure to solar, it is a positive advantage of PV (as stated in detail in the FAQ NREL, 2005a) because no other nonCO_2 resource except nuclear has anywhere near the same level of energy density/unit area and ubiquity. The above analysis completely ignores the reduction in land area requirements that would result from using PV on rooftops or other existing structures.

11.6 RISKS AND PERSPECTIVE

The analysis of major thin films tends to underestimate technical risks (despite Table 11.11) and subsequent comments. Risks are pervasive in thin film development, and major setbacks have already occurred. Perhaps the most universal cause is a lack of science base. Because thin films are almost always different from mainstream electronics materials (as opposed to x-Si, which shares much with the mainstream), thin film development is not much supported by scientific understanding outside of PV. Problems that might otherwise be trivial are magnified. Serious problems such as the Staebler–Wronski Effect in a-Si, multielement stoichiometry and uniformity in CIS, and defects and their interactions in CdTe and its contacts are even harder to overcome. Any efforts to follow through on the development of thin films for major energy production should allocate some support to improving their science base if only to reduce the risks associated with explosive growth.

Indeed, the risks associated with explosive growth are paralleled by those of getting started. The existence of one good solar cell (say 10–15 % efficiency at 1 cm^2 size) is a needed proof-of-concept; but it is still a factor of 10^9 away from the size of the annual output (in square meters of module area) needed to make a successful technology at 25 MWp/yr. Newcomers to thin films sometimes miss this developmental challenge, to their detriment. It implies both high technical and financial risk, making the period of scale up often the most challenging. Producing TWs creates a second major scale up challenge – but *only* another factor of about 10^5 to get to about 4000 GWp/yr.

Further, for PV to be actually used for TWs of energy, PV electricity storage and PV synthesized fuels (like water splitting or a reverse methanol fuel cell) will be needed. In addition to these technical and energy systems challenges, it will be favorable if PV costs could drop below even those outlined here. For that, further aggressive research work could be highly beneficial.

The point here is that due to substantial, ongoing financial and technical challenges (and the potential for great rewards), thin films need long term, financial support from the private and public sectors to allow them to reach their potential. As this chapter should make clear, achieving that potential would be well worth the investment in terms of meeting the TW Challenge.

ACKNOWLEDGMENTS

I would like to thank all those within the private sector who have contributed insights and cost inputs. Their service to clarifying the potential of thin films for meeting the TW Challenge is an important contribution as corporate citizens. I would also like to thank those who provided guidance, inputs, and challenges: especially Nate Lewis, Marty Hoffert, Tom Hansen, James Mason, Dave Mooney, Bjorn Sanden, Bob Williams, Steve Johnson, Dan Sandwich, Chip Hambro, Glen Hamer, and Dave Pearce.

Appendix 11.1 Calculating Levelized Energy Cost from System $/Wp DC Costs Using this table, one can estimate the levelized energy cost (LEC) of any system (assuming the same set of financial and other terms) by merely multiplying the system $/Wp by the proper number, above (e.g., a $5/Wp system would be five times more than the ¢/kWh level in Table 11.A1) and then adding in the O&M, which is usually very small (about 0.1 ¢/kWh for a fixed flat plate).

The LEC values in Table 11.A1 were calculated using the standard formula for amortization of cost over time, assuming the system is financed through a loan matched to the lifetime of the system.

LEC = (ICC×1000× CRF)/(CF×8760) + O&M, where

ICC = Installed Capacity Cost ($/Wp DC),

CRF = Capital Recovery Factor = (i*(i + 1)^n)/((i + 1)^n − 1),

CF = AC Capacity Factor (0.8*sunlight/8760 hours, reduced by 20 % losses to go from DC to AC),

O&M = Operation and Maintenance ($/kWh),

i = interest rate,

n = system lifetime (i.e., how many years to amortize cost of system over).

Table 11.A1 Conversion of $1/Wp (DC) to ¢/kWh (fixed flat plates) without O&M

	Average location (e.g., Kansas City)	Below average (Maine or Seattle)	Above average (Phoenix or Albuquerque)
Sunlight (kWh/m^2/yr) and capacity factor (= 0.8*sunlight/(8760)	1700 15.5 %	1300 12 %	230021 %
Levelized Energy Cost (¢/kWh)	5.9 ¢/kWh	7.7 ¢/kWh	4.4 ¢/kWh

Table 11.A2 Commercial Thin Film Modules, Data Taken from Websites (total area efficiencies)

Rated module Efficiency (%)	Description	Rated output (Wp)	Estimated price ($//Wp)	Temperature coefficient[a]
11.0	**WürthSolar** WS31050/80 (CIS)	80	Above $3/Wp	−0.36 %/°C
9.4	**Shell Solar** ST-40 (CIS)	40	Above $3/Wp	−0.6 %/°C[b]
9.0	**First Solar** FS65 (CdTe)	65	Below $3/Wp	−0.25 %/°C
6.9	**Antec-Solar** ATF50 (CdTe)	50	Below $3/Wp	−0.18 %/°C
6.3	**Kaneka** GEA/GSA (single j. a-Si)	60	Below $3/Wp	−0.2 %/°C
6.4	**Mitsubishi** Heavy MA100 (single j. a-Si, VHF deposition)	100	Below $3/Wp	−0.2 %/°C
6.3	**Uni-Solar** US-64 (triple j. amorphous silicon),	64	$3.3/Wp	−0.21 %/°C
5.3	**RWE Schott** ASI-F32/12 (same bandgap a-Si tandem)	32.2	Varies	−0.2 %/°C

Compiled by Bolko von Roedern; 8/2005

[a] Temperature coefficients will vary slightly depending on local spectral content.

[b] Company source reports −0.48 %/°C may be more accurate for recent product.

Disclaimer: Listing could be outdated or incomplete (missing manufacturers and//or some 'best' product); prices are estimates for large quantities.

Assumptions are: O&M = $0.001/kWh, i = 7 %, n = 30 (no tax credits and no accelerated depreciation); for these, CRF = 0.081.

For comparison, the LEC for an Advanced Combined Cycle Plant is currently 5.6 ¢/kWh at a capacity factor of 50 % and 7.6 ¢/kWh at a capacity factor of 25 %, under the following assumptions: Plant size = 400 MWe, Heat Rate = 6422 Btu/kWh, Capital Cost = $599/kWe, Fixed O&M = $10.34/kWyr, Variable O&M = 2.07 mil//kWh, Burner Tip Gas Price = $5/MMBtu, 20 year IRR @ 12 %, 15 year Dept @ 6 %.

Appendix 11.2 Latest (prepublication) table of thin film module efficiencies taken from websites (August 2005)

REFERENCES

B.A. Andersson (now Sanden), 2000, Materials availability for large-scale thin-film photovoltaics, *Progress in Photovoltaics*. **8**, (2000) 61–76.

P.A. Basore, 2004, Simplified processing and improved performance of crystalline silicon on glass modules, Pacific Solar Pty Ltd, in *19th European PV SEC*, (http://www.nrel.gov/ncpv/thin_film/pdfs/epvsec19.pdf) .

D.T. Colbert and R.E. Smalley, 2002, Past, present, and future of fullerene nanotubes: buckytubes, in *Perspectives of Fullerene Nanotechnology*, 3–10, Kluwer Academic Publishers.

A.E. Delahoy, Y-M. Li, J. Anna Selvan, L. Chen, T. Varvar, and H. Volltrauer, Energy Photovoltaics, Inc., 2004, Massive Parallel Processing for Low Cost a-Si Production, (http://www.nrel.gov/ncpv/thin_film/pdfs/delahoy_a-si.pdf).

R.A. Enzenroth, K.L. Barth, and W.S. Sampath, 2004, Continuous in-line processing of CdS/CdTe devices: progress towards consistent stability, *19th European Photovoltaic Solar Energy Conference and Exhibition*, Colorado State University (http://www.nrel.gov/ncpv/thin_film//pdfs/csm_2004_euro_pv_paper.pdf).

First Solar press release, May 2005, First Solar announces insurance policy to fund solar module reclamation and recycling expenses at end of product life, http://www.firstsolar.com/pdf/MD-5-704%20EU%20First%20Solar%20Announces%20Insurance%20Policy.pdf

V. Fthenakis, 2004, Life cycle impact analysis of cadmium in CdTe PV production, *Renewable and Sustainable Energy Reviews*, **8** (2004) 303–334.

S. Guha and J. Yang, 2003, *High-Efficiency Amorphous Silicon Alloy Based Solar Cells and Modules Annual Technical Progress Report*, May 30, 2002–May 31, 2003, United Solar Systems Corp.; NREL report (http://www.nrel.gov/ncpv/thin_film/pdfs/ussc_may2003.pdf).

Aklesh Gupta, 2001, Effect of CdTe thickness reduction, *Materials Research Society Symposium Proceedings*, **668**, (2001) H6.4.1.

A. Gupta and A. Compaan, 2005, *Proceedings of the IEEE PV Specialists Meeting, Orlando, FL*, Jan 2005, 235–238.

M. Hoffert, K. Caldiera, A.K. Jain, E.F. Haites, L.D. Danney Harvey, S. D. Potter, M.E. Schlesinger, S.H. Schneider, R.G. Watts, T.M.L. Wrigley, and D.J. Wuebbles, Oct. 29, 1998, Energy implications of future stabilization of atmospheric CO_2 content, *Nature*, **395** (and http://www.nrel.gov/ncpv/thin_film/pdfs/hoffert_et_al_nature2004.pdf).

K.W. Jansen, H. Volltrauer, A. Varvar, D. Jackson, B. Johnson, L. Chen, J.A. Anna Selvan, and A.E. Delahoy, 2005. Advancements in A-Si module manufacturing at Energy Photovoltaics, Inc.,(Energy Photovoltaics, Inc., 276 Bakers Basin Rd., Lawrenceville NJ, 08648, USA), 20th EUPVSC Meeting, Barcelona, Spain, June 2005.

M. Keshner and R. Arya, 2004, *Study of Potential Cost Reductions Resulting from Super-Large-Scale Manufacturing of PV Modules: Final Report, Sept. 30, 2004*; NREL Report No. SR-520-36844 and http://www.nrel.gov/docs/fy05osti/36846.pdf.

K. Ernst, A. Belaidi and R. Könenkamp, 2003, Solar cell with extremely thin absorber on highly structured substrate, *Semiconductor Science and Technology*, **18** (2003) 475–479.

Nate Lewis, 2004, A Global Energy Perspective, Caltech, The Lewis Group, http://www.its.caltech.edu/∼mmrc/nsl/energy.html.

James Mason, November 2004, *Life Cycle Analysis of a Field, Grid-Connected, Multi-Crystalline PV Plant: A Case Study of Tucson Electric Power's Springerville PV Plant*, Final report prepared for TEP.

NREL, 2005, Will we have enough materials for PV to meet the climate change Terawatt Challenge?, NREL FAQ by K. Zweibel, http://www.nrel.gov/ncpv/pvmenu.cgi?site±ncpv&idx=3&body=faq.html

NREL, 2005a, What is the energy payback of PV?, NREL FAQ by K. Zweibel, http://www.nrel.gov/ncpv/pvmenu.cgi?site±ncpv&idx=3&body=faq.html.

R.C. Powell, *Research Leading to High Throughput Manufacturing of Thin-Film CdTe PV Modules, September 2004, First Solar Thin Film Photovoltaic Partnership Program Annual Report*, NREL, First Solar, LLC, http://www.nrel.gov/ncpv/thin_film/docs/first_solar_tfppp_ann_rpt_sept_2004.doc.

M. Raugei, S. Bargiglie, and S. Ulgiati, 2005, Energy and life cycle assessment of thin film CdTe PV modules, in 20th European PVSC Conference, Barcelona, Spain.

K. Ramanathan, J. Keane, and R. Noufi, 2005, Properties of high efficiency CIGS thin film solar cells, *Proceedings of the IEEE PV Specialists Meeting, Orlando, FL*, Jan 2005, 195–198.

B.A. Sanden (formerly Andersson), 2003, Materials availability for thin film PV and the need for 'technodiversity', *EUROPV 2003*, Granada, Spain.

USGS, 2003, Historical Statistics for Mineral Commodities in the United States http://minerals.usgs.gov/minerals/pubs/of01-006//index.html.

B. von Roedern, K. Zweibel, and H. S. Ullal, 2005, The role of polycrystalline thin film technologies for achieving mid-term, market-competitive, PV modules, *Proceedings of the IEEE PV Specialists Meeting, Orlando, FL, Jan 2005*, 183–188.

R. Wieting, 2005, CIS thin film manufacturing at Shell Solar: practical techniques in volume manufacturing, *Proceedings of the IEEE PV Specialists Meeting, Orlando, FL, Jan 2005*, 177–182.

K. Zweibel, H. S. Ullal, and B. Von Roedern, October 2004, Finally: thin film PV! in *Photon International*, M. Schmela (Ed.), 48–56.

Index

Note: *italic* page numbers refer to tables and **bold** page numbers refer to figures.

a-Si:H *see* hydrogenated amorphous silicon
absorption coefficient
  amorphous silicon xx
  cadmium telluride 279, 279–80, **285**
  crystalline silicon xix-xx, 1
  defect concentration from 189
  hydrogenated amorphous silicon 173, 181–3
  microcrystalline silicon 145–6
aluminium induced crystallization 105–6
amorphous silicon *see* hydrogenated amorphous silicon
amorphous silicon cells
  applications 227–9
    largest array of modules 228, **229**
  cell structure 204–7
  design and efficiency 208–9
  development overview xx, xxii-xxiii, 173–5
    current production issues 175–6
  films
    device quality criteria *191*
    from hydrogen diluted silane 192–4
  light induced degradation 211–12
  light trapping 209–11
  modeling 218
  module fabrication 223
    encapsulation and framing 225–6
    monolithic integration of cell 225
    plasma enhanced CVD systems 223–4
    roll-roll production of flexible modules 226–7
  shunt repair 225
    transparent conductive oxide deposition 224–5
  module performance 219–21
    energy yield 221–3
  multijunction cells 212
    current matching 214
    spectrum splitting concept 215
    tandem cells 215–18
    triple junction 217–18
    tunnel recombination junction 214–15
    production capacity 223
    superstrate and substrate configurations 207–8
    transparent conductive oxides 209–11, 224–5
    see also hydrogenated amorphous silicon
atomic layer deposition 262, 295

back surface field 41, 72
bandgap
  acceptable range xix
  amorphous silicon xx, 149, 180
    tandem cells 215–16
  cadmium telluride xxi, 277–8, 279
  chalcopyrite cells xxi, 237, 265–6
  crystalline silicon xx
  group II–VI compound materials xxi
  group III–V compound materials xx-xxi
  low bandgap polymers 398
  microcrystalline silicon 149
  micromorph tandem cells 160
  organic semiconductors xxi
  silicon–germanium alloys 11, 12–15
Bragg reflectors 18–19
bulk heterojunction cells 387–8
  active layer processing techniques 392–3
  buckminsterfullerene 388–91
  cell operational principles 391–3

© 2006 John Wiley & Sons, Ltd

bulk heterojunction cells *Cont.*
charge carrier mobility/recombination
CELIV, photo-CELIV and ToF techniques 399–401
photo-CELIV measurements of solar cells 412–17
regioregular MDMO–PPV copolymers 402–7
regioregular poly(3-hexylthiophene) 407–12
thickness dependence of MDMO-0PPV/PCBM cells 418–21
compounds commonly used in cells **392**
conjugated polymers 387–8
interpenetrating network **391**
MDMO-PPV 388, **392**
MEH-PPV 389–91, **392**
regioregular MDMO-PPV copolymers 402–7
regioregular poly (3–hexylthiophene) 407–12
development 388–91
equivalent circuit model 406–7
nanomorphology-property relationships 394–5
donor-acceptor ”double cable” polymers 395–7
photoinduced electron transfer 388–91
photon harvesting, improving 397
less symmetrical fullerines 398–9
low bandgap polymers 397–8
power conversion parameters 393–4

cadmium sulfide buffer 245, 261, 283–5
cadmium telluride cells xxi, xxiv, 277–8
absorption coefficient **279**, **285**
advanced cell structures and applications 293–4
back contact structure 288–90
bandgap 277–8, 279
buffering with cadmium sulfide 283–5
cadmium telluride, toxicity 291
cadmium telluride films
activation with chlorine 286–8
dopants **282**
electrical properties 281–3
grain boundaries 292–3
optical properties 279–80
physical properties **281**
cell characterization 298
C-V measurements 300–1
I-V measurements 298–300
quantum efficiency 301–2
structural, physical and chemical 302
cell thickness issues 292
efficiencies 277, **312**
environmental issues 290–1
impurities 291–2
modeling and computer simulation (SCAPS)
contact barrier 309–10
doping profile 310–13
parameter set **308**
psuedo two-dimensional simulation 313–14
two diode model 303–6
module and cell fabrication
commercial producers 297, 460
deposition techniques 294–6
series integrated modules 296–7
superstrate structure **xxiv**
window materials 285–6, **287**
carbon dioxide sequestration 429–30
carriers *see* substrates
cell configuration *see* configuration
chalcopyrite cells 237–9
absorber film
indium free 263
materials 237, 240
multisource evaporation process 240–2
sequential process 240–1, 242–3
sodium and film growth 243–4
bandgaps xxi, 237, 265–6
carrier density and transport 250–1
cell concept 248–50
chalcopyrite compounds in common use 239
efficiencies 238, 251, 253
commercial modules 256
loss mechanisms 251–2
modules
advantages and potential 237–9
buffer 245, 261–3
cell structure and cross-section 239
diffusion layer and back contact 244, 263
monolithic integration and encapsulation 245–7
production process schematics **240**, **244**
window fabrication and cost 245
production and scaling up 254–7
cost estimations 257–8
energy payback time 238, 260

module performance **256**, 258–9
raw material availability and recycling 259–60
research and development issues 260
bifacial cells and superstrate cells 263–4
cadmium free cells 261–3
indium free absorbers 263
lightweight and flexible substrates 260–1
nonvacuum processing 264–5
novel back contacts 263
wide gap and tandem cells 265–6
chemical vapor deposition 5
electron cyclotron resonance 11
hotwire 203–4
metal organic 262, 296
plasma enhanced 10
expanding thermal plasma 202–3
and hydrogenated amorphous silicon 173, 223–4
and microcrystalline silicon 134–5
and polycrystalline silicon 108–9
radio frequency 198–201
very high frequency 201–2
reactor upscaling 25
batch type epitaxial reactor 28–9
continuous CVD reactor 25–7
convection assisted CVD 27, **28**
thermal atmospheric pressure 5, 41, 66–8
chemical yield (silicon conversion) 70
polycrystalline silicon cells 107–8
reactors 25–9, 71–2
silicon on ceramic substrates 72–5
silicon growth rate and $SiHCl_3$–H_2 68–9
chlorosilanes 66–9
CIGS/CIS and related materials xxi, 237, **239**, 240, 243–4, 251
cell schematic **xxiv**
close space vapor transport 8–9, **9**, 294–5
commercial production
amorphous silicon cells 223–5
basic module concepts xxv, xxvii
challenges and future of photovoltaics *see* Terawatt Challenge
costs xviii-xix, 1–3
dye sensitized cells 382–3
growth rate of photovoltaics xvii–xviii
process flow schematics **2**, **76**
roll-to-roll process 226–7
stringing and laminating **xxviii**
website data 460
conductive polymers 387–8
see also conjugated polymers
configurations, cell
bifacial 263–4
substrate and superstrate **xxiv**, **116**, 151, *152*, 175
cadmium telluride **294**
chalcopyrite 263–4
conjugated polymers, charge carrier photogeneration in 325–6
donor-acceptor interface 335–6
charge carrier generation and mobility 340–3
energetics and exiplexes 336–40
geminate electron-hole pair kinetics 343–5
nongeminate recombination of electron-hole pairs 345–9
exciton dissociation 349
at donor-acceptor interface 353–7
and electronegative dopants 351–3
field assisted 327–8
Onsager-Braun model 349–51
intrinsic photogeneration 326
electron-hole excitons 326–7
field assisted dissociation of excitons 327–8
sensitized photogeneration 328
doping with electronegative sensitizers 328–32
Monte Carlo simulation 332–5
see also bulk heterojunction cells
copper indium gallium selenide *see* CIGS
costs, production xviii-xix, 1–3
estimates and future of photovoltaics *see* Terawatt Challenge
crystalline silicon cells (foreign substrate) xxii-xxiii, 39–41, 85–7
cell fabrication schemes and options 75–7
passivation 77, 78–81
porosity of substrate 77
surface texturing 76–7
cell performance
on ceramic substrates 82–5
efficiencies *82*
high quality cell on SiSiC ceramic 85
large area wafer equivalents 81–2
mismatched thermal expansion coefficients 64–5, 84–5
on model (low cost) silicon substrates 78–81

crystalline silicon cells (foreign substrate) *Cont.*
epitaxial absorber layer 41
hydrogen passivation 78–81
silicon deposition 68–75
on ceramic substrates 73–5
chemical yield (silicon conversion efficiency) 70
growth rate and CVD 68–70
requirements for photovoltaics 67
research and development trends 71–3
intermediate layer 44
diffusion of impurities 47–8
light trapping 45–7
required characteristics 45
seeding layer 41, 72, 73–5
substrates
low cost and model materials 43–4, 78–81
polycrystalline silicon by CVD 72, 73–5
required characteristics 42–3
zone-melting on 64–6
zone-melting recrystallization
on ceramic substrates 64–6
development and methods 48–51
film growth and subgrain boundaries 51–3
film microstructure and defects 55–6, 58–9
grain size enhancement 53–5, 64–5
lamp heated processors 59–64
scan speed and cell performance 78–9, **80**
see also epitaxial silicon cells
crystallization, metal induced 105–6
$CuInS_2$/$CuInGaSe_2$ and related materials xxi, 237, **239**, 240, 243–4, 251
cell schematic **xxiv**

dangling bonds xx, 177, 178, 190, **195**
defect density 112–3
amorphous silicon 178, 205
and light soaking 190–1
ZMR silicon 55–6, 58–9, **60**
see also passivation
density of states 179–80
constant photocurrent method 187–8
deep level transient spectroscopy 190, **191**, **192**
defect concentration from absorption coefficient 189
dual beam photoconductivity 188
Fourier transform photocurrent spectroscopy 189
modeling 180–1
optoelectrical methods 187
photothermal deflection spectroscopy 187
space charge methods 190
deposition technologies 4, 5
atomic layer deposition 262, 295
chemical deposition 245, 296
close space vapor transport 8–9, **9**, 294–5
electrodeposition 6–8, **7**, **8**, 296
electron cyclotron resonance 11
glow discharge technique 173
high throughput/upscaling 24–5, 176
batch type epitaxial reactors 28–9, 71
continuous chemical vapor deposition reactor 25–7, 71–2
convection assisted chemical vapor deposition 27, **28**
liquid phase epitaxy reactors 29–32
ion assisted deposition 9–10, **10**
liquid phase epitaxy 6–7, 29–32, 110
low energy plasma techniques 10–11
multisource evaporation 241
requirements for silicon photovoltaics 67–8
screen printing and sintering 265, 296
solution spray 296
sputtering 242–3, 244, 245, 296
see also chemical vapor deposition
diffusion barrier 45, 47–8
diffusion length 99–100
doping 194–6
dye sensitized cell *see under* nanocrystalline injection cells 364–5

efficiencies
amorphous silicon cells 39
single junction 212, **213**, **216**
tandem 215–16
triple junction 216–17
chalcopyrite cells 238, 251, 253, 256
crystalline silicon cells (ceramic substrate) *82*
epitaxial silicon cells
industrial type *23*
laboratory type *21*, 22
microcrystalline single junction cells 154–5
micromorph tandem cells *160*, 161
nanocrystalline injection cells 363, 376–7
electrodeposition 6–8, **7**, **8**, 296
electron cyclotron resonance 11
electron-hole pairs xxi, 343–5, 345–9

energy distribution states *see* density of states
environmental issues
  cadmium telluride cells 290–1
  chalcopyrites cells 259–69, 261
epitaxial silicon cells (silicon substrate) xxii, 1–4
  buried porous silicon reflectors 18–19
  cost savings 2, 3
  cross-section schematic *xxii*, **2**
  deposition technologies 4, 5
    basic requirements for photovoltaics 67–8
    close space vapor transport 8–9
    electrodeposition from melted salts 6–8
    electron cyclotron resonance 11
    ion assisted deposition 9–10
    liquid phase epitaxy 6, 29–32
    low energy plasma techniques 10–11
    upscaling/high throughput 24–32, 71–3
    see also under chemical vapor deposition
  epitaxial lateral overgrowth 19–20
  epitaxial ZMR silicon film
    hydrogen passivation 78–81
    open circuit voltage **80**
    thickening 41, 55–6, **65**, 66–7, **66**
  germanium-silicon structures 15–17
  industrial cells 22–4
    efficiency results *23*
    front grid contacted cell 24
    local shunting paths **23**
    novel lateral epitaxial **24**
    production flow diagram **2**
  laboratory type cells 21–2
    efficiencies *21*, 22
    overview of main results *21*
  optical confinement 4, 17–20
  silicon–germanium alloys 12–15, *16*
  substrates
    choice xxii, 3
    contamination by **4**
    textured 11–12
  epitaxy, liquid phase 6–7, 29–34, 110
  excitons xxi, 326–7
    dissociation 327–8, 349–57
    exiplexes 336–40
  extremely thin absorbers xxv, **xxvi**

fullerines 388–91, **392**, 398–9

germanium–silicon structures 15–17
glow discharge deposition 135–6, 173
Graetzel cell xxv, **xxvi**
grain sizes (silicon) *see under* silicon

heterojunction cells *see* bulk heterojunction cells
hydrogenated amorphous silicon xx, 39, 133, 173
  alloying 196–7
  atomic structure 177–8
  criteria for device quality films *191*
  density of states 179–80
    determination 187–90, **191**, **192**
    modeling 180–1
  deposition techniques 197
    expanding plasma CVD 202–3
    hot wire CVD 203–4
    radio frequency plasma enhanced CVD 198–201
    very high frequency CVD 201–3
  doping 194–6
  electrical properties
    ambipolar diffusion length 185–7
    dark conductivity 183–4
    photoconductivity 184–5
  electron spin resonance 178
  film structure and hydrogen diluted silane 192–4
  hydrogen characterization by IR 178–9
  metastability 190–2
  optical properties 181–3
  Staebler-Wronski effect 190–2
  see also amorphous silicon cells
hydrogenated microcrystalline silicon xx, 39–40, 133–4
  multijunction cell schematic **xxiii**
  see also microcrystalline silicon cells

impurities, diffusion of 45–6, 47–8
indium tin oxide 151, 152
industry, photovoltaic *see* commercial production
intermediate silicon layers *see under* silicon
ion assisted deposition 9–10, **10**

Lambertian reflector 46, 98–9
laser crystallization 1, 104–5
light confinement *see* optical enhancement and confinement
light induced degradation *see* Staebler-Wronski effect
light trapping *see* optical enhancement and confinement

liquid phase epitaxy 6–7, 29–32, 110
lateral overgrowth **20**
morphology and topography **7**
reactor upscaling 29
batch type multiwafer 31
temperature difference method 30–1

μc-Si:H *see* hydrogenated microcrystalline silicon
manufacture *see* commercial production
metal imuprities *see* transition metals
metal induced crystallization 105–6
microcrystalline silicon cells 133–4, 163–5
deposition technologies
high pressure depletion technique 136–7
hot wire technique 137
microwave plasma 137
plasma enhanced chemical vapor deposition 134–5
very high frequency glow discharge 135–6
microcrystalline defined 97
microcrystalline layers 1, 137–8
crystalline growth model 143–4
density state determination 187–90
doped layers 147–8
electronic transport properties 146–7, **148**
microstructural properties 138–41
nucleation and growth 141–3
optical properties 144–6
solar cells 148–9
light management 149
single junction cells 154–9
substrate choice 150–1
tandem amorphous/microcrystalline cells xxiii, 134, 159–64
transparent conductive oxides 150–4
micromorph tandem cells xxiii, 134, 159–61, 175
light induced degradation 161–4
mobility gap 180
modeling
cadmium telluride cells 303–14
density of states 180–1
exciton dissociation in conjugated polymers 349–58
hydrogenated amorphous silicon cells 218
kinetics of geminate electron-hole pairs 343–5
microcrystalline silicon growth 143–4
Monte Carlo and charge carriers 332–5
polycrystalline cells 100–1
module manufacture *see* commercial production
molybdenum 239, 244
multicrystalline silicon
cells *see* silicon wafer cells
defined 97
multijunction cells
current matching 214
spectrum splitting concept 215
tandem cells 215–18
triple junction cells 216–18
tunnel recombination junction 214–15
types and terminology **xxiii**, 212
multisource evaporation 241

nanocrystalline injection cells 363–4
charge carrier collection 371–4
charge separation and photons to current 369–71
interfacial electron transfer **370**, 373
dye sensitized cells
commercial developments and field tests 382–3
efficiency 363, 376–7
increasing open circuit voltage 377–8
new sensitizers and redox systems 378–9
photocurrent action specta 375–8
principle 364–5
solid state cells 379
stability 379–80, 379–82
tandem concept 384
electrolyte
and charge carrier collection 372–3
redox cycles 365
light harvesting by sensitizer layer 366–8
enhanced red and infrared response 368
nanostructure
importance of 365–6
mesoscopic TiO_2 film **366**, **368**, **376**
quantum dot sensitizers 374
ruthenium polypyridyl complex dyes
adsorption at film surface 377
interfacial electron transfer 369–71
long term stability 379–82
structure **367**, **378**
semiconductor film, mesoscopic **366**, **368**, **376**
conduction band electron motion **372**
effects of morphology on performance 375–6
electron injection into 369–71, 373

and light harvesting 366–8
photoinduced processes at surface **373**
preparation 375
nanocrystalline silicon xx, 134, 138–9, **140**
defined 97

Onsager-Braun model 349–51
optical enhancement and confinement 1
amorphous silicon cells xxiii, 209–11
cells, single junction 154–9
crystalline silicon xx
germanium-silicon structures 15–17
intermediate silicon layers 45
light trapping options 46–7, 76–7, 83, 209–11
microcrystalline silicon 149
reflectors 17–20, 121
Bragg 18–19
epitaxial lateral overgrowth 1–20
intermediate layer 45
Lambertian 46, 98–9
porous silicon interlayers 18–19
transparent conductive oxides *152*
silicon-germanium alloys 12–15
texturing
glass 103
industrial epitaxial cells 22–3
microcrystalline cells 98, *152*, 154
substrates 11–12
ZMR surfaces 47
organic semiconductors xxi
cells overview xxiv-xxv, **xxvi**
see also bulk heterojunction cells; conjugated polymers

passivation, hydrogen 77, 78–81, 113–14
amorphous silicon **177**, 178
polycrystalline silicon films 118, **119**
photocurrent action spectra 375–6
photovoltaic industry *see* commercial production
plasma enhanced CVD *see under* chemical vapor deposition
polycrystalline silicon cells 97–8
active layer formation
chemical vapor deposition 106–8
ion assisted deposition 109
liquid phase epitaxy 110
plasma enhanced CVD 108–9
solid phase crystallization 110–12
defect density and activity 112–15
diffusion length 99–100
initial polycrystalline film formation 103
nucleation control 103–4
seed layer approach 72, 73–5, 104–5
light confinement 98–9
modeling 100–1
solar cell and module processing
defect passivation 118, **119**
device structure 115–17
isolation and interconnection 118–20
junction formation 117–18
substrate choice 101–3
technologies and research
crystalline silicon on glass technology 121–2
general research 122–3
solid phase crystallization-hetero junction with intrinsic thin layer 120–1
surface texture and enhanced absorption with back reflector 121
polycrystalline silicon defined 97, 134
polymorphous silicon 194
polysilicon *see* polycrystalline silicon
production *see* commercial production

quantum dot sensitizers 374

reflectors *see under* optical enhancement
ruthenium polypyridyl complex dyes *see under* nanocrystalline injection cells

screen printing and sintering 265, 296
silicon
grain sizes 97–8, 134, 194
and defect density 112
polycrystalline silicon 97–8
recrystallization of silicon 40, 49, 104–6, 110
silicon cell efficiency xxii, 1, 40, 97
layers, intermediate 41
chemical vapor deposition 72, 74–5
as diffusion barrier 45, 47–8
required properties 44–5
material definitions 97–8, 133–4, 194
wafers 1
see also amorphous silicon; hydrogenated microcrystalline silicon
silicon carbide 43, 45
silicon cells *see* amorphous; crystalline; epitaxial; microcrystalline; polycrystalline; silicon wafer
silicon nitride 43–4, 45

silicon oxide 44, 45
silicon wafer cells xvii-xviii, xxii, 40
  cost reduction 1–3
  module concepts **xxvii**
silicon-germanium alloys 12–15, 174
  dislocation and defect density 14
  efficiency comparison *16*
  growth rate graphs **13**
  hydrogenated amorphous silicon 196–7, 215–16
  internal quantum efficiency curve **15**
  structure and micrograph **12**
solar cells
  overview xvii-xxix
  see also bulk heterojunction; cadmium telluride; chalcopyrite; nanocrystalline injection; silicon cells
solar energy, future of 428–31
solid phase crystallization 110–12
solution spray 296
sputtering 242–3, 244, 245, 296
Staebler-Wronski effect xxiii, 161–3, 175–6
  hydrogenated amorphous silicon 190–2, 211–12
STAR cells 121
states *see* density of states
Stranski-Krastonov growth 15
substrates
  ceramic xxii, 1, *82*, 102
    chemical vapor deposition of silicon on 72, 73–5
    mullite 43, *83*
    porosity issues 77–8
    silicon carbide 43, 44, **65**
    silicon nitride 43–4, 53, **66**, 82, 84, 102
    zirconium silicate 43, 44
    zone-melting recrystallization on 42–4, 64–6
  for crystalline silicon ZMR cells 42–4, 78–81
  Czochralski silicon and multicrystalline silicon 44, 54, 78–81
  for epitaxial silicon cells xxii, 3
  flexible by roll-to-roll process 226–7
  glass 39, 150, 208, 255
    polycrystalline silicon cells 101–3, 121–2
  graphite xxii, 77
  intermediate silicon layer 41
  low cost and model silicon xxii, 3, 43–4
  metal 10, 154, 208
  metallurgical grade silicon 3, 25
  plastic 133, 260, 307–8
  silicon oxide 44, 45, 53, 54
  silicon ribbon 43, 44, 78
  stainless steel 150
  textured 11–12
  thermal expansion coefficients 64–5, 84–5, 101–2

Terawatt Challenge 427
  approach to estimating module costs 432–5
    BOM commonalities described and defined 431–2, 435
    characteristics of thin film designs *453*
  results of estimating module costs 435
    BOM commonalities, throughput/maturity levels for BOM commonalities 439–40, **440**
    breakdown for active materials (nonBOM) 438–9, **439**
    glass-to-glass modules BOM commaonalities 435–8, **436**, **437**
    ground mounted, large systems *448*, *449*, *450*, *452*, *453*
    long term module costs for active materials (nonBOM) 444–6
    module efficiencies, evolution of 441–2, **442**
    newer/alternate thin film technologies 442–3
    projected total module evolution costs **447**
    relative technical risk of thin film technologies 443–4, **444**
    rooftop, commercial systems *448*, *451*, *452*, *454*
    technology specific nonBOM costs 440–1, **441**
    total module costs by technology 441, **441**
  semiconductor materials, availability issues 455–8
  website data for commercial modules 460
  world energy use and future needs 428, 431
    carbon dioxide sequestration 429–30
    challenges facing solar energy 429
texturing *see under* optical enhancement
thermal annealing 1
thin film
  absorber materials xix-xxi
  defined xix
  technology overview xxi-xxix
transition metal impurities 44, 47–8

transparent conductive oxides 174, 175
amorphous silicon cells 209–11, 224–5
cadmium telluride cells 284, 285–6
chalcopyrite cell 245
microcrystalline silicon cells 150–4
reflectors *152*
TREBLE cell 100–1

VEST process 81

window materials
cadmium telluride cells 285–6, **287**
chalcopyrite cells 245
see also transparent conductive oxides

zinc oxide 151, 152–3
zirconium silicate 43, 44
zone-melting recrystallization (silicon)
development and methods 48–51
and dislocation density 55–6
electron beam ZMR 50
film growth and subgrain boundaries 51–3, 55, **56**
characteristics *50*
oxygen solubility 53
supercooling 52
film microstructure and defects 55–6, 58–9
grain size 49, 58
enhancement 53–5, 64–5
graphite stripe melting 50
high speed recrystallized layers 56–7
defect density 58–9, *60*
grain shape 58, **59**
melting zone shape 57–8
large area recrystallized wafer equivalents 81–2
laser ZMR 50, 51
linear halogen lamp heating **49**, 50–1, 59–60
process control 62–3
system setup 61–2
scan speed and cell performance 78–9, **80**
substrates
ceramics 64–6
low cost silicon 43–4
properties and requirements 42–3
thermal expansion coefficients 64, 65–6, 84–5

With kind thanks to W. F. Farrington for creation of this index.